ALLOY DISORDER, VALLEY SPLITTING, AND SHUTTLING FOR SPIN QUBITS IN SILICON/SILICON-GERMANIUM HETEROSTRUCTURES

by

Merritt Peter Rippy Losert

A dissertation submitted in partial fulfillment of

the requirements for the degree of

Doctor of Philosophy

(Physics)

at the

UNIVERSITY OF WISCONSIN-MADISON

2024

Date of final oral examination: 10/25/2024

This dissertation is approved by the following members of the Final Oral Committee:

Mark Friesen, Distinguished Scientist, Physics

Susan Coppersmith, Professor Emeritus, Physics

Mark Eriksson, Professor, Physics

Benjamin Woods, Assistant Professor, Physics

Irena Knezevic, Professor, Electrical and Computer Engineering

Abstract

Spin qubits in Si/SiGe heterostructures have several advantages as scalable qubit platforms, including their small size, their long coherence times, and their reliance upon conventional semiconductor fabrication methods. However, microscopic disorder in the semiconductor structure impact these qubits in a variety of ways, reducing qubit yield. In particular, the valley energy splitting (the energy gap between the two low-lying conduction band valley states) is widely variable, and highly sensitive to microscopic disorder. In this dissertation, we study the effects of disorder on spin qubits formed from quantum dots in Si/SiGe heterostructures, focusing particularly on the valley energy splitting. We demonstrate that alloy disorder (disorder due to the random arrangement of Si and Ge atoms in the SiGe alloy) has a profound impact on these qubits. We develop a theory to explain the impact of alloy disorder on the valley splitting, and we compare the results of this theory to a variety of experiments, finding good quantitative agreement. We demonstrate that alloy disorder determines the valley splitting in most realistic devices, and we propose a high-Ge heterostructure that enhances alloy disorder in order to increase average valley splittings. We also examine the impact of alloy disorder on flopping mode qubits, and on long-distance qubit connectivity via conveyor-mode electron shuttling. We demonstrate that alloy disorder leads to valley excitations, causing quantum information to leak out of the qubit subspace. We develop a variety of schemes to mitigate these excitations, by boosting average valley splittings, avoiding valley excitations, or mitigating their impact, providing recipes for high-fidelity spin shuttling in several device regimes.

To Mom, who couldn't see me finish, but always believed in me.

Acknowledgements

Nothing in this thesis would exist without the guidance and care of my PhD advisors, Dr. Mark Friesen and Prof. Susan Coppersmith. They have taught me to think rigorously, write clearly, and communicate effectively. They gave me the freedom to pursue new and interesting ideas, while at the same time guiding me toward productive directions. I am grateful for everything they have taught me.

I would like to thank the many experimental collaborators I've had the pleasure of working with, including but not limited to Prof. Giordano Scappucci at TU Delft, Prof. Mark Eriksson at UW Madison, and Profs. Lars Schreiber and Hendrik Bluhm at RWTH Aachen University. I did my first project in graduate school with Giordano's group, where he took a chance with a young and inexperienced student. Our collaboration continued, including projects that would ultimately form the core of this thesis. I am tremendously grateful for these opportunities. Mark Eriksson is generous with his support for and inclusion of young theory students. I've learned a lot from him, both about physics and about how to communicate it. He and his group have provided me many opportunities to work with and learn from experimentalists – an immensely valuable experience. Lars and Hendrik have been generous with their time and expertise on spin shuttling, and I've learned a tremendous amount from them. I am grateful for the opportunity to work on such a cool technology with their groups.

I would like to thank my many coauthors, including Dr. Brian Paquelet Wuetz, Dr. Sebastian Koelling, and Max Oberländer, with whom I wrote joint papers. It was a rewarding experience to work with you all on exciting projects, and I learned much from our joint

efforts. I would also like to thank Prof. Rajib Rahman, for providing invaluable help and resources for atomistic tight-binding simulations in NEMO-3D, and Profs. Chris Anderson and Mark Gyure for generously providing the MaSQE software package and helping me use it.

I would like to thank Dr. Utkan Güngördü and Dr. Charles Tahan at LPS, for inviting me into their group during the summer of 2023, and for everything I learned while I was there.

I would like to thank the many past and current members of the spin qubits groups at UW Madison – both on the theory side, including Prof. Benjamin Woods, Dr. Adam Frees, Dr. Ekmel Ercan, Dr. Leah Tom, Avani Vivrekar, Emma Brann, Owen Eskandari, Tali Oh, Hudaiba Soomro, Emily Eagen, Róbert Németh, Pedro Alves Silva Dos Santos, and Vatsal Bandaru, and on the experimental side, including Dr. J. P. Dodson, Dr. Tom McJunkin, Dr. Joelle Corrigan, Dr. Nathan Holman, Michael Wolfe, Ben Harpt, Emily Joseph, Brighton Coe, Jared Benson, Tyler Kovach, Piotr Marciniec, Sanghyeok Park, Jack Reily, Alysa Rogers, Cate Sturner, and Daniel King. I've learned a lot from all of you, and you make physics fun.

I thank my thesis committee for the time and care they have put into this work: Dr. Mark Friesen, Prof. Susan Coppersmith, Prof. Mark Eriksson, Prof. Benjamin Woods, and Prof. Irena Knezevic.

And finally, I would like to thank my friends and family for their endless love and support. I am grateful for my parents, who always gave me the freedom and support to pursue my passions, regardless what they were, and for my brother Travers for being a constant friend (and a good ski partner). I am thankful for my many friends for the endless encouragement. And I am grateful for my wonderful girlfriend Samantha, who put up with many cross-country flights and late working nights.

Contents

7   Strategies for enhancing spin-shuttling fidelities in Si/SiGe quantum wells with random-alloy disorder   **143**

List of Figures

List of Tables

Chapter 1

Introduction

The use of quantum matter as a computing platform was first considered by Paul Benioff in 1980, who realized that any Turing machine can be mapped onto the quantum dynamics of a physical system [11, 12]. Soon after, Richard Feynman conjectured that such quantum simulators could prove useful, since they avoid the exponential overhead required to simulate quantum systems on classical hardware [61]. Deutsch provided the first true quantum algorithm in 1985 [47]. Through a combination of entanglement and superposition, Deutsch's algoritm could solve a particular problem (though, not a useful one) faster than any possible classical computer. Other demonstrations of the utility of quantum computers soon followed. Grover discovered a quantum algorithm for unstructured search [73], faster than any possible classical algorithm, and Lloyd proved Feynman's initial conjecture that quantum systems can be simulated on a quantum computer [118]. And with his eponymous algorithm for factoring large composite integers, Shor provided the the most exciting quantum algorithm – one that solves a problem in polynomial time that (it is expected) a classical computer cannot [174]. Finally, Shor's demonstration of a quantum error-correcting code brought forward the real possibility of useful, scalable, fault-tolerant quantum computing [173].

Over the past four decades, tremendous progress has been made toward realizing a quantum computer. A host of physical systems are under active investigation, both by academic

and commercial laboratories. Companies like Google and IBM are developing quantum processors using superconducting qubits. Google first claimed quantum supremacy in 2019 using 53 superconducting qubits [8], and they achieved a second milestone in 2024, demonstrating a quantum error correcting surface code that improved logical qubit fidelities beyond the their underlying physical qubit fidelities [3]. Other companies are developing quantum processors based on optically trapped ions (IonQ and Quantinuum) or neutral atoms (Atom Computing, QuEra, Pasqal, and ColdQuanta). Photonic approaches, the focus of companies like PsiQuantum and Xanadu, are also promising, having also demonstrated quantum supremacy in 2020 [230]. Finally, companies like Intel, HRL, Diraq, and Silicon Quantum Computing are developing solid-state quantum processors based on trapped spins in semiconductor materials. These semiconductor spin quantum computers are the focus of this thesis.

There several flavors of semiconductor spin qubits. Perhaps the simplest, the Loss-DiVincenzo quantum computer uses electron spins as qubits [121]. These electrons are trapped laterally by gate electrodes sitting above the heterostructure, and vertically by the potential well within the heterostructure. Isolated single-spin rotations can be performed with electron spin resonance or electric dipole spin resonance, and two-qubit gates are implemented through an exchange interaction. Initial progress was made in quantum wells in lattice-matched III-V materials like GaAs/AlGaAs, but the lack of spin-zero nuclei in these systems leads to detrimental qubit dephasing [231]. More recent commercial attention has focused on silicon as a substrate, using either an oxide layer to provide confinement (as in MOS qubits, developed by companies like Diraq), or a SiGe alloy barrier region on either side of a Si quantum well (as in the devices developed by Intel and HRL). A second prominent approach to semiconductor quantum computing, the Kane quantum computer utilizes the spins of donor atoms to form qubits. These atoms are trapped within a silicon substrate and coupled together via contact hyperfine interactions with electrons, which themselves can be manipulated through gate electrodes [90]. These qubits are the focus of companies like Sili-

con Quantum Computing. Further approaches use the spins of holes in silicon or germanium as qubits [78, 162], alternative confinement structures like FinFETs or core-shell nanowires [231], and novel 2D materials, like graphene [190]. In this thesis, we focus on electron spin qubits in silicon – specifically, those confined in Si/SiGe heterostructures.

DiVincenzo outlined the five necessary criteria that any scalable quantum platform must possess [49]: (1) A scalable system with a well-defined qubit, (2) a reliable initialization scheme, (3) long coherence times, (4) a universal set of quantum gates, and (5) the ability to measure qubits. In addition, he specified two criteria needed for quantum communication schemes: (6) The ability to convert stationary qubits to flying qubits, and (7) the ability to send flying qubits from one location to another.

Spin qubits in Si/SiGe heterostructures have made progress on all of these fronts. Isolated spins in silicon have long lifetimes, on the order of seconds [206], and long (and steadily improving) dephasing times. A host of well-defined qubit archetypes have been proposed and demonstrated, including the original single-spin Loss-Divincenzo qubit [121] and a host of multi-electron qubits, like the exchange-only qubit [50], the singlet-triplet qubit [185], and the hybrid qubit [99, 172]. Spin qubits in silicon can be reliably initialized and measured. Measurement fidelities above 99% have been demonstrated [132], as have single- and two-qubit gates [131, 142, 213, 223]. Efforts are ongoing to couple silicon spin qubits to photons with high fidelity [39, 80, 86, 127], and to shuttle qubits back and forth across a heterostructure [45, 106, 109, 167, 199, 212]. But perhaps the greatest advantage of spin qubits in silicon is their inherent scalability. They are small, permitting many qubits per chip, and they are fabricated with the same processes used to build chips with billions of transistors. Commercial efforts in silicon spin qubits continue to see improvements in device quality and uniformity, and the future of this technology looks bright [76, 138].

One of the main challenges facing Si/SiGe spin qubits has been the valley degeneracy. In bulk silicon, there are 6 conduction band minima, along the $\pm x$, $\pm y$, and $\pm z$ axes of the Brillouin zone. Tensile strain in the quantum well lifts four of these valley minima in

energy, leaving two low-energy valley states along $\pm\hat{z}$ [164]. These states create an additional spin-like degree of freedom for electrons in silicon. The final valley degeneracy is lifted by effects like atomic disorder in the quantum well interface and vertical electric fields, creating an energy gap known as the valley splitting, E_v [63]. This valley splitting is known to vary widely between devices, and even across the same device, ranging from hundreds of μeV all the way to zero [19, 21, 33, 60, 79, 128, 129, 139, 143, 163, 171, 199, 225]. This variation in valley splittings can be problematic for spin qubits. Small valley splittings create low-energy leakage pathways, and they make qubit readout challenging. Understanding the valley splitting is the central goal of this thesis.

1.1 Thesis outline

This thesis is organized roughly into two parts. In the first (Chapters 1-5), we develop a theoretical understanding of the valley splitting and make comparisons to experimental results. We study E_v both in the context of Hall bar transport measurements and quantum dots. In the case of quantum dots, we develop a theory of valley splitting taking into account multiple sources of atomic disorder, including *step disorder*, the presence of mono-atomic steps in the quantum well interface, and *alloy disorer*, the random arrangement of Si and Ge atoms within the crystal lattice. We find that, contrary to prior literature, step disorder is less important in most realistic devices, and alloy disorder actually dominates the valley splitting. We find our theory can explain the observed variation of E_v, and we propose a heterostructure designed to boost E_v on average.

In the second part (Chapters 6-8), we explore the impacts that alloy-disorder-induced valley splitting will have for scaling spin qubits in Si/SiGe. We discuss the impacts of alloy disorder on the strongly driven flopping mode qubit, a promising qubit design due to its charge noise insensitivity and fast gate times. We also examine the role disorder-induced valley splitting will play in conveyor-mode electron spin shuttling, a scheme that

will enable intermediate (micron) scale connectivity in spin qubit architectures. We find that E_v variation due to alloy disorder will be a principal challenge for this technology, and we investigate several schemes to mitigate this challenge.

The chapters in this thesis are organized around various projects and papers I contributed to during my time as a graduate student. Many of these projects were collaborative efforts, often including both experimental work and theory. The individual roles I played in each of these projects is documented at the beginning of each chapter.

Chapter 2 is based on Ref. [146]. In this work, we study the valley splitting in Si/SiGe quantum wells using the integer quantum Hall effect, both experimentally and theoretically. Thermal activation measurements of longitudinal resistivities probe the valley splitting in these samples. We perform electrostatic simulations of the device and develop a model to explain the data.

Chapter 3 is based on Ref. [145]. In this work, we study the valley splitting in quantum dots formed in Si/SiGe heterostructures, again from both a theoretical and experimental perspective. We develop a theory based on the atomic disorder in the arrangement of Si and Ge atoms within the lattice – the *alloy disorder* – to explain the observed variation of valley splittings in real devices. In tandem, valley splitting measurements are performed for many quantum dots across two different heterostructures, and atom probe tomography measurements validate our disorder modeling. Finally, we propose two schemes to increase the valley splitting in quantum dot devices: (1) to increase the quantum well interface width, and (2) to add a small, uniform Ge concentration to the bottom of the quantum well.

Chapter 4 is based on Ref. [124]. In this work, we analyze the valley splittings in quantum wells with a large, oscillating Ge concentration, known as "Wiggle Wells." As expected from theory, we find large, tunable valley splittings in such devices, which we confirm with atomistic simulations of the device.

Chapter 5 is based on Ref. [119]. In this work, we elaborate on the valley splitting theory, based on alloy disorder, first described in Chapters 3 and 4. We characterise two regimes for

the valley splitting: the *deterministic regime*, where E_v is uniformly large and fixed by sharp quantum well features, and the *disordered regime*, where E_v is highly variable, dominated by alloy disorder. We demonstrate that mono-atomic steps in the quantum well interface only affect the valley splitting for devices with very sharp quantum well interfaces, which are currently out of reach to state-of-the-art processors. We also compare several different devices proposed to increase the valley splitting, and we numerically optimize quantum wells in both the deterministic and disordered regimes.

Chapter 6 is based on a project with Utkan Güngördü and Charles Tahan, started during a summer visit to LPS in 2023. In this project, we examine how a disordered valley splitting landscape impacts strongly driven flopping mode qubits. These qubits utilize the large dipole moment of an electron "flopping" between two dots in a double-dot system to enhance electric dipole spin resonance (EDSR) gate times. When driven strongly between the two dots, the charge noise sensitivity of the gate improves. However, valley phase differences across the double-dot can lead to leakage outside the qubit subspace. We quantify how and when this leakage occurs, and we discuss the relative impact of valley phase disorder on different pulse shapes. Furthermore, we quantify how charge noise may complicate these pulses.

Chapter 7 is based on Ref. [120]. In this work, we explore how a random disorder-dominated valley splitting landscape will impact proposals for conveyor-mode electron spin shuttling. We find that valley leakage is a primary difficulty for these proposals. We also propose several schemes to help mitigate this challenge, including shifting the dot position within the shuttling channel, modulating the vertical electric field, modulating the shape of the quantum dot, and modulating the shuttling velocity. We find that shifting the dot within the channel is the best single strategy, and that high-fidelity shutlting is made possible using a combination of mitigation strategies.

Chapter 8 is based on a project I worked on between 2023 and 2024. In this project, we explore an alternative scheme to achieve high-fidelity spin shuttling in silicon. Unlike the previous chapter, in this project we exploit two-electron quantum dots. As it turns out,

some two-electron states are immune to Landau-Zener-type valley excitations. We propose to encode quantum information within these states. We perform simulations of shuttling in this encoding, and we find high fidelities are achievable in certain regimes.

1.2 Other works

I have had the pleasure to participate in several other papers during my time in graduate school. While not the focus of this thesis, I briefly document them here. In Ref. [51], we explore how a quantum dot can be moved across a heterostructure, acting as a probe of the local interfacial disorder. In Ref. [66], we explore how strain from metal gates modifies the dot potential energy landscape. And in Ref. [96], we demonstrate that a quantum well annealing process introduces more germanium to a quantum well, increasing the likelihood of observing large valley splittings.

Chapter 2

Effect of quantum Hall edge strips on valley splitting in silicon quantum wells

This chapter is adapted from the article Phys. Rev. Lett. **125**, 186801 (2020), "Effect of quantum Hall edge strips on valley splitting in silicon quantum wells," by Brian Paquelet Wuetz, **Merritt P. Losert**, Alberto Tosato, Mario Lodari, Peter L. Bavdaz, Lucas Stehouwer, Payam Amin, James S. Clarke, Susan N. Coppersmith, Amir Sammak, Menno Veldhorst, Mark Friesen, and Giordano Scappucci (also available as a preprint, arXiv:2006.02305). I performed the electrostatic simulations used in this work, and with S.N.C. and M.F., I helped develop the theory used to compare to experiments.

2.1   Introduction

Silicon has proven to be a successful material platform for obtaining high-fidelity electron spin-qubits in quantum dots [195, 215, 223]. The advanced level of quantum control in these qubits makes it possible to execute two-qubit logic gates and rudimentary quantum algorithms [196, 205, 226]. In particular Si/SiGe heterostructures are promising for scalable

qubit tiles [113, 193] and the presence of low disorder has already made it possible to define a nine quantum dot array [224]. However, spin qubits in silicon suffer from a two-fold degeneracy of the conduction-band valleys [7, 101, 231], complicating quantum operation. While the valley splitting energy can be large in silicon metal-oxide-semiconductor devices [218], even allowing for qubit operation above one Kelvin [149, 216], atomic-scale disorder in Si/SiGe heterostructures at the Si quantum well top-interface yields a valley splitting energy that is typically modest and poorly controlled, with values ranging from 10 to 200 μeV in quantum dots [19, 22, 60, 79, 128, 129, 163, 171, 205, 225]. While Si/SiGe heterostructures may provide a superior host for scalable qubit arrays due to the low disorder, a key challenge is thus to increase the valley splitting energy for scalable quantum information.

The dependence of valley splitting on quantum confinement yields information about the disorder realization at the critical quantum well top-interface and hence provides tools to improve the Si/SiGe platform. The two-dimensional electron gas (2DEG) is confined laterally over the magnetic length scale $l_B = \sqrt{\hbar e/B}$, where B is the perpendicular magnetic field, which can be precisely controlled. The 2DEG is confined vertically by the quantum well heterostructure, with a confinement energy determined by the vertical electric field E_z (perpendicular to the plane of the 2DEG), which pulls the electrons against the top interface. According to the conventional theory, the valley degeneracy is lifted by the broken translational symmetry of the quantum well barriers, and is therefore proportional to the penetration of the wavefunction into the top barrier. This penetration is proportional to E_z and the two-dimensional electron density [63] $n = \epsilon E_z/e$, which is easily measured in a Hall bar geometry. However, valley splitting in Si/SiGe 2DEGs is usually probed by activation energy measurements in the quantum Hall regime [107, 139, 161, 207]. In this regime, drawing the correct relationship between valley splitting and electric field is challenging since the presence of quantum Hall edge states adds complexity to the electrostatics of the system compared to the simple electrostatics of an infinite 2DEG. Furthermore, the dependence of valley splitting upon both B and n requires activation energy measurements

over many filling factors ν because of the quantum Hall relationship $\nu = hn/eB$. This has challenged experiments so far, since measurements over many filling factors are possible in heterostructure field effect transistors (H-FETs) only if the mobility is high and the critical density for establishing metallic conduction in the channel (percolation density) is low.

In this chapter we overcome this hurdle and we study valley splitting of 2D electrons as a function of both magnetic field and density in Si/SiGe H-FETs. Benefiting from the high mobility and low percolation density achieved in industrially grown heterostructures [144], we resolve Shubnikov–de Haas (SdH) oscillations at small magnetic fields over a large range of densities and we measure activation energies in the quantum Hall regime over an unprecedented range of filling factors. We find that valley splitting increases linearly with magnetic field and is independent of Hall density. Such behavior is inconsistent with bulk transport models; we therefore present a model in which the valley splitting depends on the incremental changes in density $\Delta n = eB/h$ across quantum Hall edge strips. With this critical new insight, the experimental dependence of valley splitting upon Δn is in agreement with previous calculations for a near-ideal Si quantum well top-interface [63].

2.2   Results

Figure 2.1 shows the basic structural and magnetotransport characterization of the Si/SiGe H-FETs. The heterostructures were grown by reduced-pressure chemical vapor deposition in an industrial manufacturing CMOS fab on top of a 300 mm Si wafer. The layer sequence [Fig. 2.1(a)] comprises a step-graded $Si_{0.7}Ge_{0.3}$ strain-relaxed buffer, an 8 nm strained Si quantum well, a 34 nm $Si_{0.7}Ge_{0.3}$ barrier, and a sacrificial 3 nm Si cap. Hall-bar shaped H-FETs are fabricated with ion implanted ohmic contacts and an $Al_2O_3/Ti/Pt$ gate stack. Magnetotransport characterization of the H-FETs is performed over a temperature range $T = 50$–500 mK in a dilution refrigerator using standard four-probe low-frequency lock-in techniques. Positive bias applied to the gate induces a 2DEG and controls n in the

quantum well (see Ref. [144] for details of the heterostructure growth, device fabrication, and magnetotransport characterization). Figure 2.1(b) shows a cross-section image of the heterostructure obtained by high angle annular dark field scanning transmission electron microscopy (HAADF-STEM) to highlight the different chemistry in the layers. By fitting the HAADF-STEM intensity profile in Fig. 2.1(b) with an error function [156], we infer that the transition between Si and SiGe at the top interface of the quantum well is characterized by a distance $\lambda \approx 1$ nm[1]. Figure 2.1(c) shows the density-dependent mobility. At high density, the mobility is limited by short-range scattering from impurities within or near the quantum well and reaches a maximum value of 4.2×10^5 cm^2/Vs at $n = 4.0 \times 10^{11}$cm^{-2}. A low percolation density of 7.3×10^{10}cm^{-2} is extracted by fitting the density-dependent conductivity [Fig. 2.1(d)] to percolation theory [189]. Overall, high mobilities are observed over a wide range of densities, making these H-FETs well suited for quantum Hall measurements over many filling factors.

Figure 2.1(e) shows typical temperature-dependent measurements of the longitudinal resistivity (ρ_{xx}), plotted for clarity against filling factor ν. These measurements are performed at fixed n, by keeping the gate voltage constant while sweeping the magnetic field. We observe clear SdH oscillations that are related to the valley splitting E_v, the Zeeman splitting $g\mu_B B$, and the cyclotron gap $\hbar\omega_c$ [Fig. 2.1(f)]. The inset in Fig. 2.1(e) shows a typical temperature dependence of the SdH oscillation minimum for a valley-split level ($\nu = 5$). We observe a thermally activated dependence $\rho_{xx} \propto \exp\{(-\Delta_v/2k_B T)\}$, from which the mobility gap Δ_v is determined at a specific pair of B and n values satisfying the quantum Hall relationship $\nu = hn/eB$ when ν is an integer. As indicated in Fig. 2.1(f), the mobility gap Δ_v measures the valley splitting E_v reduced by Γ, the Landau level broadening induced by disorder.

Figure 2.2 shows Δ_v as a function of B and n on a three-dimensional (3D) plot. The data points in this graph are obtained by repeating temperature dependent ρ_{xx} measure-

---

[1]See Supplemental Material for the analysis of the HAADF-STEM intensity profile along the heterostructure growth direction
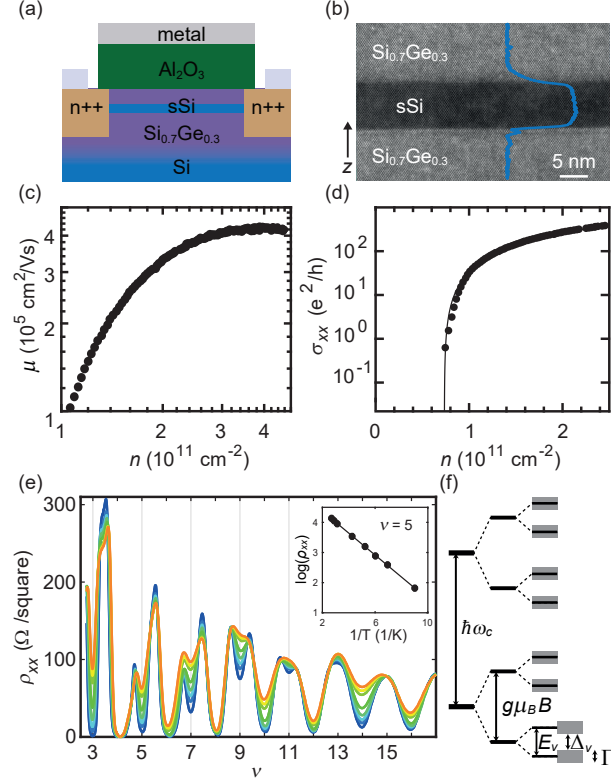
Figure 2.1: (a) Cross-section schematic of a Si/SiGe heterostructure field effect transistor. (b) High angle annular dark field scanning transmission electron (HAADF-STEM) image of the strained Si quantum well and nearby $Si_{0.7}Ge_{0.3}$ with superimposed HAADF-STEM intensity profile (blue line). The heterostructure growth direction z is indicated by a black arrow (c) Mobility μ and (d) conductivity σ_{xx} as a function of density n at a temperature of 110 mK, measured at the cold finger of the dilution refrigerator. The black line in (d) is a fit to percolation theory. (e) Resistivity ρ_{xx} as a function of filling factor ν measured at $n = 4.0 \times 10^{11} cm^{-2}$. Different colors correspond to different temperatures from 110 mK (dark blue) to 450 mK (orange). The inset reports the Arrhenius plot and fit to extract Δ_v for $\nu = 5$. (f) Single particle Landau level energy diagram. Valley split levels correspond to odd integer filling factors ν, Zeeman split levels to $\nu = (4k\text{-}2)$ ($k = 1,2,3...$), whereas spin and valley degenerate Landau levels correspond to $\nu = 4k$. The shaded areas represent the single-particle level broadening Γ due to disorder.
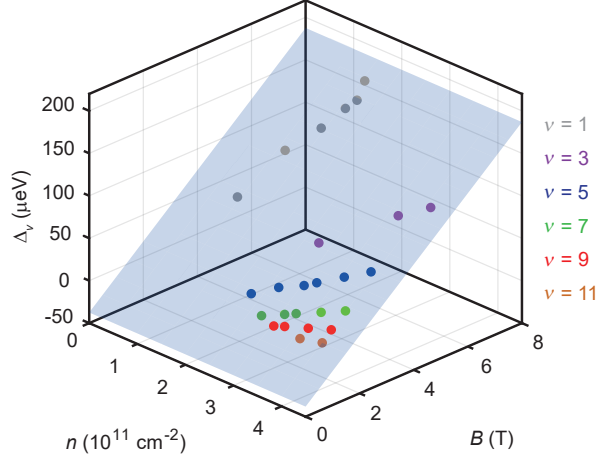
Figure 2.2: Activation energy Δ_v for odd-integer filling factors ν measured as a function of magnetic field B and Hall density n (filled circles). The blue plane defined by the equation $\Delta_v = c_B B + c_n n - \Gamma$ with $c_B = 28.1$ μeV/T, $c_n = 0.1$ μeV/10^{11}cm^{-2}, and $\Gamma = 37.5$ μeV is a fit to the experimental data points with coefficient of determination $R^2 = 0.993$.

ments at different n and by extracting Δ_v for the odd-numbered filling factors resolved at each iteration. The 3D plot shows that Δ_v increases linearly with B and—at fixed B—is independent of n. These observations are quantified by fitting the data in Fig. 2.2 to the plane $\Delta_v = c_B B + c_n n - \Gamma$ with coefficient $c_B = 28.1 \pm 1.2$ μeV/T, $c_n = 0.1 \pm 2.5$ μeV/10^{11}cm^{-2}, and $\Gamma = 37.5 \pm 10.2$ μeV. Our main experimental result, $E_v(B,n) = c_B B$, follows by considering c_n negligible and correcting for Γ[2]. Under similar experimental conditions we measure a g-factor ≈ 1.8, close to the expected value of 2[3]. This observation suggests that the measured quantum Hall gaps are not enhanced by electron-electron interactions [139] and that they represent the single particle valley splitting relevant for silicon qubits.

The conventional theory of valley splitting in a silicon quantum well predicts that E_v depends on the penetration of the electron wavefunction into the quantum well barrier, with $E_v \propto E_z$ [63]. If we assume that the 2DEG screens out electric fields from the top gate, then we should find $E_z = 0$ at the bottom of the 2DEG and $E_z = en/\epsilon$ at the top, so that $E_v \propto n$, where n is the locally varying electron density in the 2DEG. The proportionality constant is

---

[2]See Supplemental Material for theoretical justification of this fitting form

[3]See Supplemental Material for g-factor analysis
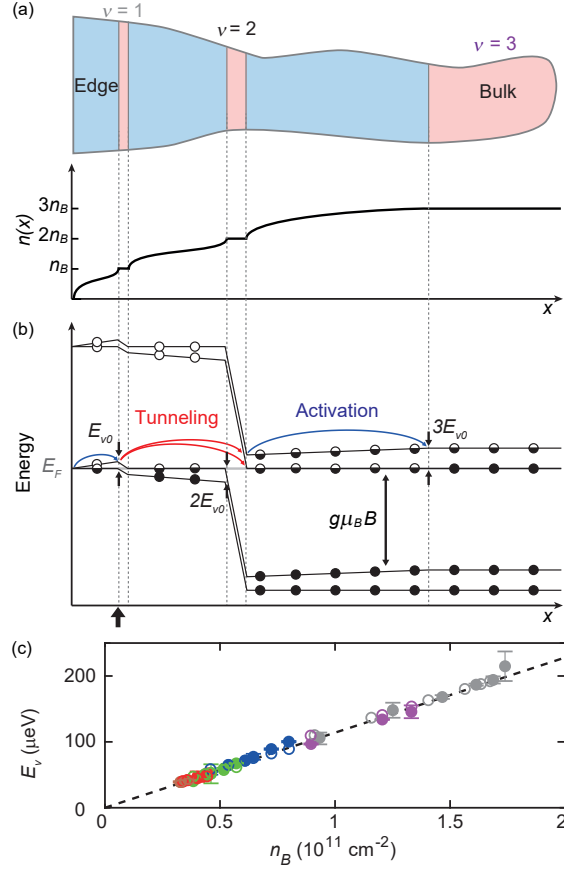
Figure 2.3: (a) Schematic representation of the charge density profile $n(x)$ on the left-hand side of a Hall bar shaped H-FET for the case of $\nu = 3$, in units of the density $n_B = eB/h$ corresponding to one completely filled Landau level. The edge of the Hall bar is at $x = 0$. The 2DEG is divided into compressible (blue) and incompressible (pink) strips. (b) Energy-level diagram, including valley and Zeeman splittings. Landau-level splittings are not present for the case of $\nu_{\mathrm{bulk}} = 3$ shown here, but would occur for larger ν_{bulk} values. Valley splittings are assumed to be proportional to the local value of n. Filled, partially filled, and empty Landau levels are indicated by filled, half-filled, and empty circles, respectively. Our model of activated transport incorporates activation and tunneling processes across the alternating compressible and incompressible strips. The thick black arrow indicates the location where the valley splitting takes its characteristic value, E_{v0}. The valley splitting increases by an amount E_{v0} in each of the compressible strips. (c) Agreement between experimental (filled circles) and simulated (open circles) data points of valley splitting E_v as a function of density $n_B = eB/h$. The dashed line is the expected valley splitting dependence on density for a disorder-free quantum well top-interface as calculated in Ref. [63].

obtained, self-consistently, in Ref. [63]. It is therefore surprising that E_v does not appear to depend on n in the Hall data reported in Fig. 2.2.

Previous experiments on quantum Hall devices were unable to separately determine the dependence of valley splitting on n and B. In particular, there was no indication of behavior inconsistent with conventional "bulk" behavior. We must therefore modify previous theories of bulk behavior [72] to account for the fact that valley splitting varies systematically across the device. Specifically, we propose that the activation energy is determined near the edges of the 2DEG, giving rise to the observed independence of E_v on n, as we now explain.

In the quantum Hall regime, the 2DEG forms alternating strips of compressible (blue) and incompressible (pink) liquid [34], as sketched in Fig. 2.3(a). The density increases by $n_B = eB/h$ in consecutive incompressible strips, where n_B is the quantized density of a filled Landau level, until reaching the bulk value $n = \nu_{\mathrm{bulk}} n_B$, measured by the Hall effect. In the compressible strips, the density varies monotonically between these quantized values, with a charge distribution that screens out electric fields parallel to the plane of the 2DEG. In this way, n varies from zero at the edge of the Hall bar to its bulk value in the center. Figure 2.3(b) is a sketch of the corresponding energy levels, assuming that E_v is proportional to the local value of n. Note that in the compressible strips and in the bulk, the highest filled levels are pinned at the Fermi level E_F [44].

To observe nonzero longitudinal resistance in our activation energy experiments, electrons must transit across the transverse width of the Hall bar. However, since all the states in the incompressible strip in the center of the Hall bar are filled for integer filling factors, this requires exciting electrons to a state above the Fermi level. Our proposed model incorporates alternating activation and tunneling processes across successive compressible strips. Each of the activation steps involves climbing "uphill" by an energy $\sim E_{v0}$, which is the change in valley splitting associated with the density change $\Delta n = n_B$. The tunneling process results in the occupation of two valley states, as indicated, since the valley quantum number is not preserved in the presence of atomic-scale roughness at the quantum-well interface

[68]. This process leads to conduction across the bulk because the valley-state lifetimes are long, so electrons can travel long distances before decaying. In this model, the characteristic energy E_{v0} is the valley splitting obtained at the position indicated by a thick black arrow in Fig. 2.3(b).

In Fig. 2.3(c) we demonstrate the consistency of this model with our experimental results and compare our results with previous effective mass theories for valley splitting in Si/SiGe [63]. Here, the experimental results from Fig. 2.2 are reported as solid circles as a function of density $n_B = eB/h$. The data points lie on a single line, irrespective of ν, as expected from the discussion of Fig. 2.2. We also report theoretical results for the valley splitting obtained from Thomas-Fermi simulations of the Hall-bar H-FET (open circles[4]). In each simulation, we adjust the top-gate voltage to obtain the desired filling factor in the bulk region. The values of n are chosen to match those used in the experiments (see Fig. 2.2). Although magnetic field does not enter the simulations explicitly, its value is determined from n and ν through the quantization relation $B = hn_{\text{bulk}}/e\nu$. We then evaluate E_z at the location of the thick black arrow in Fig. 2.3(c). Valley splitting is assumed to be proportional to E_z at the top interface of the quantum well, as described above, and we use a single fitting parameter $\beta = 134.77$ μeV·m/MV to match the simulations with the experimental results, through the relation $E_v = \beta E_z$, correcting for the offset of the experimental data at zero electric field due to Γ. The agreement between the experimental and simulated data points indicates that the proposed activation energy model agrees very well with the experimental measurements of quantum Hall gaps. Additionally, we report in Fig. 2.3(c) as a dashed line the expected value of valley splitting in Si/SiGe according to Eq. 48 of Ref. [63], which is valid for a near-ideal Si quantum well top-interface. Again, the experimental data matches the theoretical expectations. This result suggests that the atomic-scale disorder associated with the diffused SiGe barrier in Fig. 2.1(b) does not significantly suppress valley splitting, at least over lateral length scales less than the largest magnetic confinement length for electrons

---

[4]see Supplemental Material for theoretical methods, which includes Ref. [62]

$\sim 4l_B = 70$ nm in our experiments.

In summary, we have measured the valley splitting in low-disorder silicon quantum wells over a large range of odd-numbered filling factors in the quantum Hall regime. Supported by a transport model that incorporates the electrostatics of quantum Hall edge states, we demonstrate that valley splitting depends linearly upon the density eB/h rather than on the Hall density. We estimate the ratio $E_v/E_z \sim 135$ μeV·m/MV, which can be compared directly to valley splitting measurements in quantum dots.

2.3   Acknowledgements

Chapter 3

Atomic fluctuations lifting the energy degeneracy in Si/SiGe quantum dots

This chapter is adapted from the article Nat. Commun. **13**, 7730 (2022), "Atomic fluctuations lifting the energy degeneracy in Si/SiGe quantum dots," by Brian Paquelet Wuetz*, **Merritt P. Losert***, Sebastian Koelling*, Lucas E.A. Stehouwer, Anne-Marije J. Zwerver, Stephan G. J. Philips, Mateusz T. Mądzik, Xiao Xue, Guoji Zheng, Mario Lodari, Sergey V. Amitonov, Nodar Samkharadze, Amir Sammak, Lieven M. K. Vandersypen, Rajib Rahman, Susan N. Coppersmith, Oussama Moutanabbir, Mark Friesen, and Giordano Scappucci (also available as a preprint, arXiv:2112.09606). Authors marked with an (*) contributed equally. I developed the theory with R.R., S.N.C., and M.F., and I performed the simulations presented in this work.

3.1   Introduction

Advanced semiconductor manufacturing is capable of integrating billions of transistors onto a single silicon chip. The promise of leveraging the same technology for large-scale integration of qubits into a fault-tolerant quantum processing unit is a key driver for developing electron spin qubits in silicon quantum dots [194]. Although these devices bear many similarities

to transistors [233], qubits operate in the single electron regime [121], making them more sensitive to electrostatic disorder and noise arising from the surrounding environment. In strained silicon quantum wells, the electronically active part of the device is separated by an epitaxial SiGe barrier from the electronically noisy interface at the gate-stack, offering a quiet system with high mobility and low leakage between the gate and the quantum dots [122]. These properties make strained Si/SiGe heterostructures promising for scalable qubit tiles [113, 193] and have made it possible to define nine quantum dot arrays [224], run quantum algorithms [205] and entangle three-spin states [182] in natural silicon structures, and achieve two-qubit gate fidelity above 99% [142, 213] in isotopically purified silicon structures.

However, spin-qubits in silicon suffer from a two-fold degeneracy of the conduction band minima (valleys) that creates several non-computational states that act as leakage channels for quantum information[231]. These leakage channels increase exponentially with the qubit count[153], complicating qubit operation and inducing errors during spin transfers. Despite attempts to enhance the valley energy splitting, the resulting valley splittings are modest in Si/SiGe heterostructures, with typical values in the range of 20 to 100 μeV[19, 60, 128, 129, 163, 171, 205, 225] and only in a few instances in the range of 100 to 300 μeV [22, 33, 79]. Such variability in realistic silicon quantum dots remains an open challenge for scaling to large qubit systems. In particular, the probability of thermally occupying the excited valley state presents a challenge for spin initialization, and, in some cases, intervalley scattering may limit the spin coherence [91]. Furthermore, small valley splitting may affect Pauli spin blockade readout [181], which is considered in large-scale quantum computing proposals [113, 193]. Therefore, scaling up to larger systems of single-electron spin qubits requires that the valley splitting of all qubits in the system should be much larger than the typical operation temperatures ($20 - 100$ mK).

It has been known for some time that valley splitting depends sensitively on the interface between the quantum well and the SiGe barrier [63]. Past theoretical studies have considered disorder arising from the quantum well miscut angle [65] and steps in the interface [51, 64,

68, 92, 183] demonstrating that disorder of this kind can greatly decrease valley splitting in quantum dots. However, a definitive connection to experiments has proven challenging for a number of reasons. At the device level, a systematic characterisation of valley splitting in Si/SiGe quantum dots has been limited because of poor device yield associated with heterostructure quality and/or device processing. At the materials level, atomic-scale disorder in buried interfaces [14] may be revealed by atom-probe tomography (APT) in three-dimensions (3D) over the nanoscale dimensions comparable to electrically defined quantum dots. However, the current models employed to reconstruct in 3D the APT data can be fraught with large uncertainties due to the assumptions made to generate the three-dimensional representation of the tomographic data [10]. This results in limited accuracy when mapping heterointerfaces [151] and quantum wells [54, 98, 126]. These limitations prevent linking the valley splitting in quantum dots to the relevant atomic-scale material properties and hinder the development of accurate and predictive theoretical models.

Herein we solve this outstanding challenge and establish comprehensive insights into the atomic-level origin of valley splitting in realistic silicon quantum dots. Firstly, we measure valley splitting systematically across many quantum dots, enabled by high-quality heterostructures with a low disorder potential landscape and by improved fabrication processes. Secondly, we establish a new method to analyse APT data leading to accurate 3D evaluation of the atomic-level properties of the Si/SiGe buried interfaces. Thirdly, incorporating the 3D atomic-level details obtained from APT, we simulate valley splitting distributions that consider the role of random fluctuations in the concentration of Si and Ge atoms at each layer of the Si/SiGe interfaces. By comparing theory with experiments, we find that the measured random distribution of Si and Ge atoms at the Si/SiGe interface is enough to account for the measured valley splitting spread in real quantum dots. Based on these atomistic insights, we conclude by proposing a practical strategy to statistically enhance valley splitting above a specified threshold as a route to making spin-qubit quantum processors more reliable — and consequently — more scalable.
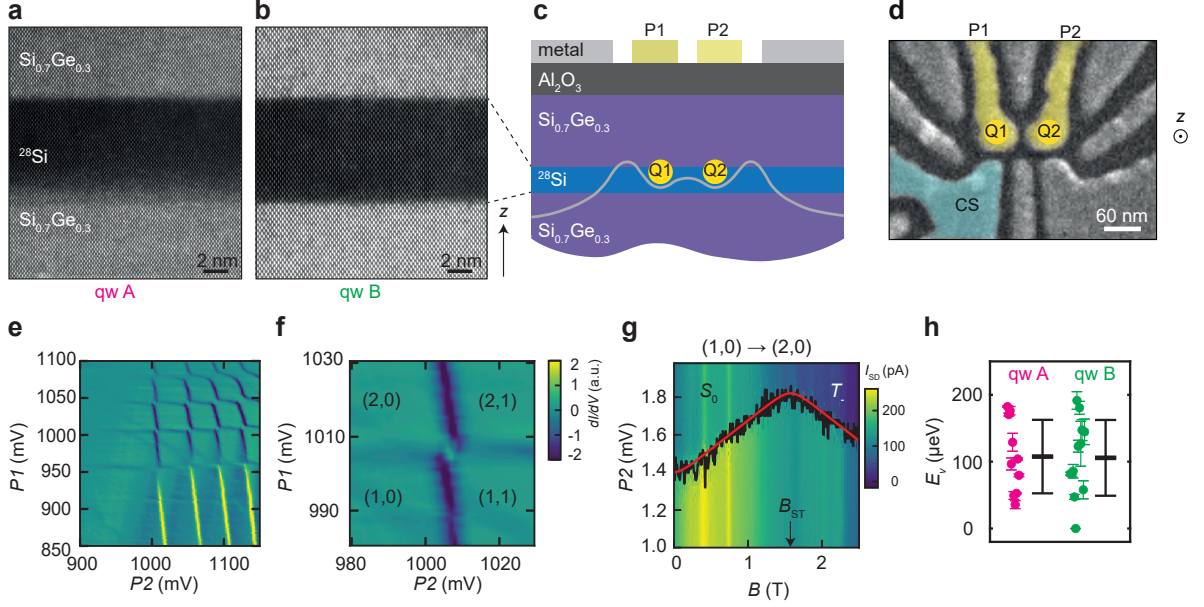
Figure 3.1: **Material stack, devices, and valley splitting measurements a,b** High-angle annular dark field scanning transmission electron microscopy (HAADF-STEM) of ^{28}Si/SiGe quantum wells A and B, respectively. **c,d** Schematic cross-section of a heterostructure with gate layout and false-coloured scanning electron microscope image of a double quantum dot, respectively. Q1 and Q2 are the quantum dots defined through confinement potentials (schematic, grey line) formed below plunger gates P1 and P2. CS is a nearby quantum dot used as a charge sensor. **e** Typical stability diagram of a double quantum dot formed by plunger gates P1 and P2 and measured by a nearby charge sensor (CS in **d**). **f** Close-up of the stability diagram in the few-electron regime. **g** Typical magnetospectroscopy of the $(1,0) \rightarrow (2,0)$ transition, used to measure singlet-triplet splittings. An offset of 1082 mV is subtracted for clarity from the gate voltage applied to P2. Black lines show the location of the maximum of the differentiated charge-sensor signal ($dI_{SD}/dP2$) of the electron charging transition. Red lines show a fit to the data, from which we extract the kink position B_{ST}. The valley splitting E_v is given by $g\mu_B B_{\mathrm{ST}}$, where $g = 2$ is the gyromagnetic ratio and μ_B is the Bohr magneton. **h** Experimental scatter plots of the valley splittings for quantum wells A (magenta) and B (green), with thick and thin horizontal black lines denoting the mean and two-sigma error bars. For quantum well B, the data point $E_V = 0$ μeV indicates that the kink in magnetospectroscopy associated with valley splitting was not observed and, consequently, that the valley splitting is below the lower bound of about 23 μeV set by our experimental measurement conditions (see Supplementary Fig. 6 and Supplementary Table 1).

3.2 Results

3.2.1 Material stacks and devices

Figure 3.1 overviews the material stack, quantum dot devices, and measurements of valley splitting. To increase statistics, we consider two isotopically purified ^{28}Si/Si$_{0.7}$Ge$_{0.3}$

heterostructures (quantum wells A and B) designed with the same quantum well width and top-interface sharpness (Methods), which are important parameters determining valley splitting [33, 63]. As shown in high angle annular dark field scanning transmission electron microscopy (HAADF-STEM), quantum well A (Fig. 3.1a) has a sharp ^{28}Si $\rightarrow$ Si-Ge heterointerface at the top and a diffused Si-Ge $\rightarrow$ ^{28}Si heterointerface at the bottom, whereas in quantum well B (Fig. 3.1b) the growth process was optimized to achieve sharp interfaces at both ends of the quantum well. These heterostructures support a two-dimensional electron gas with high mobility and low percolation density (Supplementary Figs. 1 and 2), indicating a low disorder potential landscape, and high-performance qubits [213, 214] with single- and two-qubit gates fidelity above 99% [213].

We define double-quantum dots electrostatically using gate layers insulated by dielectrics (Methods). A positive gate voltage applied to plunger gates P1 and P2 (Fig. 3.1c) accumulates electrons in the buried quantum well, while a negative bias applied to other gates tunes the confinement and the tunnel coupling between the quantum dots Q1 and Q2. All quantum dots in this work have plunger gate diameters in the range of 40-50 nm (Fig. 3.1d and Supplementary Table 1), setting the relevant lateral length scale for atomic-scale disorder probed by the electron wave function.

3.2.2   Valley splitting measurements

We perform magnetospectroscopy measurements of valley splitting E_v in dilution refrigerators with electron temperatures of about 100 mK (Methods). Figure 3.1e shows a typical charge stability diagram of a double quantum dot with DC gate voltages tuned to achieve the few electron regime, highlighted in Fig. 3.1f. We determine the 2-electron singlet-triplet energy splitting (E_{ST}) by measuring the gate-voltage dependence as a function of parallel magnetic field B along the $(0,1) \rightarrow (0,2)$ transition (Fig. 3.1g) and along the $(1,1) \rightarrow (0,2)$ transition (Supplementary Fig. 4). In Fig. 3.1g, the transition line (black line) slopes upward, because a spin $\uparrow$ electron is added to form a singlet ground state S_0. Alternatively, a spin

down electron can be added to form a T_--state, with a downward slope. A kink occurs when the S_0-state is energetically degenerate with the T_--state, becoming the new ground state of the two-electron-system. From the position of the kink ($B_{ST} = 1.57$ T) along the theoretical fit (red line) and the relation $E_{ST} = g\mu_B B_{ST}$, where $g = 2$ is the electron gyromagnetic ratio and μ_B is the Bohr magneton, we determine $E_{ST} = 182.3$ µeV for this quantum dot. E_{ST} sets a lower bound on the valley splitting, $E_v \geq E_{ST}$ [22, 57]. Due to small size, our dots are strongly confined with lowest orbital energy much larger than E_{ST} (Supplementary Fig. 3), similar to other Si/SiGe quantum dots [79, 129, 225]. Therefore, we expect exchange corrections to have negligible effects [57] and here take $E_v \approx E_{ST}$.

Here we report measurements of E_v in 10 quantum dots in quantum well A and 12 quantum dots in quantum well B (Supplementary Figs. 5 and 6) and compare the measured values in Fig. 3.1h. We observe a rather large spread in valley splittings, however we obtain remarkably similar mean values and two-standard-deviation error bars $\overline{E_v} \pm 2\sigma$ of 108 ± 55 µeV and 106 ± 58 µeV for quantum wells A and B, respectively[1]. We argue that quantum wells A and B have similar $\overline{E_v} \pm 2\sigma$ because the electronic ground state is confined against the top interface, which is very similar in the two quantum wells.

3.2.3   Atom probe tomography

We now characterise the atomic-scale concentration fluctuations at the quantum well interfaces to explain the wide range of measured valley splittings with informed theoretical and statistical models. To probe the concentrations over the dimensions relevant for quantum dots across the wafer, we perform APT on five samples each from quantum wells A and B, with a field of view of approximately 50 nm at the location of the quantum well (Methods). First, we show how to reliably reconstruct the buried quantum well interfaces, then we use this methodology to characterise their broadening and roughness.

Figure 3.2a shows a typical point-cloud reconstruction of an APT specimen from quantum

---

[1]The quantum dots all have a similar design and hence are expected to have similar electric fields across the devices with a small influence on valley splitting under our experimental conditions
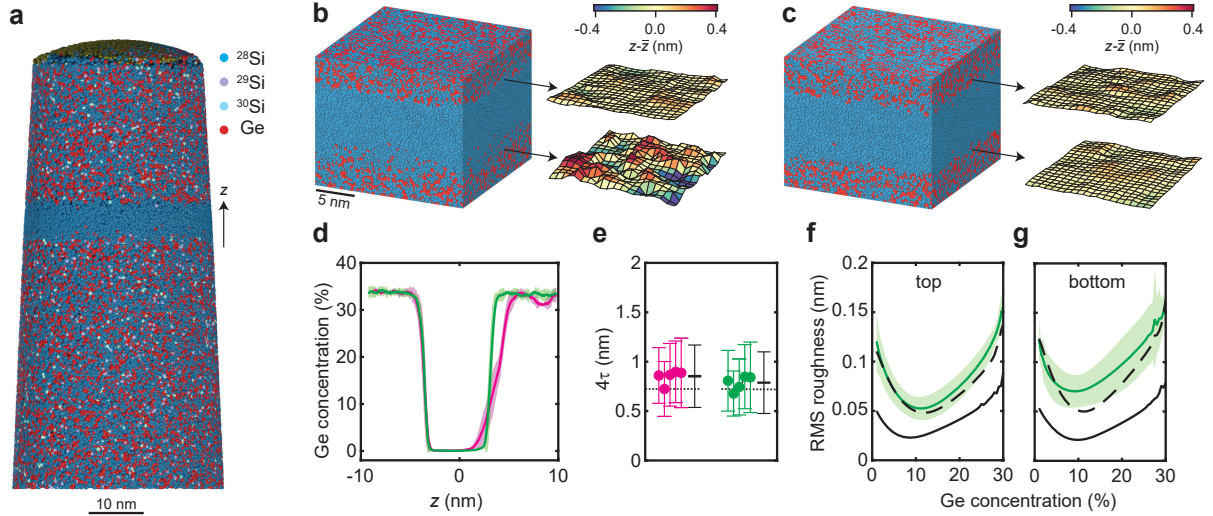
Figure 3.2: **Atom probe tomography of ^{28}Si/SiGe heterostructures. a** Point-cloud APT reconstruction of quantum well B, showing the ^{28}Si quantum well and surrounding SiGe barriers. Isotopic purification is confirmed by secondary ion mass spectroscopy (Supplementary Fig. 14). **b**, **c** Voronoi tessellation of the APT reconstructions for quantum wells A and B, respectively, and extracted isosurfaces corresponding to 8% Ge concentration. $\bar{z}$ is the average position of the 8% Ge concentration across these particular samples. We limit the lateral size of the analysis to $\approx$ 30 nm $\times$ 30 nm, reflecting the typical lateral size of a quantum dot (Fig. 3.1d). **d** Average germanium concentration depth profiles across quantum wells A (magenta) and B (green). Shaded areas mark the 95% confidence interval over each of the sets of five APT samples. **e** Statistical analysis of the top interface width 4τ determined by fitting the data for quantum wells A (magenta) and B (green) to sigmoid functions. Thick and thin horizontal black lines denote the mean and two-standard-deviation error bars for the different APT samples. Dotted black lines show 4τ results from the HAADF-STEM measurements (Supplementary Fig 13). **f**,**g** Root mean square (RMS) roughness of the concentration isosurfaces as a function of germanium concentration at the top and bottom interfaces of quantum well B (green line). Shaded areas indicate the 95% confidence interval, averaged over each set of five APT samples. The experimental data are compared to the RMS roughness of a simulated quantum well with the interface properties of **d** (dashed black line) vs. an atomically sharp quantum well (solid black line).

well B. Each point represents the estimated position of an ionized atom detected during the experiment [10]. Qualitatively, we observe an isotopically enriched ^{28}Si quantum well, essentially free of ^{29}Si, cladded in a SiGe alloy. To probe the interface properties with the highest possible resolution allowed by APT and differently from previous APT studies on Si/SiGe [54], we represent the atom positions in the acquired data sets in form of a Voronoi tessellation [200, 201] and generate profiles on an $x - y$ grid of the tessellated data, as

described in Supplementary Discussion Section 2c. A sigmoid function $[1 + \exp(z - z_0)/\tau]^{-1}$ [54] is used to fit the profiles of each tile in the $x-y$ grid. Here, z_0 is the inflection point of the interface and 4τ is the interface width. As the Voronoi tessellation of the data set does not sacrifice any spatial information, the tiling in the $x - y$ plane represents the smallest lateral length scale over which we characterise the measured disorder at the interface. Note that we do not average at all over the z axis and hence maintain the inherent depth resolution of APT. We find that for tiles as small as 3 nm × 3 nm the numerical fitting of sigmoid functions to the profiles converges reliably. Although each tile contains many atoms, their size is still much smaller than the quantum dot diameter, and may therefore be considered to be microscopic. We use the sigmoid fits for each tile stack to visualise and further characterise the interfaces (Supplementary Figs. 8–10). Importantly, Ge concentration isosurfaces as shown in Fig. 3.2b,c are constructed by determining the vertical position for which each of the sigmoids reaches a specific concentration. Note, that we oversample the interface to improve the lateral resolution by making the 3 nm × 3 nm tiles partially overlap (Supplementary Discussion Section 2c).

In Fig. 3.2d, we show the average Ge concentration profile and measurement to measurement variations from the tessellated volumes (Supplementary Discussion Section 2b,c) of all samples for both quantum wells A and B. APT confirms HAADF-STEM results in Fig. 3.1a,b: quantum wells A and B have an identical sharp top interface and quantum well A has a broader bottom interface. Furthermore, the shaded colored areas in Fig. 3.2d reveal narrow 95% confidence levels, pointing to highly uniform concentration profiles when averaged across the wafer. Strong disorder fluctuations emerge at the much smaller tile length scale. In Fig. 3.2e we show for all samples of a given quantum well the interface width mean value with two standard deviations $\overline{4\tau} \pm 2\sigma$, obtained by averaging over all the tiles in a given sample. The results indicate uniformity of $\overline{4\tau}$, and further averaging across all samples of a given heterostructure ($\mu_{\overline{4\tau}}$, black crosses) yields similar values of $\mu_{\overline{4\tau}} = 0.85 \pm 0.32$ nm and 0.79 ± 0.31 nm for quantum wells A and B, consistent with our 4τ analysis from HAADF-

STEM measurements (black dotted lines). However, the two-standard-deviation errors (2σ) of each data point can be up to 30% of the mean value $\overline{4\tau}$.

To pinpoint the root cause of atomic-scale fluctuations at the interface, in Fig. 3.2f,g we utilize the 3D nature of the APT data sets, calculate, and compare the root mean square (RMS) roughness of the interfaces (solid green lines) as measured by APT on quantum well B to two 3D models (Fig. 3.2f,g) mimicking the dimensions of an APT data set. Both models are generated with random distributions of Si and Ge in each atomic plane (Supplementary Discussion Section 2d). The first model (solid black lines) corresponds to an atomically abrupt interface where the Ge concentration drops from ∼33.5% to 0% in a single atomic layer. It hence represents the minimum roughness achievable at each isoconcentration surface given the in-plane randomness of SiGe and the method to construct the interface. The second model (dashed black lines) is generated with the experimentally determined Ge concentration profile along the depth axis (Supplementary Fig. 11). As shown in Fig. 3.2f,g, the roughness extracted from the second model fits well to the measured data, suggesting that the RMS roughness measured by APT is fully explained by the interface width and shape along the depth axis. Furthermore, as the deviation of each isosurface tile position from the isosurface's average position also matches that of the measured interfaces from the second model (Supplementary Movie 1) the APT data are consistent with a random in-plane distribution of Ge perpendicular to the interface in all data sets of quantum well B. For 2 out of 5 samples on quantum well A that we analyzed, we observe features that are compatible with correlated disorder from atomic steps (Supplementary Fig. 13). In the following, the alloy disorder observed in the APT concentration interfaces is incorporated into a theoretical model. As shown below, the calculations of valley splitting distributions associated with the 3D landscape of Si/SiGe interfaces can be further simplified into a 1D model that incorporates the in-plane random distribution of Si and Ge atoms.
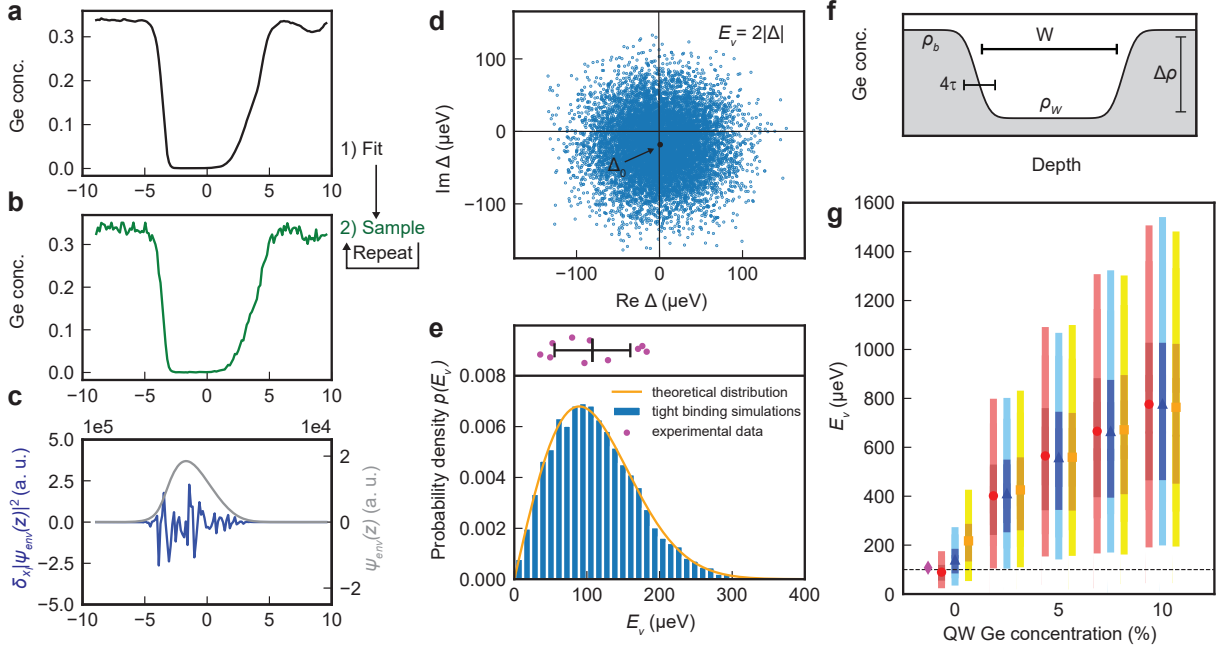
Figure 3.3: **Valley-splitting simulations. a** Average concentration profile obtained from APT data (quantum well A). **b**, Typical, randomized Ge concentration profile, derived from **a**. **c** Envelope function $\psi_{\mathrm{env}}(z)$, obtained for the randomized profile in **b** (grey curve), and the corresponding concentration fluctuations weighted by the envelope function squared: $\delta_{x_l}|\psi_{\mathrm{env}}(z_l)|^2$ (blue). Here, the wavefunction is concentrated near the top interface where the concentration fluctuations are also large; the weighted fluctuations are therefore largest in this regime. **d** Distribution of the intervalley matrix element Δ in the complex plane, as computed using an effective-mass approach, for 10,000 randomized concentration profiles. The black marker indicates the deterministic value of the matrix element Δ_0, obtained for the experimental profile in **a**. **e**, Histogram of the valley splittings from tight-binding simulations with 10,000 randomized profiles. The same profiles may be used to compute valley splittings using effective-mass methods; the orange curve shows a Rice distribution whose parameters are obtained from such effective-mass calculations (see Methods). **f**, Schematic Si/SiGe quantum well with Ge concentrations ρ_W (in the well) and $\rho_b = \rho_W + \Delta\rho$ (in the barriers), with a fixed concentration difference of $\Delta\rho = 25\%$. **g**, Distribution of valley splittings obtained from simulations with variable Ge concentrations, corresponding to ρ_W ranging from 0 to 10%, and interface widths $4\tau = 5$ ML (red circles), 10 ML (blue triangles), or 20 ML (orange squares), where ML refers to atomic monolayers. Here, the marker describes the mean valley splitting, while the darker bars represent the 25-75 percentile range and the lighter bars represent the 5-95 percentile range. Each bar reflects 2,000 randomized tight-binding simulations of a quantum well of width $W = 120$ ML. The magenta diamond at zero Ge concentration shows the average measured valley splitting of quantum well A. In all simulations reported here, we assume an electric field of $E = 0.0075$ V/nm and a parabolic single-electron quantum-dot confinement potential with orbital excitation energy $\hbar\omega = 4.18$ meV and corresponding dot radius $\sqrt{\hbar/m^*\omega}$.

3.2.4 Valley splitting simulations

We begin by considering an ideal laterally infinite heterostructure with no concentration fluctuations, and we denote the average Si concentration at layer l by $\bar{x}_l$. Due to the finite size of a quantum dot and the randomness in atomic deposition, there will be dot-to-dot concentration fluctuations. We therefore model the actual Si concentration at layer l by averaging the random alloy distribution weighted by the lateral charge density in the quantum dot, giving $x_l^d = \bar{x}_l + \delta_{x_l}$, as described in Supplementary Discussion Section 3c. Here, the random variation δ_{x_l} is computed assuming a binomial distribution of Si and Ge atoms. We find that these fluctuations can have a significant impact on the valley splitting.

We explore these effects numerically using 1D tight-binding simulations. We begin with the averaged fitted concentration profiles obtained from the APT analysis in Fig 3.2d, which enable us to directly measure the average Ge concentration in a given layer $\bar{x}_l$ (Fig. 3.3a). The variance of the concentration fluctuations is determined by the size of the quantum dot, which we assume has an orbital excitation energy of $\hbar\omega = 4.18\,\mathrm{meV}$ and corresponding radius $\sqrt{\hbar/m^*\omega}$, as well as the average Si concentration $\bar{x}_l$. Here, m^* is the effective mass of Si. Together, $\bar{x}_l$ and the variance determine the probability distribution of weighted Si and Ge concentrations. Concentration profiles are sampled repeatedly from this distribution, with a typical example shown in Fig. 3.3b. The valley splitting is then determined from a 1D tight-binding model [27]. The envelope of the effective mass wavefunction $\psi_{\mathrm{env}}(z)$ is shown in Fig. 3.3c (grey curve) for an electron confined in the quantum well of Fig. 3.3b. The procedure is repeated for 10,000 profile samples, obtaining the histogram of valley splittings shown in Fig. 3.3e. These results agree very well with calculations obtained using a more sophisticated three-dimensional 20-band sp^{3}d^{5}s* NEMO tight-binding model [93] (Supplementary Discussion Section 3b) and confirm that concentration fluctuations can produce a wide range of valley splittings. For comparison, at the top of Fig. 3.3e, we also plot the same experimental valley splittings shown in Fig. 3.1h, demonstrating good agreement in both the average value and the statistical spread. These observations support our claim that the

valley splitting is strongly affected by composition fluctuations due to random distributions of Si and Ge atoms near the quantum well interfaces, even though the experiments cannot exclude the presence of correlated disorder from atomic steps in quantum dots.

Analytical methods using effective mass theory may also be used to characterise the distribution of valley splittings. First, we model the intervalley coupling matrix element [63] as $\Delta = \int e^{-2ik_0 z_l} U(z) |\psi_{\text{env}}(z)|^2 dz$, where $k_0 = 0.82 \cdot 2\pi/a_0$ is the position of the valley minimum in the Si Brillouin zone, $a_0 = 0.543$ nm is length of the Si cubic unit cell, $\psi_{\text{env}}(z)$ is a 1D envelope function, and $U(z)$ is the quantum well confinement potential. The intervalley coupling Δ describes how sharp features in the confinement potential couple the two valley states, which would otherwise be degenerate. In general, Δ is a complex number that can be viewed as the sum of two distinct components: a deterministic piece Δ_0, arising from the average interface concentration profile, and a random piece $\delta\Delta$, arising from concentration fluctuations. The latter can be expressed as a sum of contributions from individual atomic layers: $\delta\Delta = \sum_l \delta\Delta_l$, where $\delta\Delta_l$ is proportional to $\delta_{x_l} |\psi_{\text{env}}(z_l)|^2$ (see Methods). To visualize the effects of concentration fluctuations in Fig. 3.3c, we compute $\delta\Delta_l$ using the randomized density profile of Fig. 3.3b (blue curve). We see that most significant fluctuations occur near the top interface, where $|\psi_{\text{env}}(z_l)|$ and the Ge content of the quantum well are both large. In Fig. 3.3d we plot Δ values obtained for 10,000 quantum-well realizations using this effective mass approach. The deterministic contribution to the valley splitting Δ_0 (black dot) is seen to be located near the center of the distribution in the complex plane, as expected. However, the vast majority of Δ values are much larger than Δ_0, demonstrating that concentration fluctuations typically provide the dominant contribution to intervalley coupling.

The total valley splitting is closely related to the intervalley coupling via $E_v = 2|\Delta|$, and therefore exhibits the same statistical behavior. In Fig. 3.3e, the orange curve shows the Rice distribution whose parameters are derived from effective-mass calculations of the valley splitting (see Methods), using the same concentration profiles as the histogram data. The excellent agreement between these different approaches confirms the accuracy of our

theoretical techniques (Supplementary Discussion Section 3d).

3.3   Discussion

Based on the results obtained above, we now propose two related methods for achieving large valley splittings (on average), with high yields. Both methods are derived from the key insight of Fig. 3.3c: due to random-alloy fluctuations, the valley splitting is almost always enhanced when the electronic wavefunction overlaps with more Ge atoms. In the first method, we therefore propose to increase the width of the interface (4τ) as shown in Fig. 3.3f, since this enhances the wavefunction overlap with Ge atoms at the top of the quantum well. This approach is nonintuitive because it conflicts with the conventional deterministic approach of engineering sharp interfaces. The second method, also shown in Fig. 3.3f, involves intentionally introducing a low concentration of Ge inside the quantum well. The latter method is likely more robust because it can incorporate both deterministic enhancement of the valley splitting from a sharp interface, and fluctuation-enhanced valley splitting.

We test these predictions using simulations, as reported in Fig. 3.3g, where different colors represent different interface widths and the horizontal axis describes the addition of Ge to the quantum well. For no intentional Ge in the quantum well, as consistent with the heterostructure growth profile of our measured quantum dots, the calculations show a significant increases in the valley splitting with increasing interface width. Here, the narrowest interface appears most consistent with our experimental results (magenta marker), attesting to the sharp interfaces achieved in our devices. As the Ge concentration increases in the quantum well, this advantage is largely overwhelmed by concentration fluctuations throughout the well. A very substantial increase in valley splitting is observed for all concentration enhancements, even at the low, 5% level. Here, the light error bars represent 5-95 percentiles while dark bars represent 25-75 percentiles. At the 5% concentration level, our

simulations indicate that >95% of devices should achieve valley splittings >100 µeV. This value is more than an order of magnitude larger than the typical operation temperature of spin-qubits and is predicted to yield a 99% readout fidelity [181]. This would represent a significant improvement in qubit yield for Si quantum dots. A recent report of SiGe quantum wells with oscillating Ge concentrations provides the first experimental evidence that intentionally placing Ge in the quantum well leads to significant variability and some of the highest recorded values of valley splitting [124].

In conclusion, we argue for the atomic-level origin of valley splitting distributions in realistic Si/SiGe quantum dots, providing key insights on the inherent variability of Si/SiGe qubits and thereby solving a longstanding problem facing their scaling. We relate 3D atom-by-atom measurements of the heterointerfaces to the statistical electrical characterisation of devices, and ultimately to underlying theoretical models. We observe qualitative and quantitative agreement between simulated valley splitting distributions and measurements from several quantum dots, supporting our theoretical framework. Crucially, we learn that atomic concentration fluctuations of the $^{28}\text{Si} \rightarrow \text{Si-Ge}$ heterointerface are enough to account for the valley splitting spread and that these fluctuations are largest when the envelope of the wavefunction overlaps with more Ge atoms. Moreover, while we have only incorporated random alloy disorder into our theoretical framework so far, we foresee that APT datasets including correlated disorder, such as steps, will be used to further refine our theoretical understanding of valley splitting statistics. Since atomic concentration fluctuations are always present in Si/SiGe devices due to the intrinsic random nature of the SiGe alloy, we propose to boost these fluctuations to achieve on average large valley splittings in realistic silicon quantum dots, as required for scaling the size of quantum processors. Our proposed approaches are counter-intuitive yet very pragmatic. The interface broadening approach seems viable for hybrid qubits, which require valley splitting to be large enough to be usable but not so large as to be inaccessible. For single-electron spin qubits, which don't use the valley degree of freedom, the direct introduction of Ge in the quantum well appears better suited for tar-

geting the largest possible valley splitting. By adding Ge to the Si quantum well in small concentrations we expect to achieve on average valley splitting in excess of 100 μeV. Early calculations from scattering theories [134] suggest that the added scattering from random alloy disorder will not be the limiting factor for mobility in current ^{28}Si/SiGe heterostructures. However, an approximate twofold reduction in electron mobility was recently reported when an oscillating Ge concentration of about 5% on average is incorporated in the Si quantum well [124]. We speculate that fine tuning of the Ge concentration in the quantum well will be required for enhancing the average valley splitting whilst not compromising the low-disorder potential environment, which is important for scaling to large qubit systems. We believe that our results will inspire a new generation of Si/SiGe material stacks that rely on atomic-scale randomness of the SiGe as a new dimension for the heterostructure design.

3.4 Methods

3.4.1 Si/SiGe heterostructure growth

The ^{28}Si/SiGe heterostructures are grown on a 100-mm n-type Si(001) substrate using an Epsilon 2000 (ASMI) reduced pressure chemical vapor deposition reactor equipped with a ^{28}SiH$_4$ gas cylinder (1% dilution in H$_2$) for the growth of isotopically enriched ^{28}Si. The ^{28}SiH$_4$ gas was obtained by reducing ^{28}SiF$_4$ with a residual ^{29}Si concentration of 0.08% [154]. Starting from the Si substrate, the layer sequence for quantum well A comprises a 900 nm layer of Si$_{1-x}$Ge$_x$ graded linearly from $x = 0$ to 0.3, followed by a 300 nm Si$_{0.7}$Ge$_{0.3}$ strain-relaxed buffer, an 8 nm tensily strained ^{28}Si quantum well, a 30 nm Si$_{0.7}$Ge$_{0.3}$ barrier, and a sacrificial Si cap. The layer sequence for quantum well B comprises a 1.4 μm step-graded Si$_{(1-x)}$Ge$_x$ layer with a final Ge concentration of $x = 0.3$ achieved in four grading steps ($x = 0.07$, 0.14, 0.21, and 0.3), followed by a 0.45 μm Si$_{0.7}$Ge$_{0.3}$ strain-relaxed buffer, an 8 nm tensily strained ^{28}Si quantum well, a 30 nm Si$_{0.7}$Ge$_{0.3}$ barrier, and a sacrificial Si cap. In quantum well A, the Si$_{0.7}$Ge$_{0.3}$ strain-relaxed buffer and the Si quantum well are grown

at 750 °C without growth interruption. In quantum well B the $Si_{0.7}Ge_{0.3}$ strain-relaxed buffer below the quantum well is grown at a temperature of 625 °C, followed by growth interruption and quantum well growth at 750 °C. This modified temperature profile yields a sharper bottom interface for quantum well B as compared to quantum well A.

3.4.2   Atom probe tomography

Samples for APT were prepared in a FEI Helios Nanolab 660 dual-beam scanning electron microscope using a gallium focused ion beam at 30, 16 and 5 kV and using a procedure described in detail in ref. [97]. Before preparation, a 150-200 nm thick chromium capping layer was deposited on the sample via thermal evaporation to minimize the implantation of gallium ions into the sample. All APT analyses were started inside this chromium cap with the stack fully intact underneath. APT was carried out using a LEAP 5000XS tool from Cameca. The system is equipped with a laser to generate picosecond pulses at a wavelength of 355 nm. For the analysis, all samples were cooled to a temperature of 25 K. The experimental data are collected at a laser pulse rate of 200-500 kHz at a laser power of 8-10 pJ. APT data are reconstructed using IVAS 3.8.5a34 software and visualized using the AtomBlend addon to Blender 2.79b and Blender 2.92 software. For the Voronoi tessellation the reconstructed data sets were exported to Python 3.9.2 and then tessellated using the scipy.spatial.Voronoi class of SciPy 1.6.2. Note that in these analyses the interfaces are represented as an array of sigmoid functions generated perpendicular to the respective interface on 3 nm × 3 nm tiles that are 1 nm apart. This sacrifices lateral resolution to allow for statistical sampling of the elemental concentrations but preserves the atomic resolution along the depth axis that APT is known to provide upon constructing the interface as shown in Fig. 3.2a.

3.4.3   Device fabrication

The fabrication process for Hall-bar shaped heterostructure field effect transistors (H-FETs) involves: reactive ion etching of mesa-trench to isolate the two-dimensional electron gas

(2DEG); P-ion implantation and activation by rapid thermal annealing at 700 °C; atomic layer deposition of a 10-nm-thick Al_2O_3 gate oxide; deposition of thick dielectric pads to protect gate oxide during subsequent wire bonding step; sputtering of Al gate; electron beam evaporation of Ti:Pt to create ohmic contacts to the 2DEG via doped areas. All patterning is done by optical lithography. Quantum dot devices are fabricated on wafer coupons from the same H-FET fabrication run and share the process steps listed above. Double-quantum dot devices feature a single layer gate metallization and further require electron beam lithography, evaporation of Al (27 nm) or Ti:Pd (3:27 nm) thin film metal gate, and lift-off. For linear quantum dot arrays the gate stack consists of 3 layers of Ti:Pd metallic gates (3:17, 3:27, 3:27 nm) isolated from each other by 5 nm Al_2O_3 dielectric interlayers. The fabrication processes for quantum dot devices are further detailed in Ref. [111].

3.4.4 Electrical characterisation of devices

Hall-bar measurement are performed in a Leiden cryogenic dilution refrigerator with a mixing chamber base temperature $T_{MC} = 50$mK [144]. We apply a source-drain bias of 100 µV and measure the source-drain current I_{SD}, the longitudinal voltage V_{xx}, and the transverse Hall voltage V_{xy} as function of the top gate voltage V_g and the external perpendicular magnetic field B. From here we calculate the longitudinal resistivity ρ_{xx} and transverse Hall resistivity ρ_{xy}. The Hall electron density n is obtained from the linear relationship $\rho_{xy} = B/en$ at low magnetic fields. The carrier mobility μ is extracted from the relationship $\sigma_{xx} = ne\mu$, where e is the electron charge. The percolation density n_p is extracted by fitting the longitudinal conductivity σ_{xx} to the relation $\sigma_{xx} \propto (n - n_p)^{1.31}$. Here σ_{xx} is obtained via tensor inversion of ρ_{xx} at $B = 0$. Quantum dot measurements are performed in Oxford and Leiden cryogenic refrigerators with base temperatures ranging from 10–50 mK. Quantum dot devices are operated in the few-electron regime. Further details of the 2DEG and quantum dot measurements are provided in the Supplementary Discussion Section 1.

3.4.5 Theory and simulations

The quantum-well potential at vertical position z_l is simply defined here as a linear interpolation of the conduction-band offset at the quantum-well interface: $U(z_l) = \frac{x_l^d - x_s}{x_w - x_s} \Delta E_c$, where x_l^d is the average Si concentration in layer l, x_s is the average Si concentration in the strain-relaxed SiGe barriers, x_w is the average Si concentration in the strained quantum well, and ΔE_c is the conduction band offset in the absence of fluctuations. In the effective-mass theory, the intervalley coupling matrix element can then be approximated by the sum

$$\Delta = \frac{a_0}{4} \sum_l e^{-2ik_0 z_l} \frac{x_l^d - x_s}{x_w - x_s} \Delta E_c |\psi_{\mathrm{env}}(z_l)|^2. \tag{3.1}$$

Defining the local concentration fluctuations as $x_l^d = \bar{x}_l + \delta_{x_l}$, the matrix element can then be split into its deterministic and fluctuating contributions $\Delta = \Delta_0 + \delta\Delta$, where the fluctuating term $\delta\Delta$ contains all dependence on δ_{x_l}:

$$\delta\Delta = \frac{a_0}{4} \frac{\Delta E_c}{x_w - x_s} \sum_l e^{-2ik_0 z_l} \delta_{x_l} |\psi_{\mathrm{env}}(z_l)|^2. \tag{3.2}$$

The deterministic term Δ_0 represents the matrix element of the ideal, smooth concentration profile, while $\delta\Delta$ describes the fluctuations about this value. For concentration fluctuations δ_{x_l} defined by binomial distributions of Ge and Si atoms, the resulting valley splitting $E_v = 2|\Delta_0 + \delta\Delta|$ corresponds to a Rice distribution with parameters $\nu = 2|\Delta_0|$ and $\sigma = \sqrt{2}\sqrt{\mathrm{Var}[\delta\Delta]}$ [5]. For additional details, see the Supplementary Discussion Section 3. All simulations and numerical calculations reported in this work were performed using Python 3.7.10 with the open-source libraries NumPy, SciPy, and Matplotlib. The 3D atomistic simulations were done using the large-scale Slater-Koster tight-binding solver NEMO3D. A spin resolved 20 band sp3d5s* nearest neighbour model was used. Strain optimization was done using a valence force field Keating model.

3.5   Acknowledgements

Chapter 4

SiGe quantum wells with oscillating Ge concentrations for quantum dot qubits

This chapter is adapted from the article Nat. Commun. **13**, 7777 (2022), "SiGe quantum wells with oscillating Ge concentrations for quantum dot qubits," by Thomas McJunkin, Benjamin Harpt, Yi Feng, **Merritt Losert**, Rajib Rahman, J. P. Dodson, M. A. Wolfe, D. E. Savage, M. G. Lagally, S. N. Coppersmith, Mark Friesen, Robert Joynt, and M. A. Eriksson (also available as a preprint, arXiv:2112.09765). I performed the atomistic simulations of the Wiggle Well heterostructures to interpret the experimental data.

4.1   Introduction

Quantum dots formed in silicon-germanium heterostructures are promising candidates for quantum computing, but the degeneracy of the two conduction band minima (or "valleys") in silicon quantum wells can pose a challenge for forming qubits [7, 63, 164, 205, 223, 226]. In such structures, the energy splitting between the valley states, E_v, is typically tens to a few hundred μeV and can vary widely due to heterostructure design and unintentional
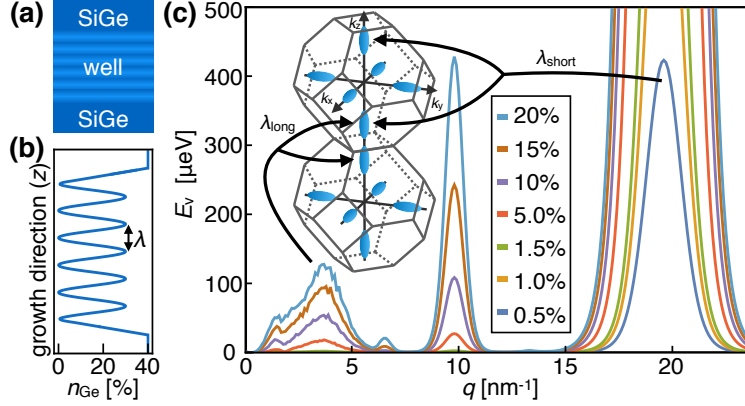
Figure 4.1: The Wiggle Well. (a) Schematic of the Wiggle Well heterostructure, showing Ge oscillations throughout the quantum well. The darker regions have higher Ge concentration. (b) Plot of Ge concentration versus position in a heterostructure with a quantum well with average concentration n_{Ge} of 15% Ge and oscillation wavelength λ, corresponding to wavevector $q = 2\pi/\lambda$. (c) EMVC predictions for valley splitting contributions (E_v versus q) due to Ge concentration oscillations in the quantum well, for n_{Ge} values shown in the inset, and a vertical electric field of 8.5 MV/m. The left inset shows two neighboring Brillouin zones in the silicon conduction band, with constant energy surfaces around the valley minima shown in blue. The peaks at $q \approx 3.5$ nm^{-1} arise from Umklapp coupling between the z valleys in neighboring Brillouin zones, and the peaks at $q \approx 20$ nm^{-1} arise from coupling between z valleys within a single zone. The peak maxima at $q \approx 20$ nm^{-1} lie between 0.4 and 18 meV and are shown on a different scale in Supplementary Fig. 1. Source data are provided as a Source Data file.

defects [21, 38, 51, 79, 88, 125, 139, 148, 166, 169, 171, 176, 225]. The small size and intrinsic variability of E_v has motivated several schemes for modifying or tuning its value. An ambitious scheme to engineer the quantum well barriers, layer-by-layer, has been proposed to increase E_v [202, 227]. Simpler heterostructure modifications have already been implemented in the laboratory. For example, including additional germanium at the quantum well interface was not found to significantly impact E_v [139], while a single spike in germanium concentration within the quantum well was found, theoretically and experimentally, to cause an approximate doubling of E_v [125]. Even more practically, E_v can be tuned after device fabrication by changing the applied vertical electric field [26, 81, 88] or the lateral dot position [51, 79, 171], though such tunability tends to be modest in a typical qubit operating range.

Here, we report theory and experiment on a novel Si/SiGe heterostructure, the Wiggle

Well, which has an oscillating concentration of germanium inside the quantum well. The wavevector is specially chosen to couple the conduction-band valleys in silicon, thereby increasing E_v. This wavevector can be chosen either to couple valleys within a single Brillouin zone or between zones. We measure a quantum dot device fabricated on a Wiggle Well heterostructure grown by chemical vapor deposition (CVD) with Ge concentrations oscillating between 0% and 9%, with wavelength of 1.8 nm, corresponding to the shortest interzone coupling wavevector. The valley splitting is measured using pulsed-gate spectroscopy [55] in a singly occupied quantum dot, obtaining results that are both large and tunable in the range of 54-239 μeV. We employ an effective mass method to treat Ge concentration variations in the virtual crystal approximation (EMVC method) to obtain an approximate picture of E_v as a function of the oscillation wavelength. We also perform tight-binding simulations of disordered heterostructures using NEMO-3D [93], which qualitatively validates our understanding from the EMVC theory and quantitatively incorporates the effects of both strain and random-alloy disorder. These simulations indicate that the magnitude and range of valley splittings observed in the current experiments can mainly be attributed to natural Ge concentration fluctuations associated with alloy disorder. These theoretical methods are also used to make predictions about a number of additional heterostructures with varying germanium oscillation wavelengths and amplitudes, in which much higher valley splitting enhancements are anticipated.

4.2 Results

We consider a spatially oscillating germanium concentration of the form $\frac{1}{2}n_{\text{Ge}}[1 - \cos(qz)]$, as illustrated in Fig. 4.1(a). Here, z is the heterostructure growth direction, n_{Ge} is the average Ge concentration in the well, and q is the wavevector corresponding to wavelength $\lambda = 2\pi/q$, as indicated in Fig. 4.1(b). The wavevector q can be chosen to greatly enhance E_v. For any Si/SiGe quantum well, the energies of the valley states split in the presence of

a sharp interface, but the Wiggle Well produces an additional contribution to E_v due to the oscillating Ge concentration, which gives rise to a potential energy term in the Hamiltonian of the form $V_{\text{osc}}(z) \propto [1 - \cos(qz)]$. The electron wavefunctions in the valleys oscillate as $\phi_{\pm}(z) \propto \exp(\pm ik_0 z)$ [63], where k_0 is the location of the conduction band minimum in the first Brillouin zone. Since k_0 occurs near the zone boundary, these oscillations are very short-wavelength. For constructive interference that would increase E_v, they must be compensated by a corresponding oscillation in the Ge concentration.

Figure 4.1(c) shows the Wiggle Well contribution to the valley splitting $E_v(q)$, calculated using the EMVC method for several values of n_{Ge}. We observe that the valley splitting is predicted to be enhanced at specific germanium oscillation wavevectors. The wavevector $q \approx 3.5$ nm^{-1}, corresponding to $\lambda_{\text{long}} = 1.8$ nm, describes coupling between valleys in two neighboring Brillouin zones, as indicated by arrows in the inset. A much larger enhancement of the valley splitting can be achieved for the wavevector $q \approx 20$ nm^{-1}, corresponding to the much shorter wavelength, $\lambda_{\text{short}} = 0.32$ nm, which describes coupling between the z-valley states within a single Brillouin zone, also shown with arrows. Thus, choosing the oscillation wavelength $\lambda = 2\pi/q$ with care enables the generation of a wavevector in the potential that couples valley minima either between or within Brillouin zones. The large difference in the heights of the two peaks is an extinction effect (destructive interference), caused by a symmetry of the diamond lattice structure. Disorder breaks the symmetry and produces a small peak. The noisy shape of the peak at $q \approx 3.5$ nm^{-1} comes from sampling error (see Supplementary Note 1). An additional peak is observed at wavevector $q \approx 10$ nm^{-1}. We identify this as a harmonic of the taller peak because its height scales as n_{Ge}^2, in contrast to the $q \approx 20$ nm^{-1} peak, which scales as n_{Ge} [59]. At small q, there are additional features associated with the details of the barrier interface.

Figure 4.2(a) shows a scanning transmission electron micrograph of a Wiggle Well heterostructure grown by chemical vapor deposition (CVD), demonstrating an oscillating concentration of germanium with $\lambda \approx 1.7$ nm, as described in Methods. Based on this result, the

growth parameters were adjusted slightly to achieve the desired λ_{long} oscillation period, with an estimated $n_{\text{Ge}} = 4.5\%$. The closest match to this value in Fig. 4.1(c) (red curve) suggests a valley splitting enhancement of about 20 μeV due to these oscillations. Hall bar devices were fabricated on the heterostructure and measured at a temperature of $\sim$2 K, revealing mobilities in the range of 1-3$\times10^4$ cm^{2}V^{-1}s^{-1} for an electron density range of 2-6$\times10^{11}$ cm^{-2}. (See Supplementary Note 2.)

To define quantum dots, atomic layer deposition was used to deposit a 5 nm layer of aluminum oxide. Electron beam lithography was used to pattern three layers of overlapping aluminum gates isolated from one another by the plasma-ash enhanced self-oxidation of the aluminum metal, following the procedure described in Ref. [52]. (See Methods.) Figure 4.2(b) shows a false-colored scanning electron micrograph of a quantum dot device lithographically identical to the one measured. The left half of the device was used for the measurements described below, with a double quantum dot formed in the lower channel and a charge sensing dot formed in the upper channel. Figure 4.2(c) shows a stability diagram of the double dot, where the absolute number of electrons can be determined by counting the number of lines crossed in the color plot. All measurements were performed using the last (leftmost) electron transition in this figure, near the magenta star, in a dilution refrigerator with a base temperature below 50 mK.

The excited-state spectrum of a singly occupied quantum dot was measured using pulsed-gate spectroscopy [51, 55, 177, 211, 217, 224], as shown in Fig. 4.2(d). Here, the differential conductance of the charge sensor is plotted as a function of the dc voltage on gate P1 vs. the amplitude of the square-wave pulse applied to P1. The data show a sudden change of color when the rate at which electrons enter or leave the dot changes significantly, allowing us to estimate the excited-state energies (see Methods). Figure 4.2(e) shows in blue the averaged result of 16 individual P1 voltage scans obtained with a 16 mV square-wave amplitude. The green curve is a numerical derivative of the blue curve with respect to V_{P1}. Here, the voltage differences corresponding to the valley splitting E_v and the orbital splitting E_{orb} are labeled

with arrows. The dips in the differentiated signal are fit to extract the voltage splittings, using the methods described in Ref. [51], and then converted into energy splittings using the appropriate lever arm (see Supplementary Note 3), yielding a valley splitting of 164±3 µeV for this particular device tuning.

To develop an understanding of how germanium concentration oscillations and fluctuations can affect the valley splitting, we make use of our ability to change the quantum dot's shape and position in-situ by changing the gate voltages. Importantly, such changes in size and shape can be made while keeping the electron occupation constant. First, we shift the dot's lateral position by changing the voltages on the screening gates S1 and S2 asymmetrically [51]. Because germanium atoms sit at discrete locations, the concentration oscillations are not identical at all locations in the quantum well; instead, each physical location represents a random instance, which only follows a smooth sine wave pattern when averaged over a wide region. Since the dot is finite in size, changes in position therefore cause it to sample local fluctuations of the Ge concentration. Moving the dot in this way also modifies the size and shape of the electron probability distribution in the plane of the quantum well. For this reason, we also perform a second experiment, in which we change the size and shape of the quantum dot while keeping the center position of the dot approximately fixed. In this case, the screening gate voltages S1 and S2 are made more negative, while P1 is made more positive, following the procedure described in Ref. [125], in which the motion of the dot was confirmed through electrostatic modeling.

The orbital and valley splittings resulting from these two different tuning schemes are shown in Fig. 4.3(a). Both tuning schemes yield a large change in the orbital splitting E_{orb}, as shown in the inset to Fig. 3(a), because both change the size and shape of the quantum dot. The valley splitting shows markedly different behavior in the two cases. The first tuning scheme, which moves the dot laterally, to sample different realizations of the Wiggle Well oscillations, yields a large change in the measured valley splitting of nearly 200 µeV. Here, the variation of E_v is monotonic because the range of motion is similar to the dot radius. The

second approach, which does not move the quantum dot, results in a much smaller change in the valley splitting. This large difference in behavior is demonstrated most obviously by the linear fits to the data, which we will compare below to numerical calculations of the valley splitting for many different atomistic realizations of the Wiggle Well. While tunable valley splittings (and closely related singlet-triplet splittings) of Si/SiGe quantum dots have recently been achieved by changing gate voltages [51, 79, 88, 125, 171], the observed range of behavior has been modest: for example, 15% tunability with a maximum of $E_v = 213$ µeV [79] or 140% tunability with a maximum of $E_v = 87$ µeV [51]. Here in contrast, we report a striking $> 440\%$ tunability with a maximum of $E_v = 239$ µeV.

The EMVC calculations presented in Fig. 1 provide intuition about how oscillating germanium concentrations affect the valley splitting: wave vectors describing the germanium-induced oscillating potential in the quantum well connect valley minima within or between Brillouin zones, as determined by the wavelength of the oscillations. However, such calculations do not provide information about the effect of different atomistic realizations of these oscillations. Moreover, from Fig. 3(a), it is clear that the variations in E_v due to atomistic randomness can be even larger than its mean value.

The strong effect of random alloy disorder on the valley splitting can also be understood from Wiggle Well theory. Due to the finite size of a quantum dot, the electron naturally experiences small layer-by-layer fluctuations of the Ge concentration, as recently explored experimentally [145]. Fourier transforming this distribution assigns random weights across the whole q spectrum in Fig. 1. In particular, weight on the $q \approx 20$ nm peak should have a random but noticeable effect on the valley splitting. In a deterministic Wiggle Well we simply emphasize the weight at certain wave vectors.

To study the competition between deterministic and random enhancements of the valley splitting, we now perform atomistic tight-binding simulations in NEMO-3D using a 20-band sp^{3}d^{5}s* strain-dependent model [93]. The quantum well concentration profile of Fig. 4.1(b) is used to construct a heterostructure atom-by-atom, where the probability that an atom is

Ge is given by the average Ge concentration at that atom's layer. For all simulations, we assume a typical electric field of 8.5 MV/m.

Figure 4.3(b) shows the results of simulations corresponding to the two experiments described in Fig. 4.3(a). The dots are modeled by the confinement potential $V(x,y) = \frac{1}{2}m_t[\omega_x^2 x^2 + \omega_y^2(y-y_0)^2]$, where $m_t = 0.19\,m_0$ is the transverse effective mass. In the left-hand panel of Fig. 4.3(b), the position of the dot (y_0) is varied by 20 nm, as consistent with electrostatic simulations reported in [125]. The dot radius along $\hat{x}$ (r_x) is also varied, by tuning the orbital energy in the range $\hbar\omega_x = $ 1-2 meV, corresponding to $r_x = \sqrt{\hbar/m_t\omega_x} = $ 14-20 nm. In the right-hand panel, only ω_x is varied, over the same range, keeping y_0 fixed. In both cases, we choose $\hbar\omega_y = 2$ meV. Each of the curves in Fig. 3(b) is a straight line connecting two simulations. These simulations have different $E_{\mathrm{orb}} = \hbar\omega_x$ values, corresponding to 1 or 2 meV, but the same disorder realization. The different curves correspond to different disorder realizations. The left-hand panel confirms that a wide range of valley splittings may be accessed by moving the dot; the experimental slope found for this tuning method (shown by the dashed line) lies within the range of simulation results. The NEMO-3D results in the right-hand panel show a much narrower range of changes in valley splittings, consistent with the experimental observations shown in blue in Fig. 3(a) (dashed line). Here, the center position of the dot does not change, so the dot samples roughly the same disorder for each value of E_{orb}. In both panels, ΔE_v is seen to increase with E_{orb} (on average); this trend can be explained by the prevalence of larger concentration fluctuations in smaller dots, yielding larger valley splittings (on average). These results highlight the ability of random-alloy disorder to affect valley splitting in this system, as compared to the more deterministic concentration oscillations, and the ability of a moving dot to sample these fluctuations.

We now use NEMO-3D tight-binding calculations to make quantitative predictions about valley splitting in other Wiggle Well structures. The top panel in Fig. 4.3(c) reports results for long-wavelength Wiggle Wells (λ_{long}=1.8 nm) with average Ge concentrations of 5%, 10%, 15%, and 20%. Here, each distribution shows the results of 40 simulations with different

realizations of alloy disorder. The bottom panel reports results for short-wavelength Wiggle Wells (λ_{short}=0.32 nm) with average Ge concentrations of 0.5%, 1%, and 1.5%. In this case, results are shown for 20 random-alloy realizations. For all simulations shown in Fig. 4.3(c), we assume an orbital excitation energy of $\hbar\omega = 2$ meV. For the long-period Wiggle Well, we see that the effects of alloy disorder are relatively large compared to the deterministic enhancement of the valley splitting caused by Ge oscillations, as indicated by the large spread in results. We also note that the 5% amplitude NEMO-3D results in the top panel are consistent with the experimental valley splittings shown in Fig. 4.3(a). For the short-period Wiggle Well, NEMO-3D predicts very large boosts in the deterministic contribution to the valley splittings, even for low-amplitude Wiggle Well oscillations.

4.3 Discussion

In summary, we have introduced a new type of silicon/silicon-germanium heterostructure with a periodically oscillating concentration of germanium within the quantum well. Using effective mass theory, we showed that the Wiggle Well can induce couplings between the z-valley states, both within a Brillouin zone and between neighboring zones, thereby enhancing the valley splitting. We reported the growth of such a heterostructure with a Ge oscillation period of 1.8 nm within the quantum well, which showed mobility large enough, and corresponding disorder small enough, to form stable and controllable gate-defined quantum dots. Pulsed-gate spectroscopy revealed large valley splittings that were widely tunable through changes in gate voltages. Tight-binding simulations were used to validate the understanding of the experiment and to make predictions about how alloy disorder and structural changes (e.g., in the amplitude and wavelength of the germanium oscillations) can be expected to influence the valley splitting. In the current experiments, simulations indicate that natural Ge concentration fluctuations play a dominant role in determining the magnitude and range of the observed valley splittings. However the short, 0.32 nm structure is predicted

to offer much larger deterministic enhancements of the valley splitting. While this spatial period is short, optimized growth methods have been shown to enable rapid changes in Ge concentrations [100]. For the short-period Wiggle Well, this method should allow 0.93% peak-to-peak Ge concentration oscillations. By further incorporating isotopically purified silicon and germanium into the growth, to suppress hyperfine interactions, the Wiggle Well offers a powerful strategy for improving both coherence times and state preparation and measurement (SPAM) fidelities, by providing reliably high valley splittings.

4.4   Methods

4.4.1   Theory

We consider a potential that couples the wavefunctions $\phi_{\pm}(\mathbf{r})$ with wavevectors near the valley minima $\mathbf{k} = \pm(0, 0, k_0)$ where $k_0 = 0.84(2\pi/a_0)$ and $a_0 = 0.543$ nm is the lattice constant. The unperturbed wavefunctions are

$$\phi_{\pm}(\mathbf{r}) = \psi(z)e^{\pm ik_0 z}\sum_{\mathbf{K}}c_{\pm}(\mathbf{K})e^{i\mathbf{K}\cdot\mathbf{r}}, \tag{4.1}$$

where ψ is an envelope function, the $\mathbf{K}$ are reciprocal lattice vectors, and the $c_{\pm}(\mathbf{K})$ are Fourier expansion coefficients of the cell-periodic part of the Bloch function. The valley splitting E_v induced by the added Ge is [158]

$$E_v = 2\left|\langle\phi_{+}|V_{\text{osc}}(z)|\phi_{-}\rangle\right| = 2\left|\sum_{\mathbf{K},\mathbf{K}'}c_{+}^{*}(\mathbf{K})c_{-}(\mathbf{K}')\delta_{K_x,K_x'}\delta_{K_y,K_y'}I(K_z - K_z')\right|, \tag{4.2}$$

where

$$I(K_z - K_z') = \int_{-\infty}^{0}|\psi(z)|^2 e^{iQz}V_0\cos(qz)dz, \tag{4.3}$$

with $Q = K_z - K_z' - 2k_0$. $|\psi(z)|^2$ is a smooth function with a single peak, so its Fourier transform has a single peak centered at zero wavevector. Hence, $I(K_z - K_z')$ will peak strongly when

$$q = \pm Q = \pm(K_z - K_z' - 2k_0). \tag{4.4}$$

Because of the sum over reciprocal lattice vectors in Eq. (4.2), $E_v(q)$ is expected to be enhanced whenever the condition $K_z - K_z' = \pm(q \pm 2k_0)$ is satisfied. However, a symmetry of the diamond lattice structure leads to a cancellation in the sum over $\mathbf{K}, \mathbf{K}'$ in Eq. (4.2) when $q = 4\pi/a - 2k_0 = 3.5 \text{ nm}^{-1}$. As described in Supplementary Note 1, the coefficients $c_\pm(\mathbf{K})$ in Eqs. (1)-(2) are determined by using the results of a pseudopotential method combined with the virtual crystal method for the disordered SiGe system. This results in a modification of the coefficients that have been previously computed using density functional theory for bulk silicon [158]. The envelope function $\psi(z)$ is found for a quantum well with a vertical electric field of 8.5 MV/m. Further details may be found in Ref. [59]

4.4.2 Heterostructure Growth.

The measured heterostructure is grown on a linearly graded SiGe alloy with a final 2 μm layer of $\text{Si}_{0.705}\text{Ge}_{0.295}$. Prior to heterostructure growth, the SiGe substrate is cleaned and prepared as described in Ref. 139. The substrate is loaded into the growth chamber and flash heated to 825 °C while silane and germane are flowing. The temperature is lowered to 600 °C, at which point a 550 nm 29.5% Ge alloy layer is grown. For the quantum well, the growth begins with a 10 second pulse of pure silane gas at 90 sccm. Then, 90 sccm of silane and 4.88 sccm of germane are introduced for 10.63 seconds followed by 10 seconds of pure silane. This SiGe–Si pulse sequence is repeated a total of 5 times. The pulse times are tuned to achieve a period of 1.8 nm and a peak Ge concentration of 9%, which was deemed small enough to prevent electrons from leaking out of the quantum well. We note that the actual heterostructure concentration will not achieve a full contrast of 9%, due to atomic diffusion.

After the quantum well, a 60 nm $Si_{0.705}Ge_{0.295}$ spacer is grown and the heterostructure is capped with a thin 1 nm layer of pure silicon.

4.4.3 Pulsed-Gate Spectroscopy

Pulsed-gate spectroscopy is used to measure the valley and orbital splitting of a singly-occupied quantum dot. A square wave voltage is applied to the plunger gate of a dot at a frequency comparable to the tunnel rate to the electron reservoir. The charge sensor current is measured with a lock-in amplifier referenced to the fundamental frequency of the square wave. When the dc voltage of the gate is swept over the dot transition, the electron is loaded and unloaded into the dot as the dot's chemical potential, split by the square wave, straddles the Fermi level of the reservoir. As the amplitude is increased, additional states such as the excited valley state and excited orbital state can be loaded during the high voltage period of the wave, modifying the tunnel rate into the dot. These changes in tunnel rate lead to a changing lock-in response. These changes can be seen in Fig. 4.2(d).

4.5 Data Availability

Raw source data for all relevant figures are available as a 'Source Data' file at `10.5281/zenodo.7374581` [123].

4.6 Code Availability

The Mathematica files used to generate Fig. 1(c) and Supplementary Fig. 1 are provided as a 'Source Code' file, available at `10.5281/zenodo.7374581` [123]. The simulations reported in Fig. 3 and described in Supplementary Note 4 were performed using NEMO-3D simulation code: `https://engineering.purdue.edu/gekcogrp/software-projects/nemo3D/`. NEMO-3D is available as open source and is also accessible at nanohub: `http://nanohub.`

`org/.`

4.7 Acknowledgements

Figure 4.2: Growth and measurement of a quantum dot device on a Wiggle Well heterostructure. (a) High-angle annular dark-field (HAADF) image of a test heterostructure demonstrating an oscillation wavelength of ∼1.7 nm. The lighter regions have higher Ge concentrations. (b) False-color scanning electron micrograph of a quantum dot device lithographically identical to the one measured. The different colors (blue, green, yellow) indicate different gate layers, and relevant gates are labeled. (c) Stability diagram of a quantum dot formed under the leftmost plunger gate in the lower channel, measured using a quantum dot charge sensor in the upper left channel. Here the differential conductance dI_{CS}/dV_{P1} is plotted, where I_{CS} is the current through the charge sensor and V_{P1} and V_{B1} are the voltages on gates P1 and B1, respectively. The dark lines (maxima in dI_{CS}/dV_{P1}) reveal the voltages at which charge transitions occur in the dots. The measurements presented here are performed at the last (leftmost) electron transition in this dot, near the magenta star. (d) Pulsed-gate spectroscopy of a singly occupied quantum dot. The dc voltage on gate P1 is swept across the 0-1 electron charging transition while simultaneously applying a square-wave voltage pulse of varying amplitude and 2 kHz frequency, revealing a characteristic V-shape in a lock-in measurement of the transconductance of the charge sensor: $|g| \approx |\delta I_{CS}/\delta V_{P1}|$, where δV_{P1} is the pulse amplitude. (e) Extraction of E_v and E_{orb}: we repeat 16 P1 voltage scans at the same device tuning as in (d), for a 16 mV pulse amplitude. The blue curve shows the averaged lock-in response and the green curve shows its derivative with respect to V_{P1}. The resulting dips allow us to determine the valley and orbital splittings, E_v and E_{orb}, as indicated. Source data are provided as a Source Data file.
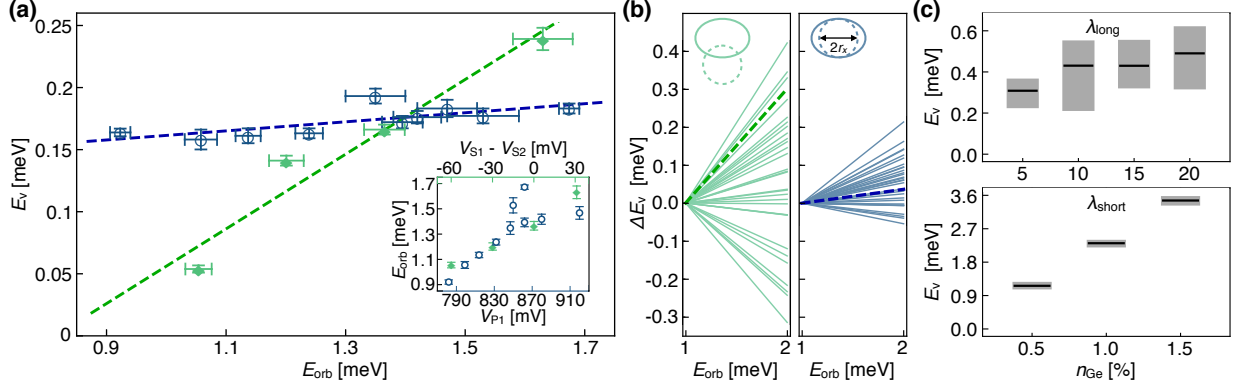
Figure 4.3: Valley and orbital excitation energies of a Wiggle Well quantum dot. The voltages applied to the dot are tuned in two ways, both of which change the orbital splitting (E_{orb}) substantially but only one of which changes the valley splitting (E_v) significantly. Case 1 (filled green diamonds): dot position depends on E_{orb}. Case 2 (open blue circles): dot position remains stationary. (a) Inset: Case 1 is achieved by asymmetrically changing voltages on screening gates S1 and S2 (top axis). Case 2 is achieved by changing voltages on S1 and S2 symmetrically, while simultaneously changing the voltage on P1 to compensate (bottom axis). Main panel: valley splittings vary by a factor of 4 for the moving dot, but much less for the stationary dot, over approximately the same range of orbital splittings. Dashed lines are linear fits through the two datasets. Valley splitting is computed by fitting to pairs of spectroscopy peaks [Fig. 2(e)]; error bars reflect the standard error in the peak fits, combined in quadrature, with errors in the lever-arm fits also added in quadrature (see Supplemental Note 3). (b) NEMO-3D tight-binding simulations of Case 1 (left panel) and Case 2 (right panel) scenarios, as depicted by the dot shapes shown in the insets. Simulations include atomistic random-alloy disorder, where the probability of choosing Si or Ge atoms is determined by the Ge concentration profile. Here each curve reflects a unique disorder realization, and we vary the orbital energies (Cases 1 and 2) and dot locations (Case 1 only). Note that E_v values are shifted to align when $E_{\mathrm{orb}} = 1$ meV. (Shifted values are labelled ΔE_v.) The dashed lines in (b) are the same as the experimental results in (a). Here they fall within the statistical range of the randomized simulations, showing consistency with the theory. (c) Statistical sampling of NEMO-3D simulations for several values of germanium concentrations n_{Ge}, for λ_{long}-period (top panel, 40 samples) or λ_{short}-period (bottom panel, 20 samples) Wiggle Wells. The mean values of the simulations are shown as black lines, along with 25 to 75 percentile ranges (gray bars). Results indicate that alloy disorder plays a dominant role in valley splitting for λ_{long} oscillations, with concentration oscillations providing a much smaller enhancement. Source data are provided as a Source Data file.

Chapter 5

Practical Strategies for Enhancing the Valley Splitting in Si/SiGe Quantum Wells

This chapter as adapted from the article Phys. Rev. B **108**, 125405 (2023), "Practical strategies for enhancing the valley splitting in Si/SiGe quantum wells," by **Merritt P. Losert**, M. A. Eriksson, Robert Joynt, Rajib Rahman, Giordano Scappucci, Susan N. Coppersmith, and Mark Friesen (also available as a preprint, arXiv:2303.02499). I principally performed the analytical calculations and simulations used in this work, with input from all authors.

5.1   Introduction

Qubits formed from quantum dots in Si/SiGe heterostructures are promising candidates for large-scale quantum computing [121, 228, 231]. Naturally abundant spin-zero nuclear isotopes and the highly developed infrastructure of the semiconductor industry lend a particular advantage to silicon-based qubits. Recently, one and two-qubit gates in spin qubits in Si/SiGe quantum dots have yielded fidelities above 99% [131, 142, 213], attesting to the viability of this materials platform.

However, qubits in Si suffer from the degeneracy of low-energy features in the conduction band, known as valleys. Although the sixfold valley degeneracy of bulk silicon is lifted by tensile strain in the quantum well, a nearly degenerate excited valley state remains accessible to electrons in quantum dots [231]. The energy splitting between these low-lying valley states, E_v, can range widely from 20 to 300 μeV [19, 22, 60, 79, 128, 129, 139, 143, 163, 171, 225], even for devices fabricated on the same chip [33, 145]. When the valley splitting is too low, the excited state provides a leakage path outside the logical space of the spins, posing a significant threat for qubit operations [231]. To date, it has not been possible to engineer devices with reliably high valley splittings.

In conventional SiGe/Si/SiGe heterostructures, the valley splitting is determined by the quantum well confinement potential. Accordingly, the variability of E_v is attributed to the variability of the interfaces. Such behavior has been well studied theoretically, using tight-binding [1, 26, 51, 57, 58, 92–95] and effective-mass methods [35, 63, 68, 69, 81, 157, 183]. Studies have focused on heterostructure parameters such as the width of the interface [33] or quantum well [26, 63]. Additional variability is caused by imperfections and disorder. Tilted interfaces and single-atom steps, in particular, have been studied extensively [20, 42, 51, 64, 65, 68, 69, 72, 81, 82, 92, 183]. Experimental work has validated some of these predictions. For example in Si metal-oxide-semiconductor (Si-MOS) stacks, where the semiconductor-dielectric interface is characteristically sharp, interface roughness has been shown to correlate with the valley splitting [69].

An additional type of disorder is present in heterostructures containing SiGe alloy. In this case, the crystal lattice sites are filled randomly with Si or Ge atoms, as determined by the average concentration profile. For Si/SiGe heterostructures, it has recently been shown that such uncorrelated, random alloy disorder can have a dominant effect on the intervalley coupling Δ [145]. Specifically, Δ can be decomposed into two components: (1) an average, 'deterministic' component Δ_0, which is largely uniform across a sample, and (2) a random component $\delta\Delta$, which varies significantly by location. Here, Δ_0 is determined by the smooth

quantum well confinement potential, while $\delta\Delta$ arises from local Ge fluctuations caused by alloy disorder. Since $E_v = 2|\Delta|$, large variations in $\delta\Delta$ lead to large variations in E_v, as verified experimentally in quantum dots [124, 145].

In this paper, we show that sharp features in the heterostructure profile, like a sharp interface, can enhance the valley splitting, while random alloy disorder strongly suppresses this effect. The crossover between these two types of behavior occurs in a regime where heterostructure features are abrupt and difficult to achieve in the laboratory. Deterministically enhanced valley splittings are therefore difficult to achieve by sharp interfaces alone.

To better understand this crossover, we consider several 'conventional' heterostructures, where we characterize competing effects like sharp interfaces vs. interface steps. We find that steps can be detrimental to valley splitting; however they have essentially no effect for interface widths of three or more atomic monolayers. In the randomly dominated regime, we show that when the electron is exposed to more Ge, it experiences a larger average valley splitting and a larger variability.

We also characterize unconventional geometries like the Wiggle Well, which yields the greatest improvements to the valley splitting, but is challenging to grow in the laboratory. We compare this to an alternative geometry, with uniform Ge in the quantum well, where the mean and standard deviation of the valley splitting are both enhanced. We argue that such structures provide a more reliable approach for improving qubits, if they can be electrostatically tuned to locations with desirable valley splittings. We finally argue that both of these approaches are superior to sharp interfaces, and show they are optimal in certain operating regimes.

The paper is organized as follows. In Sec. 5.2, we study the dominant sources of E_v variation and how they interact, and we explain these behaviors in the context of a universal theory of valley splitting. Expanding on ideas first presented in Refs. [145] and [124], we show that valley splitting depends fundamentally on the strength of the quantum well confinement potential at the special reciprocal-space wavevector $2k_0$ (we refer to this as '$2k_0$ theory'),
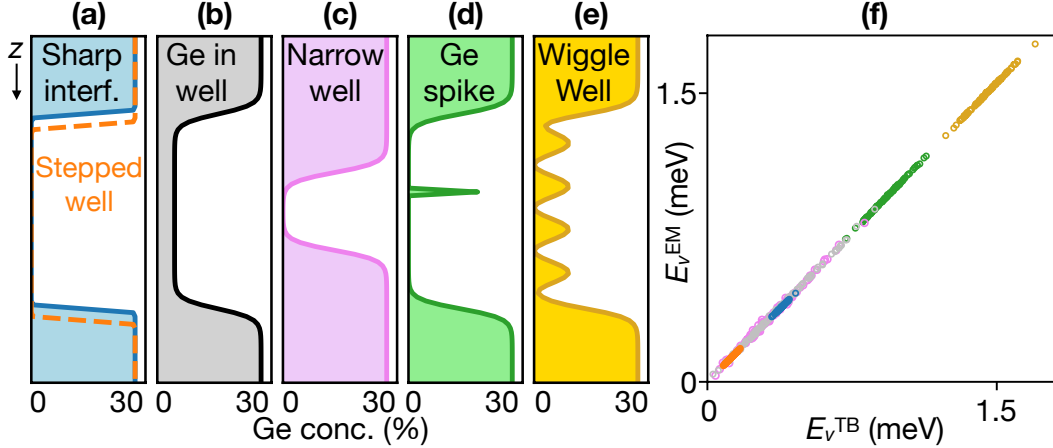
Figure 5.1: Confirmation of the universal $2k_0$ theory of valley splitting. (a)-(e) Schematic illustrations of several of the Si/SiGe heterostructures considered in this work: (a) a quantum well with a sharp interface and no interface steps (blue), or with one interface step (orange); (b) a quantum well with a uniform concentration of Ge; (c) a narrow quantum well; (d) a quantum well with a single-monolayer spike of Ge; (e) a Wiggle Well. (f) Valley-splitting correlation plot for the structures shown in (a)-(e), with the same color coding used in those panels. On one axis, we plot tight-binding (TB) results for the valley splitting, E_v^{TB}. On the other axis, we plot the universal $2k_0$ prediction, based on effective-mass (EM) theory, E_v^{EM}, as defined in Eqs. (5.8) and (5.9), where $E_v = 2|\Delta|$. (See main text for simulation details.) For each different heterostructure, we generate 100 instances of alloy disorder for a given, average Ge concentration profile, as described in the main text, using the same disorder profiles for both the TB and EM simulations. All results fall onto a universal curve, demonstrating the validity of the $2k_0$ theory.

which is the distance between the two z valleys in the first Brillouin zone. We go on to show that deterministic and random-alloy effects can both contribute to this $2k_0$ wavevector. Interface width, atomic steps, alloy disorder, and other features can therefore be studied and compared within a single analytic framework, providing intuition as well as quantitative predictions.

In Sec. 5.3, we outline the theoretical methods employed here, including tight-binding models and effective-mass theory. We investigate the effects of alloy disorder on the valley splitting in dots formed in SiGe/Si/SiGe quantum wells. This disorder leads to large E_v variations, which we show depend on the amount of Ge the wavefunction is exposed to. Such variations also increase the mean value of the valley splitting, and they significantly reduce the fraction of dots with low valley splittings. Here, we make a crucial distinction between

quantum wells in which all quantum dots (except a vanishingly small subset) have valley splittings that are large enough for qubit applications, and dots with a wide distribution of valley splittings, extending all the way to zero energy. We refer to the former category as 'deterministically enhanced' and the latter as 'randomly dominated.' By simulating many random instances of alloy disorder, we show that there is a sharp transition between these two types of behavior. We also obtain an analytical expression for the crossover, using the statistical properties of random alloys. We then show that nearly all recent experiments are of the randomly dominated type, with important implications for scaling up to large numbers of qubits. We further show that when physical limitations, such as growth constraints, do not permit the formation of heterostructures with very sharp features (on the order of 1-2 atomic layers), the resulting devices fall into the randomly dominated category. For such structures, it is generally more effective to increase the average valley splitting by increasing the wavefunction exposure to Ge.

In Sec. 5.4, we use our theoretical toolbox to examine conventional Si/SiGe heterostructures. We study the interactions between alloy disorder and interface steps in conventional Si/SiGe heterostructures as a function of the interface width [Fig. 5.1(a)]. For devices with sharp interfaces, steps are found to strongly suppress the valley splitting, as is well known. However, for devices with wider interfaces, the steps are found to have little or no effect on the valley splitting. In this regime, the valley splitting depends mainly on the local alloy disorder, and we show that this disorder leads to large E_v variations as a function of dot position.

In Sec. 5.5, we consider unconventional heterostructures proposed to boost the valley splitting [Figs. 5.1(b)-5.1(e)], by adding Ge to the interior or the boundary of the quantum well. These include Ge-rich barrier layers [139], and other more-complicated superlattice barrier structures [202, 227], single-atom spikes of Ge inside the quantum well [125], narrow quantum wells [26, 33, 63], and oscillating Ge concentrations with specially chosen oscillation wavelengths (e.g., the 'Wiggle Well' [59, 124]). We analyze these designs and characterize

their deterministic and random-alloy contributions to valley splitting, which allows us to compare ideal performance to actual operation.

To close this section, we apply optimization procedures to determine Ge concentration profiles that maximize the valley splitting, using two different optimization strategies. First, we maximize the deterministic valley splitting $E_{v0} = 2|\Delta_0|$, without including alloy disorder. This approach yields heterostructures with concentration oscillations very similar to the short-period Wiggle Well, confirming the optimality of that structure. In the second approach, we maximize the standard deviation σ_Δ, which can be shown to maximize the average valley splitting in the randomly dominated regime. This approach yields smooth Ge concentration profiles centered in the middle of the quantum well.

In Sec. 5.6, we summarize our main results, and finally in Sec. 5.7, we describe the best forward-looking strategies for enhancing the valley splitting, which can be used to guide future experiments in Si/SiGe heterostructures. Here we argue that the Wiggle Well is the preferred approach, in the deterministically enhanced regime. In the randomly dominated regime, we argue that the best approach is to introduce uniform Ge into the quantum well and then electrostatically tune the dot position, to find a location where the valley splitting is suitable.
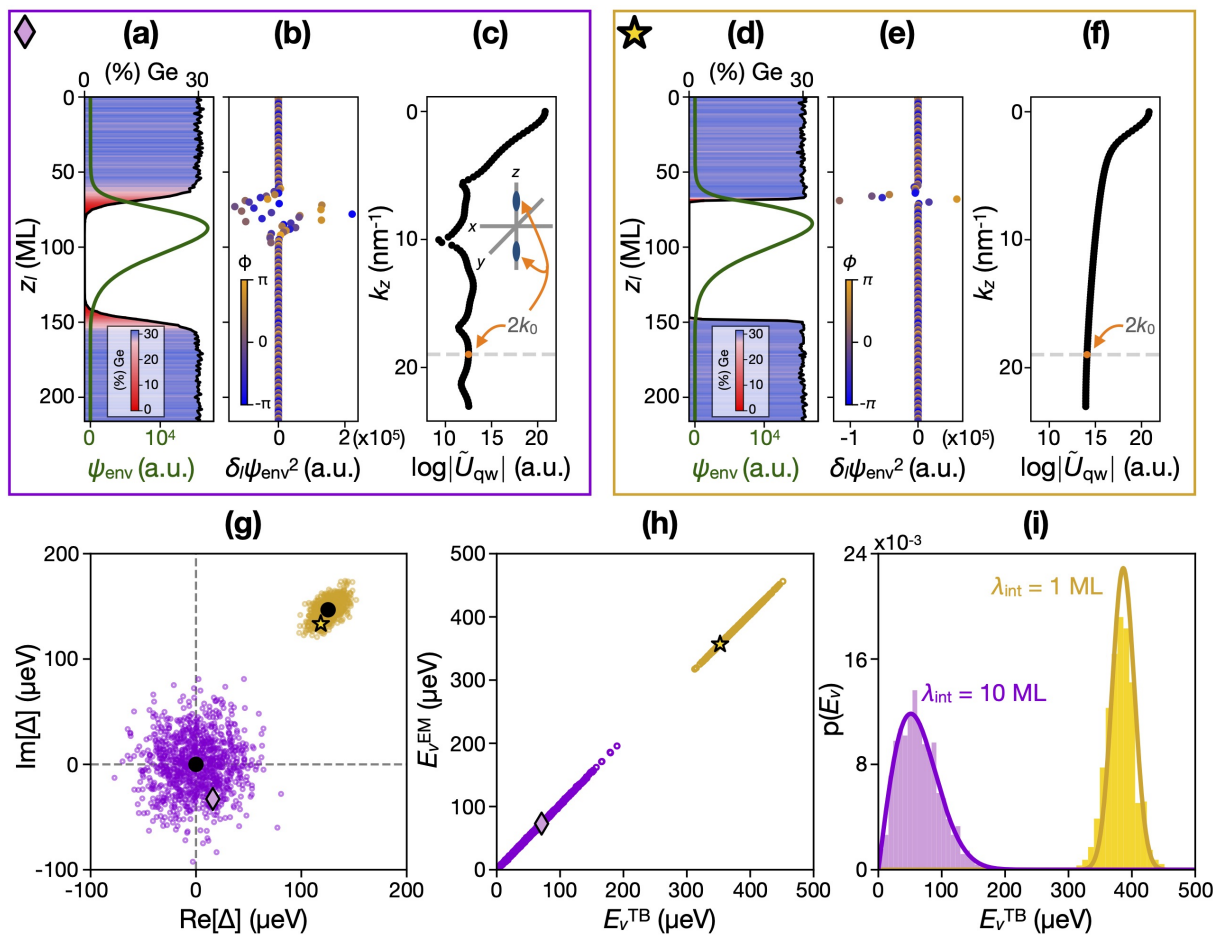
Figure 5.2 *(previous page)*: Effective-mass analysis of the effects of alloy disorder for quantum wells with (a)-(c) wide interfaces, or (d)-(f) super-sharp interfaces. (a), (d) Typical Ge concentration profiles along the growth direction ($\hat{z}$). The local Ge concentration is also shown as a color scale. Here, the average Si concentration profiles are given by sigmoid functions [Eq. (5.21)], with quantum well and substrate concentrations given by $X_w = 1$ and $X_s = 0.7$, respectively, and interface widths given by $\lambda_{\text{int}} = 10$ ML for (a) or $\lambda_{\text{int}} = 1$ ML for (d), where ML stands for atomic monolayers, corresponding to the length $a_0/4$. Small fluctuations in Ge concentration occur from location to location due to alloy disorder and the finite size of the quantum dot. We also show here the envelope functions $\psi_{\text{env}}(z)$ (solid green curves), used to calculate the intervalley matrix element Δ [Eq. (5.8)], obtained by solving a 1D Schrödinger equation for the quantum well confinement potential $U_{\text{qw}}(z)$ [Eq. (5.3)]. (b), (e) Individual terms in the the $\delta\Delta$ sum [Eq. (5.11)], plotted as a function of the vertical position z_l. The corresponding complex phases, $\phi = -2k_0 z_l$, are indicated as a color scale. (c), (f) Discrete Fourier transform $\tilde{U}_{\text{qw}}(k_z)$ of the weighted confinement potential $\tilde{U}_{\text{qw}}(z_l) = U_{\text{qw}}(z_l)|\psi_{\text{env}}(z_l)|^2$ appearing in Eq. (5.8), for the quantum wells shown in (a) and (d). The $2k_0$ wavevector component of $\tilde{U}_{\text{qw}}$ (gray dashed line) couples valleys within the first Brillouin zone, causing valley splitting. (g) Such Δ calculations are repeated for 1,000 different disorder realizations, for the same two interfaces (wide vs. sharp), obtaining the purple and gold distributions, which are plotted here on the complex plane. The highlighted points (purple diamond, gold star) correspond to the specific results shown in (a)-(f). The central black points correspond to the deterministic centers of the distributions, Δ_0. For wide interfaces (purple), we observe that the Δ distributions are broader and centered much closer to the origin. In these cases, the standard deviation of the distribution, σ_Δ, is much larger than the mean value, Δ_0, while the opposite is true for sharp interfaces (gold). (h) Effective-mass valley splittings ($E_v^{\text{EM}} = 2|\Delta|$) are obtained from (g) and plotted against 1D tight-binding calculations (E_v^{TB}), using the same disorder realizations. The collapse of the data onto a line of slope 1 indicates nearly perfect correlations between the two methods. (i) Histogram plot of the tight-binding results shown in (h). Solid lines show the computed Rice distributions [Eq. (5.14)].

5.2   A universal picture of valley splitting

A primary result of this paper is the unified understanding of how all key features in a heterostructure, from deterministic to random, work together to determine the valley splitting in Si/SiGe devices. In this section, we present an intuitive outline of the physics, with the details left to later sections.

In Si/SiGe quantum wells, the degenerate $\pm z$ valleys are separated in the first Brillouin zone by the wavevector $2k_0$, as indicated schematically in the inset of Fig. 5.2(c). The degeneracy of the valley states is lifted in a process known as 'valley splitting,' which occurs

when the quantum well confinement potential, determined by the Ge concentration profile, has Fourier components at this special wavevector. More precisely, effective-mass theory states that the valley splitting energy E_v is proportional to the Fourier transform of the quantum well potential, weighted by the dot probability density $|\psi(\mathbf{r})|^2$, evaluated at the wavevector $2k_0$. We call this the '$2k_0$ theory.'

This simple description of valley splitting has wide-ranging explanatory power, which is both qualitative and quantitative. For example, it is the basis for the short-period Wiggle Well [59, 124], which exploits heterostructures where the $2k_0$ wavevector is intentionally engineered into the quantum well. It further explains how other engineered sharp features in the confinement potential, such as sharp interfaces or Ge spikes, can enhance E_v. In the latter case, sharp features in real space produce broad Fourier spectra in k space, including components at the wavevector $2k_0$. The $2k_0$ theory also explains the random effects of alloy disorder. Here, since the heterostructure is composed of individual atoms, there will be fluctuations of the Ge concentration from layer to layer inside a finite-size dot. These random fluctuations alter the confinement potential slightly at each layer, creating a small random Fourier component at wavevector $2k_0$. Despite being small, we show in this work that such fluctuations accurately predict the wide range of valley splittings observed in recent experiments.

Finally, the $2k_0$ theory also explains the reduction of valley splitting due to interface steps. When steps are present, the z confinement potential naturally varies in different portions of the dot. Averaging over the plane of the quantum well, the step effectively causes the dot to experience a wider interface. The Fourier component of this broadened confinement potential at wavevector $2k_0$ is correspondingly reduced.

To demonstrate the universal nature of the $2k_0$ theory, in Fig. 5.1(f) we show simulation results for several types of engineered heterostructures, including conventional heterostructures with sharp interfaces, heterostructures with Ge spikes, narrow quantum wells, and heterostructures with additional, uniform Ge concentration added to the well. We also in-

clude the effects of disorder in the form of interface steps and random alloys. (Details of the specific geometries and simulations are presented in later Sections.) For each geometry, we perform 100 simulations with different realizations of random alloy, using disorder models that are consistent with atomic-scale characterization based on atom probe tomography [54, 145]. For each simulation, we compute the valley splitting using the $2k_0$ theory (the effective-mass approximation, E_v^{EM}). Then, using the same disorder profiles, we also compute the valley splitting using a two-band tight-binding model, E_v^{TB}, described below. The results show nearly perfect correlations, with all data points falling onto a universal curve. This demonstrates that the same physics governs valley splitting in deterministic vs. random structures, and it validates the $2k_0$ theory.

5.3 Modeling the quantum dot

In this section, we describe the various theoretical approaches used in this work. Our main tools are effective-mass theory [63, 65, 70] and tight-binding theory, including the two-band model of Boykin et al. [27] and the NEMO-3D 20-band sp^{3}d^{5}s* model [93, 94]. Effective-mass theory provides an intuitive understanding of valley splitting behavior in many problems of interest. Although the approach can be applied to more complicated problems [69], analytical applications are most effective for systems than can be reduced, approximately, to one dimension (1D). As we shall see, this includes many problems involving alloy disorder. In this work, we use effective-mass theory to clarify and characterize the distinct types of behavior associated with deterministic vs. randomly dominated valley splitting. For geometries that are intrinsically higher-dimensional, such as those involving atomic steps, tight-binding approaches are more effective. NEMO-3D is a sophisticated tool that provides quantitatively accurate results, over a wide energy range, and makes it possible to include atomistic details and strain. However, NEMO-3D is computationally expensive compared to effective-mass and two-band tight-binding theories. We show here that most valley-splitting physics is

well described by simplified models, and that many problems of interest can be reduced to lower-dimensional systems that are more amenable to simple approaches. We now outline the details of these different methods.

5.3.1 NEMO-3D

The most rigorous model we use to simulate Si/SiGe heterostructures is the 20-band spin-resolved sp^{3}d^{5}s* nearest-neighbour tight-binding model, known as NEMO-3D [93, 94]. Although these simulations are computationally expensive, they are truly atomistic and, therefore, the most physically accurate.

To specify a model geometry, we first define the heterostructure concentration profile, $Si_{\bar{X}_l}Ge_{1-\bar{X}_l}$, in the (nominal) growth direction [001], where $\bar{X}_l \in [0, 1]$ represents the Si concentration averaged over the entire atomic layer, with layer index l. We also use the notation X_l to refer to the Si concentration averaged over just the lateral extent of the dot in layer l, as explained in Appendix D.1. Due to the finite size of the dot, X_l is therefore a gaussian random variable fluctuating about its mean value, $\bar{X}_l$. (Note that we use the notations $Y_l = 1 - X_l$ and $\bar{Y}_l = 1 - \bar{X}_l$ interchangeably, as convenient.) In NEMO-3D, each atom in the lattice must be assigned as Si or Ge. In systems without interface steps, we therefore assign Si atoms in layer l with probability $\bar{X}_l$. In systems with interface steps, this probability also depends on the lateral position of the step (x_{step}) as

$$\bar{X}_l(x, y) = \bar{X}_l\Theta(x \leq x_{\text{step}}) + \bar{X}_{l+1}\Theta(x > x_{\text{step}}), \tag{5.1}$$

where Θ is the Heaviside step function, and we take the concentration profiles to be identical on either side of the step, except for the single-atom shift, $l \to l + 1$. Here, and throughout this work, we use lower-case (x, y) notation to refer to spatial positions and upper-case (X, Y) notation to refer to (Si,Ge) concentrations. Note that atoms in our NEMO-3D simulations are actually located on diamond lattice sites, although we often specify their positions in

continuum notation $\mathbf{r} = (x, y, z)$, for brevity. Also note that we assume the step position in Eq. (5.1) is independent of y, as consistent with a linear step oriented along [010]. This choice is made for convenience, although more nontrivial geometries may also be considered. In this way, we generate realistic 3D lattice geometries consistent with the desired, average heterostructure concentration profile. Repeating this procedure over and over yields disorder realizations that correctly reproduce the statistics of a random alloy.

Several other contributions to on-site energy terms are included in the simulation model. Local bond lengths are incorporated using a strain optimization procedure in a valence-force-field Keating model. A simple, separable lateral confinement potential is used to describe the dot, taking the parabolic form

$$U_{\mathrm{conf}}(x, y) = \frac{1}{2} m_t \omega_{\mathrm{orb}}^2 \left[(x - x_c)^2 + (y - y_c)^2 \right],\tag{5.2}$$

where $m_t \approx 0.19 m_e$ is the transverse effective mass, m_e is the bare mass of the electron, $\hbar \omega_{\mathrm{orb}}$ is the orbital excitation energy, and (x_c, y_c) is the center of the dot. This simple model is chosen for convenience, but is unlikely to affect the qualitative features of our results. We also include a uniform vertical electric field, with the corresponding potential energy $eE_z z$.

Simulations proceed by computing the energy eigenstates and eigenvalues for a given simulation geometry. The valley splitting is obtained as the energy difference between the two lowest valley states. The simulation procedure is then repeated many times, with different realizations of alloy disorder, to build up a distribution of results.

5.3.2 Modeling the quantum well potential

While NEMO-3D allows us to perform accurate, atomistic simulations of quantum dots, it is computationally expensive, making it challenging to accumulate large statistical distributions for characterizing random-alloy disorder. Numerical methods also do not provide the same theoretical guidance as analytical theories. To overcome these problems, we also make use of
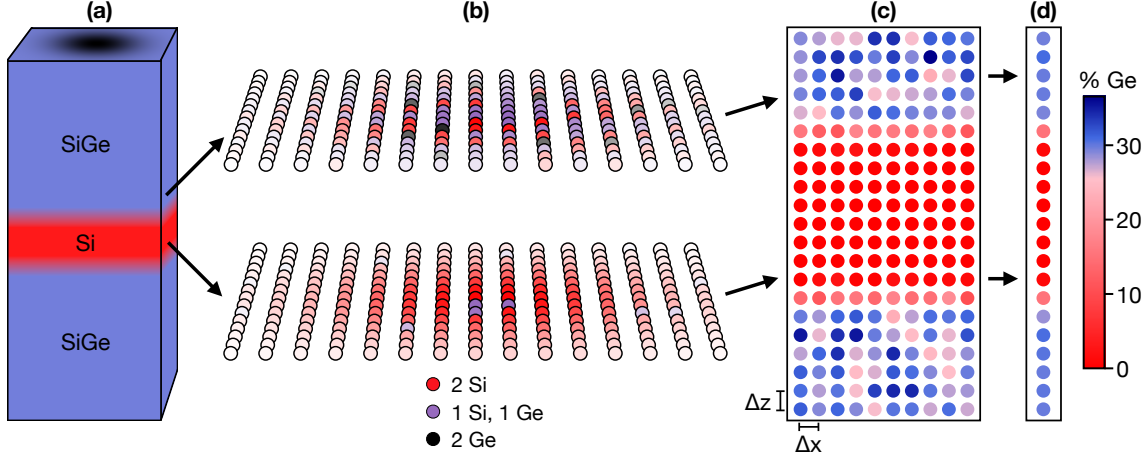
Figure 5.3: Cellular models of alloy disorder in one, two, and three dimensions. High-Ge concentration regions ($\sim 30\%$) are indicated by blue, while low-Ge concentration regions are indicated by red. (a) Schematic illustration of a Si/SiGe quantum well with diffused top and bottom interfaces. The quantum dot is located in the Si quantum well below the dark-shaded region on the top of the illustration. (b) The heterostructure is divided into rectangular 3D cells containing one or more atoms. The illustration shows two layers of cells in the high-Ge (upper) and low-Ge (lower) regions, with color intensities proportional to the wavefunction probability. (c) Effective 2D cell geometry obtained by taking a weighted average of the Ge concentration of the 3D cell geometry along the y axis, as explained in Appendix D.1. The 2D cell dimensions Δx and Δz are indicated, and the corresponding concentration fluctuations are evident. For the minimal tight-binding models used in this work, we choose $\Delta z = a_0/4$ and $\Delta x = a_0/2$, where a_0 is the width of the conventional cubic unit cell. (d) We further obtain an effective 1D cell geometry by taking weighted averages along $\hat{x}$.

minimal tight-binding and effective-mass models. In Appendix D.2, we show that all three approaches yield consistent results. However to facilitate comparisons, we need to define a mapping between the atomistic model used in NEMO-3D, and the other model schemes. This can be done for one, two, or three-dimensional models, although we will focus on 1D and 2D geometries here, taking advantage of their computational efficiency.

The mapping between simulation models uses coarse graining. We first define the notion of 'cells,' which may include one or more atoms. Cells may be defined in one, two, or three dimensions. Cells may also have different sizes; however to correctly describe valley splitting in the tight-binding theory, we require a vertical cell height of one atom [27], $\Delta z = a_0/4$, where $a_0 = 0.543$ nm is the width of the conventional cubic unit cell. Within a given cell,

we employ the virtual-crystal approximation, for which the cell as a whole takes the average properties of the atoms contained within. For a cell located at $\mathbf{r}_{\text{cell}}$, the potential energy describing the heterostructure is given by

$$U_{\text{qw}}(\mathbf{r}_{\text{cell}}) = \Delta E_c \frac{X_{\text{cell}} - X_s}{X_w - X_s}, \tag{5.3}$$

where $X_{\text{cell}} = X(\mathbf{r}_{\text{cell}})$ is the average Si concentration within the cell, X_s is the average Si concentration deep in the SiGe substrate or barrier region, and X_w is the average Si concentration in the center of the quantum well. The conduction-band offset ΔE_c describes the potential energy difference between the barrier region and the quantum well region. For simplicity, we assume the barrier is fully strain-relaxed, and that the strain state of the quantum well is reflected in ΔE_c [164]. Following [145], we model the band offset as

$$\Delta E_c = (X_w - X_s) \left[\frac{X_w}{1 - X_s} \Delta E^{\text{Si}}_{\Delta_2}(X_s) - \frac{1 - X_w}{X_s} \Delta E^{\text{Ge}}_{\Delta_2}(X_s) \right], \tag{5.4}$$

where the functions $\Delta E^{\text{Si(Ge)}}_{\Delta_2}(X)$ correspond to the Δ_2 conduction band offsets for strained Si (Ge) grown on an unstrained $\text{Si}_X\text{Ge}_{1-X}$ substrate, making use of the following linear approximations, which are approximately valid over the concentration range of interest [164]:

$$\Delta E^{\text{Si}}_{\Delta_2}(X) \approx -0.502(1 - X) \text{ (eV)},$$
$$\Delta E^{\text{Ge}}_{\Delta_2}(X) \approx 0.743 - 0.625(1 - X) \text{ (eV)}. \tag{5.5}$$

For certain quantum well geometries, where the vertical confinement along z is much stronger than the lateral confinement, it is a good approximation to treat the total confinement potential as separable [7], such that $U_{\text{total}}(\mathbf{r}) \approx U_{\text{qw}}(z) + U_{\text{conf}}(x, y)$, with the wavefunction given by $\psi(\mathbf{r}) \approx \psi_{xy}(x, y)\psi_z(z)$. When 3D alloy disorder is present, this separable approach requires performing a 2D average over the lateral extent of the dot, in each plane l. The vertical confinement potential is then given by $U_{\text{qw}}(X_l)$, where the physics of the

valleys is contained in the vertical wavefunction $\psi_z(z_l)$. For 1D calculations, the lateral confinement potential and ground-state wavefunction $|\psi_{xy}(x,y)|^2$ still play a role in computing the average Si concentrations X_l, as described in Appendix D.1.

In systems with interface steps, the lateral and vertical wavefunctions are no longer separable. However, if the step is straight and oriented along $\hat{y}$, we can write $\psi(\mathbf{r}) \approx \psi_{xz}(x,z)\psi_y(y)$. Assuming a confinement potential of form $U_{\mathrm{conf}}(y) = \frac{1}{2}m_t\omega_{\mathrm{orb}}^2(y - y_c)^2$, the wavefunction $\psi_y(y)$ is a gaussian, which we use to perform the averaging procedure along $\hat{y}$. Defining the lateral cell index along $\hat{x}$ as j, we then have $X_{\mathrm{cell}} = X_{j,l}$. Here we adopt the lateral cell dimension $\Delta x = a_0/2$. Although this particular choice is not required for Δx, we have found that it gives results consistent with other computational schemes, as described in Appendix D.2. We also note that the averaging procedure described here converts the Si diamond crystal lattice to an effective, rectangular cell structure.

The full averaging procedure is illustrated in Fig. 5.3. A typical Si/SiGe heterostructure is shown in Fig. 5.3(a). Averaging is first performed within individual cells, as shown in Fig. 5.3(b). Here, blue shading indicates dominantly Ge cells, red shading indicates dominantly Si cells, intermediate shading indicates cells with mixed Si-Ge content, and the color intensity indicates the wavefunction probability density, which is used in later steps to obtain weighted averages of the Si-Ge concentrations. Cells with higher Ge concentrations have higher potential energies, as per Eq. (5.3). The wavefunction probability distribution is used to reduce the 3D cell geometry successively to 2D [Fig. 5.3(c)] or 1D [Fig. 5.3(d)] geometries, following the procedure described in Appendix D.1. Figure 5.3 clarifies how the random nature of the original SiGe lattice is transferred to the different cell geometries – through the fractional Ge content. Although these local Ge concentration fluctuations are small, they can ultimately have a strong effect on the valley splitting.

Finally we note that, while it is possible to generate a new atomic lattice for every disorder realization (in fact, this is necessary in NEMO-3D), such 3D procedures are inefficient and unnecessary, since reduced-dimensional cell geometries may also be generated using the

statistical properties of alloy disorder [145]. To do this, we assume the Si concentration in each cell follows a binomial probability distribution with a known mean and variance, as supported by an atomistic analysis of actual Si/SiGe heterostructures using atom probe tomography [145]. For a given cell, with a given dimensionality, the mean of the distribution is given by the expected Si concentration in the cell $\bar{X}_{\text{cell}}$ (for example, based on experimental characterization), and the variance is derived from $\bar{X}_{\text{cell}}$ and the probability density of the quantum dot in the x-y plane. Unless otherwise specified, we use this statistical approach to generate the 1D and 2D cell geometries for the minimal tight-binding and effective-mass calculations described below. Full details of the method are described in Appendix D.1.

5.3.3 Minimal tight-binding model

In this work, we consider a two-band tight-binding model that accounts for physics at the very bottom of the conduction band, including the location of the valley minima $(\pm k_0 \hat{z})$ and the band curvature (i.e., the longitudinal effective mass). For a 1D model geometry oriented along [001], these parameters are given by $k_0 = 0.82 \, (2\pi/a_0)$ and $m_l = 0.916 m_e$. This minimal band structure can be mapped onto a minimal 1D tight-binding model, containing only nearest and next-nearest-neighbor hopping terms [27], given by $t_1 = 0.68$ eV and $t_2 = 0.61$ eV, respectively. For a 2D model geometry in the x-z plane, the valley minima are located at $\mathbf{k}_{0\pm} = (0, \pm k_0)$. In this case, we use the same two hopping parameters along $\hat{z}$, and we include a nearest-neighbor hopping term along $\hat{x}$, $t_3 = -2.72$ eV, which gives the correct transverse effective mass for a cell of width $\Delta x = a_0/2$. We note that this minimal model assumes a rectangular lattice geometry [159], with cells of size $(\Delta x, \Delta z)$.

In addition to the off-diagonal hopping terms, our minimal model Hamiltonian also includes on-site potential terms $U_{\text{total}}(X_{j,l})$, where (j, l) are the 1D-2D cell indices. For 2D geometries, we are particularly interested in comparing the effects of interface steps, defined in Eq. (5.1) and included in the Hamiltonian via Eq. (5.3), to alloy disorder, defined in the coarse-grained cell potentials $U_{\text{qw}}(X_{j,l})$. As for NEMO-3D, the simulations are typically

repeated for many realizations of alloy disorder to obtain statistical distributions of results, as described in Appendix D.1. When alloy disorder is not included in the simulations, we simply replace the locally fluctuating Si concentration $X_{j,l}$ by its average value $\bar{X}_l$.

5.3.4   Effective-mass theory

The effective-mass theory is similar to the minimal tight-binding theory in that it incorporates the physics of the bottom of the conduction band. The most important difference between the two approaches is that valley couplings do not arise naturally in the effective-mass theory, and must be included perturbatively. The perturbation theory is straightforward however [63], and we summarize it here for completeness.

We consider as basis states the quantum dot wavefunctions formed of Bloch states localized near the $\pm k_0 \hat{z}$ valleys in reciprocal space. For our purposes, it is a good approximation to write the real-space expressions for these wavefunctions as

$$\psi_{\pm}(\mathbf{r}) \approx e^{\pm i k_0 z} \psi_{\mathrm{env}}(\mathbf{r}), \tag{5.6}$$

where ψ_{env} is the effective-mass envelope of the ground-state wavefunction in the total confinement potential $U_{\mathrm{total}}(\mathbf{r})$. This approximation assumes weak valley-orbit coupling, so both valley states have the same envelope function. Such perturbative treatment is appropriate for many problems of interest. In the limit of large valley-orbit coupling, Eq. (5.6) should be modified to account for the differing envelope functions in the ground and excited valley states. However the simplicity of Eq. (5.6) provides considerable intuition, as discussed below. We note that the exponential phase term oscillates rapidly in Eq. (5.6), over a length scale of $2\pi/k_0$, while the confinement potential and envelope function vary slowly over this same length scale.

The intervalley-coupling matrix element is given by

$$\Delta = \langle\psi_-|U_{\mathrm{qw}}|\psi_+\rangle = \int dr^3 e^{-2ik_0 z} U_{\mathrm{qw}}(\mathbf{r})|\psi_{\mathrm{env}}(\mathbf{r})|^2, \tag{5.7}$$

and the valley splitting is given by $E_v = 2|\Delta|$. Because of the separation of length scales in Eq. (5.7), we see that Δ and E_v should approximately vanish in the limit of slowly varying $U_{\mathrm{qw}}(\mathbf{r})$. A nonvanishing valley splitting therefore requires some type of sharp feature to be present in the confinement potential. The conventional 'sharp feature' in many valley-spitting proposals is an abrupt quantum well interface.

Although effective-mass equations are conventionally expressed in a continuum description, they may also be discretized; here, such an approach helps to make contact with the tight-binding theories discussed in previous sections. We may consider 1D or 2D expressions for the intervalley matrix element:

$$\Delta_{\mathrm{1D}} = \frac{a_0}{4}\sum_l e^{-2ik_0 z_l} U_{\mathrm{qw}}(z_l)|\psi_{\mathrm{env}}(z_l)|^2, \tag{5.8}$$

$$\Delta_{\mathrm{2D}} = \frac{a_0}{4}\sum_l e^{-2ik_0 z_l}\frac{a_0}{2}\sum_j U_{\mathrm{qw}}^{\mathrm{2D}}(x_j, z_l)|\psi_{\mathrm{env}}(x_j, z_l)|^2, \tag{5.9}$$

where (j, l) are cell indices corresponding to $X_{j,l}$ in the tight binding theories, and we assume proper normalization, given by $\sum_l (a_0/4)|\psi_{\mathrm{env}}(z_l)|^2 = \sum_{j,l}(a_0^2/8)|\psi_{\mathrm{env}}(x_j, z_l)|^2 = 1$.

A key, take-away message from Eq. (5.7) is that the valley splitting can be understood, quite literally, as the $2k_0$ Fourier component (along k_z) of the quantity $U_{\mathrm{qw}}(\mathbf{r})|\psi_{\mathrm{env}}(\mathbf{r})|^2$. More simply, it is the $2k_0$ Fourier component of $U_{\mathrm{qw}}(\mathbf{r})$, weighted by the electron probability at the location where the oscillations occur. This is a powerful statement that transcends effective-mass theory. As we demonstrate in this work, such a universal description of valley splitting is quantitatively accurate for all quantum well geometries studied here, including interface steps, broadened interfaces, alloy disorder, Wiggle Wells, and other phenomena.

5.3.5 Alloy-disorder analysis

In this section, we use effective-mass methods to characterize the deterministic vs. random components of the valley splitting using an approach similar to Ref. [145], for effectively 1D geometries. Figures 5.2(a) and 5.2(d) show typical concentration fluctuations in quantum wells with wide or narrow interfaces, respectively. Below, we show that, even when Si concentrations vary only slightly from their average values, as in these examples, such small fluctuations can have an outsize effect on the valley splitting.

The intervalley coupling matrix element in Eq. (5.8) can be decomposed into its deterministic (Δ_0) and fluctuating ($\delta\Delta$) components: $\Delta_{1D} = \Delta_0 + \delta\Delta$. This assignment is unambiguous when the Si concentration in layer l, defined as $X_l = \bar{X}_l + \delta_l$, can be decomposed into its average ($\bar{X}_l$) and fluctuating (δ_l) contributions. The deterministic part of the valley splitting, $E_{v0} = 2|\Delta_0|$, is determined by the average heterostructure profile, including geometrical features like interface steps. It is computed by setting $\delta_l = 0$ in all layers. Substituting Eq. (5.3) into Eq. (5.8), we obtain

$$\Delta_0 = \frac{a_0}{4}\frac{\Delta E_c}{X_w - X_s}\sum_l e^{-2ik_0 z_l}(\bar{X}_l - X_s)|\psi_{\text{env}}(z_l)|^2. \tag{5.10}$$

The random component of the intervalley matrix element, $\delta\Delta$, arises from the alloy disorder, and is given by

$$\delta\Delta = \frac{a_0}{4}\frac{\Delta E_c}{X_w - X_s}\sum_l e^{-2ik_0 z_l}\delta_l|\psi_{\text{env}}(z_l)|^2. \tag{5.11}$$

Here, the fluctuations are contained within $\delta_l = X_l - \bar{X}_l$, which describes the concentration variations in layer l weighted by the dot probability. Since SiGe is a completely random alloy, δ_l has a binomial probability distribution, given by

$$\delta_l \sim \frac{1}{N_{\text{eff}}}\text{Binom}(N_{\text{eff}}, \bar{X}_l) \tag{5.12}$$

where $N_{\mathrm{eff}} = 4\pi a_{\mathrm{dot}}^2/a_0^2$ is the approximate number of atoms in a dot, in a given layer, and we have assumed a circular quantum dot as defined in Eq. (5.2), with orbital excitation energy $\hbar\omega_{\mathrm{orb}}$ and characteristic size $a_{\mathrm{dot}} = \sqrt{\hbar/m_t\omega_{\mathrm{orb}}}$. See Appendix D.1 for further details on the derivation of Eq. (5.12)

The individual amplitudes $\delta_l|\psi_{\mathrm{env}}(z_l)|^2$ contributing to the sum in Eq. (5.11) are plotted in Figs. 5.2(b) and 5.2(e), for the same disorder realizations shown in Figs. 5.2(a) and 5.2(d). Here, the complex phase, $-2k_0z_l$, is also indicated by the color scale. In both figures, we see that amplitudes are maximized when the wavefunction strongly overlaps with Ge. For the wide-interface geometry in Fig. 5.2(b), we find that many layers contribute significantly to the sum, while for the narrow interface shown in Fig. 5.2(e), only a few layers contribute. The total intervalley coupling Δ is therefore complex, with a large random component determined by the details of the Ge distribution. Figure 5.2(g) shows the resulting distribution of Δ values in the complex plane, for many different realizations of the alloy disorder, corresponding to the wide (purple) or narrow (gold) interfaces. The black dots indicate the deterministic components Δ_0, which are generally located at the center of the distributions. For wide interfaces, we see that $|\Delta_0|$ can be much smaller than the standard deviation of $|\Delta|$. For narrow interfaces, on the other hand, $|\Delta_0|$ can be large enough for all Δ results to be well separated from the origin. However, we note that the interface is extremely sharp in this example, with an average width of just 1 atomic monolayer (ML).

This effective-mass description of alloy disorder agrees very well with tight-binding simulations. Figure 5.2(h) shows a correlation plot of effective-mass results E_v^{EM}, obtained from Eq. (5.8), vs. tight-binding results E_v^{TB}, obtained for the same disorder realizations. The correlations between these independent methods is nearly perfect for both the purple and gold data sets in Fig. 5.2(h), emphasizing the accuracy of this analytic interpretation.
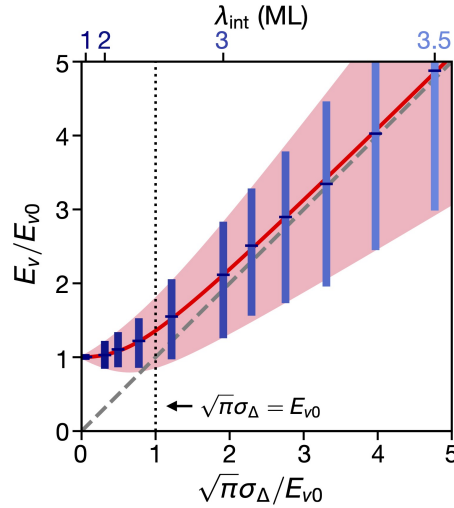
Figure 5.4: Universal crossover between deterministically and randomly dominated valley splittings, in the presence of alloy disorder. 1D effective-mass simulations are performed, using sigmoidal Ge profiles, as a function of interface width λ_{int} (top axis). 500 simulations are performed at each λ_{int} value, with 25-75 percentiles shown as vertical bars. The mean valley splittings $\bar{E}_v$ are shown as crossbars and corresponding standard deviations σ_Δ (bottom axis) are obtained from Eq. (5.13). The two energy axes are normalized by the deterministic valley splitting E_{v0}, resulting in an asymptote of $E_v/E_{v0} = 1$ in the low-σ_Δ limit, a slope of 1 in the high-σ_Δ limit, and a well-defined crossover between the two regimes at $\sqrt{\pi}\sigma_\Delta = E_{v0}$ (vertical dotted line). The red curve shows the theoretical estimate for $\bar{E}_v$, obtained from the Rician distribution in Eq. (5.15), taking E_{v0} and σ_Δ as inputs from the effective-mass simulations. The pink shaded region shows the corresponding 25-75 percentile range for the Rician distribution, which closely matches the simulation results. For all results, we assume dots with orbital splittings of $\hbar\omega_{\text{orb}} = 2$ meV, vertical electric fields of $E_z = 5$ mV/nm, and well widths of $W = 80$ ML.

5.3.6 Statistical properties of E_v

To characterize the statistical properties of Δ in the presence of alloy disorder, we first consider the case with no interface steps. From Eq. (5.11) we see that, since $\bar{\delta}_l = \mathrm{E}[\delta_l] = 0$, we must have $\mathrm{E}[\Delta] = \Delta_0$. Following [145] to compute the variance of Eq. (5.11), we then obtain

$$\sigma_\Delta^2 = \mathrm{Var}\,[\Delta] = \mathrm{Var}\,[\delta\Delta] = \frac{1}{\pi}\left[\frac{a_0^2 \Delta E_c}{8a_{\mathrm{dot}}(X_w - X_s)}\right]^2 \sum_l |\psi_{\mathrm{env}}(z_l)|^4 \bar{X}_l(1 - \bar{X}_l), \qquad (5.13)$$

where σ_Δ is the standard deviation of the Δ distribution, and we have used the fact that concentrations fluctuations in different layers are statistically independent.

If many atomic layers contribute to the sum in Eq. (5.8), then according to the central limit theorem, we can approximate the intervalley coupling Δ as a circular gaussian random variable centered at Δ_0, for which the variances of the real and imaginary parts of Δ are both $(1/2)\mathrm{Var}\,[\Delta]$. This approximation should be accurate for quantum wells with wide interfaces. For structures with very sharp interfaces, the sum in Eq. (5.8) may be dominated by just a few layers, as in Fig. 5.2(e). In this case, the central limit theorem is less accurate, and Δ may have a non-circular distribution. Nonetheless, the approximation provides reasonable estimates, even in cases where it is not well justified, and we adopt it in all cases below.

The valley splitting $E_v = 2|\Delta|$ is real. For a circular gaussian distribution of Δ values, the corresponding E_v probability distribution is Rician [5], defined as

$$f_{\mathrm{Rice}}(z|\nu, \sigma) = \frac{z}{\sigma^2} \exp\left(-\frac{z^2 + \nu^2}{2\sigma^2}\right) I_0\left(\frac{z\nu}{\sigma^2}\right), \qquad (5.14)$$

where $I_0(y)$ is a modified Bessel function of the first kind. Here, the 'center' parameter is given by $\nu = E_{v0} = 2|\Delta_0|$, and the 'width' parameter is given by $\sigma = \sqrt{2}\sigma_\Delta$. To illustrate valley splitting distributions in different limiting regimes, the tight-binding results from Fig. 5.2(h) are replotted in histogram form in Fig. 5.2(i). Here we also plot the corresponding

Rician distributions, using the parameters $E_{v0} = 2|\Delta_0|$ and σ_Δ computed in Eqs. (5.10) and (5.13). For quantum wells with wide interfaces (purple data), the predicted distributions show excellent agreement with the simulations. For wells with narrow interfaces (gold data), the Rician distribution is somewhat skewed, since the distribution of Δ is no longer perfectly circular, and the central limit theorem is less-well-satisfied. However, the Rician model still provides a reasonable estimate of the results.

We may therefore use the known properties of the Rician distribution to characterize the statistical properties of the valley splitting in the presence of disorder. The mean valley splitting is thus given by

$$\bar{E}_v = \sigma\sqrt{\pi/2}L_{1/2}(-\nu^2/2\sigma^2), \tag{5.15}$$

where $L_{1/2}(x)$ is a Laguerre polynomial [5]. In the randomly dominated regime, corresponding to $\nu \ll \sigma$ (or $|\Delta_0| \ll \sigma_\Delta$), the Rice distribution reduces to a Rayleigh distribution with $\Delta \approx \delta\Delta$ and $\bar{E}_v \approx \sqrt{\pi}\sigma_\Delta(1 + E_{v0}^2/8\sigma_\Delta^2)$. Since $\text{Var}[\Delta] = \sigma_\Delta^2$ is approximately proportional to the average Ge in the quantum well, given by Y_l in layer l, we see that the mean valley splitting can be increased by simply exposing the wavefunction to more Ge. This is an important result. In contrast, the deterministic correction to $\bar{E}_v$ (the second term in the Rayleigh expression) is proportional to $(E_{v0}/\sigma_\Delta)^2$, which has almost no effect on the valley splitting. In the opposite limit, $\nu \gg \sigma$ (or $|\Delta_0| \gg \sigma_\Delta$), the mean valley splitting is simply given by $\bar{E}_v \approx E_{v0}$. This is the expected result in the deterministically enhanced regime.

We now examine the crossover between deterministic and randomly dominated behaviors. In Fig. 5.4, we plot the total valley splitting E_v, including both deterministic and random contributions (normalized by the deterministic value, E_{v0}) as a function of the standard deviation, $\sqrt{\pi}\sigma_\Delta$ (also normalized by E_{v0}). Results are obtained from effective-mass calculations, including 500 realizations of alloy disorder. Here, the blue bars represent the 25-75 percentile range, and the crossbars indicate the mean value. The solid red line shows the Rician estimate, and the pink shading represents the corresponding 25-75 percentiles of the Rice distribution. The asymptotic behaviors derived above are then shown as the dashed
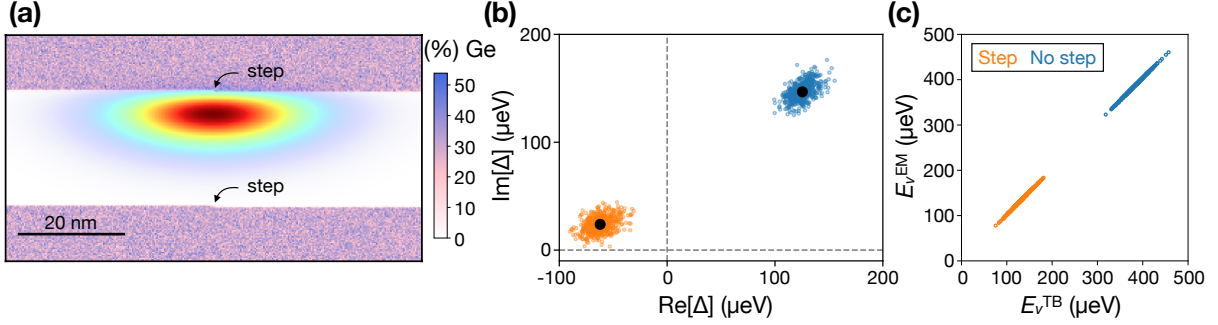
Figure 5.5: Effects of interface steps on the valley splitting for a super-sharp interface. (a) A typical 2D cell geometry and corresponding 2D envelope function, obtained in a quantum well with a single-atom step located at the center of the quantum dot confinement potential along $\hat{x}$. (b) Δ distributions obtained from Eq. (5.9), plotted on the complex plane, for 500 random-alloy realizations of the geometry shown in (a) (orange). We adopt the sigmoidal model of Eq. (5.21) for the quantum well Ge profile, with $X_s = 0.7$ and $X_w = 1$, and an interface width of $\lambda_{\mathrm{int}} = 4\tau = 1$ ML. The 2D envelope function is recomputed for each simulation, taking into account the concentration fluctuations, and we assume a vertical electric field of $E_z = 5$ mV/nm and an isotropic harmonic confinement potential of strength $\hbar\omega_{\mathrm{orb}} = 2$ meV. Blue points show results for the same geometry, but in the absence of steps. The central black points correspond to Δ_0 for each distribution. For such sharp interfaces, the presence of a step suppresses the average valley splitting by a factor of 3-4, although it has little effect on the standard deviation of the distribution. It is interesting to note that, despite being strongly suppressed, the valley splitting remains in the deterministically enhanced regime, even in the presence of a step, for the case of a super-sharp interface. (c) Correlation plot of the effective-mass valley splitting results, $E_v^{\mathrm{EM}} = 2|\Delta|$, taken from (b), vs. 2D tight-binding results obtained for the same 2D cell geometries and disorder realizations, demonstrating nearly perfect agreement. The results show that the $2k_0$ theory of valley splitting also holds for step disorder.

gray line (randomly dominated regime) and the constant value $E_v/E_{v0} = 1$ (deterministically enhanced regime). We can identify the crossover between these two regimes as

$$E_{v0} \approx \sqrt{\pi}\sigma_\Delta. \tag{5.16}$$

In practice, the crossover appears abrupt, with the deterministic valley splitting quickly becoming overwhelmed by disorder as the wavefunction is exposed to more Ge.

5.3.7 Device failure analysis

For qubit applications, a key outcome of our analysis is that valley splitting distributions exhibit qualitatively different behaviors, depending on whether they fall into the deterministically enhanced vs. disorder-dominated regimes. In general, robust qubit operations require valley splittings that are reliably large, so that excited valley states do not compete with spins as qubits, and do not interfere with spin-qubit dynamics. To form large and uniform arrays of qubits, we must therefore ensure that all quantum dots have valley splittings above a specified threshold energy value, E_v^{min}. Throughout this work, we adopt the threshold value of $E_v^{\mathrm{min}} = 100$ μeV, which corresponds to 1.2 K, or about $10\times$ the typical electron temperature in a dilution refrigerator.

We may then ask the question, what fraction of dots fail according to this criterion? For the Rice distribution, this fraction is given by

$$P_{\mathrm{fail}} = \int_0^{E_v^{\mathrm{min}}} dE\, f_{\mathrm{Rice}}(E \mid E_{v0}, \sqrt{2}\sigma_\Delta). \tag{5.17}$$

In the disorder-dominated regime ($\sigma_\Delta \gg E_{v0}$), we find that

$$P_{\mathrm{fail}} \approx 1 - \exp\left(-E_v^{\mathrm{min}2}/4\sigma_\Delta^2\right) \qquad \text{(disordered)}. \tag{5.18}$$

If we further assume that $E_v^{\mathrm{min}} > \sigma_\Delta$, as is often true for wide-interface heterostructures, we find $P_{\mathrm{fail}} \sim O(1)$. On the other hand, if we assume that $E_v^{\mathrm{min}} \lesssim \sigma_\Delta$, as found in some high-disorder heterostructures, we obtain the power law behavior

$$P_{\mathrm{fail}} \approx \left(E_v^{\mathrm{min}}/2\sigma_\Delta\right)^2 \qquad \text{(disordered)}. \tag{5.19}$$

In either case, the failure rate is found to be unacceptably high. In the deterministically

enhanced regime ($\sigma_\Delta \ll E_{v0}$), on the other hand, the failure rate is exponentially suppressed:

$$P_{\text{fail}} \propto \exp\left(-E_{v0}^2/4\sigma_\Delta^2\right) \qquad \text{(deterministic)}. \qquad (5.20)$$

In this case, it is possible that no qubits have unacceptably low valley splittings, even in large arrays. Taking an example: for a dot with the same parameters as Fig. 5.2, and a 1 ML interface width, we obtain $E_{v0} \approx 386$ μeV, $\sigma_\Delta \approx 12$ μeV, and $P_{\text{fail}} \approx 10^{-61}$, which is extremely small. However, P_{fail} also increases extremely quickly with interface width. For example, for a 2 ML interface with all other parameters unchanged, we obtain $E_{v0} \approx 79$ μeV, $\sigma_\Delta \approx 14$ μeV, and $P_{\text{fail}} \approx 0.82$. So even though 2 ML interfaces fall into the deterministically enhanced regime ($E_{v0} \gtrsim \sigma_\Delta$), since $E_{v0} < E_v^{\text{min}}$, P_{fail} can still be large. In recent experiments where quantum wells were found to have sigmoidal interfaces of width $\lambda_{\text{int}} = 0.8$ nm [145], the measured 100 μeV failure rate was found to be $\sim 50\%$. For the E_z and $\hbar\omega_{\text{orb}}$ values reported in that work, we predict a similar value of 62%, while for the $E_z = 5$ mV/nm, $\hbar\omega_{\text{orb}} = 2$ meV parameters used elsewhere in this work, we predict $P_{\text{fail}} = 99\%$. Finally we note that valley splitting distributions are not perfectly Rician when interfaces are very narrow, so the estimates given above are rough. However, these results highlight the fact that E_v can be consistently large in the deterministically enhanced regime, although this requires extremely sharp heterostructure features.

5.3.8   Interface steps

Si/SiGe heterostructures are grown on surfaces that may be intentionally miscut away from the [001] crystallographic axis, resulting in single-atom steps at all device interfaces. Steps may also arise as a consequence of strain or other natural fluctuations, which are very difficult to control at the single-atom level. Such steps are known to significantly effect the valley splitting, and are therefore very well-studied [51, 57, 64, 81, 82, 92, 183, 184]. Reductions in E_v of up to 75% for a single step have been reported theoretically, depending on the

particular step geometry, location, and other dot parameters.

The effective-mass description of valley splitting, developed in preceding sections, also applies to devices with steps. In this case, we use the 2D intervalley matrix element, Eq. (5.9). This requires first calculating the 2D envelope function $\psi(x, z)$, which we do by solving a discretized Schrödinger equation on a grid of cells, in the absence of valleys, while including alloy disorder. Figure 5.5(a) shows a typical envelope solution for the case where a step is located at the center of the quantum dot confinement potential. In Fig. 5.5(b), we show the complex Δ distributions obtained for cases with (orange) and without (blue) single-atom steps, again located at the center of the quantum dot confinement potential. In each case, the effective-mass results are obtained for 500 different disorder realizations. As we might expect, the step significantly reduces the central value of the distribution, $|\Delta_0|$, in this case, by a factor of 3-4. This particular geometry, with the step centered on the dot, is found to be a worst-case scenario for suppressing the valley splitting, although we do not consider other step geometries here. It is interesting to note however that the variances of the two distributions in Fig. 5.5(a) are nearly identical. This can be understood from the fact that the variance in Eq. (5.13) depends on quantities that vary slowly in space, such as $\psi_{\text{env}}(\mathbf{r})$ and $\bar{X}_l$. In other words, the statistical properties of the valley splitting depend on the local Ge concentration, and are not particularly sensitive to the presence of steps. It is also interesting to note that the valley splitting remains in the deterministically enhanced regime, $|\Delta_0| \gtrsim \sigma_\Delta$, even in the presence of a step, when the interface is very sharp. Below, we will show that this is no longer true for wider interfaces.

Figure 5.5(c) shows a correlation plot comparing effective-mass and tight-binding results for cell geometries and confinement parameters identical to those used in Fig. 5.5(b). Similar to Fig. 5.2(h), we observe nearly perfect correlations, including cases with and without a step. This demonstrates that the universal $2k_0$ theory of valley splitting also captures the effects of interface steps. In the following section, we explore the interplay between steps and alloy disorder more thoroughly.

5.4 Conventional Si/SiGe heterostructures

In this section, we use the theoretical tools developed above to analyze conventional Si/SiGe heterostructures. First, we more thoroughly explore the interplay between alloy disorder, interface width, and interface steps. In particular, we show that for devices with realistically broadened interfaces, step disorder is less important than alloy disorder. We then show how alloy disorder and step disorder impact the variability of valley splitting across a device. Finally, we use theoretical and numerical approaches to study how the specific profile of an interface affects its valley splitting.

5.4.1 Interplay between interface steps and interface width

(a) **(b)** **(c)**

(d) λ_{int} = 0.14 nm **(e)** λ_{int} = 1.36 nm **(f)** λ_{int} = 2.72 nm

(g) λ_{int} = 0.14 nm **(h)** λ_{int} = 1.36 nm **(i)** λ_{int} = 2.72 nm
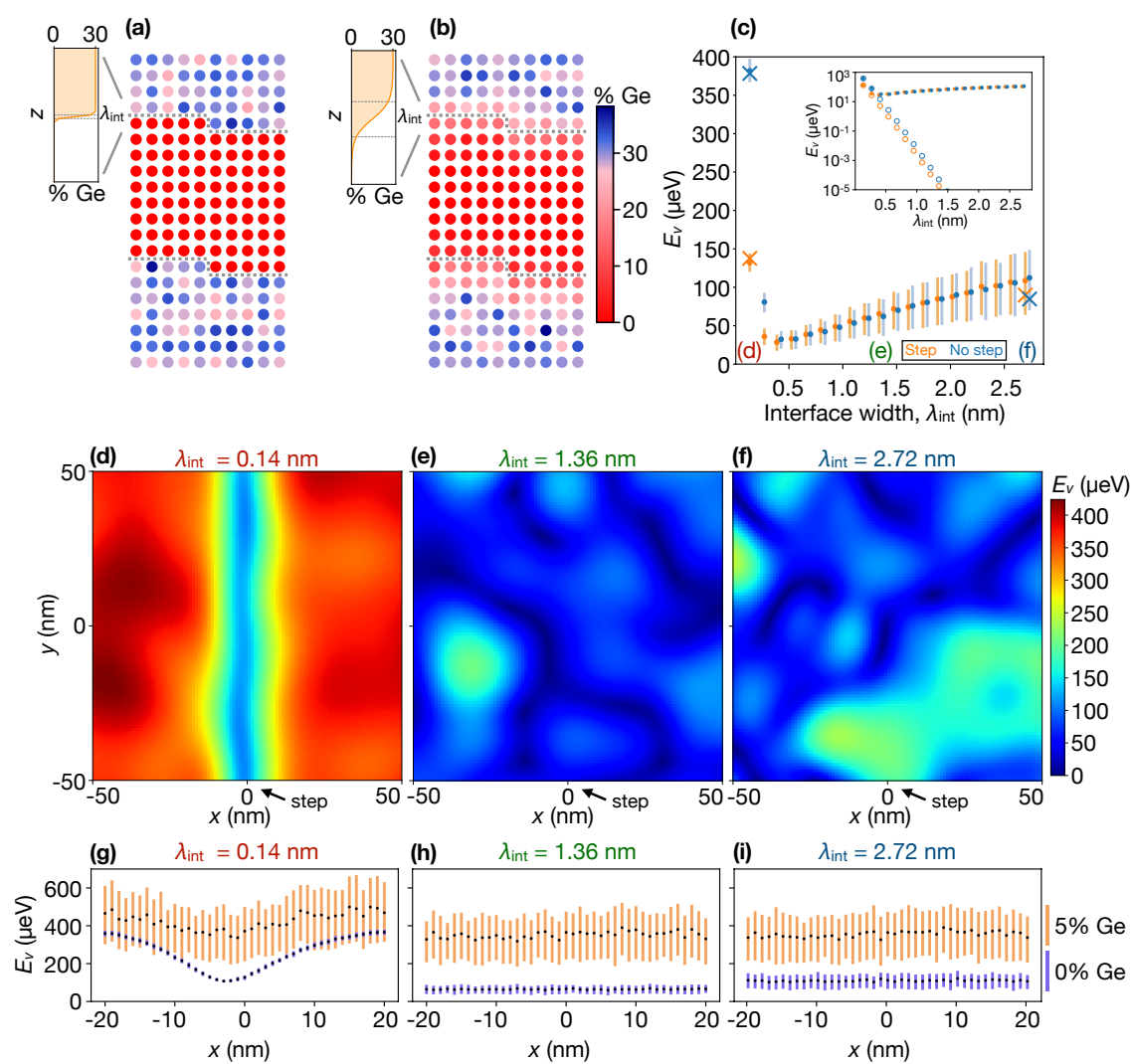
Figure 5.6 *(previous page)*: Interplay between interface step disorder and random alloy disorder. (a), (b) Schematic illustrations of 2D tight-binding models for quantum wells with (a) sharp interfaces, or (b) wider interfaces, in the presence of a single-atom step through the center of the device. Here interfaces are modelled as sigmoid functions [Eq. (5.21)] with a characteristic width of λ_{int}, as indicated by dotted lines in the insets. Quantum dots are modelled as in Eq. (5.3), with orbital energy splittings of $\hbar\omega_{\text{orb}} = 2$ meV, and a vertical electric field of $E_z = 5$ mV/nm. (c) Valley-splitting results are shown for the case of no steps at the interface (blue), or a single-atom step going through the center of the quantum dot (orange), as a function of the interface width. Circular markers show the mean values for 1,000 different alloy-disorder realizations, while error bars show the 25-75 percentile range. Inset: filled circles shown the same mean values plotted in the main panel. Open circles show the results of similar simulations, performed without alloy disorder. (d)-(f) Valley splittings as a function of dot position, in quantum wells with alloy disorder and a single-atom step at the quantum well interface, located at $x = 0$. The only difference between the three maps is the interface thickness, as indicated at the top of each panel. (g)-(i) Valley splitting results as a function of dot position, as the dot is moved across a step located at $x = 0$. Here, interface widths are the same as in (d)-(f), but the simulations are repeated for 200 realizations of alloy disorder, with circular markers showing the mean values, and error bars showing the 25-75 percentiles. Blue data: the same interface/step geometries as (d)-(f), with no additional Ge in the quantum well. Orange data: the same interface/step geometries as (d)-(f), with an average uniform concentration of 5% Ge added to the quantum well. For the orange data, we use Ge barrier concentrations of 35%, to maintain a 30% concentration offset between the barriers and the quantum well. (All other simulations, without Ge in the quantum well, use Ge barrier concentrations of 30%.)

Here we use the 2D minimal tight-binding model to explore the interplay between interface steps and interface widths on the valley splitting. We choose a smooth quantum well confinement potential defined in terms of sigmoid functions, as

$$\bar{X}(z) = X_w + \frac{X_s - X_w}{1 + \exp[(z - z_t)/\tau]} + \frac{X_s - X_w}{1 + \exp[(z_b - z)/\tau]}, \tag{5.21}$$

where we adopt the convention that $z = 0$ at the top surface of the sample, and $z > 0$ inside the sample, including in the quantum well. Here, z_t and z_b are the positions of the top and bottom interfaces of the quantum well, with $z_b - z_t = W$, and the interface width is given by $\lambda_{\text{int}} = 4\tau$. In cases with narrow interfaces, we choose z_t and z_b to lie halfway between atom sites. Steps may be included by inserting Eq. (5.21) into Eq. (5.1), with

$\bar{X}_l(x,y) = \bar{X}(x, y, z_l)$. Some typical narrow and wide-interface geometries are illustrated schematically in Figs. 5.6(a) and 5.6(b). The quantum dots are confined laterally using Eq. (5.2). Here and throughout this section, we choose the orbital excitation energy to be $\hbar\omega_{\mathrm{orb}} = 2$ meV. To reduce the 3D cell geometry to 2D, we assume the step is oriented along $\hat{y}$. As described in Sec. 5.3.2, we are then able consider a separable wavefunction, with $\psi_y(y)$ being the ground state of a harmonic oscillator along $\hat{y}$, also adopting a confinement potential with $\hbar\omega_{\mathrm{orb}} = 2$ meV. We finally take a weighted average of the Si concentration fluctuations along $\hat{y}$ for each element of the 2D cell, oriented in the x-z plane. Note that the wavefunction $\psi_y(y)$ is used only in the averaging procedure; the remainder of the 2D simulation is performed using the tight-binding model.

Narrow interfaces

Although it is extremely difficult to grow ultra-sharp interfaces of width 1 ML, or $\lambda_{\mathrm{int}} = 0.14$ nm, this limit is often considered in theoretical calculations. For example, in this limit, the valley coupling can be treated as a δ-function in effective-mass theory [63, 81, 82, 183]. We therefore also begin by considering the ultra-sharp limit here, as illustrated in Fig. 5.6(a). We further consider a $100{\times}100$ nm^2 section of heterostructure in the x-y plane, with a linear step running down the middle of the geometry. Si and Ge atoms are assigned to a 3D cell geometry after determining the average concentration for each cell. We then raster the center position of the dot across the x-y plane, apply the 3D-to-2D cell reduction procedure described above at each location (eliminating the y coordinate), and compute the valley splitting in the x-z plane using the tight-binding theory.

Figure 5.6(d) shows the resulting valley splitting as a function of dot position. Away from the step, because of the sharpness of the interface, we find that E_v can be quite high, typically on the order of 350 μeV or more. Near the step however, E_v is reduced by about 71%. Although there is some variability due to alloy disorder, the step is, without question, the dominant feature in the data. This is consistent with the fact that the ultra-sharp

interface falls within the deterministically enhanced valley-splitting regime. Indeed, using effective-mass theory to solve the the same geometry, we find that $E_{v0} \approx 386 \ \mu$eV (away from the step), while $\sigma_\Delta \approx 12 \ \mu$eV, confirming that $E_{v0} \gg \sigma_\Delta$.

Wide interfaces

Theoretically, it is well known that E_v depends sensitively on the width of the interface and decays quickly for wider interfaces [33]. Figures 5.6(e) and 5.6(f) show results for calculations similar to the previous section, but with interface widths of $\lambda_{\text{int}} = 1.36$ nm or 10 ML in panel (e), and 2.72 nm or 20 ML in panel (f). In contrast to Fig. 5.6(d), the step feature is no longer visible in either of these maps, and the valley splitting variability is fully consistent with alloy disorder. Indeed, for the 10 ML interface, we find that $E_{v0} \approx 5 \times 10^{-5} \ \mu$eV while $\sqrt{\pi}\sigma_\Delta \approx 64 \ \mu$eV, indicating that this quantum well lies deep within the disordered regime: $E_{v0} \ll \sqrt{\pi}\sigma_\Delta$.

We study the crossover between deterministic and disordered behavior in more detail in Fig. 5.6(c). Here in the main panel, we plot the valley splitting as a function of interface width for the case of no step (blue), and when the dot is centered at a step (orange). The markers indicate the mean values obtained from 1,000 minimal-model tight-binding simulations, with different disorder realizations, and the error bars show the 25-75 percentile ranges. For comparison, NEMO-3D simulation results ($\times$ markers) are also shown for several interface widths, averaged over 10 disorder realizations. The data show a distinctive *minimum* in the valley splitting, which occurs at the interface width of 3 ML. The crossover between deterministic and disordered behavior is abrupt, occurring at interface widths of 2-3 ML. The crossover is observed more clearly in the inset, where the filled circles show the same mean values as the main panel, while the open circles show E_{v0} computed in the virtual crystal approximation, where the Ge concentration in a given layer is given by $\bar{Y}_l$. The abrupt divergence of the two data sets between 2-3 ML confirms the crossover location, and clearly demonstrates that alloy disorder has essentially no effect in the deterministically

enhanced regime.

The valley splitting behavior on either side of the crossover is also distinctive. For narrow interfaces, E_v is initially large, dropping precipitously with interface width. As in Fig. 5.5, the step is seen to significantly reduce the valley splitting in both the two-band and NEMO-3D simulations. In the wide-interface regime, the valley splitting is seen to *increase* with interface width, while the error bars also grow. These effects can both be attributed to the increasing exposure to Ge. In this regime, we further note that the difference in E_v for stepped vs. non-stepped heterostructures essentially disappears.

Finally we note that the magnitude and details of the valley splitting depend on the precise shape of the interface. We also explore the relationship between interface widths and shapes in more detail in Sec. 5.4.3.

Effect of steps for very strong alloy disorder

In Fig. 5.6(c), the effects of alloy disorder were found to overwhelm step disorder for increasing levels of Ge in the quantum well. It is possible to explore the effects of even larger Ge concentrations by introducing Ge directly into the quantum well. In Figs. 5.6(g), 5.6(h), and 5.6(i), we show results for geometries similar to Figs. 5.6(d), 5.6(e), and 5.6(f). Here the blue data correspond to the same geometries as panels (d)-(f), with the same interface widths. The orange data correspond to the same geometries, but with an (average) uniform 5% concentration of Ge added to the quantum wells. In both cases, the markers show the mean valley-splitting values, averaged over 200 disorder realizations, and the error bars show the corresponding 25-75 percentile ranges, as the dot is moved across a step located at $x = 0$. For quantum wells with 5% Ge, the random component of the valley splitting is greatly enhanced, as revealed by the size of the error bars. For the narrow interfaces of Fig. 5.6(g), the effect of the step is still (barely) visible for the quantum well with 5% Ge, although it is much less prominent than in the quantum well without Ge. In Figs. 5.6(h) and 5.6(i), the interface seems to have no effect on the valley splitting, while the random fluctuations

(a) No alloy disorder

(b) With alloy disorder
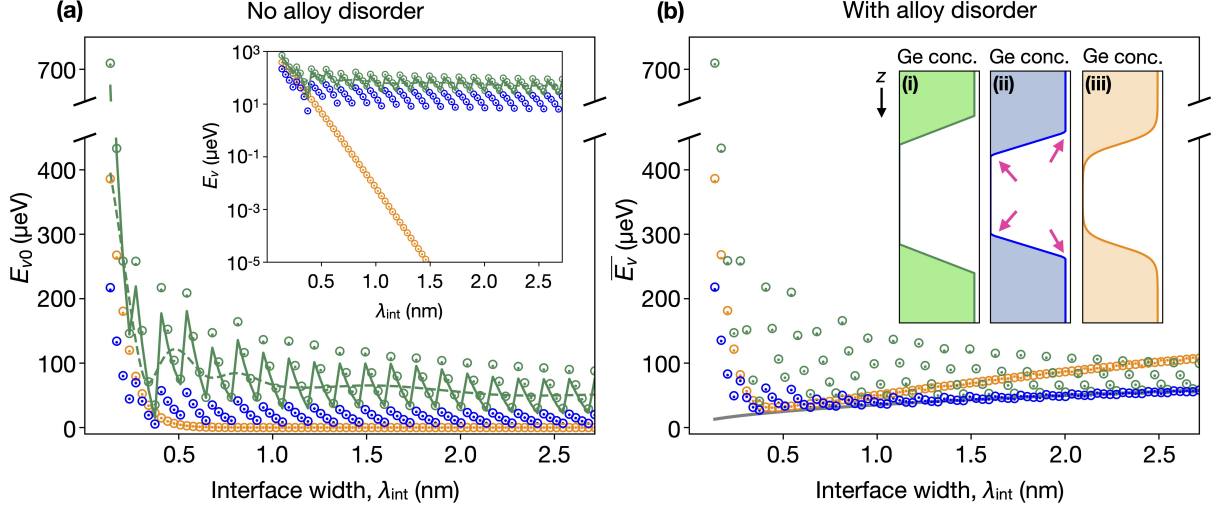
Figure 5.7: Valley splitting (E_v) depends sensitively on the width (λ_{int}) and shape of the interface, and requires alloy disorder to attain realistic results. (a) The deterministic valley splitting E_{v0} as a function of λ_{int}, obtained using the virtual crystal approximation to remove alloy disorder. Results are shown for the three Ge concentration profiles illustrated as insets in (b), with corresponding color coding. Dot markers: minimal tight-binding model. Open circles: effective-mass model. Dashed and solid green lines correspond, respectively, to a continuum variational calculation, Eq. (D.33), and the discretized version of the same calculation. Inset: the same data plotted on a semilog scale. (b) Valley splittings computed for the same geometries as (a), in the presence of alloy disorder. Dot markers: averaged value of 1,000 minimal tight-binding simulations with different disorder realizations. Open circles: averaged effective-mass model, Eq. (5.15). Insets: (i) linear interface of width λ_{int}, (ii) same linear interface with smoothed corners (see main text), (iii) sigmoidal interface of width $4\tau = \lambda_{\text{int}}$. All simulations here assume a vertical electric field of $E = 5$ mV/nm, a wide 200 ML quantum well to ensure that the wavefunction only feels the top interface, and a quantum well Ge concentration offset of $\Delta Y = 30\%$.

dominate. Importantly, we see that adding 5% Ge to the quantum well significantly increases the average valley splitting in all cases. This enhancement represents one of the main results of the present work, and we explore it in further detail in Sec. 5.5.1.

5.4.2 Valley splitting variability

One of the key feature of the valley splitting, apparent in the color maps of Figs. 5.6(d)-5.6(f), is the variability of the valley splitting across a device. In the narrow-interface regime, these variations are dominated by the presence of a step, while for wider interfaces, they are

mainly caused by alloy disorder. In both cases, the variations have a characteristic length scale arising from the self-averaging of the concentration fluctuations by the lateral extent of the quantum dot. The characteristic length scale of the variations is therefore proportional to the dot size, $a_{\mathrm{dot}} = \sqrt{\hbar/m_t\omega_{\mathrm{orb}}}$, which is of order 10-20 nm for typical excitation energies $\hbar\omega_{\mathrm{orb}} \sim 2$ meV assumed here. We therefore expect to observe significant changes in the valley splitting as the dot is moved over these length scales. Such tunability is of great practical interest, and we study it in further detail in Sec. 5.5.1. The ranges of tunability and variability of the valley splitting observed in recent experiments can be quantitatively explained by taking into account the alloy disorder, as we show below.

5.4.3   Effect of interface shape

In Sec. 5.4.1, we compared 1 ML interfaces to wider interfaces, finding that the interface shape significantly affects the valley splitting. Although it is not possible to study all possible interface profiles, we consider three representative cases here, to gain intuition.

The first geometry we consider is the only one used in our simulations so far – the sigmoidal quantum well, defined in Eq. (5.21). [See Fig. 5.7(b)iii. Note that the ultra-sharp interfaces considered in Sec. 5.4.1 were also sigmoidal, with characteristic widths of $\lambda_{\mathrm{int}} = 1$ ML.] The second geometry we consider is the linearly graded interface [Fig. 5.7(b)i]. For this profile, in the ultra-sharp limit, the interface Ge concentration jumps from its minimum value to its maximum value over a single cell width. Below, we also explore a range of linear interfaces with smaller slopes. While such interfaces are more realistic than ultra-sharp interfaces, they possess unphysically sharp corners that induce $2k_0$ components in the Fourier spectrum of $U_{\mathrm{qw}}(z)$, which artificially enhances the valley splitting. To correct this problem, we consider a third geometry [Fig. 5.7(b)ii], which is similar to the linear geometry, but includes a slight rounding of the corners, obtained by averaging the Ge concentration over three successive cell layers: $X_l \to X_l' = (X_{l-1} + X_l + X_{l+1})/3$.

Without alloy disorder

To provide a baseline for analyzing the three model geometries, we first consider the virtual crystal approximation, which does not include alloy disorder (by definition). In the next section, we solve the same geometries while including alloy disorder.

Figure 5.7(a) shows the results of valley-splitting simulations as a function of interface width, in the absence of alloy disorder. We compare the three quantum well profiles, which are color-coded to match the insets of Fig. 5.7(b). We also compare two different calculation methods: the minimal tight-binding model (dots) and effective-mass theory of Eq. (5.8) (open circles). In the latter case, the envelope function ψ_{env} is computed numerically using a Schrödinger equation. The excellent theoretical agreement again demonstrates the validity of the effective-mass approach. For all three geometries, the valley splittings are found to be larger for narrow interfaces, while quickly decreasing for wider interfaces.

Figure 5.7(a) also illustrates the strong dependence of E_v on the shape of the interface. We note that perfectly linear Ge profiles (green data) yield valley splittings that are deterministically enhanced, compared to the other two methods, due to the sharp corners. It is interesting to note that even minimal smoothing of the sharp corners causes a significant reduction of the valley splittings (blue data), compared to the sharp-corner geometry. The more realistic sigmoidal geometry has even lower valley splitting over most of its range (orange data).

The two linear geometries (blue and green) exhibit periodic oscillations, which can be explained as sampling effects, or discreteness of the atoms at the interface. We may confirm this hypothesis analytically as follows. The dashed green line in Fig. 5.7(a) shows the results for a continuum-model variational approximation for E_v, which does not take into account the discreteness of the atoms, and does not correctly reproduce the tight-binding oscillations in Fig. 5.7(a). In contrast, a numerical, but discrete, solution of the same variational model (solid green line), exhibits the same oscillations as the tight-binding results. Details of these calculations are presented in Appendix D.5.

Finally, to make contact with experiments, we consider a sigmoidal interface of width of $\lambda_{\text{int}} \approx 0.8$ nm, as consistent with recent atom probe tomography (APT) measurements [145]. The corresponding valley-splitting estimate, from Fig. 5.7(a), is given by $E_v \approx 0.1$ μeV. This predicted value is much smaller than the average measured value of $\bar{E}_v \approx 42$ μeV, indicating that random-alloy disorder is a key ingredient for understanding the experimental results. A corollary to this statement is that the quantum wells studied in Ref. [145] fall into the disorder-dominated regime, despite having interface widths below 1 nm.

With alloy disorder

Figure 5.7(b) shows the same type of valley-splitting results as Fig. 5.7(a), for the same three quantum well geometries, but now including alloy disorder. Here the sigmoidal results (orange) are the same as in Fig. 5.6(c), where we used the same quantum well geometry. In Fig. 5.7(b), the dot markers show the average of 1,000 minimal tight-binding model simulations, while open circles show effective-mass results from Eq. (5.15), where Δ_0 is taken from Fig. 5.7(a) and σ_Δ is computed in Eq. (5.13). Here again we observe excellent agreement between the two theoretical approaches.

Figures 5.7(a) and 5.7(b) are nearly identical in the deterministically enhanced regime (very low interface widths). This is expected since alloy disorder plays a weak role in this case. In the randomly dominated regime ($\lambda_{\text{int}} \gtrsim 0.4$ nm), the mean valley splitting is enhanced above its deterministic value, similar to results obtained in previous sections. In particular, for the interface width $\lambda_{\text{int}} = 0.8$ nm, we obtain $\bar{E}_v \approx 42$ μeV in the presence of alloy disorder, which is *more than two orders of magnitude higher* than the disorder-free result, and much more in line with experimental measurements [145].

While the valley splitting generally trends downward for large λ_{int} in Fig. 5.7(a), it is interesting to note that the opposite is true in Fig. 5.7(b). This is due to the wavefunction being exposed to higher Ge concentrations, and more disorder, for larger λ_{int}. The effect is especially prominent for the sigmoidal Ge profile. We also observe that the deterministic

enhancement of the valley splitting, due to unphysically sharp corners, persists into the large-λ regime. In this case, the valley splittings closely match those shown in Fig. 5.7(a), when $E_{v0} \approx \bar{E}_v$. Finally, we note that it is possible to derive an analytical estimate for $\bar{E}_v$ in the randomly dominated regime using a variational calculation, as shown by the gray line in Fig. 5.7(b) and explained in Appendix D.5.

5.5   Alternative heterostructures

Moving beyond conventional SiGe/Si/SiGe heterostructures, several alternative schemes have been proposed to boost the valley splitting. In this section, we analyze the performance of such proposals, focusing on the effects of alloy disorder. In Sec. 5.5.1, we consider quantum wells containing a uniform concentration of Ge, as proposed in Ref. [145]. Here we study the dependence of the valley splitting on Ge content and electric field, finding that the extra Ge greatly enhances the valley splitting on average, but also increases the variability. Taking this a step further, we explore how such variability allows for enhanced tuning of the valley splitting in these structures. In Sec. 5.5.2, we study narrow quantum wells and compare our simulation results to the experimental results of Ref. [33], obtaining very good agreement. In Sec. 5.5.3, we explore the effects of a narrow Ge spike centered inside a quantum well [125], focusing on how the spike width affects the valley splitting in the presence of alloy disorder. In Sec. 5.5.4, we comment on the Wiggle Well heterostructure, which contains intentional Ge concentration oscillations with a carefully chosen period [124]. Finally in Sec. 5.5.5, we develop a procedure for determining the optimal Ge profile for a quantum well, to maximize E_v in either the deterministic or disorder-dominated regime.
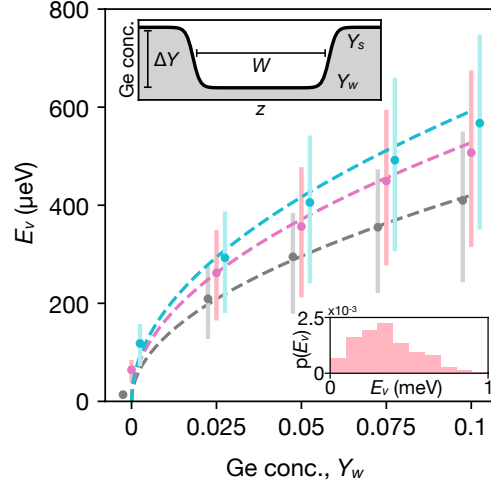
Figure 5.8: Valley splittings as a function of uniform Ge concentration Y_w inside the quantum well for three vertical electric fields: $E_z = 0$ (gray), 5 mV/nm (pink), and 10 mV/nm (blue). Here, the dots indicate mean values, and error bars indicate the 25-75 percentile range, for 1D minimal tight-binding simulations based on 1,000 different disorder realizations. (Blue and gray dots are offset to the left and right, respectively, for clarity.) Dashed lines show theoretical predictions from Eq. (5.23). The simulations assume a dot with an orbital energy splitting of $\hbar\omega_{\mathrm{orb}} = 2$ meV and are performed in a quantum well of width $W = 80$ ML, concentration offset $\Delta Y = 30\%$, and sigmoidal interface of width $\lambda_{\mathrm{int}} = 10$ ML. Top inset: schematic illustration of the quantum well simulation geometry. Bottom inset: valley-splitting distribution results, corresponding to $Y_w = 5\%$ and $E_z = 5$ mV/nm in the main plot.

5.5.1 Uniform Ge in the quantum well

Valley-splitting distributions

In Ref. [145], it was proposed to add a uniform concentration of Ge to the quantum well to significantly increase the random component of the intervalley coupling $\delta\Delta$ and the average valley splitting $\bar{E}_v$. The resulting valley splittings fall deep within the disorder-dominated regime.

Figure 5.8 shows the results of minimal-model tight-binding simulations of the valley splitting, as a function of the uniform Ge concentration Y_w, for vertical electric fields $E_z = 0$ (gray), 5 mV/nm (pink), and 10 mV/nm (blue), in quantum wells of width W as defined in the upper inset. Here we plot the average of 1,000 disorder realization (closed circles), and the corresponding 25-75 percentiles (bars). We see that even a small amount of Ge produces

a large enhancement of the valley splitting, as compared to a conventional, Ge-free quantum well ($Y_w = 0$).

We can approximate the scaling form for the mean valley splitting using $\bar{E}_v \approx \sqrt{\pi}\sigma_\Delta$ in the disorder-dominated regime, where σ_Δ is given in Eq. (5.13), and we adopt a very simple approximation for the envelope function:

$$\psi_{\mathrm{env}}(z) = \begin{cases} \sqrt{2/L_z}\sin\left(\pi z/L_z\right), & (0 \le z \le L_z), \\ 0, & (\text{otherwise}). \end{cases} \tag{5.22}$$

Approximating the sum in Eq. (5.13) as an integral, we obtain the useful scaling relation

$$\bar{E}_v \approx \sqrt{\frac{3}{32}} \frac{a_0^{3/2}}{a_{\mathrm{dot}} L_z^{1/2}} \frac{|\Delta E_c|}{X_w - X_s} \sqrt{X_w(1 - X_w)}, \tag{5.23}$$

where ΔE_c is determined by the quantum well concentration offset, taken to be $\Delta Y = 30\%$ in this section. For the case of no vertical electric field, L_z is given by the physical width of the quantum well, $W = z_t - z_b$, as defined in Eq. (5.21). When the electric field is large enough that the wavefunction does not feel the bottom of the well, the well can be treated as a triangle potential. In this case, a variational calculation using Eq. (5.22) gives

$$L_z \approx \left(\frac{2\hbar^2\pi^2}{eE_z m_l}\right)^{1/3}, \tag{5.24}$$

as described in Appendix D.5. These analytical estimates are shown as dashed lines in Fig. 5.8.

The resulting distribution of tight-binding results is plotted in the lower inset of Fig. 5.8, for the case $Y_w = 0.05$. We note that the distribution takes the characteristic Rician form expected in the disorder-dominated regime, $\sigma_\Delta \gg E_{v0}$, for which the density of states near $E_v = 0$ is nonvanishing. As the Ge concentration increases, the whole distribution moves towards higher energies, and fewer samples have low energies. In the following section, we
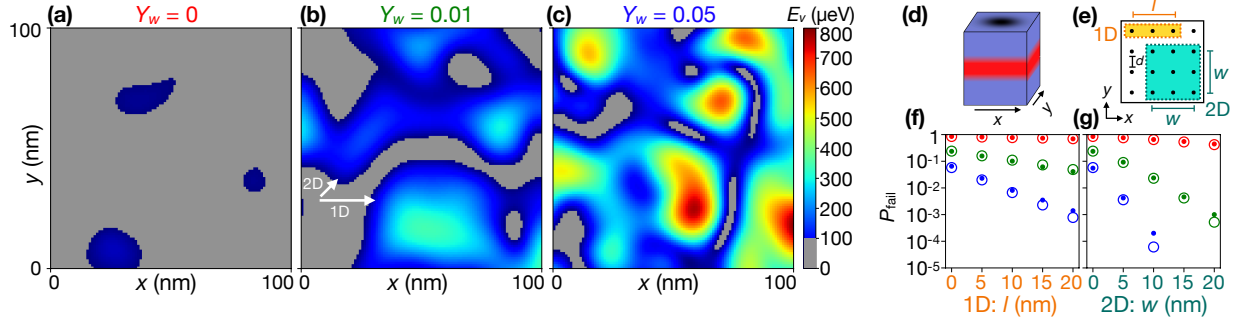
Figure 5.9: Tuning the valley splitting in quantum wells with uniform Ge concentrations. (a)-(c) The valley splitting E_v is computed as a function of the quantum dot center position (x, y), in the presence of alloy disorder. Results are shown for three uniform Ge concentrations inside the quantum well: (a) $Y_w = 0$, (b) $Y_w = 0.01$, and (c) $Y_w = 0.05$. We assume sigmoidal quantum wells with interface widths of $\lambda_{\text{int}} = 10$ ML, quantum well widths of $W = 80$ ML, quantum well offsets $\Delta Y = Y_s - Y_w = 30\%$, and vertical electric fields $E_z = 5$ mV/nm. In the color maps, valley splittings below 100 μeV are considered dangerous for qubit operation, and are shaded gray. (d) Quantum well simulation geometry, with x and y directions labeled. The quantum dot is located in the quantum well, with the density profile indicated by the shading on the top of the device. (e) Schematic illustration of the simulation procedure used to compute the failure probability P_{fail} of finding an acceptable valley splitting (i.e., with $E_v \geq 100$ μeV) when a quantum dot is allowed to explore different locations inside a 1D or 2D search box of size l or w, respectively. (See main text for details.) (f), (g) P_{fail} as a function of search-box size. For simplicity, we only consider quantum dots centered at grid points, with spacing $d = 5$ nm. Red, green, and blue markers show results for heterostructures with average Ge contents of $Y_w = 0$, 0.01, and 0.05, respectively. Solid dots correspond to numerical averages, computed from 10,000 disorder realizations. Open circles show corresponding theoretical results, as computed in Appendix D.4.

explain how to leverage this important result.

Spatial variability and tunability of the valley splitting

As the mean valley splitting increases with Ge concentration, the variability also increases. This can be seen in Figs. 5.9(a)-5.9(c), where the valley splitting is plotted as a function quantum dot position, for three different Ge concentrations. Here, the calculations are performed similarly to Fig. 5.6, although the effective simulation geometry is now reduced to 1D, since there are no interface steps. Regions with dangerously low valley splittings (here defined as $E_v < 100$ μeV) are shaded gray. These gray regions decrease in size as the Ge concentration increases, as consistent with the previous section, while the variability is seen

to increase significantly.

We can take advantage of this behavior by proposing that, when a quantum dot is initially centered at a dangerous location, the gate voltages should be adjusted to change its location. For larger Ge concentrations, such desirable locations are typically found in close proximity. Indeed, dot motion of up to 20 nm has been reported in recent experiments [51, 124], which has in turn been used to explain the large observed variations in valley splitting.

We now study the likelihood of being able to find a nearby 'safe' alloy-disorder configuration, for which $E_v \geq 100$ μeV. We consider two scenarios, illustrated schematically in Figs. 5.9(d) and 5.9(e). In the first case, the dot can be shifted in a single, fixed direction. In the second, the dot can be shifted in either of two directions. To begin, we generate valley-splitting maps, similar to Figs. 5.9(a)-5.9(c), for the same three Ge concentrations. To simplify the search procedure, we divide each map into a 2D grid of points separated by 5 nm, as shown in Fig. 5.9(e). For every grid point initially characterized as 'dangerous' (i.e., with $E_v < 100$ μeV), we search for at least one non-dangerous grid point within a 1D or 2D search box of size l or w, as illustrated in Fig. 5.9(e). Defining P_{fail} as the probability of failure, we repeat this procedure for 10,000 disorder realization and plot the average P_{fail} values in Figs. 5.9(f) and 5.9(g) (dots) as a function of l or w. Analytical results for the same disorder realizations are also shown as open circles, by accounting for the correlations between valley splittings in neighboring sites, as described in Appendix D.4. We see that the ability to search over larger regions greatly enhances the success rate of these procedures, particularly for 2D searches. For larger Ge concentrations, many orders of magnitude of improvement can be achieved in this way.

5.5.2   Narrow quantum wells

It is known from theory and experiment that narrowing a quantum well while keeping other growth and confinement parameters fixed should enhance its valley splitting [26, 63]. For example, in Fig. 5.10 we reproduce the valley-splitting results reported in Ref. [33] (open

circles), where it was found that 3 nm wells have higher valley splittings on average than wider wells. However, significant variability is also observed, and some 3 nm quantum wells are still found to have valley splittings that are dangerously low. Such behavior is in contrast with the deterministic enhancement predicted for narrow wells, but can be fully explained by alloy disorder, noting that the electron wavefunctions are forced to overlap with Ge in the barriers when the quantum wells are very narrow.

To study this behavior, we perform tight-binding simulations of the valley splitting as a function of well width, assuming sigmoidal barriers and a vertical electric field of $E_z = 5$ mV/nm, for the same well widths as Ref. [33]. Similar to theoretical calculations reported in that work, we consider a range of widths for the top interface, while keeping the bottom interface width fixed at 8 ML. In contrast with that work, we include the effects of alloy disorder by performing simulations with 1,000 different disorder realizations for each geometry. We plot our results as 10-90 percentile ranges (gray bars) in Fig. 5.10. Here we only show the results for interface widths of 2 or 3 ML and quantum dot confinement potentials $\hbar\omega_{\mathrm{orb}} = 1.5$ meV, since those values provide excellent agreement with the data, for both the mean valley splitting values and the variability. These results lend strong support for the role of alloy disorder in determining the variability of the valley splitting.

We conclude that valley splittings can be enhanced on average by using narrow quantum wells, due to increased overlap with Ge in the barrier regions. Considering the trends observed in Fig. 5.10, it is interesting to ask whether deterministically enhanced behavior (e.g., exponential suppression of small valley splittings) could potentially be achieved in ultra narrow quantum wells. We can answer this question using the crossover criterion of Eq. (5.16), finding that, for all the results shown in Fig. 5.10, only wells with interface widths of $\lambda_{\mathrm{int}}^{\mathrm{top}} = 2$ ML fall into the deterministically enhanced regime. This is consistent with our more general results for wider quantum wells, showing that deterministic enhancement of the valley splitting still requires super sharp interfaces, and indicates that there is no deterministic advantage in using narrow quantum wells. Finally, by comparing the experimental
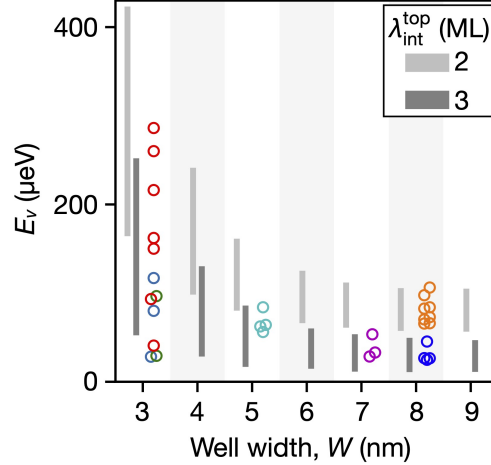
Figure 5.10: Comparison of experimental valley splitting measurements [33] (open circles) to tight-binding simulations with alloy disorder, as a function of quantum well width. Experimental data points with the same color represent quantum dots fabricated on the same chip. Bars indicate the 10-90 percentile ranges of 1,000 1D minimal tight-binding simulations, assuming a relatively sharp top interface of width $\lambda_{\text{int}}^{\text{top}} = 2$ ML (light-gray bars) or 3 ML (dark-gray bars). As in Ref. [33], the bottom interface width is taken to be $\lambda_{\text{int}}^{\text{bot}} = 8$ ML, and we assume an electric field of $E_z = 5$ mV/nm, and an orbital splitting of $\hbar\omega_{\text{orb}} = 1.5$ meV.

and theoretical results in Fig. 5.10, for $W = 3$ nm, we see that the experiments are most consistent with $\lambda_{\text{int}}^{\text{top}} = 3$ ML, whose behavior is randomly dominated. This again emphasizes the difficulty of achieving deterministically enhanced valley splittings.

5.5.3   Ge spike

In Ref. [125], it was shown that a narrow spike of Ge in the quantum well can increase the valley splitting by a factor of two, and theoretical calculations indicate that much larger enhancements are possible. However, alloy disorder was not considered in that work. In this section, we explore the interplay between optimal geometries (single monolayer spikes, which are difficult to grow), realistically diffused geometries, varying spike heights (i.e., the Ge concentrations at the top of the spike), and interface steps, and we include the effects of alloy disorder.

We first consider the case without interface steps. Figures 5.11(a)-5.11(c) show heterostructures with Ge spikes of height $Y_{\text{sp}} = 10$, 20, and 30%, respectively, and their cor-
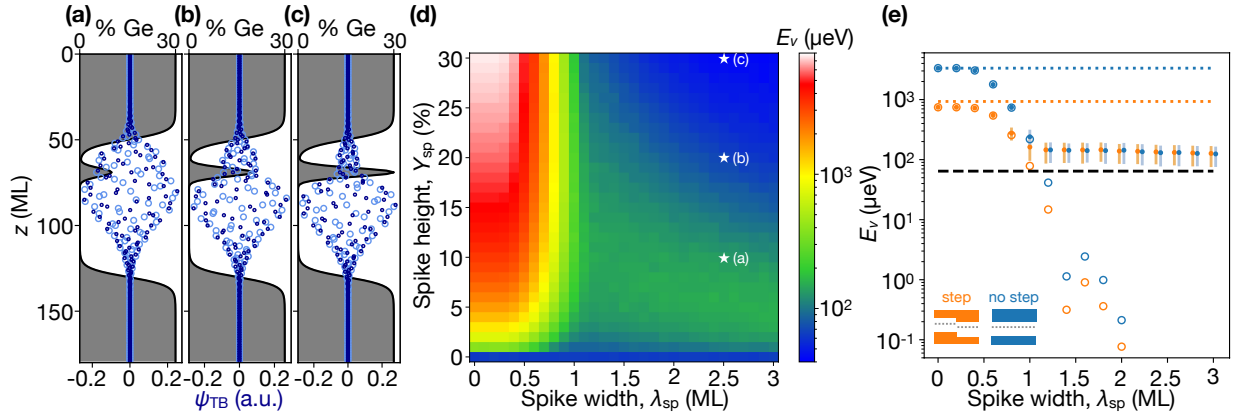
Figure 5.11: Interplay between deterministic and random contributions to the valley split-ting, for the Ge spike geometry. (a)-(c) Ge concentration profiles (gray) for spike geometries of width $\lambda_{sp} = 2.5$ ML and heights $Y_{sp} = 10$, 20, and 30%, respectively. The resulting ground-state (closed circles) and excited-valley state (open circles) tight-binding wavefunctions are also shown. For increasing spike heights, we see that the wavefunction is pushed away from the spike, resulting in lower Ge overlap and lower disorder-enhanced valley splittings. (d) Mean valley splittings (color scale) as a function of spike width λ_{sp} and spike height Y_{sp}. Here, each pixel represents an average of 1,000 1D minimal tight-binding simulations, and the results corresponding to panels (a)-(c) are indicated with stars. (e) Valley splitting as a function of spike width, for a fixed 10% Ge spike height, and a variety of device geometries, including a virtual crystal approximation without alloy disorder (E_{v0}, open circles), and av-eraged results from 1,000 random-alloy simulations ($\bar{E}_v$, closed circles, with 25-75 percentile error bars). In both cases, we consider both step-free geometries (blue), and geometries with a single step through the center of the dot (orange). Here, deterministically enhanced behavior occurs only for very narrow spikes of width < 1 ML, corresponding to a single atom in our model geometry. The black dashed line shows the average valley splitting for the same quantum well as the other simulations, including random alloy, but without the Ge spike. The blue dotted line is the maximum valley splitting, corresponding to a perfect single-atom spike geometry, computed as in Ref. [125] for a spike height of $Y_{sp} = 10\%$. The orange dotted line shows the same result for the case of a single-atom step running through the center of the dot. Here we assume the step is present on both top and bottom interfaces, as well as the single-atom spike, resulting in a suppression of the valley splitting by a factor of ~ 0.28, as explained in the main text. In all calculations reported here, we assume an isotropic quantum dot with an orbital energy splitting of $\hbar\omega_{orb} = 2$ meV and a vertical electric field of $E_z = 5$ mV/nm.

responding tight-binding wavefunctions. Here we define the Ge spike profile as $Y(z) = Y_{sp} \exp\left[-(z - z_{sp})^2/2\lambda_{sp}^2\right]$, where z_{sp} is the position of the center of the spike, and λ_{sp} is the spike width. An important effect can be observed by comparing panels (a)-(c): for increasing spike heights, the wavefunction envelope is suppressed, at and above the spike location, with consequences for disorder-induced valley coupling. We explore this dynamic in Fig. 5.11(d), where we plot the average valley splitting for varying spike widths and heights. Here, the stars labelled (a)-(c) correspond to Figs. 5.11(a)-5.11(c). We also include the singular case of a monolayer spike with no Ge outside this layer, which is defined as $\lambda_{sp} = 0$ in the figure, and is of interest because it allows for analytical estimates, as obtained in Ref. [125].

Three types of limiting behavior are observed in Fig. 5.11(d), which we also indicate with horizontal lines in Fig. 5.11(e): (i) In the limit of vanishing spike height, $Y_{sp} \to 0$, we recover results for a conventional quantum well without a spike [dashed black line in Fig. 5.11(e)], which falls into the disorder-dominated regime for the quantum well considered in Fig. 5.11; (ii) In the limit of ultra-narrow spikes, $\lambda_{sp} \to 0$, we recover the analytical predictions of Ref. [125] [dotted blue line in Fig. 5.11(e)], which fall into the deterministically enhanced regime; (iii) For larger Y_{sp} and λ_{sp}, we observe disorder-dominated behavior, characterized by larger valley splittings when the electron overlaps significantly with the Ge (lower spike heights), and smaller valley splittings otherwise (larger spike heights).

In Fig. 5.11(e), we compare several types of spike behavior, for spikes of height $Y_{sp} = 10\%$, including the case when the dot is centered at a step. For simulations with (orange) and without (blue) a step, we plot the average valley splitting values (closed circles) and the corresponding 25-75% quartiles (error bars). We also plot the corresponding deterministic, disorder-free results (open circles), obtained using the virtual-crystal approximation. These results indicate a well-defined crossover from deterministic to disorder-dominated behavior when $\lambda_{sp} \approx 1$ ML, suggesting that deterministic enhancement of the valley splitting should be difficult to achieve in this system. The theoretical maximum E_v due to a single-layer Ge spike (blue dotted line) is computed following Ref. [125], assuming a vertical electric field of

$E_z = 5$ mV/nm, obtaining $E_v \approx 3.3$ meV. We also note that, in the absence of a step, the valley splitting abruptly transitions from its deterministically enhanced upper bound (blue dotted line) to an asymptote that is slightly larger than the valley splitting in the absence of a spike (black dashed line). Such enhancement is expected in the disorder-dominated regime, as discussed in Sec. 5.4. In the presence of a step, the valley splitting asymptotes to the same value, as anticipated in Sec. 5.4.1, since the steps do not have a strong effect in this regime. In the deterministically enhanced regime however, the valley splitting approaches a value suppressed below the step-free result by a factor of $\frac{1}{2}|1 + \exp(-ik_0a_0/2)| \approx 0.28$ (orange dotted line), for the case where the step runs through the center of the dot.

5.5.4 Wiggle Well

The most effective method for deterministically enhancing the $2k_0$ component of the confinement potential $U_{qw}(z)$ in Eq. (5.7) is to add it directly to the quantum well, where it overlaps strongly with the electron wavefunction. This is accomplished by introducing Ge concentration oscillations of the form

$$Y_w(z) = A_w[1 - \cos(qz + \phi)], \qquad (5.25)$$

where A_w is the average Ge concentration and q is the oscillation wavevector. Several wavelengths were proposed to enhance the valley splitting in Refs. [124] and [59], including $\lambda = 2\pi/q = 1.8$ nm and 0.32 nm. The latter corresponds to $q = 2k_0$, which we refer to as the short-period Wiggle Well. Below, we make use of the Wiggle Well's large valley splitting to further characterize the transition between deterministic and random-dominated behavior.

In Fig. 5.12(a), we compare three closely related calculations of the valley-coupling matrix element Δ, each of which shows the averaged results of 500 alloy disorder realizations. The simulation geometries include (i) a short-period Wiggle Well with no interface steps (red dots), (ii) a short-period Wiggle Well with a single-atom step passing through the center

of the dot (blue dots), and (iii) uniform Ge in the quantum well with no concentration oscillations, but with the same average Ge concentration as the Wiggle Wells, $Y_w = A_w = 0.5\%$ (gray dots). The results reveal several interesting features. First, the red data display a striking deterministic enhancement of the valley splitting, for which the number of solutions with Δ values near zero is exponentially suppressed. This is particularly impressive given the small amplitude of the concentration oscillations. The valley splitting is strongly reduced for the blue data, due to the step; however, a significant deterministic enhancement is still apparent, attesting to the potency of Wiggle Well approach. Finally, as anticipated in Sec. 5.5.1, we see that devices formed in quantum wells with uniform Ge have Δ values centered near zero, as consistent with randomly dominated behavior. A second important observation in Fig. 5.12(a) is that the standard deviations of the three distributions about their mean values are nearly identical for the three distributions. This is consistent with the fact that the mean Ge concentration, and therefore the alloy disorder, is the same in all three cases. Thus, by moving from the Wiggle Well to the uniform-Ge geometry, we observe a clear crossover from deterministically enhanced to disorder-dominated behavior.

Finally, in Fig. 5.12(b) we show a correlation plot comparing effective-mass and tight-binding calculations, similar to Fig. 5.1(f), that includes the three data sets of Fig. 5.12(a). Here again we observe nearly perfect correlations, demonstrating that the $2k_0$ theory explains the full range of valley splitting behavior, from extreme deterministic enhancement to totally disorder-dominated.

5.5.5 Optimizing the Ge distribution

We have shown that the valley splitting can be deterministically enhanced in structures such as the Wiggle Well, or enhanced on average in quantum wells with uniform Ge. However, most schemes considered here require increasing the contact with random Ge alloy, which has the undesired side effect of decreasing the mobility [124]. It is therefore interesting to search for Ge concentration profiles that maximize the valley splitting while reducing the

total amount of Ge in the quantum well. In this section, we use a projected-gradient-descent routine to maximize the valley splitting for a specified amount of Ge. In its simplest form, this algorithm tends to remove all Ge inside or outside the quantum well, which is not the desired solution. We therefore constrain the procedure to only *add* Ge to an initial sigmoidal quantum well. The following steps are then repeated until a steady-state solution is achieved: (i) estimate the gradient of the reward function, which we take to be the valley splitting computed using the 1D minimal tight-binding method, (ii) update the Ge concentration in each layer in the direction of the gradient, (iii) renormalize the Ge concentration in all layers so that the resulting concentration profile has a fixed density of additional Ge atoms, G_{max}. (With out this renormalization step, the algorithm would continually increase the amount of Ge in the quantum well, which is also not a desired solution.) Full details of the optimization procedure can be found in Appendix D.7. Note that the total Ge content is computed by summing the contributions from individual layers in the z direction; G_{max} is therefore reported in units of atoms/nm^2. Below, we apply the routine separately for optimizations in the deterministic vs. random regimes.

Deterministically enhanced regime

Deterministically enhanced valley splittings are achieved by allowing the routine to optimize both the short-wavelength oscillations and the large-scale Ge concentration envelope that determines the shape of the wavefunction envelope. To focus on deterministic effects, we perform the optimization in the virtual crystal approximation (i.e., without including random-alloy fluctuations). Results for the added Ge concentration are shown in color in Fig. 5.13(a), for the initial sigmoidal concentration profile shown in gray. Here the color scale represents the total added Ge concentration, where $G_{\mathrm{max}} \in (0.5, 5)$ atoms/nm^2, for a fixed electric field of $E_z = 5$ mV/nm. The resulting behavior is reminiscent of the Wiggle Well.

To analyze this behavior, we Fourier transform the weighted confinement potential de-

fined in Eq. (5.7), $\tilde{U}_{qw}(z) = U_{qw}(z)|\psi_{env}(z)|^2$. Results are shown in Fig. 5.13(c) as a function of the reciprocal wavevector k_z, for the case of $G_{max} = 5$ atoms/nm^2. Here as usual, the $2k_0$ component, $\tilde{U}_{qw}(k_z = 2k_0)$, determines the valley splitting. We therefore expect to find an enhancement of $|\tilde{U}_{qw}(k_z)|$ at this wavevector (dashed-green line). Indeed this is the observed behavior, indicating that our optimization routine naturally reproduces key features of the short-period Wiggle Well.

The results also differ from the Wiggle Well in interesting ways. First, we note that approximately half the atomic layers in Fig. 5.13(a) contain no added Ge. Indeed, the secondary peak observed at $k_z \approx 8.3$ nm^{-1} in Fig. 5.13(c) corresponds to the first harmonic of $2k_0$, shifted to lower k_z values due to aliasing effects on a discrete lattice. Such harmonics are a hallmark of *truncated* sinusoids. For example, the following 'truncated Wiggle Well' yields such harmonics:

$$Y_w(z) = (\pi A_w) \max[\cos(2k_0 z + \phi), 0]. \tag{5.26}$$

As in Eq. (5.25), A_w is defined here as the average Ge concentration. However, the Fourier component of $U_{qw}(2k_0)$ for this concentration profile is $\pi/2$ times larger than for the conventional Wiggle Well, for the same value of A_w. Therefore, the truncated Wiggle Well found by our optimization procedure should improve the valley splitting of the Wiggle Well by a factor of $\pi/2$, for the same total Ge content. We confirm this prediction through simulations in Appendix D.8.

A second difference between Fig. 5.13(a) and a Wiggle Well is in the nonuniform envelope of the concentration profile, which mimics the density profile of the wavefunction $|\psi_{env}(z)|^2$. This behavior enhances the valley splitting by increasing the wavefunction overlap with Ge. (We note that the precise shape of the Ge concentration envelope depends on the quantum well profile [gray region in Fig. 5.13(a)] and the electric field.) Based on these observations, we hypothesize that the optimal Ge distribution observed in Fig. 5.13(a) should be well approximated as a truncated Wiggle Well weighted by the envelope probability, $|\psi_{env}(z)|^2$. To test this hypothesis, we fit the added Ge profile in Fig. 5.13(a), for the case of

$G_{\mathrm{max}} = 5$ atoms/nm^2, to the form

$$Y_{\mathrm{fit}}(z) = a_{\mathrm{fit}}|\psi_{\mathrm{env}}(z)|^2\mathrm{max}[0, \cos(2k_0z + \phi_{\mathrm{fit}})], \tag{5.27}$$

where a_{fit} and ϕ_{fit} are fitting parameters, and $\psi_{\mathrm{env}}(z)$ is obtained from effective-mass theory by solving a Schrödinger equation. The resulting fits are excellent, as shown in Fig. 5.13(d), where the solid line is $Y_{\mathrm{fit}}(z)$ and the red dots are the optimized simulation results.

Finally in Fig. 5.13(b), we study the statistical effects of alloy disorder by performing 1,000 valley splitting simulations for the optimized Ge profiles obtained at each G_{max} value considered in Fig. 5.13(a). Here, the markers indicate mean values and the error bars show the corresponding 25-75 percentile range. The very small standard deviations are indicative of very strong deterministic enhancements, which are robust in the presence of alloy disorder.

Randomly dominated regime

Concentration profiles like Fig. 5.13(a) are challenging to grow in the laboratory (just like the Wiggle Well), due to their short-period features. We therefore also apply a concentration-optimizing procedure in the randomly dominated valley splitting regime, where the Ge profiles are more slowly varying (analogous to quantum wells with uniform Ge). Here, to avoid obtaining a deterministically enhanced profile, we choose σ_Δ^2 as the reward function, as defined in Eq. (5.13). This has the effect of maximizing the mean valley splitting as well as the variance, since $\sigma_\Delta^2 \approx \bar{E}_v^2/\pi$ in the randomly dominated regime.

Figure 5.14(a) shows concentration profiles obtained from this procedure, where the color scale indicates the added Ge content in the range of $G_{\mathrm{max}} \in (3, 30)$ atoms/nm^2. Here we adopt the same initial quantum well and electric field as Fig. 5.13(a). The corresponding envelope functions $\psi_{\mathrm{env}}(z)$ are shown for the cases $G_{\mathrm{max}} = 3$, 15, and 30 atoms/nm^2. For low G_{max} values, the resulting Ge profiles are roughly uniform, with the Ge shifted slightly towards the top of the quantum well where $|\psi_{\mathrm{env}}(z)|^2$ is large. For high G_{max} values, the

peak of added Ge shifts towards the center of the quantum well, squeezing the electron more tightly against the top interface. (Note again that the final Ge profile depends on the precise shape of the quantum well and the electric field.) This has a two-fold effect of (i) exposing the wavefunction to more Ge in the barrier region, and (ii) causing the electron to overlap with fewer atomic layers, which also enhances the concentration fluctuations. We interpret these results as a preference for narrower quantum wells. Figure 5.14(b) shows the resulting mean values and 25-75 percentile distributions of the valley splitting, as a function of $G_{\max}$. The valley splitting enhancements here are slightly larger than for the case of uniform Ge, if we compare the same total Ge content. Overall, optimized valley splittings in the disorder-dominated regime (Fig. 5.14) are found to be much smaller than in the deterministically enhanced regime (Fig. 5.13), although the devices are much easier to grow.

5.6 Summary

In this paper, we derived a universal effective-mass theory of valley splitting in Si/SiGe heterostructures, based on the $2k_0$ reciprocal wavevector of the Fourier transform of the weighted confinement potential, $\tilde{U}_{\mathrm{qw}}(z) = U_{\mathrm{qw}}(z)|\psi_{\mathrm{env}}(z)|^2$ (Sec. III D). By comparing our results to those of tight-binding simulations, we showed that this theory accurately predicts the valley splitting across a diverse set of heterostructures and disorder models. We then used the $2k_0$ theory to identify two valley splitting regimes (Sec. III F): (i) the deterministic regime, in which the valley splitting is determined by atomistic details of the quantum well, such as the sharpness of the interface or the location of an atomic step at the interface, and (ii) the disorder-dominated regime, in which the valley splitting is fully determined by SiGe random alloy disorder. In the deterministic regime, the valley splitting is reliably large and independent of the alloy disorder, and the probability of finding a low valley splitting is exponentially suppressed (Sec. III G). In the disordered regime, valley splittings can be large on average, but there is still a good chance of finding a small valley splitting. The

crossover between these two regimes was shown to be sharp and universal (Fig. 4), since it depends only on the integrated overlap of the electron with Ge in the quantum well or the quantum well interface. However it was also shown that the crossover occurs in a regime where heterostructure features are very sharp (e.g., sharp interfaces or single-atom spikes). Such sharp features are difficult to achieve in the laboratory; therefore, deterministically enhanced valley splittings are difficult to achieve in physical devices.

Several conventional heterostructure geometries were investigated by means of simulations (Sec. IV). Sharp interfaces were found to give a large deterministic enhancement of the valley splitting (Sec. IV A 1), but only in the ultra-sharp limit ($\lambda_{int} <$3 ML), which is difficult to achieve in the laboratory. Single-atom steps at the interface were shown to suppress the valley splitting by up to 71% at ultra-sharp interfaces, but were found to have almost no effect for interfaces with $\lambda_{int} > 3$ ML (Sec. IV A 2). Indeed, the precise shape of the interface was found to be important only for the case of ultra-sharp interfaces (Sec. IV C). Wider interfaces were also shown to enhance the *variability* of the valley splitting, due to greater exposure of the electron to the SiGe random alloy (Sec. IV B). This enhanced variability has the interesting side-effect of *increasing* the average valley splitting as a function of λ_{int} in the disorder-dominated regime (Figs. 6 and 7).

Several unconventional heterostructures were also investigated (Sec. V). Uniform Ge in the quantum well was found to enhance both the average valley splitting and its standard deviation, due to significant overlap of the electron with Ge inside the quantum well, where the wavefunction is largest (Sec. V A). Similar effects occur in other geometries, including the sharp Ge spike, where the Ge concentration is maximized where the wavefunction is largest (Sec. V C), and narrow quantum wells, for which the wavefunction is squeezed into the quantum well barrier region where the Ge concentration is high (Sec. V B). The Wiggle Well geometry provides a very effective enhancement of the valley splitting by engineering the $2k_0$ wavevector directly into Ge concentration oscillations inside the quantum well. This geometry also experiences enhanced valley splitting variability due to high Ge exposure

(Sec. V D).

Such unconventional geometries are found to be *optimal,* in the following sense. When the Ge concentration profile is optimized numerically, to obtain the maximum valley splitting while allowing for short-wavelength concentration oscillations, it naturally converges to a Wiggle Well-like geometry (Sec. V E 1). This procedure can be understood as optimizing the valley splitting, *deterministically.* Alternatively, in the disorder-dominated regime, the average valley splitting is proportional to its standard deviation. Maximizing this quantity yields results similar to the geometry with uniform Ge in the quantum well (Sec. V E 2).

5.7 Conclusions: Best Strategies for Enhancing E_v

We now conclude by describing the best strategies for enhancing the valley splitting in Si/SiGe heterostructures. Just as there are two types of valley splitting behavior, there are also two approaches for obtaining large valley splittings. The first is to establish layer-by-layer growth control, which would allow for the implementation of structures like short-period Wiggle Wells, single-atom spikes, and super-sharp interfaces. We emphasize however, that if 1-2 monolayer growth accuracy cannot be achieved, then deterministic attempts to enhance the valley splitting will be overwhelmed by random-alloy disorder, and will fail. In this case, there is no benefit to striving for deterministic enhancement.

An alternative strategy for enhancing the valley splitting is to intentionally add Ge to the quantum well, to increase the exposure to disorder. This has the effect of increasing the mean value as well as the standard deviation of the valley splitting. Additionally, and just as importantly, one should arrange for electrostatic control of the dot position. The most straightforward approach for adding Ge is to choose a simple, smooth Ge profile, such as a broadened interface or uniform Ge in the quantum well, because such structures are easy to grow. Very narrow quantum wells are also effective for increasing the exposure to Ge. Finally, we note that even low Ge concentrations and modest tunability of the dot's

position can increase the probability of achieving useful valley splittings by many orders of magnitude.

5.8 Acknowledgements

Figure 5.12: Short-period Wiggle Wells provide deterministic enhancement of the valley splitting. (a) Intervalley matrix elements Δ are computed for short-period Wiggle Wells using the 1D effective-mass approach, and are plotted in the complex plane. Results are shown for geometries with (blue dots) and without (red dots) a step passing through the center of the quantum dot confinement potential. Additionally we show results for quantum wells with uniform Ge in the quantum well, but no concentration oscillations, with the same average Ge concentration as the Wiggle Wells, $Y_w = A_w = 0.5\%$ (gray dots). All three geometries include random-alloy disorder, and each simulation set is comprised of 500 disorder realizations. Additionally, we choose a quantum well offset of $\Delta Y = Y_s - \bar{Y}_w = 30\%$, a vertical electric field of $E_z = 5$ mV/nm, a quantum well width of $W = 80$ ML, and an interface width of $\lambda_{\text{int}} = 10$ ML. To ensure that $E_v < E_{\text{orb}}$ in each case, we choose $\hbar\omega_{\text{orb}} = 4$ meV for all geometries. (b) A correlation plot comparing tight-binding and effective-mass simulations of the valley splitting, for the same disorder realizations shown in (a). Nearly perfect correlations confirm the importance of the $2k_0$ wavevector for determining the valley splitting.
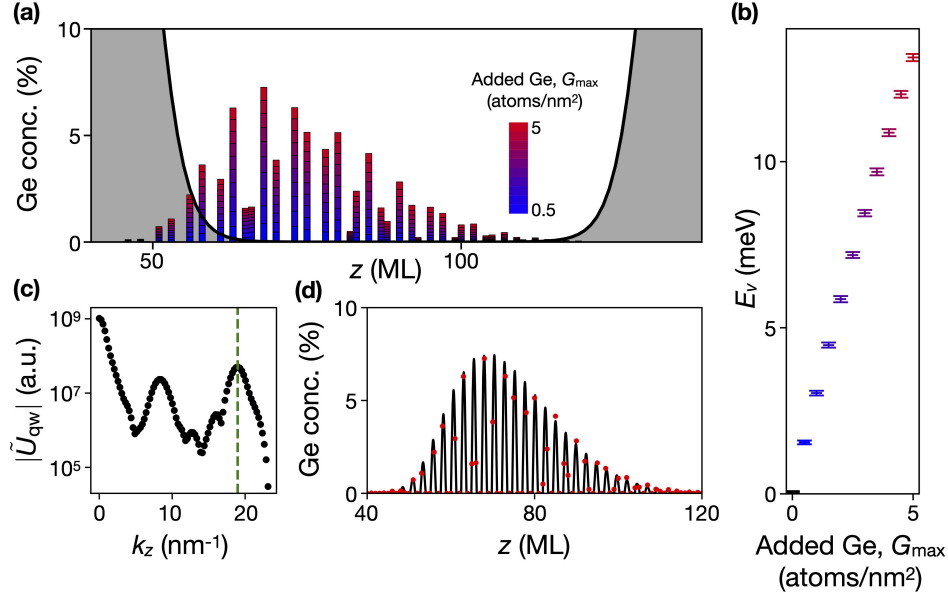
Figure 5.13: Optimizing the Ge concentration profile to provide a large deterministic enhancement of the valley splitting. (a) The initial Ge profile (gray) and added Ge content (vertical bars centered on individual atomic layers) corresponding to the G_{max} value indicated by the colorbar. Optimization is performed as described in the main text, in the absence of random-alloy disorder. The initial sigmoidal profile is defined in Eq. (5.21), with $\lambda_{\mathrm{int}} = 10$ ML and $W = 80$ ML, and with a vertical electric field of $E_z = 5$ mV/nm and quantum dot orbital splitting of $\hbar\omega_{\mathrm{orb}} = 2$ meV. (b) Optimized valley splitting distributions, including random-alloy disorder, as a function of the added Ge. Results are shown for the mean values and 25-75 percentile range of 1,000 1D tight-binding simulations at each G_{max} value. (c) Discrete Fourier transform of the weighted barrier potential $|\tilde{U}_{\mathrm{qw}}|$, as a function of the reciprocal wavevector, for the optimized concentration profile corresponding to $G_{\mathrm{max}} = 5$ atoms/nm^2. The green dashed line identifies the wavevector $q = 2k_0$ responsible for valley splitting. (d) Best fit of Eq. (5.27) (solid curve) to the optimized Ge concentration profile (red dots) shown in (a), for the case of $G_{\mathrm{max}} = 5$ atoms/nm^2.
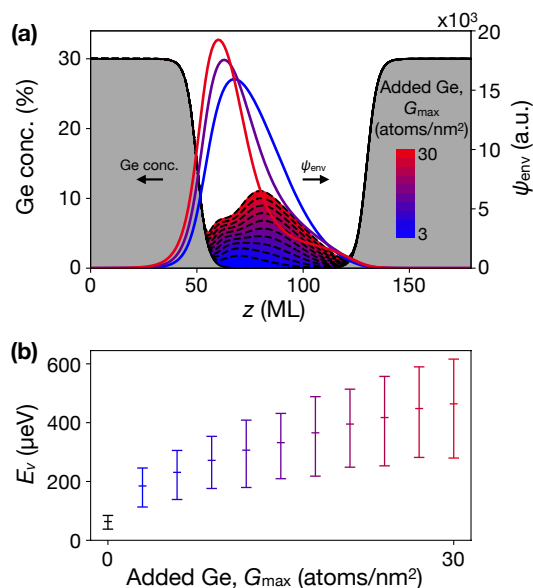
Figure 5.14: Optimized Ge profiles for enhancing the valley splitting in the disorder-dominated regime. (a) The initial Ge concentration profile (gray) and added Ge content (colored region), using the procedure described in the main text and the same quantum well as Fig. 5.13. The colorbar indicates the total added Ge concentration, G_{max}, and the resulting envelope functions $\psi_{env}(z)$ are shown for the cases of $G_{max} = 3$, 15, and 30 atoms/nm^2. (b) Optimized valley splitting distributions as a function of G_{max}, showing the mean values and 25-75 percentile ranges of 1,000 1D tight-binding simulations at each G_{max} value.

Chapter 6

The effects of alloy disorder on strongly-driven flopping mode qubits in Si/SiGe

This chapter is the output of a project I started at LPS in the summer of 2023 with Utkan Güngördü and Charles Tahan. With the guidance of Utkan, I performed the numerical simulations, and Utkan and I developed the analytics and the project direction. Utkan and Charles, as well as Mark Friesen and Susan Coppersmith, all had input to this project. A manuscript based on this work is in preparation.

6.1   Introduction

Over the past decade, spin qubits in Si/SiGe heterostructures have emerged as a leading quantum computing platform [31, 121, 231]. These qubits are small, have long coherence times, and can be fabricated using standard semiconductor processing technology, making them naturally scalable. Furthermore, single- and two-qubit fidelities above 99% have been demonstrated in these systems, demonstrating their promise as scalable qubit platforms [131, 142, 213, 223].

One of the primary sources of infidelity in Si spin qubits is charge noise, or fluctuating electric fields at the location of the spin qubit [31]. These electric field fluctuations typically have a $1/f$ spectral density, leading to low-frequency (or quasistatic) fluctuations in the qubit parameters that cause qubit dephasing [15, 41, 53, 170]. These fluctuating fields are thought to arise from charge impurities, primarily in the SiO_x layers of the heterostructure [160], and they are the dominant source of infidelity in many state-of-the-art spin qubits [36, 131, 142, 178, 213, 223].

It is possible to mitigate the impact of charge noise by designing qubits and gate operations that are inherently insensitive to these electric field fluctuations. One such qubit is the flopping-mode qubit [13, 40, 83, 186]. Flopping mode qubits utilize the delocalization of electron charge across a double quantum dot. A magnetic field gradient across the double dot induces synthetic spin-orbit coupling in the system, and by driving the inter-dot detuning, causing the electron to oscillate between the two dots, the resulting magnetic field oscillations induce single-qubit rotations in a process known as electric dipole spin resonance (EDSR). Compared to a conventional single quantum dot, flopping mode qubits maximize the dipole moment of the electron wavefunction, resulting in faster Rabi oscillations [13]. It has also been proposed to operate flopping mode qubits in the so-called "strong driving" regime, where the electron is strongly driven back and forth between the two dots [186]. This style of gate operation has two advantages: (1) it takes advantage of the full magnetic field gradient between the dots, resulting in fast gate operations, and (2) the electron spends less time at the symmetric point, where it is most sensitive to charge noise. In particular, it has been shown that by carefully shaping the detuning pulses, fast and high-fidelity single-qubit gates can be implemented, even in the presence of significant charge noise [186].

Another challenge for spin qubits in Si/SiGe is the presence of two low-lying conduction band valley states [31, 231]. Measurements of the valley-energy splitting can be as large as $300\,\mu eV$ or as low as $30\,\mu eV$ [19, 22, 33, 46, 60, 79, 128, 129, 139, 143, 163, 171, 199, 225]. Even valley splitting measurements taken on the same chip are quite variable [33]

and sensitive to small displacements in the quantum dot position [51, 79, 199]. Recent theoretical advancements have demonstrated that random-alloy disorder can explain this significant variability in the valley splitting, even between neighboring dots on the same device [115, 117, 119, 124, 145].

This valley splitting variability can create problems for strongly-driven flopping mode qubits. Since tunneling between dots need not preserve the valley quantum number, valley state variability can lead to leakage out of the computational subspace. Weaker driving can be used to avoid this valley leakage, at the expense of increased qubit sensitivity to charge noise. Thus, there is a tradeoff between valley leakage and charge noise in strongly-driven flopping mode qubits. In this work, we closely examine this tradeoff. We describe an algorithm that can optimize pulses for strongly-driven flopping-mode qubits in the presence of charge noise, accounting for differences in the valley configurations in each dot. We show that high-fidelity single-qubit gates can be realized in these systems for a wide variety of valley parameters, so long as charge noise remains relatively limited. In cases where charge noise is stronger, we can still implement high-fidelity single-qubit gates, provided that the valley splittings in each dot are large, and the valley phase difference is relatively small. Furthermore, all of these pulses require some degree of fine-tuning for the particular valley configuration of a double-dot.

Furthermore, we examine how fluctuations in the local electric fields can also lead to small quasistatic shifts in the qubit parameters, including the valley splitting in each dot, the orbital spacing in each dot, and the inter-dot tunnel coupling. While we find that noise-induced fluctuations in the orbital energies and tunnel coupling are relatively unimportant, fluctuations in the valley parameters can actually dominate the qubit infidelity in some cases. This is especially true when the valley splitting is small and the charge noise fluctuations are very large. However, we find that slightly weaker qubit driving can significantly mitigate these errors, and we propose a pulse shape that is more robust to these errors. Thus, we consider many sources of infidelity in this work, including the valley configuration across the

Valley splitting and valley phase	Sec. 6.4
Detuning fluctuations	Sec. 6.4
Valley fluctuations	Sec. 6.6
Orbital energy fluctuations	Sec. 6.6 and App. E.6
Tunnel coupling fluctuations	Sec. 6.6 and App. E.7

Table 6.1: Summary of the potential sources of infidelity in flopping-mode qubits, and where we analyze them in this work.

double-dot, charge noise fluctuations to the qubit detuning, and fluctuations to the other qubit parameters. Table 6.1 summarizes where in the paper each of these effects is analyzed.

This paper is organized as follows. In Sec. 6.2, we review our model of the flopping mode qubit, and we discuss the impact of alloy disorder on the valley parameters of the qubit. In Sec. 6.3, we discuss our algorithm for optimizing flopping-mode qubits, taking into account charge noise and differences in the valley configuration. In Sec. 6.4, we discuss in detail the performance of flopping mode qubits under varying valley configurations. In Sec. 6.5, we address the generalizability of flopping mode qubits, and we come to the conclusion that these qubits should be fine-tuned for any given valley configuration. In Sec. 6.6, we analyze charge-noise-induced fluctuations to the qubit parameters besides the detuning, including the orbital energies in each dot, the tunnel coupling between dots, and the valley parameters in each dot. In Sec. 6.7, we evaluate schemes to avoid low-fidelity configurations, and we discuss the implications for scalable quantum processors based on the flopping mode qubit.

6.2 Modelling strongly-driven flopping mode qubits

6.2.1 Model Hamiltonian

A flopping-mode qubit consists of a single-electron double quantum dot with a magnetic field gradient between the dots. By modulating the detuning ε, we can drive the dot back and forth between the left (L) and right (R) dot. Since the field gradient induces a synthetic spin-orbit
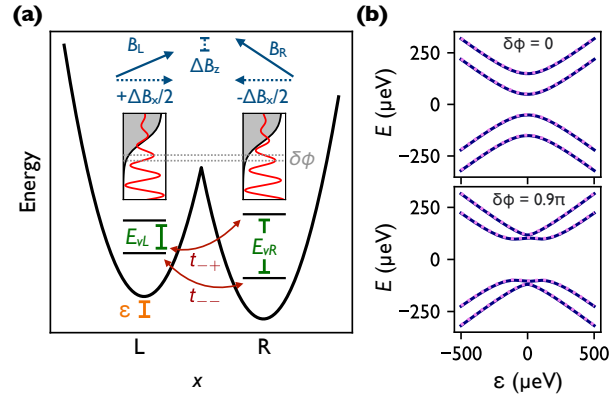
Figure 6.1: Schematic of the flopping mode qubit. (a) Structure of the double quantum dot system, where the left and right dots are labeled L and R. The detuning ε controls the energy splitting between the two dots Within each dot, there are separate valley splittings E_{vL} and E_{vR}. If the valley phase difference between the two dots $\delta\phi \neq 0$, tunneling between the dots need not preserve the valley index, and both valley-preserving and valley-flipping tunneling is allowed. Two such processes are labeled in red, where t_{--} and t_{-+} are defined in Eq. (6.10). Differences in the local magnetic fields between the two dots, labeled B_L and B_R, enable spin spin rotations as the electron is driven back and forth between the dots. (b) Sample energy spectra of the double dot system as a function of detuning, with representative valley parameters, $E_{vL} = E_{vR} = 100$ µeV. The top figure shows the spectrum for $\delta\phi = 0$, and the bottom spectrum for $\delta\phi = 0.9\pi$. Since the spin splitting is small, we use different colors for bands with different spin quantum numbers. All other parameters are those outlined in Sec. 6.2.

coupling, this modulation induces rotations between the spin states. Each dot also has two low-lying valley states. We label the inter-valley couplings in each dot $\Delta_{L(R)} = e^{i\phi_{L(R)}}|\Delta_{L(R)}|$, where the valley splitting $E_{vL(R)} = 2|\Delta_{L(R)}|$ and $\phi_{L(R)}$ is the valley phase [63]. These valley parameters are, in general, different for each dot, complicating the qubit operation, as described below. A schematic of this qubit can be seen in Fig. 6.1(a).

To model strongly-driven flopping mode qubits, we start with an 8-level Hamiltonian in the charge, spin, and valley space. The full Hamiltonian is given by

$$
\begin{aligned}
H(\varepsilon) =& \frac{\varepsilon(t)}{2}\tau_z + t_c\tau_x + \frac{g\mu_B B_z}{2}\sigma_z + \frac{g\mu_B}{2}(\Delta B_x\sigma_x + \Delta B_z\sigma_z)\tau_z \\
&+ \frac{\tau_0 + \tau_z}{2}|\Delta_L|(\gamma_x\cos\phi_L - \gamma_y\sin\phi_L) + \frac{\tau_0 - \tau_z}{2}|\Delta_R|(\gamma_x\cos\phi_R - \gamma_y\sin\phi_R) \quad (6.1)
\end{aligned}
$$

where τ_j are the Pauli operators operating in the basis of the left and right dot (so $\tau_z = |L\rangle\langle L| - |R\rangle\langle R|$ and $\tau_x = |L\rangle\langle R| + |R\rangle\langle L|$), σ_j are Pauli operators in spin space, and γ_j are the Pauli operators in valley space. The detuning between the left and right dots is given by $\varepsilon(t)$, and t_c is the tunnel coupling between the dots. For simplicity, we fix our tunnel coupling $t_c = 100\ \mu\text{eV}$, which was found to achieve good performance for strongly-driven qubits in Ref. 186. We assume there is a magnetic field gradient $\Delta B_x = 2$ mT and $\Delta B_z = 0.4$ mT, and a constant background magnetic field $B_z = 20$ mT, where we have taken these parameters from Ref. 186. We can equivalently write this Hamiltonian in a basis that simultaneously diagonalizes the left and right-dot valleys:

$$
\begin{aligned}
H(\varepsilon) =& \frac{\varepsilon(t)}{2}\tau_z + t_c U_v\tau_x U_v^\dagger + \frac{E_z}{2}\sigma_z + \frac{g\mu_B}{2}(\Delta B_x\sigma_x + \Delta B_z\sigma_z)\tau_z \\
&+ \frac{1}{2}(|\Delta_L| + |\Delta_R|)\gamma_z + \frac{1}{2}(|\Delta_L| - |\Delta_R|)\tau_z\gamma_z \quad (6.2)
\end{aligned}
$$

where

$$U_v = P_L U_L + P_R U_R \tag{6.3}$$

$$U_{L(R)} = \frac{1}{\sqrt{2}} \left[\gamma_0 + i\cos\left(\phi_{L(R)}\right)\gamma_y + i\sin\left(\phi_{L(R)}\right)\gamma_x \right]$$

and $P_{L(R)} = |L(R)\rangle\langle L(R)|$ projects the system into the left (right) subspace. Equation (6.2) forms the basis of our gate optimization procedure, described in Sec. 6.3.

To gain intuition for how pulses to the detuning, $\varepsilon(t)$, perform spin rotations, we make the simplistic assumption that the valley splitting and orbital splittings are sufficiently large, so evolution is adiabatic with respect to excited valley and orbital states. (We derive a precise condition on $\dot{\varepsilon}$ to avoid orbital excitations in Appendix E.1; we consider valley excitations later.) We also assume the spin terms in the Hamiltonian are small and can be treated as perturbations. In this regime, we can replace τ_z by its expectation value in the ground state spin subspace, $\langle\tau_z\rangle$, where

$$\langle\tau_z\rangle_\varepsilon = \frac{1}{2}\left({}_\varepsilon\langle 0|\tau_z|0\rangle_\varepsilon + {}_\varepsilon\langle 1|\tau_z|1\rangle_\varepsilon \right) \tag{6.4}$$

where $|0\rangle_\varepsilon$ and $|1\rangle_\varepsilon$ and the ground and first-excited (spin) instantaneous eigenstates of the system for a given detuning ε. This approximation results in a simple two-level spin Hamiltonian

$$H_{\text{eff}}(\varepsilon) = \frac{g\mu_B B_z}{2}\sigma_z + \frac{g\mu_B}{2}\langle\tau_z\rangle_\varepsilon \left(\Delta B_x \sigma_x + \Delta B_z \sigma_z\right) \tag{6.5}$$

where we have discarded valley and orbital terms. If we also discard the relatively small ΔB_z term, we have the simple Hamiltonian of a driven two-level system, where the drive amplitude is given by $g\mu_B B_x \langle\tau_z\rangle/2$. By pulsing the detuning $\varepsilon(t)$, we modulate the ground state charge expectation value $\langle\tau_z\rangle_\varepsilon$ from -1 to 1. And, by driving at the resonant frequency $E_z/\hbar$, where $E_z = g\mu_B B_z$ is the Zeeman splitting, we can perform a rotation about the

x-axis in spin space by angle θ:

$$U_\theta = \cos(\theta/2) - i\sin(\theta/2)\sigma_x. \tag{6.6}$$

Including virtual *z* gates, these single-qubit rotations are enough to implement all single-qubit rotations. In this work, we choose a representative case $\theta = \pi$.

6.2.2 Alloy disorder and valley splitting

One potential difficulty for spin qubits in general, and for strongly-driven flopping mode qubits in particular, is the variation of valley parameters between dots. Recent theoretical work suggests that the valley splitting in most realistic devices is primarily due to the random-alloy disorder in the SiGe buffer layers [119, 145]. In this regime, termed the *disordered* valley splitting regime, both the valley splitting and the valley phase difference are randomized between the two dots. It is possible to create heterostructures with deterministically large valley splittings, for example by engineering very sharp quantum well interfaces ≤ 3 atomic monolayers (ML) in width [119], or by a combination of shear strain and Ge concentration modulation [210]. However, these deterministically enhanced devices are relatively difficult to fabricate. In this paper, we restrict ourselves to devices in the disordered valley splitting regime.

The inter-valley coupling is a complex quantity, and in the disordered valley splitting regime, its statistics can be described rather simply. Following Refs. 145 and 119, it can be shown from effective mass theory that the variance of the inter-valley coupling for a single quantum dot, averaged over configurations of random alloy disorder, is given by

$$\sigma_\Delta^2 := \mathbb{V}[\Delta] = \frac{1}{\pi}\left[\frac{a_0^2 \Delta E_c}{8 a_{\text{dot}}(X_w - X_s)}\right]^2 \sum_l |\psi_{\text{env}}(z_l)|^4 \bar{X}_l(1 - \bar{X}_l) \tag{6.7}$$

where $a_0 = 0.543$ nm is the Si lattice constant, ΔE_c is the conduction band offset between the Si quantum well and the SiGe barriers (≈ 150 meV for a typical quantum well), X_w is

the Si concentration in the quantum well, X_s is the Si concentration in the SiGe barrier (substrate), and $a_{\text{dot}} = \sqrt{\hbar/m_t\omega_{\text{orb}}}$ is the dot radius, assuming the dot is confined in an isotropic harmonic confinement potential with characteristic level spacing $\hbar\omega_{\text{orb}}$ and $m_t = 0.19m_e$ is the transverse effective mass of an electron in Si. The sum in Eq. (6.7) is over the layers in the heterostructure, and the quantities $\bar{X}_l$ are the expected Si concentrations at layer l, when averaged over the whole device. Finally, ψ_{env} is a 1D envelope function for the quantum dot wavefunction, ignoring effects of valley-orbit coupling. In the disordered valley-splitting regime, the average valley splitting is given by [119]

$$E_v = \sqrt{\pi}\sigma_\Delta \tag{6.8}$$

Observing Eqs. (6.7) and (6.8), we see that the valley splitting depends strongly on the Ge concentration in the quantum well, $1-\bar{X}_l$. Devices with nonzero minimum Ge concentrations (G_{min}) have been proposed to boost average E_v. However, a larger σ_Δ will also lead to larger spatial variations in the valley splitting. We examine the consequences of this spatial variability in Sec. 6.6 and 6.7.

We also note that Δ is a complex quantity, so $\mathbb{V}[\text{Re}[\Delta]] = \mathbb{V}[\text{Im}[\Delta]] = \sigma_\Delta^2/2$. Thus, between two dots, the valley phase $|\delta\phi|$ is randomized uniformly between 0 and π, assuming the dots are spatially well-separated and there is no deterministic inter-valley coupling. This creates complications for a strongly-driven flopping-mode qubit. We can expand the tunneling term in Eq. (6.2) in the basis $\{|L,+\rangle, |L,-\rangle, |R,+\rangle, |R,-\rangle\}$ where $\pm$ labels the ground/excited valley:

$$t_c U_v \tau_x U_v^\dagger = \begin{pmatrix} 0 & 0 & t_{++} & t_{+-} \\ 0 & 0 & t_{-+} & t_{--} \\ t_{++}^* & t_{-+}^* & 0 & 0 \\ t_{+-}^* & t_{--}^* & 0 & 0 \end{pmatrix} \tag{6.9}$$

where the matrix elements

$$t_{++} = t_{--}^* = \frac{t_c}{2}\left(1 + e^{i(\phi_L - \phi_R)}\right)$$
$$t_{+-} = -t_{-+}^* = \frac{t_c}{2}\left(e^{i\phi_L} - e^{i\phi_R}\right). \tag{6.10}$$

If $\phi_L = \phi_R$, then $t_{+-} = t_{-+} = 0$, and all tunneling between the left and right dot is valley-preserving. In Fig. 6.1(b), we plot the qubit spectrum as a function of ε for $\delta\phi = 0$, where we observe no valley anticrossing. However, if $\phi_L \neq \phi_L$, valley-flipping tunneling between the left and right dots is allowed. As a result, a valley anticrossing emerges in the qubit spectrum, as we observe in Fig. 6.1(b) for $\delta\phi = 0.9\pi$. We highlight two of these tunneling elements in red in Fig. 6.1(a). This poses a leakage pathway for strongly driven flopping mode qubits. If $\delta\phi = \phi_L - \phi_R \neq 0$ and the detuning is strongly driven, the dot can tunnel into the excited valley. In the rest of this paper, we examine the consequences of the valley leakage pathway for pulse optimization (Sec. 6.3), pulse fidelity (Sec. 6.4, 6.5, and 6.6), and scalability (Sec. 6.7).

6.3   Gate optimization

In this section, we outline a straightforward procedure to optimize gates in strongly driven flopping mode qubits, given variations in the valley parameters. Then, we analyze these pulses and their resulting fidelities, focusing on the role of the valley splitting in each dot and the valley phase difference between dots.

We consider three pulse types in this work. First, we consider cosine and smoothed-
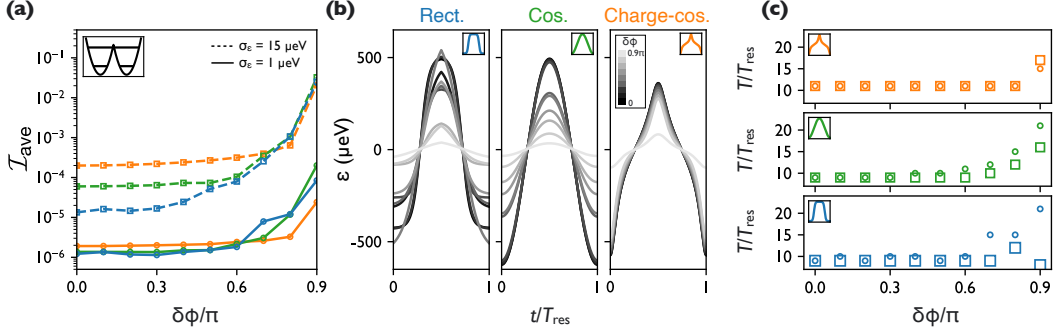
Figure 6.2: Performance comparison of the three pulse families described in Sec. 6.3 for fixed valley splittings $E_{vL} = E_{vR} = 100$ μeV [indicated by the inset to (a)], as we increase the valley phase difference $\delta\phi$ from 0 to 0.9π. (a) Infidelities of the optimized pulses, including the effects of charge noise, for three pulse families: the rectangular pulse (blue), the cosine pulse (green), and the spin-cosine pulse (orange). We consider two charge noise regimes: an optimistic regime given by $\sigma_\varepsilon = 1$ μeV, and a pessimistic regime given by $\sigma_\varepsilon = 15$ μeV. (b) We plot one period of the optimized pulse shapes for the three pulse families as we increase the $\delta\phi$ from 0 to 0.9π. These pulses were optimized for $\sigma_\varepsilon = 1$ μeV (c) The total pulse time, in units of T_{res}, for each of the optimized pulses.

rectangular pulses similar to those considered in Ref. [186]:

$$\varepsilon_{\cos}(t) = C + A\cos(2\pi t/T_{\text{res}})$$

$$\varepsilon_{\text{rect}}(t) = C + A \begin{cases} \tanh\big(2R(\tilde{t} - (1 + c_{\text{dc}})/4)\big), & \tilde{t} \leq 1/2 \\ -\tanh\big(2R(\tilde{t} - (3 - c_{\text{dc}})/4)\big), & \tilde{t} > 1/2 \end{cases} \tag{6.11}$$

where $T_{\text{res}} = 2\pi/E_z$. In both pulses, A represents the pulse amplitude, and C is a constant offset. In all simulations, we limit the maximum detuning $|\varepsilon| \leq \varepsilon_{\max}$, where $\varepsilon_{\max} = 1$ meV. In the rectangular pulse, R represents the steepness of the transition, c_{dc} is a duty-cycle coefficient which we restrict between 0 and 1, and $\tilde{t} = t \pmod{T_{\text{res}}}$. The smooth rectangular pulse parameterization enables pulses that drive quickly through the anticrossing, limiting the qubit's sensitivity to charge noise.

We also consider a third pulse form, which we term the "charge-cosine" or "cc" pulse,

defined as a cosine function within the charge subspace:

$$\langle \tau_z \rangle_{\text{cc}}(t) = C + A \cos(2\pi t / T_{\text{res}}). \tag{6.12}$$

Again, A is the pulse amplitude, in this space, and C is the pulse offset. Since this pulse is defined in terms of the charge expectation value $\langle \tau_z \rangle$, we need a map from $\langle \tau_z \rangle \to \varepsilon$ to determine the detuning function $\varepsilon(t)$. We obtain this map by diagonalizing $H(\varepsilon)$ across the full range of ε, computing $\langle \tau_z \rangle_\varepsilon$ according to Eq. (6.4). Then, by inverting the relationship in Eq. (6.4), we obtain $\varepsilon(t)$. Examples of these optimized pulses are shown in Fig. 6.2(b), where we illustrate just one period of the periodic pulse. As we see in Fig. 6.2(b), the charge-cosine pulse drives more softly across the charge anticrossing, compared to the strong driving of the rectangular and cosine pulses. For all pulses, we set the maximum detuning to ± 1 meV, and we limit $R \le 20$ for the rectangular pulse.

Now, we outline the algorithm used to optimize our pulses. As well as the pulse parameters in Eqs. (6.11) and (6.12), we need to optimize the pulse length $T = n T_{\text{res}}$, which is an integer multiple of the resonant period. For each possible pulse length T, we choose pulse parameters that minimize the following heuristic cost function:

$$\mathcal{C} = \mathcal{I}_0 + \mathcal{L}_{\text{charge}} + \mathcal{L}_{\text{leak}}. \tag{6.13}$$

We define the trace infidelity of a pulse as follows:

$$\mathcal{I}_{\delta\varepsilon} = 1 - \left[\frac{\left| \text{tr} \left(\mathcal{P} U_{\delta\varepsilon}(T) \mathcal{P}^\dagger U_\theta^\dagger \right) \right|}{2} \right]^2, \tag{6.14}$$

where the $U_{\delta\varepsilon}(T)$ is the propagator of the pulse evaluated at time T, in the presence of a quasistatic detuning fluctuation $\delta\varepsilon$ (see below). The propagator is determined by solving the Schrodinger equation

$$i\hbar \dot{U}_{\delta\varepsilon} = H(\varepsilon(t) + \delta\varepsilon) U_{\delta\varepsilon} \tag{6.15}$$

where $\varepsilon(t)$ is the pulse we seek to optimize. The ideal infidelity $\mathcal{I}_0$ is the trace infidelity in the absence of any detuning fluctuations, obtained by setting $\delta\varepsilon = 0$ in Eq. (6.15). The projector $\mathcal{P} = |0(T)\rangle\langle 0(T)| + |1(T)\rangle\langle 1(T)|$ projects the system into the subspace spanned by the instantaneous ground and first excited states at time T, and U_θ is the ideal pulse defined in Eq. (6.6). The quantity $\mathcal{L}_{\mathrm{charge}}$ is an estimate of the infidelity due to charge noise, and $\mathcal{L}_{\mathrm{leak}}$ is an estimate of the infidelity due to leakage outside the computational subspace. More details on the components of $\mathcal{C}$ are given in Appendix E.2.

Because charge noise sensitivity will increase for longer and weaker pulses, while leakage and infidelity errors tend to decrease, we expect a minimum $\mathcal{C}$ for a particular pulse length. Because this analysis is approximate, we then select the five pulses yielding the lowest overall cost for further analysis. By choosing five pulses, we increase the likelihood of finding the true best-performing pulse. At this stage, we randomize and re-optimize the pulse parameters for each of the five best-performing pulses, performing this randomization and re-optimization ten times. We find this procedure helps avoid some local minima, especially for the rectangular pulse family, and results in better overall fidelity. After ten iterations, we select the optimized pulse parameters that resulted in the lowest overall $\mathcal{C}$. Then, for each of five best-performing pulses (which have now been fine-tuned by randomization and re-optimization), we estimate the total infidelity in the presence of charge noise. We account for charge noise as a quasistatic fluctuation to the detuning, where $\tilde{\varepsilon}(t) = \varepsilon_{\mathrm{pulse}}(t) + \delta\varepsilon$. We assume $\delta\varepsilon$ is sampled from a normal distribution with zero mean and standard deviation σ_ε. We consider two charge noise regimes in this work: an optimistic $\sigma_\varepsilon^{\mathrm{opt}} = 1$ µeV, and a pessimistic $\sigma_\varepsilon^{\mathrm{pes}} = 15$ µeV. At the low end, our optimistic charge noise strength is similar to the measured charge noise spectral densities at 1 Hz [36, 37, 46, 103]. To estimate the gate infidelity in the presence of charge noise, we sample 51 values of $\Delta\varepsilon$, ranging from $-4\sigma_\varepsilon$ to $4\sigma_\varepsilon$ and take the weighted average of the resulting ideal infidelities:

$$\mathcal{I}_{\mathrm{avg}} = \sum_{-4\sigma_\varepsilon}^{4\sigma_\varepsilon} \mathcal{I}_{\delta\varepsilon}\, p(\Delta\varepsilon) \tag{6.16}$$
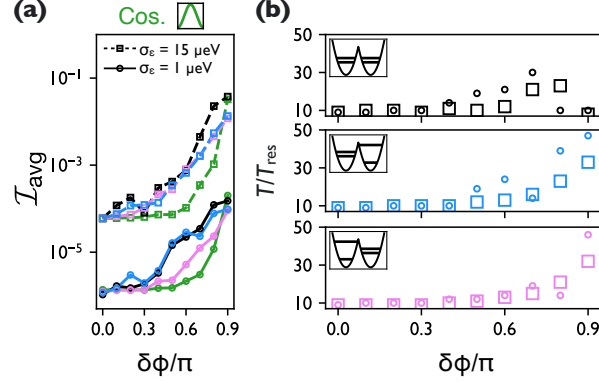
Figure 6.3: Evaluation of the cosine pulse family for varying valley configurations. (a) Average infidelity $\mathcal{I}_{\mathrm{avg}}$, defined in Eq. (6.16), for optimal pulses as $\delta\phi$ is varied from 0 to 0.9π, assuming $\sigma_\varepsilon = 1$ µeV (circles and solid lines) and 15 µeV (squares and dashed lines). We plot results for $E_{vL} = E_{vR} = 100$ µeV (green), the same data as shown in Fig. 6.2. We also show results for $E_{vL} = 100$ and $E_{vR} = 20$ µeV (pink), $E_{vL} = 20$ and $E_{vR} = 100$ µeV (blue), and $E_{vL} = E_{vR} = 20$ µeV (black). (The insets in (b) refer to the valley configuration in the left and right dots.)

where $\mathcal{I}_{\delta\varepsilon}$ is given by Eq. (6.14). Of the five pulses under consideration, we select the pulse with minimal $\mathcal{I}_{\mathrm{charge}}$.

6.4 Dependence of gate fidelity on the inter-valley coupling

Using the pulse optimization procedure outlined above, we now evaluate the performance of the three pulse families described in Eqs. (6.11) and (6.12) in the presence of variations in the inter-valley coupling between the two dots. We start with a favorable valley splitting configuration, $E_{vL} = E_{vR} = 100$ µeV [indicated by the inset in Fig. 6.2(a)], where we vary the valley phase difference $\delta\phi$ from 0 to 0.9π. The resulting average infidelities, for both optimistic and pessimistic charge noise configurations, are plotted in Fig. 6.2(a), and the corresponding optimized pulse shapes in (b) [for $\sigma_\varepsilon = 1$ µeV] and pulse lengths in (c). In the optimistic charge noise regime, pulse infidelities are fairly uniform around 10^{-6} for each pulse type, across a wide range of $\delta\phi$. In the pessimistic charge noise regime, as highlighted

in Ref. [186], the smoothed rectangular pulses perform best for smaller phase differences, and the charge-cosine pulse the worst. Since the rectangular pulse allows for more rapid driving across the double-dot, the system spends less time near $\varepsilon = 0$, where it is most sensitive to charge noise fluctuations. Since the charge-cosine pulse is driven more gently through $\varepsilon = 0$, it is more sensitive to charge noise. As the valley phase difference increases above $\sim 0.6\pi$, the fidelities of all pulse types in both charge noise regimes start to deteriorate. This is due to the emergence of a valley anticrossing, visible in the energy spectra of Fig. 6.1(b), which causes strongly-driven pulses to leak into the excited valley state. As a result, the pulses must in general be made weaker and longer, as we observe in Figs. 6.2(b) and (c). (Sometimes, for the very worst valley configurations, like the rectangular pulse at $\delta\phi = 0.9\pi$ under pessimistic charge noise, much shorter pulses are actually preferred. Regardless, these pulses have very poor fidelities; see App. E.3 for a discussion.) These pulses spend more time around $\varepsilon = 0$, and are hence more sensitive to charge noise.

Next, we examine pulses in less favorable valley configurations. In Fig. 6.5(a), we plot optimized infidelities for the cosine pulse as a function of $\delta\phi$ for three valley splitting regimes: $E_{vL} = 100$ μeV and $E_{vR} = 20$ μeV (pink), $E_{vL} = 20$ μeV and $E_{vR} = 100$ μeV (blue), and $E_{vL} = E_{vR} = 20$ μeV (black). For comparison, we include infidelities for $E_{vL} = E_{vR} = 100$ μeV shown in Fig. 6.2 (green). As expected, as we reduce the valley splitting in one or both dots, gate infidelity increases across most $\delta\phi$. This effect is small for $\delta\phi \lesssim 0.3\pi$, but worsens for larger phase differences. Nonetheless, in the optimistic charge noise regime, there is still a wide range of $\delta\phi$ supporting charge-noise-induced gate infidelities $< 10^{-4}$. This picture is qualitatively similar for the other two pulse families as well (seep App. E.3). Thus, as long as charge noise is limited, we expect that strongly-driven flopping mode qubits are achievable across a wide range of valley parameters.

While each pulse family performs similarly here, there are some notable differences between each optimized pulse. To see this, we examine a representative case. In Fig. 6.4(a), we plot the evolution of a state $|\psi(t)\rangle$ under the action of a pulse from each optimized family,
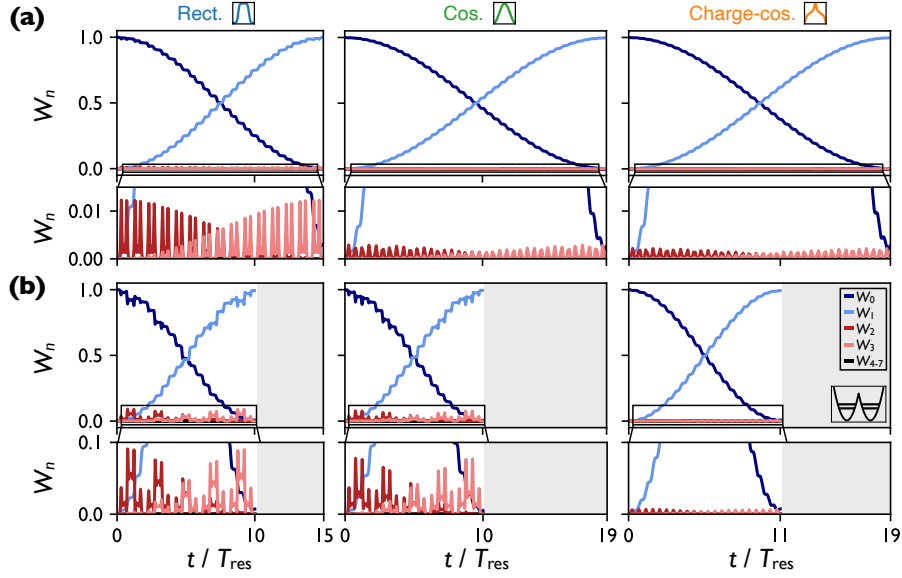
Figure 6.4: Wavefunction evolution under an optimized pulse from each pulse family, assuming $E_{vL} = E_{vR} = 20$ µeV and $\delta\phi = 0.5\pi$. We plot the wavefunction weight W (as defined in the main text) in each of the 8 instantaneous eigenstates for the duration of the pulse, assuming $|\psi(0)\rangle$ is the ground state of the Hamiltonian. Curves in blue show the weight for the ground (dark blue) and first excited (light blue) spin states. Curves in red show the weight in the third (dark red) and fourth (light red) excited valley states. We plot pulses optimized for $\sigma_\varepsilon = 1$ µeV (a) and 15 µeV (b). We also include a zoomed-in view of the evolution of the lowest two excited valley states for both (a) and (b). To highlight the relative length of each pulse, we plot all pulses on the same x-axis scale. For all three pulse families, the optimized pulses for $\sigma_\varepsilon = 15$ µeV are significantly shorter.

for the case $E_{vL} = E_{vR} = 20$ µeV, $\delta\phi = 0.5\pi$, and $\sigma_\varepsilon = 1$ µeV. We take the state $|\psi(0)\rangle$ to be the instantaneous ground state at $t = 0$. We can express $|\psi\rangle$ in the basis of instantaneous eigenstates, $|\psi(t)\rangle = \sum_n c_n(t)|n(t)\rangle$, where $c_n(t)$ is the component of $|\psi\rangle$ in eigenstate $|n\rangle$ at time t. In Fig. 6.4, we plot $W_n = |c_n(t)|^2$, where we color the two lowest (spin) eigenstates blue, and the next two excited (valley) eigenstates red. In the lower portion of Fig. 6.4(a), we plot a zoomed-in picture of the evolution of the lowest two valley eigenstates. While there is nonzero wavefunction weight in the excited valley states for all pulses, this weight is visibly much larger for the rectangular pulses. Due to their stronger driving through the anticrossing, these pulses create more Landau-Zener tunneling from the ground to excited valley state. While all three pulses perform similarly in the presence of detuning fluctuations, the greater excited valley occupation in the rectangular pulse family make it more sensitive to fluctuations in other parameters, like the inter-valley coupling. We analyze this effect more in Sec. 6.6.

As we increase the strength of the charge noise, this effect becomes even more apparent. In Fig. 6.4(b), we plot the wavefunction evolution for optimized pulses for the same valley configuration as in (a), assuming a charge noise parameter $\sigma_\varepsilon = 15$ µeV. First, we note that these pulses are all shorter than the pulses in (a). Since the impact of charge noise compounds for longer pulses, the optimization favors shorter pulse duration in this case. Second, the excited valley occupation is not significantly larger for the rectangular and cosine pulses than for the charge-cosine pulse, since these two pulses have much stronger driving through the valley anticrossing. As a result, these two pulses are much more sensitive to small fluctuations in the valley parameters. In fact, for the rectangular and cosine pulses, we expect small fluctuations in the valley parameters to be the dominant source of infidelity in this regime, as we illustrate in Sec. 6.6. On the other hand, by avoiding valley excitations, the charge-cosine pulse is relatively resilient to these valley fluctuations.
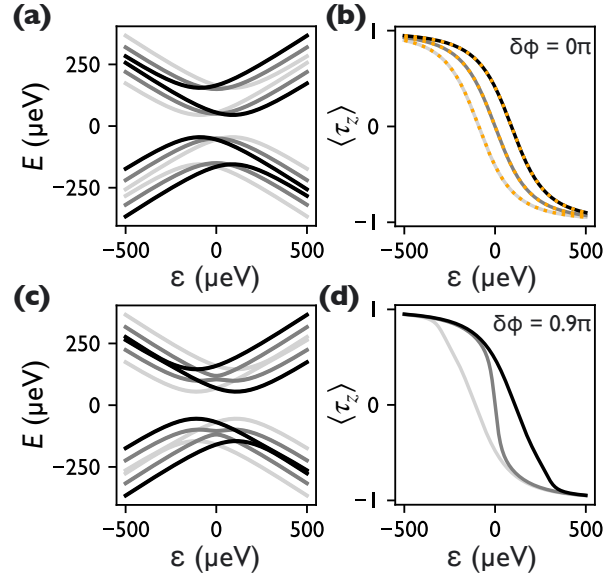
Figure 6.5: Differing valley splittings (and valley phases) between the left and right dots necessitates valley-dependent pulse optimization. (a) Energy spectrum of the double quantum dot for $E_{vL} = 20$, $E_{vR} = 100$ μeV (light gray), $E_{vL} = E_{vR} = 100$ μeV (gray), and $E_{vL} = 100$, $E_{vR} = 20$ μeV (black), where the valley phase difference $\delta\phi = 0$. [Note: the spin splitting is too small to be resolved in this plot.] (b) The expectation $\langle \tau_z \rangle$, averaged between the ground and first excited state, as a function of detuning ε for the same three cases considered in (a). Orange dotted lines indicate the theoretical results from Eq. (E.5). The same quantities are plotted in (d) and (e), for a valley phase difference $\delta\phi = 0.9\pi$.

6.5   The necessity of fine-tuning

In our optimization of flopping-mode pulses, we fine-tune each pulse for a given set of valley parameters. While generalized pulses that work across all valley configurtations may be more desirable, we show in this section that this fine-tuning is necessary to achieve very high-fidelity qubit operations. In the disordered valley splitting regime, valley parameters can vary significantly from dot to dot, so any given qubit will have random E_v and ϕ_v distributions. As we show below, gates optimized for one set of valley parameters perform poorly when used on others.

First, we analyze the energy spectrum, as a function of detuning, for several different valley configurations. Figure 6.5(a) shows the energy spectrum for three such configurations, each with $\delta\phi = 0$: light gray lines show $E_{vL} = 20$ μeV and $E_{vR} = 200$ μeV, dark gray lines

show $E_{vL} = E_{vR} = 100$ µeV, and black lines show $E_{vL} = 200$ µeV and $E_{vR} = 20$ µeV. Clearly, the energy spectrum as a function of ε differs significantly for different E_{vL} and E_{vR}, since the valley splitting is of the same order of magnitude as the orbital level spacing. Moreover, these spectral differences lead to different effective spin Hamiltonians. To see this, we plot the charge expectation value $\langle \tau_z \rangle_\varepsilon$ in the ground state spin subspace, defined in Eq. (6.4), as a function of ε in Fig. 6.5(b), for each of the three configurations in (a). Again, we see significant variation across the three cases. As described in Sec. 6.2 and Eq. (6.5), the quantity $\langle \tau_z \rangle_\varepsilon$ is approximately proportional to the pulse amplitude *in spin space*. So, if the function $\langle \tau_z \rangle_\varepsilon$ is not constant across the three valley configurations, then the same detuning pulse $\varepsilon(t)$ will implement *different* spin rotations. In this regime where $\delta\phi = 0$, we can also derive the simple analytical formula for $\langle \tau_z \rangle_\epsilon$, given in Eq. (E.5) and plotted as orange dotted lines in (b) [see Appendix E.1]. The picture is complicated further by a valley phase difference, $\delta\phi$. In Fig. 6.5(c), we again plot spectra for the three valley splitting configurations considered in (a), this time assuming a valley phase difference $\delta\phi = 0.9\pi$. In Fig. 6.5(d), we plot the resulting $\langle \tau_z \rangle_\varepsilon$ for the three spectra in (c). Thus, the resulting spin pulse amplitude depends both on the valley splitting configuration, as well as the valley phase difference, across the double-dot.

Now, we analyze how failure to account for differences in valley splitting and valley phase results in poorer gate fidelities. First, we consider a cosine pulse, optimized for $E_{vL} = E_{vR} = 100$ µeV, with $\delta\phi = 0$. In this configuration, the pulse achieves infidelity $\mathcal{I}_0 \approx 10^{-6}$ in the absence of charge noise, as we see in Fig. 6.6(a). Then, we modulate the underlying valley configuration, by varying E_{vL} (orange line) or E_{vR} (black dashed line), and we plot the resulting pulse infidelity as a function of $\Delta E_v = E_{vL} - E_{vR}$ in Fig. 6.6(a). Away from the optimal point $\Delta E_v = 0$ in either direction, we see that $\mathcal{I}_0$ quickly grows. For comparison, we include pulse infidelities for gates optimized for each valley configuration (orange and black circles), which remain around 10^{-6} across the full range of parameters here. Thus, if we do not fine-tune our pulses for a given valley configuration, we cannot expect high-fidelity
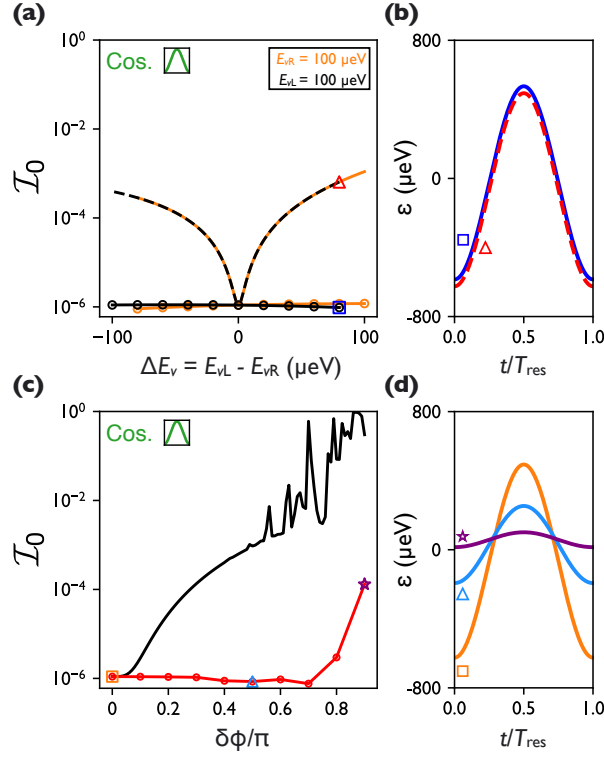
Figure 6.6: Failing to account for individual valley parameters results in poor pulse fidelities. (a) We plot gate infidelities for cosine pulses without any charge noise ($\mathcal{I}_0$) as we modulate the valley splitting. First, we show infidelities of pulses fine-tuned for each valley configuration, for double dots with $E_{vR} = 100$ µeV (orange circles) and $E_{vL} = 100$ µeV (black circles). We also show the infidelity of a single pulse, fine-tuned for $E_{vL} = E_{vR} = 100$ µeV, as manipulate the valley splitting configuration (orange and black dashed lines). (b) The relatively small difference between a pulse fine-tuned for $E_{vL} = E_{vR} = 100$ µeV (red) and a pulse fine-tuned for $E_{vL} = 200$ µeV and $E_{vR} = 10$ µeV (blue). These pulses correspond to the infidelities marked with a red triangle and blue square in (a). (c) For a double-dot with $E_{vL} = E_{vR} = 100$ µeV, we vary $\delta\phi$ and plot the resulting fidelities wihtout charge noise. We show fidelities for pulses fine-tuned for each $\delta\phi$ (red circles), and the infidelity of a single pulse, fine-tuned for $\delta\phi = 0$ (black). (d) For the three cases marked in (c), we plot a single period of the fine-tuned pulse, showing clear differences in amplitude and offset.

pulses. Finally, we highlight the small difference between an optimized and un-optimized pulse. In Fig. 6.6(b), we plot one period of a pulse optimized for $E_{vL} = E_{vR} = 100$ μeV (red), as well as a pulse optimized for $E_{vL} = 100$ μeV and $E_{vR} = 20$ μeV (blue). These pulses correspond to the red triangle and blue square in Fig. 6.6(a), and they differ by about 40 μeV across their duration, resulting in a difference in infidelity of nearly three orders of magnitude.

The variation between optimal and sub-optimal pulses becomes more apparent when we allow changes to $\delta\phi$. In Fig. 6.5(c), we plot the infidelity $\mathcal{I}_0$ for pulses optimized for $\delta\phi$ between 0 and 0.9π (red circles). Again, we consider valley splittings $E_{vL} = E_{vR} = 100$ μeV. We also consider the performance of a single pulse optimized for $\delta\phi = 0$ as we modify the underlying $\delta\phi$ (black). Clearly, as $\delta\phi$ increases from 0, the infidelity of the non-fine-tuned pulse quickly grows, while the fine-tuned pulses remain high-fidelity across a wide range of $\delta\phi$. For the three positions marked in Fig. 6.5(c), we plot a single period of the fine-tuned pulses in (d), displaying clear differences in the optimal pulse amplitude and offset. Hence, in a quantum computing architecture based on the flopping-mode qubit, we expect each single-qubit gate to require valley-dependent fine-tuning to achive very high fidelities.

6.6   Other sources of infidelity

In the optimization procedure we describe in Sec. 6.3, we have designed pulses that account for detuning fluctuations $\delta\varepsilon$ between each dot in the double-dot qubit. These detuning fluctuations occur due to fluctuating lateral electric fields, $\delta\mathbf{E}_{\text{lat}} = \delta E_{\text{lat},x}\hat{x} + \delta E_{\text{lat},y}\hat{y}$, due to fluctuating charge impurities in the heterostructure [58]. If the double-dot detuning axis is along $\hat{x}$, then a lateral field fluctuation produces a detuning fluctuation

$$\delta\varepsilon = ed\delta E_{\text{lat},x}, \tag{6.17}$$
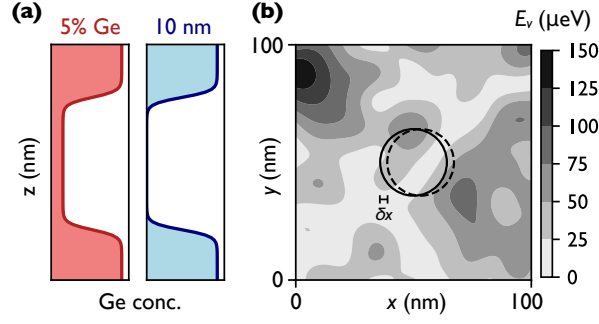
Figure 6.7: Schematic illustration of how charge noise results in valley splitting fluctuations. (a) Illustrations of the two heterostructure types we consider in this work: a QW with 5% Ge in the QW center (red), and a conventional 10 nm QW (blue). (b) Simulation of E_v across a 100×100 nm^2 region of heterostructure for a conventional 10 nm QW. The circle of radius a_{dot} represents a quantum dot, which is displaced by an amount δx in the presence of a lateral electric field fluctuation.

where d is the inter-dot distance. In this work, we consider $d = 60$ nm, resulting in a $t_c \approx 100$ µeV (see Appendix E.7). Fidelity estimates for spin qubits in Si/SiGe often focus on these detuning fluctuations [13, 15, 41, 105, 186].

However, these direct detuning fluctuations are not the only possible source of qubit infidelity. Given a quasistatic lateral electric field fluctuation $\delta E_{\text{lat},x}$, the center of the dot confinement potential shifts by an amount

$$\delta x = \frac{e \delta E_{\text{lat},x}}{m_t \omega_{\text{orb}}^2}, \tag{6.18}$$

resulting in a small shift in the dot center. This causes the dot to sample a slightly different disorder landscape, due to both the random-alloy disorder and interface steps inevitable in Si/SiGe heterostructures. In turn, this disorder causes small shifts in the qubit parameters of Eq. (6.1), like the orbital levels, tunnel coupling, and inter-valley coupling. This effect is illustrated schematically in Fig. 6.7(b), where we have simulated a map of E_v across a 100×100 nm^2 region of heterostructure. The two circles represent a dot which has been shifted by an amount δx in response to a lateral field. (This shift has been greatly exaggerated for visual effect.) By moving the dot across a fluctuating E_v landscape, charge

noise slightly modulates the valley coupling parameters Δ_L and Δ_R. The same picture holds for fluctuations to the orbital energies in each dot as well as the tunnel coupling. We analyze the impact of these fluctuations below.

To simulate the disorder landscape, we also need to specify the type of heterostructure used. As described in Sec. 6.2.2, the average valley splitting depends on the disorder parameter σ_Δ, which in turn depends on the wavefunction overlap with high-Ge layers in the heterostructure. In heterostructures with larger Ge overlap, we can expect larger fluctuations to all three quantities consider here. To make concrete estimates, we therefore analyze two representative heterostructures, illustrated in Fig. 6.7(a): a conventional $10\,\mathrm{nm}$ QW with no additional Ge (labeled 0% Ge) and a heterostructure with uniform 5% Ge in the QW. These high-Ge heterostructrues have been proposed to boost the average valley splitting in quantum dots [119, 145], which would benefit flopping mode qubits, as discussed above. For example, using Eqs. (6.7) and (6.8), we estimate $\bar{E}_v \approx 360$ µeV in the 5% Ge QW, while $\bar{E}_v \approx 49$ µeV for the conventional 0% Ge QW. However, this large average E_v comes with an increased sensitivity to charge noise in some regimes, which we analyze below. More details on the design of each heterostructure and the calculation of their average valley splittings is given in Appendix E.4

6.6.1   Orbital energy and tunnel coupling fluctuations

First, we analyze the impact of small shifts in each dot's orbital confinement energy, due to both alloy disorder and interface steps. If the fluctuation δE_{orb} is different in each dot, the result is an effective detuning fluctuation, $\delta\varepsilon_{\mathrm{eff}} = \delta E_{\mathrm{orb},L} - \delta E_{\mathrm{orb},R}$. However, we find these shifts to be subdominant compared to the direct detuning fluctuations $\delta\varepsilon$, given by Eq. (6.17). We provide details of this analysis in Appendix E.6.

Next, we analyze the impact of small shifts to the tunnel coupling t_c in the presence of lateral field fluctuations, due to both alloy disorder and interface steps. For the charge noise regimes considered in this work, these fluctuations are $\lesssim 10^{-1}$ µeV. Again, we find these
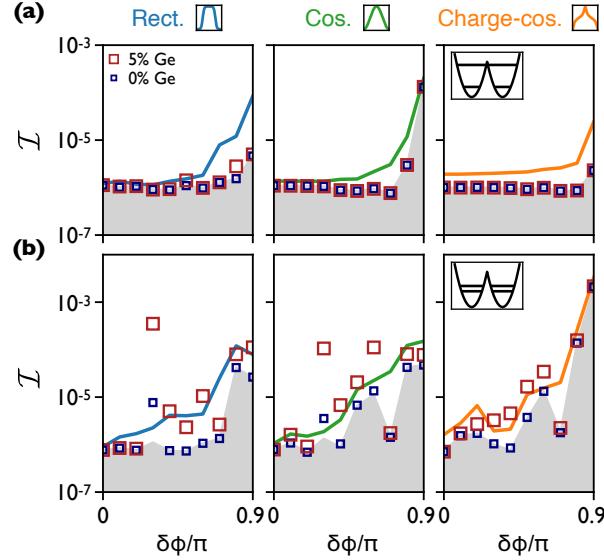
Figure 6.8: Infidelity due to valley fluctuations in the *optimistic* charge noise regime. For each pulse family (rectangular, cosine, and charge-cosine), we plot the expected infidelity due to charge noise $\mathcal{I}_{\text{ave}}$, computed with Eq. (6.16) (colored lines) for both $E_{vL} = E_{vR} = 100$ µeV (a) and $E_{vL} = E_{vR} = 20$ µeV (b), as we vary $\delta\phi$ between 0 and 0.9π. (The insets in the right panels indicate the valley splitting configuration.) The $\mathcal{I}_{\text{ave}}$ curves plotted in (a) are the same as in Fig. 6.2(a). We also indicate the expected infidelity due to *valley fluctuations*, as described in the main text, for conventional 10 nm QWs (blue squares) and 5% Ge QWs (red squares). The gray region indicates the baseline pulse infidelity with no charge noise and serves as an effective lower bound.

have little impact on qubit fidelity, and we leave our detailed analysis to Appendix E.7.

6.6.2 Valley coupling fluctuations

Next, we analyze the impact of small shifts to the inter-valley coupling parameters Δ_L and Δ_R due to lateral field fluctuations. Unlike fluctuations in the orbital energy and tunnel coupling, these effects can have a dominant impact on qubit infidelity in some regimes. Firsrt, we need to estimate the expected size of these fluctuations. As derived in Refs. 119, the spatial covariance between the inter-valley coupling in a single dot, measured at two positions in the heterostructure separated by a distance δr, is given by

$$\text{Cov}[\Delta_1, \Delta_2] = e^{-\delta r^2/2a_{\text{dot}}^2}\sigma_\Delta^2 \tag{6.19}$$

where Δ_1 and Δ_2 indicate the inter-valley couplings measured with a spacing of δx. Thus, the *difference* in inter-valley coupling $\delta\Delta = \Delta_2 - \Delta_1$ is given by a complex normal distribution with variance

$$\mathbb{V}[\delta\Delta] = \left(1 - e^{-\delta r^2/2a_{\text{dot}}^2}\right)\sigma_\Delta^2. \tag{6.20}$$

Thus, for any given displacement of the dot center δr, we can determine the distribution of the resulting valley fluctuations using Eq. (6.20). The above analysis has been performed for an isotropic and harmonically confined single quantum dot, not a double-dot. However, we expect this analysis to approximately hold for each dot in the double-dot qubit, as long as each dot is well-separated.

Now, we need to relate the detuning fluctuations $\delta\varepsilon$ to electric field fluctuations δE_{lat}. Examining Eq. (6.17), we observe that our charge noise metric σ_ε is related to a lateral field fluctuation by the following:

$$\sigma_\varepsilon = ed\sigma_{E_x} \tag{6.21}$$

where $\sigma_{E_x} = \text{Std}[\delta E_{\text{lat},x}]$. Here, we have assumed $E_{\text{lat},x}$ is zero-mean and normally distributed. We further assume lateral field fluctuations in the $\hat{x}$ and $\hat{y}$ direction are isotropically distributed and equally likely, so we have $\sigma_E := \sigma_{E_x} = \sigma_{E_y}$. Thus, by specifying the charge noise parameter σ_ε, we can determine the expected distribution of lateral field fluctuations, given by σ_E.

Now, we can examine the impact of inter-valley coupling simulations. To do so, we use the following Monte Carlo simulation procedure. First, we specify the charge noise regime σ_ε and the valley configuration E_{vL}, E_{vR}, and $\delta\phi$. We also specify a heterostructure type (either a conventional 0% Ge or a 5% Ge device), which determines the disorder parameter σ_Δ. Then, we obtain the optimized pulse for these parameters, following the steps in Sec. 6.3. Next, we perform 500 iterations of the following steps: (1) Randomly generate a lateral field fluctuation in the $\hat{x}$ and $\hat{y}$ direction according to Eq. (6.21); (2) For a given $E_{\text{lat},x}$ and $E_{\text{lat},y}$, we compute the dot displacement $\delta r = \sqrt{\delta x^2 + \delta y^2}$, where δx and δy are computed

according to Eq. (6.18); (3) For a given δr, we randomly generate inter-valley coupling fluctuations for each dot in the double-dot qubit, $\delta\Delta_L$ and $\delta\Delta_R$, according to Eq. (6.20); (4) We apply the fluctuations $\delta\Delta_L$ and $\delta\Delta_R$ to the Hamiltonian, and we simulate the fidelity of the optimized pulse under these new conditions. By averaging the resulting infidelities over 500 iterations, we obtain the expected infidelity due to Δ fluctuations, averaged over lateral field fluctuations and random alloy disorder, for a *fixed* set of valley parameters. Importantly, we do not include detuning fluctuations ($\delta\varepsilon$) in our estimate of the pulse infidelity. Thus, this procedure computes the infidelity attributable to inter-valley coupling fluctuations alone.

First, we consider the optimistic charge noise regime, $\sigma_\varepsilon = 1$ µeV, and a favorable valley configuration, $E_{vL} = E_{vR} = 100$ µeV. We summarize infidelities for this configuration, for all three pulse families, in Fig. 6.8(a). In these plots, red and blue squares indicate infidelity due to Δ fluctuations *alone*, for conventional $10\,\mathrm{nm}$ QWs (blue) and 5% Ge QWs (red). We also indicate the expected infidelities due to detuning fluctuations, computed with Eq. (6.16) [colored lines, same data as in Fig. 6.2(a)]. The gray boundary highlight the baseline infidelities $\mathcal{I}_0$, with neither detuning fluctuations nor Δ-fluctuations, and serves as an effective lower-bound fidelity for each pulse. Examining Fig. 6.8(a), we see that the infidelities including Δ-fluctuations are not much worse than baseline infidelities, and the expected infidelity due to detuning fluctuations is generally much larger. Furthermore, across all three pulse families, we can reliably achieve total infidelity $< 10^{-4}$ for $\delta\phi \leq 0.9\pi$, estimated by summing the contributions from ε-fluctuations and Δ-fluctuations.

Next, we examine a slightly worse valley configuration, $E_{vL} = E_{vR} = 20$ µeV, in Fig. 6.8(b). This time, Δ fluctuations are no longer negligible; in many instances, the infidelity due to valley fluctuations exceeds that of detuning fluctuations. This effect is larger for the 5% Ge QWs, where $\delta\Delta$ can be much larger for the same lateral field. For the 5% Ge QW, there are even points with fairly small $\delta\phi$ where the infidelity exceeds 10^{-4}, especially for the rectangular and cosine pulse families. Nonetheless, this problem is less extreme for the charge-cosine pulse, due to its weaker driving through the anticrossing. For this pulse,
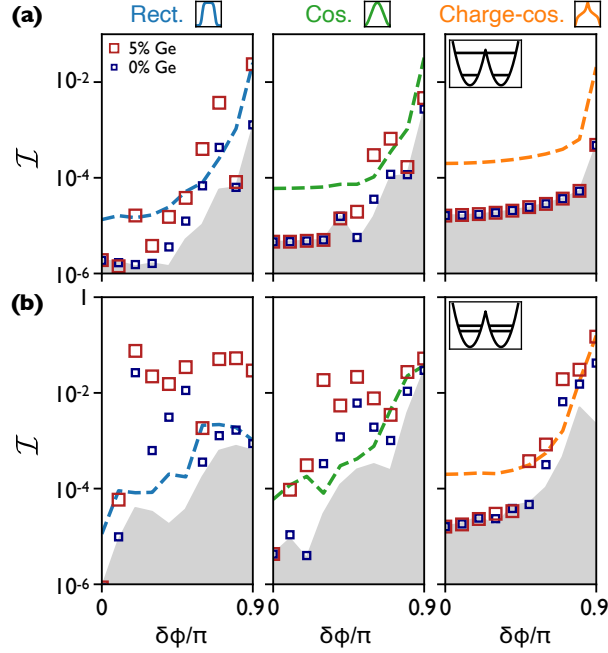
Figure 6.9: Infidelity due to valley fluctuations in the *pessimistic* charge noise regime. All plots show the same data as in Fig. 6.8, but we use $\sigma_\varepsilon = 15$ μeV when optimizing pulses and evaluating charge noise.

we note that the total infidelity, estimated by summing the infidelities due to Δ-fluctuations and detuning fluctuations, remains below 10^{-4} for $\delta\phi \leq 0.7$.

Finally, we examine the pessimistic charge noise regime, $\sigma_\varepsilon = 15$ μeV, for the same two valley configurations considered above. For the configuration $E_{vL} = E_{vR} = 100$ μeV, there is a modest range of $\delta\phi \leq 0.5\pi$ that achieves infidelities $< 10^{-4}$ for the rectangular and cosine pulses, as we see in Fig. 6.9(a). Nonetheless, both pulses are somewhat sensitive to valley fluctuations, especially at larger $\delta\phi$. The charge-cosine pulse, on the other hand, is not sensitive to valley fluctuations in this regime, but due to its weaker driving, it is more sensitive to charge noise. Hence, this pulse does not achieve infidelities $< 10^{-4}$ for $\sigma_\varepsilon = 15$ μeV.

In the less favorable valley configuration $E_{vL} = E_{vR} = 20$ μeV, the picture is considerably worse. For both the rectangular and the cosine pulse families, valley fluctuations totally dominate detuning fluctuations, even for fairly small $\delta\phi$. Except for $\delta\phi = 0$, there is no configuration with infidelities reliably below 10^{-4}. In this regime, the charge-cosine pulse

performs significantly better, since it is relatively insensitive to valley fluctuations, achieving a total infidelity $\leq 3 \times 10^{-4}$ for $\delta\phi$ between 0 and 0.4π. Yet, across our three pulse families, we find no true high-fidelity pulses.

6.6.3   Lessons for future pulse optimization schemes

We have shown above that for favorable valley configurations and low levels of charge noise, detuning fluctuations are the dominant source of infidelity in strongly-driven flopping mode qubits. In these circumstances, it suffices to model the noise as a detuning fluctuation and to optimize pulses as we have done in Sec. 6.3. However, in configurations with unfavorable valley splittings or large charge noise, infidelity due to valley fluctuations can be larger than the infidelity due to detuning fluctuations alone. This is especially true for high-Ge heterostructures. In this regime, pulse optimization schemes must account for these valley fluctuations. This not only requires a full characterization of the valley splittings and valley phase difference in the double-dot system, but also a characterization of the valley response to nearby noise sources. This will further complicate the pulse optimization procedure, adding overhead to the tune-up process in a large quantum processor. We view this as additional evidence that, to build scalable quantum processors, it is tremendously important to (1) reduce charge noise, and (2) reliably increase valley splittings. Doing so not only boosts qubit fidelities, but also makes qubit optimization more straightforward.

6.7   The scalability of flopping-mode qubits

Here, we discuss implications of our work for the scalability of flopping-mode qubits. In particular, for heterostructures in the disordered valley splitting regime, the valley parameters E_v and $\delta\phi$ are randomized from dot to dot. As we note above, flopping-mode qubit operations are, in some cases, very sensitive to these valley parameters. So, there is no guarantee that any given double-dot will enable a successful flopping-mode qubit. For example,
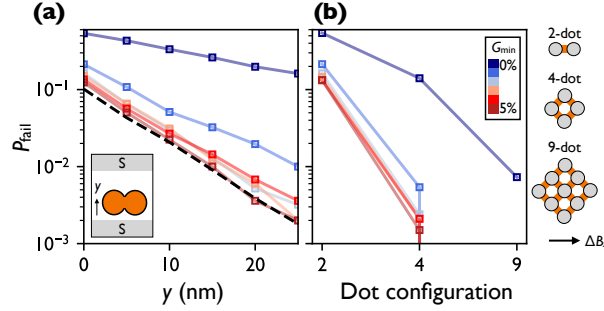
Figure 6.10: By engineering some tunability to our quantum computing architecture, we significantly improve the probability of finding high-quality qubits. (a) We plot P_{fail}, computed using Eq. (6.22), as we allow the dot some lateral adjustability within the range $[0, \Delta y]$, illustrated schematically in the inset. Each data point is computed from 2,500 instantiations of random alloy disorder. We use heterostructures with minimum Ge concentrations from 0 to 5%. For comparison, we include the lower bound P_{phase}, computed using Eq. (6.23). (b) We plot P_{fail} for quantum dot grids of various sizes, as illustrated on the right, for the same G_{min} shown in (a). Each data point computed from 10,000 random instantiations of the valley parameters in each dot. We note that for $G_{\text{min}} \geq 1\%$, the numerically calculated P_{fail} goes to zero.

in double-dots with small $E_{vL(R)}$ or valley phase differences $\delta\phi \sim \pi$, high-fidelity operations may not be possible. Given such an unfavorable configuration, though, it is possible to tune the system into a better-performing state by taking advantage of the random nature of the valley parameters. Here, we explore two strategies to improve qubit fidelities, assuming an optimistic charge noise regime $\sigma_\varepsilon = 1$ µeV.

First, we utilize lateral displacement of the double-dot system along a direction perpendicular to the detuning axis, which can be accomplished by modulating the screening gate potentials [pictured in the inset to Fig. 6.10(a)]. By moving the dot across the heterostructure, we sample a different instantiation of random alloy disorder, which modifies the valley parameters. Lateral displacements of up to 20 nm have already been demonstrated experimentally [51, 79], so we view this as a realistic scaling strategy. Second, we consider sparse grids of quantum dots, as depicted in Fig. 6.10(b), where any two neighboring dots can be used as a flopping mode qubit. For a system with two dots, there is only one possible flopping mode qubit. However, for a system with four dots in a diamond configuration, there are four possible flopping-mode qubits, indicated as orange links in Fig. 6.10(b). If a magnetic

field gradient can be produced across $\hat{x}$, each of the four qubits will have roughly the same magnetic parameters. Likewise, for a nine-dot grid, there are 12 potential double-dot qubits. By increasing the grid size, we increase the probability that any two neighboring dots will realize a high-fidelity flopping mode qubit. This method achieves better qubit operations at the expense of creating more dots. However, since quantum dots in Si are small, we view this is a reasonable price to pay.

Finally, we also consider the impact of high-Ge quantum wells in both of the strategies outlined above. Adding Ge to the quantum well can boost average E_v, making it likelier to achieve a high-fidelity valley configuration. Moreover, in Sec. 6.6, we showed that the impact of the resulting charge-noise-induced valley fluctuations can be mitigated by operating at large E_v or by careful pulse shaping. Here, we consider QWs with minimum Ge concentrations $G_{\min}$ ranging frmo 0 to 5%.

6.7.1 Defining a success criterion

Before we proceed, we must estimate the likelihood that any one double-dot will enable a high-fidelity gate. Examining Fig. 6.8(a), we note that there is a wide space of valley parameters where we expect total infidelities $< 10^{-4}$ are achievable under our optimistic charge noise assumption, $\sigma_\varepsilon = 1$ µeV. We conservatively estimate that if E_{vL} and $E_{vR} \geq 100$ µeV and $|\delta\phi| \leq 0.9\pi$, a good quality gate can be constructed for any of the three pulse families. Additionally, from Fig. 6.8(b), we estimate that even in less favorable valley configurations, if E_{vL} and $E_{vR} \geq 20$ µeV and $|\delta\phi| \leq 0.7\pi$, a low-infidelity gate can be made from the charge-cosine pulse family. If either of the two above conditions are met, we claim that a given qubit will succeed. Now, our goal is to estimate P_{fail}, the probability that *neither* of the conditions is met:

$$P_{\text{fail}} = 1 - P\left[E_{vL}, E_{vR} \geq 100 \text{ eV}, \delta\phi \leq 0.9\pi \text{ or } E_{vL}, E_{vR} \geq 20 \text{ eV}, \delta\phi \leq 0.7\pi\right]. \quad (6.22)$$

Equation (6.22) defines our approximate success criterion.

6.7.2 Lateral displacement

First, we consider lateral displacements of the dot position in the heterostructure. For each iteration, we simulate the valley splitting in each of the two dots as it is displaced by up to 25 nm across the heterostructure. We assume E_v in the left and right dots are uncorrelated, but E_v in either dot is correlated with itself as the dot moves over small distances (see Appendix E.8 for more details). Then, for a given amount of lateral displacement Δy, we compute whether or not the success criterion is met for some position y in the interval $[0, \Delta y]$. Repeating this procedure for 2,500 instantiations of random alloy disorder, we can estimate P_{fail}. We perform the above analysis for displacements up to 25 nm and for heterostructures with G_{min} ranging from 0 to 5%.

The resulting estimates of P_{fail} are plotted in Fig. 6.10(a). For heterostructures with a modest amount of Ge in the QW, the lateral tunability significantly improves success rates. For $G_{\text{min}} \geq 3$ %, we find that $P_{\text{fail}} \leq 1$ % for $\Delta y = 20$ nm. We also observe that the P_{fail} curves for different G_{min} saturate for $G_{\text{min}} \geq 3$ %, with no significant improvement observed beyond 3% Ge. For heterostructures with a modest amount of Ge, the valley splitting in each dot is no longer the limiting constraint. Instead, it is the phase difference $\delta\phi$, which is uncorrelated with the average valley splitting in a quantum well. To see this, we can also estimate the probability that the phase condition is not met, ignoring the valley splitting condition:

$$P_{\text{phase}} = P\left(|\delta\phi| > 0.9\pi \text{ for all } y \in [0, \Delta y]\right). \tag{6.23}$$

Estimates of P_{phase} from Eq. (6.23) are plotted as a dashed black line in Fig. 6.10(a). We see that P_{phase} forms a lower-bound on P_{fail}. Furthermore, since P_{phase} is independent of G_{min}, increasing the Ge content of the QW cannot reduce P_{fail} beyond this bound.

6.7.3 Sparse quantum dot grids

Next, we consider grids of quantum dots, within which we select two neighboring dots to house our qubit. As described above, such sparsely-populated grids come with a space overhead, but they allow us to sample from more possible valley parameters to select a good qubit. As described above, there is one possible qubit for a two-dot configuration, four possible qubits in a four-dot configuration, and twelve possible qubits in a nine-dot configuration. To estimate P_{fail}, we generate 10,000 values of the inter-valley coupling Δ for each dot in the n-dot system. Again, we assume Δ is uncorrelated for neighboring dots. Then, we evaluate if any of the dot pairings highlighted in Fig. 6.10(b) meet our success criterion. Results are plotted in Fig. 6.10(b). Notably, we see that if $G_{\text{min}} > 0$, P_{fail} drops below 1% for the four-dot configuration. In the nine-dot configuration, we find *zero* configurations where no suitable qubit cannot be found for all $G_{\text{min}} > 0$. Thus, by manufacturing sparse quantum dot grids, combined with a small amount of Ge in the quantum well to boost average E_v, we can engineer systems with many high-fidelity qubits with high success probability. We also analyze linear grids of qubits in Appendix E.9, where we find they have slightly larger P_{fail} than square grids of the same size, but they nonetheless significantly reduce P_{fail} compared to the base case.

6.8 Conclusion

In this work, we analyze the performance of flopping-mode quantum dot qubits in Si/SiGe. We develop an algorithm to optimize single-qubit rotations in the presence of charge noise and random valley disorder. We show that in the weak-noise limit, high-fidelity pulses can be achieved across a range of valley parameters. In the strong-noise limit, high fidelity pulses can still be achieved, provided the valley splitting in each dot is large and the valley phase difference between dots is relatively small. In addition to the typical detuning noise, we analyze the impact of small noise-induced fluctuations to the other qubit parameters.

We find that, in some regimes, small fluctuations to the valley parameters are actually the dominant source of infidelity, but this infidelity can be mitigated by softening the driving through the valley anticrossing. Finally, we analyze schemes to avoid unfavorable valley configurations, including lateral displacement of the double-dot and sparse grids of quantum dots. We find both schemes significantly enhance the probability of achieving high-fidelity qubit rotations.

6.9 Acknowledgments

Chapter 7

Strategies for enhancing spin-shuttling fidelities in Si/SiGe quantum wells with random-alloy disorder

This chapter is adapted from the preprint arXiv:2405.01832, "Strategies for enhancing spin-shuttling fidelities in Si/SiGe quantum wells with random-alloy disorder," by **Merritt P. Losert***, Max Oberländer*, Julian D. Teske, Mats Volmer, Lars R. Schreiber, Hendrik Bluhm, S. N. Coppersmith, and Mark Friesen. This was a collaborative effort between our group at Wisconsin and the group of Lars Schreiber and Hendrik Bluhm at RWTH Aachen University. Max Oberländer and I were equal contributors to this work. Max developed the numerical spin shuttling simulations, I generated the valley splitting landscapes and valley theory, and together we conceived of the strategies to improve shuttling fidelities outlined in this paper, with input from all the authors.

7.1 Introduction

Quantum dots formed in Si/SiGe heterostructures are a promising technology for scalable quantum computing. Their strengths include the fact that silicon and germanium both

have abundant zero-spin isotopes and are compatible with existing semiconductor fabrication technologies. Moreover, one- and two-qubit gate fidelities in Si/SiGe have now exceeded 99% [131, 142, 213]. However, scalable quantum computing also requires the coupling of distant qubits, which is not possible via short-ranged exchange interactions. Coupling qubits beyond the nearest neighbor is therefore a topic of great current interest [28, 80, 150, 155, 168, 188, 191, 203, 204]. Among other approaches [108, 155, 175], one promising strategy consists of physically shuttling the qubits over distances of one or more microns [24, 67, 87, 106, 109, 133, 141, 167, 179, 212, 222, 232].

Two main shuttling schemes have been proposed for quantum dot qubits: the *bucket-brigade* mode and the *conveyor* mode. In the bucket-brigade mode, the electron is moved serially along a line of quantum dots, by modulating the detuning potential between nearest neighbors [109, 133]. In the conveyor mode, which is the topic of this work, phase-shifted sinusoidal potentials are applied to interleaved clavier gates along a channel defined by two screening gates, yielding a moving potential well that carries the electron across a device [109]. A schematic illustration of a conveyor-mode device is shown in Figs. 7.1(a) and 7.1(b).

Experimentally, high-fidelity charge shuttling of electrons has now been demonstrated in silicon over distances of $\sim 20\,\mu$m [133, 167, 212], while phase-coherent shuttling has been demonstrated over distances of $\sim 400\,$nm [179] and over a cumulative distance of $10\,\mu$m using four of the dots in a 6-dot device [45]. Other experiments have demonstrated transfer across a double dot [141], and repeated transport of spins, without spin flips, through a short dot array [232]. However, an important question remains: what are the dominant limitations to coherent spin transfer over extended distances?

One of the main challenges for Si/SiGe qubits, which also affects spin shuttling, is the near-degeneracy of the two low-lying valley states [31, 231]. The energy spacing between these states, known as the valley splitting, can be as large as $300\,\mu$eV in some cases, but can also be lower than $30\,\mu$eV [19, 22, 60, 79, 128, 129, 139, 143, 163, 171, 225]. Recent theoretical advancements have shown that, for current state-of-the-art heterostructures, random-alloy
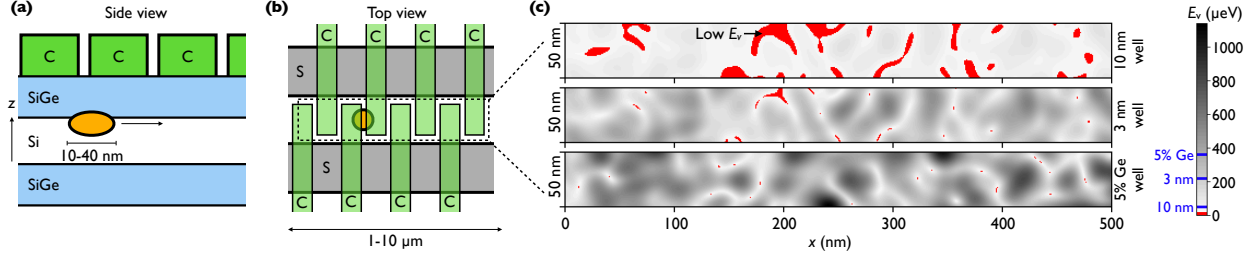
Figure 7.1: Schematic illustration of a conveyor-mode spin-shuttling device: (a) side view; (b) top view. A quantum dot in a Si quantum well is confined vertically by the SiGe barriers, and laterally by the electrostatic potential from screening gates (S) and stacked clavier (C) gates. Phase-shifted sinusoidal ac fields are applied to the C gates, yielding a moving potential minimum that carries the electron across the device [109]. (c) Simulated valley-splitting landscapes (top view), as described in Sec. 7.3.2, for quantum wells of width 10 nm (top) or 3 nm (middle), and a 10 nm quantum well with a uniform 5% concentration of Ge (bottom). Results are shown for a 500×50 nm^2 shuttling channel, where "dangerous" regions with $E_v \leq 20\,\mu\text{eV}$ are highlighted in red. We also indicate the average valley splittings for these three quantum wells on the colorbar.

disorder in the quantum well barriers is the source of the wide valley-splitting variability [115, 119, 145, 147]. Crucially, large valley-splitting fluctuations are even observed in neighboring dots formed on the same chip [117, 119, 124]. These fluctuations inevitably lead to local regions with relatively low valley splittings [199]. While a stationary spin qubit can potentially be shifted away from such a region [51, 79, 171], such fluctuations pose a greater challenge for spin shuttling experiments, where a quantum dot is rapidly shuttled across an extended and highly variable valley-splitting landscape.

Previous theoretical work has considered both the bucket-brigade and conveyor modes of shuttling [23, 30, 71, 104, 109, 114, 229]. Detailed models have been employed to study spin transfer; however at present, an extensive analysis of valley-splitting variations is still lacking for realistic heterostructures. In the current work, we incorporate a realistic statistical description of valley-splitting variations caused by alloy disorder, and we apply this to a conveyor-mode shuttling process. In particular, we apply the valley-splitting theory derived in Refs. [119, 145] to an effective dynamical model that captures the relevant effects in the parameter regime of interest. Our results show that large valley-splitting variations can cause leakage to the excited valley state, posing a significant challenge for conveyor-mode

shuttling architectures where the valley splitting is dominated by alloy disorder. To address this problem, we consider variations of the conventional quantum-well heterostructure that reduce the size of regions with low valley splitting. We also propose and investigate several control strategies to suppress valley-state excitations. By combining these strategies, we show that shuttling fidelities can be improved by several orders of magnitude, enabling high-fidelity shuttling over distances of $10\,\mu\text{m}$. A summary description of these strategies is given in Table 7.1.

The paper is organized as follows. In Sec. 7.2, we provide an intuitive explanation for the dangers of low valley splitting in shuttling experiments. In Sec. 7.3, we review the theory of valley splitting in the presence of alloy disorder. Section 7.4 describes the numerical model we use to simulate spin shuttling, and outlines possible tuning strategies that mitigate the effects of valley excitations. In Sec. 7.5, we describe the results of shuttling simulations across a $10\,\mu\text{m}$ device, while employing different mitigation strategies. In Sec. 7.6, we comment on the potential scalability of these schemes. Finally in Sec. 7.7, we summarize our findings and discuss future paths for spin shuttling. Additional details are provided in the Appendices.

7.2 Effects of valley leakage on spin shuttling

In this section, we outline the problems caused by small valley splittings in spin shuttling experiments, leaving mathematical and computational details for later sections. The main problem is leakage outside the computational subspace caused by Landau-Zener transitions from the valley ground state to the valley excited state. Since the Landé g factor differs by a small amount δg for these two states, valley excitations cause undesired spin rotations and dephasing. For example, for an external magnetic field of 0.5-1 T [60, 152], the inter-valley Zeeman energy difference can be of order $\Delta E_B/h = 10\,\text{MHz}$, yielding spin rotation errors in about $100\,\text{ns}$. In principle, fast valley relaxation processes could mitigate this problem, as we discuss briefly in a later section. However, we do not attempt to leverage this effect here,

and we simply consider valley excitations as errors.

Recent theoretical work has identified two valley-splitting regimes: *disordered* vs *deterministic* [119]. Since deterministically enhanced valley splittings are extremely difficult to achieve in the laboratory, we focus mainly on the disordered case here.

In the disordered regime, valley splitting variability is attributed mainly to alloy disorder, due to the electron overlap with the SiGe alloy. As the Ge exposure increases (for example, by adding Ge to the quantum well), the variability and average value of the valley splitting E_v also increase. This trend is evident in Fig. 7.1(c), where we show results of valley-splitting simulations for three different quantum-well profiles, all in the disordered regime. Here in red, we highlight regions where $E_v < 20\,\mu\text{eV}$, which pose a significant risk for shuttling at speeds of a few meters per second, due to enhanced Landau-Zener tunneling into the excited valley state. (See Section F.3 for details.) In the top panel, we consider a conventional quantum well of width 10 nm, and top and bottom interface widths of 1 nm. Here, large portions of the device exhibit dangerously low valley splittings. In the lower two panels, the Ge exposure is further enhanced: the middle panel shows a narrow 3 nm quantum well with 1 nm interfaces, while the lower panel shows a 10 nm quantum well, with a uniform 5% Ge concentration inside the quantum well. As consistent with our expectations, the size of the dangerous regions decreases in these examples. However, regions of low E_v still persist. Indeed, as shown in Sec. 7.3.2, such regions are statistically *guaranteed* to exist in the disordered regime. For a long-enough shuttling trajectory, a dot is very likely to encounter at least one such region, resulting in valley excitations and subsequent phase errors. In the disordered regime, additional tuning strategies are therefore needed to achieve high shuttling fidelities, as described in Sec. 7.5.

In Sec. 7.5.7, we also briefly consider the possibility of valley excitations in the deterministic regime. In this case, the valley splitting can be made uniformly large, with no randomly small values. Inter-valley leakage is then strongly reduced, even in the presence of interfacial disorder, so that high-fidelity spin shuttling is relatively easy to achieve. (See Fig. F.1,

below, and Section F.1 for further details.) However, as noted above, this regime is very difficult to reach experimentally, since it requires the presence of very abrupt features in the quantum-well profile (e.g., super-sharp interfaces, narrower than three atomic monolayers, or 0.4 nm [119]). State-of-the-art growth processes have been shown to produce quantum well interfaces with characteristic widths of 0.8 nm, which do not fall into the deterministic regime [145].

Recent work has therefore suggested alternative strategies for achieving consistently large valley splittings in Si/SiGe systems. For example, shear-strain is known to affect valley splitting in Si systems [4, 180, 192], and recent theories have proposed to use shear strain to boost valley splittings in Si/SiGe quantum dots [210]. However, some of these techniques may likewise be challenging to implement in the laboratory. Consequently, we expect the great majority of Si/SiGe devices should fall into the disordered regime, which is more consistent with current fabrication techniques. We therefore focus mainly on the disordered regime in this work.

7.3 Valley-splitting model

7.3.1 Effective-mass theory

In this work, we adopt an effective-mass envelope-function formalism to study the valley states, as outlined in Refs. [119, 145]. In this model, the $\pm z$ valley wavefunctions are approximated by

$$\psi_\pm(\mathbf{r}) = e^{\pm ik_0 z}\psi_{\mathrm{env}}(\mathbf{r}), \tag{7.1}$$

where $k_0 = 0.82(2\pi/a_0)$ is the position of the valley minimum in the first Brillouin zone and $a_0 = 0.543\,\mathrm{nm}$ is the size of the conventional Si unit cell. For our purposes, the envelope function ψ_{env} is approximately identical for both valleys. The inter-valley coupling matrix

element is defined as

$$\Delta = \langle \psi_- | H | \psi_+ \rangle = \int d^3r \, e^{-2ik_0 z} U_{\mathrm{qw}}(\mathbf{r}) |\psi_{\mathrm{env}}(\mathbf{r})|^2, \tag{7.2}$$

where the quantum-well confinement potential U_{qw} is the only term in the Hamiltonian H that significantly couples the two valley states. Since the Ge concentration of the atomic layers along $\hat{z}$ plays an important role in determining the valley splitting, we may discretize the integral in Eq. (7.2) as follows:

$$\Delta = \frac{a_0}{4} \sum_l e^{-2ik_0 z_l} U_{\mathrm{qw}}(z_l) |\psi_{\mathrm{env}}(z_l)|^2, \tag{7.3}$$

where l is the atomic layer index. The resulting valley splitting is given by $E_v = 2|\Delta|$.

The principal observation of Refs. [119, 145] is that alloy disorder partially randomizes Δ. We therefore write $\Delta = \Delta_0 + \delta\Delta$, where Δ_0 is the deterministic contribution to Δ, and $\delta\Delta$ arises from random variations of the Ge concentration. To compute these quantities, we define the Si concentration in layer l as X_l, where X_l is averaged over the area of a quantum dot, while the mean concentration $\bar{X}_l$ is averaged over the whole atomic layer. In Appendix F.5, we provide more precise definitions of these quantities, and we describe the relation between X_l and $U_{\mathrm{qw}}(z_l)$, where the latter also depends on the dot size and location.

Following Refs. [119, 145], we characterize the statistical properties of Δ in terms of the variance of $\delta\Delta$, given by

$$\sigma_\Delta^2 = \mathrm{Var}[\delta\Delta] = \frac{1}{\pi a_x a_y} \left[\frac{a_0^2 \Delta E_c}{8(X_w - X_s)} \right]^2 \sum_l |\psi_{\mathrm{env}}(z_l)|^4 \bar{X}_l (1 - \bar{X}_l). \tag{7.4}$$

Here, we assume the dot is in the ground state of a lateral harmonic confinement potential with characteristic level spacings $\hbar\omega_{x(y)}$ along the principle $x(y)$ axes, and characteristic length scales $a_{x(y)} = \sqrt{\hbar/m_t \omega_{x(y)}}$, where $m_t = 0.19 m_e$ is the transverse effective mass in Si. The quantity ΔE_c defines the conduction-band energy offset between the strained quantum
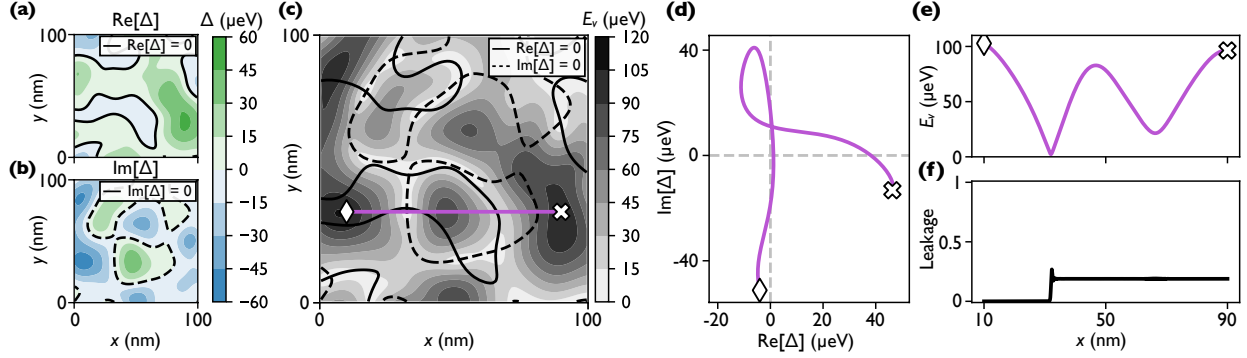
Figure 7.2: Points of vanishing valley splitting are topologically guaranteed to occur in the disordered regime. (a),(b) Real and imaginary components of the inter-valley coupling Δ, computed across a typical 100×100 nm^2 region of heterostructure, as described in the main text. Solid and dashed lines highlight contours where $\text{Re}[\Delta] = 0$ and $\text{Im}[\Delta] = 0$, respectively. (c) The valley splitting $E_v = 2|\Delta|$, obtained from (a) and (b), with the same contours superimposed. Correlations are observed between these contours and regions with low E_v. Intersections between the contours correspond to points of vanishing E_v. A sample path across the heterostructure (purple line) passes nearby one such intersection. (d) The inter-valley coupling Δ, and (e) the valley splitting E_v, along the same path shown in (c). (f) Leakage to the excited valley state caused by Landau-Zener tunneling, simulated for a dot traveling at a velocity of 1 m/s along the same path.

well and the strain-relaxed SiGe barriers. While the quantum well is conventionally formed of pure Si, we also consider more general situations where the well is formed of SiGe alloy, with a different composition than the barriers. The variables X_w and X_s then indicate the Si concentrations of the quantum well and the SiGe substrate (i.e., the barriers), respectively. Generally, $\bar{X}_l$ transitions smoothly between X_s and X_w, while X_l deviates slightly from $\bar{X}_l$ due to local fluctuations within a quantum dot.

While full details of the derivation of Eq. (7.4) are left to Refs. [145] and [119], we can provide some physical intuition here. First, we note that the quantum-well confinement energy U_{qw} is proportional to both ΔE_c and the Si concentration X_l, normalized by the concentration differential $(X_w - X_s)$. Moreover, fluctuations related to alloy disorder are expected to vanish in the limit of very large dots, due to large-scale averaging, as captured by the ratio $a_0^2/a_x a_y$. When characterizing the effects of alloy disorder, dominant contributions arise from layers with higher wavefunction density. (Note that the fourth power of the wavefunction is commonly observed in standard-deviation calculations.) Finally, we note

that SiGe alloy disorder vanishes in either limit, $\overline{X}_l \to 0$ or 1, resulting in the scaling factor $\overline{X}_l(1 - \overline{X}_l)$.

From Eq. (7.3), we note that Δ is a complex quantity, which can be decomposed into its real and imaginary components: $\Delta = \Delta_R + i\Delta_I$. Under realistic assumptions about the width of the quantum-well interface, Δ_R and Δ_I are well described here as Gaussian random variables [119], each having a variance of $\sigma_\Delta^2/2$. As we show in the following section, this property leads to the existence of regions of arbitrarily small E_v.

Finally we note that Eq. (7.4) allows us to directly characterize the valley splitting of a given heterostructure as deterministically enhanced vs disordered, based on the crossover between these two regimes, which occurs at $\sqrt{\pi}\sigma_\Delta = 2|\Delta_0|$ [119]. In the deterministic regime, we observe $|\Delta_0| > |\delta\Delta|$ with high probability, and an average valley splitting of $\bar{E}_v \approx 2|\Delta_0|$. (For example, quantum wells with ultra-sharp interfaces exhibit such behavior.) In contrast, in the disordered regime, we find $|\Delta_0| < |\delta\Delta|$ with high probability, and [119]

$$\bar{E}_v \approx \sqrt{\pi}\sigma_\Delta. \tag{7.5}$$

For conventional heterostructures, like those considered in this work, typical interfaces are not ultra-sharp, and the valley splitting falls into the disordered regime.

7.3.2 Valley-coupling landscape and excitations

As described above, in the disordered regime, the real and imaginary components of Δ are independent Gaussian random fields. We now show that this guarantees the existence of regions with arbitrarily small E_v, scattered across a heterostructure. Figures 7.2(a) and 7.2(b) illustrate typical instances of $\text{Re}[\Delta]$ and $\text{Im}[\Delta]$ for a $100{\times}100\,\text{nm}^2$ lateral region of a device. To compute these landscapes, the heterostructure is modeled atomistically by assigning each atom in the crystal lattice as either Si or Ge. The probability of choosing Si at a given lattice site in layer l is given by $\bar{X}_l$. We then perform the one-dimensional

(1D) summation in Eq. (7.3) via the following procedure. First we compute the local Si concentration X_l by performing the weighted average described in Eq. (F.14), for a dot with orbital energies $\hbar\omega_x = \hbar\omega_y = 2\,\text{meV}$, centered at (x_0, y_0). Next, we use Eq. (F.7) to convert the Si concentration profile X_l to a quantum-well confinement potential $U_{\text{qw}}(z_l)$. $\psi_{\text{env}}(z_l)$ is then computed from $U_{\text{qw}}(z_l)$ by solving a discretized Schrödinger equation, as described in Section F.5. Equation (7.3) then gives Δ as a function of dot position (x_0, y_0), yielding the real and imaginary components shown in Figs. 7.2(a) and 7.2(b). The corresponding valley splitting $E_v = 2|\Delta|$ is plotted in Fig. 7.2(c).

In Figs. 7.2(a) and 7.2(b), we highlight contours where $\text{Re}[\Delta] = 0$ and $\text{Im}[\Delta] = 0$. The same contours are also plotted in Fig. 7.2(c), where they are seen to correlate with regions of low valley splitting. Points where the contours intersect correspond to zero valley splitting. Importantly, such points are randomly distributed across the heterostructure and are guaranteed to exist in the disordered regime. Their spatial distribution is determined by the dot size, and in the disordered regime, we note that this distribution does not depend on the average valley splitting. Thus, distributions with similar topologies are observed in systems with large average E_v.

We note that a recent spin shuttling experiment has confirmed the presence of such regions of low valley splitting, scattered throughout a 2D heterostructure [199], while another shuttling experiment has demonstrated high-fidelity shuttling over a similar length scale, with no indication of low E_v [45]. Given the random nature of the valley splitting landscape, we expect larger-scale shuttling and E_v-mapping experiments to provide further clarity on the presence of these valley minima. We explore the statistics of low-E_v locations further in Appendix F.11.

The regions of low valley splitting near $\Delta \approx 0$ are dangerous for spin shuttling, because the electron can potentially tunnel into the excited valley state via a Landau-Zener process, leading to shuttling errors. This process is illustrated in Figs. 7.2(c)-7.2(f). First in Fig. 7.2(c), we highlight a shuttling path in purple that passes through a region of low E_v.
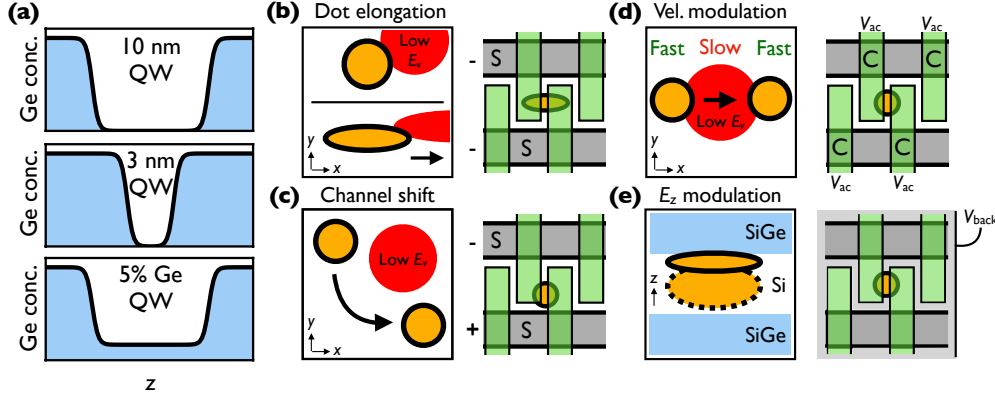
Figure 7.3: Overview of the heterostructure tuning strategies considered in this work. (a) Three different quantum wells, including a conventional 10 nm Si quantum well, a narrow 3 nm Si quantum well, and a 10 nm quantum well with a uniform 5% Ge concentration in the middle of the well. (b)-(e) Four strategies proposed for avoiding valley excitations: (b) elongating the dot along the shuttling direction while squeezing the dot in the transverse direction, by applying appropriate voltages to screening gates (S); (c) shifting the position of the dot in the channel to avoid low-E_v regions, by modulating the voltages on S gates; (d) slowing the dot velocity near E_v minima, by manipulating the ac voltages V_{ac} applied to the clavier gates (C); (e) modulating the vertical field E_z, e.g., by introducing a back gate (V_{back}).

In Fig. 7.2(d), the inter-valley coupling Δ is plotted along the same path, where it passes very near the origin of the complex plane, $\Delta = 0$. The valley splitting, $E_v = 2|\Delta|$, is also shown along this path in Fig. 7.2(e). In Fig. 7.2(f), we solve the dynamical evolution of the shuttling electron with regards to the two valley states, assuming the valley splitting shown in Fig. 7.2(e), using the methods described in Sec. 7.4, below. Specifically, we plot the leakage into the excited valley state, observing a sudden jump near the Δ minimum, caused by Landau-Zener tunneling. We expect a similar jump in the shuttling infidelity whenever a shuttling path passes through a region of low valley splitting. We also note that valley excitations across an avoided crossing require a fluctuating valley phase, in addition to a low valley splitting. (If the valley phase were constant across a region of low E_v, no excitation would occur.) However, like the valley splitting, the valley phase is also spatially random, as determined by the microscopic alloy disorder at the location of the dot. So, we generally expect some degree of valley excitation at these avoided crossings, and our simulations fully

account for the effects of valley phase variability.

In the above discussion, we have ignored effects like strain fluctuations and valley-orbit interactions that lift the valley-state degeneracy near points of low E_v. However, these effects are weak, and we expect leakage induced by Landau-Zener processes to remain prevalent in real devices.

Finally, we note that the atomistic method for generating valley-splitting landscapes, described above, is inefficient for determining large-scale statistical properties. To make this process more efficient, we turn instead to a statistical assignment of valley splittings, using the methods described in Section F.6. This assignment makes use of the fact that the real and imaginary components of Δ are Gaussian random variables. We note that, to a very good approximation, in the disordered regime, the center of these Gaussian distributions is given by $|\Delta_0| \approx 0$ [119]. The full statistical description of Δ then requires one additional piece of information: the spatial two-point covariance functions for $\text{Re}[\Delta]$ and $\text{Im}[\Delta]$, which were obtained in Ref. [119] as

$$\text{Cov}(\text{Re}[\Delta], \text{Re}[\Delta']) = \text{Cov}(\text{Im}[\Delta], \text{Im}[\Delta']) = \frac{1}{2} e^{-\delta_x^2/2a_x^2 - \delta_y^2/2a_y^2} \sigma_\Delta^2. \tag{7.6}$$

Here, Δ and Δ' are separated by the spatial vector (δ_x, δ_y) in the xy-plane. Obtaining valley-coupling landscapes with this method yields results like those shown in Fig. 7.1(c), which exhibit the correct statistical properties.

7.4 Simulating quantum dynamics

7.4.1 Physical device

Figures 7.1(a) and 7.1(b) schematically illustrate the devices we consider in this work. During conveyor-mode operation, oscillating voltages are applied to the clavier gates, to produce a moving potential pocket capable of carrying an electron across the device [167]. Unless

otherwise specified, we model this potential pocket as an isotropic harmonic confinement potential with orbital splittings $\hbar\omega_x = \hbar\omega_y = 2\,\mathrm{meV}$, and we assume the pocket moves with constant speed along the shuttling trajectory. The clavier gates generate a vertical electric field that squeezes the electron against the top quantum-well interface. In some cases, we assume this field can be tuned, for example, by including a back-gate. However, unless otherwise specified, we consider a fixed vertical field of $E_z = 5\,\mathrm{mV\,nm^{-1}}$. In Sec. 7.4.3, we consider several additional tuning capabilities that allow us to mitigate the effects of low valley splitting. These include the ability to vary the shuttling velocity, the position of the electron transverse to the shuttling trajectory, and the dot shape (e.g., with $\omega_x \neq \omega_y$). In all cases, we consider a total shuttle length of $10\,\mathrm{\mu m}$, as consistent with a recent architecture proposal involving a medium-range coupler [106].

We also consider three types of quantum wells, as illustrated in Fig. 7.3. These include a conventional 10 nm quantum well, and two other wells proposed to give larger average valley splittings: a narrow 3 nm quantum well and a structure containing a uniform 5% Ge concentration inside the quantum well. These are meant to illustrate a range of realistic heterostructures. We model the quantum-well interfaces using sigmoid functions, as described in Section F.5, and assume interface widths of $\lambda = 1\,\mathrm{nm}$, unless otherwise specified. (Note that our current goal is not to optimize heterostructure parameters, but to characterize schemes for mitigating the effects of small valley splittings.) As previously noted, the deterministic contribution to the inter-valley coupling can be safely ignored in these heterostructures, with $\Delta_0 \approx 0$, since they fall into the disordered regime. The key difference between the heterostructures is therefore their σ_Δ values, which are related to the average valley splittings through Eq. (7.5). For the heterostructures described above, we obtain the average values $\langle E_v(10\,\mathrm{nm})\rangle \approx 50\,\mathrm{\mu eV}$, $\langle E_v(3\,\mathrm{nm})\rangle \approx 220\,\mathrm{\mu eV}$, and $\langle E_v(5\%)\rangle \approx 360\,\mathrm{\mu eV}$, respectively. For our dynamical shuttling simulations, we generate many random valley-splitting landscapes, as described in Sec. 7.3.2, obtaining results like those shown in Fig. 7.1 for the three different heterostructures.

7.4.2   Spin-shuttling model

Hamiltonian

We employ a minimal model to investigate decoherence during shuttling. The model is comprised of two spin and two valley states. In particular, we ignore the presence of orbitally excited states, which relax quickly and are sufficiently separated in energy (1-2 meV) that they play a much smaller role than the valley excited state [109]. Here, we first present the model, then provide discussion of some assumptions built into it. The model is given by

$$H = \frac{E_B}{2}\sigma_z + \mathbf{\Delta}(x) \cdot \boldsymbol{\tau} + \frac{\Delta E_B}{4}[\hat{\mathbf{n}}_\Delta(x) \cdot \boldsymbol{\tau}] \otimes \sigma_z, \tag{7.7}$$

where $E_B = g\mu_B B$ is the Zeeman energy, $g \approx 2$ is the Landé g factor, μ_B is the Bohr magneton, B is the magnetic field along the spin quantization axis, which does not necessarily coincide with the crystallographic z axis, $\Delta E_B = (\delta g)\mu_B B$ is the difference in Zeeman splittings for the two valley states, $\mathbf{\Delta} = (\Delta_R, \Delta_I)^T$ is the inter-valley coupling (which varies from location to location), $\hat{\mathbf{n}}_\Delta = \mathbf{\Delta}/|\mathbf{\Delta}|$ denotes the valley quantization axis, and σ_z and $\boldsymbol{\tau} = (\tau_x, \tau_y)^T$ are Pauli matrices acting on the spin- and valley-spaces, respectively.

Several comments are in order for Eq. (7.7). First, we note that the ΔE_B term ignores any dependence on the magnitude or angular orientation of the magnetic field, as well as local variations of the applied electric field, all of which can affect δg. Moreover, we note that δg also varies slightly by location, due to interface steps and random-alloy disorder [60, 152, 209]. However, we observe almost no dependence of our results on ΔE_B (see Appendix F.7), and we therefore set it here to a fixed value of $10\,\mathrm{MHz}$, reflecting a typical difference in spin-resonance frequencies between the two valley states, as consistent with experimental observations [60, 152].

Second, we note that the model, above, does not include dephasing or relaxation effects, which we now discuss briefly. One relaxation process that could affect shuttling in silicon is the spin-valley hot spot, at which the Zeeman and valley energy splittings are nearly equal,

giving rise to fast spin relaxation [79]. An electron could potentially encounter many such hot spots when traversing a wildly varying landscape of valley splittings. We could suppress the effects of these hot spots by shuttling past them as quickly as possible; however, this has other potential pitfalls. A simpler approach is to reduce the number of hot spots by operating at low magnetic fields where the Zeeman splitting is much smaller than the average valley splitting [109]. In this work, we consider low external fields of $B = 50\,\mathrm{mT}$ [84], which moves the hot spots to below $10\,\mathrm{\mu eV}$. Although occasional hot spots are still encountered in this regime, Landau-Zener processes are also present, and since they are also detrimental to the shuttling fidelity, it reasonable to ignore the hot spots in favor of Landau-Zener processes.

Spin dephasing of the shuttling electron occurs over a time scale of T_2^*, due to the presence of charge or magnetic noise [109]. In Sec. 7.5.6, we treat these effects phenomenologically, finding that the presence of both dephasing and leakage suggests that there will be an optimal shuttling speed.

Fast valley relaxation processes present interesting opportunities for solving the valley-state leakage problem, which we will investigate in a future publication. In the present work, we note that experimental measurements of valley relaxation are scarce, but likely of order $10\,\mathrm{ms}$ for valley splittings of order $50\,\mathrm{\mu eV}$ [148], which is several orders of magnitude slower than dephasing, and therefore irrelevant. We note that these measurements were taken in static systems, and there may exist complications for dynamic, shuttled quantum dots. On the other hand, valley lifetimes scale as the inverse-fifth power of the valley splitting [109, 218], so valley and dephasing timescales could become comparable for very large valley splittings of order $500\,\mathrm{\mu eV}$ (assuming $\Delta E_B / h = 10\,\mathrm{MHz}$). Such large valley splittings may exist in certain heterostructures, but are unlikely to be widespread across a device. In this work we simply take the conservative approach of assuming no inter-valley relaxation; any nonzero valley relaxation would improve shuttling fidelities beyond what is described here.

Fidelity metrics

To quantify the fidelity of our shuttling simulations, we compute the process fidelity, defined as [208]

$$F_{\text{process}}(U) = \frac{1}{d_1^2} \left| \text{tr} \left\{ V^\dagger U_{\text{trunc}} \right\} \right|^2 , \tag{7.8}$$

where V is the target unitary in the spin subspace, $U = U_{\mathbb{B} \to \mathbb{B}'} U_t$ is the full evolution operator, including the effects of non-adiabatic evolution, $U_{\mathbb{B} \to \mathbb{B}'}$ is the transformation matrix from the initial to the instantaneous eigenbasis, U_t is the evolution operator in the initial eigenbasis of our model, and the subscript 'trunc' denotes truncation to the two-dimensional ($d_1 = 2$) spin subspace of the instantaneous valley ground state. Equation (7.8) compares the evolution of a real shuttling process to an ideal, adiabatic process, while accounting for leakage errors, which can be independently quantified as [208]

$$L = 1 - \text{tr} \left\{ U_{\text{trunc}}^\dagger U_{\text{trunc}} \right\} / d_1 . \tag{7.9}$$

When applying Eq. (7.8), we note that g-factor fluctuations cause random phases to accumulate during shuttling, even when the system remains in the ground state. Since such fluctuations are static, they can be compensated in experiments. It is therefore reasonable to remove these phase shifts from our fidelity estimates. We do this here by setting $V = \mathbb{1}$. We then apply a virtual z rotation to U_{trunc} and choose the phase of this rotation to maximize the shuttling fidelity. On the other hand, phase differences between the ground and excited valley states represent true dephasing errors, and cannot be removed. However, as no valley relaxation is assumed, these errors only directly affect U_{trunc} through a (weak) second-order Landau-Zener process, involving valley excitation followed by de-excitation. Thus, although leakage formally sets a lower bound on the infidelity (defined as $I = 1 - F$), to a good approximation, we find that $I \approx L$. Our four-level shuttling fidelity calculations could therefore be replaced by a two-level problem involving just the valley levels. For better accuracy, we still perform four-level calculations using Eq. (7.8); however, we expect leakage

to be the dominant source of infidelity.

Computational framework

The following computational procedure is used in our simulations. First, we calculate the time evolution of Eq. (7.7) using an adapted version of the Python-based software package `qopt`, described in [187]. The total propagator of the time evolution is calculated by splitting up the matrix exponential into a product of piecewise-constant Hamiltonians with appropriately small time steps. These time steps are chosen in the range of 2-4 ps, depending on the quantum well and the shuttling velocity, to achieve sufficient convergence of the final results. We check the time step used against test cases with steps as small as 0.5 ps, which indicate that the shape and the median of the distribution have both converged well forthe coarser time step. The main computational back-end used to calculate the propagators is given by the JAX package [29] (with 64-bit precision enabled), and its functions `jax.scipy.linalg.expm` and `jax.numpy.dot`. After obtaining the propagator, the fidelity is computed from Eq. (7.8) and post-optimized as described above, using the Python routine `jax.scipy.optimize.minimize` to perform phase calibration.

7.4.3 Tuning strategies

In Figs. 7.3(b)-7.3(e), we illustrate the four tuning strategies used in this work to suppress valley excitations when shuttling near points of low valley splitting: (1) elongating the quantum dot along the shuttling trajectory while squeezing it in the transverse direction (this keeps the total dot area fixed, thereby maintaining the same average E_v, to allow a fair comparison with other strategies, and ensures that the elongated electron wavefunction sees the same amount of Ge, on average), (2) shifting the lateral position of the dot within the shuttling channel, (3) modifying the shuttling velocity, and (4) varying the vertical electric field of the dot. The effects of these strategies can be understood intuitively as follows. Methods (2) and (4) simply avoid the points of low E_v. Method (3) directly suppresses the

Landau-Zener tunneling process. Method (1) causes three important effects that increase the shuttling fidelity. First, by elongating the dot along x, we reduce the length scale of the shuttling process, relative to the dot size. This causes the dot to experience fewer local E_v minima, reducing the probability of Landau-Zener valley excitations. Second, for a fixed shuttling velocity, this length scale modification also reduces the rate of change of Δ, further limiting the probability of valley excitation near E_v minima. Finally, by squeezing the dot along y by the same factor, we maintain the same average valley splitting, and we enhance our ability to tune E_v by using lateral channel shifts, for a fixed channel width. In this paper, we consider shifts from an isotropic dot with $\hbar\omega_x = \hbar\omega_y = 2$ meV to an elongated dot with $\hbar\omega_x = 1$ meV and $\hbar\omega_y = 4$ meV. Section F.10 elaborates further on the physics of the elongation strategy. The final results obviously depend quantitatively on the imposed parameter constraints. Here we have chosen experimentally reasonable constraints; an exploration of different parameter ranges is given in Section F.3.

7.5   Results

7.5.1   Evolution without applying tuning strategies

As a baseline, we first characterize spin shuttling across a spatially varying valley-splitting landscape, at a velocity of 5 m/s, without applying any fine-tuning strategies. Figure 7.4(a) shows the medians (markers) and 25-75 percentile ranges (bars) of the infidelity, computed according to Eq. (7.8), for 300 shuttling simulations, each with a different, random valley-splitting landscape. The results are reported as a function of position along the shuttling trajectory. (Here, we only show results for the initial 1 μm portion of the trajectory.) We include results for the 10 nm, 3 nm, and 5% Ge quantum wells illustrated in Fig. 7.3(a). Despite experiencing different average valley splittings, these three heterostructures exhibit similar behaviors, characterized by a rapid increase of the infidelity over short distances, to levels that are incompatible with quantum computing on a sparse-grid architecture [106]. The main

contribution to the infidelities observed in these simulations is the Landau-Zener excitation of the upper valley state, caused by momentary dips in E_v, as illustrated in Figs. 7.2(e) and 7.2(f). The simplest approach for suppressing such excitations is to uniformly reduce the shuttling velocity, which unfortunately leads to a competition between the shuttling and decoherence timescales. Other suppression strategies are therefore required, which we now include in our simulations.

7.5.2   Electric-field modulation

Local modulation of the vertical electric field E_z causes the electron wavefunction to shift vertically, as illustrated in Fig. 7.3(e), exposing it to a slightly different Ge distribution, and modifying its valley splitting [119]. It may therefore be beneficial to modify E_z when a low valley-splitting region is encountered. While any E_z value can be used in the simulations, we adopt some procedural constraints, to make our theoretical methods more compatible with experiments, and to reduce computing times. First, we restrict the E_z range to lie between 0 and 10 mV/nm. ($E_z < 0$ can also be considered, but does not change our results significantly.) We note that even larger changes in E_z may be possible when using a back gate. However, the range chosen here includes relatively high fields [79], and should therefore be sufficient for evaluating the feasibility of E_z modulations. Second, we do not allow the field to be adjusted continuously; rather, we assume piece-wise constant E_z values over 1 μm segments. To optimize the E_z values used in each shuttling segment, for a given valley landscape, we apply a graph traversal algorithm, as described in Section F.8. This path seeks to avoid regions of low valley splittings, while making as few changes to the tuning parameters as possible. In real devices with no a-priori knowledge of the valley splitting, such optimization would require either obtaining a high-resolution map of $E_v(\mathbf{r})$ [199] or applying trial-and-error methods.

Simulation results for infidelity vs shuttling distance are presented in Fig. 7.4(b) (light-gray triangles) where we show results only for the 5% Ge quantum well. We assume a single,
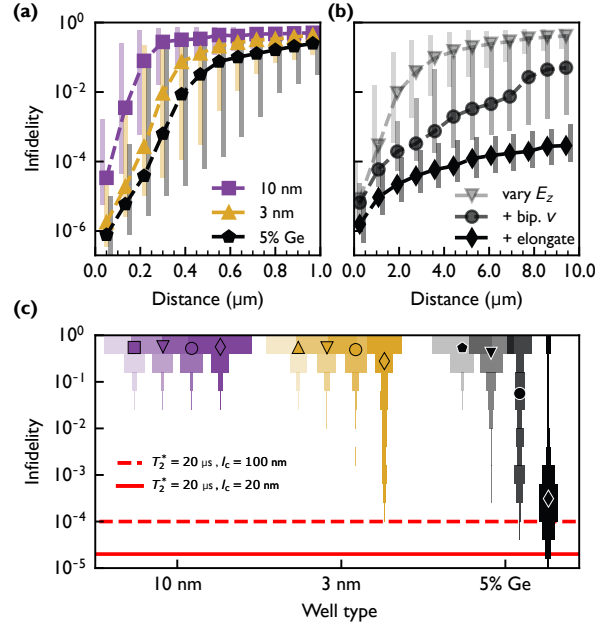
Figure 7.4: A comparison of shuttling infidelities: (a) without, vs (b) with several of the tuning strategies depicted in Figs. 7.3(b)-7.3(e), for an average shuttling velocity of 5 m/s. (a) Infidelity as a function of shuttling distance, for the three quantum wells shown in Fig. 7.3(a). (b) Infidelity computed using the following tuning strategies, for the 5% Ge quantum well: (i) E_z modulation only (gray triangles); (ii) E_z modulation plus bipartite velocity modulation (dark-gray circles); or (iii) E_z modulation, bipartite velocity modulation, and elongated dots (black diamonds). For (a) and (b), the markers represent the median values obtained from 300 different disorder realizations, while the vertical bars show the 25-75 percentiles. (Note the different horizontal scales.) (c) Histograms of results like those shown in (a) and (b), for the full shuttling distance of $10 \, \mu m$, in all three quantum wells (color coded). Within each color grouping, the tuning methods are coded with the same marker styles as in (a) and (b). Only the 5% Ge well, with either two or three tuning strategies (last two histogram columns), provides significant improvements of the shuttling fidelity. Red lines are estimates for infidelity due to spin dephasing and correspond to Eq. (7.10) evaluated for magnetic noise (solid red line) and charge noise (dashed red line), as explained further in Section 7.5.6.

fixed velocity of $5\,\mathrm{m\,s^{-1}}$, corresponding to a total shuttling time of $2\,\mathrm{\mu s}$, which is slightly shorter than commonly observed T_2^* times of a few microseconds [131, 142, 178, 223]. As indicated here, the E_z-modulation procedure provides some improvement over the baseline results shown in Fig. 7.4(a) (note the different horizontal scales in these two panels); however, the shuttling infidelities remain quite poor over the full shuttling range of $10\,\mathrm{\mu m}$.

7.5.3 Bipartite velocity modulation

To further improve the shuttling fidelity, we next consider velocity modulation as a tuning strategy for suppressing Landau-Zener excitations in regions of low valley splitting. In this case, we adopt the constraint that only two shuttling velocities are allowed (rather than a continuous range): v_{fast} and $v_{\mathrm{slow}} = v_{\mathrm{fast}}/5$. As described in Section F.3, the slower velocity is applied whenever E_v falls below a threshold value, defined as 10% of the mean value of E_v, or $20\,\mathrm{\mu eV}$, whichever is greater. These choices strike a balance between sufficiently reducing v_{slow} while retaining a reasonable total shuttling velocity. As a safety margin, we also apply v_{slow} within a $\pm 10\,\mathrm{nm}$ window around these valley-splitting minima, while setting the velocity to v_{fast} elsewhere. On average, since fewer than ten slow-downs occur per trace under these constraints, we still maintain an average velocity of approximately $5\,\mathrm{m\,s^{-1}}$, which is nearly equal to v_{fast}. Results for such bipartite velocity modulations, combined with E_z modulations, are shown in Fig. 7.4(b) (dark-gray circles). By combining tuning strategies in this way, we obtain an approximate order of magnitude improvement in the fidelity for the 5% Ge quantum well, as compared to the case where only E_z is modulated. However, the error bars of the infidelity are seen to be quite large. In Appendix F.4, we explore the effects of applying different combinations of control strategies. In particular, we consider the separate effects of velocity modulation and dot elongation, without including E_z modulation or channel shifting. This shows that velocity modulation (and dot elongation) are only effective when used in combination with an evasion strategy (e.g., E_z modulation or channel shifting). This can be understood because velocity modulation does not directly address the

problem of low valley splitting.

7.5.4   Elongated dots

Finally, we consider the shuttling of an elongated quantum dot, in which the orbital confinement energy in the shuttling direction $\hbar\omega_x$ is reduced from 2 to 1 meV (elongating the dot along $\hat{x}$), while increasing the confinement energy in the transverse direction $\hbar\omega_y$ from 2 to 4 meV (squeezing the dot along $\hat{y}$). In the current work, we do not explore potential pitfalls of this elongation strategy, although they may occur in some settings [109]. Results of such elongated-dot simulations, combined with E_z and velocity modulations, are shown in Fig. 7.4(b) (black diamonds). In this case, we obtain significant improvement over previous results, by over an order of magnitude for longer shuttling distances. Figure 7.4(c) summarizes the results of these simulations, including the base case, for all three types of quantum wells. It is interesting to note that, while simultaneously applying multiple strategies is found to improve the shuttling fidelity for the 5% Ge quantum well, much weaker improvements are found for the 10 nm and 3 nm quantum wells. In Section F.9, we show that this tepid response is a consequence of using the E_z-modulation strategy, because E_z does not provide effective tuning of E_v for the other two heterostructures.

7.5.5   Channel shifting

Since the E_z modulation scheme is not found to be effective universally, we also explore the channel-shifting strategy, depicted in Fig. 7.3(c), where the position of the electron is shifted along $\hat{y}$ to avoid regions of low valley splitting. We expect this method to be more effective than E_z modulation because E_v typically varies much more as a function of y than as a function of E_z within the parameter constraints we consider. Moreover, since lateral shifting is not sensitive to the vertical Ge confinement profile, we expect the effectiveness to depend only on the variability of the valley splitting σ_Δ, rather than other features of the quantum well.
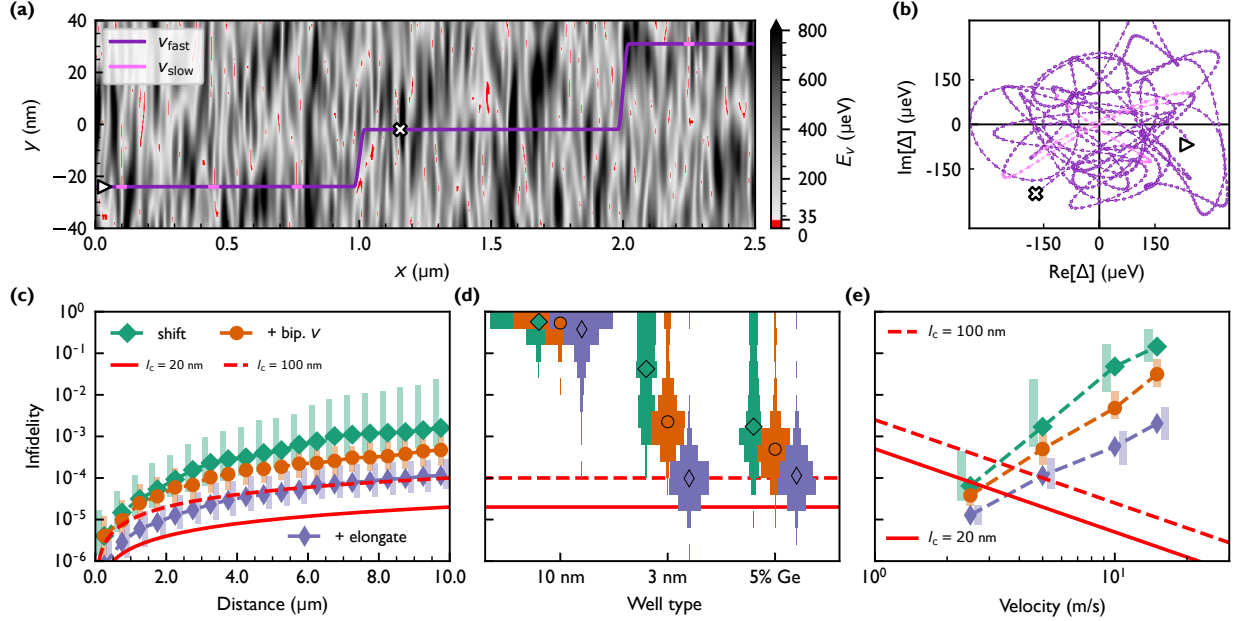
Figure 7.5: Shuttling results involving lateral channel shifting. (a) Typical valley-splitting landscape for a 5% Ge quantum well, with regions of relatively low valley splitting highlighted in red (10% or less of the average value of E_v, or about $35\,\mu\text{eV}$). An optimized, segmented shuttling trajectory is shown in purple (see main text). In the few remaining regions of low valley splitting, the shuttling velocity may be reduced to v_{slow} (indicated in pink), to suppress Landau-Zener excitations. (b) Inter-valley coupling Δ along the same path shown in (a). (c) Shuttling infidelities computed using the following tuning strategies for the 5% Ge quantum well and average shuttling velocity 5 m/s: (i) lateral channel shifting only (green diamonds); (ii) channel shifting plus bipartite velocity modulation (rust-colored circles); or (iii) channel shifting, bipartite velocity modulation, and elongated dots (narrow violet diamonds). Here, the markers represent the median values obtained from 300 different disorder realizations, while the vertical bars show the 25-75 percentiles. (d) Histograms of results like those shown in (c), for the full shuttling distance of $10\,\mu\text{m}$, in all three quantum wells. Here, the tuning methods are coded by both color and marker styles, as in (c). (e) Shuttling infidelities like those shown in (c), for the full shuttling distance of $10\,\mu\text{m}$, as a function of average shuttling velocity. Red lines in panels (c), (d) and (e) show infidelity estimates for magnetic noise (solid red line) or charge noise (dashed red line), based on Eq. (7.10), with the indicated correlation lengths l_c.

Similar to E_z modulation, we determine the optimal shuttling trajectory by applying a graph-traversal algorithm. In this case, we again consider a full $10\,\mu$m shuttling channel formed of piecewise-constant $1\,\mu$m segments. We also constrain the trajectory to lie within the channel width given by $y = \pm 50$ nm. Figure 7.5(a) illustrates one such optimized shuttling trajectory for the case of a 5% Ge quantum well, where the valley-splitting landscape is shown as grayscale, with regions of $E_v < 35\,\mu$eV highlighted in red. Here, the compromises caused by limiting the shifts to $1\,\mu$m segments are easy to visualize, because not all red regions can be avoided. Figure 7.5(b) illustrates the complicated evolution of the inter-valley coupling Δ, following along this same trajectory. While most of this evolution exhibits a sufficiently large $|\Delta|$, a small portion still approaches $|\Delta| \approx 0$, causing leakage. Averaging such results over 300 valley-splitting landscapes yields the infidelity results shown as green diamonds in Fig. 7.5(c). Here we observe immediate improvement over the E_z modulation; we even observe improvement over the best-case results in Fig. 7.4(b), obtained for the 5% Ge quantum well.

Taking the same approach as Fig. 7.4, we now include additional tuning methods in Fig. 7.5(c): the rust-colored circles show the combined results of channel-shifting and bipartite velocity modulation (using the same two velocities as Fig. 7.4), while the purple diamonds show the combined results of channel-shifting, velocity modulation, and dot elongation. In each case, we observe some fidelity improvement. Results of these different tuning schemes are shown as histograms in Fig. 7.5(d) for all three types of quantum wells. Here the best results are obtained for the 3 nm and 5% Ge quantum wells, which have much higher average valley splittings to begin with. These two quantum wells show similar results when applying multiple tuning strategies, obtaining infidelities consistently below 10^{-3}, except for a small minority of outlier cases. Importantly, the 5% Ge quantum well shows a low average infidelity when applying *only* the channel-shifting strategy, although a significant fraction of results still give poor fidelities. Finally we note that the 10 nm quantum well – with a small average valley splitting of $50\,\mu$eV – experiences particularly small E_v minima too

frequently to be compensated by any tuning method, for any reasonable velocity, for the tuning constraints we have imposed in this work.

7.5.6 Transport velocity

As previously noted, transport velocity plays an important role in determining the leakage during shuttling, since the probability of Landau-Zener excitations depends exponentially on velocity. This strong dependence is evident in Fig. 7.5(e), where we plot simulation results like those in Fig. 7.5(d) for the 5% Ge quantum well, but we now consider a range of velocities. As in Fig. 7.5(d), we adopt three tuning strategies, using the same color coding as before. Here, when bipartite velocity modulations are employed, we note that it is the *average* velocity that is reported on the horizontal axis. [The results shown in Fig. 7.5(d) correspond to the velocity of 5 m/s in Fig. 7.5(e).] As expected, we find that lower velocities cause less leakage, and the shuttling fidelity depends sensitively on the choice of velocity.

On the other hand, slower shuttling speeds also increase the risk of decoherence, so the velocity should be carefully chosen. Although we do not include decoherence directly in our shuttling model, we now provide analytical estimates, to illustrate the emergence of an optimal shuttling velocity. In Ref. [109], it was argued that the main sources of decoherence during shuttling are time-varying Overhauser magnetic fields and low-frequency charge noise, which both cause dephasing of the spin over the time scale T_2^*. The same reference obtains an approximate expression for the noise-induced shuttling infidelity, which we have adapted to the present context (note the slight difference from [109]), as discussed in Section F.2:

$$I \approx \frac{l_c L_s}{(v T_2^*)^2} \,, \tag{7.10}$$

where l_c denotes the correlation length of the quasistatic noise source, L_s=10 µm is the shuttling distance, v is the average velocity, and we note that motional narrowing has been taken into account [179].

In Fig. 7.5(c)-(e), we include two representative infidelity estimates from Eq. (7.10), obtained using l_c=20 nm (solid red lines), for the case where nuclear spin noise dominates, and l_c=100 nm (dashed red lines), for the case where charge noise dominates [109]. We also include the same infidelity estimates in Fig. 7.4(c). In both cases, we take a cautiously optimistic value of $T_2^*\approx20$ μs, as consistent with Refs. [178, 222, 223]. This analysis confirms the presence of an optimal velocity value, which depends on the tuning strategies used and the dominant noise source, but generally corresponds to a few m/s. The analysis also shows that an appropriate choice of tuning strategies and velocities should yield, in principle, shuttling infidelities below 10^{-3}.

7.5.7 Sharp interfaces with steps

Up to this point, we have only considered quantum wells with valley splittings that are determined mainly by alloy disorder, since most current devices are expected to fall into this regime [119]. For completeness, we also briefly consider the opposite regime, where alloy disorder plays a minor role. The most common quantum-well geometry for this purpose has a super-sharp interface, with an interface width of less than three atomic monolayers. For such geometries, the valley splitting should be enhanced, and the dominant form of disorder and E_v variability should arise from atomic steps at the quantum-well interface [119]. To study this situation, we perform simulations of shuttling with super-sharp interfaces and sparse step disorder, as described in Section F.1. Our results indicate that high-fidelity shuttling can be achieved in the presence of sparse step disorder, even without applying additional tuning methods. The fact that step disorder and alloy disorder can obtain such different results highlights the importance of including realistic disorder models that accurately account for random alloys.

7.6   Implementing the tuning schemes

We close by commenting on the added complexity that comes with the tuning methods proposed here, and their consequences for scalability. First, we note that dot size and shape in the elongation scheme are closely tied to the predetermined gate-electrode spacing. Some additional fine-tuning is possible; however, a truly scalable pulsing scheme favors applying the same ac signals to all the clavier gates across a quantum processor [167], suggesting that the dots (and the gate pitch) should all have a uniform size.

For the vertical or lateral channel-shifting schemes, we have proposed to divide the channel into smaller segments, which may then be manipulated in two ways, as we now explain. The most versatile approach involves manipulating each segment independently. For vertical shifting, this requires independent control of the clavier gates within each segment, while for lateral shifting it requires independent control of the screening gates in each segment. While such an approach is highly versatile, it also adds significant overhead to the wiring costs, effectively negating many of the global benefits of our shuttling scheme. The second approach involves applying tailored shift pulses to *all* the clavier gates or *all* the screening gates. This has the advantage of not requiring new control lines but has the disadvantage of affecting all the electrons within the conveyor. Thus, if multiple electrons are shuttled simultaneously, it would require a more-sophisticated path-traversal algorithm.

Hence, any channel shifting scheme will require some additional wiring costs. And, as we demonstrate in this work, we view some degree of channel shifting as necessary for achieving high-fidelity shuttling. However, this additional wiring is not infeasible. For example, if low-resolution control of the dot position within a channel suffices, the screening gates within each segment can be modulated by introducing just a few new DC lines; this represents a moderate increase in wiring complexity, which is not dissimilar from wiring requirements for achieving high-fidelity gates. Moreover, these screening gate voltages can be locked in after an initial tune-up stage. Advances in automation techniques ("auto-tuning"), allowing for the simultaneous tune-up of each shuttling channel, will reduce the initial time spent in the

tune-up stage. Altogether, this additional complexity is reasonable.

Similar considerations apply to bipartite velocity modulations, although we note that slow shuttling in a region with high valley splitting is harmless, so multi-electron shuttling is less fraught in this case. On the other hand, true global control could become a challenge, if a large number of slow-downs are needed.

Finally, we note that all proposed tuning strategies require the valley-splitting landscape to be carefully characterized. However, since the valley splitting is a static and materials-dependent property of the device, this characterization only needs to be performed once per shuttling channel. A recent experiment demonstrates that such mappings can be implemented effectively, within the same shuttling framework [199].

7.7 Summary

In this work, we have shown that leakage from the ground valley to the excited valley state is a major source of decoherence for conveyor-mode spin shuttling in Si/SiGe quantum wells. This leakage is caused by Landau-Zener excitations across a narrow energy gap, as electrons traverse the wildly varying valley-splitting energy landscape caused by alloy disorder. In turn, leakage causes dephasing of the spin, due to the presence of different g-factors in the ground and excited valley states.

Using the most current understanding of random-alloy disorder, we perform simulations of the shuttling evolution within an effective four-level Hamiltonian spanning the spin and valley degrees of freedom. For quantum wells falling into the "deterministically enhanced" valley-splitting regime (e.g., with interfaces narrower than three atomic monolayers), we find that Landau-Zener excitations do not pose a significant challenge for shuttling. It is hoped that such structures will become available for qubit implementations in the future.

Existing devices are not expected to fall into the deterministically enhanced regime, and our simulations indicate that coherent transport may be unfeasible in common 10 nm

quantum wells in this "disorder-dominated" regime. In this case, we have also performed simulations of alternative quantum wells with much higher average valley splittings, including narrow 3 nm quantum wells and quantum wells with a significant concentration of Ge in the middle of the well. We have also explored a number of tuning strategies, including shifting the location of the electron inside the shuttling channel (either vertically or laterally), to avoid passing through a valley-splitting minimum, slowing down the shuttling velocity when it passes too close to a mininum, and elongating the quantum dot to change its effective velocity. In our simulations, we have optimized these tuning strategies, and we have also simultaneously applied multiple strategies, obtaining several orders of magnitude improvement in the shuttling fidelity. Since slower shuttling velocities suppress Landau-Zener excitations but lead to dephasing, we have also optimized the velocity, finding that velocities on the order of several m/s can provide shuttling infidelities below 10^{-3}.

Finally, we note that the tuning strategies proposed here come with a nontrivial experimental overhead, which must be accounted for in scalable implementations. The valley-splitting landscape only needs to be mapped out once, however. In the future, we argue that fidelity-improving strategies like those considered here must be employed in any high-performance shuttling implementation in Si/SiGe quantum wells.

7.8 Acknowledgments

Table 7.1: Summary of the heterostructure modifications and control strategies used here to boost the shuttling fidelity.

Heterostructure modification	Effect
Narrow quantum well	Increase wavefunction overlap with Ge in the barrier regions.
High-Ge quantum well	Increase wavefunction overlap with Ge in the quantum well.
Control Strategy	Effect
Channel shift	Steer around low-E_v regions using screening gates. (Most effective single strategy.)
E_z modulation	Modulate vertical electric field to tune E_v. Requires high-Ge quantum wells, for which E_v is more tunable.
Velocity modulation	Shuttle slowly in regions of low E_v to reduce Landau-Zener excitations. (Most effective in combination with other strategies.)
Dot elongation	Elongate the dot in the shuttling direction to reduce the number of local minima and the magnitude of E_v fluctuations. (Most effective in combination with other strategies.)

Chapter 8

High-fidelity spin shuttling with very low valley splittings in Si/SiGe heterostructures

This chapter is based on work I performed with Susan Coppersmith and Mark Friesen. I performed the analytical calculations and simulations used in this work, with input from all authors.

8.1 Introduction

Spin qubits in Si/SiGe heterostructures have a number of potential advantages, including their small size and long coherence times [31, 121, 231]. High-fidelity single- and two-qubit gates have been demonstrated in these platforms [131, 142, 213, 223], and device yield and uniformity continues to improve as device design and process nodes are optimized [76, 138].

Spin qubits in quantum well heterostructures have natural nearest-neighbor connectivity though exchange interactions. Much progress has also been made in engineering longer-scale connectivity between qubits in Si/SiGe, over the scale of microns [28, 80, 108, 150, 155, 168, 175, 188, 191, 203, 204]. One particularly promising technology is the so-called *conveyor-*
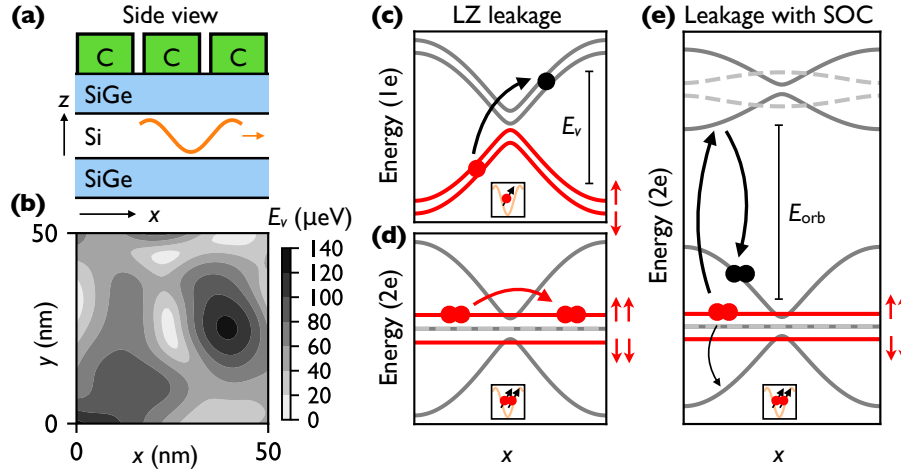
Figure 8.1: Certain two-electron states are immune to Landau-Zener-like excitations near valley minima. (a) Schematic illustration of shuttling in the conveyor mode, where interleaved clavier [C] gates create a traveling potential pocket that can drive a quantum dot across the heterostructure. (b) Variation of the valley-energy splitting E_v across a 50×50 nm^2 region of heterostructure. (c) Single-electron quantum dots are susceptible to Landau-Zener-like excitations near E_v minima. (d) Certain two-electron quantum dots (valley singlets) are immune to these excitations. (e) Leakage is the dominant error mechanism for valley-singlet two-electron states, including (weak) first-order leakage through spin-orbit coupling, and (stronger) second-order leakage via virtual occupation of excited orbital states.

mode shuttling architecture [24, 67, 87, 106, 109, 130, 141, 167, 179, 212, 222, 232]. In this scheme, oscillating sinusoidal potentials are applied to clavier gates interleaved across a shuttling channel, creating potential pockets that can drive an electron across a device, as illustrated schematically in Fig. 8.1(a).

A critical challenge for Si/SiGe spin qubits, and conveyor-mode shuttling in particular, is the presence of low-lying valley states. The Si band structure of a strained Si quantum well has two conduction band minima, creating a low-energy excited valley state. The energy gap between the ground and first-excited valley state, called the valley splitting, is known to vary significantly across a device. Valley splittings have been measured as large as $300\,\mu\text{eV}$ and as small as $30\,\mu\text{eV}$ have been measured [19, 21, 33, 60, 79, 128, 129, 139, 143, 163, 171, 199, 225]. Theoretical work has demonstrated that random alloy disorder is the dominant contributor to the valley splitting, leading to large fluctuations of the valley splitting across a device [115, 119, 145, 147]. A simulation of such a disorder-dominated valley energy landscape is

shown in Fig. 8.1(b). Importantly, this disorder creates regions of vanishing valley splitting, scattered across a device [120]. If a dot is shuttled through such a region, Landau-Zener-like excitations can cause the dot to leak outside of the computational subspace, as illustrated in Fig. 8.1(c) [116, 120]. These low-valley-splitting regions are a primary challenge for conveyor-mode shuttling, motivating much theoretical work in the field [43, 116, 120].

In this work, we explore an alternative qubit encoding for shuttling spin qubits in the conveyor mode. We demonstrate that certain two-electron states – in particular, states formed from valley singlets and polarized spin triplets – are immune to the Landau-Zener type transitions that plague single-electron shuttling, as illustrated in Fig. 8.1(d). Since the spins in these states are aligned, a transition to any other low-energy state requires a spin flip. Since the spin-valley coupling (mediated by the spin-orbit interaction) is weak in silicon, such leakage is suppressed. Instead of Landau-Zener transitions, the main leakage source for these qubits is the second-order virtual excitation of excited orbital states, as illustrated in Fig. 8.1(e), with spin-orbit coupling providing a weaker first-order leakage pathway. We demonstrate that, in certain regimes, high-fidelity spin shutting is possible *without* fine-tuning the shuttling path. Furthermore, in contrast to the single-electron case, these logical encodings actually benefit from very small valley splittings.

8.2   Physical model

We start with a description of the valley physics of one electron, before moving to the two-electron picture. We use the effective-mass approximation (EMA) to describe the valley physics, in which the single-electron valley states are formed from linear combinations of states at the Si band structure minima at $\pm k_0$ along the z-axis in the Brillouin zone, where $k_0 = 0.82 \times 2\pi/a_0$ and $a_0 = 0.543$ nm is the lattice constant of the silicon diamond cubic

lattice [63]. In the $|z_{\pm}\rangle$ basis, the single-electron valley Hamiltonian is given by

$$H_v = \begin{pmatrix} \epsilon_0 & \Delta_0 \\ \Delta_0^* & \epsilon_0 \end{pmatrix}. \tag{8.1}$$

To first order, the inter-valley coupling Δ_0 and intra-valley coupling ϵ_0 are given by

$$\begin{aligned} \Delta_0 &:= \langle z_- | U_{\mathrm{qw}} | z_+ \rangle = \int d\mathbf{r} \, e^{-2ik_0 z} \psi_0^2 U_{\mathrm{qw}} \\ \epsilon_0 &:= \langle z_{\pm} | U_{\mathrm{qw}} | z_{\pm} \rangle = \int d\mathbf{r} \, \psi_0^2 U_{\mathrm{qw}} \end{aligned} \tag{8.2}$$

where ψ_0 is the ground-state envelope function (often, assumed to be the ground-state of a harmonic confinement potential) and the quantum well potential U_{qw} is determined by the concentration of Ge atoms within the SiGe alloy barrier regions. (We note that, in general, U_{qw} includes terms due to random alloy disorder, interface width, and mono-atomic steps in the interface.) The valley splitting $E_v = 2|\Delta_0|$ [63]. Previously, it has been shown that for realistic quantum wells (with quantum well interfaces ≥ 3 atomic monolayers), Δ_0 is due primarily to alloy disorder, and is thus randomized [119]. In this limit, Δ_0 is well-described as an isotropic complex Gaussian random variable with zero mean and complex variance $\sigma_{\Delta_0}^2$, where the real and imaginary components are independent. In general, the value of σ_{Δ_0} depends on the quantum well profile and confinement strength. But these heterostructure details are not critical to our model, so we take the single-electron σ_{Δ_0} as an input to our theory. (We later comment on the relationship between σ_{Δ_0} and σ_{Δ_s}, the two-electron equivalent, in the Supplement.)

The one-electron Hamiltonian Eq. (8.1) can be transformed from the static $z_{\pm}$ basis into the basis of ground and excited valley states $|v_{g(e)}\rangle$ through the rotation

$$U_v = \frac{1}{\sqrt{2}} \begin{pmatrix} -e^{-i\phi_0} & 1 \\ e^{-i\phi_0} & 1 \end{pmatrix} \tag{8.3}$$

where $\phi_0 = \mathrm{Arg}\Delta_0$. Since ϕ_0 varies across the heterostructure, this is not a static transformation, and the effective time-dependent single-electron Hamiltonian obtains a dynamical correction:

$$\tilde{H}_v = U_v H_v U_v^\dagger - i\hbar U_v \dot{U}_v^\dagger = \frac{1}{2}\begin{pmatrix} -E_v + \hbar\dot{\phi}_0 & -\hbar\dot{\phi}_0 \\ -\hbar\dot{\phi}_0 & E_v + \hbar\dot{\phi}_0 \end{pmatrix}. \tag{8.4}$$

(Here and throughout this work, we use tildes to indicate quantities in the basis of instantaneous valley eigenstates.) We see that terms proportional to valley phase fluctuations $\hbar\dot{\phi}_0$ directly couple the ground and excited valley states. This coupling leads to Landau-Zener-like excitations wherever $\hbar\dot{\phi}$ is large and E_v is small, as often occurs near valley minima, as illustrated in Fig. 8.1(c).

Now, we consider the two-electron physics. There are two important differences from the single-electron case. First, the Coulomb interaction between the two electrons modifies the quantum dot envelope functions and reduces the orbital splitting compared to single-electron case [57]. We assume the lateral confinement potential is strong enough that excited orbital states are well-separated and can be treated perturbatively. Second, we must take care that our basis states preserve Fermion parity. There are three degrees of freedom relevant to our system: orbital, valley, and spin. Within the low-energy orbital subspace, there are six states obeying Fermion anti-symmetry. Three are valley singlet, spin triplet states:

$$|0\rangle = |S^{\mathrm{val}} T_-^{\mathrm{spin}}\rangle$$
$$|1\rangle = |S^{\mathrm{val}} T_+^{\mathrm{spin}}\rangle \tag{8.5}$$
$$|2\rangle = |S^{\mathrm{val}} T_0^{\mathrm{spin}}\rangle,$$

where $|S^{\mathrm{val}}\rangle = (|z_+ z_-\rangle - |z_- z_+\rangle)/\sqrt{2}$, $|T_-^{\mathrm{spin}}\rangle = |\downarrow\downarrow\rangle$, $|T_+^{\mathrm{spin}}\rangle = |\uparrow\uparrow\rangle$, and $|T_0^{\mathrm{spin}}\rangle = (|\uparrow\downarrow\rangle - |\downarrow\uparrow\rangle)/\sqrt{2}$. (We have omitted T_-^{orb} labels for clarity.) The remaining three states are

valley triplets and spin singlets:

$$|3\rangle = |T_-^{\mathrm{val}} S^{\mathrm{spin}}\rangle$$

$$|4\rangle = |T_+^{\mathrm{val}} S^{\mathrm{spin}}\rangle \tag{8.6}$$

$$|5\rangle = |T_0^{\mathrm{val}} S^{\mathrm{spin}}\rangle,$$

where $|T_-^{\mathrm{val}}\rangle = |z_- z_-\rangle$, $|T_+^{\mathrm{val}}\rangle = |z_+ z_+\rangle$, and $|T_0^{\mathrm{val}}\rangle = (|z_+ z_-\rangle + |z_- z_+\rangle)/\sqrt{2}$. In this basis, the spin-valley Hamiltonian to lowest order, excluding spin-orbit coupling, is given by

$$H_{\mathrm{sv}}^{2e} = \begin{pmatrix} \epsilon_s - E_z & 0 & 0 & 0 & 0 & 0 \\ 0 & \epsilon_s + E_z & 0 & 0 & 0 & 0 \\ 0 & 0 & \epsilon_s & 0 & 0 & 0 \\ 0 & 0 & 0 & \epsilon_s & 0 & \sqrt{2}\Delta_s \\ 0 & 0 & 0 & 0 & \epsilon_s & \sqrt{2}\Delta_s^* \\ 0 & 0 & 0 & \sqrt{2}\Delta_s^* & \sqrt{2}\Delta_s & \epsilon_s \end{pmatrix} \tag{8.7}$$

where Δ_s and ϵ_s are given by Eq. (8.2), replacing the single-electron envelope function ψ_0 with the two-electron envelope ψ_s, accounting for Coulomb interactions. In deriving Eq. (8.7), we have used the two-electron quantum well potential $U_{\mathrm{qw}}^{2e} = U_{\mathrm{qw}}^{(1)} \otimes I^{(2)} + I^{(1)} \otimes U_{\mathrm{qw}}^{(2)}$ (the superscript labels the electron), and we have used the fact that both electrons share the same envelope function to lowest order.

As we did in the single-electron case, we can diagonalize the Hamiltonian of Eq. (8.7) by applying a valley rotation,

$$U_v^{2e} = \begin{pmatrix} -e^{-i\phi_s} & 0 & 0 & 0 \\ 0 & \frac{1}{2}e^{-2i\phi_s} & \frac{1}{2} & -\frac{1}{\sqrt{2}}e^{-i\phi_s} \\ 0 & \frac{1}{2}e^{-2i\phi_s} & \frac{1}{2} & \frac{1}{\sqrt{2}}e^{-i\phi_s} \\ 0 & -\frac{1}{\sqrt{2}}e^{-2i\phi_s} & \frac{1}{\sqrt{2}} & 0 \end{pmatrix} \tag{8.8}$$

in the basis $\{|S^{\mathrm{val}}\rangle, |T_-^{\mathrm{val}}\rangle, |T_+^{\mathrm{val}}\rangle, |T_0^{\mathrm{val}}\rangle\}$, where $\phi_s = \mathrm{Arg}[\Delta_s]$. It is important to note that U_v^{2e} is a rotation purely in *valley* space, so it leaves spin states unmodified. As we shall see below, this property leads to the stability of valley singlets against Landau-Zener leakage. Once again, since Δ_s varies across the heterostructure, this is not a static basis transformation, and the effective time-dependent Hamiltonian obtains a dynamical correction $-i\hbar U_v^{2e}\dot{U}_v^{2e\dagger}$.

Electrons in Si/SiGe quantum dots are also known to experience weak spin-orbit coupling, which nonetheless plays an important role in spin shuttling. We use the spin-orbit coupling model of Woods et al. [209], including both inter-valley and intra-valley Rashba and Dresselhaus terms. For a single particle in the $z_\pm$ valley basis, $H_{\mathrm{so}} = \alpha\tau_0(k_x\sigma_y - k_y\sigma_x) + (\beta\tau_- + \beta^*\tau_+)(k_x\sigma_x - k_y\sigma_y)$, where σ_i are Pauli matrices in spin space, τ_i are Pauli matrices in the $z_\pm$ valley basis, $\tau_\pm = (\tau_x \pm i\tau_y)/2$ are valley raising and lowering operators, and α and $\beta = |\beta|e^{i\phi_\beta}$ are the Rashba and Dresselhaus spin-orbit coupling parameters. We take $\alpha = 2\ \mu\mathrm{eV\ nm}$ and $|\beta| = 12\ \mu\mathrm{eV\ nm}$ [209], and we set $\phi_\beta = 0$ for simplicity. The equivalent two-electron Hamiltonian is $H_{\mathrm{so}}^{2e} = H_{\mathrm{so}}^{(1)} \otimes I^{(2)} + I^{(1)} \otimes H_{\mathrm{so}}^{(2)}$. Transforming to a frame co-moving with the quantum dot, we replace $k_j \to k_j + m_t v_j/\hbar$, where v_j is the dot velocity along axis $j \in \{x, y\}$. After applying the valley rotation of Eq. (8.8), we obtain an effective spin-orbit Hamiltonian in our low-energy subspace.

Taken all together, we have the following effective first-order two-electron Hamiltonian:

$$\tilde{H}_{\mathrm{sv}}^{2e} = \begin{pmatrix} -E_z & 0 & \sqrt{2}m_{\mathrm{so}} & 0 & 0 & 0 \\ 0 & E_z & \sqrt{2}m_{\mathrm{so}}^* & 0 & 0 & 0 \\ \sqrt{2}m_{\mathrm{so}}^* & \sqrt{2}m_{\mathrm{so}} & 0 & 0 & 0 & 0 \\ 0 & 0 & 0 & -E_{v,2e} & 0 & -\frac{\hbar\dot{\phi}}{\sqrt{2}} \\ 0 & 0 & 0 & 0 & E_{v,2e} & -\frac{\hbar\dot{\phi}}{\sqrt{2}} \\ 0 & 0 & 0 & -\frac{\hbar\dot{\phi}}{\sqrt{2}} & -\frac{\hbar\dot{\phi}}{\sqrt{2}} & 0 \end{pmatrix} + (2\epsilon_s + \hbar\dot{\phi})I_{6\times6} \qquad (8.9)$$

where $E_{v,2e} = 2|\Delta_s|$, $m_{\mathrm{so}} = im_t v_x \alpha/\hbar$, and v is the shuttling speed. The first two rows of

$\tilde{H}^{2e}_{\mathrm{sv}}$ are spanned by the computational basis,

$$|0_L\rangle = |\tilde{S}^{\mathrm{val}}T^{\mathrm{spin}}_-\rangle \text{ and } |1_L\rangle = |\tilde{S}^{\mathrm{val}}T^{\mathrm{spin}}_+\rangle. \tag{8.10}$$

Note that the valley components of these states are written in terms of instantaneous eigenstates, i.e. $|\tilde{S}^{\mathrm{val}}\rangle = (|v_e v_g\rangle - |v_g v_e\rangle)/\sqrt{2}$. The remaining rows are spanned by the leakage states

$$
\begin{aligned}
|l_2\rangle = |\tilde{S}^{\mathrm{val}}T^{\mathrm{spin}}_0\rangle, \ |l_3\rangle = |\tilde{T}^{\mathrm{val}}_- S^{\mathrm{spin}}\rangle, \\
|l_4\rangle = |\tilde{T}^{\mathrm{val}}_+ S^{\mathrm{spin}}\rangle, \ |l_5\rangle = |\tilde{T}^{\mathrm{val}}_0 S^{\mathrm{spin}}\rangle.
\end{aligned}
\tag{8.11}
$$

In general, the spin-orbit terms depend on both the shuttling direction and magnetic field orientation, and the values in Eq. (8.9) are computed assuming an in-plane magnetic field $\mathbf{B} = B\hat{x}$ and shuttling along $\hat{x}$.

Some comments on Eq. (8.9) are in order. First, the terms proportional to $\hbar\dot{\phi}$ are the dynamical terms due to motion through a fluctuating valley landscape. Importantly, the logical subspace (rows 0 and 1) are not coupled to any other states via dynamical terms. Such a coupling would necessarily require a spin flip, but the valley-diagonalizing rotation of Eq. (8.8) is spin-independent. Thus, in the absence of spin-valley coupling, Landau-Zener dynamics in valley space do not impact spin, and these states are immune to Landau-Zener-type excitations. Second, spin-orbit coupling induces leakage pathways of the form $\langle 0(1)_L | H_{\mathrm{eff}} | l \rangle$. Thus, we expect leakage outside the qubit subspace to be the dominant source of shuttling infidelity, as illustrated schematically in Fig. 8.1(e). Our choice of magnetic field orientation and shuttling direction remove first-order spin-orbit coupling-induced leakage from the logical subspace to states $|l_4\rangle$, $|l_5\rangle$, and $|l_6\rangle$. In this case, $\mathbf{B}$ is aligned with $\mathbf{v}$, so only valley-preserving Rashba spin-orbit terms contribute to leakage. However, as we demonstrate in the Supplement, this choice does not significantly impact our results. It turns out that second-order virtual coupling to excited orbital states provide a stronger leakage
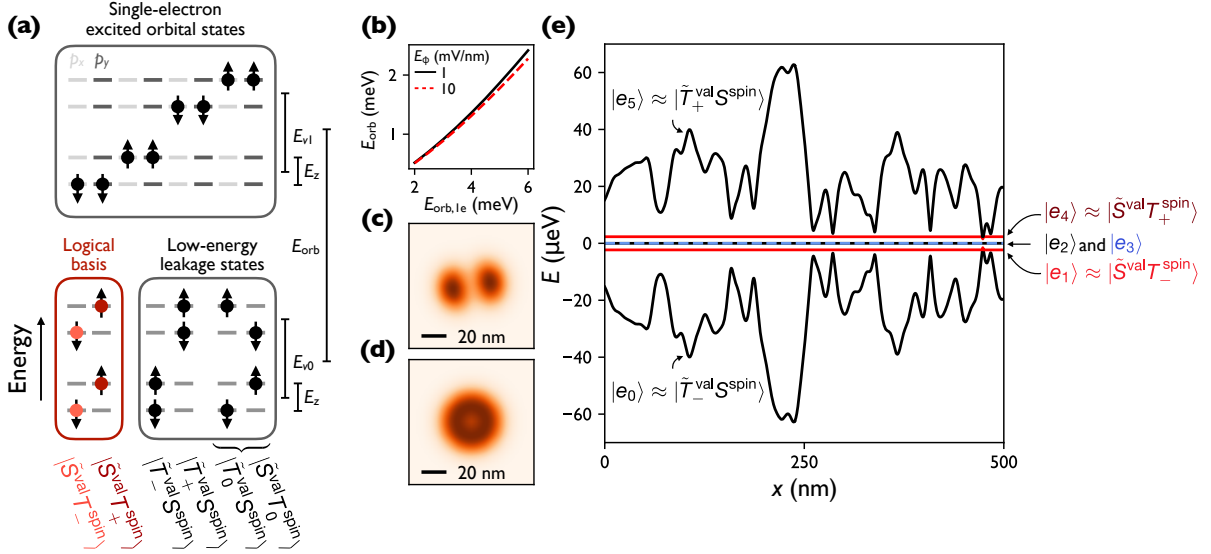
Figure 8.2: Energy level structure of two-electron quantum dots. (a) Schematic illustration of the energy levels in a doubly-occupied quantum dot, including the logical basis (red) and low-lying leakage states. The 8 single-electron excited orbital states are also illustrated, and each two-electron excited orbital state is formed from one of the 8 single-electron excited states and one low-energy state. (b) Two-electron orbital energies as a function of the confinement strength $E_{\mathrm{orb},1e}$, computed with FI methods without alloy disorder, for vertical fields $E_\phi = 1$ and $10\,\mathrm{mV\,nm^{-1}}$. (c) Electron density of the first excited orbital state. (d) Electron density of the ground orbital state. (e) Energies of the six low-lying instantaneous eigenstates (labeled $|e_j\rangle$) across a heterostructure, for a randomly generated disorder landscape, including the two qubit states $|S^{\mathrm{val}}T_\pm^{\mathrm{spin}}\rangle$ (red), and the remaining low-energy leakage states. We have ignored dynamical terms $\propto \dot{\phi}$ to compute these levels.

pathway, which we consider in the following section. Finally, in the above derivation, we ignore inter-valley g-factor variations. According to Woods et al., the g-factor fluctuations are largely equal and opposite in the ground and excited valley states, so they vanish for our logical basis states. For the remaining states, these small energy changes are dominated by the other energies in the system.

8.3   Second-order effects

In addition to spin-orbit coupling, there are second-order leakage pathways via virtual coupling to excited orbital states. There are two sources of this coupling: (1) spin-preserving valley-orbit transitions induced by alloy disorder, and (2) spin-flipping transitions induced

by spin-orbit coupling. Each of these terms induces matrix elements of the form $\langle s|H|p \rangle$, where orbital $|s\rangle$ states form our 6-level low-energy subspace, and orbital $|p\rangle$ states contain one orbital excitation. Including both p_x and p_y states, there are 32 excited orbital levels that obey Fermion parity. The low-lying and excited orbital energy levels are illustrated in Fig. 8.2(a). We assume the excited orbital states are well-separated from the low-energy subspace, so they can be treated perturbatively according to the Schrieffer-Wolf transform, leading to the second-order contributions

$$H'_{ij} = \frac{1}{2} \sum_k H_{ik} H_{kj} \left(\frac{1}{E_i - E_k} + \frac{1}{E_j - E_k} \right) \tag{8.12}$$

where i and j label states within the 6-level subspace, k runs over the 32 possible excited orbital states, H_{ik} are couplings between low-energy and excited-orbital subspaces (evaluated in the static valley basis), E_i are the diagonal terms of Eq. (8.9), and E_k are the diagonal terms of the p_x and p_y excited orbital subspace. There $6 \times 32 = 192$ possible matrix elements of the form $\langle i|H|k \rangle$, so we leave the details of this calculation to the Supplement. However, we comment here on the scaling dependencies of these leakage mechanisms. First, all second order terms are approximately proportional to $1/E_{\mathrm{orb}}$. So, leakage is reduced for more strongly-confined systems. Spin-transition matrix elements are proportional to βk_{sp}, where β is a spin-orbit coupling parameter and k_{sp} is the coupling of the form $\langle s|k|p \rangle$. Spin-preserving valley-orbit transitions, on the other hand, are proportional to integrals of the form

$$\int d\mathbf{r}\ \psi_s \psi_p U_{\mathrm{qw}} \sim \int d\mathbf{r}\ e^{-2ik_0 z} \psi_s \psi_p U_{\mathrm{qw}} \sim \sigma_\Delta. \tag{8.13}$$

Any second-order leakage pathway outside of the logical subspace requires at least one spin transition, induced by spin-orbit coupling, and one spin-preserving valley-orbit transition, scaling like $\beta k_{sp} \sigma_\Delta / \hbar$. Because leakages scale with β, this scheme benefits from the small spin-orbit coupling in Si. And because leakages scales with σ_Δ, leakage is suppressed in systems with low alloy disorder and, therefore, low valley splittings.

As described above, all second-order couplings scale like $\sim 1/E_{\text{orb}}$. To determine the size of second-order effects, we need to determine E_{orb}. In two-electron systems, the orbital energy is reduced by electron-electron Coulomb interactions [57, 58]. Thus, we must solve the fully interacting two-electron problem to accurately determine E_{orb}. By combining the effective mass approximation (EMA) and FCI methods in the MaSQE software package [6], we simulate two electrons confined by the potential $U_\phi = \frac{1}{2} m_t \omega^2 [(x - x_0)^2 + (y - y_0)^2] + e E_\phi z + U_{\text{qw}}^{\text{vc}}$, where (x_0, y_0) is the dot center, $E_{\text{orb},1e} = \hbar\omega$ is the characteristic single-electron confinement energy, E_ϕ is a vertical electric field, and $U_{\text{qw}}^{\text{vc}}$ is the quantum well potential in the virtual crystal approximation (ignoring random alloy disorder). We use a 10 nm wide quantum well, with interface widths 0.8 nm, consistent with state-of-the-art fabrication techniques [46, 145]; see the Supplement for further details. We obtain the two-electron orbital splittings E_{orb} for vertical fields $E_\phi = 1 \text{ mV nm}^{-1}$ and 10 mV nm^{-1}, plotted in Fig. 8.2(b). We also illustrate the ground-state and first-excited orbital wavefunctions in Figs. 8.2(d) and (c), demonstrating their s- and p-like character. In our shuttling simulations, for a given $E_{\text{orb},1e}$, we use E_{orb} averaged between the $E_\phi = 1$ and 10 mV nm^{-1} values.

8.4 Shuttling simulations

To evaluate the performance of our spin triplet shuttling scheme, compared to single-electron shuttling, we perform simulations of spin shuttling across 5 µm of heterostructure. To parameterize the amount of disorder in the system, we fix the size of the single-electron inter-valley coupling distribution, σ_{Δ_0}. The statistical properties of the two-electron inter-valley coupling, Δ_s, as well as valley-orbit coupling to excited orbitals, are related to σ_{Δ_0}, so we can now randomly generate these matrix elements as they fluctuate across a heterostructure, as detailed in the Supplement. We plot the instantaneous eigen-energies across a heterostructure of one such random disorder landscape in Fig. 8.2(e), where we can clearly see the energies of the polarized valley states ($|\tilde{T}_-^{\text{val}}\rangle$ and $|T_+^{\text{val}}\rangle$) fluctuate widely. The remaining

states are composed of both a ground and excited valley and have flat energy dispersions. For each disorder landscape, we numerically solve the Schrodinger equation in terms of the time evolution propagator, $i\hbar\dot{U} = HU$. In the two-electron case, $H = \tilde{H}^{2e}_{\text{sv}} + \tilde{H}'$, where $\tilde{H}^{2e}_{\text{sv}}$ is given in Eq. (8.9). The second-order contribution $\tilde{H}' = U^{2e}_v H' U^{2e\dagger}_v$, where U^{2e}_v is given in Eq. (8.8) and H' is given in Eq. (8.12). By repeating this process five times for each σ_{Δ_0}, we build up a distribution of shuttling through different instantiations of random alloy disorder.

To evaluate shuttling performance, we compute the trace infidelity [120, 208]

$$I = 1 - \left[\frac{1}{2} | \operatorname{Tr} \mathcal{P} U \mathcal{P}^\dagger U^\dagger_{\text{id}}| \right]^2 \tag{8.14}$$

where $\mathcal{P} = |0_L\rangle\langle 0_L| + |1_L\rangle\langle 1_L|$ projects the system into the logical subspace, and U_{id} is the time-evolution under an "ideal" Hamiltonian with all second-order contributions and spin-orbit terms removed.

We summarize the results of our two-electron shuttling simulations in Fig. 8.3. In panels (a) and (b), we plot the trace infidelities computed with Eq. (8.14) for total shutting distances of $2\,\mu\text{m}$ (a) and $5\,\mu\text{m}$ (b), for $\sigma_{\Delta_0} \sim \{10, 20, 50\}$ µeV, and for $E_{\text{orb},1e}$ from 2 to $6\,\text{meV}$. In these simulations, we adopt a constant shuttling velocity $v_x = 10$ m s^{-1}. Across all sets of simulations, we observe average infidelities improve with increasing $E_{\text{orb},1e}$. We also observe lower infidelities for smaller σ_{Δ_0}, as expected.

We also explore how shuttling infidelity scales with shuttling velocity. For the same set of σ_{Δ_0} and $E_{\text{orb},1e} = 4$ meV, we simulate shuttling at $v_x = 1$, 10, and $100\,\text{m s}^{-1}$, illustrated in Fig. 8.3(c). As we increase shuttling speed, we note an reduced shuttling infidelity in all cases. This is a demonstration of motional narrowing – by moving quickly through a landscape of disorder, the disorder is more rapidly averaged toward zero [109]. For shuttling at $100\,\text{m s}^{-1}$, we observe that shuttling infidelities consistently $< 10^{-3}$ are achievable in the strong-confinement, small-E_v regime.

To benchmark the performance of our two-electron shuttling scheme, we also simulate

single-electron shuttling through landscapes with the same alloy disorder characteristics. In this case, we randomly generate the single-electron inter-valley coupling Δ_0 as above. The single-electron Hamiltonian is given by $H^{1e} = \tilde{H}_v \otimes E_z\sigma_z/2$, where the single-electron valley Hamiltonian $\tilde{H}_v$ is given in Eq. (8.1). Since Landau-Zener-like excitations dominate the infidelity, we ignore all other sources of leakage, like spin-orbit coupling. In the single-electron case, the logical basis is formed by the ground valley spin states.

For $\sigma_{\Delta_0} = 10$ µeV and $E_{\mathrm{orb},1e} = 4$ meV, we plot the trace infidelity of one-electron shuttling as a function of distance, over 5 µm (light blue lines), as well as the average infidelity (dark blue line) in Fig. 8.3(d). For comparison, we include the trace infidelities of 5 single-electron shuttling simulations using the same parameters (light gray lines), as well as their average (black line). Clearly, the two-electron shuttling outperforms the single-electron shuttling – the two-electron average infidelity at 5 µm is $\sim 10^{-3}$, while the average single-electron infidelity is of order 1.

8.5 Summary

In this paper, we have proposed a scheme based on two-electron quantum dots for spin shuttling in Si devices with disordered valley landscapes. By encoding the quantum information in polarized spin triplet states, the shuttling process is immune to Landau-Zener valley excitations. Leakage is dominated by second-order virtual excitations of excited orbital states, which are reduced in systems with large orbital splittings and small valley-orbit couplings (and valley splittings). In this regime, shuttling with infidelity $< 10^{-3}$ is achievable. Moreover, no fine-tuning of the shuttling path is required. This stands in stark contrast to other proposals for high-fidelity shuttling in silicon, which require engineering large valley splittings as well as some degree of tunability in the shuttling protocol. We hope this work encourages future study of other unconventional qubit encodings, which may have desirable properties yet to be discovered.
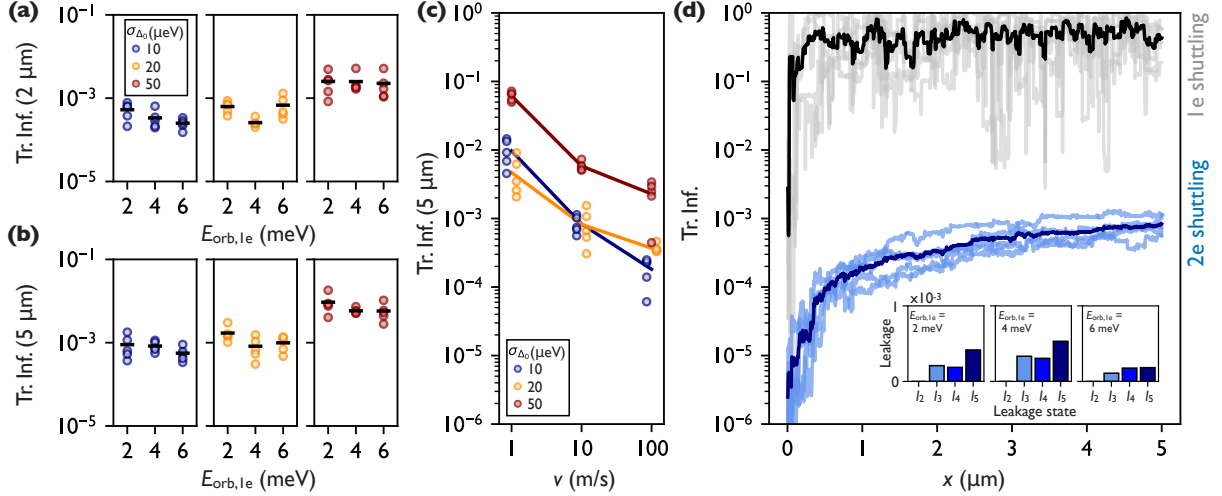
Figure 8.3: Shuttling infidelities across a range of disorder and confinement strengths. (a) Shuttling infidelity computed with Eq. (8.14) computed at distance $2\,\mu m$ for a variety of confinement strengths and σ_{Δ_0}, at shuttling speed $v = 10\ \mathrm{m\,s^{-1}}$. Black lines indicate the mean infidelity across the 5 simulations. (b) Same as (a), now at shuttling distance $5\,\mu m$. (c) Shuttling infidelities at $5\,\mu m$ for $E_{\mathrm{orb},1e} = 4$ meV for a variety of shuttling velocities. (d) For $E_{\mathrm{orb},1e} = 4$ meV and $\sigma_{\Delta_0} = 10$ µeV, we plot the trace infidelity as a function of distance for all 5 random alloy configurations (light blue), as well as the mean infidelity (dark blue). For comparison, we plot trace infidelities for one-electron shuttling under the same conditions. Inset: leakage probabilities to each of the four leakage states, averaged over 5 disorder realizations, for $E_{\mathrm{orb},1e} = 2$, 4, and 6 meV and $\sigma_{\Delta_0} = 10$ µeV.

8.6   Acknowledgements

Chapter 9

Conclusion

In this thesis, we have examined many aspects of the physics of valley splitting in Si/SiGe heterostructures. First, we examined the microscopic origins of the valley splitting, making frequent comparisons between our theories and experiments. In Chapter 2, we examined the valley splitting in the quantum Hall regime. In Chapter 3, we examine the physics of valley splitting in quantum dots. In particular, we describe the role of random alloy disorder, and we derive a theory of valley splitting that can explain the wide variation of valley splittings observed in real devices. This theory is compared to measurements of E_v in many quantum dots, showing good agreement. Furthermore, we propose a heterostructure that can boost average E_v by incorporating a uniform Ge concentration into the quantum well. In Chapter 4, we provide further experimental evidence for the role of alloy disorder in valley splitting through measurements and simulations of a Wiggle Well heterostructure. And in Chapter 5, we elaborate on the theory outlined in Chapters 3 and 4. We describe a crossover between *deterministic* and *disordered* valley splitting regimes. Quantum wells with very sharp features are in the deterministic regime, having uniformly large valley splittings. On the other hand, most realistic devices are in the disordered regme, where alloy disorder dominates and valley splittings vary widely. We demonstrate that monoatomic steps in the interface have little impact in the disordered regime, and we evaluate the performance of

many devices proposed to boost E_v.

In the second half of this thesis, we examined the impact of disorder-dominated valley splitting on scaling spin qubits in silicon. In Chapter 6, we examine the impact of E_v on strongly-driven flopping mode qubits. We show that qubit performance is strongly limited by low valley splittings and large valley phase differences across the double-dot. We also examine how various sources of disorder, combined with charge noise, impact qubit performance. In Chapter 7, we examine the impact of disorder-dominated E_v on spin shuttling. We demonstrate that regions of vanishing valley splitting are guaranteed to exist, leading to leakage during shuttling. We propose several schemes to avoid this leakage and achieve high-fidelity shuttling. And in Chapter 8, we explore an alternative qubit encoding in the polarized spin-triplet states of a two-electron quantum dot. These states are immune to Landau-Zener-type excitations, and they enable high-fidelity spin shuttling in some regimes.

Appendices

Appendix A

Supplementary Information for Chapter 2

A.1 Theoretical Methods (Supplemental Materials)

Figure 3 of the main text presents theoretical estimates for the valley splitting as a function of the magnetic field, B, and the two-dimensional electron density, n. This Supplementary Section presents details of the calculations.

The final goal of the simulation procedure is to determine the vertical electric field in the quantum Hall edge states. As a first step, we calculate the energy of a two-dimension electron gas (2DEG), which has two predominant contributions. The first is electrostatic, arising from voltages applied to top-gates, and electron-electron interactions in the 2DEG that yield screening. The second is from vertical confinement of the 2DEG (perpendicular to the 2DEG), caused by the quantum well and the vertical electric field. In the quantum Hall regime, the density of states in the 2DEG splits into highly degenerate quantized levels; however, these energy splittings are significantly smaller than the electrostatic and vertical confinement energies [34]. This separation of energy scales allows the vertical and lateral confinement problems to be solved independently, via the Born-Oppenheimer approxima-

tion, and it also allows us to apply Thomas-Fermi quasiclassical methods to describe the electrostatic screening [34]. Below, we combine the Born-Oppenheimer and Thomas-Fermi methods in a single self-consistent scheme.

For a 2DEG, the Born-Oppenheimer approximation allows us to treat the vertical (z) and lateral (x-y) confinement problems independently, beginning with the former. The vertical confinement and the electrostatics can be solved simultaneously and self-consistently using the Hartree approximation [44]. The full three-dimensional (3D) electron density takes the form $n_{3D} \approx |\psi(z)|^2 n(x, y)$, where ψ is the vertical (one-dimensional) wavefunction, and n is the usual 2D electron density. Note that $\psi(z)$ depends implicitly on x and y through n, which is taken to be a constant in this calculation. Since the electric fields used to accumulate electrons in a 2DEG are quite large, we use the method described in Ref. [63] to include important corrections arising from the wavefunction penetration into the quantum well barrier. At low temperatures, we find that electrons are confined to the lowest quantum well subband with a confinement energy given by

$$E_{\text{sb}} = \frac{5}{16}\left(\frac{33}{2}\right)^{2/3}\left[\frac{\hbar^2}{2m_l}\left(\frac{e^2 n}{\epsilon}\right)^2\right]^{1/3} - \frac{5}{3}\sqrt{\frac{2}{33}}\frac{e^2 n}{\epsilon}\sqrt{\frac{\hbar^2}{m_l \Delta E_c}}, \tag{A.1}$$

where $m_l \simeq 0.92 m_0$ is the longitudinal effective mass in silicon, $\epsilon \simeq 11.4\epsilon_0$ is the dielectric constant in low-temperature silicon, and ΔE_c is the conduction band offset of the $\text{Si}_{1-x}\text{Ge}_x/\text{Si}/\text{Si}_{1-x}\text{Ge}_x$ quantum well, which we take to be $\Delta E_c = 0.15$ eV for the $x = 0.3$ heterostructures used in this experiment. The first term in Eq. (A.1) is the leading-order contribution from confinement in an approximately triangular quantum well. The second term is the correction for the penetration of the electron wavefunction into the SiGe barrier.

Next we solve the full, 3D electrostatics, taking into account the lateral variations of $n(x, y)$. In this case, we treat the 2DEG as strictly two-dimensional, in a plane located 2 nm below the top of the quantum well. In the Thomas-Fermi method, the electron density $n(x, y)$ and the electrostatic potential $\phi(x, y, z)$ are determined self-consistently. Typically [62], n

is determined by integrating the density of states, from the lowest available electron energy in the conduction band $(-e\phi)$ up to the Fermi level, E_F, which corresponds to the global chemical potential. Here, we use the same method, but we replace the lower limit of the integration with the full quasiclassical energy, $-e\varphi + E_{\text{sb}}$. The resulting Thomas-Fermi approximation for the 2DEG density is given by

$$n = \frac{g_{\text{Si}} m_t}{2\pi\hbar^2}(E_F + e\varphi - E_{\text{sb}})\Theta[E_F + e\varphi - E_{\text{sb}}], \tag{A.2}$$

where $g_{\text{Si}} = 4$ is the band degeneracy factor for strained silicon, including two spin and two valley degrees of freedom, $m_t \simeq 0.19 m_0$ is the transverse effective mass, and $\Theta[\cdot]$ is the Heaviside step function.

Several of the terms in Eq. (A.2) depend on n. However, the term originating from the first term in Eq. (A.1), which is proportional to $n^{2/3}$, is considerably larger than the others. It is therefore convenient to adopt an approximation of the form

$$n \simeq \frac{3n_t^{1/3} n^{2/3}}{2} - \frac{n_t}{2} \tag{A.3}$$

for the smaller, linear-in-n terms in Eq. (A.2), which is valid for $n \simeq n_t$, where n_t is a typical value of the electron density. In practice, we find that Eq. (A.3) provides accurate results over the entire experimental range of interest when choosing $n_t = 2 \times 10^{11}$ cm^{-2}. Rearranging terms, the improved Thomas-Fermi approximation can be rewritten as

$$\frac{n}{n_t} = \left[\frac{E_F + e\varphi}{\frac{3\pi\hbar^2 n_t}{4m_t} - \frac{5e^2 n_t}{2\epsilon}\sqrt{\frac{2\hbar^2}{33m_l \Delta E_c}} + \frac{5}{32}\left(\frac{\hbar^2}{m_l}\right)^{1/3}\left(\frac{33e^2 n_t}{\epsilon}\right)^{2/3}} \right]^{3/2} \Theta\left[E_F + e\varphi\right], \tag{A.4}$$

where we have absorbed a global constant into the definition of E_F. For the parameters assumed here, this simplifies to

$$n = 1.6 \times 10^{46}(E_F + e\varphi)^{3/2}\Theta[E_F + e\varphi], \tag{A.5}$$

where we have assumed SI units. It is interesting to note that the scaling dependence $n \sim (E_F + e\varphi)^{3/2}$ observed in Eq. (A.5) is consistent with the 3D Thomas-Fermi approximation. This is a natural outcome of accounting for the confinement energy in Eq. (A.1), which arises from the third spatial dimension, perpendicular to the 2DEG. Since this confinement energy is relatively large, and depends strongly on n, it suggests that the more conventional 2D Thomas-Fermi approximation is likely to yield inaccurate results.

The Fermi level E_F appearing in Eq. (A.5) is constant across the whole sample, and its value is chosen to yield the desired electron density in the bulk region. For our activation energy experiments, the bulk density is given by $n_{\mathrm{bulk}} = \nu_{\mathrm{bulk}} n_B$, where $n_B = eB/h$ is the density of a single filled level [44], and ν_{bulk} is an integer. The values of n reported in the figures in the main text correspond to $n = n_{\mathrm{bulk}}$. However, the theoretical valley splittings reported in the main text are obtained from the same simulations by evaluating the vertical electric field E_z in the outer edge channel, at the position where $n = n_B$.

Finally, for completeness, we present the full energy of a 2DEG in the quantum Hall regime, including lateral quantization effects, although it is not used in our simulations:

$$\varepsilon(n, B, n_{\mathrm{LL}}, m_s, m_v) = -e\varphi(x, y) + E_{\mathrm{sb}}(x, y) + (n_{\mathrm{LL}} + \frac{1}{2})\frac{e\hbar B}{m_t} + m_s g^* \mu_B B + m_v E_v. \quad (\mathrm{A.6})$$

Here, $n_{\mathrm{LL}} = 0, 1, 2, \ldots$ is the Landau level index, $m_s = \pm 1/2$ is the spin quantum number, g^* is the Landé g-factor, $m_v = \pm 1/2$ is the valley quantum number, and E_v is the valley splitting.

Appendix B

Supplementary Information for Chapter 3

B.1 Electrical characterization

B.1.1 Magnetotransport characterisation of Hall-bar shaped heterostructure field effect transistors
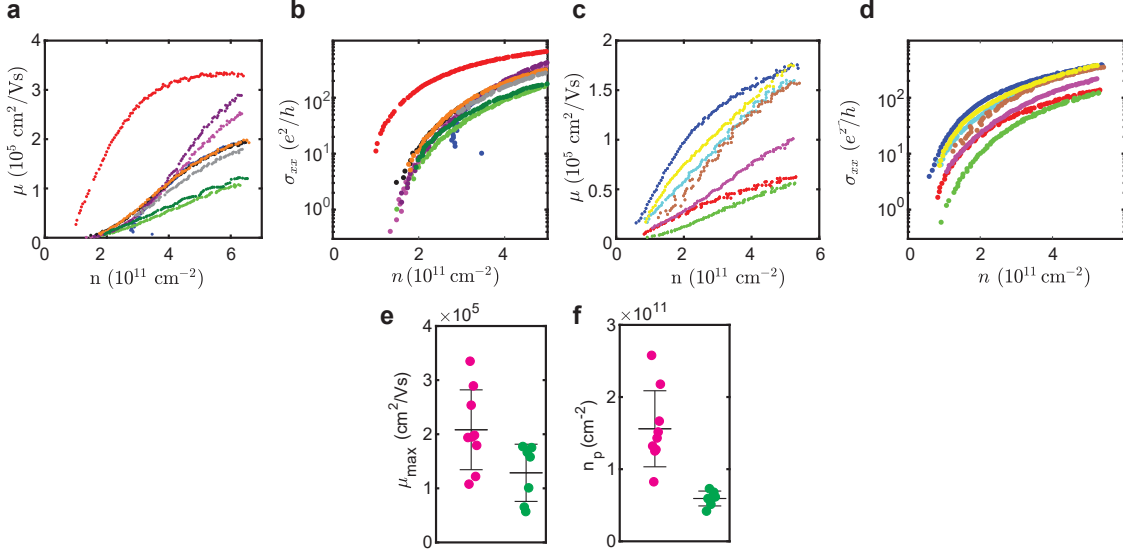
Figure B.1: **a,b**. Mobility μ and conductivity σ_{xx} as a function of Hall density n measured for quantum well A. **c**, **d** Mobility μ and conductivity σ_{xx} as a function of Hall density n measured for quantum well B. **e** Maximum mobility μ_{max} for quantum well A (magenta) and quantum well B (green) extracted from **a** and **c**. Black crosses are the mean and standard deviation. For quantum well A we find $\overline{\mu_{max}} = 129.000 \pm 53.000$ cm^2/Vs and for quantum well B we find $\overline{\mu_{max}} = 208.000 \pm 74.000$ cm^2/Vs. **f** Percolation density n_p for quantum well A (magenta) and quantum well B (green) extracted by fitting the conductivity-density curves in **b** and **d** to the relationship $\sigma_{xx} \propto (n - n_p)^{1.31}$ [189]. Since this percolation theory is valid only at low densities, for each sample we chose a fitting range that goes from the lowest measured density n_{min} to a density $n_{max,fit}$ that yields the best fitting results. For the devices from quantum well A in **b** we have $n_{max,fit} = 3.2 \times 10^{11}$ cm^{-2}, 2.2×10^{11} cm^{-2}, 2×10^{11} cm^{-2}, 2×10^{11} cm^{-2}, 2.2×10^{11} cm^{-2}, 2.2×10^{11} cm^{-2}, 2.5×10^{11} cm^{-2}, 4×10^{11} cm^{-2}, 5.8×10^{11} cm^{-2}. For the devices from quantum well B in **d** we have $n_{max,fit} = 1.35 \times 10^{11}$ cm^{-2}, 1.35×10^{11} cm^{-2}, 1.6×10^{11} cm^{-2}, 1.6×10^{11} cm^{-2}, 1.6×10^{11} cm^{-2}, 1.8×10^{11} cm^{-2}, 1.35×10^{11} cm^{-2} Black crosses are the mean and standard deviation of the percolation density. For quantum well A we find $\overline{n_p} = 1.56 \pm 0.53 \times 10^{11}$ cm^{-2} and for quantum well B we find $\overline{n_p} = 0.59 \pm 0.1 \times 10^{11}$ cm^{-2}.

B.1.2 Singlet-triplet energy splitting in quantum dots

The singlet-triplet energy splitting is computed according to the configurations in Fig. B.4.

In the configuration in Fig. B.4a the red line can be fitted to compute E_{ST} with the formula [51]:

$$V_P = \frac{1}{\alpha\beta_e} \ln \frac{e^{\frac{1}{2}\kappa B + \beta_e E_{ST}}(e^{\kappa B} + 1)}{e^{\kappa B} + e^{2\kappa B} + e^{\kappa B + \beta_e E_{ST}} + 1}, \tag{B.1}$$

where α is the lever arm converting gate voltage to energy, V_P is the gate voltage, $\kappa = g\mu_B\beta_e$ where $\beta_e = 1/k_BT_e$, g is the Lande-g-factor in silicon, μ_B is the Bohr magneton, B is the magnetic field, k_B is Boltzmann's constant, and T_e is the electron temperature [51].

In the configuration in Fig. B.4b the Hamiltonian of the T$-$ state is given by:

$$\hat{H} = \begin{pmatrix} E_{S0} & t_c \\ t_c & E_{T-} \end{pmatrix} \tag{B.2}$$

where E_{S0} is the energy evolution of the singlet state, E_{T-} is the energy evolution of the triplet minus-state, and the off-diagonal element t_c is the tunnel coupling between the (1,1)-state and the the (2,0)-state in the double quantum dot. Diagonalization of the Hamiltonian yields:

$$\mu_n(T-) = \frac{1}{2}(E_{S0} + E_{T-} + \sqrt{(E_{S0} - E_{T-})^2 + 4t_c^2}\,) \tag{B.3}$$

To fit the red line from Fig. B.4b we use $E_{S0} = 0$ and $E_{T_-} = \alpha(g\mu_B B + E_{ST})$, where α is the lever arm, g is the single particle g-factor, B is the magnetic field, and E_{ST} is the singlet-triplet splitting.
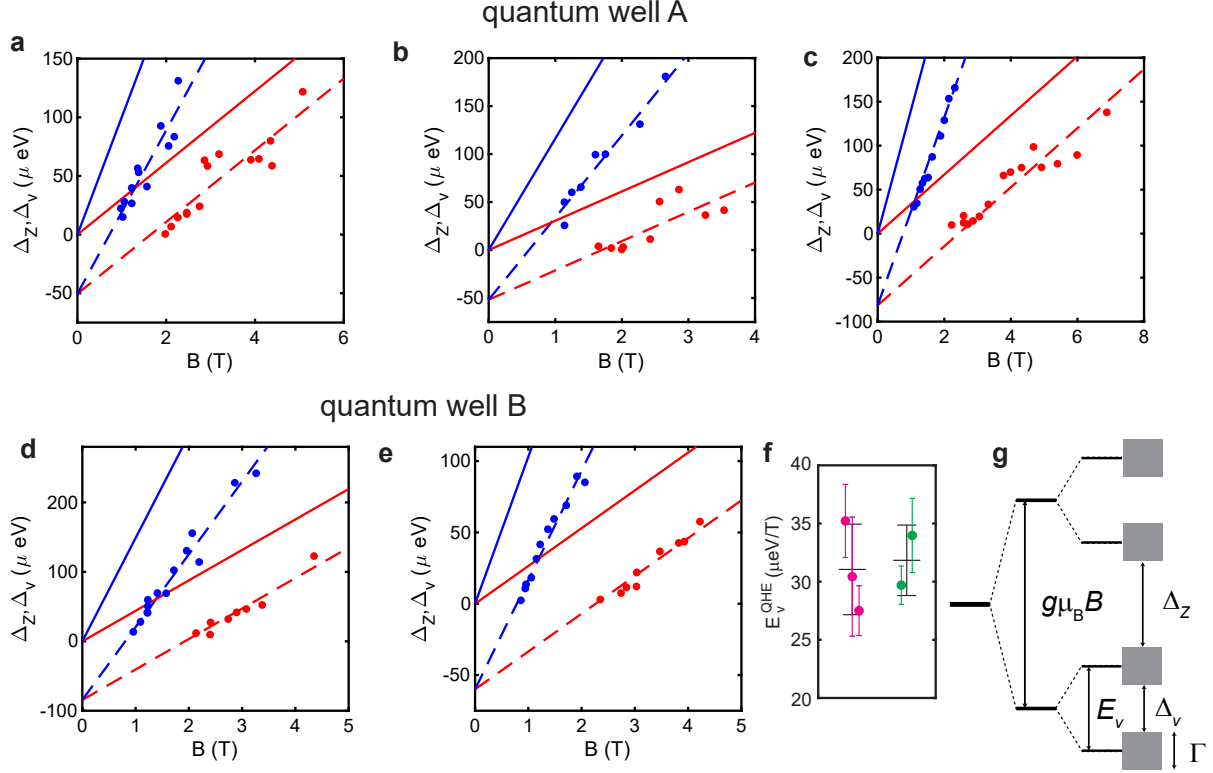
Figure B.2: **a-c** Activation energy measurements of the valley gap Δ_v (red circles) and Zeeman gap Δ_Z (blue circles) as a function of the magnetic field B for three different devices from quantum well A. Δ_v is measured at the $2n-1$ quantum Hall filling factors and Δ_Z is measured at the $4n-2$ filling factors. We follow the same methodology as in Ref. [146]. The blue and red dashed lines are theoretical fits to the experimental data using the equations $\Delta_Z = g^*\mu_B B - c_B B - \Gamma$ and $\Delta_v = c_B B - \Gamma$, where g^* is the effective Landé-g-factor, μ_B is the Bohr magneton, c_B is the proportionality factor of the valley splitting with B, and Γ is the Landau level broadening induced by disorder. We obtain $c_B = 30.64 \pm 3.14\,\mu\text{eV/T}$, $30.43\pm5.12\,\mu\text{eV/T}$, $32.46\pm2.14\,\mu\text{eV/T}$, and $g^* = 1.74\pm0.16$, 2 ± 0.21, 2.36 ± 0.12 respectively. The blue and red solid lines correspond to the estimated Zeeman and valley energy gaps, respectively. **d, e** Activation energy measurements and fits of the valley gap and Zeeman gap as in **a-c** for two devices from quantum well B. We obtain $c_B = 26.28 \pm 1.65\,\mu\text{eV/T}$, $43.15 \pm 3.19\,\mu\text{eV/T}$, and $g^* = 1.77 \pm 0.13$, 2.54 ± 0.17 respectively. **f** Rate of increase of valley splitting with magnetic field E_V^{QHE} for quantum well A (magenta) and quantum well B (green) extracted from the fitting analysis of **a-e**. We calculate E_V^{QHE} by setting $E_V^{QHE} = c_B g/g^*$, thereby scaling c_B with a coefficient g/g^* that normalizes the fitted g^* to the value $g = 2$ in silicon. This normalization is a way to take into account the modest electron-electron interaction present in different devices, allowing for a comparison across different quantum wells. Black crosses are the mean and standard deviation of E_V^{QHE}. For quantum well A we find $\overline{E_V^{QHE}} = 31.1\pm3.9\,\mu\text{eV/T}$ and for quantum well B we find $\overline{E_V^{QHE}} = 31.8\pm3\,\mu\text{eV/T}$. **g**, Schematic drawing of a Landau level split into Zeeman and valley energy levels, showing all relevant energy separations. Shaded areas represent the single-particle Landau level broadening Γ due to disorder [146].
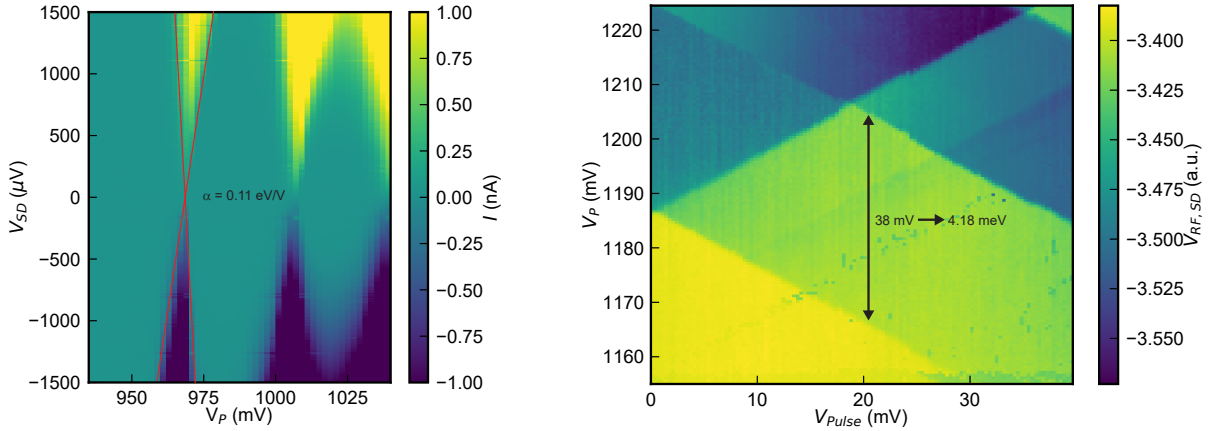
Figure B.3: **A** Coulomb blockade measurements of QD1, device 5 (see Table S3). The current through the QD is monitored while scanning the gate voltage and the bias voltage applied between the source and the drain, resulting in Coulomb diamonds. From the leftmost Coulomb diamond (indicated by the red lines) we extract a leverarm $\alpha = 0.11$ eV/V using the method described in the supplementary information of Ref. [37]. **b** Pulsed gate spectroscopy for the same quantum dot. The time-averaged RF reflectometry signal/sensing dot response is plotted as a function of the dc gate voltage V_P and the square pulse amplitude V_{pulse} with a pulse frequency of 25 kHz, both applied to the same gate. The arrow indicates the orbital splitting, which we extract as $E_{orb} = \alpha V_{orb} = 4.18$ meV, consitent with other values reported in literature [79, 129, 225].
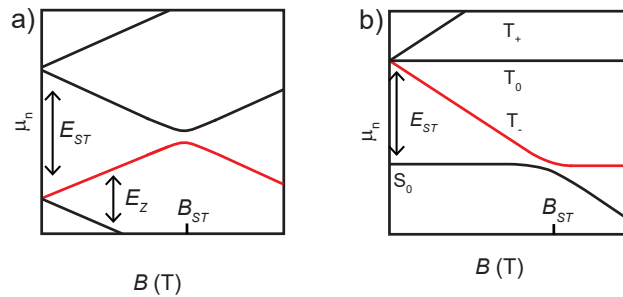
Figure B.4: **a**, Energy evolution of the ground state and first excited state in a single quantum dot as a function of the magnetic field. The red line shows the expected spin filling for the charge transition $N = 1 \rightarrow 2$. At $B = B_{ST}$ the typical kink can be observed, where the Zeeman energy E_Z is equal to the singlet-triplet splitting energy E_{ST}. **b**, Energy evolution of the four lowest lying energy states in a double quantum dot as a function of the magnetic field with fixed electron number $N = 2$. The red line represents the T_- energy state measured along the $(1,1) \rightarrow (2,0)$ transition. At $B = B_{ST}$ the singlet state S_0 and the triplet state T_- are equal in energy, resulting in an anticrossing.
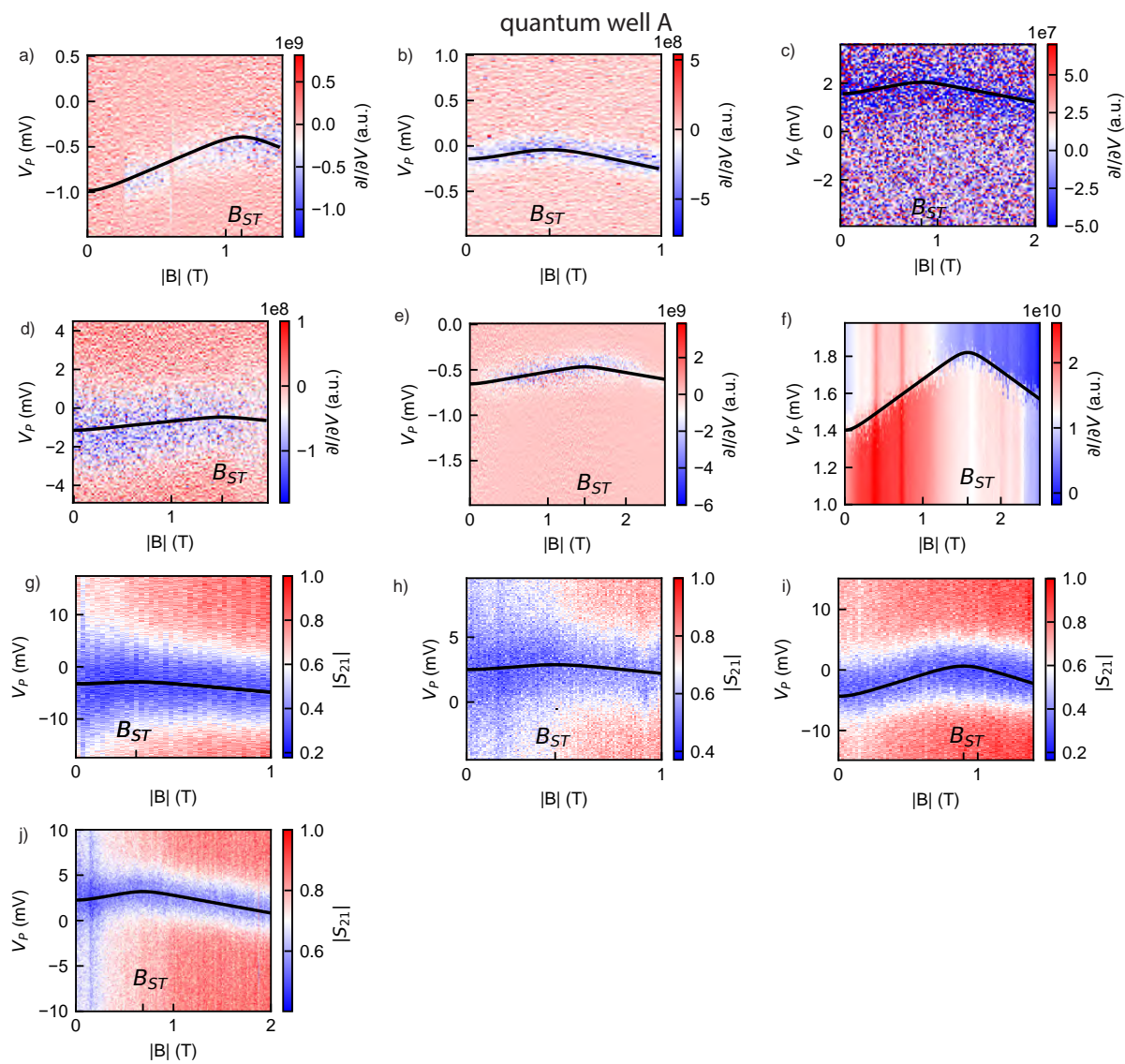
quantum well A

Figure B.5 *(previous page)*: Magnetospectroscopy of quantum dots fabricated on quantum well A. V_P is the gate voltage applied to the plunger gate forming the quantum dot. For clarity, we subtract from V_P in panels a) - j) an offset that depends is on the quantum dot being measured. a) - f) Magnetospectroscopy data measured along the $N = 1 \rightarrow 2$ transition of five different quantum dots on three different samples in quantum well A. The signal is measured by monitoring the derivative of the current through a nearby charge sensor. a), A charge fluctuation occurred during the measurement and to optimize the fitting routine, we shifted the data in the range 0.3-0.6 T upwards by 1 mV. a) - f), Due to low tunnel rates, for each gate Voltage sweep at the different magnetic fields, we determine the points with the highest derivative of the current $\frac{\partial I}{\partial V}$ through the charge sensor as the $N = 1 \rightarrow 2$ charge transition. We then use these points as the input of eq. B.1. With this equation we can fit the charge transition as a function of the magnetic field (black curve). g) - j) Magnetospectroscopy data measured along the $N = 1 \rightarrow 2$ transition of four different quantum dots on two different samples in quantum well A. The quantum dot is probed via gate-based sensing using an on-chip superconducting resonator in these measurements [155]. The magnitude of the transmitted microwave signal S_{21} through a feed line that is capacitively coupled to the resonator is plotted here. For each gate Voltage sweep at the different magnetic fields, we use a Lorentzian function to find the resonance peak of the signal. The resonance peaks then are used as input of eq. B.1. With this equation we can fit the charge transition as a function of the magnetic field (black curve).
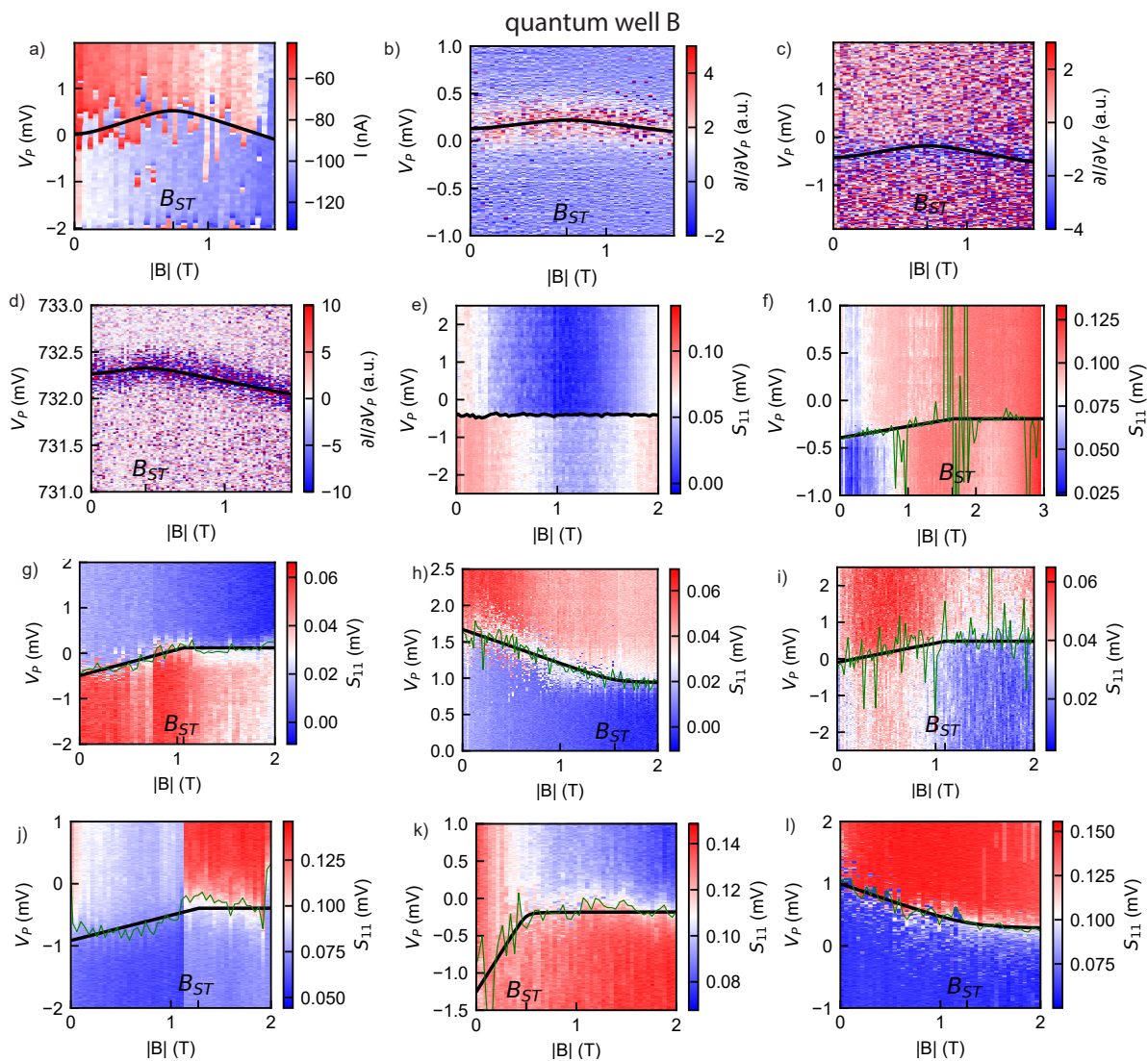
quantum well B

Figure B.6 *(previous page)*: Magnetospectroscopy of quantum dots fabricated on quantum well B. V_P is the gate voltage applied to the plunger gate forming the quantum dot. For clarity, we subtract from V_P in panels a) - l) an offset that depends is on the quantum dot being measured. a) -d) Magnetospectroscopy data measured along the $N = 1 \rightarrow 2$ transition of four different quantum dots on two different samples in quantum well B. The signal is measured by monitoring **a**, the current I through a nearby charge sensor, or **b** - **d** by monitoring the derivative of the current $\frac{\partial I}{\partial V}$ through a nearby charge sensor. **a** - **d**, To extract the inflection point of the electron charge transition, we fit the signal of the detuning for every magnetic field to eq. (2) from Ref. [48]. The inflection points then are used as input of eq. B.1. With this equation we can fit the charge transition as a function of the magnetic field (black curve). e) - l) Magnetospectroscopy data measured along the $N = (1, 1) \rightarrow (2, 0)$ transition of eight different quantum dots on two different samples in quantum well B. The signal is measured by monitoring the reflected amplitude of the rf readout signal through a nearby charge sensor. To extract the inflection point of the electron charge transition, we fit the signal of the detuning for every magnetic field to eq. (2) from Ref. [48]. Here we superimpose the inflection points as green curves, to help the reader to follow the charge transitions. To extract B_{ST} we use the crossing point of two linear fits (black solid lines) along the T_- and S_0-state. On top of these samples there is a micromagnet lowering the magnetic field strength at the center of the sample by up to 0.2 T corresponding to 23 μeV which is taken as a lower bound for measurable E_{ST}.

Stack	Wafer ID	database processing ID	Figure	device ID	transition	B_{ST} (T)	E_{ST} (µeV)	d_p (nm)
QW A	QT428	DEMO 13	S4a	D1 2-dot, P2	$(0,1) \rightarrow (0,2)$	1.11	129±1.1	50
QW A	QT428	DEMO 13	S4b	D1 2-dot, P1	$(0,1) \rightarrow (0,2)$	0.42	49.4±2.2	50
QW A	QT428	DEMO 21	S4c	D2 2-dot, P1	$(0,1) \rightarrow (0,2)$	0.83	96.6±6.3	50
QW A	QT428	DEMO 21	S4d	D2 2-dot, P2	$(0,1) \rightarrow (0,2)$	1.47	170.4±9.0	50
QW A	QT428	DEMO 15	S4e	D3 2-dot, P1	$(0,1) \rightarrow (0,2)$	1.52	176.3±13.4	50
QW A	QT428	DEMO 15	1f, S4f	D3 2-dot, P2	$(0,1) \rightarrow (0,2)$	1.57	182.3±5.8	50
QW A	QT539	SQ19-193-1-3-03	S4, g	D4 2-dot, P1	$(0,1) \rightarrow (0,2)$	0.31	35.7±5.9	50
QW A	QT539	SQ19-193-1-3-03	S4, h	D4 2-dot, P2	$(0,1) \rightarrow (0,2)$	0.45	52.6±0.8	50
QW A	QT539	SQ19-193-1-3-04	S4, i	D5 2-dot, P1	$(0,1) \rightarrow (0,2)$	0.9	104±1.6	50
QW A	QT539	SQ19-193-1-3-04	S4, j	D5 2-dot, P2	$(0,1) \rightarrow (0,2)$	0.69	79.6±2.0	50
QW B	QT592	SQ20-20-5-25-2	S5, a	D1 5-dot, P4	$(0,1) \rightarrow (0,2)$	0.74	85.7±2.0	40
QW B	QT592	SQ20-20-5-25-2	S5, b	D1 5-dot, P1	$(0,1) \rightarrow (0,2)$	0.71	82.1±3.7	40
QW B	QT592	SQ20-20-5-25-2	S5, c	D1 5-dot, P2	$(0,1) \rightarrow (0,2)$	0.7	81.7±10.1	40
QW B	QT553	SQ19-228-2-44-2	S5, d	D6 2-dot, P2	$(0,1) \rightarrow (0,2)$	0.41	47.2±3.68	50
QW B	QT592	SQ20-20-5-18-4	S5, e	D1 6-dot, P3	$(1,1) \rightarrow (0,2)$	0	0±0	50
QW B	QT592	SQ20-20-5-18-4	S5, f	D1 6-dot, P4	$(1,1) \rightarrow (0,2)$	1.73	191.5±13.2	50
QW B	QT637	SQ20-205-2-12	S5, g	D2 6-dot, P1	$(1,1) \rightarrow (0,2)$	1.06	123.1±8.9	40
QW B	QT637	SQ20-205-2-12	S5, h	D2 6-dot, P2	f $(1,1) \rightarrow (0,2)$	1.56	180.5±9.7	40
QW B	QT637	SQ20-205-2-12	S5, i	D2 6-dot, P3	$(1,1) \rightarrow (0,2)$	1.1	126.8±33.6	40
QW B	QT637	SQ20-205-2-12	S5, j	D2 6-dot, P4	$(1,1) \rightarrow (0,2)$	1.27	147.3±15.7	40
QW B	QT637	SQ20-205-2-12	S5, k	D2 6-dot, P5	$(1,1) \rightarrow (0,2)$	0.5	57.9±13.5	40
QW B	QT637	SQ20-205-2-12	S5, l	D2 6-dot, P6	$(1,1) \rightarrow (0,2)$	1.25	144.6±19.1	40

Table B.1: Summary of quantum dot valley splitting measurements. Among all devices measured, in one case (data point $E_{ST} = 0$ µeV) we did not observe in magnetospectroscopy the signature kink associated with valley splitting. This indicates a very small valley splitting, below the lower bound of about 23 µeV set by our experimental measurement conditions. While very small valley splitting values are within the predicted theoretical distributions in the main text, previous theories [63] suggest that they could also originate from the presence of an atomic step within the quantum dot.

B.2   Material characterization

B.2.1   Atom Probe Tomography analysis of interfaces

Atom Probe analysis (APT) of the interfaces is done in 5 steps. All of them explained in detail below. First, the entire measurement is reconstructed using the standard reconstruction algorithms [10]. Second, a cube approximately representing the size of an electrical defined quantum in the x,y-plane and comfortably comprising the entire quantum well in the z-direction/depth-direction is extracted from the reconstructed data. This is done to have comparable sizes for each measurement, to limit the known reconstruction artefacts of APT [151] and to enable a direct comparison to simulations in step 5. Third, the three-dimensional point cloud created in the usual APT reconstruction [10] is tessellated using a Voronoi tessellation [200, 201]. The Voronoi tessellation is used for all subsequent steps. It can be viewed as a smoothing operation that "spreads out" the detected ions/atoms to a finite volume rather than representing them as zero-dimensional points. Forth, a x,y-grid is defined on the cube and for each cell of the grid a profile based on the Voronoi tessellation along the z-axis is created that is than fitted with a sigmoid function. The collection of sigmoid functions is then used to represent the interface and calculate the interface positions as well as the isoconcentration surfaces. Fifth, the profile extracted from the Voronoi grid of the entire cube is used to create a model structure with the known crystal structure of SiGe and a pseudo-random distribution of Si and Ge atoms in the x-y plane, enforcing the same profile along the depths direction as given by the Voronoi grid and the same percentage of atoms in the volume as expected from the detection efficiency of the Atom Probe (here: 80 % detection efficiency of the LEAP 5000XS). These model structures interface are then compared to the measurement results. All data treatment is done in Python 3.9 using numpy 1.20.3 and scipy 1.6.3.

B.2.2 Extraction of the cubes and Voronoi tessellation

The cubes are manually extracted from the reconstructed volume as exemplary shown in Fig. B.7 a-b). After a cube containing the quantum well with the approximate size of an electrically defined quantum dot ($\sim$ 30x30x20 nm) is extracted a Voronoi tessellation is performed on the point cloud representing APT data inside the cube. A result of such a tessellation in exemplary shown in Fig. B.7 c).
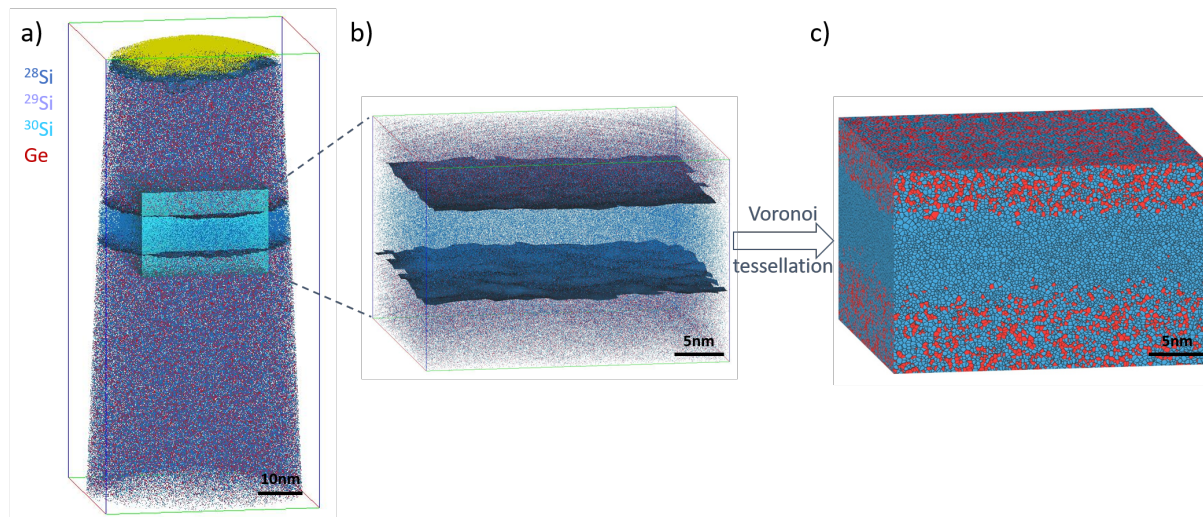
Figure B.7: Visualization of the extraction (a) of the cube (b) from the full data set (a) and Voronoi tessellation of the cube (c)

B.2.3 Construction of the interface

Interfaces are constructed based on the Voronoi tessellated data sets. The process is depicted in Fig. B.8. A grid is created in the x,y-plane of the tessellated data set (Fig. B.8 a-b). For each cell of the grid a one-dimensional profile along the z-axis is generated using the tessellation. As opposed to "regular" APT data [10] where profiles are created utilizing small bins along the z-axis and concentrations are then calculated from the ions/atoms within the bin [110], the profiles on the tessellated data are created by a set of cutting planes. The process works by cutting the tessellation at each depth and use every ion/atom whose volume is cut as part of the plane and hence have it contribute to the concentration measured within

that plane and at that depth.This can be viewed as a smoothing operation that spreads out the detected ions/atoms to a finite volume.
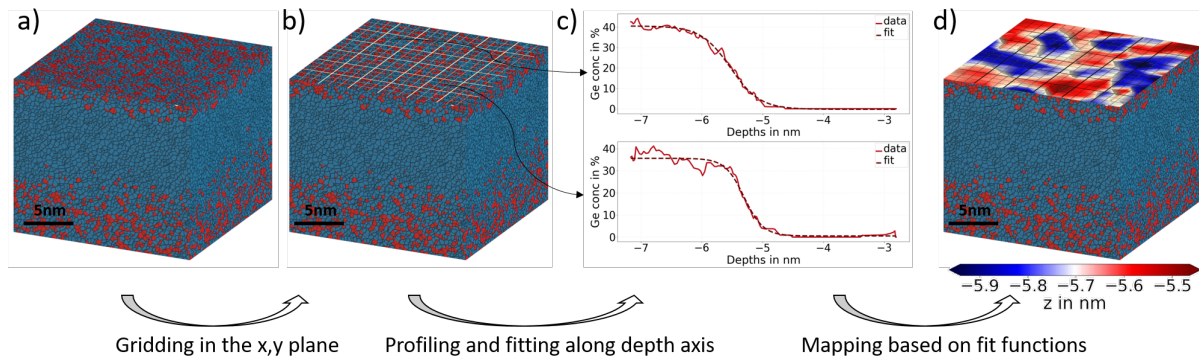
Figure B.8: Creation of a map from the Voronoi tessellated cube (a) by applying an x,y-grid (b) and fitting of profiles along z-axis with a sigmoid function in each cell (c). The profiles can then be used to calculate the position of e.g. the 25 % Germanium isoconcentration surface (d).

Each x,y-cell (typically 3x3 nm wide spaced 1 nm apart and hence partially overlapping) generates a profile and is then fitted using sigmoid function [54] as shown in Fig. B.8 c). The sigmoid functions are then used to represent the interface in the following way:

- The inflection point of the sigmoid represents the position of the interface in each cell (Fig. B.8 d)

- Isoconcentration surfaces [110] Chapter 6.3.2 are created by plotting the position where the sigmoid of each cell reaches the respective concentration

Fig. B.9 and B.10 show examples of the interface positions maps and isoconcentration surface maps generated in this way for the top and bottom interfaces of a QW A and a QW B sample. Note, that the data can now readily be used to calculate the average roughness and root mean square roughness in the usual way [75].
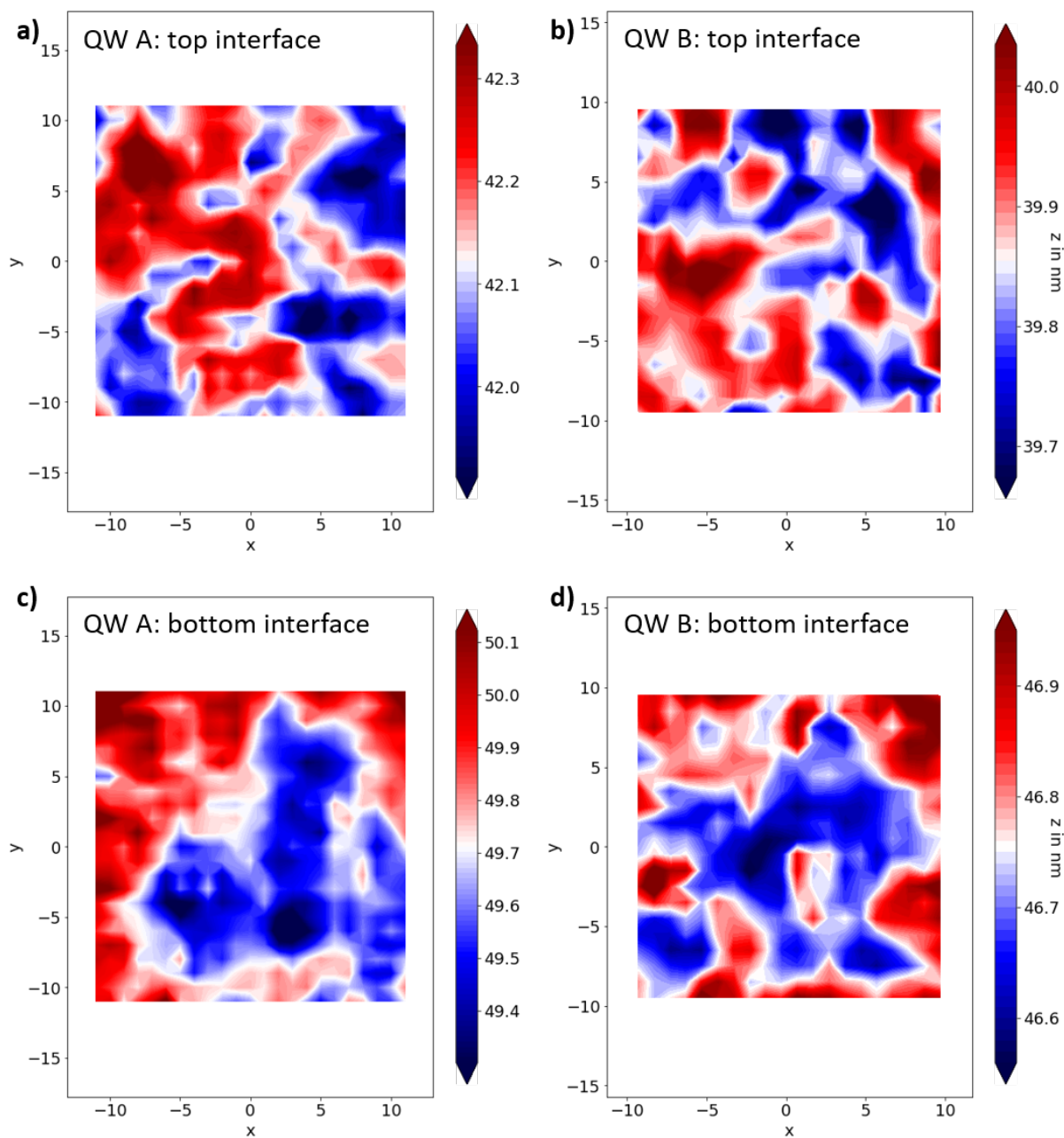
Figure B.9: Examples of position maps of top (a, b) and bottom (c, d) Germanium interfaces for both Quantum wells A and B. For each cell the depth plotted on the map is extracted from inflection point the sigmoid fit to the profile extracted from the cell (Fig. B.8 b-c).
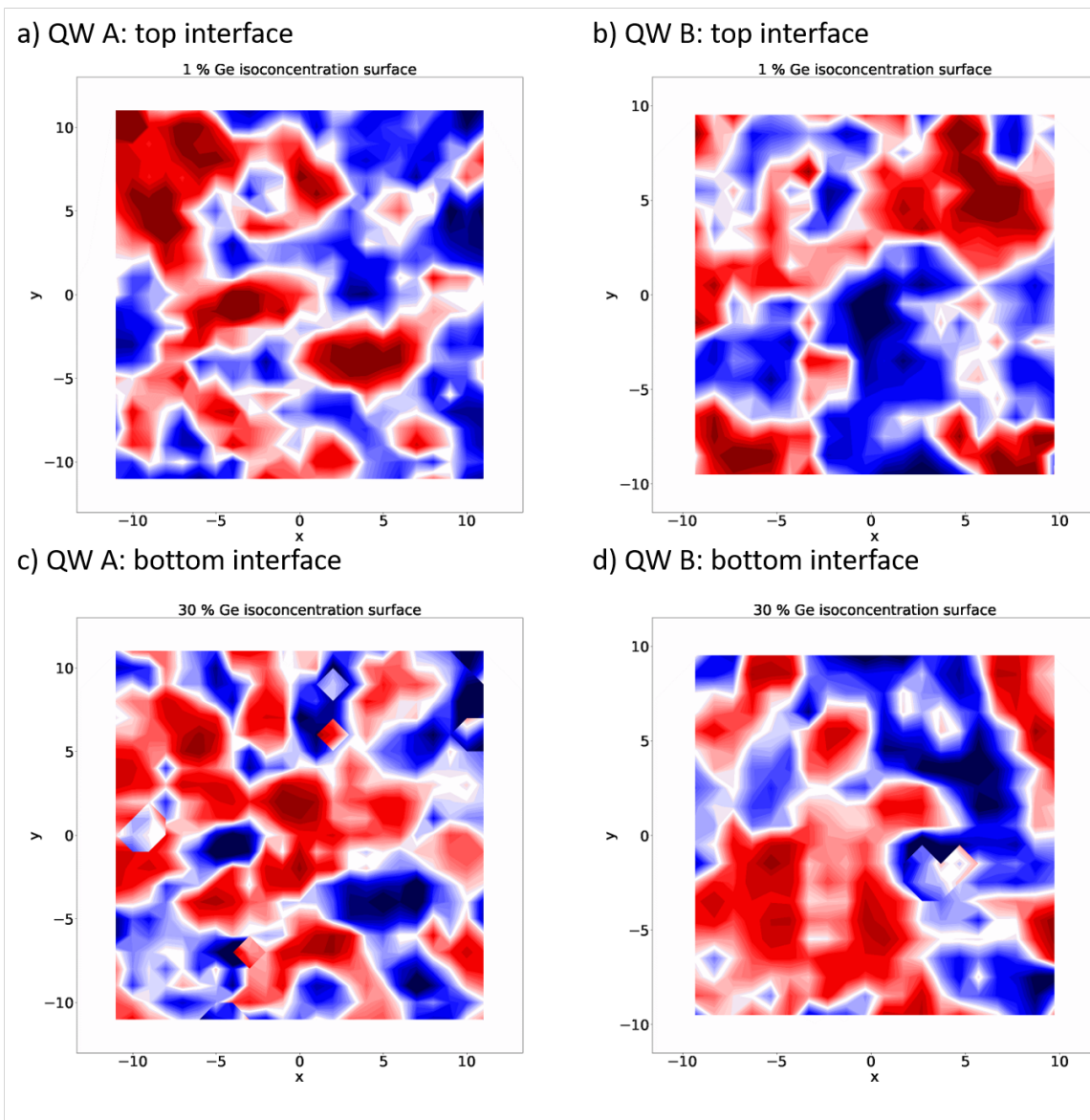
Figure B.10: Example of Germanium isoconcentration surfaces or the top (a, b) and bottom (c, d) interfaces of both Quantum Wells A and B. The plots reported here show one particular isosurface, 1% in a, b and 30% in c,d. Animated short clips provided as Supplementary Movies show the evolution across the interfaces of each isoconcentration surfaces, from 1-30 % Ge. As before the depth for each map can be extracted from the sigmoid fits to the profile in each cell.

B.2.4 Generating model data

Model data are generated based on the known crystal properties of $Si_{66.5}Ge_{33.5}$. A crystal of the same size as the cubes extracted from the data ($\sim$ 30x30x20 nm) is generated digitally and then 20 % of the atoms in the crystal are pseudo-randomly removed to account for the detection efficiency of the LEAP5000XS system used in the APT analysis.
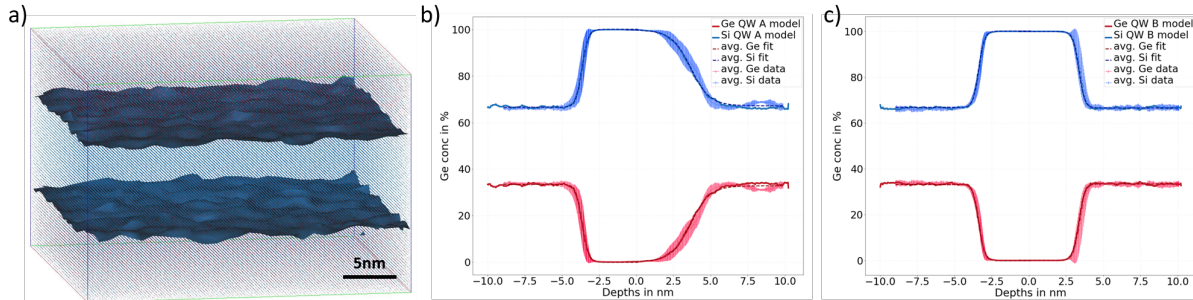
Figure B.11: Example of a crystalline cube of QW A (a) and a comparison of the average profiles of the measured quantum wells (see Fig. 2(c) of the main text) and profiles from a generated cube of Quantum Well A (b) and Quantum Well C (c).

Along the depth axis of the cube the average measured APT profile of the Si and Ge concentration of QW A and QW B as shown in Fig. 2c) of the main text is enforced. The result of the generation of such a cube for QW A and the comparison of the depth profile extracted from a cube of QWA and QW B to the average profile of QW A and QW B respectively are shown in Fig. B.11. In Fig. B.12 interface position maps of these model structures are shown. They should be compared to Fig. B.9 where the same maps are extracted from measured data sets. The root mean square roughness as measured from the model is compared to the data measured from the APT data in Fig 2 of the main text.

Note: the animation in the file Supplementary_ Movie_1.m4v shows for the top interface of quantum well B (for increasing Ge concentration) the deviation of each isosurface tile position from the isosurface's average position. Here we benchmark the experimental data from our APT analysis (at each frame of the animation) against average and min-max range covered by 100 random models.
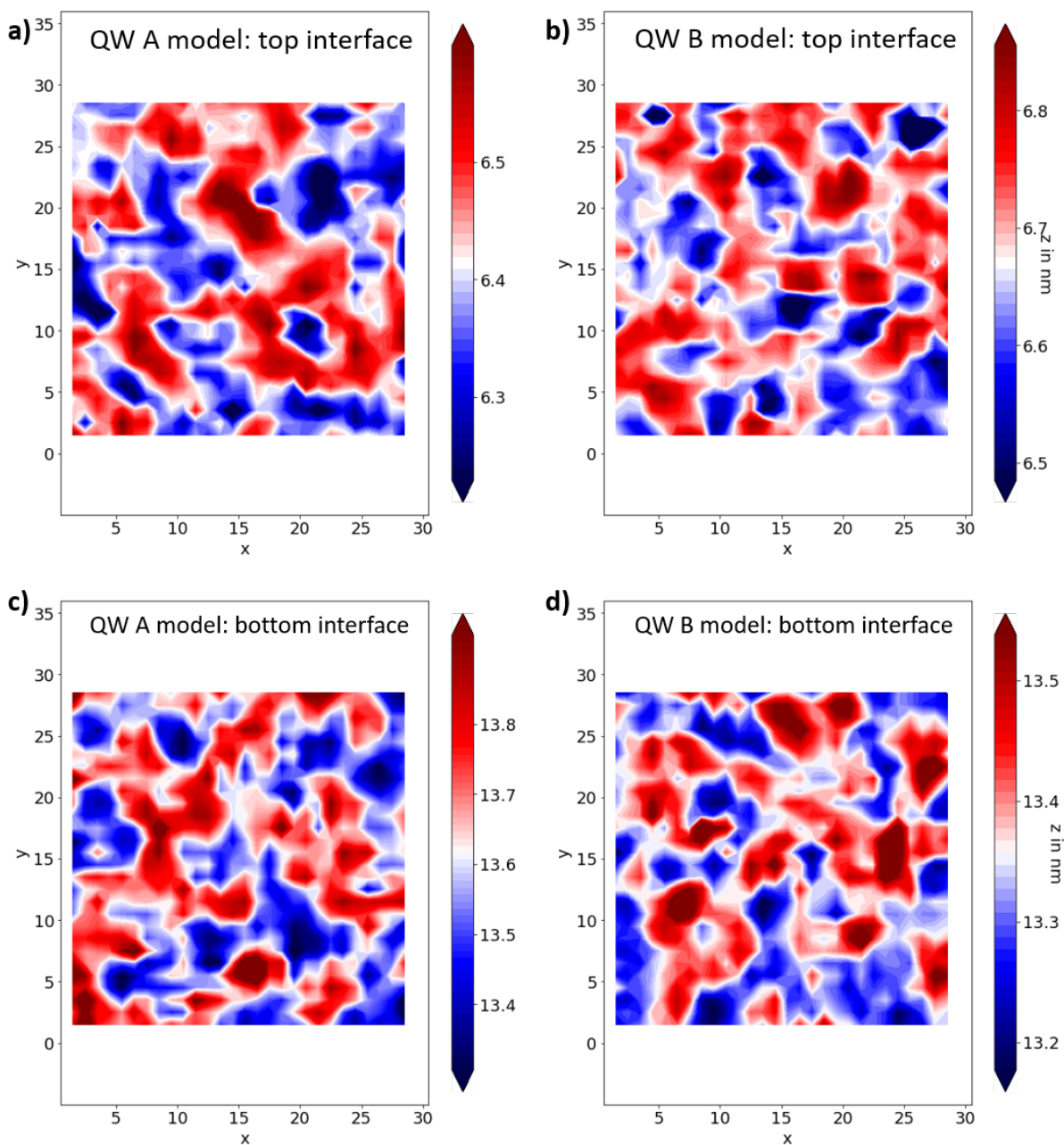
Figure B.12: Examples of position maps of top (a, b) and bottom (c, d) Germanium interfaces for model data sets of both Quantum wells A and B. As in Fig. B.9 the depth plotted on the map is extracted from the inflection point of the sigmoid fit for the profile along the depth axis generated in each cell (Fig. B.8 b-c).

B.2.5 Atomic steps, Quantum well width, and bottom interfaces
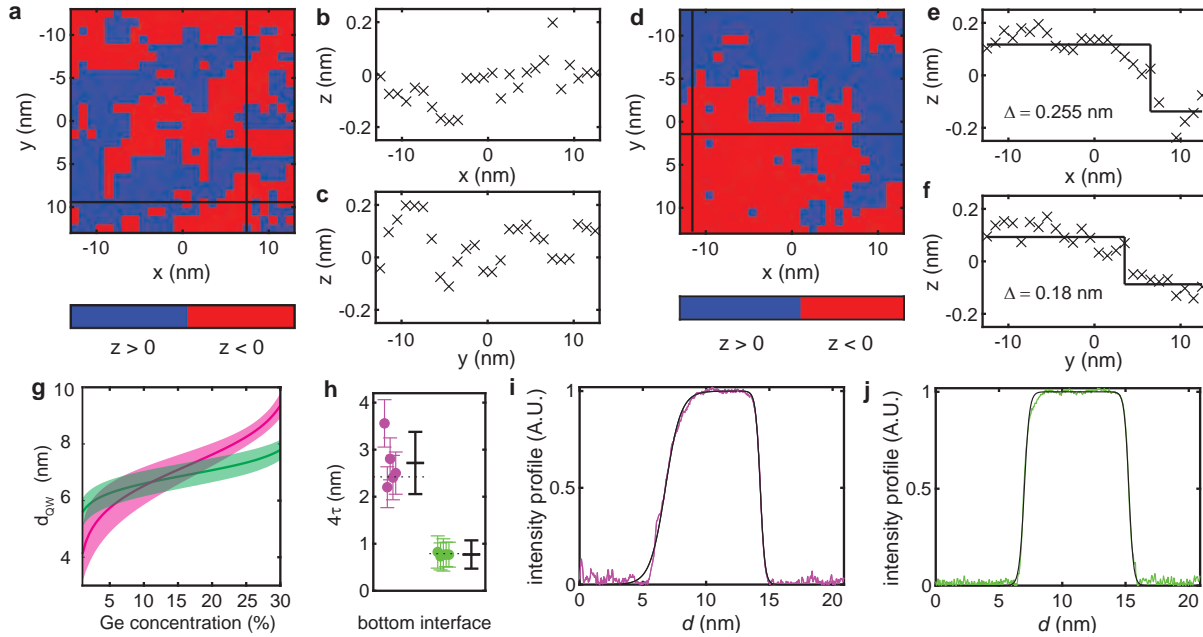
Figure B.13: **a** 10% isoconcentration surface from a Stack A sample without step. Blue areas are below and red areas above the average height (defined as $z = 0$) of the isoconcentration surface. The black lines are the positions of the line cuts in **b** and **c**. **b** line cut along the x direction of the isoconcentration surface. in **a**. **c** line cut along the y-direction of the isoconcentration surface. The z-position randomly oscillates around the mean value. **d** 10% isoconcentration surface from a Stack A sample with clear spatial division of the blue and red areas. The black lines are the positions of the line cuts in **e** and **f**. **e** line cut along the x-direction of **d**. A step with height $\Delta = 0.255$ nm occurs at $x = 7$ nm, corresponding to approximately 2 monoatomic layers. The black line represents the Heavyside step function with the highest C and the step height is determined by taking average z-position of the line cut before and after the step. **f** line cut along the y-direction of **c**. A step with $\Delta = 0.18$ nm occurs at $x = 3$ nm, corresponding to approximately 1.5 monoatomic layers. The black line represents the average z-position before and after the step. **g**, Average width of quantum well A (magenta line) and B (green line) as a function of the Ge concentration of the isoconcentration surfaces. Shaded areas represent the standard deviation of the quantum wells. **h**, Statistical analysis of the bottom 4τ interface widths derived from the fitting the data for quantum well A (magenta) and quantum well B (green). Black crosses are the mean and standard deviation for data from the different APT samples, highlighting the uniformity of the interfaces. **i**, **j**, HAADF-STEM intensity profile for stack A and B (magenta and green line, respectively) along the heterostructure growth direction (see TEMs in the main section). The black lines are fits of the data in the interface regions, using a sigmoid function.

To evaluate the presence of atomic steps from isoconcentration surfaces, we consider one-dimensional line cuts along the x- and y-axis of an isosurface. If a line cut crosses an atomic

step along the isosurface, the line cut should resemble a Heavyside step function H:

$$H(x - x_s) = h_0 + \begin{cases} -a/2, & \text{for } x < x_s. \\ a/2, & \text{for } x \geq x_s. \end{cases} \tag{B.4}$$

where a is the step height, x_s is the step position and the offset h_0. To quantify the resemblance between a line cut and the step function, we determine the correlation coefficient C between the two with:

$$C = \frac{\sum_k (z_k - \bar{z})(h_k - \bar{h})}{\sqrt{\sum_k (z_k - \bar{z})^2} \sqrt{\sum_k (h_k - \bar{h})^2}} \tag{B.5}$$

where z_k are the z-values of the line cut, $\bar{z}$ is the mean value of the line cut, k is the index of the, h_k are the values of the step function, and $\bar{h}$ the mean value of the step function. If $C \geq 0.75$ we consider the linecut to represent a step. We subsequently can determine a by taking the difference between the two plateaux $\Delta = \bar{z}_{k+} - \bar{z}_{k-}$, where $\bar{z}_{k+}$ and $\bar{z}_{k-}$ are the average z-position before and after x_s, respectively.

B.2.6 SIMS and crosshatch pattern
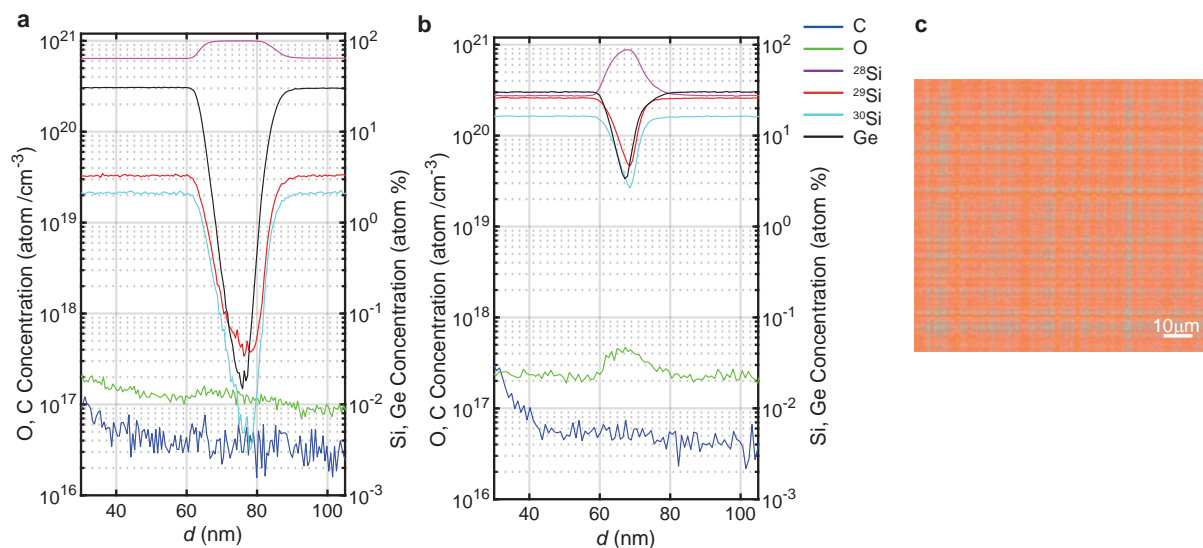
Figure B.14: **a**, **b**, Depth concentration SIMS profile of quantum well A and quantum well B respectively. Analyzed elements are ^{28}Si (red), ^{29}Si (blue), ^{30}Si (purple), Ge (black), oxygen (green) and carbon (blue). In quantum well A both carbon and oxygen concentrations are below their respective detection limits of 3×10^{16} cm^{-3} and 1×10^{17} cm^{-3}. In quantum well A only carbon is below the detection limits, while there is a residual oxygen content of 4×10^{17} cm^{-3} in the quantum well. **c** typical cross-hatch pattern from the surface of the wafers.

B.3 Theoretical model

All numerical simulations and analysis in this section were performed in Python, using the open-source libraries NumPy, SciPy, and Matplotlib.

B.3.1 Tight-binding model

In our analysis, we use the one-dimensional two-band tight-binding model of Boykin *et al.* [27]. Here, the nearest-neighbor and next-nearest-neighbor hopping amplitudes, chosen to yield the correct valley minimum wavevector and out-of-plane effective mass, are $v = 0.683$ and $u = 0.612$, respectively. The onsite energy ε is the sum of the contributions from the electrostatic potential energy eEz, for a vertical electric field $E = 0.0125$ V/nm, and the quantum well confinement potential $U(z)$. The conduction band offset is taken to be a linear interpolation:

$$\Delta E_c = (x_w - x_s) \left[\frac{x_w}{1 - x_s} \Delta E_{\Delta_2}^{\mathrm{Si}}(x_s) - \frac{1 - x_w}{x_s} \Delta E_{\Delta_2}^{\mathrm{Ge}}(x_s) \right], \tag{B.6}$$

where x_w is the Si concentration inside the well and x_s is the Si concentration in the quantum well barriers (the substrate). The functions $\Delta E_{\Delta_2}^{\mathrm{Si(Ge)}}(x)$ describe the Δ_2 conduction band offsets for strained Si (Ge) grown on an unstrained $\mathrm{Si}_x\mathrm{Ge}_{1-x}$ substrate. These functions are approximately linear in x over their entire range, with limiting behaviors [164]

$$\begin{aligned} \Delta E_{\Delta_2}^{\mathrm{Si}}(x) &\approx -0.502(1 - x) \text{ (eV)}, \\ \Delta E_{\Delta_2}^{\mathrm{Ge}}(x) &\approx 0.743 - 0.625(1 - x) \text{ (eV)}, \end{aligned} \tag{B.7}$$

when $x \to 0$. The linearization scheme employed here agrees well with theoretical calculations [164].

As described in Methods, for our one-dimensional model, we determine the quantum well potential $U(z_l)$ at each atomic layer position z_l by linearly interpolating the conduction band

offset between the barriers and the bottom of the well, yielding

$$U(z_l) = \frac{x_l^d - x_s}{x_w - x_s} \Delta E_c, \tag{B.8}$$

where x_l^d is the Si concentration at layer l, averaged over the lateral probability distribution of the quantum dot wavefunction, as explained in subsection c, below. To simulate many different quantum wells, we allow for random fluctuations of x_l^d, due to the finite size of a quantum dot. Below, we derive the statistical distribution of x_l^d, as reported in Eq. (B.18).

B.3.2   Comparison with NEMO-3D

The two-band tight-binding model has the advantage of being computationally inexpensive, allowing us to perform many random samplings, to obtain accurate statistics. To validate the model, we compare our results to those of a more sophisticated 20-band sp^{3}d^{5}s* NEMO-3D tight-binding model (including spin) [94]. NEMO-3D heterostructures are generated atom by atom. Each atom is randomly chosen to be either Si or Ge, with the probability of choosing Si given by the concentration profile $\bar{x}_l$ for a given atomic layer l. The valley splitting is computed as the energy difference between the two lowest conduction states.

First, we consider the quantum well confinement profile shown in the inset of Fig. B.15(c) for a quantum dot with a lateral parabolic confinement potential, corresponding to an orbital splitting of $\hbar\omega = 2.83$ meV, and a vertical electric field of $E = 0.0125$ V/nm. Note that in the two-band model, the resulting three-dimensional wavefunction is simply used to obtain a set of weighted one-dimensional layer concentrations, x_l^d. The results of these NEMO-3D simulations are plotted as histograms in Fig. B.15(a), while the corresponding results from the two-band model are plotted in Fig. B.15(b). Although fewer random samples are obtained in the NEMO-3D case, due to computational constraints, the two distributions appear to agree well. The NEMO-3D distribution is found to have a mean of 87.4 μeV and

a standard deviation of 50.1 μeV, while the two-band distribution is found to have a mean of 104.7 μeV and a standard deviation of 55.7 μeV. Qualitatively, the two distributions have similar shapes. NEMO valley splittings are on average slightly smaller, which is consistent with previous results [27].

To analyze the relationship between 2-band and NEMO simulations in more detail, we compute E_v with the 1D 2-band model using the same 60 heterostructures we used in Fig. B.15(a). To do so, we took the heterostructure, computed the weighted average Si concentration at each layer, and plugged it into the 1D 2-band model. We assumed the wavefunction was in the ground state of a 2D isotropic harmonic oscillator potential, with characteristic energy $\hbar\omega = 2.83$ meV. Resulting valley splittings from NEMO (E_v^{NEMO}) and the 2-band model (E_v^{TB}) are plotted against each other in Fig. B.15(c). We can see that there is a clear, strong linear correlation between the two. Fitting these data to the relationship $E_v^{\mathrm{NEMO}} = kE_v^{\mathrm{TB}}$, we find $k = 0.86$ with standard error 0.018. Again, the fact that NEMO valley splittings are slightly less than 2-band TB valley splittings is consistent with prior results [27].

Next, we analyze the relationship between 2-band and NEMO simulations as a function of the Ge content in the well. Using the same heterostructures for both 2-band and NEMO simulations, we compute valley splittings with both models, performing 20 simulations for quantum wells with each of 0%, 5%, and 10% Ge. The resulting data are shown in Fig. B.16(a). Again, there is a strong linear correlation between E_v^{TB} and E_v^{NEMO}. This correlation is tightest for 0% Ge, but still clear with Ge in the well. Again, we fit all the data to $E_v^{\mathrm{NEMO}} = kE_v^{\mathrm{TB}}$, finding $k = 0.76$ with standard error 0.053, indicated in the inset of Fig. B.16(a). We also perform the same fit for each of the 0%, 5%, and 10% Ge data individually, also shown in the inset of Fig. B.16(a), and we find that the resulting k values are not significantly different. We also note that these fit parameters are different than those from Fig. B.15(c), indicating that there may be some interface-dependence for k. For these
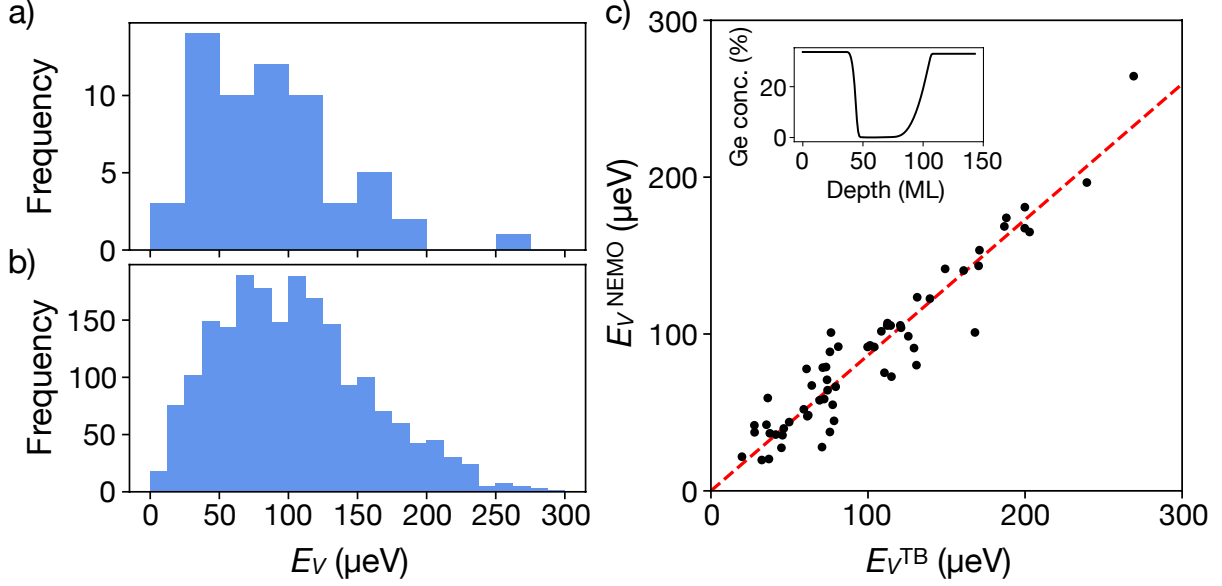
Figure B.15: A comparison of simulations with NEMO-3D and the 1-dimensional 2-band tight-binding model. (a) Histogram of 60 randomized valley-splitting simulations using NEMO-3D. (b) Histogram of 2,000 randomized valley-splitting simulations using the one-dimensional two-band tight-binding model. (c) We directly compare simulations using NEMO-3D and the 2-band model for the 60 heterostructures shown in (a). For each heterostructure, we plot its valley splitting with the 2-band model (E_v^{TB}) against it's valley splitting with NEMO (E_v^{NEMO}). The red dashed line shows the fit $E_v^{\mathrm{NEMO}} = kE_v^{\mathrm{TB}}$ with $k = 0.86$. All simulations assume an orbital splitting of $\hbar\omega = 2.83$ meV, and a vertical electric field of $E = 0.0125$ V/nm.

simulations, we used dots with characteristic orbital energy $\hbar\omega = 2$ meV and vertical field $E = 0.0125$ V/nm. We use 80 ML wide wells and sigmoid interfaces with widths $4\tau = 10$ ML.

Fig. B.16(b) shows the mean and 25-75 percentile range of the valley splittings computed with NEMO as a function of the quantum well Ge concentration. As presented in the main text, the average valley splitting clearly grows with increasing Ge content. This is a nice validation of the main results obtained with the simple 1D model.

B.3.3 Statistical distribution of intervalley couplings

Here, we examine the derivation of the statistical distribution of the intervalley coupling matrix element in more detail. From Methods, we have the intervalley coupling matrix
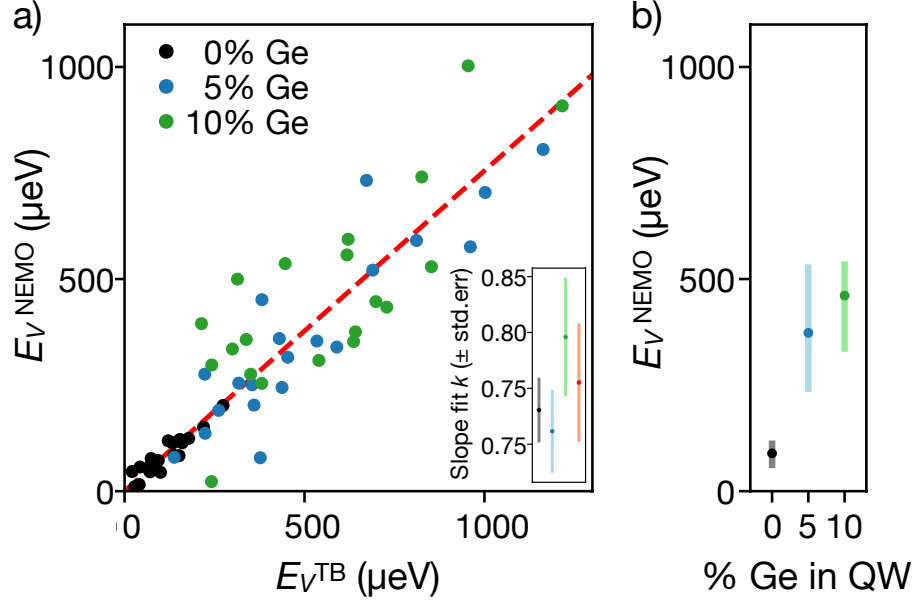
Figure B.16: (a) A comparison of valley splittings computed with the 2-band TB model (E_v^{TB}) and NEMO-3D (E_v^{NEMO}). Valley splittings for each point were computed using the same heterostructure on both methods. Black, blue, and green data correspond to quantum wells with 0%, 5%, and 10% Ge, respectively. The red dashed line indicates the best fit $E_v^{\mathrm{NEMO}} = kE_v^{\mathrm{TB}}$, where $k = 0.76$ with standard error 0.026, shown in red in the inset. Also shown in the inset are fit values k and their standard errors for each subset of data individually. (b) The mean and 25-75 percentile range of E_v^{NEMO} for quantum wells with 0%, 5%, and 10% Ge. For all simulations, we use quantum wells with widths of 80 ML and interface widths of $4\tau = 10$ ML. We assume a parabolic confinement potential with strength $\hbar\omega = 2$ meV and vertical field $E = 0.0125$ V/nm.

element

$$\Delta = \frac{a_0}{4} \sum_l e^{-2ik_0 z_l} \frac{x_l^d - x_s}{x_w - x_s} \Delta E_c |\psi_{\mathrm{env}}(z_l)|^2, \tag{B.9}$$

where the valley splitting $E_v = 2|\Delta|$. As above, x_l^d represents the Si concentration in atomic layer l, weighted by the probability distribution of the electron charge density in the dot. We can split Eq. (B.9) into its deterministic and random contributions, using the definition $x_l^d = \bar{x}_l + \delta_l$, where $\bar{x}_l$ is the ideal, smooth concentration profile of the heterostructure and δ_l are the random fluctuations about this profile. The random contribution to the matrix element can then be expressed as

$$\delta\Delta = \frac{a_0 \Delta E_c}{4(x_w - x_s)} \sum_l e^{-2ik_0 z_l} \delta_l |\psi_{\mathrm{env}}(z_l)|^2. \tag{B.10}$$

We now calculate the variance of the matrix element. First, we note that the random fluctuations only occur in $\delta\Delta$, so that $\text{Var}\,[\Delta] = \text{Var}\,[\delta\Delta]$. Second, we recall that the variance of a complex random variable is the sum of the variances of its real and imaginary components. Third, since we assume the fluctuations in different layers are independent, the variance of the sum in Eq. (B.10) must be equal to the sum of the variances in each layer. In this way, we obtain

$$\text{Var}\,[\Delta] = \left[\frac{a_0 \Delta E_c}{4(x_w - x_s)}\right]^2 \sum_l |\psi_{\text{env}}(z_l)|^4 \text{Var}\,[\delta_l]. \tag{B.11}$$

To compute $\text{Var}[\delta_l]$, we note again that x_l^d represents the fluctuating Si concentration in layer l, weighted by the electron charge density. We first describe the weighting function, which is defined in a single two-dimensional layer, and is proportional to the squared amplitude of the wavefunction. In the lowest-subband approximation [65], the dot wavefunction is separable, so the in-plane component of the wavefunction $\psi_t(x, y)$ does not depend on the layer index. For a circular, parabolically confined dot with orbital excitation energy $\hbar\omega_{\text{dot}}$, the normalized wavefunction is given by $\psi_t(x, y) = (\pi a_{\text{dot}}^2)^{-1/2} \exp(-r^2/2a_{\text{dot}}^2)$, where the dot is taken to be centered at the origin, $a_{\text{dot}} = \sqrt{\hbar/m_t \omega_{\text{dot}}}$ is a characteristic dot dimension, $m_t = 0.19\, m_e$ is the transverse effective mass, and $r = \sqrt{x^2 + y^2}$. Let us consider the dot weighting function $w(a)$, which is defined only at the atom locations $a \in A_l$, where A_l is the set of all atom positions in layer l. Since $w(a)$ is defined discretely, while $\psi_t(x, y)$ is continuous, their normalizations are different. To determine the normalization of $w(a)$, we require that $\sum_{a \in A_l} w(a) = 1$, which is analogous to the wavefunction normalization $\int_{-\infty}^{\infty} dx\, dy |\psi_t(x, y)|^2 = 1$. The correspondence between between the sum, $\sum_{a \in A_l}$, and the integral, $\int_{-\infty}^{\infty} dx\, dy$, must take into account the fact that there are two atoms in every two-dimensional unit cell of size $a_0 \times a_0$, for a diamond cubic crystal like Si. Normalizing

over a single unit cell, the correct correspondence is therefore given by

$$\sum_{a \in A_l} \rightarrow \frac{2}{a_0^2} \int_{-\infty}^{\infty} dx\, dy. \tag{B.12}$$

Next, we define $w(a) = c|\psi_t(r_a)|^2$, where c is a proportionality constant, to be determined below, and $\mathbf{r}_a = (x_a, y_a)$ is the 2D coordinate location of atom a. Using the correspondence in Eq. (B.12), we obtain the appropriate normalization for $w(a)$:

$$w(a) = \frac{a_0^2}{2\pi a_{\text{dot}}^2} e^{-r_a^2/a_{\text{dot}}^2}. \tag{B.13}$$

Now, according to its definition, the weighted Si concentration in layer l is given by

$$x_l^d = \sum_{a \in A_l} \mathbb{1}\left[a = \text{Si}\right] w(a), \tag{B.14}$$

where the indicator function, $\mathbb{1}\left[a = \text{Si}\right]$, takes the value 1 if a is a Si atom and 0 otherwise. The fluctuating part of the concentration is given by $\delta_l = x_l^d - \bar{x}_l$. Calculating $\text{Var}\left[\delta_l\right]$, we then obtain

$$
\begin{aligned}
\text{Var}\left[\delta_l\right] &= \text{Var}\left[\sum_{a \in A_l} \mathbb{1}\left[a = \text{Si}\right] w(a)\right] \\
&= \sum_{a \in A_l} w^2(a) \text{Var}\left[\mathbb{1}\left[a = \text{Si}\right]\right] \\
&= \bar{x}_l(1 - \bar{x}_l) \sum_{a \in A_l} w^2(a).
\end{aligned} \tag{B.15}
$$

Here, in the second line, we use the fact that the atoms in the random alloy are chosen independently. In the third line, we use the fact that each indicator function in the sum is a Bernoulli trial with variance given by $p(1 - p)$ [16], where the probability of success is given by $p = \bar{x}_l$. Making use of Eqs. (B.12) and (B.13), we arrive at

$$\text{Var}[\delta_l] = \bar{x}_l(1 - \bar{x}_l) \frac{a_0^2}{4\pi a_{\text{dot}}^2}, \tag{B.16}$$

and

$$\text{Var}\,[\Delta] = \frac{1}{\pi} \left[\frac{a_0^2 \Delta E_c}{8 a_{\text{dot}}(x_w - x_s)} \right]^2 \sum_l |\psi_{\text{env}}(z_l)|^4 \bar{x}_l (1 - \bar{x}_l). \tag{B.17}$$

To complete the calculation of Var[Δ], we need to evaluate $\psi_{\text{env}}(z_l)$. In this work, we compute $\psi_{\text{env}}(z_l)$ numerically, for the ideal concentration profile $\bar{x}_l$, and the corresponding confinement potential $U(z_l)$ obtained from Eq. (B.8), by discretizing the Schrodinger equation on the atomic lattice sites z_l.

Although analytical methods can be used to characterize $x_l^d = \bar{x}_l + \delta_l$, as in Eq. (B.16), we also perform other types of randomized numerical simulations, as described in the main text. To do this, we could assign atoms in a 3D array, with each atom in layer l having the probability $\bar{x}_l$ of being silicon. The statistical properties of such an array derive from a binomial distribution. In principle, for real wave functions, such calculations could involve a very large number of atoms, to accurately describe the wavefunction tails. Alternatively, we may consider a much smaller number atoms N_{eff}, for which

$$x_l^d \sim \frac{1}{N_{\text{eff}}} \text{Binom}\left(N_{\text{eff}}, \bar{x}_l\right), \tag{B.18}$$

where Binom (n, p) is the binomial distribution with n trials and probability of success p. The question now becomes, how should we determine N_{eff}? The answer is that N_{eff} should be chosen to yield the correct statistical properties for x_l^d, including its mean and variance. Using the known variance of the binomial distribution, $N_{\text{eff}} \bar{x}_l (1 - \bar{x}_l)$, and comparing to Eq. (B.16), we see that we should choose $N_{\text{eff}} = 4\pi a_{\text{dot}}^2/a_0^2$. This corresponds to an effective dot radius of $r_{\text{eff}} = \sqrt{2}\, a_{\text{dot}} = \sqrt{2\hbar/m_t \omega_{\text{dot}}}$.

B.3.4 Statistical distribution of valley splittings

Since the intervalley coupling Δ is a complex random variable and is the sum of many independent random variables (corresponding to the different layers), it follows a 2D Gaussian distribution in the complex plane. In Eq. (B.17), we derived the variance of the intervalley

coupling Δ due to concentration fluctuations. We now examine the distribution of valley splittings $E_v = 2|\Delta|$. The magnitudes of points sampled from a circular Gaussian distribution in the complex plane follow a Rice distribution [5], whose probability density function is given by

$$f_{\text{Rice}}(z|\nu, \sigma) = \frac{z}{\sigma^2} \exp\left(-\frac{z^2 + \nu^2}{2\sigma^2}\right) I_0\left(\frac{z\nu}{\sigma^2}\right) \tag{B.19}$$

where ν is the distance from the origin to the center of the circular Gaussian, σ is the width of the Gaussian along one of its axes, and $I_0(y)$ is a modified Bessel function of the first kind. Since the Gaussian distribution for Δ is centered on the deterministic value Δ_0, the probability density function for valley splittings $f_{\text{Rice}}(E_z|\nu, \sigma)$ is centered at $\nu = 2|\Delta_0|$. The variances of the real and imaginary components are both given by $(1/2)\text{Var}[\delta\Delta]$, such that $\sigma = \sqrt{2}\sqrt{\text{Var}[\delta\Delta]}$.

B.3.5 Effects of interface width and QW Ge concentration on average valley splitting

Both the average Ge concentration and the width of the interface have an effect on the valley splitting in a quantum well. Here, we analyze the contributions of both. Figure B.17(a) provides an extended version of Fig. 3(g) in the main text, showing the valley splitting distributions at different quantum well Ge concentrations and interface widths. The valley splittings at interface width $4\tau = 0$ are consistently large, regardless of quantum well Ge concentration, due to the large deterministic component for this (somewhat unphysical) geometry. For more realistic, nonzero interface widths, increasing the Ge concentration in the quantum well increases the valley splitting. At low Ge concentration, wider interfaces can actually increase average valley splitting, because the wavefunction sees layers with more Ge. Figure B.17(b) provides an extended dataset, showing the average valley splitting at several combinations of interface width vs. Ge concentration in the well. For very narrow interfaces, E_v is large, regardless of the Ge concentration in the well. For wider interfaces,

adding Ge to the well consistently boosts the valley splitting. The grey line in Fig. B.17(b) delineates quantum wells for which $\geq 95\%$ of simulations have $E_v \geq 100$ μeV (the large, upper-left portion of the plot). For realistic electric fields, we find that any well with $> 5\%$ Ge, regardless of interface width, should have $E_v \geq 100$ μeV at least 95% of the time.

Figure B.17(c) shows a sample wavefunction in a quantum well with an interface width of $4\tau = 20$ ML. The wavefunction is colored according to the Ge concentration in each layer, illustrating how a wide interface can expose the wavefunction to more layers with nonzero Ge content.

a)

b)

c)
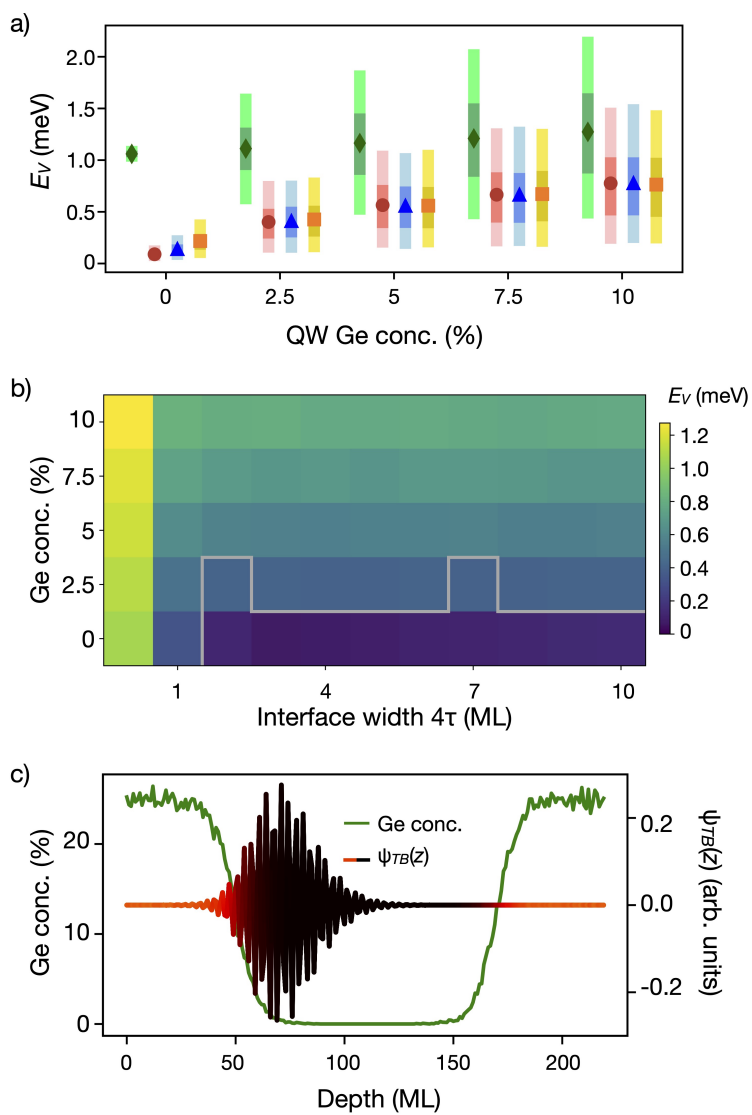
Figure B.17 *(previous page)*: Valley splitting simulations. (a) An extended version of Fig. 3(g) in the main text. Valley splitting distributions are shown for quantum well Ge concentrations from 0 to 10% and interface widths of $4\tau = 0$ ML (green diamonds), $4\tau = 5$ ML (red circles), $4\tau = 10$ ML (blue triangles), and $4\tau = 20$ ML (orange squares). The symbol represents the mean valley splitting, while the dark bars represent the 25-75 percentile range, and the light color bars represent the 5-95 percentile range. Each bar represents 2,000 simulations using the one-dimensional two-band tight-binding model. (b) The mean valley splitting is shown for a range of interface widths 4τ and quantum well Ge concentrations. Each pixel corresponds to 2,000 simulations using the one-dimensional two-band tight-binding model. All pixels above the grey line have $E_v \geq 100$ μeV in more than 95% of the simulations; all pixels below have $E_v \geq 100$ μeV less than 95% of the time. (c) A sample simulation of a quantum well with 0% Ge and an interface width of $4\tau = 20$ ML. The green curve shows the Ge concentration profile, and the red-black curve shows the ground state tight-binding wavefunction. The color of the wavefunction illustrates the Ge concentration of each layer, with red corresponding to high concentrations. Clearly, a significant portion of the wavefunction is found in a region with nonzero Ge content. All simulations in this figure were performed with an electric field of 0.0075 V/nm, for the quantum well depicted in Fig. 3(g) of the main text.

B.3.6 Effect of vertical electric field on average valley splitting

In this section, we investigate the effect of the vertical electric field on the valley splitting distributions in quantum well A and B. Fig. B.18 shows the mean and 25-75 percentile range of 1000 1D 2-band tight-binding simulations of E_v with various vertical fields E_z, for both quantum wells A and B. Increasing the vertical field leads to larger mean E_v and larger spreads in E_v as the quantum dot wavefunction penetrates the top interface, thereby increasing the alloy disorder. That said, even wells with zero vertical field still show a sizeable spread in E_v due to alloy disorder. In this paper, we use $E_z = 0.0075$ V/nm because the resulting E_v distributions agree well with the data.
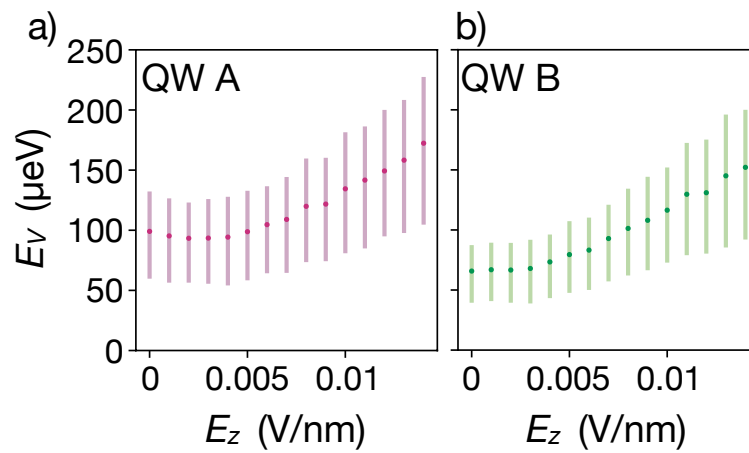
Figure B.18: The variation of the valley splitting distributions in quantum wells A (a) and B (b) as a function of the vertical electric field E_z. Each bar shows the mean and 25-75 percentile range of 1000 simulations using the 1D 2-band tight-binding model. We assume an orbital energy $\hbar\omega = 4.18$ meV.

Appendix C

Supplementary Information for

Chapter 4

C.1   Details of the Effective Mass Virtual Crystal Calculation of the Wiggle Well Valley Splitting

The effective mass virtual crystal (EMVC) approximation calculations of the valley splitting E_v shown in Fig. 1(c) of the main text and Supplementary Fig. 1 were performed as follows. The electron is confined by a barrier and an applied electric field in the z direction. Averaging over the lateral directions gives a one-dimensional, two-component Schrödinger equation for the envelope functions $\phi_{\pm}(z)$ that appear in Eq. (2) of the Methods section of the main text. The equation uses the longitudinal effective mass, $m_l = 0.92 m_0$, for the kinetic energy term. The diagonal intravalley potential for the model is $V(z) = V_F(z) + V_B(z) + V_{\mathrm{osc}}(z)$. The external electrostatic potential energy is given by $V_F(z) = -eFz$, where $F = 8.5$ MV/m. The barrier potential is $V_B(z) = \frac{B}{2}[1 + \tanh(z/w)]$ with the barrier height $B = 0.15$ eV and barrier width $w = 1$ nm. The Wiggle Well potential is $V_{\mathrm{osc}}(z) = n_{\mathrm{Ge}} V_0 [1 - \cos(qz)]/2$, where V_0 is the difference in site energies between the s-like conduction-band levels of Si and Ge. We take this as $V_0 = -1.53$ eV from Table I of Ref. [140]. The off-diagonal intervalley potential
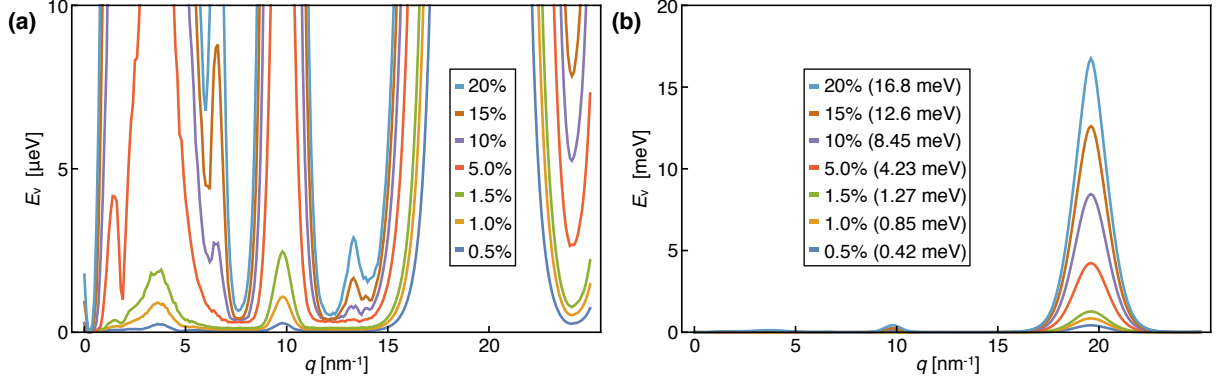
Figure C.1: The contribution to the valley splitting E_v due to a sinusoidal Ge concentration in the quantum well as a function of the wavevector q, similar to Fig. 1(c) in the main text, with a smaller scale (a) to show the low-concentration peaks at low q and a larger scale (b) to show the peaks at $q \approx 20$ nm^{-1}. The average concentration n_{Ge} of Ge in the quantum well of each curve is shown in the inset legend. The energy splittings listed in the inset are the maximum E_v calculated for each concentration. Source data are provided as a Source Data file.

that connects $\phi_+(z)$ to $\phi_-(z)$ has the additional factor $\exp[\pm i(K_z - K_z' - 2k_0)z]$ with the contributions of the reciprocal lattice vectors weighted by the appropriate combinations of $c_{\pm}(\mathbf{K})$, the coefficients of the cell-periodic parts of the Bloch functions. These coefficients are given in Table I of Ref. [157] for bulk Si. Extinction effects in the Si lattice turn out to be extremely important for the calculation of E_v for the long-period Wiggle Well, with E_v actually vanishing at the oscillation period λ_{long} in the absence of disorder. Even when disorder is present, E_v at λ_{long} is much less than E_v at λ_{short}, as seen in Fig. 1(c) of the main text and in Supplementary Fig. 1. This means that $c_+(\mathbf{K})$ must be recalculated when Ge is present. This is also done using a virtual crystal approximation in which 59 $c_{\pm}(\mathbf{K})$ coefficients are used [59]. The calculation requires disorder averaging, which leads to a certain amount of noise in the calculated $E_v(q)$ plots in Supplementary Fig. 1.

C.2 Fabrication Details and Hall Measurement

Hall bars and quantum dot devices were fabricated simultaneously on the same ~10 mm chip. A 15 nm layer of aluminum oxide gate dielectric is grown by atomic layer deposition
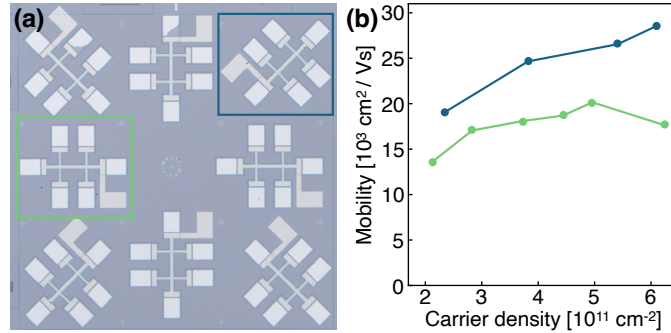
Figure C.2: Wiggle Well Hall Bars. (a) Optical image of Hall bar devices measured. The length of the Hall bar between the central ohmics is 200 µm. The Hall bar top gate is isolated from the heterostructure by 20 nm of ALD-grown aluminum oxide. All deposited metal is a Ti/Pd stack. (b) Transport mobility results of two Hall bar devices highlighted in (a), performed at ∼2 K. Source data are provided as a Source Data file.

(ALD) at 200 °C. This oxide is etched by dilute HF in a 30 µm square region centered around the dot region. Another 5 nm of aluminum oxide is then deposited. This results in 5 nm of deposited oxide over the dot region and 20 nm over the Hall bars. The chip then undergoes a 15 min, 450 °C forming gas anneal. The Hall bar gate metal is a bi-layer of titanium and palladium, patterned by photo-lithography. The quantum dot gate design has three layers of aluminum patterned by electron-beam-lithography. Each gate layer is isolated by the self oxidation of the aluminum, enhanced by a 15 min downstream oxygen plasma ash. Supplementary Fig. C.2 shows an optical image of the Hall bars measured and the transport mobility results of the measurements as a function of carrier density, measured at ∼2 K. The peak mobility reported here is 5-10 times lower than other recently reported values for pure silicon quantum wells [139, 144, 165]. However, the estimated electronic mean-free path in this device is ∼ 1 μm, so we do not expect this mobility to be a limiting factor for qubit formation or performance.

C.3   Gate Lever Arms for Dot Tuning

The lever arm α of the plunger gate P1 to the dot used for pulsed-gate spectroscopy is measured by thermally broadening the charge-sensed electron charging transition. The gate
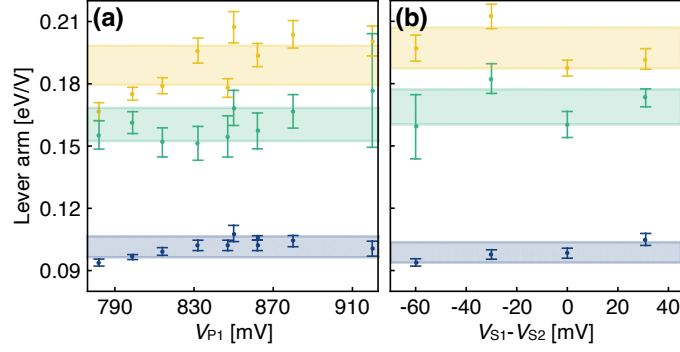
Figure C.3: Lever arms for voltage tunings. (a) Lever arms for gates S1 (yellow), S2 (green), and P1 (blue), as a function of the corresponding voltages, for the 'symmetric' voltage tuning method described in the main text. (b) Lever arms for S1 (yellow), S2 (green), and P1 (blue) of the 'asymmetric' voltage tuning method described in the main text. In both plots, the shaded regions are ±5% around the average. Error bars correspond to the standard error in the fit to Supplemental Eq. (2). Source data are provided as a Source Data file.

voltage is swept over the transition as the mixing chamber temperature is increased, and the current through the charge sensor is fit to [102]

$$I_{\text{CS}}(V) = A \tanh\left[\frac{\alpha(V - V_0)}{2k_B T_e}\right] + bV + I_0, \tag{C.1}$$

in order to extract $\tau = T_e/\alpha$ as a function of the mixing chamber temperature T_{MC}, where k_B is Boltzmann's constant, T_e is the electron temperature, and A, b, V_0 and I_0 are additional fitting parameters. The lever arm α, as well as the base electron temperature T_{e_0}, are determined by fitting τ as a function of T_{MC} to the phenomenological expression

$$\tau = \frac{1}{\alpha}\sqrt{T_{\text{MC}}^2 + T_{e_0}^2}. \tag{C.2}$$

For the 'symmetric' tuning method where both screening gates S1 and S2 are changed in the same voltage direction, the lever arm is measured at every other voltage tuning. For voltage tunings where the P1 lever arm is not explicitly measured, the average of the two nearest tunings is used. For the 'asymmetric' tuning method where S1 and S2 are changed in opposite directions, the lever arm is measured at every tuning. Relative lever arms between
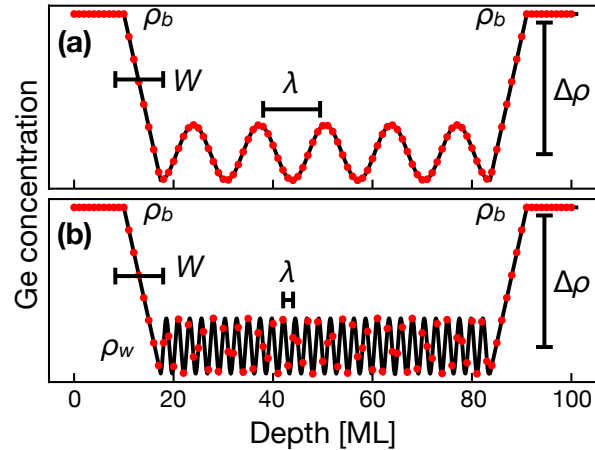
Figure C.4: Illustration of (a) the long-period Wiggle Well, and (b) the short-period Wiggle Well, simulated using NEMO-3D. Black lines represent the ideal concentration profile, and red points represent the concentrations sampled at each layer. Both wells have a linearly graded interface concentration with width $W = 1$ nm. The difference in Ge concentration between the bulk (ρ_b) and the well (ρ_w) is $\Delta\rho$, which is always fixed at 0.25 to prevent the wavefunction from spilling out of the quantum well. The concentration oscillation periods are $\lambda = 1.8$ nm in (a) and $\lambda = 0.32$ nm in (b). The amplitude of the concentration oscillation was adjusted, such that $\rho_w = A$, where A is the oscillation amplitude. Depth is reported in units of monolayers (ML). Source data are provided as a Source Data file.

a screening gate and P1 are determined by measuring the slope of a transition line as both gate voltages are changed. Using the absolute lever arm of P1 and the relative lever arms for the screening gates, their absolute lever arms to the dot are calculated.

Supplementary Fig. C.3 shows these lever arms for both the 'symmetric' and 'asymmetric' tuning methods. As shown, the lever arms for all three gates stays within 5% of the average value for most tunings. There is no noticeable difference in the lever arms between the tuning methods, despite the significant difference in valley splitting tuning. This may indicate that this method of tracking the lever arms is not a sensitive enough technique to measure the lateral movement expected in the 'asymmetric' tuning scheme. Our assumption that the dot remains approximately stationary for the 'symmetric' tuning scheme is based on a previous study of valley splitting in a device with a gate structure nearly identical to the one used here [125]. In that study, the tuning scheme is identical to the 'symmetric' tuning scheme here and the dot location is determined through COMSOL simulations over the experimental

tuning range. These simulations showed the center of mass of the dot remained stationary, to within 1 nm.

C.4   Additional Details of NEMO simulations

Supplementary Fig. C.4 shows schematic illustrations of the Ge concentration profiles used to generate the lattice simulated in NEMO-3D. At a given layer, each atom in the lattice is assigned to be either Si or Ge, where the probability of choosing Ge is given by the average concentration in a given layer.

Appendix D

Supplementary Information for

Chapter 5

D.1   Theoretical treatment of alloy disorder in 1D and 2D models

In this Appendix, we describe how to account for alloy disorder in the coarse-grained 1D and 2D models we use in both tight-binding and effective-mass simulations. First, we consider how to compute the weighted average Si concentration in each cell, starting from a fully atomistic, 3D model of the heterostructure. Then, we derive effective probability distributions for the Si concentrations in each cell. These effective distributions allow us to sample many realizations of alloy disorder without generating fully atomistic, 3D models, thus greatly improving our computational efficiency.

D.1.1   Averaging method for obtaining Si and Ge concentrations

As described in Section 5.3.2, for 1D models, the Si concentration in each cell $X_{\text{cell}} = X_l$, where X_l is the average Si concentration at layer l, weighted by the dot probability density.

We can define this quantity as follows:

$$X_l = \sum_{a \in A_l} \mathbb{1}\left[a = \text{Si}\right] w(a) \tag{D.1}$$

where A_l is the set of atoms in layer l, $a = \{\text{Si}, \text{Ge}\}$ is a Si or Ge atom, and $\mathbb{1}\left[a = \text{Si}\right]$ is the indicator function which returns 1 if $a = \text{Si}$ and 0 otherwise. The weight function $w(a)$ is proportional to the dot probability density, which we assume to be the ground state of a 2D isotropic harmonic oscillator. Following Ref. [145], $w(a)$ should be normalized such that $\sum_{a \in A_l} w(a) = 1$. Because there are two atoms in each layer of the Si cubic unit cell, spread out over an area of size a_0^2, we can approximate the sum over atoms as an integral using the transformation

$$\sum_{a \in A_l} \rightarrow \frac{2}{a_0^2} \int_{-\infty}^{+\infty} dx \, dy. \tag{D.2}$$

Hence, the correctly normalized weight function is

$$w(a) = \frac{a_0^2}{2\pi a_{\text{dot}}^2} e^{-r_a^2 / a_{\text{dot}}^2} \tag{D.3}$$

where r_a is the distance of atom a from the center of a dot of radius $a_{\text{dot}} = \sqrt{\hbar / m_t \omega_{\text{orb}}}$, $m_t = 0.19 m_e$ is the transverse effective mass in Si, m_e is the bare electron mass, and $\hbar\omega_{\text{orb}}$ is the characteristic energy level spacing of the confinement potential. So, starting from a fully atomistic model of a heterostructure, we can incorporate concentration fluctuations into a 1D cell model by taking the weighted average Si concentration in each cell, where the weight function is given by Eq. (D.3). As noted in the main text, we assume a cell size of $\Delta z = a_0 / 4$ here.

For 2D models, we divide the atoms on layer l into cells of width Δx. We assume the dot envelope function is separable, $\Psi(x, y, z) = \psi_{xz}(x, z)\psi_y(y)$, and we take $\psi_y(y)$ to be the ground state of a parabolic confinement potential with characteristic orbital splitting $\hbar\omega_y$.

The Si concentration in each cell, weighted by the dot wavefunction, is given by

$$X_{j,l} = \sum_{a \in A_{j,l}} \mathbb{1}\left[a = \text{Si}\right] w_{2\text{D}}(a) \tag{D.4}$$

where $A_{j,l}$ is the set of atoms in the jth cell along $\hat{x}$, in the lth layer, $\mathbb{1}$ is the indicator function, and $w_{2\text{D}}(a)$ is proportional to the dot orbital wavefunction in the y direction. Proper normalization should ensure that

$$\sum_{a \in A_{j,l}} w_{2\text{D}}(a) = 1. \tag{D.5}$$

Because there are 2 atoms per unit cell per layer, we can approximate the sum as an integral using

$$\sum_{a \in A_{j,l}} \rightarrow \frac{2\Delta x}{a_0^2} \int_{-\infty}^{\infty} dy. \tag{D.6}$$

Thus, we find

$$w_{2\text{D}}(a) = \frac{a_0^2}{2\Delta x a_y \sqrt{\pi}} e^{-y_a^2/a_y^2}, \tag{D.7}$$

where y_a is measured from the center of the dot, and $a_y = \sqrt{\hbar/m_t \omega_y}$. In this case, we adopt the same vertical cell dimension Δz as the 1D model, and a lateral cell width of $\Delta x = a_0/2$ for the 2D cell model. Thus, we account for concentration fluctuations in each cell of a 2D model by taking the weighted average Si concentration in each cell of size $\Delta x \times \Delta z$, where the weight function is given by Eq. (D.7).

D.1.2 Generating probability distributions for Si and Ge concentrations

In the previous section, we took alloy disorder into account by generating fully 3D heterostructures atomistically, then populating each cell of a coarse-grained model by computing the weighted average Si concentration in each 1D or 2D cell. However, it is slow and
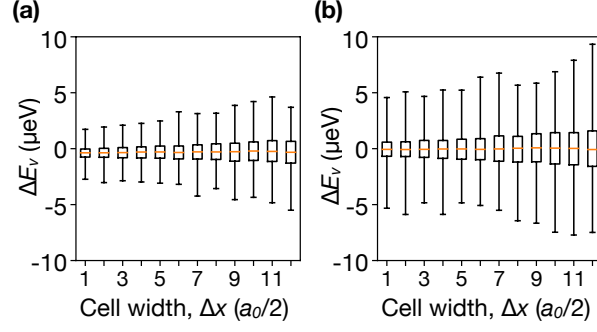
Figure D.1: Discrepancy between 1D and 2D tight-binding models in systems without steps. (a), (b) Plots show the median values (red lines), quartile ranges (boxes), and maximum ranges (whiskers) of $\Delta E_v = E_v^{2\mathrm{D}} - E_v^{1\mathrm{D}}$, for the same disorder realizations in 1D and 2D cell geometries (see main text and Appendix D.1), as a function of the cell size Δx. Here we consider quantum wells with smoothed linear interface profiles, as described in Section 5.4.3, with interface widths of (a) $\lambda_{\mathrm{int}} = 1$ ML, and (b) $\lambda_{\mathrm{int}} = 10$ ML, and well widths of $W = 80$ ML. For all simulations we assume a vertical electric field of $E_z = 5$ mV/nm and an isotropic orbital energy splitting of $\hbar\omega_{\mathrm{orb}} = 2$ meV.

computationally expensive to repeat this procedure for every simulation. Here, we show that we can generate valley splitting distributions by randomly sampling the Si concentration in each cell from known probability distributions based on the Si/Ge concentration profile.

In Ref. [145], by examining the statistical properties of Eq. (D.1), we showed that the Si concentration in each cell of a 1D model can be described as a binomial random variable:

$$X_l \sim \frac{1}{N_{\mathrm{eff}}} \mathrm{Binom}(N_{\mathrm{eff}}, \bar{X}_l), \qquad (D.8)$$

where $N_{\mathrm{eff}} = 4\pi a_{\mathrm{dot}}^2/a_0^2$ is the number of Si atoms per layer inside a 2D dot of radius $\sqrt{2}\,a_{\mathrm{dot}}$ [145] and $\bar{X}_l$ is the average Si concentration in layer l. Here, we derive a similar sampling rule for cells in a 2D model. Taking the variance of Eq. (D.4), we find

$$
\begin{aligned}
\mathrm{Var}\left[X_{j,l}\right] &= \bar{X}_{j,l}(1 - \bar{X}_{j,l}) \sum_{a \in A_{j,l}} w_{2\mathrm{D}}^2(a) \\
&= \bar{X}_{j,l}(1 - \bar{X}_{j,l}) \frac{1}{2\sqrt{2\pi}} \frac{a_0^2}{a_y \Delta x} \\
&= \frac{\bar{X}_{j,l}(1 - \bar{X}_{j,l})}{N_{\mathrm{eff}}^{2\mathrm{D}}},
\end{aligned}
\qquad (D.9)
$$

where $N_{\mathrm{eff}}^{\mathrm{2D}} = 2\sqrt{2\pi}a_y\Delta x/a_0^2$ and $\bar{X}_{j,l}$ is the expected Si concentration of the 2D cell with indices (j, l), obtained by averaging uniformly over the entire layer ($\bar{X}_{j,l} = \bar{X}_l$, for the case of no step), or by using Eq. (5.1) (for the case of a step). Comparing these relations to the known properties of a binomial distribution, we can identify

$$X_{j,l} \sim \frac{1}{N_{\mathrm{eff}}^{\mathrm{2D}}}\mathrm{Binom}(N_{\mathrm{eff}}^{\mathrm{2D}}, \bar{X}_{j,l}). \tag{D.10}$$

In this way, we can account for alloy disorder in the 1D and 2D models by sampling each cell according to Eqs. (D.8) and (D.10), rather than generating a full 3D lattice geometry and explicitly averaging the Ge concentration in every cell.

D.2   Characterizing tight-binding models

D.2.1   Comparing NEMO-3D, two-band tight-binding model, and effective-mass theory

In this Appendix, we compare results obtained from NEMO-3D, the minimal two-band tight-binding model, and effective-mass theory in heterostructures without steps. We first construct a 3D crystal lattice atom by atom, including alloy disorder. Taking the dot to be in the orbital ground state of a harmonic confinement potential with a characteristic strength of $\hbar\omega_{\mathrm{orb}} = 2$ meV, we then reduce the 3D model to an effective 1D cell geometry as described in Appendix D.1. This geometry can be solved immediately, using the 1D minimal tight-binding model to obtain the valley splitting. For the effective-mass model, we use the same 1D concentration profile to numerically solve for $\psi_{\mathrm{env}}(z)$, and then compute E_v^{EM} from Eq. (5.8). Figures D.2(a) and D.2(c) show correlation plots for valley splittings computed this way for 10 disorder realizations, obtaining nearly perfect agreement between the two methods, for both (a) wide and (c) sharp interfaces.

The full 3D crystal lattice geometries used in these simulations are then used to obtain
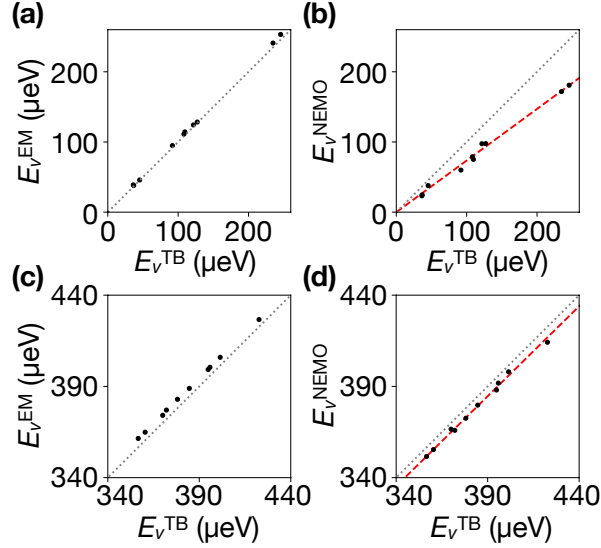
Figure D.2: Valley splitting comparisons between effective-mass theory, two-band tight-binding, and NEMO-3D models. (a), (b) Using the same 10 alloy disorder realizations, we calculate valley splittings in three ways. In (a), we compare valley splittings computed from the minimal tight-binding model (E_v^{TB}) and effective-mass theory [E_v^{EM}, from Eq. (5.8)], obtaining nearly perfect agreement. In (b), we compare the minimal tight-binding model to NEMO-3D (E_v^{NEMO}). The red dashed line indicates the best fit to $E_v^{\text{NEMO}} = \alpha E_v^{\text{TB}}$ with $\alpha = 0.74$. Gray dotted lines indicate $y = x$. For both (a) and (b), we use quantum wells of width $W = 80$ ML and sigmoid interfaces of width $\lambda_{\text{int}} = 20$ ML. (c), (d) show the same data as (a), (b) for 10 heterostructures with $\lambda_{\text{int}} = 1$ ML. In (d), the red line indicates the best fit, with $\alpha = 0.99$. In all simulations, we assume a vertical electric field of $E_z = 5$ mV/nm and an orbital energy splitting of $\hbar\omega_{\text{orb}} = 2$ meV. The NEMO-3D valley splitting results shown here are the same used in Fig. 5.6(c).
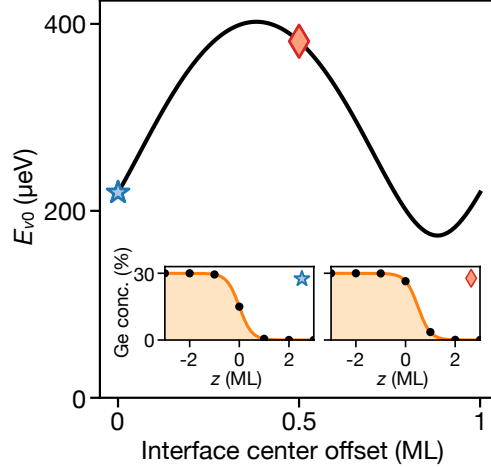
Figure D.3: For quantum wells with sharp interfaces, the deterministic valley splitting E_{v0} depends sensitively on the interface position. Here we compute E_{v0} for quantum wells with sigmoid interfaces, and interface widths of $\lambda_{\text{int}} = 1$ ML, as the center of the interface is varied between two adjacent atomic layers. Insets: (blue star) an interface centered exactly on an atomic layer; (red diamond) an interface centered halfway between atomic layers.

the valley splitting in NEMO-3D. Figures D.2(b) and D.2(d) show correlation plots for the same 10 heterostructures, now comparing the minimal tight-binding model to the NEMO-3D model, for (b) wide and (d) sharp interfaces. The NEMO-3D valley splitting results consistently fall slightly below the minimal tight-binding values; however the results are very strongly correlated, and well-approximated by a linear scaling relation, $E_v^{\text{NEMO}} \approx \alpha E_v^{\text{(TB)}}$, where $\alpha = 0.74$ for wide interfaces and $\alpha = 0.99$ for sharp interfaces. Thus, the effect of the higher bands ignored in the two-band model are effectively captured by a modest linear scaling of the valley splitting, which depends on interface width.

D.2.2 Comparing 1D and 2D tight-binding models

In this paper, we employ the 1D tight-binding model in systems without steps, and the 2D tight-binding model in systems with steps, assuming a cell width of $\Delta x = a_0/2$. In this section, we show that these choices yield consistent results.

We first choose a value for the cell width. We generate a full 3D crystal lattice atom-by-atom, including alloy disorder. We then create a coarse-grained 2D cell geometry using

the methods described in Appendix D.1, and solve this using the 2D minimal tight-binding model. Next, we coarse grain the model a second time, as described in Appendix D.1, to obtain a 1D cell geometry, and solve this using the 1D minimal tight-binding model. We then compute the corresponding differences $\Delta E_v = E_v^{2D} - E_v^{1D}$. This procedure is repeated for 1,000 realizations of random alloy disorder. Δx is then modified, choosing values that are integer multiples of $a_0/2$. The results are plotted in Fig. D.1 for a range of Δx values, showing the resulting median values (red lines), 25-75% quartiles (boxes), and maximum ranges (whiskers). The very small values obtained for ΔE_v indicate excellent consistency between the 1D and 2D models for systems without steps. Since the smallest cell width, $\Delta x = a_0/2$, is found to provide the best agreement, we adopt this as the cell width for our 2D model.

D.3 Choosing the center of the quantum well interface

In quantum wells with very sharp interfaces, the exact location of the interface [e.g., z_b or z_t in Eq. (5.21)] strongly affects the deterministic valley splitting E_{v0}. Figure D.3 shows this variation in E_{v0} for a $\lambda_{int} = 1$ ML sigmoidal interface, as the center of the sigmoid is moved between two adjacent atomic monolayers. While all interfaces in Fig. D.3 are drawn from the same sigmoid profile, E_{v0} nonetheless varies by a factor of 2. In this work, whenever narrow interfaces are considered, we choose the center of the interface to be exactly halfway between two adjacent monolayers, as shown in the inset labeled with a red diamond.

D.4 Valley splitting spatial correlations

In this Appendix, we theoretically compute the probability P_{fail} of measuring a valley splitting lower than a nominal threshold value E_v^{min}, as defined in Sec. 5.5.1 of the main text. In that Section, we considered geometries with uniform Ge in the quantum well, which are always disorder-dominated, with $|\Delta_0| \ll \sigma_\Delta$. The probability of failure for a single valley splitting
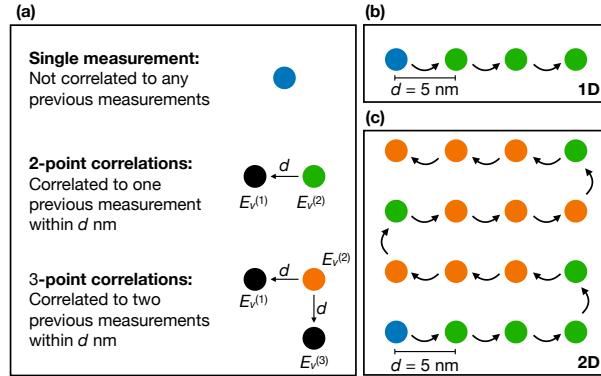
Figure D.4: An explanation of the types of correlations taken into account when computing P_{fail}. (a) The difference between a single E_v measurement, two-point correlations between neighboring measurements, and three-point correlations between neighboring measurements. We only consider these three types of correlations in our model. (b) Illustration of a series of E_v measurements, in increments of d, along a 1D line. The first measurement is uncorrelated to anything prior, and the next 3 are correlated to one prior measurement. (c) Illustration of a series of E_v measurements along a square grid with spacing d. We see one initial measurement, six measurements correlated to one prior measurement within distance d, and 9 measurements correlated to two prior measurements within distance d.

measurement is therefore given by Eq. (5.18):

$$p_1 := P(E_v < E_v^{\text{min}}) \approx 1 - \exp\left[-(E_v^{\text{min}})^2/4\sigma_\Delta^2\right]. \tag{D.11}$$

In the protocol described in Sec. 5.5.1, a dot is allowed to sample either a 1D or 2D region of a device, along a set of grid points with spacing 5 nm. If n sites are sampled, a naive estimate for P_{fail} would be p_1^n. However, this estimate is inaccurate because the quantum dot is larger than the grid spacing, so the valley splittings measured when the dot is centered on nearby grid points are not independent. A more accurate estimate of P_{fail} should therefore account for correlations between nearby grid points. Empirically, for the setup described in Sec. 5.5.1 and Fig. 5.9(e), we find that it is sufficient to account for nearest-neighbor correlations between sites separated by ≤ 5 nm.

Figure D.4 illustrates the different types of correlations relevant to the 1D and 2D simulation schemes shown in Fig. 5.9(e). In Fig. D.4(b), we consider four neighboring sites in a 1D geometry. To explain the correlation analysis, we can think of the valley splitting simulations

at each of these sites as 'measurements' performed in a particular order, as indicated by the arrows. The first measurement (blue dot) clearly has no prior measurements to correlate with, so its probability of failure is simply given by p_1 in Eq. (D.11). However, the next three measurements (green dots) are all correlated with the prior measurement. If we define the conditional probability of failure at site (2), given failure at site (1), as

$$p_2 := P(E_v^{(2)} < E_v^{\min}|E_v^{(1)} < E_v^{\min}). \tag{D.12}$$

then the total estimated probability of failure for the linear geometry shown in Fig. D.4(b) is given by $P_{\text{fail}} \approx p_1 p_2^3$. In general, for a 1D chain of n sites, we have

$$P_{\text{fail}} \approx p_1 \, p_2^{n-1}. \tag{D.13}$$

Figure D.4(c) illustrates a series of valley splitting measurements exploring a 2D region, on a 4×4 grid. If we imagine performing these measurements by snaking across the lattice as indicated by the arrows, we see there is only one measurement (blue dot) having no prior correlations. There are six measurements (green dots) correlated with one prior measurement, and nine measurements (orange dots) correlated with two prior measurements. If we define the conditional probability function

$$p_3 := P(E_v^{(2)} < E_v^{\min}|E_v^{(1)} < E_v^{\min}, E_v^{(3)} < E_v^{\min}) \tag{D.14}$$

for measurements at sites (1), (2), and (3) in Fig. D.4(a), then we can estimate $P_{\text{fail}} \approx p_1 p_2^6 p_3^9$. In general, for an $n \times n$ lattice, we have

$$P_{\text{fail}} \approx p_1 \, p_2^{2n-2} \, p_3^{(n-1)^2}. \tag{D.15}$$

In Appendix D.4.1 (below) we compute the probability p_2, and in Appendix D.4.2 we

compute p_3. Numerical values for p_1, p_2, and p_3 are given in Table D.1, and the resulting P_{fail} values are given in Tables D.2 and D.3.

D.4.1 Two-point correlations

We consider quantum dots centered at two neighboring grid sites, (1) and (2). The corresponding dot positions in the x-y plane are $\mathbf{r}_1$ and $\mathbf{r}_2$, and we assume the dots are separated by the grid spacing $d = |\mathbf{r}_2 - \mathbf{r}_1|$. We want to compute p_2, the conditional probability that $E_v^{(2)} < E_v^{\text{min}}$, given that $E_v^{(1)} < E_v^{\text{min}}$, where as usual, the valley splittings are related to the intervalley couplings through $E_v^{(1)} = 2|\Delta_1|$ and $E_v^{(2)} = 2|\Delta_2|$. In the disorder-dominated regime, we simply assume the deterministic intervalley couplings are zero, such that Δ_1 and Δ_2 become complex random variables centered at zero. The probability distributions of Δ_1 and Δ_2 are assumed to be circular gaussian distributions in the complex plane. To account for the correlations between Δ_1 and Δ_2, we need to compute the covariances between real and imaginary components of Δ_1 and Δ_2, defined as Δ_1^R, Δ_1^I, Δ_2^R, and Δ_2^I.

We begin with the following identity for covariances:

$$\text{Cov}\,[X, Y] = \frac{1}{2}\left(\text{Var}\,[X] + \text{Var}\,[Y] - \text{Var}\,[X - Y]\right). \tag{D.16}$$

Previously, we have found that $\text{Var}[\Delta^R] = \text{Var}[\Delta^I] = \sigma_\Delta^2/2$, or $\text{Var}[\Delta] = \sigma_\Delta^2$. Following Ref. [145], we also find that

$$\text{Var}\,[\Delta_2 - \Delta_1] = \left(\frac{a_0}{4}\frac{\Delta E_c}{X_w - x_s}\right)^2 \sum_l |\psi_{\text{env}}(z_l)|^4 \text{Var}\left[\delta_l^{(2)} - \delta_l^{(1)}\right], \tag{D.17}$$

where from Eq. (D.1) we have

$$\delta_l^{(j)} = X_l^{(j)} - \bar{X}_l^{(j)} = \sum_{a \in A_l} \mathbb{1}\,[a = \text{Si}]\,w_j(a) - \bar{X}_l^{(j)}. \tag{D.18}$$

Here, $X_l^{(j)}$ are the weighted Si concentrations at sites $j = 1, 2$, and the properly normalized

probability density for site j is given by

$$w_j(a) = \frac{a_0^2}{2\pi a_{\text{dot}}^2} e^{-|\mathbf{r}_a - \mathbf{r}_j|^2/a_{\text{dot}}^2}, \tag{D.19}$$

where $\mathbf{r}_a$ is the position of atom a in layer l. Using Eqs. (D.17), (D.18), (D.19), and the sum-to-integral transformation Eq. (D.2), we can evaluate

$$\text{Var}\left[\Delta_2 - \Delta_1\right] = 2\left(1 - e^{-d^2/2a_{\text{dot}}^2}\right)\sigma_\Delta^2. \tag{D.20}$$

Using Eq. (D.16), we then have

$$\text{Cov}\left[\Delta_2^R, \Delta_1^R\right] = \text{Cov}\left[\Delta_2^I, \Delta_1^I\right] = \frac{1}{2}e^{-d^2/2a_{\text{dot}}^2}\sigma_\Delta^2. \tag{D.21}$$

We can now construct the joint probability density function for Δ_1 and Δ_2. For the basis ordering $\left\{\Delta_1^R, \Delta_1^I, \Delta_2^R, \Delta_2^I\right\}$ the covariance matrix is given by

$$\boldsymbol{\Sigma} = \frac{\sigma_\Delta^2}{2}\begin{pmatrix} 1 & 0 & A & 0 \\ 0 & 1 & 0 & A \\ A & 0 & 1 & 0 \\ 0 & A & 0 & 1 \end{pmatrix}, \tag{D.22}$$

where

$$A = \exp\left(-d^2/2a_{\text{dot}}^2\right). \tag{D.23}$$

Using the standard definition of conditional probability, we now have

$$p_2 = \frac{P(E_v^{(2)} < E_v^{\text{min}}, E_v^{(1)} < E_v^{\text{min}})}{p_1}. \tag{D.24}$$

We can evaluate the numerator using the joint probability density function, giving

$$P(E_v^{(2)} < T, E_v^{(1)} < T) = \frac{1}{\sqrt{(2\pi)^4 |\boldsymbol{\Sigma}|}} \int\limits_{\substack{|\Delta_1| < E_v^{\min}/2 \\ |\Delta_2| < E_v^{\min}/2}} d\Delta_1 d\Delta_2 \exp\left(-\frac{1}{2}\mathbf{v}^T \boldsymbol{\Sigma}^{-1} \mathbf{v}\right) \tag{D.25}$$

where we define $\mathbf{v} = \left(\Delta_1^R, \Delta_1^I, \Delta_2^R, \Delta_2^I\right)^T$, and $d\Delta_j$ is shorthand for $d\Delta_j^R d\Delta_j^I$. This integral can be evaluated numerically for a given set of parameters σ_Δ, d, and a_{dot}. Numerical results for p_2, for a typical set of parameters, are presented in Table D.1, and the corresponding results for P_{fail} are reported in Table D.2 for a 1D grid geometry.

D.4.2 Three-point correlations

The conditional probability p_3 is computed similarly to p_2. In this case, there are three intervalley couplings, so the covariance matrix becomes

$$\boldsymbol{\Sigma} = \frac{\sigma_\Delta^2}{2} \begin{pmatrix} 1 & 0 & A & 0 & B & 0 \\ 0 & 1 & 0 & A & 0 & B \\ A & 0 & 1 & 0 & A & 0 \\ 0 & A & 0 & 1 & 0 & A \\ B & 0 & A & 0 & 1 & 0 \\ 0 & B & 0 & A & 0 & 1 \end{pmatrix}, \tag{D.26}$$

in the basis $\left\{\Delta_1^R, \Delta_1^I, \Delta_2^R, \Delta_2^I, \Delta_3^R, \Delta_3^I\right\}$, where A is given in Eq. (D.23) and $B = \exp(-d^2/a_{\mathrm{dot}}^2)$, which differs from A because the distance between sites (1) and (3) is given by $\sqrt{2}d$. Similar to Eq. (D.24), we apply the standard definition of conditional probability,

$$p_3 = \frac{P(E_v^{(1)} < E_v^{\min}, E_v^{(2)} < E_v^{\min}, E_v^{(3)} < E_v^{\min})}{P(E_v^{(1)} < E_v^{\min}, E_v^{(3)} < E_v^{\min})}. \tag{D.27}$$

	σ_Δ (μeV)	p_1	p_2	p_3
0% Ge	36.21	0.8515	0.9531	0.98
1% Ge	96.43	0.2357	0.6763	0.83
5% Ge	203.82	0.0584	0.3397	0.53

Table D.1: Numerical parameters used to calculate P_{fail}. To compute σ_Δ, we use Eq. (5.13), and we assume quantum wells with a sigmoidal profile defined by $\lambda_{\text{int}} = 10$ ML and $W = 80$ ML, an isotropic harmonic confinement potential of strength $\hbar\omega_{\text{orb}} = 2$ meV, corresponding to $a_{\text{dot}} \approx 14$ nm, and a vertical electric field of $E_z = 5$ mV/nm. To compute p_2 and p_3, we set $d = 5$ nm.

Here, the denominator can be evaluated using Eq. (D.25), while the numerator is given by

$$
P(E_v^{(1)} < E_v^{\text{min}}, E_v^{(2)} < E_v^{\text{min}}, E_v^{(3)} < E_v^{\text{min}}) =
$$

$$
\int_{\substack{|\Delta_1|<E_v^{\text{min}}/2 \\ |\Delta_2|<E_v^{\text{min}}/2 \\ |\Delta_3|<E_v^{\text{min}}/2}} d\Delta_1 d\Delta_2 d\Delta_3 \frac{1}{\sqrt{(2\pi)^6 |\boldsymbol{\Sigma}|}} \exp\left(-\frac{1}{2}\mathbf{v}^T \boldsymbol{\Sigma}^{-1} \mathbf{v}\right),
\tag{D.28}
$$

where now, $\mathbf{v} = \left(\Delta_1^R, \Delta_1^I, \Delta_2^R, \Delta_2^I, \Delta_3^R, \Delta_3^I\right)^T$. Numerical results for p_3 are presented in Table D.1, and the corresponding results for P_{fail} are reported in Table D.3 for a 2D grid geometry.
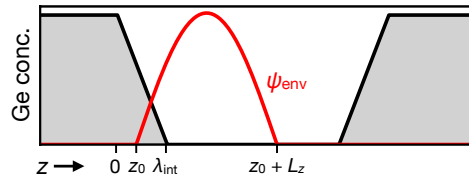
Figure D.5: Schematic illustration of the sinusoidal variational envelope function $\psi_{\text{env}}(z)$ and the variational parameters z_0, λ_{int}, and L_z used to study linear interfaces.

	Calc. P_{fail}	Sim. P_{fail}
0% Ge		
$n = 1$	0.85	0.8510
$n = 2$	0.81	0.8111
$n = 3$	0.77	0.7715
$n = 4$	0.74	0.7328
$n = 5$	0.70	0.6936
1% Ge		
$n = 1$	0.24	0.2358
$n = 2$	0.16	0.1576
$n = 3$	0.11	0.1013
$n = 4$	0.073	0.0617
$n = 5$	0.049	0.0411
5% Ge		
$n = 1$	0.058	0.0650
$n = 2$	0.020	0.0230
$n = 3$	0.0067	0.0081
$n = 4$	0.0023	0.0035
$n = 5$	0.00078	0.0014

Table D.2: Numerical and simulated values of P_{fail} for a 1D grid geometry, using the same parameters as Table D.1. These are the same values plotted in Fig. 5.9(f) in the main text. Calculated values are computed using the methods described in Appendix D.4. Simulated values are obtained by averaging 10,000 tight-binding simulations, as described in the main text.

D.5 Variational approach for studying E_v vs. interface width

In this Appendix, we use a variational method to derive the valley splitting as a function of interface width, both with and without alloy disorder, as described in Sec. 5.4.3. In both cases, we use the perfectly linear interface model described in Section 5.4.3 and Fig. 5.7(b)i.

	Calc. P_{fail}	Sim. P_{fail}
0% Ge		
$n = 1$	0.85	0.8473
$n = 2$	0.76	0.7588
$n = 3$	0.65	0.6548
$n = 4$	0.53	0.5503
$n = 5$	0.42	0.4441
1% Ge		
$n = 1$	0.24	0.2359
$n = 2$	0.090	0.0925
$n = 3$	0.023	0.0237
$n = 4$	0.0042	0.0046
$n = 5$	5.2×10^{-4}	0.0010
5% Ge		
$n = 1$	0.058	0.0552
$n = 2$	0.0036	0.0042
$n = 3$	6.1×10^{-5}	2×10^{-4}
$n = 4$	3.0×10^{-7}	0
$n = 5$	4.0×10^{-10}	0

Table D.3: Numerical and simulated values of P_{fail} for a 2D grid geometry, using the same parameters as Table D.1. These are the same values plotted in Fig. 5.9(f) in the main text. Calculated values are computed using the methods described in Appendix D.4. Simulated values are obtained by averaging 10,000 tight-binding simulations, as described in the main text.

We consider the variational envelope function

$$
\psi_{\text{env}} = \begin{cases} \sqrt{2/L_z} \sin\left[\pi(z - z_0)/L_z\right], & z_0 \leq z \leq z_0 + L_z, \\ 0 & (\text{otherwise}), \end{cases} \tag{D.29}
$$

with variational parameters z_0 and L_z, shown schematically in Fig. D.5. Since the calculation only depends on the wavefunction near the top interface, a simple sinusoidal envelope suffices [63]. The variational energy is given by $\langle H \rangle = \langle T \rangle + \langle \phi \rangle + \langle U_{\text{qw}} \rangle$, where the kinetic
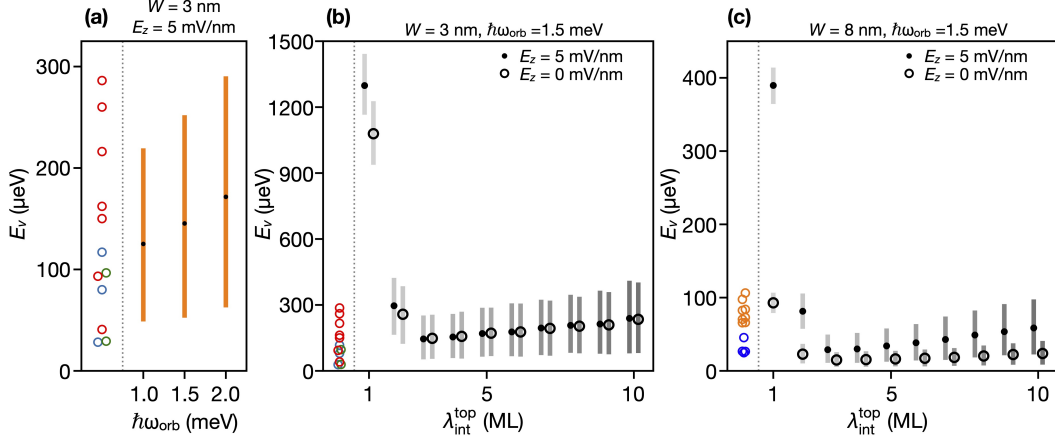
Figure D.6: Narrow quantum wells: our choice of vertical field E_z and orbital splitting $\hbar\omega_{\mathrm{orb}}$ yield simulation results consistent with experimental data considered in Sec. 5.5.2. (a) The mean values (dots) and 10-90 percentile range (bars) obtained from 1,000 1D two-band tight-binding simulations of E_v, with orbital energies $\hbar\omega_{\mathrm{orb}}$ between 1 and 2 meV. Here we use an electric field $E_z = 5$ mV/nm, a top-interface width of $\lambda_{\mathrm{int}}^{\mathrm{top}} = 3$ ML, and a well width of $W = 3$ nm. E_v data from Ref. [33], for the 3 nm quantum wells, are included for comparison (open circles). (b), (c) The 10-90 percentile ranges (bars) and mean values (dots and open circles) from 1,000 1D two-band tight-binding simulations of E_v, for different $\lambda_{\mathrm{int}}^{\mathrm{top}}$ and E_z. Dots are used for $E_z = 5$ mV/nm, and open circles are used for $E_z = 0$ mV/nm. (b) Results for a well width of $W = 3$ nm, including E_v data from Ref. [33]. (c) Results for a well width of 8 nm, including experimental E_v data from Ref. [33]. Dots and circles have the same meaning as in (b). Both (b) and (c) assume an orbital splitting $\hbar\omega_{\mathrm{orb}} = 1.5$ meV.

component $\langle T \rangle = \hbar^2\pi^2/2m_l L_z^2$ and the vertical field component $\langle \phi \rangle = (1/2)eE_z(L_z + 2z_0)$. The quantum well has barriers with Ge concentration $Y_s = 1 - X_s$ and linear interfaces of width λ_{int}, as illustrated in Fig. D.5. In the remainder of this section, we drop the subscript on λ to avoid clutter. In this section, to simplify the variational calculation, we set $z = 0$ at the top of the interface, as indicated in Fig. D.5, and we use the quantum well potential

$$U_{\mathrm{qw}}(z) = |\Delta E_c| \left(1 - \frac{X(z) - X_s}{1 - X_s} \right). \tag{D.30}$$

Equation (D.30) is equivalent to Eq. (5.3), offset by a constant, so that $U_{\mathrm{qw}} = 0$ in the middle of the quantum well.

D.5.1 No alloy disorder

First, we examine the system without alloy disorder. This is accomplished by employing the virtual crystal approximation, $X(z) = \bar{X}_z$. We separate the calculation into two cases: $z_0 < 0$ or $z_0 \geq 0$. The quantum well contribution to the variational energy is then given by

$$\langle U_{\text{qw}} \rangle = \frac{|\Delta E_c|}{4\pi^2 L_z \lambda_{\text{int}}} \times \begin{cases} 2\pi^2 \lambda_{\text{int}}^2 - 4\pi^2 \lambda_{\text{int}} z_0 + L_z^2 \cos\left[\frac{2\pi(\lambda_{\text{int}} - z_0)}{L_z}\right] \\ \quad -L_z^2 \cos\left(\frac{2\pi z_0}{L_z}\right), & z_0 < 0, \\ -L_z^2 + 2\pi^2(\lambda_{\text{int}} - z_0)^2 + L_z^2 \cos\left(\frac{2\pi(\lambda_{\text{int}} - z_0)}{L_z}\right), & z_0 \geq 0. \end{cases} \tag{D.31}$$

We then expand the cosine functions to fourth order and solve for the variational parameters by minimizing the variational energy, yielding

$$z_0 \approx \begin{cases} \frac{\lambda_{\text{int}}}{2} - \frac{1}{2\pi}\left(\frac{2eE_z L_z^3}{|\Delta E_c|} - \frac{\pi^2 \lambda_{\text{int}}^2}{3}\right)^{1/2}, & z_0 < 0, \\ \lambda_{\text{int}} - \left(\frac{3eE_z L_z^3}{2|\Delta E_c|\pi^2}\right)^{1/3} \lambda_{\text{int}}^{1/3}, & z_0 \geq 0, \end{cases} \tag{D.32}$$

$$L_z \approx \left(\frac{2\hbar^2 \pi^2}{eE_z m_l}\right)^{1/3}.$$

Applying these parameters to the envelope function, Eq. (D.29), we can compute the intervalley coupling and the valley splitting, using Eq. (5.8). The results are plotted as a solid green line in Fig. 5.7(a), showing very good agreement with numerical tight-binding and effective mass solutions. Thus, this simple variational model captures most of the interface physics.

We can also derive a continuum approximation for the intervalley coupling by transforming the sum in Eq. (5.8) to an integral and approximating the envelope function as linear
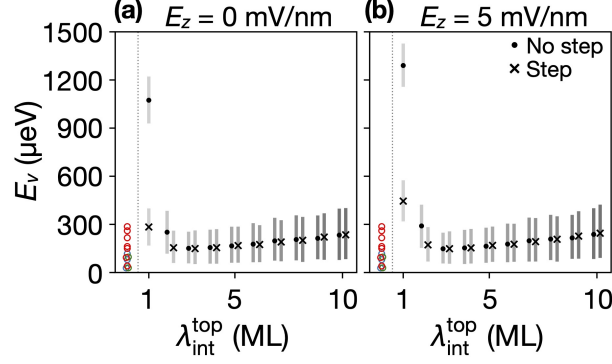
Figure D.7: Step disorder has the strongest effect on valley splitting in narrow wells with sharp top interfaces. (a), (b) The mean values (dots and × markers) and the 10-90 percentile range (bars) for 1,000 2D two-band tight-binding valley splitting simulations of the quantum wells described in Section 5.5.2, with varying top interface widths $\lambda_{\text{int}}^{\text{top}}$, performed with no step at the interface (dots), or with a single step at the center of the dot confinement potential (× markers). We use electric fields of (a) $E_z = 0$ mV/nm, or (b) $E_z = 5$ mV/nm, a well width $W = 3$ nm, and orbital energy splittings $\hbar\omega_{\text{orb}} = 1.5$ meV. E_v data for the 3 nm quantum wells in Ref. [33] are included for comparison (open circles).

near the interface, yielding

$$
\begin{aligned}
\Delta_0 &\approx \int_{z_0}^{\lambda_{\text{int}}} dz\, e^{-2ik_0 z} U_{\text{qw}}(z)\psi_{\text{env}}^2(z) \\
&\approx \frac{|\Delta E_c|\pi^2}{k_0^3 L_z^3}\left[e^{-2ik_0\lambda_{\text{int}}}\left(i + \frac{3}{4k_0\lambda_{\text{int}}} - \frac{\lambda_{\text{int}}k_0}{2} + z_0 k_0 - \frac{iz_0}{\lambda_{\text{int}}} - \frac{z_0^2 k_0}{2\lambda_{\text{int}}}\right)\right. \\
&\quad + \left.\begin{cases} \frac{i}{2}e^{-2ik_0 z_0} + \left(\frac{iz_0}{\lambda_{\text{int}}} + \frac{z_0^2 k_0}{2\lambda_{\text{int}}} - \frac{3}{4k_0\lambda_{\text{int}}}\right), & z_0 < 0 \\ e^{-2ik_0 z_0}\left(\frac{i}{2} - \frac{3}{4k_0\lambda_{\text{int}}} - \frac{iz_0}{2\lambda_{\text{int}}}\right), & z_0 \geq 0 \end{cases}\right].
\end{aligned}
\tag{D.33}
$$

Using z_0 and L_z defined above and taking $E_v = 2|\Delta_0|$ gives an analytical expression for the valley splitting, plotted as a green dashed line in Fig. 5.7(a). Again, this model captures the significant decay of Δ_0 for wide interfaces, although we find the continuum result lacks some of the structure captured by the discrete sum. This is due to the finite spacing between layers, as explained in Sec. 5.4.3.

D.5.2 Including alloy disorder

Here, we study the same variational system with linear interfaces as above, using it to derive a scaling law for the average valley splitting $\bar{E}_v$ in the presence of alloy disorder, due to the overlap of the wavefunction with Ge in wide quantum well interfaces. In the wide interface limit, we can restrict our analysis to $z_0 \geq 0$. As discussed in Section 5.4.3, the deterministic valley splitting Δ_0 is suppressed for wide interfaces, so we only need to consider the contributions due to alloy disorder, $\delta\Delta$. Using Eq. (5.13) for $\mathrm{Var}\,[\Delta]$ and approximating the discrete sum as an integral, we obtain

$$\mathrm{Var}\,[\Delta] \approx \frac{1}{\pi} \left[\frac{a_0^2 \Delta E_c}{8 a_{\mathrm{dot}}(1 - X_s)} \right]^2 \frac{4}{a_0} \int_{z_0}^{\lambda_{\mathrm{int}}} dz\, \psi_{\mathrm{env}}^4(z) \bar{X}(z) \left[1 - \bar{X}(z) \right]. \tag{D.34}$$

We can further simplify the calculation by approximating $\bar{X}(1 - \bar{X}) \approx 1 - \bar{X}$, for $\bar{X} \approx 1$. We then introduce the variational solution for the envelope function, Eq. (D.29), and again apply a linear approximation near the interface, yielding

$$\sigma_\Delta^2 = \mathrm{Var}\,[\Delta] \approx \frac{3}{160\pi} \frac{a_0^3 m_t \omega_{\mathrm{orb}} e^2 E_z^2}{(1 - X_s)\hbar} \lambda_{\mathrm{int}}. \tag{D.35}$$

We then finally obtain the result

$$\bar{E}_v \approx \sqrt{\pi \mathrm{Var}\,[\Delta]} = \frac{1}{4} \sqrt{\frac{3}{10}} \left[\frac{a_0^3 m_t \omega_{\mathrm{orb}} e^2 E_z^2}{(1 - X_s)\hbar} \lambda_{\mathrm{int}} \right]^{1/2}. \tag{D.36}$$

Equation (D.36) is plotted in gray in Fig. 5.7(b), giving good agreement with simulation data for smoothed linear interfaces. For perfectly linear interfaces, this formula is still valid and acts as a lower bound; however, Fourier components arising from the sharp corners raise $\bar{E}_v$ above this bound for the simulation results.

Algorithm 1 for optimizing Ge distributions, to maximize the valley splitting.

Require: An array (Y_l^{init}) of minimum Ge concentrations for each layer l
Require: A maximum amount of Ge (G_{max}) that can be added to the total heterostructure, in units of atoms/nm^2
Require: $\epsilon > 0$
  1: $Y^{\text{curr}} \leftarrow Y^{\text{init}}$
  2: **while** not converged **do**
  3:     Estimate grad_l
  4:     $Y_l^{\text{next}} \leftarrow \min\left[1, \max\left(Y_l^{\text{curr}} + \epsilon \cdot \text{grad}_l, Y_l^{\text{init}}\right)\right]$ ▷ Ensure that Y_l^{next} is a valid concentration
  5:     $\delta Y_l^{\text{next}} \leftarrow Y_l^{\text{next}} - Y_l^{\text{init}}$
  6:     $Y_l^{\text{next}} \leftarrow Y_l^{\text{init}} + \delta Y_l^{\text{next}} \times \min\left[1, \left(\frac{1}{2}(10^9 a_0)^2 G_{\text{max}} / \sum_l \delta Y_l^{\text{next}}\right)\right]$ ▷ Limit the additional Ge added to G_{max}
  7:     $Y_l^{\text{curr}} \leftarrow Y_l^{\text{next}}$
  8: **end while**

D.6   Simulations of narrow quantum wells

In this Appendix, we present additional simulations of the narrow wells considered in Sec. 5.5.2, justifying the parameter choices we made there. Figure D.6(a) illustrates how the choice of orbital energy affects the simulation results. Here we show the 10-90 percentile range for E_v, from 1,000 tight-binding simulations of a 3 nm quantum well with $\lambda_{\text{int}}^{\text{top}} = 3$ ML interfaces, for various orbital energy splittings $\hbar\omega_{\text{orb}}$, assuming an isotropic dot. Larger orbital energies lead to larger average valley splittings because they give smaller dots, for which the Ge concentration fluctuations are larger. According to Eq. (5.13), we expect the valley splitting in the disordered regime to scale as $\sqrt{\omega_{\text{orb}}}$. We find that using $\hbar\omega_{\text{orb}} = 1.5$ meV yields results consistent with the experimental data.

Figures D.6(b) and D.6(c) show how the choice of vertical electric field, interface width, and well width interact. Larger vertical fields have a larger impact on wide wells, where they strongly increase the penetration of the wavefunction into the top barrier. On the other hand, the wavefunction in narrower wells is already strongly confined, so increasing the field has a smaller effect. Figures D.6(b) and D.6(c) show the 10-90 percentile ranges of E_v, for quantum wells of width 3 nm and 8 nm, respectively, with various top interface widths $\lambda_{\text{int}}^{\text{top}}$

and vertical fields $E_z = 0$ and 5 mV/nm. We find that the field only modestly affects E_v in the 3 nm well, but a larger field significantly increases E_v in the 8 nm well. In particular, we find that the parameters $\lambda_{\text{int}}^{\text{top}} = $ 2-3 ML and $E_z = $ 5 mV/nm yield results consistent with the data.

Figures D.7(a) and D.7(b) illustrate the effect of steps on a narrow quantum well. In this case, we consider a 3 nm well with varying $\lambda_{\text{int}}^{\text{top}}$, and the electric fields (a) $E_z = 0$, or (b) $E_z = $ 5 mV/nm, where simulations were performed with and without a step through the center of the confinement potential. Results show that steps strongly affect the valley splitting for very narrow interfaces, but the effect of a step becomes weak for $\lambda_{\text{int}}^{\text{top}} \geq$ 3 ML. For the range of parameters simulated in Sec. 5.5.2, steps are found to have a modest impact on E_v. Nonetheless, we find that alloy disorder is capable of explaining the full range of E_v variations observed in the experimental data.

D.7 Optimizing the Ge distribution

In this Appendix, we provide details about the algorithm used in Sec. 5.5.5 to optimize Ge concentrations in the quantum well. The algorithm pseudocode is outlined in Algorithm 1. We begin with a realistic heterostructure profile Y_l^{init} [shaded in gray in Figs. 5.13(a) and 5.14(a)], and we allow the algorithm to only add Ge to this initial profile. We use an algorithm based on the method of projected gradient ascent. At each iteration, the gradient of the reward function with respect to the Ge concentration (grad_l) is computed for each layer l, and the corresponding Ge concentrations (Y_l) are adjusted by a small amount in the direction of the gradient. At each iteration, the resulting concentrations are then projected onto an acceptable parameter space as follows. First, we ensure that the Ge concentration is never reduced below its initial value: $Y_l^{\text{init}} \leq Y_l \leq 1$; this is accomplished by setting $Y_l = Y_l^{\text{init}}$ if Y_l is too small, or $Y_l = 1$ if Y_l is too large. Second, we ensure that the total Y_l never exceeds the maximum allowed density of additional Ge atoms, G_{max}, defined in units

of atoms/nm^2. This is accomplished by scaling the additional Ge added at each layer (δY_l) by a common factor:

$$\delta Y_l \leftarrow \delta Y_l \times \min\left[1, \left(\frac{1}{2}\frac{(10^9 a_0)^2\, G_{\max}}{\sum_l \delta Y_l}\right)\right]. \tag{D.37}$$

If less Ge is added than $G_{\max}$, this factor is equal to 1, and nothing is changed. However, if the added Ge is greater than $G_{\max}$, the added Ge at each layer is rescaled such that the density remains fixed at $G_{\max}$. [Note that the other factors appearing in Eq. (D.37) convert $G_{\max}$, in units of atoms/nm^2, to units consistent with $\sum_l \delta Y_l$.] Convergence is achieved when the change in the reward function is no longer positive, for a small enough step size.

When we optimize Y_l in the deterministic regime, as in Fig. 5.13, the tight-binding valley splitting is used as the reward function. Here, the gradient function is defined as $\mathrm{grad}_l = \delta E_v^{\delta l}/\delta Y$, and is estimated as follows. First, we compute E_v for the existing concentration profile. Then, separately for each layer l, we modify the concentration by a small amount, δY, and recompute the resulting valley splitting $E_v^{\delta l}$, which includes this change. The ratio $(E_v^{\delta l} - E_v)/\delta Y$ provides an estimate of the gradient for each layer. In this work we choose $\delta Y = 10^{-8}$, and we find the algorithm step factor $\epsilon = 10^{-3}$ to be effective for this protocol. (See Algorithm 1.)

When we optimize Y_l in the disordered regime, as in Fig. 5.14, $\mathrm{Var}\,[\Delta]$ is used as the reward function, as explained in the main text. We can re-express Eq. (5.13) in terms of Ge concentrations as follows:

$$\mathrm{Var}\,[\Delta] = \frac{1}{\pi}\left[\frac{a_0^2 \Delta E_c}{8 a_{\mathrm{dot}}(Y_s - Y_w)}\right]^2 \sum_l |\psi_l|^4 Y_l(1 - Y_l), \tag{D.38}$$

where Y_s is the Ge concentration in the barriers, Y_w is the Ge concentration in the quantum well before adding extra Ge (set to 0 in this case), Y_l is the Ge concentration at layer l, and ψ_l is the value of the envelope function at layer l. In this case, we again consider small layer-by-layer variations of $\mathrm{Var}[\Delta]$. We then define the gradient functions as $\mathrm{grad}_l = \delta \mathrm{Var}[\Delta]^{\delta l}/\delta Y$ and proceed as in the previous paragraph. In this case, we also find the algorithm step factor

$\epsilon = 10^3$ yields suitable results.

D.8 The truncated Wiggle Well

In this Appendix, we validate the performance of the truncated Wiggle Well, which was the learned outcome of our optimization algorithm in Section 5.5.5. To do this, we consider both normal and truncated Wiggle Wells, where the Ge concentration oscillations are given by Eqs. (5.25) and (5.26), respectively. The inset to Fig. D.8(a) schematically illustrates both types of wells. Figures D.8(b) and D.8(c) show the Fourier components of the weighted quantum well potential $|\tilde{U}_{\mathrm{qw}}|$, for the same average Ge concentration $A_w = 0.01$, as described in the main text. We see in Fig. D.8(b) that the truncated Wiggle Well has a Fourier peak at $k_z = 2k_0$, and that the truncation also introduces higher harmonics into the spectrum, including a large peak at $4k_0$. In the figure, the peak appears at lower k_z values due to an aliasing effect caused by the finite spacing between layers. By zone folding, the aliased $4k_0$ peak location is given by $8\pi/a_0 - 4k_0$. On the other hand, the normal Wiggle Well shown in Fig. D.8(c) has a peak at $k_z = 2k_0$ but no additional harmonics. As demonstrated in Fig. D.8(a), for a fixed average Ge concentration A_w, the truncated Wiggle Well produces larger E_v values than the normal Wiggle Well. The relation between the valley splittings for truncated (E_v^{tr}) vs. normal (E_v^w) Wiggle Wells is very well represented by the theoretical estimate given in the main text, $E_v^{\mathrm{tr}} = (\pi/2)E_v^w$, which is shown in Fig. D.8(a) as gray circles.
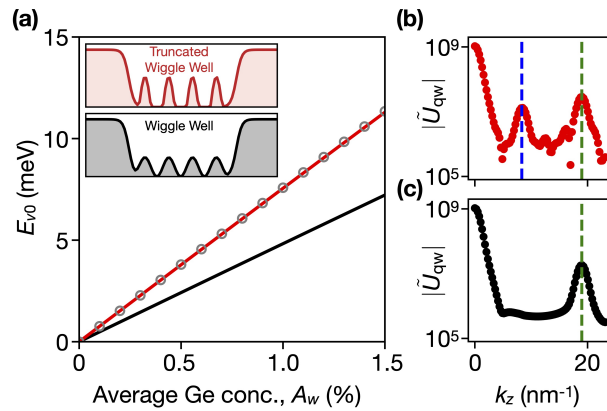
Figure D.8: For a fixed average Ge concentration in the quantum well A_w, the truncated Wiggle Well yields larger E_v than the normal Wiggle Well. (a) Deterministic valley splitting values E_{v0}, for normal (E_{v0}^w, black) and truncated (E_{v0}^{tr}, red) Wiggle Wells, plotted against the average Ge concentration in the quantum well, A_w. The theoretical estimate $E_{v0}^{tr} = (\pi/2)E_{v0}^w$ is also shown with gray circles. Inset: schematic illustrations of the truncated (red) and normal (black) Wiggle Wells. (b), (c) The weighted Fourier transforms of the weighted quantum well potentials $|\tilde{U}_{qw}|$ for (b) truncated and (c) normal Wiggle Wells, for the Ge concentrations $A_w = 0.01$. Vertical green dashed lines in (b) and (c) highlight the wavevector $k_z = 2k_0$, and the vertical blue dashed line in (b) highlights the wavevector $k_z = 4k_0$, aliased down to a lower value by the discrete lattice spacing. All simulations are performed with a vertical electric field of $E_z = 5$ mV/nm, a quantum well width of $W = 80$ ML, a sigmoidal interface of width $\lambda_{int} = 10$ ML, and Ge barrier concentration of $Y_s = 0.3$.

Appendix E

Supplementary Information for

Chapter 6

E.1 Additional analysis of the qubit Hamiltonian

In this Appendix, we include some further analysis of the qubit Hamiltonian. Starting with the Hamiltonian of Eq. 6.2, we discard the spin terms, since $g\mu_B B \ll |\Delta|, t_c$ and they can be treated as perturbations. The remaining valley-orbit Hamiltonian is given by

$$H_{\mathrm{vo}} = \begin{pmatrix} |\Delta_L| + \frac{\varepsilon}{2} & 0 & t_{++} & t_{+-} \\ 0 & -|\Delta_L| + \frac{\varepsilon}{2} & t_{-+} & t_{--} \\ t_{++}^* & t_{-+}^* & |\Delta_R| - \frac{\varepsilon}{2} & 0 \\ t_{+-}^* & t_{--}^* & 0 & -|\Delta_R| - \frac{\varepsilon}{2} \end{pmatrix} \tag{E.1}$$

in the basis $\{|L, +\rangle, |L, -\rangle, |R, +\rangle, |R, -\rangle\}$, where the t_{ij} are defined in the main text. The general solutions of H_{vo} involve fourth-order polynomials, but we can simplify the problem

in the limit where $\delta\phi = 0$. In this case, $t_{++} = t_{--} = t_c$ and $t_{-+} = t_{+-} = 0$, and

$$H_{\text{vo}}^{\delta\phi=0} = \begin{pmatrix} |\Delta_L| + \frac{\varepsilon}{2} & 0 & t_c & 0 \\ 0 & -|\Delta_L| + \frac{\varepsilon}{2} & 0 & t_c \\ t_c & 0 & |\Delta_R| - \frac{\varepsilon}{2} & 0 \\ 0 & t_c & 0 & -|\Delta_R| - \frac{\varepsilon}{2} \end{pmatrix} \tag{E.2}$$

In this regime, we can obtain simple expressions for the eigenvalues of the system:

$$\begin{aligned} E_0 &= \frac{1}{2}\left(-\Delta_+ - \sqrt{(\varepsilon - \Delta_-)^2 + 4t_c^2}\right) \\ E_1 &= \frac{1}{2}\left(\Delta_+ - \sqrt{(\varepsilon + \Delta_-)^2 + 4t_c^2}\right) \\ E_2 &= \frac{1}{2}\left(-\Delta_+ + \sqrt{(\varepsilon - \Delta_-)^2 + 4t_c^2}\right) \\ E_3 &= \frac{1}{2}\left(\Delta_+ - \sqrt{(\varepsilon + \Delta_-)^2 + 4t_c^2}\right) \end{aligned} \tag{E.3}$$

where $\Delta_\pm = |\Delta_L| \pm |\Delta_R|$. The corresponding (un-normalized) eigenstates are

$$\begin{aligned} |v_0\rangle &= \begin{pmatrix} 0 & \frac{1}{2t_c}\left(-\Delta_- + \varepsilon - \sqrt{(\varepsilon - \Delta_-)^2 + 4t_c)^2}\right) & 0 & 1 \end{pmatrix}^T \\ |v_1\rangle &= \begin{pmatrix} \frac{1}{2t_c}\left(\Delta_- + \varepsilon - \sqrt{(\varepsilon + \Delta_-)^2 + 4t_c)^2}\right) & 0 & 1 & 0 \end{pmatrix}^T \\ |v_2\rangle &= \begin{pmatrix} 0 & \frac{1}{2t_c}\left(-\Delta_- + \varepsilon + \sqrt{(\varepsilon - \Delta_-)^2 + 4t_c)^2}\right) & 0 & 1 \end{pmatrix}^T \\ |v_3\rangle &= \begin{pmatrix} \frac{1}{2t_c}\left(\Delta_- + \varepsilon + \sqrt{(\varepsilon + \Delta_-)^2 + 4t_c)^2}\right) & 0 & 1 & 0 \end{pmatrix}^T \end{aligned} \tag{E.4}$$

From these eigenstates, can compute $\langle\tau_z\rangle_\epsilon$:

$$\langle\tau_z\rangle_\epsilon = \frac{\langle v_0|\tau_z|v_0\rangle}{\langle v_0|v_0\rangle} = \frac{\Delta_- - \varepsilon}{\sqrt{(\varepsilon - \Delta_-)^2 + 4t_c^2)}}. \tag{E.5}$$

The results for Eq. (E.5) are included in Fig. 6.5(b) in the main text.

We can also extract limits on charge excitations in the $\delta\phi = 0$ limit. We define R_0 as the unitary that diagonalizes $H_{\text{vo}}^{\delta\phi=0}$, whose rows are given by $\langle v_i|$ in Eq. (E.4). Since ε

is a function of time, the transformation R_0 is also time-dependent, and the transformed Hamiltonian can be computed as

$$H'_{\delta\phi=0} = R_0 H^{\delta\phi=0}_{\text{vo}} R_0^\dagger - i\hbar R_0 \dot{R}_0^\dagger, \tag{E.6}$$

resulting in

$$H'_{\delta\phi=0} = \begin{pmatrix} E_0 & 0 & \frac{i\hbar t_c \dot{\epsilon}}{(\varepsilon-\Delta_-)^2+4t_c^2} & 0 \\ 0 & E_1 & 0 & \frac{i\hbar t_c \dot{\epsilon}}{(\varepsilon+\Delta_-)^2+4t_c^2} \\ \frac{-i\hbar t_c \dot{\epsilon}}{(\varepsilon-\Delta_-)^2+4t_c^2} & 0 & E_2 & 0 \\ 0 & \frac{-i\hbar t_c \dot{\epsilon}}{(\varepsilon+\Delta_-)^2+4t_c^2} & 0 & E_3 \end{pmatrix} \tag{E.7}$$

where now the Hamiltonian is expressed in the basis of instantaneous eigenstates, and the E_j are the eigenvalues given in Eq. (E.3). Thus, the regime in which we can ignore orbital excitations is given by $\dot{\varepsilon} \ll ((\varepsilon\pm\Delta_-)^2+4t_c^2)/\hbar$. Of course, in most scenarios, valley excitations will create a much tighter limit on $\dot{\varepsilon}$.

Finally, we can also extract approximate expressions for the rate of valley excitation in this system in certain limits. Namely, if $|\Delta_{L(R)}| \ll t_c$, then the valley terms in Eq. (6.1) can also be treated perturbatively. In this limit, we can diagonalize the orbital Hamiltonian through the rotation $R_{\text{orb}} = \exp\left[\frac{i}{2}\arctan\left(\frac{2t_c}{\varepsilon}\right)\tau_y\right]$. Starting with Eq. (6.1), dropping the valley and spin terms as perturbations, and performing $H'_{\text{orb}} = R_{\text{orb}} H R_{\text{orb}}^\dagger - i\hbar R_{\text{orb}} \dot{R}_{\text{orb}}^\dagger$, we obtain

$$H'_{\text{orb}} = \sqrt{\varepsilon^2 + 4t_c^2}\,\tilde{\tau}_z + \frac{\hbar t_c \dot{\varepsilon}}{4t_c^2 + \varepsilon^2}\tilde{\tau}_y \tag{E.8}$$

where $\tilde{\tau}_j$ are the Pauli matrices in the transformed basis. Now, we assume evolution is adiabatic with respect to orbital levels, so we remain within the $\langle\tilde{\tau}_z\rangle = -1$ subspace, and we can replace $\tilde{\tau}_z \to -1$ and remove the term proportional to $\tilde{\tau}_y$. Now, we add the valleys as a

perturbation, resulting in the Hamiltonian

$$
\begin{aligned}
H'_{|\Delta|\ll t_c} = & -\sqrt{\varepsilon^2 + 4t_c^2} \\
& + \frac{1 + \langle\tau_z\rangle_\varepsilon}{2}|\Delta_L|(\gamma_x \cos\phi_L - \gamma_y \sin\phi_L) \\
& + \frac{1 - \langle\tau_z\rangle_\varepsilon}{2}|\Delta_R|(\gamma_x \cos\phi_R - \gamma_y \sin\phi_R) \\
& := V_x(t)\gamma_x + V_y(t)\gamma_y
\end{aligned}
\tag{E.9}
$$

In this regime, we can use Eq. (E.5) for $\langle\tau_z\rangle_\varepsilon$, setting $\Delta_- = 0$. Now, we diagonalize the valley space with the rotation

$$
R_v = e^{-i\frac{\pi}{4}\gamma_y}e^{\frac{i}{2}\arctan\left[\frac{V_y(t)}{V_x(t)}\right]\gamma_z}
\tag{E.10}
$$

resulting in another transformed Hamiltonian $H''_{|\Delta|\ll t_c} = R_v H'_{|\Delta|\ll t_c} R_v^\dagger - i\hbar R_v \dot{R}_v^\dagger$, where

$$
H''_{|\Delta|\ll t_c} = -\sqrt{\varepsilon^2 + 4t_c^2} + \sqrt{V_x(t)^2 + V_y(t)^2}\tilde{\gamma}_z + S\tilde{\gamma}_x
\tag{E.11}
$$

where $\tilde{\gamma}_j$ are the Pauli matrices in the rotated valley space, and

$$
S = \frac{V_x(t)V'_y(t) - V_y(t)V'_x(t)}{2(V_x(t)^2 + V_y(t)^2)}
\tag{E.12}
$$

Solving for S, we obtain

$$
S = \frac{-\hbar|\Delta_L||\Delta_R|\sin(\phi_L - \phi_R)\frac{d\langle\tau_z\rangle_\varepsilon}{dt}}{|\Delta_+|^2 + 2(|\Delta_L|^2 - |\Delta_R|^2)\langle\tau_z\rangle_\varepsilon + |\Delta_-|^2\langle\tau_z\rangle_\varepsilon^2}
\tag{E.13}
$$

Equation (E.13) can be used to place approximate limits on the driving strength $d\langle\tau_z\rangle_\varepsilon/dt$ to avoid valley excitations, which can in turn place limits on $\dot{\varepsilon}$.
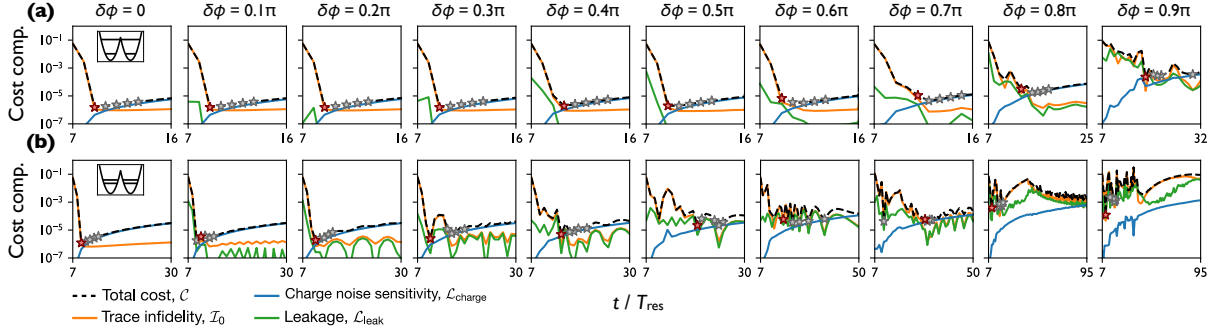
Figure E.1: Here, we illustrate the behavior of the three components to our cost function, $\mathcal{C}$, across a variety of valley configurations. We show results for the cosine pulse family, assuming an optimistic charge noise regime, $\sigma_\varepsilon = 1$ µeV. Each individual plot represents the cost landscape for a particular valley configuration: in the top row (a), we use $E_{vL} = E_{vR} = 50$ µeV, and in the bottom row (b) we use $E_{vL} = E_{vR} = 20$ µeV. Each column represents a value of $\delta\phi$, which we vary from 0 to 0.9π. The stars indicate the five pulses that minimized the total cost, and the red star indicates the pulse ultimately selected by the algorithm.

E.2   Pulse optimization algorithm

In this Appendix, we provide additional details on our pulse-optimization algorithm outlined in Sec. 6.3. First, we provide details on the quantities $\mathcal{L}_{\text{charge}}$ and $\mathcal{L}_{\text{leakage}}$, used in our heuristic cost function Eq. (6.13).

E.2.1   Computing $\mathcal{L}_{\text{charge}}$

As described in Sec. 6.3 in the main text, to develop high-fidelity pulses, we want to estimate the pulse sensitivity to charge noise. To do so, we utilize a formalism based on a general 2-level Hamiltonian [32, 74]

$$H = H_c + \delta H \tag{E.14}$$

where H_c is the desired (time-dependent) control Hamiltonian, and the leakage term

$$\delta H = \chi_x(t)\sigma_x + \chi_z(t)\sigma_z \tag{E.15}$$

where $\chi_j(t)$ are time-dependent noise amplitudes. For weak noise, the propagator associated with error can be solved from the first order Magnus expansion

$$U_{\mathrm{err}} = \exp\left(-\frac{i}{\hbar}\sum_j \mathcal{E}_j(T)\right) \tag{E.16}$$

where

$$\mathcal{E}_j(T) = \int_0^T dt\, U_c^\dagger(t)\,[\chi_j(t)\sigma_j]\,U_c(t). \tag{E.17}$$

and $U_c(t)$ is the propagator associated with H_c. The noise sensitivity of the logical subspace to σ_j errors can be estimated by

$$N_j = \frac{1}{2}||\mathcal{E}_j(T) - \mathrm{tr}[\mathcal{E}_j(T)/2]||^2 \tag{E.18}$$

where $\mathcal{E}_j$ represents the characteristic strength of the noise amplitude χ_j [74].

Now, we apply the above formalism to estimate the impact of charge noise in our flopping mode qubits. For computational efficiency, we reduce the full 8-level Hamiltonian to an effective 2-level system, following Eq. (6.5). We note that, while this effective Hamiltonian does not exactly describe the spin dynamics of the system, it is good enough to estimate charge-noise sensitivity. However, to compute the true gate fidelity $\mathcal{I}_0$, we retain the full 8-level system; see Sec. 6.3.

Given a quasistatic fluctuation in the detuning, $\delta\varepsilon$, there is a resulting fluctuation in $\langle\tau_z\rangle$, which produces the effective noise Hamiltonian

$$\delta H_{\mathrm{eff}} = \frac{\delta\langle\tau_z\rangle}{2}\left(\delta E_x\sigma_x + \delta E_z\sigma_z\right). \tag{E.19}$$

where $\delta E_{x(z)} = g\mu_B\Delta B_{x(z)}$. We can approximate

$$\delta\langle\tau_z\rangle \approx \delta\varepsilon\frac{d\langle\tau_z\rangle}{d\varepsilon}, \tag{E.20}$$

where the derivative $\frac{d\langle\tau_z\rangle}{d\varepsilon}$ is evaluated numerically from the 8-level Hamiltonian, and $\delta\varepsilon$ is the approximate size of a detuning fluctuation. In our optimization algorithm, we use $\delta\varepsilon = \sigma_\varepsilon$. If we associate the noise amplitudes of Eq. (E.15) with our spin system, we have

$$\chi_x^{\text{spin}}(t) = \frac{\delta\varepsilon}{2} \frac{d\langle\tau_z\rangle}{d\varepsilon} \delta E_x \tag{E.21}$$

$$\chi_z^{\text{spin}}(t) = \frac{\delta\varepsilon}{2} \frac{d\langle\tau_z\rangle}{d\varepsilon} \delta E_z. \tag{E.22}$$

We can obtain the resulting noise sensitivity by using the approximate noise amplitudes of Eq. (E.21) in the above noise-sensitivity estimation. So, in our cost function, we include

$$\mathcal{L}_{\text{charge}} = \frac{1}{2} \left[N_x(T) + N_z(T) \right]. \tag{E.23}$$

To estimate the error propagator U_{err}, we time-evolve the 2-level effective noise Hamiltonian of Eq. (E.19).

E.2.2 Computing $\mathcal{L}_{\text{leak}}$

While we restrict ourselves to the 2-level spin subspace to approximate the gate sensitivity to charge noise, we need to consider leakage out of this subspace while performing gate operations. To do so, at each step, we simulate the evolution of the full 8-level system from $t = 0$ to $t = T \coloneqq nT_{\text{res}}$ under the Schrodinger equation, including a quasistatic detuning fluctuation, using Eq. (6.15). For a given propagator, we can estimate the leakage outside of the ground state subspace by computing the quantity

$$L_{\delta\varepsilon} = \frac{1}{2} \sum_{n=2}^{7} \left(|\langle n|U_{\delta\varepsilon}|0\rangle|^2 + |\langle n|U_{\delta\varepsilon}|1\rangle|^2 \right) \tag{E.24}$$

where $\{|n\rangle\}_{n=0}^{7}$ are the 8 eigenstates of the system at $t = T$. Finally, we obtain $\mathcal{L}_{\text{leak}}$ by averaging $L_{\delta\varepsilon}$ over 9 simulations using uniformly spaced $\delta\varepsilon$ between $-2\sigma_\varepsilon$ and $2\sigma_\varepsilon$, each weighted by the normal distribution $N(0, \sigma_\varepsilon)$. Finally, we obtain $\mathcal{L}_{\text{leak}}$ by averaging $L_{\delta\varepsilon}$ over

9 uniformly spaced detuning fluctuations $\delta\varepsilon$, between $-2\sigma_\varepsilon$ and $2\sigma_\varepsilon$, each weighted by the normal distribution $N(0, \sigma_\varepsilon)$.

E.2.3 Comparison of cost components

In Fig. E.1, we plot the components of the total cost $\mathcal{C}$ for a variety of valley configurations. Here, we show results for the cosine pulse family, assuming an optimistic $\sigma_\varepsilon = 1$ µeV. In Fig. E.1(a), we assume $E_{vL} = E_{vR} = 100$ µeV, and in (b) we assume $E_{vL} = E_{vR} = 20$ µeV. Each column represents a different valley phase difference $\delta\phi$, which we vary from 0 to 0.9π. We see that, for most configurations, the infidelity $\mathcal{I}_0$ and leakage $\mathcal{L}_{\text{leak}}$ fall as pulse time increases, while the charge noise sensitivity $\mathcal{I}_{\text{charge}}$ grows. For very short pulses, $\mathcal{I}_0$ and $\mathcal{L}_{\text{leak}}$ dominate $\mathcal{C}$, while for longer pulses, $\mathcal{L}_{\text{charge}}$ dominates $\mathcal{C}$. This results in a minimum $\mathcal{C}$ for some optimial pulse length. For each configuration, the five pulses that minimze $\mathcal{C}$ are marked with a star, and the red star indicates the pulse ultimately selected by our algorithm. These are the five pulses that enter the next stage of randomization and re-optimization, described in the following section. We also note that the loss landscape is significantly complicated for large $\delta\phi$, especially for small E_v. In this regime, the optimal $\mathcal{C}$ is sometimes much larger, and, in the very worst cases, realized at short pulse lengths. We comment on this more in App. E.3.

E.2.4 Randomization and re-optimization

As described in the main text, after optimizing the pulse parameters and computing $\mathcal{C}$ for a range of total pulse lengths, we select the five best-performing pulses, and we randomize and re-optimize the pulse parameters for these pulses, to help avoid local minima. We represent the pulse parameters as a vector p. We convert this vector to the pulse parameters according to the following prescriptions. For the rectangular pulse family, the amplitude is $A = \varepsilon_{\text{max}}|\sin(p_0)|$, the offset is $C = |\varepsilon_{\text{max}} - A|\sin(p_1)$, the steepness $R = R_{\text{max}}|\sin(p_2)|$, and the duty cycle coefficient $c_{\text{dc}} = |\sin(p_3)|$. We use the same amplitude and offset definitions

for the cosine pulse. For the charge-cosine pulse, the amplitude $A = \langle \tau_z \rangle_{\max} |\sin(p_0)|$ and the offset $C = |\langle \tau_z \rangle_{\max} - A| \sin(p_1)$, where $\langle \tau_z \rangle_{\max}$ is the maximum achievable $\langle \tau_z \rangle_\varepsilon$ for $|\varepsilon| \leq \varepsilon_{\max}$. To randomize and re-optimize a pulse, we take the p obtained by the first optimization iteration, and we add a uniform random value between ± 0.1 to each p_n. This randomized p serves as the initial condition for the next round of optimization.

E.2.5 Additional details

To perform our pulse optimization and simulation, we use the Julia programming language [17]. Optimizations are performed with the Nelder-Mead method [137]. We select initial conditions such that the optimized pulse performs a single rotation from $\theta = 0$ to π, and not multiple rotations. Data analysis, plotting, and other computations are performed in the Python programming language, including the libraries NumPy [77], SciPy [197], and Matplotlib [85].

E.3 Optimized pulses in unfavorable valley configurations

In this Appendix, we provide further analysis of the optimized pulses in unfavorable valley conditions. In Fig. E.2, for both the charge-cosine (a-b) and rectangular (c-d) pulse families, we plot the average infidelity due to detuning fluctuations ($\mathcal{I}_{\text{ave}}$) as a function of valley phase difference $\delta\phi$, for valley configurations $E_{vL} = 100$, $E_{vR} = 20$ μeV (light gray), $E_{vL} = 20$, $E_{vR} = 100$ μeV (dark gray), and $E_{vL} = E_{vR} = 20$ μeV (black). This is the same data as in the main text Fig. 6.3, for the charge-cosine and rectangular pulse families. Qualitatively, all pulse families behave similarly. Worse valley configurations lead to worse fidelities, and larger $\delta\phi$ lead to worse fidelities and longer pulses. We understand this as a leakage-noise tradeoff, as discussed in the main text.

We note that, in the very worst cases, such as $E_{vL} = E_{vR} = 20$ μeV and $\delta\phi = 0.9\pi$, the
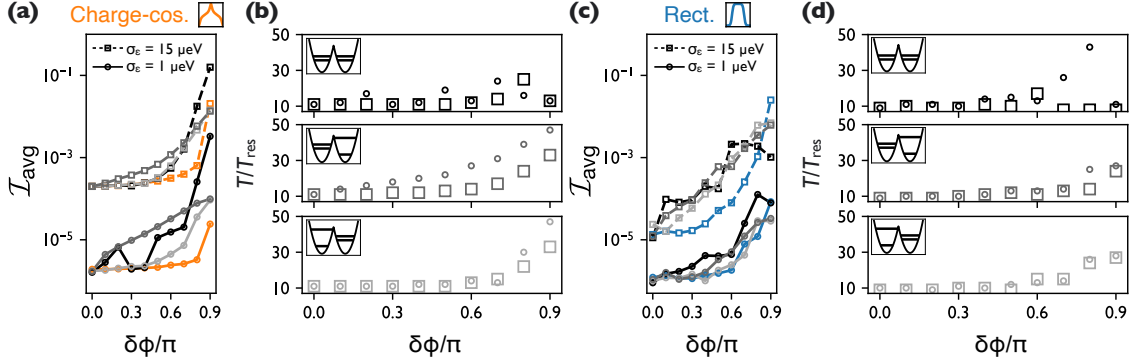
Figure E.2: For completeness, we include the same data as shown in Fig. 6.3 of the main text, for the charge-cosine pulse family (a)-(b) and the rectangular pulse family (c)-(d). (a) Expected qubit infidelities due to charge noise computed with Eq. (6.16), as we vary $\delta\phi$ from 0 to 0.9π, for valley splittings $E_{vL} = E_{vR} = 100$ µeV [orange; same data as in Fig. 6.2(a)], $E_{vL} = 100$ µeV and $E_{vR} = 20$ µeV [light gray lines], $E_{vL} = 20$ µeV and $E_{vR} = 100$ µeV [dark gray lines], and $E_{vL} = E_{vR} = 20$ µeV [black lines]. We include data for both the optimistic (circles) and pessimistic (squares) charge noise regimes. (b) The total pulse times, for each of the pulses illustrated in (a). (c)-(d) The same data as in (a) and (b), for the rectangular pulse family.

optimized pulses are much shorter, as we see in Fig. 6.3(b) and Fig. E.2(b) and (d). This may be due to a number of effects. First, the presence of strong valley interference may make it too difficult for the algorithm to find cost minima for long pulses, since valley interference patterns are sensitive to even small changes in pulse parameters.

Second, shorter pulses with fewer pulse oscillations may actually be less sensitive overall to detuning fluctuations in this regime. In these very unfavorable valley configurations, valley excitations are nearly unavoidable. For example, in Fig. E.3, we analyze the cosine pulse family, assuming the unfavorable valley configuration described above, under pessimistic charge noise $\sigma_\varepsilon = 15$ µeV. Assuming our qubit starts in the ground state, we plot the wavefunction weight in the first two excited valley eigenstates $W_{\mathrm{val}} = W_2 + W_3$, where W_n are defined in the main text. We analyze all five of the total pulse lengths that yielded the lowest overall cost $\mathcal{C}$, ranging from 8 to 19 resonant periods. (The shortest pulse, shown in (a) for $T = 8T_{\mathrm{res}}$, is the pulse selected by our algorithm and marked with a red star.) First, we plot the excited valley weight assuming zero detuning fluctuations, $\delta\varepsilon = 0$ (red solid lines). We observe that, for all pulses regardless of length, the excited valleys are
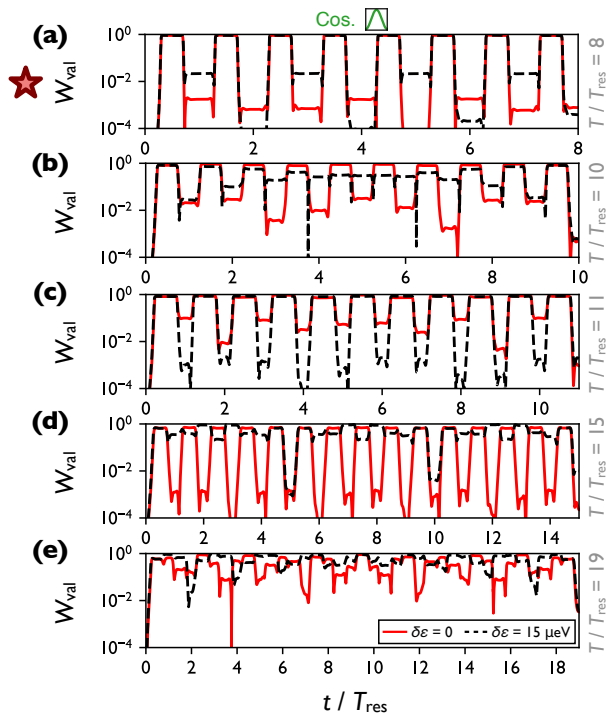
Figure E.3: In very unfavorable valley conditions, complicated patterns of valley interference emerge. We plot the fraction of the wavefunction weight in the first excited valley eigenstates, W_{val} as defined in Appendix E.3, for optimized pulses from the cosine family, at each of the five total pulse lengths that best minimized the total cost $\mathcal{C}$. The pulse plotted in (a), for $T = 8T_{res}$, was the pulse ultimately selected by our algorithm and marked with a red star. For each of the five cases, we plot the excited valley weight assuming zero detuning fluctuations, $\delta\varepsilon = 0$ (red solid lines), and a detuning fluctuation $\delta\varepsilon = 15$ μeV (black dashed lines).

populated with weight near unity for a significant fraction of the pulse duration. Moreover, as the pulses get longer, more complicated patterns of valley interference emerge, which the pulse optimization algorithm must account for. This picture is further complicated by the presence of detuning fluctuations. In Fig. E.3, we also plot the excited valley weight assuming a quasistatic detuning fluctuation $\delta\varepsilon = 15$ μeV (black dashed lines). We note that the valley interference pattern changes dramatically, compared with the $\delta\varepsilon = 0$ case. Moreover, the changes in interference patterns are potentially more dramatic in the longer pulses, since any small change in valley interference is compounded over the longer pulse duration. Thus, in such unfavorable valley configurations, shorter pulses may have more controllable valley interference patterns. Of course, for very long and very weak pulses, we expect valley leakage to eventually die away. But, at this point, charge noise will dominate the infidelity, resulting in worse pulses overall.

E.4 Heterostructure parameters

Here, we elaborate on the parameters of the heterostructures we consider in the main text. Following Ref. 119, we define the expected Si concentration at position z according to the following function:

$$\bar{X}_l = X_w + \frac{X_s - X_w}{1 - \exp[(z - z_t)/\tau]} + \frac{X_s - X_w}{1 - \exp[(z_b - z)/\tau]} \tag{E.25}$$

where $z_{t(b)}$ mark the position of the top (bottom) QW interface, and $\lambda = 4\tau$ is the characteristic interface width. We use interface width $\lambda = 1$ nm and well width $|z_t - z_b| = 10$ nm in this work. In cases where the minimum Ge concentration $G_{\min} = 1 - X_w > 0$, we set $X_s = X_w - 0.3$, maintaining a 30% Ge concentration difference between the barrier and quantum well regions.

E.5 Effective mass simulations

In this work, we use both 1D and 3D effective mass simulations. We use the 1D simulations to calculate σ_Δ (and therefore the average valley splitting) for the heterostructures considered in this work. In Appendices E.6 and E.7, we use 3D effective mass simulations to model the orbital energy of a single dot and the tunnel coupling in a double dot, respectively. In this Appendix, we outline these effective mass simulations.

E.5.1 1D simulations

To obtain σ_Δ for a given heterostructure according to Eq. (6.7), we need to compute the envelope function ψ_{env}. To do so, a 1D effective mass model suffices. We solve the 1D effective mass Hamiltonian

$$H_{\text{EM}}^{\text{1D}} = T_{1D} + U_\phi + U_{\text{qw}} \tag{E.26}$$

where T_{1D} is a discretized 1D kinetic energy operator, $U_\phi = eE_z z$ is the potential due to a vertial electric field E_z, and U_{qw} is the quantum well potential. We assume $E_z = 5\,\text{meV}\,\text{nm}^{-1}$. The quantum well potential at position $\mathbf{r}$ is given by

$$U_{\text{qw}}(\mathbf{r}) = \frac{X(\mathbf{r}) - X_s}{X_w - X_s} \Delta E_c \tag{E.27}$$

where $X(\mathbf{r})$ is the Si concentration at position $\mathbf{r}$. In the 1D model, we can replace $\mathbf{r} \to z_l$, where l is the layer index, and we use Eq. (E.25) to define the Si concentration profile. Following Refs. [119, 145], the conduction band offset is given by

$$\Delta E_c = (X_w - X_s) \left[\frac{X_w}{1 - X_s} \Delta E_{\Delta_2}^{\text{Si}}(X_s) - \frac{1 - X_w}{X_s} \Delta E_{\Delta_2}^{\text{Ge}}(X_s) \right] \tag{E.28}$$

where $\Delta E_{\Delta_2}^{\text{Si}(Ge)}$ are the Δ_2 conduction band offsets for strained Si (Ge) grown on unstrained $\text{Si}_X\text{Ge}_{1-X}$ substrate [164], approximated as

$$\begin{aligned}
\Delta E_{\Delta_2}^{\text{Si}}(X) &= -0.502(1 - X) \text{ (eV)} \\
\Delta E_{\Delta_2}^{\text{Ge}}(X) &= 0.743 - 0.625(1 - X) \text{ (eV)}
\end{aligned} \tag{E.29}$$

By diagonalizing Eq. (E.26), we obtain the envelope function and can compute σ_Δ, whose values are reported in the main text. We note that, to compute ψ_{env}, we use the virtual crystal approximation and do not include random alloy disorder in the quantum well potential. In this computation, unless otherwise specified, we assume the lateral confinement potential is parabolic and isotropic with characteristic level spacing $\hbar\omega_{\text{orb}} = 2$ meV.

E.5.2   3D simulations

We also employ 3D effective mass simulations to describe the orbital energy and tunnel coupling fluctuations due to alloy disorder. We note that these simulations contain no valley physics, since their purpose is only to describe the orbital energies of the system. Following the methods of Ref. 119, we use a coarse-grained model of the Si/SiGe heterostructure in three dimensions. We discretize the heterostructure into cells of size $(\Delta x, \Delta y, \Delta z) = (a_0, a_0, a_0/4)$, where $a_0 = 0.543$ nm is the Si lattice constant. In this model, each cell contains exactly two Si/Ge atoms. On this discretized lattice, we solve the following effective-mass Hamiltonian:

$$H_{\text{EM}}^{3D} = T_{3D} + U_{\text{conf}} + U_\phi + U_{\text{qw}}, \tag{E.30}$$

where T_{3D} is the discretized 3D kinetic energy operator and U_{qw} is the quantum well potential, given in Eq. (E.27). The lateral confinement potential U_{conf} depends on whether we consider a single or a double-dot system. For example, for a single quantum dot, we use the confinement potential

$$U_{\text{conf}}^{\text{sd}} = \frac{1}{2} m_t \omega_{\text{orb}}^2 \left((x - x_0)^2 + y^2 \right), \tag{E.31}$$

where the dot is centered at $(x_0, 0)$. Again, unless otherwise specified, we consider single-dot unperturbed orbital splittings $\hbar\omega_{\mathrm{orb}} = 2$ meV, and vertical fields $E_z = 5$ mV nm^{-1}. We elaborate on the double-dot system in Appendix E.7.

The quantum well potential is given by Eq. (E.27), where we define $X(x_j, y_k, z_l) \coloneqq X_{j,k,l}$ as the Si concentration of a cell at $\mathbf{r} = (x_j, y_k, z_l)$, labeled with indices (j, k, l). In a system with alloy disorder, the atoms in any given cell will be randomly assigned as Si or Ge, where the probability of choosing a Si atom is given by the average (or expected) Si concentration at the position of the cell. To separate the effects of alloy disorder from those intrinsic to the shape of the interface, we decompose U_{qw} into two components, one due to the average Si concentrations in a given cell ($\bar{U}_{\mathrm{qw}}$), and one due to the random fluctuations of the Si concentration in a given cell due to random alloy disorder ($U_{\mathrm{qw}}^{\mathrm{dis}}$). Hence, $U_{\mathrm{qw}} = \bar{U}_{\mathrm{qw}} + U_{\mathrm{qw}}^{\mathrm{dis}}$, where

$$
\begin{aligned}
\bar{U}_{\mathrm{qw}}(x_j, y_k, z_l) &= \frac{\bar{X}_{j,k,l} - X_s}{X_w - X_s} \Delta E_c \\
U_{\mathrm{qw}}^{\mathrm{dis}}(x_j, y_k, z_l) &= \frac{\delta X_{j,k,l} - X_s}{X_w - X_s} \Delta E_c
\end{aligned}
\tag{E.32}
$$

where $\bar{X}_{j,k,l}$ is the expected Si concentration in a cell, and $\delta X_{j,k,l} = X_{j,k,l} - \bar{X}_{j,k,l}$ is the difference between the actual and expected Si concentrations in a cell.

We model the top and bottom quantum well interfaces as smooth sigmoid functions. Without interface steps, the expected Si concentration at layer l, $\bar{X}_l$, is give by Eq. (E.25). With an interface step, we model the expected Si concentration for a cell at (x_j, y_k, z_l) as

$$
\bar{X}_{j,k,l} = \bar{X}_l \Theta(x_j \geq x_{\mathrm{step}}) + \bar{X}_{l+1} \Theta(x < x_{\mathrm{step}})
\tag{E.33}
$$

where $\bar{X}_l$ is given by Eq. (E.25), x_{step} is the lateral position of the interface step, and $\Theta(\cdot)$ is the Heaviside step function. Here, we consider a step oriented along the $\hat{y}$ direction.

Finally, in Appendices E.6 and E.7, we consider systems both with and without alloy disorder. To model a system without alloy disorder, we use the virtual crystal approxima-
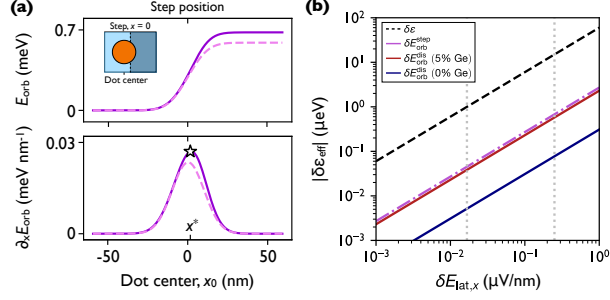
Figure E.4: Comparison of effective detuning fluctuations due to the direct effects of fluctuating lateral fields and indirect effects due to alloy disorder and interface steps. (a) The orbital energy of a single dot, centered at x_0, as it moves across a single interface step at $x_{\text{step}} = 0$, simulated with a 3D effective mass model using the virtual crystal approximation (solid line), and the results for the same system computed with first-order perturbation theory (dashed line) [see Appendix E.6]. (b) The gradient of the orbital energy with respect to the dot center, $\partial_{x_0} E_{\text{orb}}$, for the same system as in (a), again computed with 3D effective mass simulations (solid line) and perturbation theory (dashed line). (c) For a lateral field fluctuation along the $\hat{x}$ direction, we plot the resulting direct detuning fluctuations for the double dot (black dashed line), as well as the indirect effective detuning fluctuations due to alloy disorder, for both conventional (blue) and 5% Ge QWs (red), and step disorder (pink dot-dashed line).

tion, setting $U_{\text{qw}}^{\text{dis}} = 0$. In systems with alloy disorder, we populate each cell with exactly two atoms. The probability each atom in a cell is Si is given by $\bar{X}_{i,j,k}$, the expected Si concentration at that cell. The resulting Si concentration in the cell defines $X_{i,j,k}$, as used in Eq. (E.27).

E.6   Orbital energy fluctuations

In this section, we elaborate on how fluctuations to the ground state orbital energy due to local disorder affect flopping mode qubit fidelities. In the presence of a quasistatic lateral field fluctuation $\delta\mathbf{E}_{\text{lat}} = \delta E_{\text{lat},x}\hat{x} + \delta E_{\text{lat},y}\hat{y}$, there is a corresponding fluctuation in the inter-dot detuning, $\delta\varepsilon = ed\delta E_{\text{lat},x}$, where d is the inter-dot spacing, and we have assumed the detuning axis of the double dot system is along $\hat{x}$. Here, we assume an inter-dot spacing $d = 60$ nm (see Appendix E.7). In Fig. E.4(b), we plot this detuning fluctuation as a function of $\delta E_{\text{lat},x}$ (black dashed line). However, this detuning fluctuation is not the only possible effect. In

the presence of fluctuating lateral fields, the center of a dot is shifted by a small amount δx, as described in Eq. (6.18) of the main text. These lateral shifts cause the dot to sample slightly different disorder landscapes, both due to the presence of steps in the quantum well interface and alloy disorder. If the orbital energy fluctuations are different for each dot in the double-dot qubit, the result is an effective detuning fluctuation, $\delta \varepsilon_{\text{eff}} = \delta E_{\text{orb},2} - \delta E_{\text{orb},1}$, where $\delta E_{\text{orb},i}$ labels the orbital energy fluctuation in dot i. We examine the effects of both sources below, where we find both steps and alloy disorder have much smaller impacts on the effective detuning than the direct detuning fluctuations described above. Thus, we do not expect the orbital energy fluctuations due to alloy disorder or interface steps to materially impact flopping mode qubit fidelities.

E.6.1 Alloy disorder

As described above, alloy disorder can induce small shifts in the orbital energy in the presence of fluctuating lateral electric fields. From effective mass theory, the first-order correction to the orbital energy due to alloy disorder is given by

$$E_{\text{orb}}^{\text{dis}} = \int d\mathbf{r} |\psi_0(\mathbf{r})|^2 U_{\text{qw}}^{\text{dis}}(\mathbf{r}) \tag{E.34}$$

where ψ_0 is the zeroth order envelope function, and $U_{\text{qw}}^{\text{dis}}$ is defined in Eq. (E.32). We assume $\psi_0(\mathbf{r}) = \phi_0(x)\phi_0(y)\psi_z(z)$, where ϕ_0 is the ground state wavefunction of a 1D harmonic oscillator confinement potential, and ψ_z is the ground state of the z-confinement potential, determined by the quantum well profile and the vertical field (see Appendix E.5). Since we consider a coarse-grained model of heterostructure, we can replace the integral with a sum, according to the formula

$$\int d\mathbf{r} \rightarrow \frac{a_0^3}{4} \sum_{x_j, y_k, z_l} \tag{E.35}$$

where the sum is over all cells in the heterostructure. To understand the statistical properties of $E_{\text{orb}}^{\text{dos}}$, following Ref. 119 we take the variance in the resulting quantity, resulting in

$$\mathbb{V}[E_{\text{orb}}^{\text{dis}}] = \sigma_\Delta^2 \tag{E.36}$$

where we have used

$$a_0 \sum_{x_j} \phi_0^4(x_j) \approx \int dx\, \phi_0^4(x) = \sqrt{\frac{m_t \omega}{2\pi \hbar}} \tag{E.37}$$

and

$$\mathbb{V}[U_{\text{qw}}^{\text{dis}}(x_j, y_k, z_l)] = \left(\frac{\Delta E_c}{X_w - X_s}\right)^2 \mathbb{V}[\delta X_{j,k,l}] = \frac{1}{2}\left(\frac{\Delta E_c}{X_w - X_s}\right)^2 \bar{X}_{j,k,l}(1 - \bar{X}_{j,k,l}) \tag{E.38}$$

Hence, the orbital energy fluctuation due to alloy disorder in any single dot is a normal random variable, with zero mean and variance given by Eq. (E.36).

Now, we introduce charge noise, in the form of fluctuating lateral electric fields. As discussed above, these field fluctuations induce small shifts in the dot position δx, given by Eq. (6.18). Following the methods of Ref. 119 and 120, it can be shown that the gradient $\partial_x E_{\text{orb}}^{\text{dis}}$ is also a random variable, with variance given by $\mathbb{V}[\partial_x E_{\text{orb}}^{\text{dis}}] = \sigma_\Delta^2/a_{\text{dot}}^2$. So, in response to a small lateral perturbation δx, the resulting detuning fluctuation $\delta E_{\text{orb}}^{\text{dis}} = E_{\text{orb}}^{\text{dis}}(\delta x) - E_{\text{orb}}^{\text{dis}}(0)$ will have the variance

$$\mathbb{V}[\delta E_{\text{orb}}^{\text{dis}}] = \mathbb{V}[\delta x\, \partial_x E_{\text{orb}}^{\text{dis}}] = \frac{\delta x^2 \sigma_\Delta^2}{a_{\text{dot}}^2}. \tag{E.39}$$

Finally, since each dot in the double-dot qubit will have a nearly-uncorrelated alloy disorder profile, it will experience a different change in orbital energy. The resulting detuning fluctuation $\delta \varepsilon_{\text{eff}} = \delta E_{\text{orb},2}^{\text{dis}} - \delta E_{\text{orb},1}^{\text{dis}}$ will have variance

$$\mathbb{V}[\delta \varepsilon_{\text{eff}}^{\text{dis}}] = \frac{2\delta x^2 \sigma_\Delta^2}{a_{\text{dot}}^2} \tag{E.40}$$

Once again, this is a normal random variable with zero mean and variance given by Eq. (E.40). Since these fluctuations can be both positive and negative, we consider the magnitude $|\delta\varepsilon_{\text{eff}}^{\text{dis}}|$. The distribution of $|\delta\varepsilon_{\text{eff}}^{\text{dis}}|$ is folded-normal, with mean

$$\mathbb{E}[|\delta\varepsilon_{\text{eff}}^{\text{dis}}|] = \sqrt{\frac{2}{\pi}\mathbb{V}[\delta\varepsilon_{\text{eff}}^{\text{dis}}]} = 2\sqrt{\frac{2}{\pi}}\frac{\delta x \sigma_\Delta}{a_{\text{dot}}} \tag{E.41}$$

The predictions of Eq. (E.41) for a given lateral field fluctuation $E_{\text{lat},x}$ are shown in Fig. E.4(b), for both the conventional QW (blue) and the 5% Ge QW (red). We see that the effects of alloy disorder are much smaller than the effects of direct detuning fluctuations for a double dot.

E.6.2 Interface steps

Now, we consider the effect of an interface step on the detuning fluctuations in a flopping mode qubit. First, we determine the effects of an interface step on the orbital levels of a single quantum dot. We obtain the ground state orbital energy E_{orb} by diagonalizing the effective mass Hamiltonian Eq. (E.30), varying the dot center x_0 relative to the step at $x_{\text{step}} = 0$ [illustrated schematically in the inset of Fig. E.4(a)]. We use the virtual crystal approximation described in Appendix E.5 to avoid the effects of alloy disorder. We plot the resulting values of $E_{\text{orb}}(x_0)$ in the top panel of Fig. E.4(a) [solid line]. We see that, on either side of the step, the orbital energy levels out, but near the step, the E_{orb} shifts by about $0.7\,\text{meV}$.

Given E_{orb} as a function of dot position x, we can also compute the gradient relative to the dot center, $\partial_{x_0} E_{\text{orb}}$, plotted in the lower panel of Fig. E.4(a) [solid line]. The gradient peaks at the position labeled x^*, marked with a star in Fig. E.4, which is nearly equal to x_{step}. Given a lateral electric field fluctuation $\delta E_{\text{lat},x}$, the dot shifts by an amount δx, given in Eq. (6.18). We can estimate the resulting detuning fluctuation at the position of maximal

gradient,

$$\delta E_{\mathrm{orb}} = \delta x \partial_{x_0} E_{\mathrm{orb}}|_{x_0=x^*} \tag{E.42}$$

Furthermore, if we assume one dot in the double-dot qubit is centered along a step, Eq. (E.42) describes an effective detuning shift $\delta\varepsilon_{\mathrm{eff}}$ between the two dots. This detuning shift is plotted in Fig. E.4(b) [pink dot-dashed line] as a function of $\delta E_{\mathrm{lat},x}$. The resulting $\delta\varepsilon_{\mathrm{eff}}$ is about as large as the expected detuning fluctuation due to alloy disorder in the 5% Ge QW. However, even at the position of the maximal E_{orb} gradient, this shift is still about an order of magnitude smaller than the shift due to direct E-field induced detuning fluctuations.

Finally, we can compare our effective mass simulations with first-order perturbation theory. The first-order correction to the orbital energy due to an interface step is given by

$$E_{\mathrm{orb}}^{\mathrm{step}} = \int d\mathbf{r} |\psi_0(\mathbf{r})|^2 U_{\mathrm{step}}(\mathbf{r}) \tag{E.43}$$

where ψ_0 is the unperturbed ground state envelope function, and U_{step} is the perturbation to the quantum well potential by a step. Using Eqs. (E.32) and (E.33), in the virtual crystal approximation, the potential perturbation due to a step is given by

$$U_{\mathrm{step}}(x_j, y_k, z_l) = \Theta(x < x_{\mathrm{step}}) \frac{\bar{X}_{l+1} - \bar{X}_l}{X_w - X_s} \Delta E_c \tag{E.44}$$

Using the integral-to-sum relation Eq. (E.35), and noting that the step is oriented along $\hat{y}$, we have

$$E_{\mathrm{orb}}^{\mathrm{step}} = \frac{a_0^2 \Delta E_c}{4(X_w - X_s)} \sum_{x_j < x_{\mathrm{step}}} |\psi_0(x_j)|^2 \sum_{z_l} |\psi_z(z_l)|^2 (\bar{X}_{l+1} - \bar{X}_l) \tag{E.45}$$

The results of Eq. (E.45), and the derivative $\partial_{x_0} E_{\mathrm{orb}}^{\mathrm{step}}$, are plotted in Fig. E.4(a) as dashed lines, showing good agreement with the effective mass simulations.
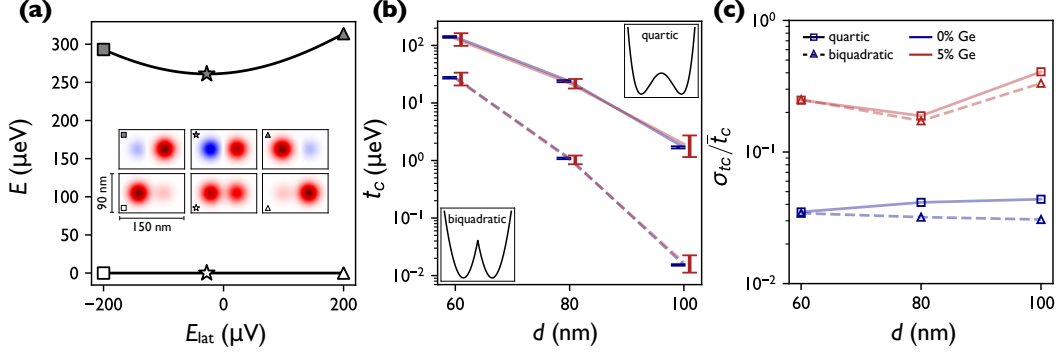
Figure E.5: Computation of the tunnel coupling distribution using effective mass simulations. (a) An example diagram of the ground and first-excited orbital energies, for a single alloy disorder configuration, as we modulate the lateral field E_{lat}. Inset: the ground (white shapes) and first-excited (dark shapes) wavefunctions, plotted at three different E_{lat} configurations, indicated by their shapes. (b) Errorbars represent the 25-75 percentile range of 20 simulations of t_c, where each simulation has a different random-alloy disorder configuration, as we modulate the inter-dot distance d. We consider conventional QWs (blue) and QWs with 5% Ge (red), and we consider quartic (upper series, solid lines) and biquardratic (lower series, dashed lines) double-dot potentials. Connecting lines are a guide to the eye. (c) For each configuration in (b), we plot the standard deviation of the 20 tunnel coupling calculations (σ_{tc}), normalized by the average of the 20 calculations ($\bar{t}_c$).

E.7 Tunnel coupling fluctuations

As well as fluctuations in the effective double-dot detuning, fluctuating lateral electric fields can also produce shifts in the double-dot tunnel coupling t_c. First, we assume charge impurities are distant from the qubit, so the effective lateral field fluctuations are constant across the double-dot. As in Appendix E.6, these cause the double-dot system to displace slightly, sampling a slightly different disorder profile, leading to tunnel coupling fluctuations, δt_c. In the case where charge impurities are nearby, lateral field fluctuations may displace two dots differently, effectively modulating the inter-dot spacing and therefore the tunnel coupling. In this Appendix, we estimate the resulting tunnel coupling fluctuations due to alloy disorder, interface steps, and inter-dot distance modulations. In all cases, as expected, we find tunnel coupling fluctuations are not the dominant source of flopping mode qubit infidelity.
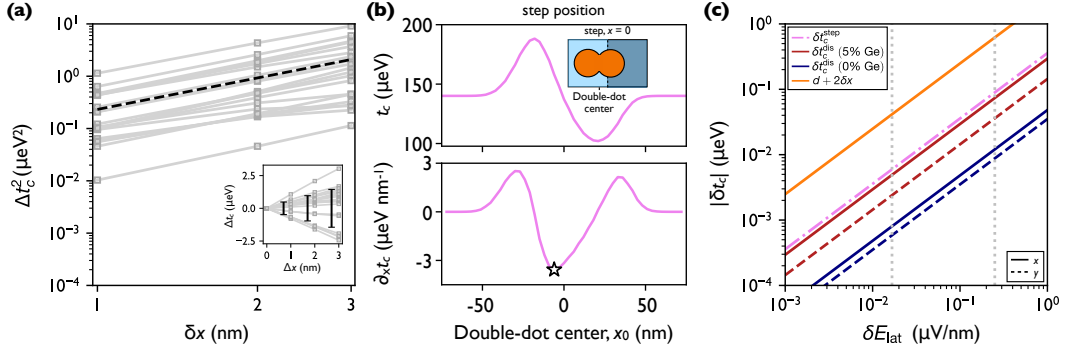
Figure E.6: Estimating the size of tunnel coupling fluctuations due to charge noise. (a) Starting with a double-dot centered at (x_0, y_0), we move the system slightly along the $\hat{x}$ direction, computing the resulting change in tunnel coupling, Δt_c, as described in Appendix E.7. We plot Δt_c^2 against δx for 20 instantiations of random-alloy disorder, as well as the best-fit line for $\mathbb{E}[\Delta t_c^2]$ [see Eq. (E.48)]. For these simulations, we use a conventional QW, quartic double-dot potential, and inter-dot distnace $d = 60$ nm. (b) For a system without alloy disorder, we compute t_c as the double-dot potential moves across a single step in the QW interface at $x_{\text{step}} = 0$ (upper panel). We also indicate the gradient of t_c relative to the double-dot center, $\partial_{x_0} t_c$ (lower panel). We indicate the position of maximal sensitivity to fluctuations in x_0 with a star. (c) For a given lateral field fluctuation δE_{lat}, we estimate the resulting t_c fluctuation, δt_c, due to steps and alloy disorder. First, we consider a double-dot with a single interface step, at the position of maximal sensitivity to changes in x_0 (pink dot-dashed line), ignoring the effects of disorder. We also consider systems with random-alloy disorder and without interface steps, for fluctuations along $\hat{x}$ (solid lines) and y (dashed lines), for conventional QWs (blue) and 5% Ge QWs (red). Finally, we include the δt_c due to fluctuations in the inter-dot position (orange line), where we assume δE_{lat} is equal and opposite in each dot, arranged such that the inter-dot distance $d \to d + 2\delta x$, for δx defined in Eq. (6.18).

E.7.1 Alloy disorder

First, we evaluate the role of alloy disorder on the tunnel coupling in a double dot. To do so, we consider two models of the lateral confinement potential: biquadratic and quartic, following Ref. 112, given by the following

$$
\begin{aligned}
U_{\text{bi}} &= \frac{1}{2}m_t\omega^2 \left\{ \text{Min}\left[\left(x - x_0 - \frac{d}{2}\right)^2, \left(x - x_0 + \frac{d}{2}\right)^2 \right] + (y - y_0)^2 \right\} \\
U_{\text{qu}} &= \frac{1}{2}m_t\omega^2 \left[\frac{1}{d^2}\left((x - x_0)^2 - \frac{d^2}{4} \right)^2 + (y - y_0)^2 \right].
\end{aligned}
\tag{E.46}
$$

where the detuning axis is along $\hat{x}$, d is the inter-dot spacing, the double-dot system is centered at (x_0, y_0), and the orbital energy in each dot is approximately given by $\hbar\omega = 2\,\text{meV}$. These potentials are illustrated schematically in Fig. E.5(b). We note that these models are fairly crude, and real devices allow for control over individual plunger gates and tunnel barriers. Nonetheless, the allow us to make estimates of the impact of disorder on tunnel couplings. We also include the potential due to a lateral electric field,

$$
U_{\text{lat}} = eE_{\text{lat}}x.
\tag{E.47}
$$

This lateral field effectively modulates the detuning of the double-dot system, allowing us to estimate the tunnel coupling, as described below.

To obtain the tunnel coupling for a given disordered crystal lattice, we diagonalize the effective mass Hamiltonian Eq. (E.30), with the double-dot confinement potential given by Eq. (E.46) and lateral field potential given by Eq. (E.47), obtaining energies for the ground and first-excited orbital states, E_g and E_e. Then, we adjust the lateral field strength E_{lat} to find the configuration that minimizes the ground state energy gap, $\Delta E = E_e - E_g$. The tunnel coupling is approximately half this gap, $t_c \approx \Delta E/2$. This procedure is illustrated for one example in Fig. E.5(a), where we have plotted both E_g and E_e as we modulate E_{lat}. We also plot the ground state wavefunction (white markers) and the first excited

state wavefuntions (gray markers) at three different configurations. We see that at the position of minimal ΔE, indicated with stars, the wavefunctions are given by symmetric and antisymmetric combinations of left- and right-dot orbital states with nearly equal weights. Using this procedure, we compute t_c for 20 instantiations of random-alloy disorder.

We perform the above procedure for inter-dot spacings $d = 60$, 80, and 100 nm, for both the quartic and biquadratic confinement potentials defined in Eq. (E.46). We consider both conventional QWs (blue) and QWs with 5% Ge (red), and the resulting t_c distributions are plotted in Fig. E.5(b), where errorbars represent the $25 - 75$ percentile range across the 20 instantiations of random-alloy disorder. The upper series of data (connected with solid lines) indicate results for the quartic potential, and the lower series (dashed lines) the biquadratic potential. We observe that the average t_c varies over many orders of magnitude for the inter-dot spacings considered here. This is the expected behavior, given the exponential dependence of t_c on d. We also see that the variation in t_c is much larger in the QWs with 5% Ge than the conventional QWs. To illustrate this further, we plot the size of σ_{tc}, the standard deviation of the t_c distribution, relative to the average $\bar{t}_c$ in Fig. E.5(c). We see that for both quartic and biquadratic models, σ_{tc} is about 20% of $\bar{t}_c$ in the 5% Ge heterostructures, while only about 3% of $\bar{t}_c$ for the conventional QWs.

Next, we consider the effects of charge noise. We assume that a lateral field fluctuation δE_{lat} will slightly modify the center coordinates (x_0, y_0) of the double-dot qubit, causing the qubit to sample a slightly different disorder landscape. Again, we assume δE_{lat} is constant across the double-dot, which is true if the charge defects producing δE_{lat} are far from the qubit. We consider a quartic potential with dot spacing $d = 60$ nm, which produces average $\bar{t}_c$ closest to $100\,\mu\text{eV}$ [see Fig. E.5(b)]. For each of the 20 alloy disorder configurations, for both the conventional and 5% Ge QW, we slightly perturb the double-dot center coordinates. We consider perturbations in both the x- and y-directions. By computing the change in tunnel couplings due to these lateral shifts, labeled Δt_c, we can extract the statistics of t_c fluctuations. Like other disorder-influenced quantities, we assume $\mathbb{V}[\Delta t_c] = \mathbb{E}[\Delta t_c^2]$

	$\bar{t}_c$ (µeV)	σ_{tc} (µeV)	$a_{tc,x}$ (nm)	$a_{tc,y}$ (nm)
0% Ge	140	4.9	10	14
5% Ge	131	32	11	22

Table E.1: Numerical parameters describing t_c sensitivity due to lateral perturbations of the double-dot center coordinates, as described in Appendix E.7.

scales quadratically with displacement and is proportional to the underlying tunnel coupling variance, σ_{tc}^2. Hence, we fit the data to the relationship

$$\mathbb{E}[\Delta t_c^2] = \sigma_{tc}^2 \Delta x^2 / a_{tc,x}^2, \tag{E.48}$$

where σ_{tc} is determined empirically from the initial 20 simulations, and $a_{tc,x}$ is the fitting parameter. The parameter $a_{tc,x}$ has units of distance, so this parameter captures the length scales over which t_c varies in a double dot, and the subscript x indicates that the displacement Δx occurred along $\hat{x}$. We plot one dataset of Δt_c^2 vs δx^2 in Fig. E.6(a), for small displacements along the $\hat{x}$ axis in a conventional QW. We also plot the fit given by Eq. (E.48) [black dashed line]. Clearly, the tunnel coupling fluctuations are well-described by Eq. (E.48). In the inset, we also plot Δt_c vs. δx, indicating with scale bars how $\text{Std}[\Delta t_c] = \sqrt{\mathbb{E}[\Delta t_c^2]}$ grows with distance. We repeat this procedure for displacements along the $\hat{y}$ direction as well, for both conventional and 5% Ge QWs. The resulting fit parameters are summarized in Table E.1. We note that the fluctuation length scales are all on the order of the dot size.

Finally, we can relate these tunnel coupling fluctuations to a lateral field fluctuation. As before, we assume that a lateral field fluctuation δE_{lat} shifts the dot by a small distance δx, as given in Eq. (6.18), resulting in a small shift δt_c. In Fig. E.6(b), we plot E_{lat} vs the expected rms tunnel coupling fluctuations, for both conventional (blue) and 5% Ge (red) QWs and displacements along $\hat{x}$ (solid lines) and $\hat{y}$ (dashed lines). Again, we note the expected δE_{lat} corresponding to our optimistic and pessimistic charge noise configurations. We see that, for the charge noise regimes considered in this work, we expect tunnel coupling fluctuations

much less than $1\,\mu\text{eV}$ due to alloy disorder.

E.7.2 Interface steps

Next, we investigate the role of interface steps in tunnel coupling fluctuations. As above, we use 3D effective mass simulations to determine t_c for different step configurations. In this case, we exclude alloy disorder by using the virtual crytal approximation. Again, we use the quartic potential model and an inter-dot separation $d = 60$ nm in Eq. (E.46). We plot the resulting t_c as we move the double-dot across a step at $x_{\text{step}} = 0$ in Fig. E.6(b) [top panel]. In the bottom panel, we plot the resulting gradient, $\partial_{x_0} t_c$. At the position of maximal gradient x^*, we find $|\partial_{x_0} t_c|_{x_0 = x^*} \approx 3.6\,\mu\text{eV}\,\text{nm}^{-1}$. Then, using Eq. (6.18), we relate the t_c fluctuation to a lateral field fluctuation, using

$$\delta t_c \approx \delta x \partial_{x_0} t_c|_{x_0 = x^*}. \tag{E.49}$$

The resulting δt_c are plotted in Fig. E.6(c) [pink dot-dashed line]. For the charge noise regime considered here, we expect $\delta t_c \ll 1\,\mu\text{eV}$.

E.7.3 Fluctuations in the inter-dot distance

Lastly, we investigate the role of fluctuations in the inter-dot distance due to charge noise. In the case where charge defects live near the qubit, each dot could experience electric field fluctuations in opposite directions. These could have the effect of moving the two dots slightly closer or slightly farther apart. To estimate the effect these fluctuations would have on the tunnel coupling, we use the data in Fig. E.5(b) to estimate how t_c scales with distance. Using the data for the 0% Ge QWs in quartic potentials at $d = 60$ and $80\,\text{nm}$, we approximate $\log t_c \approx -3.57 - 0.088d$, for t_c in eV and d in nm. Using this relationship, we can estimate δt_c for small shifts in d. To relate shifts in d to lateral field fluctuations δE_x, we again use Eq. (6.18). This time, we assume the lateral field fluctuations are equal and opposite for
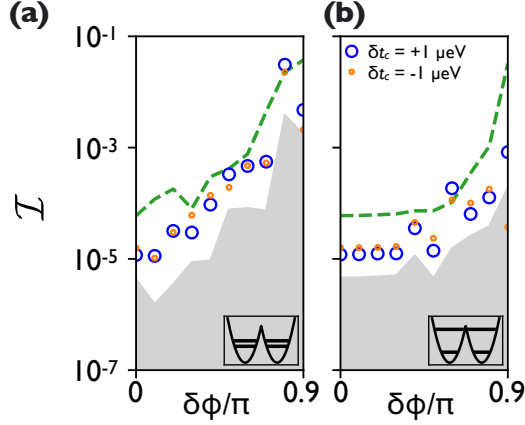
Figure E.7: Estimating the pulse infidelity due to fluctuations in the tunnel coupling t_c. For $\delta\phi$ from 0 to 0.9π, we compute the infidelity resulting from tunnel coupling fluctuations $\delta t_c = \pm 1$ µeV, for valley splittings $E_{vL} = E_{vR} = 20$ µeV (a) and $E_{vL} = E_{vR} = 100$ µeV (b), for pulses optimized for $\sigma_\varepsilon = 15$ µeV. We also plot the average infidelity due to detuning fluctuations for the cosine pulse, computed with Eq. (6.16) [green dashed lines]. The gray regions indicate the infidelity without charge noise, $\mathcal{I}_0$, and serves as a lower bound on pulse fidelity.

each dot, so the double-dot spacing d is shifted by $\pm 2\delta x$, for δx given by Eq. (6.18). We plot the resulting $|\delta t_c|$ as a function of δE_{lat}, assuming $d \to d + 2\delta x$, in Fig. E.6(c) [orange line]. We see this type of shift can have a much larger impact on t_c than alloy disorder and interface steps.

E.7.4   Impact of δt_c on gate fidelity

To estimate the expected infidelity due to tunnel coupling fluctuations, we examine the cosine pulse family, in the pessimistic $\sigma_\varepsilon = 15$ µeV charge noise regime. We expect the effects of charge noise to be more apparent for large noise amplitudes. Starting with a pulse optimized for either $E_{vL} = E_{vR} = 20$ µeV or $E_{vL} = E_{vR} = 100$ µeV, we then apply a t_c fluctuation equal to ± 1 µeV to the Hamiltonian, and we compute the resulting pulse infidelity under the modified Hamiltonian. Results are shown as circles in Fig. E.7 for $E_{vL} = E_{vR} = 20$ µeV (a) and $E_{vL} = E_{vR} = 100$ µeV (b), where large blue circles show infidelities for $\delta t_c = +1$ µeV, and small red circles show infidelities for $\delta t_c = -1$ µeV. The green dashed lines in (a) and (b) indicate the infidelity due to detuning fluctuations, and the gray boundary indicates the

baseline infidelity $\mathcal{I}_0$, as described in the main text. We note that $\delta t_c = \pm 1\,\mu\text{eV}$ is quite a large fluctuation. In our simulations above, we only find δt_c approaching $1\,\mu\text{eV}$ when a fluctuating lateral field has opposite direction in each dot. Alloy disorder and interface steps produce δt_c's that are about an order of magnitude smaller, given the same lateral fields. Of course, precise quantification of the true δt_c distribution will require atomistic simulations including charge traps and other impurities. However, we view this as an approximate upper bound on δt_c. In Fig. E.7 (a) and (b), despite these very large fluctuations in t_c, we observe that the infidelity due to t_c fluctuations is almost always smaller than the expected infidelity due to detuning fluctuations. Hence, for the qubits considered in this work, we do not expect tunnel coupling fluctuations to be a dominant source of infidelity.

E.8 Simulations of random E_v landscapes

In both Sec. 6.6 and 6.7, we have performed simulations of the spatial distribution of valley splittings along a 1D or 2D landscape. We use the GSTools python library [136] to generate these landscapes, assuming the real and imaginary components of Δ are uncorrelated, and the spatial covariance of Δ is given by Eq. (6.19).

E.9 Linear quantum dot array

In Section 6.7 of the main text, we considered sparse grids of quantum dots, showing that they enable a much higher probability of finding a high-fidelity qubit. Here, we perform the same analysis for linear arrays of quantum dots, illustrated in the inset to Fig. E.8. As in the main text, we estimate P_{fail} for each configuration of dots, assuming the valley parameters are uncorrelated between neighboring dots, from 10,000 simulations of random alloy disorder, assuming a minimum QW Ge concentration G_{min} from 0 to 5%. Like we found for sparse grids of dots, we find that P_{fail} falls dramatically as the number of dots in the grid is increased. For the same number of dots, we find the square grid configuration achieves
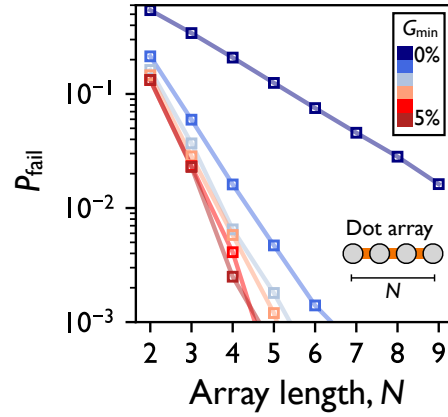
Figure E.8: We plot P_{fail}, defined in Eq. 6.22, for linear arrays of quantum dots with size N. Each data point is computed from 10,000 instantiations of random alloy disorder, assuming E_v is uncorrelated between neighboring dots. Colors indicate the minimum Ge concentration G_{min}, which we vary from 0 to 5 %.

slightly smaller P_{fail} than the linear chain, since more qubits can be formed in the square grid. For example, for 0% Ge quantum wells, we find 9 dots arranged in a line achieves $P_{\text{fail}} \approx 1.6$ %, while 9 dots arranged in a square grid achieves $P_{\text{fail}} \approx 0.7$ %.

Appendix F

Supplementary Information for Chapter 7

F.1 Super-sharp interfaces with atomic step disorder

In the main text, we considered the limit of disorder-dominated quantum wells, for which random-alloy disorder is the main source of variability in the valley splitting. In this Appendix, we consider the opposite, deterministically enhanced valley-splitting limit, which can be achieved, for example, in quantum wells with super-sharp interfaces. In this case, the dominant source of disorder is from single-atom steps at the quantum well interface. We now briefly show that such disorder from sparse steps has a very different effect on shuttling than random-alloy disorder, and that the resulting infidelities are greatly reduced in accordance with much larger minimal E_v.

When the QW interfaces are very sharp, monoatomic steps in the QW interfaces are the dominant source of E_v fluctuations. To study shuttling in this regime, we examine the case of a single atomic step, traversed at different shuttling velocities. We assume an orbital splitting of $2\,\mathrm{meV}$ and a vertical electric field of $5\,\mathrm{mV\,nm^{-1}}$ inside a well of width $10\,\mathrm{nm}$, with perfectly sharp interfaces and a single atomic step in the interface. We use 2D effective mass
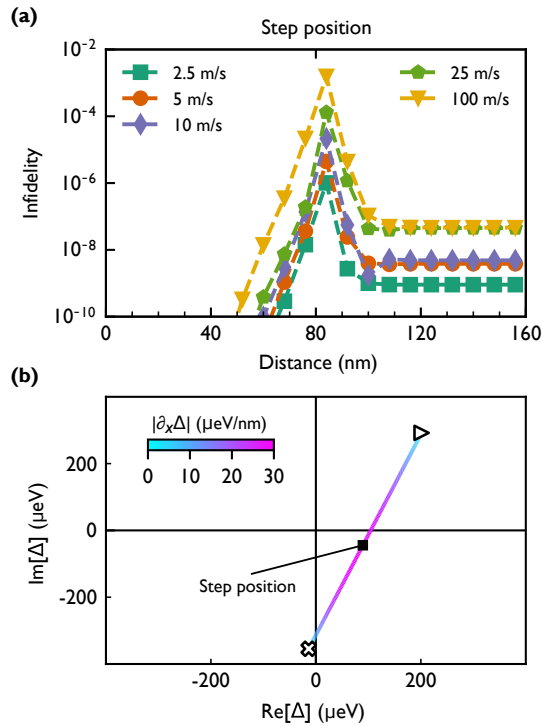
Figure F.1: Traversal of a single monoatomic step. (a) Infidelities as a function of shuttling distance, for a quantum well with a perfectly sharp interface containing a single atomic step centered in the middle of the shuttling path, for several different shuttling velocities (color coded). Working in the basis of instantaneous eigenstates, we observe an infidelity peak at the center of the Landau-Zener transition, as expected from theory [135, 198]. The infidelity then remains low after crossing the step, even for velocities up to $100\,\mathrm{m\,s^{-1}}$. Compared to the disorder-dominated regime, this represents several orders of magnitude of improvement in the infidelity. (b) The inter-valley coupling Δ plotted in the complex plane for the same shuttling path. Here, the lowest valley splitting occurs at the step location, with a value of $200\,\mathrm{\mu eV}$. The color code represents $|\partial_x \Delta|$.

theory to simulate the inter-valley coupling as the dot moves across the step (see Section F.5). The evolution of Δ as the dot traverses the step is shown in Fig. F.1(b), where at the step position, the dot has a minimum E_v of about $200\,\mu\text{eV}$. We plot the resulting infidelity as function of shuttling distance in Fig. F.1(a). We see spikes in the infidelity near the step position in Fig. F.1(a). These correspond to the position with maximized $|\partial_x\Delta|$, the rate of change in Δ as a function of distance, shown in Fig. F.1(b). However, as the minimal E_v at the step position is much larger than typical minima present in the disordered regime, even velocities an order of magnitude higher than those considered in the main text converge to low infidelity values beyond the step. An ideal sharp interface with only occasional single monolayer steps can therefore enable high-fidelity transport even without applying tuning methods. It should be noted that multiple steps in close vicinity, i.e. on the order of the dot size, may decrease E_v^{min} again and induce larger infidelity, as considered in Ref. [109].

F.2 Prefactor of the noise-induced shuttling infidelity

Here, we briefly clarify the different prefactor appearing in Eq. (7.10), as compared to Ref. [109], which we have adapted to match the infidelity metric described in Sec. 7.4.2. For a noise Hamiltonian given by

$$H_{\text{noise}} = \frac{\hbar}{2}\Phi(t)\sigma_z \,, \tag{F.1}$$

our metric can be rewritten as

$$F = \frac{1}{d^2}\left|\text{Tr}\{\underbrace{V^\dagger}_{\mathbb{1}} U_{\text{noise}}(t)\}\right|^2 \tag{F.2}$$

$$= \frac{1}{d^2}\left|e^{i\Phi(t)/2} + e^{-i\Phi(t)/2}\right|^2 , \tag{F.3}$$

where $U_{\text{noise}}(t)$ is the time evolution operator for H_{noise}. Assuming a Gaussian ensemble average of qubit phases Φ of zero mean and rms $\delta\Phi$, and with a dimension $d = 2$, this

evaluates to

$$\langle F \rangle = \frac{1}{d^2} \left(2 + 2e^{-\delta\Phi^2/2} \right) \tag{F.4}$$

$$\xrightarrow{d=2} \langle I \rangle = 1 - \langle F \rangle = \frac{1}{2} \left(1 - e^{-\delta\Phi^2/2} \right) \approx \frac{\delta\Phi^2}{4}, \tag{F.5}$$

which implies an additional factor of 1/2 compared to Ref. [109].

F.3 Parameter choices for two tuning methods

In this Appendix, we examine how parameter choices for two of the tuning strategies in the main text affect the shuttling infidelities. This discussion is not meant to provide a comprehensive analysis; rather, it is to illustrate some of the compromises that must be considered when making these choices.

We first examine how the segment length and channel width affect shuttling infidelities for the channel-shifting strategy. In Fig. F.2(a), we modify both the length of each segment and the width of the shuttling channel (the "lateral range"). We calculate the shuttling infidelities for the 3 nm QW at 10 μm distance for each parameter choice, while simultaneously applying bipartite velocity modulation, with an average shuttling velocity of $5\,\mathrm{m\,s^{-1}}$. As expected, both parameters have a significant effect on shuttling infidelities of at least several orders of magnitude. Increasing the lateral range makes it easier to avoid regions with low valley splittings, while smaller segment lengths allow for more frequent adjustments to the optimal path. For both parameters, the range of parameters considered in Fig. F.2(a) does not result in asymptotic behavior of the infidelity; however, the range is imaginable for experimental realizations. On the other hand, the results suggest the existence of thresholds, beyond which the infidelities deteriorate significantly: for channel widths, this occurs below about 60 nm, and for segment lengths, it occurs above 1 μm. The threshold for both parameters depends on the dot size, since valley splitting values are essentially uncorrelated when the
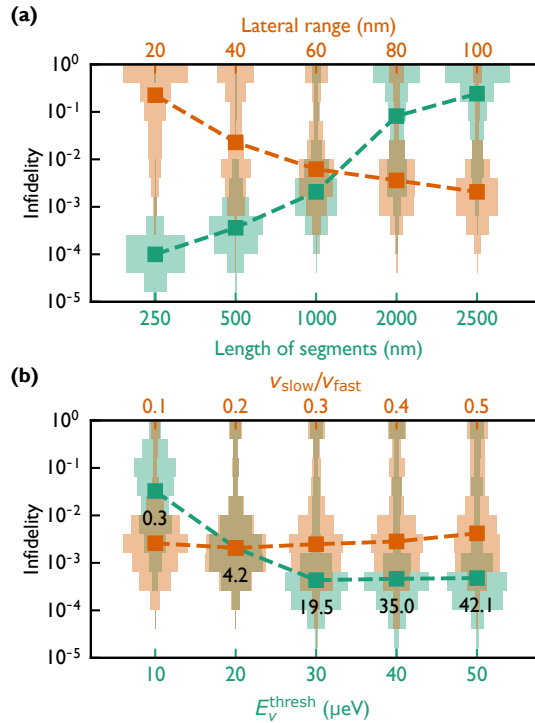
Figure F.2: Comparison of different simulation constraint parameters, for two tuning methods. (a) Exploration of shuttling infidelities as we vary parameters used in the channel-shifting simulations. Rust-colored histograms show results for several different lateral shift ranges. Green histograms show results for several different segment lengths. Larger lateral ranges and smaller segment lengths are seen to give higher fidelities. Here, results are obtained for a $10\,\mu\mathrm{m}$ shuttling trajectory, for an average velocity of $5\,\mathrm{m\,s^{-1}}$, in the $3\,\mathrm{nm}$ quantum well, and we simultaneously apply bipartite velocity modulation but no dot elongation. (b) Exploration of shuttling infidelities as we vary parameters related to bipartite velocity modulations. Rust-colored histograms show results for several values of the ratio $v_\mathrm{slow}/v_\mathrm{fast}$. Green histograms show results for several values of the threshold valley splitting E_v^thresh, below which the slower velocity is applied. While increasing the ratio $v_\mathrm{slow}/v_\mathrm{fast}$ has a weak effect on the median infidelity values, it has a stronger effect on the number of very poor infidelity results. On the other hand, setting a low valley splitting threshold value causes the infidelity to increase significantly. Black numbers indicate the average number of valley splitting dips below E_v^min that occur over the full shuttle length. Other parameters are the same as in (a).

dot is moved by the distance of a dot diameter. We therefore expect that smaller dots do not require a wide channel to achieve high shuttling fidelities; however they do require shorter segment lengths. At the threshold values for these tuning parameters, in addition to increasing median infidelity, we note that the infidelity distribution also becomes problematic, with a much higher portion of infidelities occurring at higher values.

Second, we examine parameters related to bipartite velocity tuning. In Fig. F.2(b), we analyze the choice of the "slow" velocity used near locations of low valley splitting, v_{slow}, and we study the choice of threshold valley splitting, E_v^{thresh}, below which the velocity is reduced. Again, we consider simulations of the $3\,\text{nm}$ QW evaluated at $10\,\mu\text{m}$, with a fixed average velocity of $5\,\text{m}\,\text{s}^{-1}$, and we apply both bipartite velocity modulation and channel shifting techniques. We see that increasing the ratio $v_{\text{slow}}/v_{\text{fast}}$ only slightly increases the median infidelity, but it significantly widens the tails of the distribution at large infidelities. Setting a higher threshold E_v^{thresh} for velocity switching causes the median infidelity to move to lower infidelities; however, this occurs at the cost of significantly more velocity switches per trace, as indicated by the black numbers accompanying the data points.

F.4 Effect of individual tuning methods

In this Appendix, we briefly show that strategies to evade points of low E_v (e.g., modulating the electric field or channel shifting) are a necessary component of high-fidelity shuttling. Velocity modulation and dot elongation can improve upon these fidelities, but they do not provide high-fidelity shuttling on their own. In Fig. F.3, we separate out the performance of velocity modulation and dot elongation for the 5% Ge quantum well. While both strategies yield improvements over the unmodified shuttling procedure, after $2\,\mu\text{m}$ no practical improvement is obtained, even for the quantum well with the largest average valley splitting studied here.
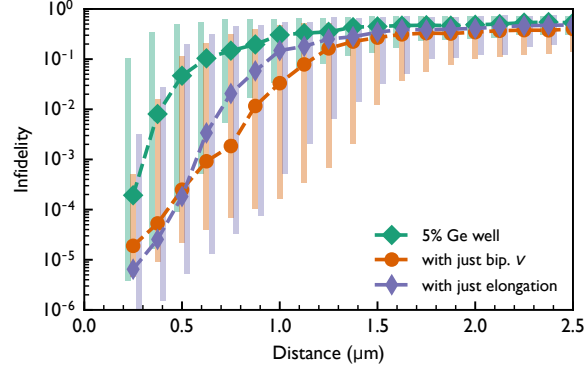
Figure F.3: Simulation results showing that velocity modulation and dot elongation do not provide high-fidelity shuttling on their own. Here, we plot the shuttling infidelities as a function of distance for the 5% Ge quantum well without any modifications (green), then including either velocity modulation (orange) or dot elongation (purple). Note that we use neither channel shifting nor electric field modulation. We find that neither the velocity modulation nor the elongation strategy provides reliable improvements over extended distances, with improvements that are limited to length scales below $2\,\mu m$.

F.5 Effective-mass theory of valley splitting

In this section, we elaborate on the effective-mass envelope-function model for the valley states outlined in Refs. [119, 145] and referenced in Sec. 7.3. We start with Eq. (7.2) in the main text, describing the inter-valley coupling Δ. For a fully separable system, we can reduce Eq. (7.2) to a 1D integral over z. Moreover, following Refs. [119, 145], we transform the integral to a sum over atomic monolayers (MLs) to account for the discrete layers of the Si diamond cubic crystal structure, yielding Eq. (7.3) for Δ_{1D} in the main text. When monoatomic steps are present at the interface, our system is no longer fully separable, and the reduction to 1D is no longer sufficient. In this case, we can easily generalize to 2D or 3D. For example, to simulate a system with a monoatomic step in the y direction, we can still separate the wavefunction as $\psi_{env}(\mathbf{r}) = \psi_{env}(x,z)\psi_{env}(y)$. We now perform a weighted average of the Ge distribution in only one (y) direction, resulting in a 2D description in the variables (x,z). Discretizing our system into cells of size $(\Delta x, \Delta z) = (a_0, a_0/4)$ yields the

2D effective mass equation

$$\Delta_{2D} = \frac{a_0^2}{4} \sum_{j,l} e^{-2ik_0 z_l} U_{\text{qw}}(x_j, z_l)|\psi_{\text{env}}(x_j, z_l)|^2. \tag{F.6}$$

Here, the sum is over indices j and l, which label the x and z coordinates of each cell, respectively.

To a very good approximation, the quantum well potential U_{qw} is a linear function of the Ge concentration:

$$U_{\text{qw}}(\mathbf{r}) = \frac{X_{\mathbf{r}} - X_s}{X_w - X_s} \Delta E_c \tag{F.7}$$

where $X_{\mathbf{r}}$ is the Si concentration at position $\mathbf{r}$ in the heterostructure, X_w is the average Si concentration in the quantum well, X_s is the average Si concentration in the SiGe barrier/substrate region, and ΔE_c is the conduction-band offset of the quantum well. For 1D systems, we can use $X_{\mathbf{r}} = X_l$, where l is the layer index. In this work, unless otherwise stated, we model our interfaces as sigmoid functions, where the average Si concentration at layer l is defined by

$$\bar{X}_l = X_w + \frac{X_s - X_w}{1 + \exp[(z_l - z_t)/\tau]} + \frac{X_s - X_w}{1 + \exp[(z_b - z_l)/\tau]}, \tag{F.8}$$

where z_t and z_b label the positions of the top and bottom interfaces, and $\lambda = 4\tau$ is the characteristic interface width. Unless otherwise specified, we use $\lambda = 4\tau = 1\,\text{nm}$.

In the case of monoatomic steps, the Si concentration $X_{\mathbf{r}}$ adopts some lateral dependence. In this case, we can define the expected Si concentrations for a system with a step at lateral position $x = 0$:

$$\bar{X}_{j,l} = \bar{X}_l \Theta(x_j \leq 0) + \bar{X}_{l+1} \Theta(x_j > 0) \tag{F.9}$$

where $\bar{X}_l$ is given by Eq. (F.8) and $\Theta(\cdot)$ is the Heaviside step function.

Both Eqs. (7.3) and (F.6) depend on the envelope function ψ_{env}. To compute ψ_{env}, we discretize and solve a Schrodinger equation *without* valley physics. In the 1D case, we

discretize and solve the effective 1D Hamiltonian

$$H_{1D} = -\frac{\hbar^2}{2m_l}\partial_z^2 + \bar{U}_{qw}(z) + U_\phi(z) \tag{F.10}$$

where $m_l = 0.916m_e$ is the longitudinal effective mass of the electron, m_e is the bare electron mass, $U_\phi(z) = eE_z z$ is the potential due to a vertical electric field E_z, and $\bar{U}_{qw}$ is the quantum well potential without alloy-disorder-induced fluctuations. In the 2D case, we discretize and solve the effective 2D Hamiltonian

$$H_{2D} = -\frac{\hbar^2}{2m_l}\partial_z^2 - \frac{\hbar^2}{2m_t}\partial_x^2 + \bar{U}_{qw}(x,z) + U_\phi(z) + \frac{1}{2}m_t\omega_x^2(x-x_0)^2 \tag{F.11}$$

where ω_x is the orbital confinement energy in the x-direction, and x_0 is the center location of the dot. In Section F.1, we considered shuttling across a mono-atomic step, where it was necessary to apply Eq. (F.11). However, in the rest of this work, it is sufficient to use the 1D approximation of Eq. (F.10).

To model the conduction-band offset, we follow Ref. [145]:

$$\Delta E_c = (X_w - X_s)\left[\frac{X_w}{1 - X_s}\Delta E_{\Delta_2}^{Si}(X_s) - \frac{1 - X_w}{X_s}\Delta E_{\Delta_2}^{Ge}(X_s)\right], \tag{F.12}$$

where $\Delta E_{\Delta_2}^{Si(Ge)}(X)$ are the Δ_2 conduction-band offsets for strained Si (Ge) grown on unstrained Si_XGe_{1-X} substrate, and we approximate these functions as [164]

$$\Delta E_{\Delta_2}^{Si}(X) \approx -0.502(1 - X) \text{ (eV)}$$
$$\Delta E_{\Delta_2}^{Ge}(X) \approx 0.743 - 0.625(1 - X) \text{ (eV)}. \tag{F.13}$$

Since the crystal lattice itself is composed of discrete atomic sites, the averaged concentration inside a finite-sized dot has an intrinsic uncertainty, given by $X_l = \bar{X}_l + \delta_l$, where $\bar{X}_l$ is the mean Si concentration at layer l, and δ_l is the fluctuation for a particular dot. The Si concentration X_l in layer l can be computed as a weighted average, where the contribution

of each atom is weighted by the dot probability density at that atom:

$$X_l = \frac{1}{N_l} \sum_{a \in A_l} \mathbb{1}[a = \text{Si}]|\psi_{\text{env}}(a)|^2 = \bar{X}_l + \delta_l \tag{F.14}$$

where the sum is taken over A_l, the set of atoms in layer l, $\mathbb{1}[a = \text{Si}]$ is the indicator function that returns 1 if a is Si and 0 otherwise, and $\psi_{\text{env}}(a)$ is the value of the envelope function at the position of atom a. The normalization constant $N_l = \sum_{a \in A_l} |\psi_{\text{env}}(a)|^2$. The inter-valley coupling of Eq. (7.3) can likewise be broken into fixed and random components Δ_0 and $\delta\Delta$:

$$\begin{aligned} \Delta_0 &= \frac{a_0 \Delta E_c}{4(X_w - X_s)} \sum_l e^{-2ik_0 z_l}(\bar{x}_l - x_s)|\psi_{\text{env}}(z_l)|^2, \\ \delta\Delta &= \frac{a_0 \Delta E_c}{4(X_w - X_s)} \sum_l e^{-2ik_0 z_l}\delta_l|\psi_{\text{env}}(z_l)|^2. \end{aligned} \tag{F.15}$$

In Eq. (F.15), Δ_0 is the inter-valley coupling due to larger-scale features of the heterostructure, like the interface width or interface steps. On the other hand, $\delta\Delta$ is a local fluctuation about Δ_0, caused by alloy disorder. We can then compute the variance $\sigma_\Delta^2 = \text{Var}[\delta\Delta]$, as given in Eq. (7.4) in the main text.

F.6 Generating valley-splitting landscapes

To obtain accurate statistics of shuttling fidelities, we need to generate many realistic examples of inter-valley couplings, Δ, which vary spatially across the device. That is, we need many examples of $\Delta(x, y)$. To do so, we use the GSTools python library, which generates spatially random fields [136]. The real and imaginary components of Δ are generated independently, with variances given by $\sigma_\Delta^2/2$ and spatial covariances defined in Eq. (7.6).

The above approach works for spatially varying inter-valley couplings, $\Delta(x, y)$. However, to test the efficacy of modulating the electric field, we also need to generate many sample fields of the form $\Delta(x, E_z)$. Unlike the relationship between Δ and x, the statistical relationship between Δ and E_z is not given by a simple covariance equation that can be

randomized. Instead, the effect of E_z depends on the shape of the quantum well interfaces, the quantum well width, and the Ge content in the quantum well. So, rather than randomly generating the field Δ, we instead generate the local Si concentrations across the device, for each atomic layer of the quantum well. Since the dot is finite in extent, as it shuttles across the device, the effective Si concentrations experienced by the dot at each layer in the heterostructure fluctuate slightly. Thus, the effective Si concentrations in the quantum well become position-dependent. We then indicate the Si concentration at layer l and lateral position x by $X_l(x)$. Using GSTools, we create many examples of $X_l(x)$. Then, for a given position and vertical field value, we use these local Si concentrations in our effective mass model, outlined above, to compute $\Delta(x, E_z)$. Below, we outline how we obtain these spatially fluctuating Si concentrations.

Previous work has shown that X_l can be approximately sampled from a binomial distribution, $X_l \sim \frac{1}{N_{\text{eff}}}\text{Binom}(N_{\text{eff}}, \bar{X}_l)$, where $N_{\text{eff}} = 4\pi a_{\text{dot}}^2/a_0^2$ [119]. In turn, this is approximately equal to a normal distribution with mean $\bar{X}_l$ and variance $\sigma_X^2 = N_{\text{eff}}\bar{X}_l(1 - \bar{X}_l)$. Therefore, X_l can be approximately sampled as

$$X_l \sim \frac{1}{N_{\text{eff}}}N(\bar{X}_l, N_{\text{eff}}\bar{X}_l(1 - \bar{X}_l)), \tag{F.16}$$

where $N(\mu, \sigma^2)$ is the normal distribution with mean μ and variance σ^2. The spatial covariance is then given by

$$\text{Cov}[X_l, X_l'] = \exp\left(-\delta_x^2/2a_x^2\right)\sigma_X^2, \tag{F.17}$$

where δ_x indicates the distance between two points along the shuttling trajectory. Equations (F.16) and (F.17) describe the complete spatial statistics of $X_l(x)$, which we can input into GSTools, to generate fluctuating Si concentrations. Now, for each position x, we have a complete Si concentration profile $X_l(x)$, which we simulate using effective mass theory Eq. (7.3) to compute Δ. Thus, we can build up sample fields of the form $\Delta(x, E_z)$.
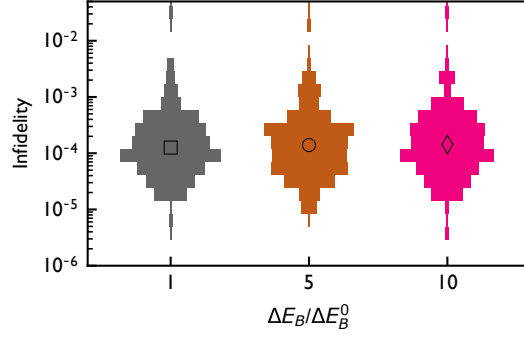
Figure F.4: Infidelity histograms for the channel-shifted 5% Ge quantum well, including all tuning methods applied, as in Fig. 7.5(d), as a function of the Zeeman splitting difference ΔE_B between the ground and excited valley states. Here, ΔE_B^0 is the characteristic value of 10 MHz used in the main text.

F.7   Dependence on ΔE_B

We briefly comment on the dependence of the simulations on the difference in Zeeman splittings ΔE_B between the ground and excited valley states. In Fig. F.4, we illustrate the dependence of the shuttling infidelity distribution on ΔE_B for the highest-fidelity simulations used in this work: shuttling in a 5% Ge quantum well with all tuning methods applied. We see that the distribution of infidelities changes only slightly when increasing the value of ΔE_B by an order of magnitude. We can understand this result as follows. The metric used to evaluate the fidelity in this work considers, as a conservative assumption, only the population ending up in the ground state [208]. In the absence of fast relaxation dynamics, as discussed in the main text, we do not expect dots in the excited valley state to return to the ground state with significant probability. Since the energy scale of the ΔE_B term has little effect on the Landau-Zener transition mechanism, ΔE_B is not a determining factor for the infidelity results, as confirmed in Fig. F.4.
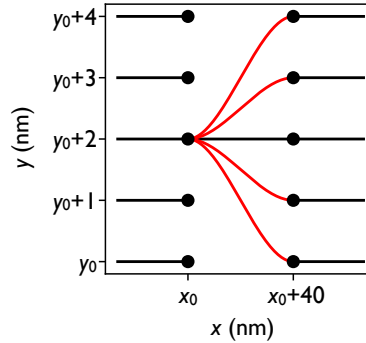
Figure F.5: Schematic illustration of the possible paths a dot can take across a device, implemented in our path traversal algorithm. Straight segments of fixed length are connected by transition zones of length $40\,\text{nm}$ along the shuttling direction ($\hat{x}$). The possible transitions from one such straight segment are illustrated, including the option to continue straight ($\Delta p = \Delta y = 0$), shown in black, and the option to modify the parameter ($|\Delta p| = |\Delta y| > 0$), shown in red.

F.8   Path selection algorithm

To implement segmented channel-shifting strategies, we need to carefully choose our path across the valley splitting landscape, either by modifying the y coordinate of the dot or by modifying the vertical electric field E_z. In this work, we adopt a heuristic graph traversal algorithm to make this path selection. The valley splitting landscape is discretized into pixels of size $1\,\text{nm} \times 1\,\text{nm}$ for y tuning, or $0.1\,\text{mV/nm} \times 1\,\text{nm}$ for E_z-tuning. To make use of common graph traversal algorithms, we define a graph representing the possible paths across this discretized landscape. The edges of the graph represent possible paths the dot could take across the device. These paths include straight segments of a fixed length with $40\,\text{nm}$ transition zones between the segments. (We set all segment lengths to $1\,\mu\text{m}$ in this work, except briefly in Appendix F.3.) [See Fig. 7.5(a) for an example trajectory, and Fig. F.5 for an illustration of the method.] The parameter being optimized (either y or E_z) remains constant along a straight segment (black lines in Fig. F.5), but is modified smoothly and continuously in the transition zones (red lines in Fig. F.5). Transitions between the optimized segments are heuristically defined as cubic polynomial functions whose derivatives go to zero at the endpoints of the transition.

An ideal path should have the following properties: (1) the minimum valley splitting along each segment should be large enough to avoid Landau-Zener transitions between the valley states, and (2) the transitions between segments should be as short as possible, to avoid increasing the effective shuttling velocity along long, steep transitions. To achieve paths that globally optimize these two properties, we assign weights $w(e)$ to each edge e according to the following rules, which penalize both low minimum valley splittings ($\min_e E_v$) along a given segment, and transitions with large changes Δp in the optimization parameter, where $p = y$ or E_z :

$$w(e) = \begin{cases} 100 \cdot \frac{|\Delta p|}{\Delta p^{\mathrm{max}}} & \min_e E_v \geq T_v, \\ N + 100 \cdot \frac{|\Delta p|}{\Delta p^{\mathrm{max}}} + \frac{(T_v - \min_e E_v)^2}{1\mu\mathrm{eV}^2} & \min_e E_v < T_v, \end{cases} \tag{F.18}$$

where T_v is a threshold value for the valley splitting (measured in µeV), Δp^{max} is the maximum variation of p allowed between the segments, and $N > 100$ is a large number chosen such that a transition edge with $\min_e E_v \geq T_v$ has a smaller weight than a straight edge with $\min_e E_v < T_v$. We note that the exact values of the weights assumed in Eq. (F.18) are relatively unimportant for our purposes, as long as both low-E_v minima and transitions with large changes $|\Delta p|$ are penalized, relative to paths with large minimum E_v and no transitions. In this work, we choose $T_v = 50\,\mu\mathrm{eV}$ and $N = 1000$, with $\Delta p^{\mathrm{max}} = 100\,\mathrm{nm}$ for the channel-shifting protocol and $\Delta p^{\mathrm{max}} = 10\,\mathrm{mV\,nm^{-1}}$ for E-field modulation. After assigning weights to each edge in the graph, the graph traversal algorithm minimizes w to generates an optimized path across a given E_v landscape.

F.9 Further characterization of the E_z modulation strategy

In this Appendix, we further examine the performance of the electric-field (E_z) modulation strategy. In Section 7.5.2, we highlighted that E_z modulation offers improvements in shut-
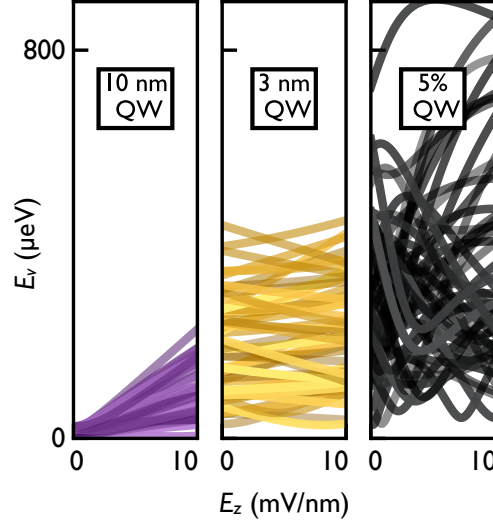
Figure F.6: Dependence of valley splitting on the vertical electric field, for the 10 nm quantum well (left), the 3 nm quantum well (middle), and the 5 % Ge quantum well (right). Each plot shows the variation of E_v as a function of E_z for 100 instantiations of alloy disorder.

tling fidelity for 5% Ge quantum wells, but not for the other quantum wells analyzed in this work. We now explain these differences. First, for devices with sharp interfaces, it is well known that the valley splitting scales linearly with E_z, as stronger E_z increases the wavefunction penetration into the top barrier [63]. For more realistic quantum wells with diffuse interfaces, we expect the average valley splitting to also scale linearly with E_z, as increasing E_z forces the wavefunction to overlap with more high-Ge layers [119]. However, for recently demonstrated heterostructures, like narrow quantum wells or quantum wells with a high Ge concentration, E_v has a nontrivial dependence on E_z, which we characterize below.

In Fig. F.6, we show the variation of E_v as a function of E_z for 100 instantiations of each quantum well. For the 10 nm quantum well (left), we notice that E_v is largely monotonically increasing with E_z, since larger E_z pulls the dot strongly into the top barrier, increasing its overlap with high-Ge layers.

For the 3 nm quantum well (middle), E_v is no longer a monotonic function of E_z. Moreover, since the dot is tightly confined inside the narrow well, the dot position (and thus E_v) is not very tunable as a function of E_z. In contrast, for the 5 % Ge quantum well (right), the quantum well is much wider and has strong local fluctuations of the Ge concentration,
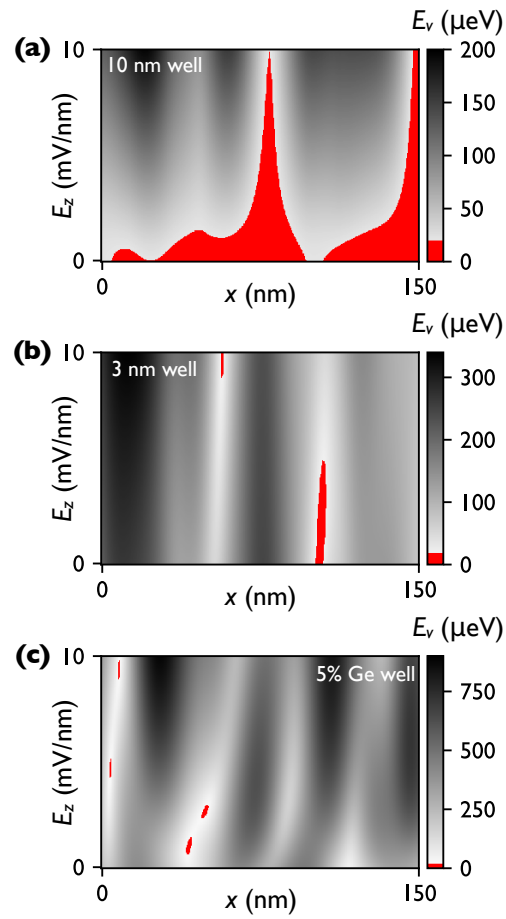
Figure F.7: Sample valley splitting landscapes as a function of position, x, and vertical field E_z, for (a) a 10 nm QW, (b) a 3 nm QW, and (c) a 5% Ge QW. In all panels, we highlight regions where $E_v < 20\,\mu$eV in red.

so small shifts in the wavefunction position can significantly alter E_v as a function of E_z. In this case, if we want to use E_z as a tuning knob to avoid low-E_v regions, this scheme can be very effective.

Figures F.7(a)-F.7(c) show sample valley splitting landscapes as a function of position, x, and vertical field, E_z, for the case of (a) a 10 nm quantum well, (b) a 3 nm quantum well, and (c) a 5% Ge quantum well. In all plots, regions with $E_v < 20$ µeV are highlighted in red. As consistent with data in Fig. F.6, we see in Fig. F.7(a) that E_v tends to increase monotonically with E_z, for any location in a 10 nm quantum well. However, since this quantum well has a relatively low average E_v, despite the large vertical field, significant regions of low E_v cannot be avoided. Indeed, we see in Fig. F.7(a) two x locations where $E_v < 20$ µeV regardless of E_z. For the 3 nm well, we have a larger average E_v, and therefore fewer zones where E_v is dangerously small. However, since E_v is not highly tunable as a function of E_z in these quantum wells, regions of low E_v tend to persist over a wide range of E_z. When E_z is held constant over a distance of 1 µm, these regions are difficult to avoid.

The situation is somewhat improved for the 5% Ge well in Fig. F.7(c). First, the large amount of alloy disorder creates much larger average valley splittings. Additionally, E_v has a non-monotonic dependence on E_z, which makes it more likely that we can find an E_z value that avoids all low E_v for a given shuttling trajectory. We find, however, that taking advantage of such non-monotonicity requires imposing fairly short segments of constant E_z. If segments are too large, one is always likely to encounter low E_v values. Still, for the 1 µm segments used in the simulations reported in the main text, we find E_z modulation does offer improved fidelities for the 5% Ge quantum well.

F.10 Further characterization of the dot-elongation strategy

In this Appendix, we provide further details on the performance of the dot-elongation tuning strategy. As a reminder, we have considered isotropic dots with orbital splittings $\hbar\omega_x = \hbar\omega_y = 2\,\mathrm{meV}$, and "elongated" dots with orbital splittings $\hbar\omega_x = 1\,\mathrm{meV}$ and $\hbar\omega_y = 4\,\mathrm{meV}$. While these choices yield dots with the same area, we find that they yield very different shuttling infidelities.

Elongating the dot in the shuttling direction has three main effects on the shuttling procedure. First, it increases the size of the dot along the shuttling direction, thereby reducing the effective length scale of the shuttling process. Since the characteristic length of valley splitting correlations depends entirely on the dot size, this means the moving dot will encounter proportionately fewer regions of low E_v on average. In Fig. F.8(a), we plot the valley splitting for an isotropic (orange) vs an elongated (blue) dot, for the same landscape; here we can clearly see the longer correlation length scale in the blue data, and the larger number of regions with low E_v in the orange data. To create these plots, we generate an atomistic model of a heterostructure and raster the lateral confinement potential across this heterostructure, computing Δ for each potential center x, using the method outlined in the main text. In Fig. F.8(b), we histogram the number of local E_v minima observed along 300 straight shuttling trajectories, for both isotropic (yellow) and elongated (blue) dots. To avoid the massive computational overhead of populating $10\,\mathrm{\mu m}$-wide heterostructures atom-by-atom, we generate these E_v landscapes randomly, using the methods outlined in Appendix F.6. Results are shown for a trajectory length of $10\,\mathrm{\mu m}$ in a $3\,\mathrm{nm}$ quantum well. Clearly, there are fewer local minima for elongated dots, leading to fewer opportunities for Landau-Zener excitations. Here, we also indicate the expected number of local minima in each case [vertical lines in Fig. F.8(b)], as derived later in this Appendix.

The second effect of dot elongation is to increase the tunability of the valley splitting

via the channel-shifting technique. Just as elongating the dot in the shuttling direction increases the characteristic length scale of valley splitting fluctuations along $\hat{x}$, narrowing the dot transverse to the shuttling trajectory reduces the characteristic fluctuation length scale along $\hat{y}$. Thus, for a fixed channel width, when we employ the channel-shifting strategy, the path-selection algorithm is effectively able to search over more variations in the E_v landscape, allowing it to identify better shuttling trajectories.

Finally, the third impact of elongating the dot is to reduce the effective shuttling velocity. This is important when passing through a narrow energy gap, because it reduces the probability of Landau-Zener excitations. To clarify this point, we examine the rate of change of the inter-valley coupling of the moving dot, $\partial_t \Delta$. Using the chain rule, we have

$$\partial_t \Delta = v \partial_x \Delta = v \left(\partial_x \Delta_R + i \partial_x \Delta_I \right) \tag{F.19}$$

where v is the shuttling velocity (assumed to be in the x-direction) and $\Delta_{R/I}$ refer to the real and imaginary components of Δ. The rate of change of Δ is therefore directly related to the spatial derivative $\partial_x \Delta$. In Fig. F.8(c), we plot histograms of $|\partial_x \Delta|$ along 300 shuttling trajectories for the 3 nm quantum well, for both isotropic (yellow) and elongated (blue) dots, using the same set of landscapes as in (b). While both of these distributions exhibit some spread, the average gradient is clearly smaller for the elongated dots. Here, we also indicate the theoretically calculated mean gradients (vertical dashed lines) and probability density functions (solid lines) for $|\partial_x \Delta|$, as derived below.

Calculation of the $\partial_x \Delta$ distributions. Since the inter-valley coupling Δ fluctuates throughout the device, the derivatives on the right-hand-side of Eq. (F.19) are random variables,
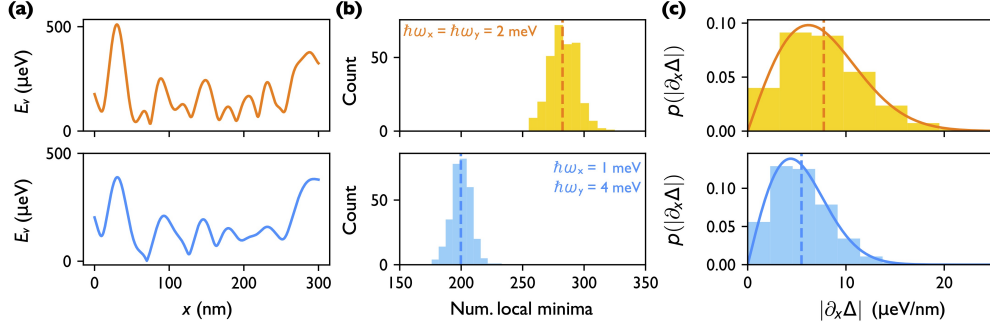
Figure F.8: Elongating the dot in the shuttling direction, and squeezing the dot in the transverse direction, reduces the magnitude of E_v fluctuations, significantly boosting shuttling fidelities. (a) Example E_v traces as a function of position for the $3\,\text{nm}$ QW, for isotropic (top, orange) and elongated (bottom, blue) quantum dots. (b) Histograms of the number of local E_v minima along a $10\,\mu\text{m}$ shuttling path, for 300 iterations with the $3\,\text{nm}$ QW, using isotropic (top, yellow) and elongated (bottom, blue) dots. Dashed lines indicate the expected number of local minima in each case ($E[N] \approx 282$ for isotropic dots and ≈ 200 for elongated dots), computed with Eq. (F.39). (c) Histograms of $|\partial_x \Delta|$ across the same 300 shuttling trajectories. Solid lines indicate the theoretical probability density functions, computed with Eq. (F.21). Dashed lines indicate the expected mean gradient, $E[|\partial_x \Delta|]$, computed with Eq. (F.23), which are 7.7 for isotropic dots and 5.5 for elongated dots.

and we may evaluate their statistics. To do so, we compute the variance of $\partial_x \Delta$:

$$
\begin{aligned}
\text{Var}\left[\partial_x \Delta\right] &= 2\text{Var}\left[\partial_x \Delta_R\right] \\
&= 2\text{Var}\left[\lim_{\delta_x \to 0} \frac{1}{\delta_x}\left(\Delta_R(x+\delta_x) - \Delta_R(x)\right)\right] \\
&= 2\lim_{\delta_x \to 0} \frac{1}{\delta_x^2}\left(\text{Var}[\Delta_R(x+\delta_x)] + \text{Var}[\Delta_R(x)]\right. \\
&\qquad\qquad\qquad \left. - 2\text{Cov}[\Delta_R(x+\delta_x), \Delta_R(x)]\right) \\
&= 2\lim_{\delta_x \to 0} \frac{1}{\delta_x^2}\left(\sigma_\Delta^2 - e^{-\delta_x^2/2a_x^2}\sigma_\Delta^2\right) \\
&= \frac{\sigma_\Delta^2}{a_x^2}
\end{aligned}
\tag{F.20}
$$

In the first line of Eq. (F.20), we use the identity $\text{Var}[A + iB] = \text{Var}[A] + \text{Var}[B]$ and the symmetry between Δ_R and Δ_I. In the second line, we use the definition of a derivative. In the third line, we interchange the order of the variance and the limit, and we use the identity $\text{Var}[A - B] = \text{Var}[A] + \text{Var}[B] - 2\text{Cov}[A, B]$. In the fourth line, we use $\text{Var}[\Delta_R(x+\delta_x)] =$

$\text{Var}[\Delta_R(x)] = \sigma_\Delta^2/2$, and we use Eq. (7.6) to evaluate $\text{Cov}[\Delta_R(x+\delta_x), \Delta_R(x)]$. Finally, in the fifth line, we evaluate the limit. As consistent with the central-limit theorem, the quantity $\partial_x \Delta$ is thus seen to be a circular complex Gaussian random variable, centered at the origin, with variance given by Eq. (F.20).

Since $\partial_x \Delta$ is complex, it is also interesting to evaluate the distribution of $|\partial_x \Delta|$. This quantity will have a Rayleigh distribution, whose probability density function is given by

$$p_{\text{Rayleigh}}(z) = \frac{z^2}{\sigma^2} \exp\left(-z^2/2\sigma^2\right), \tag{F.21}$$

where we define the spread parameter as

$$\sigma = \frac{1}{2}\text{Var}\left[\partial_x \Delta\right] = \frac{\sigma_\Delta^2}{2a_x^2}. \tag{F.22}$$

The probability density functions for $|\partial_x \Delta|$ from Eq. (F.21) are shown as solid lines in Fig. F.8(c). The expected value of $|\partial_x \Delta|$ is likewise given by

$$E[|\partial_x \Delta|] = \sqrt{\frac{\pi}{2}}\sigma. \tag{F.23}$$

Evaluating $E[|\partial_x \Delta|]$ for the elongated and isotropic dots gives the results plotted as vertical dashed lines in Fig. F.8(c).

Estimating the number of valley-splitting minima. We now compute the expected number of valley splitting minima along a straight shuttling trajectory. Typical results are shown with vertical dashed lines in Fig. F.8(b). We follow the approach of Ref. [18], which we reproduce below for completeness. Note that we restrict the analysis to just one spatial dimension.

Using the Kac-Rice formula, the number of local minima is given by [9]

$$N = \frac{1}{2}\int_x dx \; \delta(\partial_x E_v^2)|\partial_x^2 E_v^2|, \tag{F.24}$$

where the factor of $1/2$ accounts for the fact that half of the extrema points (where $\partial_x E_v^2 = 0$) are minima, and $\delta(\partial_x E_v^2)$ is a delta-function that activates when E_v^2 is at an extremum. Using the identity

$$\delta(f(x)) = \sum_i \frac{\delta(x - x_i)}{|f'(x_i)|}, \text{ where } f(x_i) = 0, \tag{F.25}$$

we see that the remaining factor $|\partial_x^2 E_v^2|$ allows the integral to count the number of extrema in E_v^2. Here, we use E_v^2 instead of E_v to simplify the calculation, without changing the results. Mathematically, the quantity E_v^2 is a χ^2 random field with two contributing Gaussian random fields, $E_v^2 = 4\Delta_R^2 + 4\Delta_I^2$. The derivatives of E_v^2 are given by

$$\partial_x E_v^2 = 8\Delta_R \partial_x \Delta_R + 8\Delta_I \partial_x \Delta_I,$$
$$\partial_x^2 E_v^2 = 8(\partial_x \Delta_R)^2 + 8\Delta_R \partial_x^2 \Delta_R + 8(\partial_x \Delta_I)^2 + 8\Delta_I \partial_x^2 \Delta_I. \tag{F.26}$$

We compute the expectation value, $E[N]$, by averaging over all possible configurations of the inter-valley coupling:

$$E[N] = \frac{1}{2} \int d\Phi \; P(\Phi) \int_x dx \; \delta(8\Delta_R \partial_x \Delta_R + 8\Delta_I \partial_x \Delta_I) |\partial_x^2 E_v^2|, \tag{F.27}$$

where we use Φ as shorthand notation for the random field configurations of $\Delta_R(x)$, $\Delta_I(x)$, and their derivatives. More explicitly, the integral element is given by

$$d\Phi = d\Delta_R d\Delta_I d(\partial_x \Delta_R) d(\partial_x \Delta_I) d(\partial_x^2 \Delta_R) d(\partial_x^2 \Delta_I), \tag{F.28}$$

and the total probability density function is given by

$$P(\Phi) = P_{\Delta, \partial_x^2 \Delta}(\Delta_R, \partial_x^2 \Delta_R) P_{\Delta, \partial_x^2 \Delta}(\Delta_I, \partial_x^2 \Delta_I) P_{\partial_x \Delta}(\partial_x \Delta_R) P_{\partial_x \Delta}(\partial_x \Delta_I). \tag{F.29}$$

Note that we do not include higher order derivatives here, since they do not appear in the integrand. Also note that the random fields Δ_R and Δ_I are independent by definition, and

any covariance of the form $\langle \Delta_i(x)\partial_x\Delta_i(x)\rangle$ or $\langle \partial_x^2\Delta_i(x)\partial_x\Delta_i(x)\rangle$ must vanish due to the $x \to -x$ symmetry of the integral, where we use angle brackets $\langle \cdot \rangle$ to denote the expectation value of a quantity over its field configurations. Thus, we are left with two probability density functions to compute: one for the first derivatives of the field, $P_{\partial_x\Delta}(\partial_x\Delta_j)$, as well as the joint probability density function for the fields and their second derivatives, $P_{\Delta,\partial_x^2\Delta}(\Delta_j, \partial_x^2\Delta_j)$. We showed above that $\partial_x\Delta_R$ and $\partial_x\Delta_I$ are Gaussian random variables with zero mean and variance $\sigma_\Delta^2/2a_x^2$. We therefore have

$$P_{\partial_x\Delta}(\partial_x\Delta_j) = \frac{a_x}{\sqrt{\pi}\sigma_\Delta} \exp\left(-(\partial_x\Delta_j)^2 a_x^2/\sigma_\Delta^2\right). \tag{F.30}$$

Finally, we compute $P_{\Delta,\partial_x^2\Delta}(\Delta_j, \partial_x^2\Delta_j)$. To do this, we need covariances of the form $\langle \Delta_j(x)\partial_x^2\Delta_j(x)\rangle$. By expressing the random fields in the reciprocal basis,

$$\Delta_j = \int \frac{dk}{2\pi} e^{ikx} \tilde{\Delta}_j(k), \tag{F.31}$$

we can evaluate

$$\langle \Delta_j(x)\partial_x^2\Delta_j(x)\rangle = -\frac{1}{2\pi} \int dk \, k^2 P(k), \tag{F.32}$$

where the power spectrum $P(k)$ is the Fourier transform of the covariance function $\langle \Delta_j(x)\Delta_j(x')\rangle$, which is provided in Eq. (7.6). Hence, we find

$$P(k) = a_x\sigma_\Delta^2\sqrt{\pi/2}\exp\left(-a_x^2 k^2/2\right). \tag{F.33}$$

We then evaluate Eq. (F.32), obtaining

$$\langle \Delta_j(x)\partial_x^2\Delta_j(x)\rangle = -\frac{\sigma_\Delta^2}{2a_x^2}. \tag{F.34}$$

Using the same technique, we can evaluate the variance as

$$\langle (\partial_x^2 \Delta_j(x))^2 \rangle = \frac{1}{2\pi} \int dk k^4 P(k) = \frac{3\sigma_\Delta^2}{2a_x^4}. \tag{F.35}$$

Since the fields Δ_j and their derivatives are Gaussian random variables with zero mean, we can define the joint probability density function as

$$
\begin{aligned}
&P_{\Delta,\partial_x^2\Delta}(\Delta_j, \partial_x^2\Delta_j) \\
&= \frac{1}{\sqrt{(2\pi)^2|\Sigma|}} \exp\left(-\frac{1}{2}\mathbf{v}^T \Sigma^{-1} \mathbf{v}\right) \\
&= \frac{a_x^2}{\sqrt{2\pi\sigma_\Delta^2}} \exp\left(-\frac{3\Delta_j^2 + 2a_x^2 \Delta_j \partial_x^2\Delta_j + a_x^4 (\partial_x^2\Delta_j)^2}{2\sigma_\Delta^2}\right),
\end{aligned}
\tag{F.36}
$$

where $\mathbf{v}^T = (\Delta_j, \partial_x^2\Delta_j)$ and the covariance matrix is given by

$$\Sigma = \frac{\sigma_\Delta^2}{2} \begin{pmatrix} 1 & -a_x^{-2} \\ -a_x^{-2} & 3a_x^{-4} \end{pmatrix}. \tag{F.37}$$

Here, we used Eq. (F.34) to populate the off-diagonal elements of Σ, and Eq. (F.35) to populate the remaining diagonal element.

We are then in a position to evaluate Eq. (F.27). First, we eliminate the δ-function and the integral over $\partial_x(\Delta_I)$ by setting $\partial_x\Delta_I = -\Delta_R\partial_x\Delta_R/\Delta_I$, which yields

$$
\begin{aligned}
E[N] &= \frac{1}{2} \int_x dx \int d\Delta_R \, d\Delta_I \, d(\partial_x\Delta_R) \, d(\partial_x^2\Delta_R) \, d(\partial_x^2\Delta_I) \\
&\times P_{\Delta,\partial_x^2\Delta}(\Delta_R, \partial_x^2\Delta_R) P_{\Delta,\partial_x^2\Delta}(\Delta_I, \partial_x^2\Delta_I) P_{\partial_x\Delta}(\partial_x\Delta_R) P_{\partial_x\Delta}\left(\frac{-\Delta_R\partial_x\Delta_R}{\Delta_I}\right) |\partial_x^2 E_v^2| \, (|8\Delta_I|)^{-1}.
\end{aligned}
\tag{F.38}
$$

Here, the probability density functions are given in Eq. (F.30) and Eq. (F.36), and the term $|\partial_x^2 E_v^2|$ is given in Eq. (F.26). The final term $(|8\Delta_I|)^{-1}$ comes from the evaluation of the δ-function, where we have used Eq. (F.25). Finally, we evaluate Eq. (F.38) numerically,
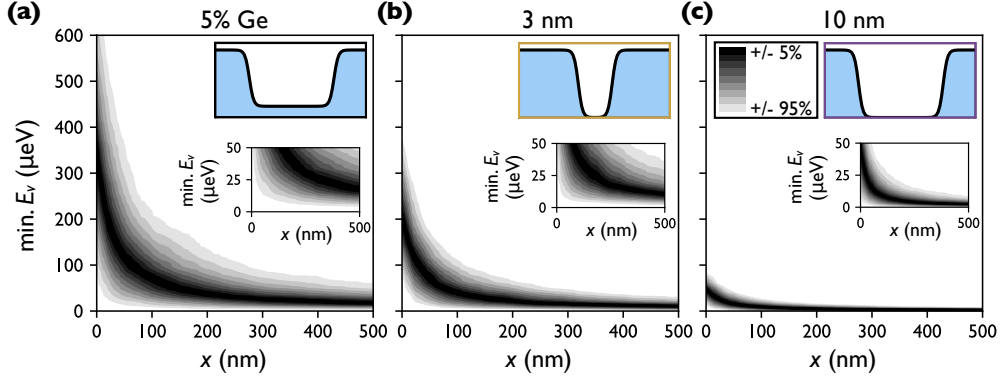
Figure F.9: The expected minimum E_v along a 1D shuttling channel quickly falls toward zero as the shuttling channel length increases. (a) For the 5% Ge quantum well, we plot the distribution of the minimum E_v experienced over 1000 simulated shuttling channels, as the length of the shuttling channel grows. We assume a vertical electric field of $E_z = 5\,\mathrm{mV\,nm^{-1}}$ and orbital energy splittings of $\hbar\omega_{\mathrm{orb}} = 2$ meV. In (b) and (c) we plot results obtained in the same way for the 3 nm and 10 nm quantum wells, respectively. The insets display the same data over a reduced y-axis range.

obtaining

$$E[N] \approx 0.4 \times \frac{x_{\mathrm{tot}}}{a_x}, \tag{F.39}$$

where x_{tot} is the total shuttling distance. The dashed lines indicating $E[N]$ in Fig. F.8(b) were computed using Eq. (F.39). Since $E[N]$ scales as $1/a_x$, we see that reducing the orbital energy from 2 to 1 meV, should cause $E[N]$ to drop by a factor of $1/\sqrt{2}$.

F.11 Minimum E_v along a shuttling channel

In this Appendix, we compute the expected minimum valley splitting along a 1D shuttling channel to justify our claim that heterostructure modification, alone, is insufficient for achieving high-fidelity shuttling results. In the disordered regime, even in heterostructures with large average E_v, a quantum dot is extremely likely to encounter regions of low E_v during shuttling, for realistically long shuttling channels, as demonstrated in Fig. F.9. For the 5% Ge quantum well, the 3 nm quantum well, and the 10 nm quantum well, we plot the distribution of the minimum valley splitting experienced along a 1D shuttling channel, as

we increase the channel distance. These distributions are determined empirically from 1,000 simulations of random valley splitting landscapes, as described in Appendix F.6. For the 10 nm quantum well, we observe that the expected minimum E_v is below $10 \, \mu\text{eV}$ for $500 \, \text{nm}$ shuttling distances. Even in high E_v quantum wells, like the 5% Ge device, we expect a minimum E_v of $\sim 20 \, \mu\text{eV}$ at distances of $500 \, \text{nm}$.

Appendix G

Supplementary Information for Chapter 8

G.1 FCI simulations

We utilize two forms of full-configuration-interaction simulations in this work, both performed within the MaSQE software package, based on the simulations of Refs. [6]. It is known that few-electron quantum dot wavefunctions are strongly impacted by Coulomb interactions [2, 38, 56–58, 219–221]. Hence, these methods are necessary to obtain accurate descriptions of these systems. The first form, which we label as "effective mass (EM)" FCI, does not account for valley physics, and is used to determine the orbital splittings in a two-electron quantum dot. The second form, which we label as "tight-binding (TB)" FCI, does account for valley physics, employing the two-band tight-binding model of Boykin et al. [25, 26] as the kinetic energy operator. In this section, we outline the procedure used in both of these simulations.

G.1.1   EM FCI simulations

For the EM FCI simulations, we start with the Hamiltonian

$$H_{\text{EM}}^{2e} = \sum_{i=1}^{2} H_{\text{EM}}^{1e}(\mathbf{r}_i) + \frac{e^2}{4\pi\epsilon_0\epsilon_r} \frac{1}{|\mathbf{r}_1 - \mathbf{r}_2|} \tag{G.1}$$

where $H_{\text{EM}}^{1e} = T + U_\phi + U_{\text{qw}}^{\text{vc}}$. T is a discretized kinetic energy operator that takes into account the longitudinal and transverse effective masses in Si, and $U_\phi = \frac{1}{2}m_t\omega_{\text{orb},1e}^2[(x - x_0)^2 + (y-y_0)^2] + eE_\phi z$ is the electrostatic confinement term, including both lateral parabolic confinement and a vertical electric field. The single-particle orbital spacing $E_{\text{orb},1e} = \hbar\omega_{\text{orb},1e}$. The quantum well potential is computed in the virtual crystal approximation, without alloy disorder:

$$U_{\text{qw}}^{\text{vc}} = \Delta E_c \frac{\bar{X}_l - 1}{X_s - 1} \tag{G.2}$$

where $\bar{X}_l$ is the expected Si concentration at layer l, averaged over the whole device, $X_s = 0.7$ is the Si concentration in the SiGe barrier (substrate), and $\Delta E_c = 150.6$ is the conduction band offset between the relaxed $\text{Si}_{0.7}\text{Ge}_{0.3}$ quantum well barrier and the strained Si quantum well [145, 164]. We model the Si concentration profile as a sigmoid function,

$$\bar{X}_l = 1 + \frac{X_s - 1}{1 + \exp[(z - z_t)/\tau]} + \frac{X_s - 1}{1 + \exp[(z_b - z)/\tau]} \tag{G.3}$$

where the quantum well top and bottom interface positions are given by z_t and z_b, the well width $W = |z_b - z_t| = 10$ nm and the interface widths $\lambda_{\text{int}} = 4\tau = 6$ ML or 0.8 nm, consistent with state-of-the-art fabrication techniques [46, 145]. These FCI simulations ignore the valley degree of freedom entirely, as well as valley-orbit effects due to steps in the quantum well interface. In order to simulate the system, we discretize our crystal lattice into rectangular cells of size $(\Delta x, \Delta y, \Delta z) = (2a_0, 2a_0, a_0/4)$. The quantum well and electrostatic confinement potentials are added as onsite parameters.

G.1.2 TB FCI simulations

For the TB FCI simulations, we adopt the same form of the two-electron FCI Hamiltonian as Eq. (G.1), where $H_{\mathrm{TB}}^{\mathrm{1e}} = T + U_\phi + U_{\mathrm{qw}}$. In the TB simulations, the kinetic operator T is given by the two-band tight-binding model of Boykin et al. in the $\hat{z}$ direction, which reproduces the position and effective mass of valley states along the $\pm z$ axis of the Brillouin zone [25, 26]. Furthermore, since these simulations aim to capture valley physics, we do not employ the virtual crystal approximation in defining U_{qw}. Instead, we adopt a model that accounts for alloy disorder. Again discretizing the system into cells of size $(\Delta x, \Delta y, \Delta z) = (2a_0, 2a_0, a_0/4)$, we model the quantum well potential as

$$U_{\mathrm{qw}}(j, k, l) = \Delta E_c \frac{1 - X_{jkl}}{1 - X_s}. \tag{G.4}$$

where X_{jkl} is the true Si concentration in the cell with indices (j, k, l). Since each cell in our lattice contains 8 atoms in the diamond cubic crystal lattice of Si/SiGe, we sample X_{jkl} from a binomial distribution according to

$$X_{jkl} \sim \mathrm{Binom}(\bar{X}_{jkl}, n_c)/n_c \tag{G.5}$$

where $\mathrm{Binom}(p, n)$ is a binomial distribution of n trials with p probability of success, $\bar{X}_{jkl}$ is the expected average Si concentration in the cell, and n_c is the number of Si/Ge atoms per cell. For our cell size, $n_c = 8$ For systems without an interface step, we set $\bar{X}_{jkl} = \bar{X}_l$, where $\bar{X}_l$ is defined in Eq. (G.3). For systems with a step, we define

$$\bar{X}_{jkl} = \bar{X}_l \Theta\left(x \leq x_{\mathrm{step}}\right) + \bar{X}_{l+1} \Theta\left(x > x_{\mathrm{step}}\right) \tag{G.6}$$

where once again $\bar{X}_l$ is given in Eq. (G.3) and $\Theta(\cdot)$ is the Heaviside step function.

G.2 Detailed description of the model Hamiltonian

In this section, we provide more details on the model Hamiltonian used in our shuttling simulations. First, we derive the spin-orbit coupling terms within the low-energy subspace, reported in Eq. (8.9) in the main text. Then, we describe the two mechanisms that can couple low-energy states to these excited orbital states: (1) valley-orbit coupling induced by alloy disorder, and (2) spin-orbit coupling. These second-order couplings lead to leakage out of the qubit subspace, so it is crucial to account for these states correctly. We consider excited states with a single orbital excitation - that is, orbital singlets S^{orb} and unpolarized triplets $T_{0,x}^{\text{orb}}$ and $T_{0,y}^{\text{orb}}$. comprised of either p_x and p_y orbital excitations. Thus, we have in total 32 states with excited orbital quantum numbers that obey Fermion antisymmetry.

G.2.1 Spin-orbit coupling within the low-energy subspace

To compute the low-energy spin-orbit Hamiltonian, we need to compute matrix elements of the form $\langle L|H_{\text{so}}^{2e}|L'\rangle$, where $|L\rangle$ and $|L'\rangle$ both come from the six-level low-energy subspace. The two-electron spin-orbit interaction decomposes into single-electron components,

$$H_{\text{so}}^{2e} = H_{\text{so}}^{(1)} \otimes I^{(2)} + I^{(1)} \otimes H_{\text{so}}^{(2)} \tag{G.7}$$

where the spin-orbit Hamiltonian is defined according to Woods et al.,

$$H_{\text{so}}^{(1)} = \alpha\tau_0(k_x\sigma_y - k_y\sigma_x) + (\beta\tau_- + \beta^*\tau_+)(k_x\sigma_x - k_y\sigma_y). \tag{G.8}$$

where τ_j are Pauli operators in valley space $\{z_-, z_+\}$, α is the Rashba spin-orbit parameter, and β is the Desselhaus spin-orbit parameter. We compute two-electron matrix elements by

expressing the basis states as product states and applying Eq. (G.7). For example,

$$
\begin{aligned}
\langle T_-^{\mathrm{spin}} S^{\mathrm{val}} | H_{\mathrm{so}} | S^{\mathrm{spin}} T_-^{\mathrm{val}} \rangle &= \frac{1}{2} \left[\langle \downarrow z_+; \downarrow z_- | - \langle \downarrow z_-; \downarrow z_+ | \right] H_{\mathrm{so}} \left[| \uparrow z_-; \downarrow z_- \rangle - | \downarrow z_-; \uparrow z_- \rangle \right] \\
&= \frac{1}{2} \left[\langle \downarrow z_+; \downarrow z_- | H_{\mathrm{so}} | \uparrow z_-; \downarrow z_- \rangle + \langle \downarrow z_-; \downarrow z_+ | H_{\mathrm{so}} | \downarrow z_-; \uparrow z_- \rangle \right] \\
&= \langle \downarrow z_+ | H_{\mathrm{so}} | \uparrow z_- \rangle
\end{aligned}
$$

$$(G.9)$$

Transforming to a frame co-moving with the quantum dot, we replace $k_j \to k_j + m_t v_j / \hbar$. Terms proportional to k vanish within the low-energy subspace, leaving just the velocity-dependent terms. In the static valley basis, we obtain the spin-orbit Hamiltonian

$$
H_{\mathrm{so}} = \begin{pmatrix}
0 & 0 & \sqrt{2}\alpha R^{\downarrow\uparrow} & \beta^* D^{\downarrow\uparrow} & -\beta D^{\downarrow\uparrow} & 0 \\
0 & 0 & \sqrt{2}\alpha R^{\uparrow\downarrow} & -\beta^* D^{\uparrow\downarrow} & \beta D^{\uparrow\downarrow} & 0 \\
\sqrt{2}\alpha R^{\downarrow\uparrow *} & \sqrt{2}\alpha R^{\uparrow\downarrow *} & 0 & 0 & 0 & 0 \\
\beta D^{\downarrow\uparrow *} & -\beta D^{\uparrow\downarrow *} & 0 & 0 & 0 & 0 \\
-\beta^* D^{\downarrow\uparrow *} & \beta^* D^{\uparrow\downarrow *} & 0 & 0 & 0 & 0 \\
0 & 0 & 0 & 0 & 0 & 0
\end{pmatrix}
$$

$$(G.10)$$

where the Rashba and Dresselhaus components

$$
\begin{aligned}
R^{ij} &= \frac{m_t}{\hbar} \left(v_x \sigma_y^{ij} - v_y k_x^{ij} \right) \\
D^{ij} &= \frac{m_t}{\hbar} \left(v_x \sigma_x^{ij} - v_y \sigma_y^{ij} \right)
\end{aligned}
$$

$$(G.11)$$

and the spin matrix elements $\sigma_\nu^{ij} = \langle i | \sigma_\nu | j \rangle$, for $i, j \in \{\uparrow, \downarrow\}$. For a magnetic field $\mathbf{B} = B(\sin\theta_B \cos\phi_B, \sin\theta_B \sin\phi_B, \cos\theta_B)$, the spin eigenstates are

$$
\begin{aligned}
| \downarrow \rangle &= -e^{-i\phi_B/2} \sin(\theta_B/2) | \uparrow_z \rangle + e^{i\phi_B/2} \cos(\theta_B/2) | \downarrow_z \rangle \\
| \uparrow \rangle &= e^{-i\phi_B/2} \cos(\theta_B/2) | \uparrow_z \rangle + e^{i\phi_B/2} \sin(\theta_B/2) | \downarrow_z \rangle
\end{aligned}
$$

$$(G.12)$$

where $|\uparrow_z\rangle$ and $|\downarrow_z\rangle$ are the eigenstates of σ_z. For an in-plane magnetic field ($\theta_B = \pi/2$), the spin matrix elements are given by

$$
\begin{aligned}
\sigma_x^{\uparrow\uparrow} &= -\sigma_x^{\downarrow\downarrow} = \cos\phi_B = 1 \\
\sigma_x^{\uparrow\downarrow} &= \left(\sigma_x^{\downarrow\uparrow}\right)^* = i\sin\phi_B = 0 \\
\sigma_y^{\uparrow\uparrow} &= -\sigma_y^{\downarrow\downarrow} = \sin\phi_B = 0 \\
\sigma_y^{\uparrow\downarrow} &= \left(\sigma_y^{\downarrow\uparrow}\right)^* = -i\cos\phi_B = -i
\end{aligned}
\tag{G.13}
$$

In this work, we set B along $\hat{x}$, so $\phi_B = 0$, resulting in the values reported on the right-hand-side of Eq. (G.13). In our simulations in the main text, we set $v_x = v$ and $v_y = 0$. If we apply the valley rotation operator U_v of Eq. (8.8), we obtain the spin-orbit terms shown in the main text. For nonzero v_x and v_y (and B along $\hat{x}$) we obtain

$$
\tilde{H}_{\text{so}} =
\begin{pmatrix}
0 & 0 & \frac{i\sqrt{2}\alpha m_t v_x}{\hbar} & -\frac{|\beta|m_t v_y}{\hbar}\sin(\phi-\phi_\beta) & -\frac{|\beta|m_t v_y}{\hbar}\sin(\phi-\phi_\beta) & -\frac{i\sqrt{2}|\beta|m_t v_y}{\hbar}\cos(\phi-\phi_\beta) \\
\cdot & 0 & -\frac{i\sqrt{2}\alpha m_t v_x}{\hbar} & -\frac{|\beta|m_t v_y}{\hbar}\sin(\phi-\phi_\beta) & -\frac{|\beta|m_t v_y}{\hbar}\sin(\phi-\phi_\beta) & -\frac{i\sqrt{2}|\beta|m_t v_y}{\hbar}\cos(\phi-\phi_\beta) \\
\cdot & \cdot & 0 & 0 & 0 & 0 \\
\cdot & \cdot & \cdot & 0 & 0 & 0 \\
\cdot & \cdot & \cdot & \cdot & 0 & 0 \\
\cdot & \cdot & \cdot & \cdot & \cdot & 0 \\
\cdot & \cdot & \cdot & \cdot & \cdot & 0
\end{pmatrix}.
\tag{G.14}
$$

The remaining terms are found by Hermitian conjugation.

G.2.2 Disorder-induced valley-orbit coupling

Here, we examine coupling to excited orbital states through disorder-induced valley-orbit coupling. There exist inter- and intra-valley couplings between states in the same orbital and states of different orbitals. These are spin-independent couplings, so all valley-orbit coupling terms preserve spin. These couplings depend on the forms of the envelope functions used for the single-particle states. For electrons in the ground state orbital manifold, we have access to

the single-electron envelope functions using EM FCI simulations, since both electrons share the shame envelope to lowest order. We label these states ψ_s. States in the first-excited orbital manifold (S^{orb} and T_0^{orb}) are composed of two single-electron wavefunctions, where one is s-like and one is p-like. We note that the s-like single-electron envelope function in an excited orbital state is, in general, not equal to ψ_s, since the different charge distribution of the p-state modifies the Coulomb potential. For simplicity, we assume that these excited orbital states are composed of one SHO ground state ψ_0 and one SHO p-state, ψ_{p_μ}, where $\mu \in \{x, y\}$:

$$
\begin{aligned}
\psi_0(x, y) &= \left(\frac{m_t\omega}{\pi\hbar}\right)^{1/4} \exp\left[-\frac{x^2 + y^2}{2a_{\text{dot}}^2}\right] \\
\psi_{p_\mu}(x, y) &= \left(\frac{m_t\omega}{\pi\hbar}\right)^{1/4} \left[\frac{\sqrt{2}\mu}{a_{\text{dot}}}\right] \exp\left[-\frac{x^2 + y^2}{2a_{\text{dot}}^2}\right]
\end{aligned} \tag{G.15}
$$

We assume the z components of ψ_s, ψ_0, and ψ_{p_μ} are identical.

Armed with these envelope functions, we can compute matrix elements. As described above, all two-particle matrix elements reduce to single-electron integrals. We compute these couplings in the static valley basis, with valley states $\{z_-, z_+\}$. First, we compute matrix elements coupling our low-energy subpsace with higher orbital states. The valley-preserving terms are given by

$$
\begin{aligned}
\langle T_-^{\text{orb}} S^{\text{val}}|U_{\text{qw}}|T_0^{\text{orb}} S^{\text{val}}\rangle &= \langle T_-^{\text{orb}} T_-^{\text{val}}|U_{\text{qw}}|T_0^{\text{orb}} T_-^{\text{val}}\rangle = \langle T_-^{\text{orb}} T_0^{\text{val}}|U_{\text{qw}}|T_0^{\text{orb}} T_0^{\text{val}}\rangle \\
&= \langle T_-^{\text{orb}} T_+^{\text{val}}|U_{\text{qw}}|T_0^{\text{orb}} T_+^{\text{val}}\rangle = \sqrt{2}\left(O_{sp_\mu}\epsilon_{ss'} + O_{ss'}\epsilon_{sp_\mu}\right)
\end{aligned} \tag{G.16}
$$

where $\mu \in \{x, y\}$, depending on whether the excited orbital state is of x or y type, and the

single-particle integrals O and ϵ are defined below. The valley-flipping terms are given by

$$\langle T_-^{\mathrm{orb}} S^{\mathrm{val}} | U_{\mathrm{qw}} | S^{\mathrm{orb}} T_-^{\mathrm{val}} \rangle = \Delta_{sp_\mu}^* O_{s0} - \Delta_{s0}^* O_{sp_\mu}$$

$$\langle T_-^{\mathrm{orb}} S^{\mathrm{val}} | U_{\mathrm{qw}} | S^{\mathrm{orb}} T_+^{\mathrm{val}} \rangle = \Delta_{s0} O_{sp_\mu} - \Delta_{sp} O_{s0}$$

$$\langle T_-^{\mathrm{orb}} S^{\mathrm{val}} | U_{\mathrm{qw}} | S^{\mathrm{orb}} T_0^{\mathrm{val}} \rangle = 0$$

$$\langle T_-^{\mathrm{orb}} T_-^{\mathrm{val}} | U_{\mathrm{qw}} | T_0^{\mathrm{orb}} T_0^{\mathrm{val}} \rangle = \Delta_{sp_\mu} O_{s0} + \Delta_{s0} O_{sp_\mu}$$

$$\langle T_-^{\mathrm{orb}} T_+^{\mathrm{val}} | U_{\mathrm{qw}} | T_0^{\mathrm{orb}} T_0^{\mathrm{val}} \rangle = \Delta_{sp_\mu}^* O_{s0} + \Delta_{s0}^* O_{sp_\mu} \qquad \text{(G.17)}$$

$$\langle T_-^{\mathrm{orb}} T_0^{\mathrm{val}} | U_{\mathrm{qw}} | T_0^{\mathrm{orb}} T_+^{\mathrm{val}} \rangle = \Delta_{sp_\mu} O_{s0} + \Delta_{s0} O_{sp_\mu}$$

$$\langle T_-^{\mathrm{orb}} T_0^{\mathrm{val}} | U_{\mathrm{qw}} | T_0^{\mathrm{orb}} T_-^{\mathrm{val}} \rangle = \Delta_{sp_\mu}^* O_{s0} + \Delta_{s0}^* O_{sp_\mu}$$

$$\langle T_-^{\mathrm{orb}} T_0^{\mathrm{val}} | U_{\mathrm{qw}} | S^{\mathrm{orb}} S^{\mathrm{val}} \rangle = 0.$$

Alloy disorder also induces diagonal corrections to the orbital energies within both the ground and first-excited manifolds, given by

$$\delta E_s = 2\epsilon_s$$
$$\delta E_{p_\mu} = \epsilon_0 + \epsilon_{p_\mu} \qquad \text{(G.18)}$$

We define the following disorder-induced single-particle integrals. First, the overlap terms:

$$O_{s0} := \langle z_\pm, s | z_\pm, 0 \rangle = \int d\mathbf{r} \, \psi_s \psi_0$$
$$O_{sp_\mu} := \langle z_\pm, s | z_\pm, p_\mu \rangle = \int d\mathbf{r} \, \psi_s \psi_{p_\mu}. \qquad \text{(G.19)}$$

Since we consider symmetric confinement potentials, we assume $O_{sp_\mu} = 0$. For a given confinement potential, we compute O_{s0} for $E_z = 1$ and $10\,\mathrm{mV\,nm^{-1}}$, taking the average of the two. We find that $O_{s0} = \{0.93, 0.95, 0.97\}$ for $E_{\mathrm{orb,1e}} = \{2, 4, 6\}$ meV. Next, the

valley-preserving single-particle integrals:

$$\epsilon_s := \langle z_\pm, s|U_{\mathrm{qw}}|z_\pm, s\rangle = \int d\mathbf{r}\, \psi_s^2 U_{\mathrm{qw}}$$

$$\epsilon_0 := \langle z_\pm, 0|U_{\mathrm{qw}}|z_\pm, 0\rangle = \int d\mathbf{r}\, \psi_0^2 U_{\mathrm{qw}}$$

$$\epsilon_{p_\mu} := \langle z_\pm, p_\mu|U_{\mathrm{qw}}|z_\pm, p_\mu\rangle = \int d\mathbf{r}\, \psi_{p_\mu}^2 U_{\mathrm{qw}} \tag{G.20}$$

$$\epsilon_{s0} := \langle z_\pm, s|U_{\mathrm{qw}}|z_\pm, 0\rangle = \int d\mathbf{r}\, \psi_s \psi_0 U_{\mathrm{qw}}$$

$$\epsilon_{sp_\mu} := \langle z_\pm, s|U_{\mathrm{qw}}|z_\pm, p_\mu\rangle = \int d\mathbf{r}\, \psi_s \psi_{p_\mu} U_{\mathrm{qw}}$$

And finally, the valley-flipping single-particle integrals:

$$\Delta_s := \langle z_-, s|U_{\mathrm{qw}}|z_+, s\rangle = \int d\mathbf{r}\, e^{-2ik_0 z}\psi_s^2 U_{\mathrm{qw}}$$

$$\Delta_{s0} := \langle z_-, s|U_{\mathrm{qw}}|z_+, 0\rangle = \int d\mathbf{r}\, e^{-2ik_0 z}\psi_s \psi_0 U_{\mathrm{qw}} \tag{G.21}$$

$$\Delta_{sp_\mu} := \langle z_-, s|U_{\mathrm{qw}}|z_+, p_\mu\rangle = \int d\mathbf{r}\, e^{-2ik_0 z}\psi_s \psi_{p_\mu} U_{\mathrm{qw}}$$

Thus, we can describe all valley-orbit coupling terms due to alloy disorder in terms of the integrals in Eqs. (G.19), (G.20), and (G.21).

G.2.3 Spin-orbit coupling to excited orbitals

Now, we examine coupling to excited orbital states through the spin-orbit interaction. Once again, we start with the spin-orbit Hamiltonian given in Eq. (G.8). This time, we examine coupling between different orbital manifolds. For these states, terms proportional to v vanish, leaving just terms proportional to k_j. To compute matrix elements of the form $\langle s|k_j|j\rangle$, we use the trick $\langle B|\mathbf{p}|A\rangle = \frac{im_t}{\hbar}(E_B - E_A)\langle B|\mathbf{r}|A\rangle$, allowing us to relate spin-orbit matrix elements to dipolar operators:

$$\langle s|k_\mu|p_\mu\rangle := k_{sp_\mu} = \frac{-im_t E_{\mathrm{orb}}}{\hbar^2} r_{sp_\mu} \tag{G.22}$$

where the dipolar operator r_{sp_μ} is defined as

$$r_{sp_\mu} = \int d\mathbf{r}\ \mu\ \psi_s \psi_{p_\mu}. \tag{G.23}$$

Plugging into Eq. (G.8), we obtain the matrix elements coupling to excited orbital states. Again, we work in the static valley basis, $\{z_+, z_-\}$. For example, spin-orbit matrix elements connecting $|T_-^{\mathrm{orb}} S^{\mathrm{val}} T_-^{\mathrm{spin}}\rangle$ to higher-energy orbital states are

$$
\begin{aligned}
\langle T_-^{\mathrm{orb}} S^{\mathrm{val}} T_-^{\mathrm{spin}} | H_{\mathrm{so}} | S^{\mathrm{orb}} S^{\mathrm{val}} S^{\mathrm{spin}} \rangle &= \frac{1}{2} O_{s0} \left(H_{--,\mu}^{\downarrow\uparrow} + H_{++,\mu}^{\downarrow\uparrow} \right) \\
\langle T_-^{\mathrm{orb}} S^{\mathrm{val}} T_-^{\mathrm{spin}} | H_{\mathrm{so}} | S^{\mathrm{orb}} T_-^{\mathrm{val}} T_0^{\mathrm{spin}} \rangle &= \frac{1}{\sqrt{2}} O_{s0} H_{+-,\mu}^{\downarrow\uparrow} \\
\langle T_-^{\mathrm{orb}} S^{\mathrm{val}} T_-^{\mathrm{spin}} | H_{\mathrm{so}} | S^{\mathrm{orb}} T_0^{\mathrm{val}} T_0^{\mathrm{spin}} \rangle &= \frac{1}{2} O_{s0} \left(H_{++,\mu}^{\downarrow\uparrow} - H_{--,\mu}^{\downarrow\uparrow} \right) = 0 \\
\langle T_-^{\mathrm{orb}} S^{\mathrm{val}} T_-^{\mathrm{spin}} | H_{\mathrm{so}} | S^{\mathrm{orb}} T_+^{\mathrm{val}} T_0^{\mathrm{spin}} \rangle &= -\frac{1}{\sqrt{2}} O_{s0} H_{+-,\mu}^{\downarrow\uparrow} \\
\langle T_-^{\mathrm{orb}} S^{\mathrm{val}} T_-^{\mathrm{spin}} | H_{\mathrm{so}} | T_0^{\mathrm{orb}} S^{\mathrm{val}} T_0^{\mathrm{spin}} \rangle &= \frac{1}{2} O_{s0} \left(H_{--,\mu}^{\downarrow\uparrow} + H_{++,\mu}^{\downarrow\uparrow} \right) \\
\langle T_-^{\mathrm{orb}} S^{\mathrm{val}} T_-^{\mathrm{spin}} | H_{\mathrm{so}} | T_0^{\mathrm{orb}} T_-^{\mathrm{val}} S^{\mathrm{spin}} \rangle &= \frac{1}{\sqrt{2}} O_{s0} H_{+-,\mu}^{\downarrow\uparrow} \\
\langle T_-^{\mathrm{orb}} S^{\mathrm{val}} T_-^{\mathrm{spin}} | H_{\mathrm{so}} | T_0^{\mathrm{orb}} T_0^{\mathrm{val}} S^{\mathrm{spin}} \rangle &= \frac{1}{2} O_{s0} \left(-H_{--,\mu}^{\downarrow\uparrow} + H_{++,\mu}^{\downarrow\uparrow} \right) = 0 \\
\langle T_-^{\mathrm{orb}} S^{\mathrm{val}} T_-^{\mathrm{spin}} | H_{\mathrm{so}} | T_0^{\mathrm{orb}} T_+^{\mathrm{val}} S^{\mathrm{spin}} \rangle &= -\frac{1}{\sqrt{2}} O_{s0} H_{-+,\mu}^{\downarrow\uparrow}
\end{aligned}
\tag{G.24}
$$

where once again $\mu \in \{x, y\}$ labels the p_x or p_y character of the excited orbital state, and we note that the spin-orbit interaction does not couple s and 0 single-particle orbitals, since they are both rotationally symmetric about the origin. The single-electron matrix elements

$H^{s_a s_b}_{z_i z_j, \mu}$ are given by

$$
\begin{aligned}
H^{s_a s_b}_{++,x} = H^{s_a s_b}_{--,x} &= -\alpha k_{sp_x} \sigma^{s_a s_b}_y \\
H^{s_a s_b}_{++,y} = H^{s_a s_b}_{--,y} &= \alpha k_{sp_y} \sigma^{s_a s_b}_x \\
H^{s_a s_b}_{+-,x} &= \beta e^{-i\phi_\beta} k_{sp_x} \sigma^{s_a s_b}_x \\
H^{s_a s_b}_{+-,y} &= -\beta e^{-i\phi_\beta} k_{sp_y} \sigma^{s_a s_b}_y \\
H^{s_a s_b}_{-+,x} &= \beta e^{i\phi_\beta} k_{sp_x} \sigma^{s_a s_b}_x \\
H^{s_a s_b}_{-+,y} &= -\beta e^{i\phi_\beta} k_{sp_y} \sigma^{s_a s_b}_y
\end{aligned}
\tag{G.25}
$$

where $s_a, s_b \in \{\uparrow, \downarrow\}$, and $\sigma^{s_a s_b}_{x(y)}$ are given in Eq. (G.13)

G.3 Generating random valley coupling fields

In this section, we describe how we generate random valley coupling fields for use in shuttling experiments. These random fields are listed in Eqs. (G.20) and (G.21). All of these terms depend on the form of the quantum well potential U_{qw}, which induces these valley-flipping and valley-preserving random fields. We can mode the quantum well potential as a sum of a deterministic (or "virtual crystal") component and a random component:

$$
U_{\mathrm{qw}} = U^{\mathrm{vc}}_{\mathrm{qw}} + \delta U_{\mathrm{qw}}
\tag{G.26}
$$

where $U^{\mathrm{vc}}_{\mathrm{qw}}$ is given in Eq. (G.2), and

$$
\delta U_{\mathrm{qw}} = \Delta E_c \frac{\delta X_{jkl}}{1 - X_s}
\tag{G.27}
$$

where $\delta X_{jkl} = X_{jkl} - \bar{X}_{jkl}$, X_{jkl} is the Si concentration in cell at position (x_j, y_k, z_l), and $\bar{X}_{jkl}$ is the expected Si concentration in this cell, as determined by the heterostructure profile. Alloy disorder contributes to the random term, δU_{qw}, whereas step disorder in the quantum

well interface modifies $U_{\mathrm{qw}}^{\mathrm{vc}}$. As we justify in Appendix G.5, we ignore interface steps in our simulations. In this regime, it suffices to replace U_{qw} with δU_{qw} in the field definitions, allowing us to derive simple statistical relationships between these fields.

Single-electron shuttling

In our single-electron shuttling experiments, we do not include any coupling to excited orbitals, since Landau-Zener-like leakage between the ground and excited valley states dominates the infidelity. Thus, there is only one disorder-dependent field to generate: the intervalley coupling

$$\Delta_0 = \int d\mathbf{r} \; e^{-2ik_0 z} \psi_0^2 \delta U_{\mathrm{qw}} \tag{G.28}$$

Following Ref. [120], this field can be modeled as a complex Gaussian random variable, with spatial covariance function

$$\langle \Delta_0(0)^* \Delta_0(x,y) \rangle = \sigma_{\Delta_0}^2 \exp\left(-\frac{x^2 + y^2}{2a_{\mathrm{dot}}^2}\right). \tag{G.29}$$

For completeness, we include a derivation of Eq. (G.29) below. We can express the spatial covariance of Δ_0 as

$$\langle \Delta_0(0)^* \Delta_0(x,y) \rangle = \langle \int d\mathbf{r}' \int d\mathbf{r}'' \; \psi_0^2(x',y') \psi_0^2(x''-x,y''-y) \psi_z^2(z) \psi_z^2(z') \delta U_{\mathrm{qw}}(\mathbf{r}') \delta U_{\mathrm{qw}}(\mathbf{r}'') \rangle \tag{G.30}$$

We approximate each integral as a discrete sum, using the transformation

$$\int d\mathbf{r} \to \Delta x \Delta y \Delta z \sum_{x,y,z}, \tag{G.31}$$

where the sum is over discrete, rectangular cells, as described in Appendix G.1. Using Eq. (G.31), we obtain

$$
\langle \Delta_0(0)^* \Delta_0(x,y) \rangle
$$
$$
= (\Delta x \Delta y \Delta z)^2 \sum_{x',y',z'} \sum_{x'',y'',z''} \psi_0^2(x',y')\psi_0^2(x''-x,y''-y)\psi_z^2(z)\psi_z^2(z')\langle \delta U_{\mathrm{qw}}(\mathbf{r}')\delta U_{\mathrm{qw}}(\mathbf{r}'') \rangle
$$
$$(G.32)$$

Since δU_{qw} is zero-mean, $\langle \delta U_{\mathrm{qw}}(\mathbf{r}')\delta U_{\mathrm{qw}}(\mathbf{r}'') \rangle = 0$ for $\mathbf{r}' \neq \mathbf{r}''$. Furthermore,

$$
\langle U_{\mathrm{qw}}^2(\mathbf{r}) \rangle = \frac{1}{n_c}\left(\frac{\Delta E_c}{X_w - X_s} \right)^2 \bar{X}_{\mathbf{r}}(1 - \bar{X}_{\mathbf{r}}),
\tag{G.33}
$$

where $\bar{X}_{\mathbf{r}}$ is the expected Si concentration at position $\mathbf{r}$, derived by taking the variance of the binomial distribution of Eq. (G.5). So, we can simplify Eq. (G.32), resulting in

$$
\langle \Delta_0(0)^* \Delta_0(x,y) \rangle = (\Delta x \Delta y \Delta z)^2 \sum_{x',y',z'} \psi_0^2(x',y')\psi_0^2(x'-x,y'-y)\psi_z^4(z)\langle \delta U_{\mathrm{qw}}^2(\mathbf{r}') \rangle
$$
$$
= \frac{\eta}{16}\frac{\Delta x \Delta y}{n_c}\left(\frac{\Delta E_c}{X_w - X_s} \right)^2 \int dx' dy' \; \psi_0(x',y')\psi_0(x'-x,y'-y) \quad (G.34)
$$

where we have converted the sums over x and y back to integrals. We have defined

$$
\eta = a_0^2 \sum_z \psi_z^4(z)\bar{X}_z(1 - \bar{X}_z)
\tag{G.35}
$$

and we have assumed $\Delta z = a_0/4$, which is the natural lattice spacing in the z direction, and that the expected Si concentration $\bar{X}_z$ is only a function of z (i.e. that there are no interface steps). The ratio $\Delta x \Delta y / n_c = a_0^2/2$, since there are 2 atoms per unit cell per layer in Si/SiGe. Evaluating the integral in Eq. (G.34), we obtain the covariance relation reported
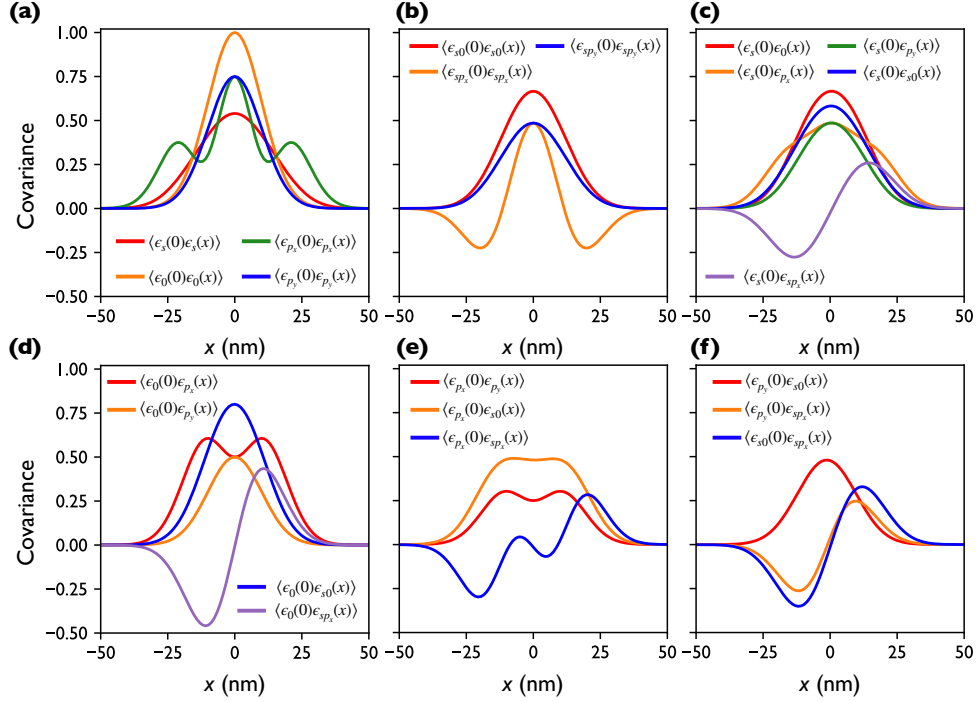
Figure G.1: Spatial covariance functions between the real fields used in shuttling simulations, in units where $\sigma_{\Delta_0}^2 = 1$. (a), (b) The autocorrelation functions for each of the 7 real fields. The remaining panels illustrate the nonzero cross-correlation functions, like those involving ϵ_s (c), ϵ_0 (d), ϵ_{p_x} (e), ϵ_{p_y} and ϵ_{s0} (f). Covariance functions are computed for $E_{\mathrm{orb},1e} = 4$ meV.

in Eq. (G.29), where we note that [119]

$$\sigma_{\Delta_0}^2 = \frac{\eta}{\pi} \left[\frac{a_0 \Delta E_c}{8 a_{\mathrm{dot}}(X_w - X_s)} \right]^2 \tag{G.36}$$

Furthermore, we assume Re Δ_0 and Im Δ_0 are uncorrelated, each with vrariance $\sigma_{\Delta_0}^2/2$. Using the Python library GSTools [136], we generate random fields with the correct covariance relationship.

G.3.1 Two-electron shuttling

For our two-electron shuttling simulations, there are more fields that need to be generated in a self-consistent manner. We have both real and complex fields, which we assume are uncorrelated with each other. We also assume the real and imaginary components of each

complex field are uncorrelated. We discretize our shuttling segment into pieces of size $1\,\mathrm{nm}$, and we compute the covariance between each field at x, with each other field at x'. For the real fields, this produces the covariance matrix

$$
\Sigma = \begin{pmatrix}
\Sigma_{\epsilon_s\epsilon_s} & \Sigma_{\epsilon_s\epsilon_0} & \Sigma_{\epsilon_s\epsilon_{px}} & \Sigma_{\epsilon_s\epsilon_{py}} & \Sigma_{\epsilon_s\epsilon_{s0}} & \Sigma_{\epsilon_s\epsilon_{spx}} & \Sigma_{\epsilon_s\epsilon_{spy}} \\
\Sigma^T_{\epsilon_s\epsilon_0} & \Sigma_{\epsilon_0\epsilon_0} & \Sigma_{\epsilon_0\epsilon_{px}} & \Sigma_{\epsilon_0\epsilon_{py}} & \Sigma_{\epsilon_0\epsilon_{s0}} & \Sigma_{\epsilon_0\epsilon_{spx}} & \Sigma_{\epsilon_0\epsilon_{spy}} \\
\Sigma^T_{\epsilon_s\epsilon_{px}} & \Sigma^T_{\epsilon_0\epsilon_{px}} & \Sigma_{\epsilon_{px}\epsilon_{px}} & \Sigma_{\epsilon_{px}\epsilon_{py}} & \Sigma_{\epsilon_{px}\epsilon_{s0}} & \Sigma_{\epsilon_{px}\epsilon_{spx}} & \Sigma_{\epsilon_{px}\epsilon_{spy}} \\
\Sigma^T_{\epsilon_s\epsilon_{py}} & \Sigma^T_{\epsilon_0\epsilon_{py}} & \Sigma^T_{\epsilon_{px}\epsilon_{py}} & \Sigma_{\epsilon_{py}\epsilon_{py}} & \Sigma_{\epsilon_{py}\epsilon_{s0}} & \Sigma_{\epsilon_{py}\epsilon_{spx}} & \Sigma_{\epsilon_{py}\epsilon_{spy}} \\
\Sigma^T_{\epsilon_s\epsilon_{s0}} & \Sigma^T_{\epsilon_0\epsilon_{s0}} & \Sigma^T_{\epsilon_{px}\epsilon_{s0}} & \Sigma^T_{\epsilon_{py}\epsilon_{s0}} & \Sigma_{\epsilon_{s0}\epsilon_{s0}} & \Sigma_{\epsilon_{s0}\epsilon_{spx}} & \Sigma_{\epsilon_{s0}\epsilon_{spy}} \\
\Sigma^T_{\epsilon_s\epsilon_{spx}} & \Sigma^T_{\epsilon_0\epsilon_{spx}} & \Sigma^T_{\epsilon_{px}\epsilon_{spx}} & \Sigma^T_{\epsilon_{py}\epsilon_{spx}} & \Sigma^T_{\epsilon_{s0}\epsilon_{spx}} & \Sigma_{\epsilon_{spx}\epsilon_{spx}} & \Sigma_{\epsilon_{spx}\epsilon_{spy}} \\
\Sigma^T_{\epsilon_s\epsilon_{spy}} & \Sigma^T_{\epsilon_0\epsilon_{spy}} & \Sigma^T_{\epsilon_{px}\epsilon_{spy}} & \Sigma^T_{\epsilon_{py}\epsilon_{spy}} & \Sigma^T_{\epsilon_{s0}\epsilon_{spy}} & \Sigma^T_{\epsilon_{spx}\epsilon_{spy}} & \Sigma_{\epsilon_{spy}\epsilon_{spy}}
\end{pmatrix}
\tag{G.37}
$$

Each of the $\Sigma_{\alpha\beta}$, for fields α and β, is an $N \times N$ covariance matrix, where N is the number of discretized points in the shuttling segment (at intervals of $1\,\mathrm{nm}$). These matrices are constructed such that $\Sigma^{ij}_{\alpha\beta} = \langle \alpha(x_i)\beta(x_j)\rangle$, where $\langle \cdot \rangle$ is the expectation value, and x_i is a position along the shuttling segment. For the real and imaginary components of the complex fields, we have a similar covariance matrix:

$$
\Sigma = \frac{1}{2}\begin{pmatrix}
\Sigma_{\Delta^*_s\Delta_s} & \Sigma_{\Delta^*_s\Delta_{s0}} & \Sigma_{\Delta^*_s\Delta_{spx}} & \Sigma_{\Delta^*_s\Delta_{spy}} \\
\Sigma^T_{\Delta^*_s\Delta_{s0}} & \Sigma_{\Delta^*_{s0}\Delta_{s0}} & \Sigma_{\Delta^*_{s0}\Delta_{spx}} & \Sigma_{\Delta^*_{s0}\Delta_{spy}} \\
\Sigma^T_{\Delta^*_s\Delta_{spx}} & \Sigma^T_{\Delta^*_{s0}\Delta_{spx}} & \Sigma_{\Delta^*_{spx}\Delta_{spx}} & \Sigma_{\Delta^*_{spx}\Delta_{spy}} \\
\Sigma^T_{\Delta^*_s\Delta_{spy}} & \Sigma^T_{\Delta^*_{s0}\Delta_{spy}} & \Sigma^T_{\Delta^*_{spx}\Delta_{spy}} & \Sigma_{\Delta^*_{spy}\Delta_{spy}}
\end{pmatrix}
\tag{G.38}
$$

The factor of $\frac{1}{2}$ comes from the division of the variance into the real and imaginary components, $\langle \alpha\beta \rangle = \langle \mathrm{Re}\,\alpha\,\mathrm{Re}\,\beta \rangle + \langle \mathrm{Im}\,\alpha\,\mathrm{Im}\,\beta \rangle$, for independent, zero-mean real and imaginary components. The complex field covariance matrices are related to the real field covariance matrices by $\Sigma_{\Delta^*_\alpha\Delta_\beta} = \Sigma_{\epsilon_\alpha\epsilon_\beta}$.

To define these covariance matrices, we need covariance functions between the different fields, $\langle \alpha(x)\beta(x')\rangle = \langle \alpha(0)\beta(x'-x)\rangle$. Some of these can be computed theoretically. Direct

calculations, like that above, yield

$$\langle\epsilon_0(x)\epsilon_0(x')\rangle = \sigma_{\Delta_0}^2 \exp\left[-\frac{(x'-x)^2}{2a_{\text{dot}}^2}\right]$$

$$\langle\epsilon_{p_x}(x)\epsilon_{p_x}(x')\rangle = \frac{\sigma_{\Delta_0}^2}{4}\left(3 - \frac{2(x'-x)^2}{a_{\text{dot}}^2} + \frac{(x'-x)^4}{a_{\text{dot}}^4}\right)\exp\left[-\frac{(x'-x)^2}{2a_{\text{dot}}^2}\right]$$

$$\langle\epsilon_{p_y}(x)\epsilon_{p_y}(x')\rangle = \frac{3\sigma_{\Delta_0}^2}{4}\exp\left[-\frac{(x'-x)^2}{2a_{\text{dot}}^2}\right]$$

$$\langle\epsilon_0(x)\epsilon_{p_x}(x')\rangle = \frac{\sigma_{\Delta_0}^2}{2}\left(1 + \frac{(x'-x)^2}{a_{\text{dot}}^2}\right)\exp\left[-\frac{(x'-x)^2}{2a_{\text{dot}}^2}\right] \tag{G.39}$$

$$\langle\epsilon_0(x)\epsilon_{p_y}(x')\rangle = \frac{\sigma_{\Delta_0}^2}{2}\exp\left[-\frac{(x'-x)^2}{2a_{\text{dot}}^2}\right]$$

$$\langle\epsilon_{p_x}(x)\epsilon_{p_y}(x')\rangle = \frac{\sigma_{\Delta_0}^2}{4}\left(1 + \frac{(x'-x)^2}{a_{\text{dot}}^2}\right)\exp\left[-\frac{(x'-x)^2}{2a_{\text{dot}}^2}\right]$$

Note that, since we consider shuttling along x, the y-coordinate of all fields remains constant, simplifying some of the covariance relationships. Other covariance functions can be set to zero on symmetry grounds. For example,

$$\langle\epsilon_s(x)\epsilon_{sp_y}(x')\rangle = 0$$

$$\langle\epsilon_0(x)\epsilon_{sp_y}(x')\rangle = 0$$

$$\langle\epsilon_{p_x}(x)\epsilon_{sp_y}(x')\rangle = 0$$

$$\langle\epsilon_{s0}(x)\epsilon_{sp_y}(x')\rangle = 0 \tag{G.40}$$

$$\langle\epsilon_{s1}(x)\epsilon_{sp_y}(x')\rangle = 0$$

$$\langle\epsilon_{p_y}(x)\epsilon_{sp_y}(x')\rangle = 0$$

The remaining covariance relationships involving ψ_s must be computed numerically, which can be done using the envelope functions ψ_s, ψ_0, and ψ_1. The envelope function ψ_s is obtained through FCI simulations, detailed above. The x and y components of ψ_0 and ψ_1 are given in Eq. (G.15); we assume these wavefunctions share the same z component as ψ_s. For example,

to compute the covariance between ϵ_s and ϵ_0, we perform the following calculation:

$$\langle \epsilon_s(\mathbf{r})\epsilon_0(\mathbf{r}') \rangle = \int d\mathbf{r}''\, \psi_s^2(\mathbf{r}'';\mathbf{r})\psi_0^2(\mathbf{r}'';\mathbf{r}')\langle H_{\text{dis}}^2 \rangle = \xi \int dx''dy''\psi_s^2(x'',y'';x,y)\psi_0^2(x'',y'';x',y)$$

$$= \sigma_{s0}^2 \frac{\int dx''dy''\, \psi_s^2(x'',y'';x,y)\psi_0^2(x'',y'';x',y)}{\int dx\, dy\, \psi_s^2(x,y;0,0)\psi_0^2(x,y;0,0)} \quad \text{(G.41)}$$

where $\xi = \int dz\, \psi_z^4(z)\langle H_{\text{dis}}^2(z)\rangle$, $\mathbf{r} = (x,y,z)$, and $\mathbf{r}' = (x',y,z)$. The integrals over z factors out, since we do not include interface steps. As a result, ψ are separable and $\langle H_{\text{dis}}^2 \rangle$ is a function only of z. Thus, if we can provide $\sigma_{s0}^2 = \langle \epsilon_{s0}^2 \rangle$, we need only to compute the wavefunction overlaps on the right-hand side, which form the correlation function. We can estimate σ_{s0}^2 by relating it to σ_{Δ_0}, which we take as a free parameter in this work:

$$\sigma_{s0}^2 = \sigma_{\Delta_0}^2 \frac{\int d\mathbf{r}\, \psi_s^2(\mathbf{r})\psi_0^2(\mathbf{r})}{\int d\mathbf{r}\, \psi_0^4(\mathbf{r})} \quad \text{(G.42)}$$

Thus, through these overlap integrals, we can compute all covariance relations numerically. These covariance relationships are illustrated in Fig. G.1. All numerical covariance relationships are computed for $E_\phi = 1$ and $10\,\text{mV}\,\text{nm}^{-1}$, which are averaged to produce the covariances shown in Fig. G.1.

With these covariance matrices, we can generate random instantiations of the fields in question, following the methods of Woods et al. First, we diagonalize Σ through the rotation $\Sigma' = U\Sigma U^\dagger$, where Σ' is a diagonal matrix. Now, we generate N random Gaussian variables, stored in vector $\mathbf{v}'$, using covariance Σ', where $N = 7n$ for the real fields, and $N = 4n$ for the complex fields. Transforming $\mathbf{v}'$ back to the original basis, $\mathbf{v} = U^\dagger \mathbf{v}'$, we have the fields stored in $\mathbf{v}$ with the correct covariance structure.

To generate random fields over $5\,\mu\text{m}$ is computationally demanding. To reduce the computational overhead, we instead generate segments of length $1\,\mu\text{m}$. Then, we interpolate between these segments at their ends. For example, between the first and second segments,
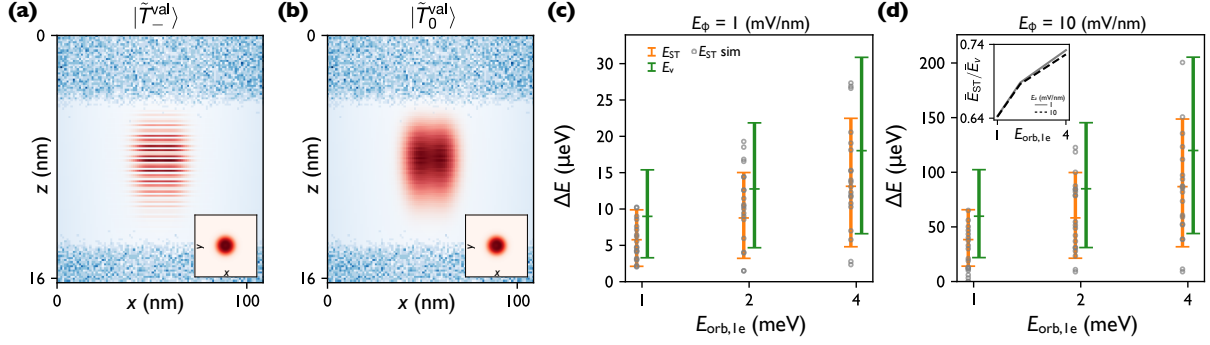
Figure G.2: (a) Ground state and (b) first excited state electron densities of a sample TB FCI simulation, computed for a heterostructure with lateral confinement $E_{\mathrm{orb},1e} = 4$ meV and vertical field $E_\phi = 1$ mV nm^{-1}. (c) Mean and 10-90 percentile ranges for the single-electron valley splitting (green) and the singlet-triplet splitting (orange) for varying lateral confinement energies $E_{\mathrm{orb},1e}$ and a vertical field $E_\phi = 1$ mV nm^{-1}. Also included are 20 TB FCI simulations of E_{ST} computed for the same heterostructure, where each point represents a different random alloy configuration (gray circles). (d) The same data as (c) for vertical fields $E_\phi = 10$ mV nm^{-1}.

we use

$$\alpha(x) = \sqrt{1 - \left(\frac{x - (l - l_{\mathrm{int}})}{l_{\mathrm{int}}}\right)^2} \alpha_0(x) + \left(\frac{x - (l - l_{\mathrm{int}})}{l_{\mathrm{int}}}\right)^2 \alpha_1(x - (l - l_{\mathrm{int}})) \qquad \text{(G.43)}$$

$l = 1$ µm is the segment length, and l_{int} is the interpolation length, x ranges from 0 to l, and $\alpha_0(x)$ and $\alpha_1(x)$ are segments that have been independently generated for x from 0 to l, The interpolation length l_{int} should be much larger than the dot correlation length a_{dot} and much smaller than the overall segment length l. We choose $l_{\mathrm{int}} = 200$ nm. While non-standard, the interpolation form used above preserves the total variance of α (a linear interpolation, for example, would reduce the variance of α).

G.4 Comparing the valley splitting and the singlet-triplet splitting

In this section, we comment on the relationship between the valley splitting and the two-electron zero magnetic field singlet-triplet splitting. The singlet-triplet splitting is known to
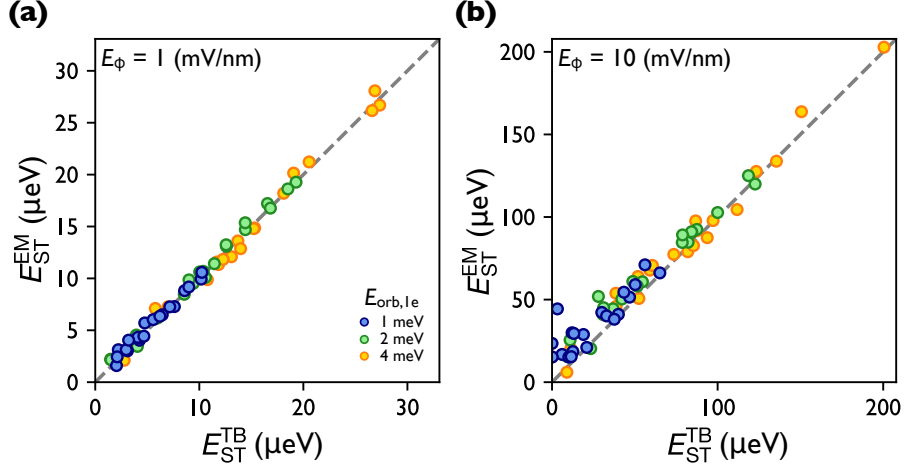
Figure G.3: Comparing TB FCI simulations with effective mass theory. We plot the singlet triplet splitting extracted from TB FCI simulations of disordered quantum wells, $E_{\mathrm{ST}}^{\mathrm{TB}}$, with the singlet-triplet splittings computed from Eq. (G.44), $E_{\mathrm{ST}}^{\mathrm{EM}}$. Each point represents a different instantiation of random alloy disorder. We include results for lateral confinement strengths $E_{\mathrm{orb},1e} = 1$ (blue), 2 (green), and $4\,\mathrm{meV}$ (orange), and for vertical fields $E_\phi = 1\mathrm{mV\,nm}^{-1}$ (a) and $10\,\mathrm{mV\,nm}^{-1}$.

depend sensitively on the symmetry of the confinement potential [57, 58]. For symmetric confinement potentials, it is limited by the valley splitting. On the other hand, for asymmetric potentials, electron-electron interactions lead to the renormalization of the singlet-triplet splitting, which is now of orbital character and often much smaller than the valley splitting. Here, we consider only the symmetric case, so the singlet-triplet splitting is well-described as a valley splitting.

To lowest order, the single-particle valley splitting is $E_v = 2|\Delta_0|$, where Δ is given in the main text Eq. (8.2). Likewise, for two electrons, the (valley) singlet-triplet splitting is given by $E_{ST} = 2|\Delta_s|$, where Δ_s is computed with Eq. (G.21). At this order, the only difference between E_v and E_{ST} is the form of the ground state envelope function. Thus, we can make a statistical comparison of these two quantities. From Ref. [119], we know the average valley splitting $\bar{E}_v = \sqrt{\pi}\sigma_{\Delta_0}$ for the one-electron case, where $\sigma_{\Delta_0}^2 = \langle \Delta_0^2 \rangle$ is the variance of the single-electron Δ_0. Likewise, in the two-electron case, using the same arguments, the average singlet-triplet splitting $\bar{E}_{ST} = \sqrt{\pi}\sigma_{\Delta_s}$, where $\sigma_{\Delta_s}^2 = \langle \Delta_s^2 \rangle$ is the variance of Δ_s. To obtain statistical properties of Δ_0 and Δ_s, we use the integral-to-sum transformation of Eq. (G.31),

resulting in

$$\Delta_{0(s)} = \frac{\Delta E_c V_c}{1 - X_s} \sum_i \sum_j \sum_k e^{-2ik_0 z_l}(1 - X_{jkl})\psi_{0(s)}^2(x_i, y_j, z_l) \tag{G.44}$$

where $V_c = \Delta x \Delta y \Delta z$ is the discretized cell volume. Computing the variance yields

$$\sigma_{\Delta_{0(s)}}^2 = \left(\frac{\Delta E_c V_c}{1 - X_s}\right)^2 \frac{1}{n_c} \sum_i \sum_j \sum_l \psi_{0(s)}(x_i, y_j, z_l)^4 \bar{X}_l(1 - \bar{X}_l), \tag{G.45}$$

where n_c is the number of atoms per cell (8 in our case). Using σ_Δ, we can characterize the distribution of resulting valley (or singlet-triplet) splittings, which are given by the Rayleigh distribution [119],

$$f_{\text{Rayleigh}}(z) = \frac{z^2}{\sigma^2} \exp\left[-\frac{z^2}{2\sigma^2}\right] \tag{G.46}$$

where $\sigma = \sqrt{2}\sigma_\Delta$. We can also define the ratio of the mean singlet-triplet splitting to the mean valley splitting for a given heterostructure,

$$\frac{\bar{E}_{ST}}{\bar{E}_v} = \frac{\sigma_{\Delta_s}}{\sigma_{\Delta_0}} \tag{G.47}$$

where $\bar{E}_v$ and $\bar{E}_{ST}$ are averaged over alloy disorder configurations. Using the EM FCI simulations described in Section G.1, we compute the single- and two-electron envelope functions for $E_{\text{orb,1e}}$ from 1 to 4 meV, and for $E_\phi = 1$ and $10\,\text{mV}\,\text{nm}^{-1}$. Using these envelope functions, we can compute σ_{Δ_s} and σ_{Δ_0}. The expected valley splitting distributions, computed from Eq. (G.46), are illustrated as colored error bars in Fig. G.2(c) and (d). In the inset to Fig. G.2(d), we plot the ratio $\bar{E}_{ST}/\bar{E}_v$, computed from Eq. (G.47). We notice that E_{ST} is consistently smaller than E_v, where $\bar{E}_{ST}/\bar{E}_v$ is between 0.64 and 0.74, depending on the confinement strength. This effect has a simple origin: since the two-electron envelope function is broadened by the Coulomb repulsion between electrons, the two-electron state is larger in area, averaging over more atomic disorder and therefore reducing σ_{Δ_s} compared to σ_{Δ_0}.

We can also use the TB FCI simulations described in Section G.1 to confirm our statistical analysis. Each of these simulations represents one instantiation of alloy disorder. Using the

same range of device parameters as above, we compute the ground state energy gap in 20 random instantiations of alloy disorder, plotted in Fig. G.2(c) and (d) [gray circles]. These data agree well with the statistical distributions of E_{ST} computed above, validating our envelope function description of these systems. For one of these simulations, we plot the ground state and first-excited state electron densities in Fig. G.2(a) and (b). We see that the ground state has clear $|T_-^{\mathrm{val}}\rangle$ character: since both electrons occupy the ground valley, the fast valley oscillations along z are visible in the electron density. Since the first excited state contains both ground and excited valley components, these fast valley oscillations are averaged out.

Finally, we can directly compare our effective mass description of the singlet-triplet splitting with tight-binding simulations, using the same 20 simulations of E_{ST} in disordered quantum wells. To do so, we compare the singlet-triplet splitting computed from TB FCI, $E_{\mathrm{ST}}^{\mathrm{TB}}$, with the singlet-triplet splitting computed from Eq. (8.2), $E_{\mathrm{ST}}^{\mathrm{EM}}$. We use ψ_s computed with the EM FCI simulations, which completely ignore the valley degree of freedom. In Fig. G.3, we plot the correlation between these quantities for electric fields $E_\phi = 1 \ \mathrm{mV\,nm}^{-1}$ (a) and $10 \ \mathrm{mV\,nm}^{-1}$ (b). Included in both plots are results for lateral confinement strengths $E_{\mathrm{orb},1e} = 1$, 2, and 4 meV. In all cases the points lie near the line $y = x$ (gray dashed line), indicating that the first-order effective mass theory is capturing most of the physics involved. This agreement is particularly strong for $E_\phi = 1 \ \mathrm{mV\,nm}^{-1}$, where vertical confinement is relatively weak, leading to small, disorder-dominated valley splittings – the regime of interest for this work.

G.5 Valley-orbit coupling due to interface steps

In this section, we discuss the role of interface steps in the quantum well. For single-electron quantum dots, single-monolayer steps in the quantum well interface have been explored as a source of valley splitting and valley-orbit coupling variation [42, 51, 58, 64, 72, 81, 92, 183].
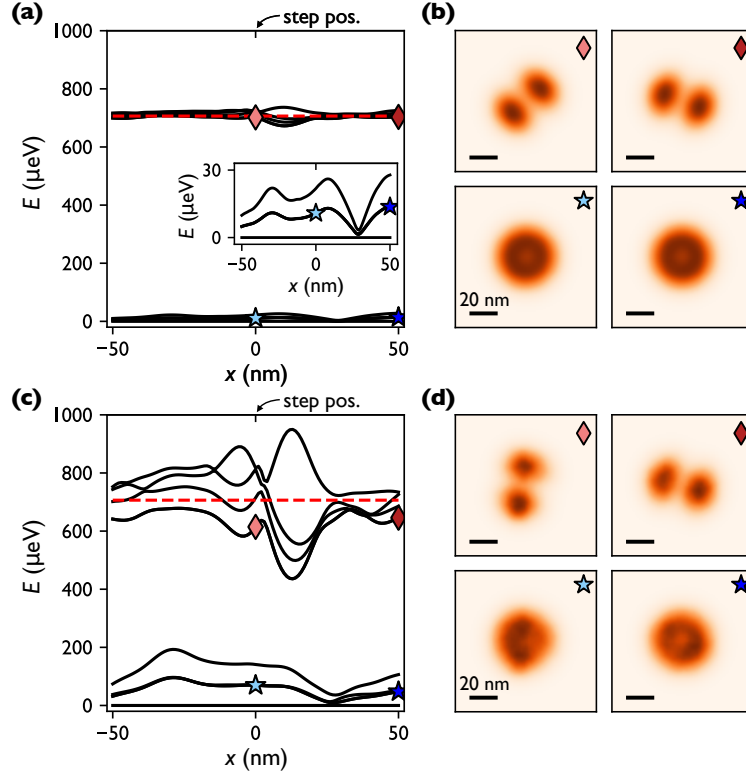
Figure G.4: Low-energy spectrum as a dot moves a cross a single-monolayer interface step. (a) We plot several of the low-lying energies of a dot moving across an interface step, computed with TB FCI simulations. The orbital splitting, computed with EM FCI, is indicated as a red dashed line. Inset: the low-lying ground state orbital energies. We use a vertical field $E_\phi = 1$ mV nm^{-1}. (b) Sample electron densities for the states marked in (a) are plotted for dots positioned on the step and far from the step. (c) and (d) show the same data as (a) and (b), computed for $E_\phi = 10$ mV nm^{-1}

More recently, it has been shown that steps are less important for the single-electron valley splitting in quantum wells without atomically sharp interfaces [119]. The same is true for inter-valley dipole moments [89]. The picture is similar in the two-electron case. Following Chapter 8, we can treat the step as a perturbation:

$$H_{\text{step}}(x, z) = \frac{\Delta E_c}{1 - X_s} \delta X_l \Theta(x > x_{\text{step}}), \tag{G.48}$$

where $\delta X_l = X_l - X_{l+1}$. We can compute the contribution of H_{step} to coupling terms in a two-electron quantum dot. For example,

$$\langle T_-^{\text{val}}|H_{\text{step}}|T_0^{\text{val}}\rangle = \sqrt{2}\langle z_-|H_{\text{step}}|z_+\rangle = \sqrt{2}\int d\mathbf{r}\, e^{-2ik_0 z}\psi_s^2 H_{\text{step}}$$
$$= \frac{\sqrt{2}}{2}\frac{\Delta E_c a_0}{4(1-X_s)}\sum_l e^{-2ik_0 z_l}\delta X_l \psi_s(z_l)^2 \quad \text{(G.49)}$$

where in the first step we have transformed the two-electron matrix element into single-particle integrals, and in the last step we have discretized the integral into a sum over cells using Eq. (G.31), and we have performed the x and y integrations. (We have assumed the step is at the center of the dot wavefunction, so the x-integration produces a factor of $\frac{1}{2}$.) In Eq. (G.49), we note that the sum over layers l includes a rapidly oscillating term, $e^{-2ik_0 z_l}$. In the case of a perfectly sharp quantum well interface, δX_l is nonzero only within one monolayer. In this case, the rapidly oscillating term does not impact the sum, and we obtain large inter-valley couplings. (This has been widely demonstrated in prior works, where interfaces have been assumed to be atomically sharp.) However, in heterostructures with wider interfaces, δX_l is nonzero across many monolayers, so the sum over a rapidly oscillating term rapidly converges to zero. Thus, for more realistic models, we do not expect steps to meaningfully contribute to inter-valley matrix elements.

While they do not meaningfully contribute to inter-valley matrix elements, steps do contribute to intra-valley terms. For example,

$$\langle T_-^{\text{val}}|H_{\text{step}}|T_-^{\text{val}}\rangle = 2\langle z_-|H_{\text{step}}|z_-\rangle = 2\int d\mathbf{r}\, \psi_s^2 H_{\text{step}} = \frac{\Delta E_c a_0}{4(1-X_s)}\sum_l \delta X_l \psi_s^2(z_l), \quad \text{(G.50)}$$

In this case, we have no rapidly oscillating term. So, as long as δX_l and $\psi_s(z_l)$ have some overlap, the intra-valley contribution of a step is non-zero. Moreover, if there is a large vertical field, ψ_s is drawn closer to the top interface, increasing the product $\delta X_l \psi_s^2(z_l)$ and therefore increasing the intra-valley coupling. While different intra-valley matrix elements

will involve different envelope functions, this observation is generic.

One way these intra-valley terms manifest is as corrections to the orbital energies. In Fig. G.4, we plot the low-energy landscape for a two-electron quantum dot as it moves across a step positioned at $x = 0$, simulated with TB FCI methods, for a particular instantiation of random alloy disorder. Results are shown for vertical fields $E_\phi = 1$ mV nm^{-1}(a) and 10 mV nm^{-1} (c). We observe two separated manifolds, one corresponding to ground state orbital levels, and one to first-excited orbital states. Electron densities for states in both manifolds, near the step and far away from it, are illustrated in Figs. G.4(b) and (d). The orbital splitting computed with EM FCI is indicated as a red dashed line in (a) and (c). In both cases, we observe fluctuations of the excited orbital energies near the position of the step (as well as fluctuations due to alloy disorder). These fluctuations are weak for small vertical fields $E_\phi = 1$ mV nm^{-1}, but much larger for strong vertical fields $E_\phi = 10$ mV nm^{-1}.

Thus, in general, steps do contribute to intra-valley terms in the Hamiltonian, even for quantum well interfaces that are not atomically sharp. However, in this work we are interested in the weak vertical field, small valley splitting limit, where these fluctuations are relatively small. Moreover, simulations of realistic heterostructures indicate the vertical field is closer to $E_\phi = 1$ mV nm^{-1} [79]. Thus, for simplicity, we ignore interface steps in this work, focusing our simulations on landscapes determined exclusively by alloy disorder.

G.6 The role of first-order spin-orbit coupling

In this section, we evaluate the role of first-order spin-orbit coupling in our simulations. In the main text, we claimed that this leakage is much weaker than second-order processes. In Fig. G.5, we compare shuttling with $E_{\mathrm{orb},1e} = 4$ meV, $\sigma_{\Delta_0} = 20$ μeV, and $v = 10$ m s^{-1} for shuttling along $\hat{x}$, shuttling at a 45 degree angle from x, and shuttling along $\hat{y}$. Since ψ_s is isotropic, we use the same 5 randomly generated fields Δ_s and ϵ_s for each shuttling direction. For these simulations, we have also removed all second-order processes, to isolate
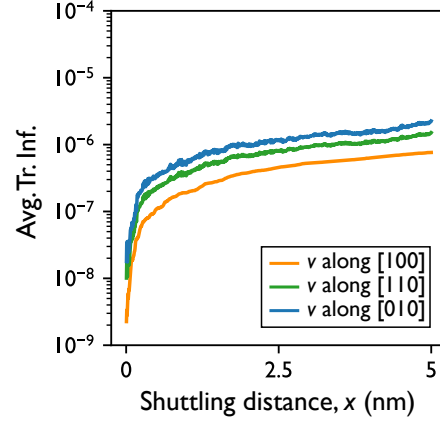
Figure G.5: First-order spin-orbit coupling is not a dominant source of infidelity. Here, we show average infidelities across 5 random disorder landscapes for shuttling along [100] (orange), [110] (green), and [010] (blue), where we have removed all second-order processes. We see that average infidelities are well below 10^{-4} in all cases.
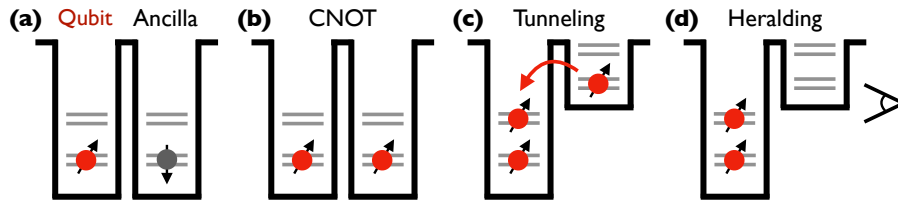
Figure G.6: Schematic illustration of a scheme to prepare the two-electron logical states from two Loss-Divincenzo qubits. (a) The spin qubit in the left dot contains the quantum information we wish to shuttle, and the right dot contains an ancilla qubit initialized in a known state $|\downarrow\rangle$. (b) A CNOT operation, controlled on the left dot, entangles the two spins. Now, our qubit is a linear combination of T_-^{spin} and T_+^{spibn}. (c) The detuning in the right dot is lifted above the valley energy of the left dot, allowing the right electron to tunnel into the left dot. (d) The tunneling process can be heralded by measuring the charge occupation of the right dot.

the dephasing associated with first-order spin-orbit coupling. In all cases, we find infidelities much smaller than those reported in the main text. Hence, regardless of shuttling direction, we expect second-order processes to dominate the shuttling infidelity.

G.7 Preparing logical basis states

The shuttling scheme explored in this work relies on two-electron spin states of the form $\alpha|\downarrow\downarrow\rangle + \beta|\uparrow\uparrow\rangle$. This is an unusual basis for a spin qubit. Here, we briefly discuss one possible

scheme to initialize these states from more typical single-spin Loss-Divincenzo qubits. We start with a double quantum dot in the (1,1) charge configuration. In the left dot, qubit $|q_1\rangle = \alpha|\downarrow\rangle + \beta|\uparrow\rangle$ contains the quantum information we wish to shuttle, and in the right dot, an ancilla qubit is initialized as $|q_2\rangle = |\downarrow\rangle$, as illustrated in Fig. G.6(a). By performing a CNOT, controlled on $|q_1\rangle$, we prepare the state $\alpha|\downarrow\downarrow\rangle + \beta|\uparrow\uparrow\rangle$, illustrated in Fig. G.6(b). This state has the correct spin configuration, but it is dispersed across a double dot. By lifting the detuning in the right dot above the excited valley energy in the left dot, the electron in the right dot may tunnel into the left dot, as illustrated in Fig. G.6(c). Since the two electrons have identical spin, the only possible configuration for the two electrons is a valley singlet. The resulting state is $\alpha|S^{\mathrm{val}}T_-^{\mathrm{spin}}\rangle + \beta|S^{\mathrm{val}}T_+^{\mathrm{spin}}\rangle$. Finally, the tunneling can be heralded by measuring the occupation in the right dot, as depicted in Fig. G.6(d).

Bibliography

[1] J. C. Abadillo-Uriel, Brandur Thorgrimsson, Dohun Kim, L W Smith, C B Simmons, Daniel R Ward, Ryan H Foote, J Corrigan, D E Savage, M G Lagally, M J Calderón, S N Coppersmith, M A Eriksson, and Mark Friesen. "Signatures of atomic-scale structure in the energy dispersion and coherence of a Si quantum-dot qubit". *Physical Review B* 98.16 (2018), p. 165438.

[2] José C. Abadillo-Uriel, Biel Martinez, Michele Filippone, and Yann-Michel Niquet. "Two-body Wigner molecularization in asymmetric quantum dot spin qubits". *Phys. Rev. B* 104 (2021), p. 195305.

[3] Rajeev Acharya et al. *Quantum error correction below the surface code threshold.* 2024. arXiv: 2408.13687 [quant-ph].

[4] Christoph Adelsberger, Stefano Bosco, Jelena Klinovaja, and Daniel Loss. "Valley-Free Silicon Fins Caused by Shear Strain". *Phys. Rev. Lett.* 133 (2024), p. 037001.

[5] Santiago Aja-Fernández and Gonzalo Vegas-Sánchez-Ferrero. *Statistical Analysis of Noise in MRI: Modeling, Filtering and Estimation.* Springer, 2016.

[6] Christopher R. Anderson, Mark F. Gyure, Sam Quinn, Andrew Pan, Richard S. Ross, and Andrey A. Kiselev. "High-precision real-space simulation of electrostatically confined few-electron states". *AIP Advances* 12 (2022).

[7] T Ando, A B Fowler, and F Stern. "Electronic properties of two-dimensional systems". *Rev. Mod. Phys.* 54.2 (1982), pp. 437–672.

[8] Frank Arute et al. "Quantum supremacy using a programmable superconducting processor". *Nature* 574.7779 (2019), pp. 505–510.

[9] J. M. Bardeen, J. R. Bond, N. Kaiser, and A. S. Szalay. "The Statistics of Peaks of Gaussian Random Fields". *Astrophysical Journal* 304 (1986), p. 15.

[10] P. Bas, A. Bostel, B. Deconihout, and D. Blavette. "A general protocol for the reconstruction of 3D atom probe data". *Applied Surface Science* 87-88 (1995), pp. 298–304.

[11] Paul Benioff. "Quantum Mechanical Models of Turing Machines That Dissipate No Energy". *Phys. Rev. Lett.* 48 (1982), pp. 1581–1585.

[12] Paul Benioff. "The computer as a physical system: A microscopic quantum mechanical Hamiltonian model of computers as represented by Turing machines". *Journal of Statistical Physics* 22.5 (1980), pp. 563–591.

[13] M. Benito, X. Croot, C. Adelsberger, S. Putz, X. Mi, J. R. Petta, and Guido Burkard. "Electric-field control and noise protection of the flopping-mode spin qubit". *Phys. Rev. B* 100 (2019), p. 125430.

[14] Samantha E. Bennett, Tim M. Smeeton, David W. Saxey, George D. W. Smith, Stewart E. Hooper, Jonathan Heffernan, Colin J. Humphreys, and Rachel A. Oliver. "Atom probe tomography characterisation of a laser diode structure grown by molecular beam epitaxy". *Journal of Applied Physics* 111.5 (2012), p. 053508.

[15] Adam Bermeister, Daniel Keith, and Dimitrie Culcer. "Charge noise, spin-orbit coupling, and dephasing of single-spin qubits". *Applied Physics Letters* 105.19 (2014), p. 192102.

[16] "Bernoulli Distribution". *Statistical Distributions*. Hoboken, NJ, USA: John Wiley & Sons, Inc., 2010, pp. 53–54.

[17] Jeff Bezanson, Alan Edelman, Stefan Karpinski, and Viral B Shah. "Julia: A fresh approach to numerical computing". *SIAM review* 59.1 (2017), pp. 65–98.

[18] Jolyon K. Bloomfield, Stephen H. P. Face, Alan H. Guth, Saarik Kalia, Casey Lam, and Zander Moss. *Number Density of Peaks in a Chi-Squared Field.* 2016. arXiv: `1612.03890 [math-ph]`.

[19] F. Borjans, D. M. Zajac, T. M. Hazard, and J. R. Petta. "Single-Spin Relaxation in a Synthetic Spin-Orbit Field". *Phys. Rev. Applied* 11 (2019), p. 044063.

[20] Péter Boross, Gábor Széchenyi, Dimitrie Culcer, and András Pályi. "Control of valley dynamics in silicon quantum dots in the presence of an interface step". *Physical Review B* 94.3 (2016), p. 035438.

[21] M. G. Borselli, K. Eng, E. T. Croke, B. M. Maune, B. Huang, R. S. Ross, A. A. Kiselev, P. W. Deelman, I. Alvarado-Rodriguez, A. E. Schmitz, M. Sokolich, K. S. Holabird, T. M. Hazard, M. F. Gyure, and A. T. Hunter. "Pauli spin blockade in undoped Si/SiGe two-electron double quantum dots". *Appl. Phys. Lett.* 99 (2011), p. 063109.

[22] M. G. Borselli, R. S. Ross, A. A. Kiselev, E. T. Croke, K. S. Holabird, P. W. Deelman, L. D. Warren, I. Alvarado-Rodriguez, I. Milosavljevic, F. C. Ku, W. S. Wong, A. E. Schmitz, M. Sokolich, M. F. Gyure, and A. T. Hunter. "Measurement of valley splitting in high-symmetry Si/SiGe quantum dots". *Applied Physics Letters* 98.12 (2011), p. 123118. eprint: `https://doi.org/10.1063/1.3569717`.

[23] Stefano Bosco, Ji Zou, and Daniel Loss. "High-Fidelity Spin Qubit Shuttling via Large Spin-Orbit Interactions". *PRX Quantum* 5 (2024), p. 020353.

[24] Jelmer M Boter, Juan P Dehollain, Jeroen P. G. Van Dijk, Yuanxing Xu, Toivo Hensgens, Richard Versluis, Henricus W. L. Naus, James S Clarke, Menno Veldhorst, Fabio Sebastiano, et al. "Spiderweb array: a sparse spin-qubit array". *Physical Review Applied* 18.2 (2022), p. 024053.

[25] T B Boykin, N Kharche, and G Klimeck. "Valley splitting in finite barrier quantum wells". *Phys. Rev. B* 77.24 (2008), p. 245320.

[26] T. B. Boykin, G. Klimeck, M. A. Eriksson, M. Friesen, S. N. Coppersmith, P. von Allmen, F. Oyafuso, and S. Lee. "Valley splitting in strained silicon quantum wells". *Appl. Phys. Lett.* 84 (2004), pp. 115–117.

[27] T. B. Boykin, G. Klimeck, M. Friesen, S. N. Coppersmith, P. von Allmen, F. Oyafuso, and S. Lee. "Valley splitting in low-density quantum-confined heterostructures studied using tight-binding models". *Phys. Rev. B* 70 (2004), p. 165325.

[28] F. R. Braakman, P. Barthelemy, C. Reichl, W. Wegscheider, and L. M. K. Vandersypen. "Long-distance coherent coupling in a quantum dot array". *Nature Nanotechnology* 8.6 (2013), pp. 432–437.

[29] James Bradbury, Roy Frostig, Peter Hawkins, Matthew James Johnson, Chris Leary, Dougal Maclaurin, George Necula, Adam Paszke, Jake VanderPlas, Skye Wanderman-Milne, and Qiao Zhang. *JAX: composable transformations of Python+NumPy programs.* Version 0.3.13. 2018.

[30] Brandon Buonacorsi, Benjamin Shaw, and Jonathan Baugh. "Simulated coherent electron shuttling in silicon quantum dots". *Physical Review B* 102.12 (2020), p. 125406.

[31] Guido Burkard, Thaddeus D. Ladd, Andrew Pan, John M. Nichol, and Jason R. Petta. "Semiconductor spin qubits". *Rev. Mod. Phys.* 95 (2023), p. 025003.

[32] Donovan Buterakos, Sankar Das Sarma, and Edwin Barnes. "Geometrical Formalism for Dynamically Corrected Gates in Multiqubit Systems". *PRX Quantum* 2 (2021), p. 010341.

[33] Edward H. Chen, Kate Raach, Andrew Pan, Andrey A. Kiselev, Edwin Acuna, Jacob Z. Blumoff, Teresa Brecht, Maxwell D. Choi, Wonill Ha, Daniel R. Hulbert, Michael P. Jura, Tyler E. Keating, Ramsey Noah, Bo Sun, Bryan J. Thomas, Matthew G. Borselli, C.A.C. Jackson, Matthew T. Rakher, and Richard S. Ross. "Detuning Axis Pulsed Spectroscopy of Valley-Orbital States in Si/Si-Ge Quantum Dots". *Physical Review Applied* 15.4 (2021), p. 044033.

[34] D. B. Chklovskii, B. I. Shklovskii, and L. I. Glazman. "Electrostatics of edge channels". *Physical Review B* 46.7 (1992), pp. 4026–4034.

[35] Sucismita Chutia, S. N Coppersmith, and Mark Friesen. "Multiscale theory of valley splitting in the conduction band of a quantum well". *Phys Rev B* 77.19 (2008), p. 193311.

[36] Elliot J. Connors, J. Nelson, Lisa F. Edge, and John M. Nichol. "Charge-noise spectroscopy of Si/SiGe quantum dots via dynamically-decoupled exchange oscillations". *Nature Communications* 13.1 (2022), p. 940.

[37] Elliot J. Connors, JJ Nelson, Haifeng Qiao, Lisa F. Edge, and John M. Nichol. "Low-frequency charge noise in Si/SiGe quantum dots". *Phys. Rev. B* 100 (2019), p. 165305.

[38] J. Corrigan, J. P. Dodson, H. Ekmel Ercan, J. C. Abadillo-Uriel, Brandur Thorgrimsson, T. J. Knapp, Nathan Holman, Thomas McJunkin, Samuel F. Neyens, E. R. MacQuarrie, Ryan H. Foote, L. F. Edge, Mark Friesen, S. N. Coppersmith, and M. A. Eriksson. "Coherent Control and Spectroscopy of a Semiconductor Quantum Dot Wigner Molecule". *Phys. Rev. Lett.* 127 (2021), p. 127701.

[39] J. Corrigan, Benjamin Harpt, Nathan Holman, Rusko Ruskov, Piotr Marciniec, D. Rosenberg, D. Yost, R. Das, William D. Oliver, R. McDermott, Charles Tahan, Mark Friesen, and M.A. Eriksson. "Longitudinal coupling between a Si/Si$_{1-x}$Ge$_x$ double quantum dot and an off-chip TiN resonator". *Phys. Rev. Appl.* 20 (2023), p. 064005.

[40] X. Croot, X. Mi, S. Putz, M. Benito, F. Borjans, G. Burkard, and J. R. Petta. "Flopping-mode electric dipole spin resonance". *Phys. Rev. Res.* 2 (2020), p. 012006.

[41] Dimitrie Culcer, Xuedong Hu, and S. Das Sarma. "Dephasing of Si spin qubits due to charge noise". *Appl. Phys. Lett.* 95 (2009), p. 073102.

[42] Dimitrie Culcer, Xuedong Hu, and S. Das Sarma. "Interface roughness, valley-orbit coupling, and valley manipulation in quantum dots". *Phys. Rev. B* 82 (2010), p. 205315.

[43] Alessandro David, Akshay Menon Pazhedath, Lars R. Schreiber, Tommaso Calarco, Hendrik Bluhm, and Felix Motzoi. *Long distance spin shuttling enabled by few-parameter velocity optimization.* 2024. arXiv: 2409.07600 [quant-ph].

[44] J. H. Davies. *The Physics of Low-Dimensional Semiconductors.* Cambridge, UK: Cambridge University Press.

[45] Maxim De Smet, Yuta Matsumoto, Anne-Marije J Zwerver, Larysa Tryputen, Sander L de Snoo, Sergey V Amitonov, Amir Sammak, Nodar Samkharadze, Önder Gül, Rick NM Wasserman, et al. *High-fidelity single-spin shuttling in silicon.* 2024. arXiv: 2406.07267 [cond-mat.mes-hall].

[46] Davide Degli Esposti, Lucas E. A. Stehouwer, Önder Gül, Nodar Samkharadze, Corentin Déprez, Marcel Meyer, Ilja N. Meijer, Larysa Tryputen, Saurabh Karwal, Marc Botifoll, Jordi Arbiol, Sergey V. Amitonov, Lieven M. K. Vandersypen, Amir Sammak, Menno Veldhorst, and Giordano Scappucci. "Low disorder and high valley splitting in silicon". *npj Quantum Information* 10.1 (2024), p. 32.

[47] D Deutsch. "Quantum-theory, the Church-Turing Principle and the unviversal quantum computer". *P. Roy. Soc. Lond. A Mat.* 400.1818 (1985), pp. 97–117.

[48] L. DiCarlo, H. J. Lynch, A. C. Johnson, L. I. Childress, K. Crockett, C. M. Marcus, M. P. Hanson, and A. C. Gossard. "Differential Charge Sensing and Charge Delocalization in a Tunable Double Quantum Dot". *Phys. Rev. Lett.* 92.22 (2004), p. 226801.

[49] D. P. DiVincenzo. "The physical implementation of quantum computation". *Fortschr. Phys.* 48.9-11 (2000), pp. 771–783.

[50] D. P. DiVincenzo, D. Bacon, J. Kempe, G. Burkard, and K. B. Whaley. "Universal quantum computation with the exchange interaction". *Nature* 408.6810 (2000), p. 339.

[51] J. P. Dodson, H. Ekmel Ercan, J. Corrigan, Merritt P. Losert, Nathan Holman, Thomas McJunkin, L. F. Edge, Mark Friesen, S. N. Coppersmith, and M. A. Eriksson. "How Valley-Orbit States in Silicon Quantum Dots Probe Quantum Well Interfaces". *Phys. Rev. Lett.* 128 (2022), p. 146802.

[52] J P Dodson, Nathan Holman, Brandur Thorgrimsson, Samuel F Neyens, E R MacQuarrie, Thomas McJunkin, Ryan H Foote, L F Edge, S N Coppersmith, and M A Eriksson. "Fabrication process and failure analysis for robust quantum dots in silicon". *Nanotechnology* 31.50 (2020), p. 505001.

[53] P. Dutta and P. M. Horn. "Low-frequency fluctuations in solids: $\frac{1}{f}$ noise". *Rev. Mod. Phys.* 53 (1981), pp. 497–516.

[54] O. Dyck, D. N. Leonard, L. F. Edge, C. A. Jackson, E. J. Pritchett, P. W. Deelman, and J. D. Poplawsky. "Accurate Quantification of Si/SiGe Interface Profiles via Atom Probe Tomography". *Adv. Mater. Interfaces* 4 (2017), p. 1700622.

[55] J. M. Elzerman, R. Hanson, L. H. Willems van Beveren, L. M. K. Vandersypen, and L. P. Kouwenhoven. "Excited-state spectroscopy on a nearly closed quantum dot via charge detection". *Appl. Phys. Lett.* 84 (2004), pp. 4617–4619.

[56] H. Ekmel Ercan, Christopher R. Anderson, S. N. Coppersmith, Mark Friesen, and Mark F. Gyure. *Multielectron dots provide faster Rabi oscillations when the core electrons are strongly confined.* 2023. arXiv: 2303.02958 [cond-mat.mes-hall].

[57] H. Ekmel Ercan, S. N. Coppersmith, and Mark Friesen. "Strong electron-electron interactions in Si/SiGe quantum dots". *Phys. Rev. B* 104 (2021), p. 235302.

[58] H. Ekmel Ercan, Mark Friesen, and S. N. Coppersmith. "Charge-Noise Resilience of Two-Electron Quantum Dots in Si/SiGe Heterostructures". *Phys. Rev. Lett.* 128 (2022), p. 247701.

[59] Yi Feng and Robert Joynt. "Enhanced valley splitting in Si layers with oscillatory Ge concentration". *Phys. Rev. B* 106 (2022), p. 085304.

[60] Rifat Ferdous, Erika Kawakami, Pasquale Scarlino, MichałP. Nowak, D. R. Ward, D. E. Savage, M. G. Lagally, S. N. Coppersmith, Mark Friesen, Mark A. Eriksson, Lieven M. K. Vandersypen, and Rajib Rahman. "Valley dependent anisotropic spin splitting in silicon quantum dots". *npj Quantum Information* 4.1 (2018), p. 26.

[61] Richard P. Feynman. "Simulating physics with computers". *International Journal of Theoretical Physics* 21.6 (1982), pp. 467–488.

[62] Adam Frees, John King Gamble, Daniel R Ward, Robin Blume-Kohout, MA Eriksson, Mark Friesen, and SN Coppersmith. "Compressed optimization of device architectures for semiconductor quantum devices". *Physical Review Applied* 11.2 (2019), p. 024063.

[63] M Friesen, S Chutia, C Tahan, and S N Coppersmith. "Valley splitting theory of SiGe/Si/SiGe quantum wells". *Phys. Rev. B* 75 (2007), p. 115318.

[64] M. Friesen, M. A. Eriksson, and S. N. Coppersmith. "Magnetic field dependence of valley splitting in realistic Si/SiGe quantum wells". *Appl. Phys. Lett.* 89 (2006), p. 202106.

[65] Mark Friesen and S. N Coppersmith. "Theory of valley-orbit coupling in a Si/SiGe quantum dot". *Phys. Rev. B* 81.11 (2010), p. 115324.

[66] Collin C. D. Frink, Benjamin D. Woods, Merritt P. Losert, E. R. MacQuarrie, M. A. Eriksson, and Mark Friesen. *Reducing strain fluctuations in quantum dot devices by gate-layer stacking.* 2024. arXiv: 2312.09235 [cond-mat.mes-hall].

[67] Takafumi Fujita, Timothy Alexander Baart, Christian Reichl, Werner Wegscheider, and Lieven Mark Koenraad Vandersypen. "Coherent shuttle of electron-spin states". *npj Quantum Information* 3.1 (2017), p. 22.

[68] John King Gamble, M. A. Eriksson, S. N. Coppersmith, and Mark Friesen. "Disorder-induced valley-orbit hybrid states in Si quantum dots". *Phys. Rev. B* 88 (2013), p. 035310.

[69] John King Gamble, Patrick Harvey-Collard, N Tobias Jacobson, Andrew D Baczewski, Erik Nielsen, Leon Maurer, Inès Montaño, Martin Rudolph, MS Carroll, CH Yang, A Rossi, AS Dzurak, and Richard P Muller. "Valley splitting of single-electron Si MOS quantum dots". *Appl. Phys. Lett.* 109.25 (2016), p. 253101.

[70] John King Gamble, N. Tobias Jacobson, Erik Nielsen, Andrew D. Baczewski, Jonathan E. Moussa, Inès Montaño, and Richard P. Muller. "Multivalley effective mass theory simulation of donors in silicon". *Phys. Rev. B* 91 (2015), p. 235318.

[71] Florian Ginzel, Adam R. Mills, Jason R. Petta, and Guido Burkard. "Spin shuttling in a silicon double quantum dot". *Phys. Rev. B* 102 (2020), p. 195418.

[72] S. Goswami, K. A. Slinker, M. Friesen, L. M. McGuire, J. L. Truitt, C. Tahan, L. J. Klein, J. O. Chu, P. M. Mooney, D. W. van der Weide, R. Joynt, S. N. Coppersmith, and M. A. Eriksson. "Controllable valley splitting in silicon quantum devices". *Nat. Phys.* 3 (2007), pp. 41–45.

[73] LK Grover. "Quantum mechanics helps in searching for a needle in a haystack". *Phys. Rev. Lett.* 79.2 (1997), pp. 325–328.

[74] Utkan Güngördü and J. P. Kestner. "Robust quantum gates using smooth pulses and physics-informed neural networks". *Phys. Rev. Res.* 4 (2022), p. 023155.

[75] *Gwyddion documentation, Chapter 4: One-Dimensional Roughness Parameters.* http://gwyddion.net/documentation/user-guide-en/roughness-iso.html. Accessed: 2021-06-29.

[76] Wonill Ha, Sieu D. Ha, Maxwell D. Choi, Yan Tang, Adele E. Schmitz, Mark P. Levendorf, Kangmu Lee, James M. Chappell, Tower S. Adams, Daniel R. Hulbert, Edwin Acuna, Ramsey S. Noah, Justine W. Matten, Michael P. Jura, Jeffrey A. Wright, Matthew T. Rakher, and Matthew G. Borselli. "A Flexible Design Platform for Si/SiGe Exchange-Only Qubits with Low Disorder". *Nano Lett.* 22 (2022), 1443–1448.

[77] Charles R. Harris et al. "Array programming with NumPy". *Nature* 585.7825 (2020), pp. 357–362.

[78] Nico W. Hendrickx, William I. L. Lawrie, Maximilian Russ, Floor van Riggelen, Sander L. de Snoo, Raymond N. Schouten, Amir Sammak, Giordano Scappucci, and Menno Veldhorst. "A four-qubit germanium quantum processor". *Nature* 591.7851 (2021), pp. 580–585.

[79] Arne Hollmann, Tom Struck, Veit Langrock, Andreas Schmidbauer, Floyd Schauer, Tim Leonhardt, Kentarou Sawano, Helge Riemann, Nikolay V. Abrosimov, Dominique Bougeard, and Lars R. Schreiber. "Large, Tunable Valley Splitting and Single-Spin Relaxation Mechanisms in a Si/Si_xGe_{1-x} Quantum Dot". *Phys. Rev. Applied* 13 (2020), p. 034068.

[80] Nathan Holman, D. Rosenberg, D. Yost, J. L. Yoder, R. Das, William D. Oliver, R. McDermott, and M. A. Eriksson. "3D integration and measurement of a semiconductor double quantum dot with a high-impedance TiN resonator". *npj Quantum Information* 7.1 (2021), p. 137.

[81] Amin Hosseinkhani and Guido Burkard. "Electromagnetic control of valley splitting in ideal and disordered Si quantum dots". *Phys. Rev. Research* 2 (2020), p. 043180.

[82] Amin Hosseinkhani and Guido Burkard. "Relaxation of single-electron spin qubits in silicon in the presence of interface steps". *Phys. Rev. B* 104 (2021), p. 085309.

[83] Rui-Zi Hu, Rong-Long Ma, Ming Ni, Yuan Zhou, Ning Chu, Wei-Zhu Liao, Zhen-Zhen Kong, Gang Cao, Gui-Lei Wang, Hai-Ou Li, and Guo-Ping Guo. "Flopping-mode spin qubit in a Si-MOS quantum dot". *Applied Physics Letters* 122.13 (2023), p. 134002.

[84] Jonathan Y. Huang et al. *High-fidelity operation and algorithmic initialisation of spin qubits above one kelvin*. 2023. arXiv: `arXiv:2308.02111` [`quant-ph`].

[85] J. D. Hunter. "Matplotlib: A 2D graphics environment". *Computing in Science & Engineering* 9.3 (2007), pp. 90–95.

[86] A. Imamoḡlu, D. D. Awschalom, G. Burkard, D. P. DiVincenzo, D. Loss, M. Sherwin, and A. Small. "Quantum Information Processing Using Quantum Dot Spins and Cavity QED". *Phys. Rev. Lett.* 83 (1999), pp. 4204–4207.

[87] Baptiste Jadot, Pierre-André Mortemousque, Emmanuel Chanrion, Vivien Thiney, Arne Ludwig, Andreas D. Wieck, Matias Urdampilleta, Christopher Bäuerle, and Tristan Meunier. "Distant spin entanglement via fast and coherent electron shuttling". *Nature Nanotechnology* 16.5 (2021), pp. 570–575.

[88] A.M. Jones, E.J. Pritchett, E.H. Chen, T.E. Keating, R.W. Andrews, J.Z. Blumoff, L.A. De Lorenzo, K. Eng, S.D. Ha, A.A. Kiselev, S.M. Meenehan, S.T. Merkel, J.A. Wright, L.F. Edge, R.S. Ross, M.T. Rakher, M.G. Borselli, and A. Hunter. "Spin-Blockade Spectroscopy of Si/Si-Ge Quantum Dots". *Phys. Rev. Applied* 12 (2019), p. 014026.

[89] David W. Kanaar, H. Ekmel Ercan, Mark F. Gyure, and J. P. Kestner. *Proposed real-time charge noise measurement via valley state reflectometry*. 2024. arXiv: `2402.14765` [`cond-mat.mes-hall`].

[90] B E Kane. "A silicon-based nuclear spin quantum computer". *Nature* 393.6681 (1998), pp. 133–137.

[91] E. Kawakami, P. Scarlino, D. R. Ward, F. R. Braakman, D. E. Savage, M. G. Lagally, M. Friesen, S. N. Coppersmith, M. A. Eriksson, and L. M. K. Vandersypen. "Electrical control of a long-lived spin qubit in a Si/SiGe quantum dot". *Nat. Nanotechnol.* 9 (2014), pp. 666–670.

[92] N Kharche, M Prada, T B Boykin, and G Klimeck. "Valley splitting in strained silicon quantum wells modeled with 2° miscuts, step disorder, and alloy disorder". *Appl. Phys. Lett.* 90.9 (2007), p. 092109.

[93] G. Klimeck, S.S. Ahmed, Hansang Bae, N. Kharche, S. Clark, B. Haley, Sunhee Lee, M. Naumov, Hoon Ryu, F. Saied, M. Prada, M. Korkusinski, T.B. Boykin, and R. Rahman. "Atomistic Simulation of Realistically Sized Nanodevices Using NEMO 3-D—Part I: Models and Benchmarks". *IEEE Transactions on Electron Devices* 54.9 (2007), pp. 2079–2089.

[94] Gerhard Klimeck, Shaikh Shahid Ahmed, Neerav Kharche, Marek Korkusinski, Muhammad Usman, Marta Prada, and Timothy B. Boykin. "Atomistic Simulation of Realistically Sized Nanodevices Using NEMO 3-D—Part II: Applications". *IEEE Transactions on Electron Devices* 54.9 (2007), pp. 2090–2099.

[95] Jan Klos, Fabian Hassler, Pascal Cerfontaine, Hendrik Bluhm, and Lars R. Schreiber. "Calculation of tunnel couplings in open gate-defined disordered quantum dot systems". *Phys. Rev. B* 98 (2018), p. 155320.

[96] Jan Klos, Jan Tröger, Jens Keutgen, Merritt P. Losert, Nikolay V. Abrosimov, Joachim Knoch, Hartmut Bracht, Susan N. Coppersmith, Mark Friesen, Oana Cojocaru-Mirédin, Lars R. Schreiber, and Dominique Bougeard. "Atomistic Compositional Details and Their Importance for Spin Qubits in Isotope-Purified Silicon Quantum Wells". *Advanced Science* (2024), p. 2407442.

[97] Sebastian Koelling, Simone Assali, Mahmoud Atalla, Aashish Kumar, Anis Attiaoui, Mario Lodari, Amir Sammak, Giordano Scappucci, and Oussama Moutanabbir. "*(Invited)* Probing Semiconductor Heterostructures from the Atomic to the Micrometer Scale". *ECS Transactions* 98.5 (2020), pp. 447–455.

[98] Sebastian Koelling, Matthieu Gilbert, Jozefien Goossens, Andriy Hikavyy, Olivier Richard, and Wilfried Vandervorst. "High depth resolution analysis of Si/SiGe multilayers with the atom probe". *Applied Physics Letters* 95.14 (2009), p. 144106.

[99] T. S. Koh, J. K. Gamble, M. Friesen, M. A. Eriksson, and S. N. Coppersmith. "Pulse-gated quantum dot hybrid qubit". *Phys. Rev. Lett.* 109 (2012), p. 250503.

[100] David Kohen, Vijay D'Costa, Nupur Bhargava, and John Tolle. "Abrupt SiGe-to-Si interface: influence of chemical vapor deposition processes and characterization by different metrology techniques". *Semiconductor Science and Technology* 33.10 (2018), p. 104003.

[101] B. Koiller, X. Hu, and S. Das Sarma. "Exchange in Silicon-Based Quantum Computer Architecture". *Phys. Rev. Lett.* 88.2 (2001), p. 027903.

[102] L. P. Kouwenhoven, C. M. Marcus, P. L. McEuen, S. Tarucha, R. M. Westervelt, and N. S. Wingreen. "Mesoscopic Electron Transport". Ed. by L. L. Sohn, L.P. Kouwenhoven, and G. Schön. Vol. 345. Kluwer, 1997. Chap. Electron Transport in Quantum Dots, p. 105.

[103] Ludwik Kranz, Samuel Keith Gorman, Brandur Thorgrimsson, Yu He, Daniel Keith, Joris Gerhard Keizer, and Michelle Yvonne Simmons. "Exploiting a Single-Crystal Environment to Minimize the Charge Noise on Qubits in Silicon". *Advanced Materials* 32.40 (2020), p. 2003361.

[104] Jan A Krzywda and Łukasz Cywiński. *Decoherence of electron spin qubit during transfer between two semiconductor quantum dots at low magnetic fields.* 2024. arXiv: 2405.12185 [cond-mat.mes-hall].

[105] Jan A. Krzywda. "Interplay of charge noise and coupling to phonons in adiabatic electron transfer between quantum dots". *Phys. Rev. B* 104 (2021), p. 075439.

[106] Matthias Künne, Alexander Willmes, Max Oberländer, Christian Gorjaew, Julian D. Teske, Harsh Bhardwaj, Max Beer, Eugen Kammerloher, René Otten, Inga Seidler, Ran Xue, Lars R. Schreiber, and Hendrik Bluhm. "The SpinBus architecture for scaling spin qubits with electron shuttling". *Nature Communications* 15.1 (2024), p. 4977.

[107] K. Lai, W. Pan, D. C. Tsui, S. Lyon, M. Mühlberger, and F. Schäffler. "Two-Flux Composite Fermion Series of the Fractional Quantum Hall States in Strained Si". *Physical Review Letters* 93.15 (2004), p. 156805.

[108] Andreas J Landig, Jonne V Koski, Pasquale Scarlino, UC Mendes, Alexandre Blais, Christian Reichl, Werner Wegscheider, Andreas Wallraff, Klaus Ensslin, and T Ihn. "Coherent spin–photon coupling using a resonant exchange qubit". *Nature* 560.7717 (2018), pp. 179–184.

[109] Veit Langrock, Jan A. Krzywda, Niels Focke, Inga Seidler, Lars R. Schreiber. "Blueprint of a Scalable Spin Qubit Shuttle Device for Coherent Mid-Range Qubit Transfer in Disordered Si/SiGe/SiO$_2$". *PRX Quantum* 4 (2023), p. 020305.

[110] D. J. Larson, T. J. Prosa, R. M. Ulfig, B. P. Geiser, and T. F. Kelly. *Local electrode atom probe tomography.* Vol. 4. Springer, 2013, p. 020305.

[111] W. I. L. Lawrie, H. G. J. Eenink, N. W. Hendrickx, J. M. Boter, L. Petit, S. V. Amitonov, M. Lodari, B. Paquelet Wuetz, C. Volk, S. G. J. Philips, G. Droulers, N. Kalhor, F. van Riggelen, D. Brousse, A. Sammak, L. M. K. Vandersypen, G. Scappucci, and M. Veldhorst. "Quantum dot arrays in silicon and germanium". *Applied Physics Letters* 116.8 (2020), p. 080501.

[112] Qiuzi Li, Dimitrie Culcer, Xuedong Hu, and S. Das Sarma. "Exchange coupling in silicon quantum dots: Theoretical considerations for quantum computation". *Phys. Rev. B* 81 (2010), p. 085313.

[113] Ruoyu Li, Luca Petit, David P. Franke, Juan Pablo Dehollain, Jonas Helsen, Mark Steudtner, Nicole K. Thomas, Zachary R. Yoscovits, Kanwal J. Singh, Stephanie Wehner, Lieven M. K. Vandersypen, James S. Clarke, and Menno Veldhorst. "A crossbar network for silicon quantum dot qubits". *Science Advances* 4 (2018), p. 7.

[114] Xiao Li, Edwin Barnes, Jason P Kestner, and S Das Sarma. "Intrinsic errors in transporting a single-spin qubit through a double quantum dot". *Physical Review A* 96.1 (2017), p. 012309.

[115] Jonas R. F. Lima and Guido Burkard. "Interface and electromagnetic effects in the valley splitting of Si quantum dots". *Mater. Quantum. Technol.* 3 (2023), p. 025004.

[116] Jonas R. F. Lima and Guido Burkard. *Superadiabatic Landau-Zener transitions.* 2024. arXiv: 2408.03173 [quant-ph].

[117] Jonas R. F. Lima and Guido Burkard. "Valley splitting depending on the size and location of a silicon quantum dot". *Phys. Rev. Mater.* 8 (2024), p. 036202.

[118] S Lloyd. "Universal quantum simulators". *Science* 273.5278 (1996), pp. 1073–1078.

[119] Merritt P. Losert, M. A. Eriksson, Robert Joynt, Rajib Rahman, Giordano Scappucci, Susan N. Coppersmith, and Mark Friesen. "Practical strategies for enhancing the valley splitting in Si/SiGe quantum wells". *Phys. Rev. B* 108 (2023), p. 125405.

[120] Merritt P. Losert, Max Oberländer, Julian D. Teske, Mats Volmer, Lars R. Schreiber, Hendrik Bluhm, S. N. Coppersmith, and Mark Friesen. *Strategies for enhancing spin-shuttling fidelities in Si/SiGe quantum wells with random-alloy disorder*. 2024. arXiv: 2405.01832 [cond-mat.mes-hall].

[121] D. Loss and D. P. DiVincenzo. "Quantum computation with quantum dots". *Phys. Rev. A* 57.1 (1998), pp. 120–126.

[122] B. M. Maune, M. G. Borselli, B. Huang, T. D. Ladd, P. W. Deelman, K. S. Holabird, A. A. Kiselev, I. Alvarado-Rodriguez, R. S. Ross, A. E. Schmitz, M. Sokolich, C. A. Watson, M. F. Gyure, and A. T. Hunter. "Coherent singlet-triplet oscillations in a silicon-based double quantum dot". *Nature* 481.7381 (2012), pp. 344–347.

[123] Thomas McJunkin, Benjamin Harpt, Yi Feng, Merrit P. Losert, Rajib Rahman, J. P. Dodson, M. A. Wolfe, D. E. Savage, M. G. Lagally, S. N. Coppersmith, Mark Friesen, Robert Joynt, and M. A. Eriksson. *Source Data and Source Code for "SiGe quantum wells with oscillating Ge concentrations for quantum dot qubits"*. 2022. eprint: 10.5281/zenodo.7374581.

[124] Thomas McJunkin, Benjamin Harpt, Yi Feng, Merritt Losert, Rajib Rahman, J. P. Dodson, M. A. Wolfe, D. E. Savage, M. G. Lagally, S. N. Coppersmith, Mark Friesen, Robert Joynt, and M. A. Eriksson. "SiGe quantum wells with oscillating Ge concentrations for quantum dot qubits". *Nature Commun.* 13 (2022), p. 7777.

[125] Thomas McJunkin, E. R. MacQuarrie, Leah Tom, S. F. Neyens, J. P. Dodson, Brandur Thorgrimsson, J. Corrigan, H. Ekmel Ercan, D. E. Savage, M. G. Lagally, Robert Joynt, S. N. Coppersmith, Mark Friesen, and M. A. Eriksson. "Valley splittings in Si/SiGe quantum dots with a germanium spike in the silicon well". *Phys. Rev. B* 104 (2021), p. 085406.

[126] D. Melkonyan, C. Fleischmann, L. Arnoldi, J. Demeulemeester, A. Kumar, J. Bogdanowicz, F. Vurpillot, and W. Vandervorst. "Atom probe tomography analysis of SiGe fins embedded in SiO_2: Facts and artefacts". *Ultramicroscopy* 179 (2017), pp. 100–107.

[127] X. Mi, M. Benito, S. Putz, D. M. Zajac, J. M. Taylor, Guido Burkard, and J. R. Petta. "A coherent spin–photon interface in silicon". *Nature* 555 (2018), p. 599.

[128] X. Mi, S. Kohler, and J. R. Petta. "Landau-Zener interferometry of valley-orbit states in Si/SiGe double quantum dots". *Phys. Rev. B* 98 (2018), 161404(R).

[129] X. Mi, Csaba G. Péterfalvi, Guido Burkard, and J. R. Petta. "High-Resolution Valley Spectroscopy of Si Quantum Dots". *Phys. Rev. Lett.* 119 (2017), p. 176803.

[130] A. R. Mills, M. M. Feldman, C. Monical, P. J. Lewis, K. W. Larson, A. M. Mounce, and J. R. Petta. "Computer-automated tuning procedures for semiconductor quantum dot arrays". *Applied Physics Letters* 115.11 (2019), p. 113501.

[131] Adam R. Mills, Charles R. Guinn, Michael J. Gullans, Anthony J. Sigillito, Mayer M. Feldman, Erik Nielsen, and Jason R. Petta. "Two-qubit silicon quantum processor with operation fidelity exceeding 99%". *Science Advances* 8.14 (2022), eabn5130.

[132] A.R. Mills, C.R. Guinn, M.M. Feldman, A.J. Sigillito, M.J. Gullans, M.T. Rakher, J. Kerckhoff, C.A.C. Jackson, and J.R. Petta. "High-Fidelity State Preparation, Quantum Control, and Readout of an Isotopically Enriched Silicon Spin Qubit". *Phys. Rev. Appl.* 18 (2022), p. 064028.

[133] AR Mills, DM Zajac, MJ Gullans, FJ Schupp, TM Hazard, and JR Petta. "Shuttling a single charge across a one-dimensional array of silicon quantum dots". *Nature Communications* 10.1 (2019), p. 1063.

[134] Don Monroe, Y. H. Xie, E. A. Fitzgerald, P. J. Silverman, and G. P. Watson. "Comparison of mobility-limiting mechanisms in high-mobility Si1-xGex heterostructures". *Journal of Vacuum Science & Technology B: Microelectronics and Nanometer Structures Processing, Measurement, and Phenomena* 11.4 (1993), pp. 1731–1737.

[135] Kieran Mullen, Eshel Ben-Jacob, Yuval Gefen, and Zeev Schuss. "Time of zener tunneling". *Phys. Rev. Lett.* 62.21 (1989), p. 2543.

[136] Sebastian Müller and Lennart Schüler. *GeoStat-Framework/GSTools: v1.5.0 'Nifty Neon'*. Version v1.5.0. 2023.

[137] J. A. Nelder and R. Mead. "A simplex method for function minimization". *Computer Journal* 7 (2010), pp. 308–313.

[138] Samuel Neyens et al. "Probing single electrons across 300-mm spin qubit wafers". *Nature* 629.8010 (2024), pp. 80–85.

[139] Samuel F. Neyens, Ryan H. Foote, Brandur Thorgrimsson, T. J. Knapp, Thomas McJunkin, L. M. K. Vandersypen, Payam Amin, Nicole K. Thomas, James S. Clarke, D. E. Savage, M. G. Lagally, Mark Friesen, S. N. Coppersmith, and M. A. Eriksson. "The critical role of substrate disorder in valley splitting in Si quantum wells". *Appl. Phys. Lett.* 112 (2018), p. 243107.

[140] Y. M. Niquet, D. Rideau, C. Tavernier, H. Jaouen, and X. Blase. "Onsite matrix elements of the tight-binding Hamiltonian of a strained crystal: Application to silicon, germanium, and their alloys". *Phys. Rev. B* 79 (2009), p. 085313.

[141] Akito Noiri, Kenta Takeda, Takashi Nakajima, Takashi Kobayashi, Amir Sammak, Giordano Scappucci, and Seigo Tarucha. "A shuttling-based two-qubit logic gate for linking distant silicon quantum processors". *Nature Communications* 13.1 (2022), p. 5740.

[142] Akito Noiri, Kenta Takeda, Takashi Nakajima, Takashi Kobayashi, Amir Sammak, Giordano Scappucci, and Seigo Tarucha. "Fast universal quantum gate above the fault-tolerance threshold in silicon". *Nature* 601.7893 (2022), pp. 338–342.

[143]   Seong Woo Oh, Artem O. Denisov, Pengcheng Chen, and Jason R. Petta. "Cryogen-free scanning gate microscope for the characterization of $Si/Si_{0.7}Ge_{0.3}$ quantum devices at milli-Kelvin temperatures". *AIP Advances* 11.12 (2021), p. 125122.

[144]   B. Paquelet Wuetz, P. L. Bavdaz, L. A. Yeoh, R. Schouten, H. van der Does, M. Tiggelman, D. Sabbagh, A. Sammak, C. G. Almudever, F. Sebastiano, J. S. Clarke, M. Veldhorst, and G. Scappucci. "Multiplexed quantum transport using commercial off-the-shelf CMOS at sub-kelvin temperatures". *npj Quantum Information* 6.6 (2020), p. 43.

[145]   Brian Paquelet Wuetz, Merritt P. Losert, Sebastian Koelling, Lucas E. A. Stehouwer, Anne-Marije J. Zwerver, Stephan G. J. Philips, Mateusz T. Mądzik, Xiao Xue, Guoji Zheng, Mario Lodari, Sergey V. Amitonov, Nodar Samkharadze, Amir Sammak, Lieven M. K. Vandersypen, Rajib Rahman, Susan N. Coppersmith, Oussama Moutanabbir, Mark Friesen, and Giordano Scappucci. "Atomic fluctuations lifting the energy degeneracy in Si/SiGe quantum dots". *Nature Communications* 13.1 (2022), p. 7730.

[146]   Brian Paquelet Wuetz, Merritt P. Losert, Alberto Tosato, Mario Lodari, Peter L. Bavdaz, Lucas Stehouwer, Payam Amin, James S. Clarke, Susan N. Coppersmith, Amir Sammak, Menno Veldhorst, Mark Friesen, and Giordano Scappucci. "Effect of Quantum Hall Edge Strips on Valley Splitting in Silicon Quantum Wells". *Phys. Rev. Lett.* 125 (2020), p. 186801.

[147]   Luis Fabián Peña, Justine C. Koepke, Joseph Houston Dycus, Andrew Mounce, Andrew D. Baczewski, N. Tobias Jacobson, and Ezra Bussmann. "Modeling Si/SiGe quantum dot variability induced by interface disorder reconstructed from multiperspective microscopy". *npj Quantum Information* 10.1 (2024), p. 33.

[148]   Nicholas E. Penthorn, Joshua S. Schoenfield, Lisa F. Edge, and HongWen Jiang. "Direct Measurement of Electron Intervalley Relaxation in a Si/Si-Ge Quantum Dot". *Phys. Rev. Applied* 14 (2020), p. 054015.

[149]   L. Petit, H. G. J. Eenink, M. Russ, W. I. L. Lawrie, N. W. Hendrickx, S. G. J. Philips, J. S. Clarke, L. M. K. Vandersypen, and M. Veldhorst. "Universal quantum logic in hot silicon qubits". *Nature* 580.7803 (2020), pp. 355–359.

[150]   Haifeng Qiao, Yadav P. Kandel, Saeed Fallahi, Geoffrey C. Gardner, Michael J. Manfra, Xuedong Hu, and John M. Nichol. "Long-Distance Superexchange between Semiconductor Quantum-Dot Electron Spins". *Phys. Rev. Lett.* 126 (2021), p. 017701.

[151]   Nicolas Rolland, François Vurpillot, Sébastien Duguay, Baishakhi Mazumder, James S. Speck, and Didier Blavette. "New Atom Probe Tomography Reconstruction Algorithm for Multilayered Samples: Beyond the Hemispherical Constraint". *Microscopy and Microanalysis* 23.2 (2017), pp. 247–254.

[152]   Rusko Ruskov, Menno Veldhorst, Andrew S. Dzurak, and Charles Tahan. "Electron g-factor of valley states in realistic silicon quantum dots". *Phys. Rev. B* 98 (2018), p. 245424.

[153]   Maximilian Russ, Csaba G Péterfalvi, and Guido Burkard. "Theory of valley-resolved spectroscopy of a Si triple quantum dot coupled to a microwave resonator". *Journal of Physics: Condensed Matter* 32.16 (2020), p. 165301.

[154] D. Sabbagh et al. "Quantum Transport Properties of Industrial ^{28}Si / ^{28}SiO$_2$". *Phys. Rev. Applied* 12 (2019), p. 014013.

[155] N Samkharadze, G Zheng, N Kalhor, D Brousse, A Sammak, U C Mendes, A Blais, G Scappucci, and L M K Vandersypen. "Strong spin-photon coupling in silicon". *Science* 359 (2018), p. 1123.

[156] Amir Sammak, Diego Sabbagh, Nico W. Hendrickx, Mario Lodari, Brian Paquelet Wuetz, Alberto Tosato, LaReine Yeoh, Monica Bollani, Michele Virgilio, Markus Andreas Schubert, Peter Zaumseil, Giovanni Capellini, Menno Veldhorst, and Giordano Scappucci. "Shallow and Undoped Germanium Quantum Wells: A Playground for Spin and Hybrid Quantum Technology". *Advanced Functional Materials* 29.14 (2019), p. 1807613.

[157] A. L. Saraiva, M. J. Calderón, Rodrigo B. Capaz, Xuedong Hu, S. Das Sarma, and Belita Koiller. "Intervalley coupling for interface-bound electrons in silicon: An effective mass study". *Phys. Rev. B* 84 (2011), p. 155320.

[158] A. L. Saraiva, M. J. Calderon, Xuedong Hu, S. Das Sarma, and Belita Koiller. "Physical mechanisms of interface-mediated intervalley coupling in Si". *Phys. Rev. B* 80 (2009), 081305(R).

[159] A. L. Saraiva, B. Koiller, and M. Friesen. "Extended interface states enhance valley splitting in Si/SiO$_2$". *Phys. Rev. B* 82 (2010), p. 245314.

[160] Andre Saraiva, Wee Han Lim, Chih Hwan Yang, Christopher C. Escott, Arne Laucht, and Andrew S. Dzurak. "Materials for Silicon Quantum Dots and their Impact on Electron Spin Qubits". *Advanced Functional Materials* 32.3 (2022), p. 2105488.

[161] Kohei Sasaki, Ryuichi Masutomi, Kiyohiko Toyama, Kentarou Sawano, Yasuhiro Shiraki, and Tohru Okamoto. "Well-width dependence of valley splitting in Si/SiGe quantum wells". *Applied Physics Letters* 95.22 (2009), p. 222109.

[162] Giordano Scappucci, Christoph Kloeffel, Floris A. Zwanenburg, Daniel Loss, Maksym Myronov, Jian-Jun Zhang, Silvano De Franceschi, Georgios Katsaros, and Menno Veldhorst. "The germanium quantum information route". *Nature Reviews Materials* 6.10 (2021), pp. 926–943.

[163] P. Scarlino, E. Kawakami, T. Jullien, D. R. Ward, D. E. Savage, M. G. Lagally, Mark Friesen, S. N. Coppersmith, M. A. Eriksson, and L. M. K. Vandersypen. "Dressed photon-orbital states in a quantum dot: Intervalley spin resonance". *Physical Review B* 95.16 (2017), p. 165429.

[164] F Schäffler. "High-mobility Si and Ge structures". *Semicond. Sci. Tech.* 12.12 (1997), pp. 1515–1549.

[165] F Schaffler, D Tobben, H J Herzog, G Abstreiter, and B Hollander. "High-electron-mobility Si/SiGe heterostructures: influence of the relaxed SiGe buffer layer". *Semicond Sci Tech* 7 (1992), p. 260.

[166] Joshua S. Schoenfield, Blake M. Freeman, and HongWen Jiang. "Coherent manipulation of valley states at multiple charge configurations of a silicon quantum dot device". *Nature Commun.* 8.1 (2017), p. 64.

[167] Inga Seidler, Tom Struck, Ran Xue, Niels Focke, Stefan Trellenkamp, Hendrik Bluhm, and Lars R. Schreiber. "Conveyor-mode single-electron shuttling in Si/SiGe for a scalable quantum computing architecture". *npj Quantum Information* 8.1 (2022), p. 100.

[168] Marcel Serina, Christoph Kloeffel, and Daniel Loss. "Long-range interaction between charge and spin qubits in quantum dots". *Phys. Rev. B* 95 (2017), p. 245422.

[169] N. Shaji, C. B. Simmons, M. Thalakulam, L. J. Klein, H. Qin, H. Luo, D. E. Savage, M. G. Lagally, A. J. Rimberg, R. Joynt, M. Friesen, R. H. Blick, S. N. Coppersmith, and M. A. Eriksson. "Spin blockade and lifetime-enhanced transport in a few-electron Si/SiGe double quantum dot". *Nat. Phys.* 4.7 (2008), pp. 540–544.

[170] M. Mohamed El Kordy Shehata, George Simion, Ruoyu Li, Fahd A. Mohiyaddin, Danny Wan, Massimo Mongillo, Bogdan Govoreanu, Iuliana Radu, Kristiaan De Greve, and Pol Van Dorpe. "Modeling semiconductor spin qubits and their charge noise environment for quantum gate fidelity estimation". *Phys. Rev. B* 108 (2023), p. 045305.

[171] Z. Shi, C. B. Simmons, J.R. Prance, John King Gamble, Mark Friesen, D. E. Savage, M. G. Lagally, S. N. Coppersmith, and M. A. Eriksson. "Tunable singlet-triplet splitting in a few-electron Si/SiGe quantum dot". *Appl. Phys. Lett.* 99 (2011), p. 233108.

[172] Zhan Shi, C. B. Simmons, J. R. Prance, John King Gamble, Teck Seng Koh, Yun-Pil Shim, Xuedong Hu, D. E. Savage, M. G. Lagally, M. A. Eriksson, Mark Friesen, and S. N. Coppersmith. "Fast Hybrid Silicon Double-Quantum-Dot Qubit". *Phys. Rev. Lett.* 108 (2012), p. 140503.

[173] Peter W. Shor. "Scheme for reducing decoherence in quantum computer memory". *Phys. Rev. A* 52 (1995), R2493–R2496.

[174] PW Shor. "Polynomial-time algorithms for prime factorization and discrete logarithms on a quantum computer". *SIAM J. Comput.* 26.5 (1997), pp. 1484–1509.

[175] AJ Sigillito, MJ Gullans, LF Edge, M Borselli, and JR Petta. "Coherent transfer of quantum information in a silicon double quantum dot using resonant swap gates". *npj Quantum Information* 5.1 (2019), p. 110.

[176] C. B. Simmons, Teck Seng Koh, Nakul Shaji, Madhu Thalakulam, L. J. Klein, Hua Qin, H. Luo, D. E. Savage, M. G. Lagally, A. J. Rimberg, Robert Joynt, Robert Blick, Mark Friesen, S. N. Coppersmith, and M. A. Eriksson. "Pauli Spin Blockade and Lifetime-Enhanced Transport in a Si/SiGe double quantum dot". *Phys. Rev. B* 82 (2010), p. 245312.

[177] C. B. Simmons, J. R. Prance, B. J. Van Bael, Teck Seng Koh, Zhan Shi, D. E. Savage, M. G. Lagally, R. Joynt, Mark Friesen, S. N. Coppersmith, and M. A. Eriksson. "Tunable Spin Loading and T_1 of a Silicon Spin Qubit Measured by Single-Shot Readout". *Phys. Rev. Lett.* 106.15 (2011), p. 156804.

[178] Tom Struck, Arne Hollmann, Floyd Schauer, Olexiy Fedorets, Andreas Schmidbauer, Kentarou Sawano, Helge Riemann, Nikolay V. Abrosimov, Łukasz Cywiński, Dominique Bougeard, and Lars R. Schreiber. "Low-frequency spin qubit energy splitting noise in highly purified 28Si/SiGe". *npj Quantum Information* 6.1 (2020), p. 40.

[179] Tom Struck, Mats Volmer, Lino Visser, Tobias Offermann, Ran Xue, Jhih-Sian Tu, Stefan Trellenkamp, Łukasz Cywiński, Hendrik Bluhm, and Lars R Schreiber. "Spin-EPR-pair separation by conveyor-mode single electron shuttling in Si/SiGe". *Nature Communications* 15.1 (2024), p. 1325.

[180] Viktor Sverdlov and Siegfried Selberherr. "Electron subband structure and controlled valley splitting in silicon thin-body SOI FETs: Two-band k·p theory and beyond". *Solid-State Electronics* 52.12 (2008). Selected Papers from the EUROSOI '08 Conference, pp. 1861–1866.

[181] M. L. V. Tagliaferri, P. L. Bavdaz, W. Huang, A. S. Dzurak, D. Culcer, and M. Veldhorst. "Impact of valley phase and splitting on readout of silicon spin qubits". *Physical Review B* 97.24 (2018), p. 245412.

[182] Kenta Takeda, Akito Noiri, Takashi Nakajima, Jun Yoneda, Takashi Kobayashi, and Seigo Tarucha. "Quantum tomography of an entangled three-qubit state in silicon". *Nature Nanotechnology* 16.9 (2021), pp. 965–969.

[183] Bilal Tariq and Xuedong Hu. "Effects of interface steps on the valley-orbit coupling in a Si/SiGe quantum dot". *Phys. Rev. B* 100 (2019), p. 125309.

[184] Bilal Tariq and Xuedong Hu. "Impact of the valley orbit coupling on exchange gate for spin qubits in silicon". *npj Quantum Inf.* 8.1 (2022), p. 53.

[185] J. M. Taylor, H. A. Engel, W. Dur, A. Yacoby, C. M. Marcus, P. Zoller, and M. D. Lukin. "Fault-tolerant architecture for quantum computation using electrically controlled semiconductor spins". *Nat. Phys.* 1 (2005), pp. 177–183.

[186] Julian D. Teske, Friederike Butt, Pascal Cerfontaine, Guido Burkard, and Hendrik Bluhm. "Flopping-mode electron dipole spin resonance in the strong-driving regime". *Phys. Rev. B* 107 (2023), p. 035302.

[187] Julian David Teske, Pascal Cerfontaine, and Hendrik Bluhm. "qopt: An experiment-oriented software package for qubit simulation and quantum optimal control". *Physical Review Applied* 17.3 (2022), p. 034036.

[188] Guilherme Tosi, Fahd A. Mohiyaddin, Vivien Schmitt, Stefanie Tenberg, Rajib Rahman, Gerhard Klimeck, and Andrea Morello. "Silicon quantum processor with robust long-distance qubit couplings". *Nature Communications* 8.1 (2017), p. 450.

[189] L. A. Tracy, E. H. Hwang, K. Eng, G. A. Ten Eyck, E. P. Nordberg, K. Childs, M. S. Carroll, M. P. Lilly, and S. Das Sarma. "Observation of percolation-induced two-dimensional metal-insulator transition in a Si MOSFET". *Phys. Rev. B* 79 (2009), p. 235307.

[190] Bjorn Trauzettel, Denis Bulaev, Daniel Loss, and Guido Burkard. "Spin qubits in graphene quantum dots". *Nature Physics* 3.3 (2007), pp. 192–196.

[191] Luka Trifunovic, Oliver Dial, Mircea Trif, James R. Wootton, Rediet Abebe, Amir Yacoby, and Daniel Loss. "Long-Distance Spin-Spin Coupling via Floating Gates". *Physical Review X* 2 (2010), p. 011006.

[192] Enzo Ungersboeck, Siddhartha Dhar, Gerhard Karlowatz, Viktor Sverdlov, Hans Kosina, and Siegfried Selberherr. "The Effect of General Strain on the Band Structure and Electron Mobility of Silicon". *IEEE Transactions on Electron Devices* 54.9 (2007), pp. 2183–2190.

[193] L. M. K Vandersypen, H. Bluhm, J. S. Clarke, A. S. Dzurak, R. Ishihara, A. Morello, D. J. Reilly, L. R. Schreiber, and M. Veldhorst. "Interfacing spin qubits in quantum dots and donors: hot, dense, and coherent". *npj Quantum Inf.* 3 (2017), p. 34.

[194] Lieven M. K. Vandersypen and Mark A. Eriksson. "Quantum computing with semiconductor spins". *Physics Today* 72.8 (2019), pp. 38–45.

[195] M. Veldhorst, J. C. C. Hwang, C. H. Yang, A. W. Leenstra, B. de Ronde, J. P. Dehollain, J. T. Muhonen, F. E. Hudson, K. M. Itoh, A. Morello, and A. S. Dzurak. "An addressable quantum dot qubit with fault-tolerant control-fidelity". *Nat. Nanotechnol.* 9.12 (2014), pp. 981–985.

[196] M. Veldhorst, C. H. Yang, J. C. C. Hwang, W. Huang, J. P. Dehollain, J. T. Muhonen, S. Simmons, A. Laucht, F. E. Hudson, K. M. Itoh, A. Morello, and A. S. Dzurak. "A two-qubit logic gate in silicon". *Nature* 526 (2015), p. 410.

[197] Pauli Virtanen et al. "SciPy 1.0: Fundamental Algorithms for Scientific Computing in Python". *Nature Methods* 17 (2020), pp. 261–272.

[198] N. V. Vitanov. "Transition times in the Landau-Zener model". *Physical Review A* 59.2 (1999), p. 988.

[199] Mats Volmer, Tom Struck, Arnau Sala, Bingjie Chen, Max Oberländer, Tobias Offermann, Ran Xue, Lino Visser, Jhih-Sian Tu, Stefan Trellenkamp, Łukasz Cywiński, Hendrik Bluhm, and Lars R. Schreiber. "Mapping of valley splitting by conveyor-mode spin-coherent electron shuttling". *npj Quantum Information* 10.1 (2024), p. 61.

[200] Georges Voronoi. "Nouvelles applications des paramètres continus à la théorie des formes quadratiques. Deuxième mémoire. Recherches sur les parallélloèdres primitifs." *Journal für die reine und angewandte Mathematik (Crelles Journal)* 1908.134 (1908), pp. 198–287.

[201] Georges Voronoi. "Nouvelles applications des paramètres continus à la théorie des formes quadratiques. Premier mémoire. Sur quelques propriétés des formes quadratiques positives parfaites." *Journal für die reine und angewandte Mathematik (Crelles Journal)* 1908.133 (1908), pp. 97–102.

[202] Gang Wang, Zhi-Gang Song, Jun-Wei Luo, and Shu-Shen Li. "Origin of giant valley splitting in silicon quantum wells induced by superlattice barriers". *Phys. Rev. B* 105 (2022), p. 165308.

[203] Zeheng Wang, MengKe Feng, Santiago Serrano, William Gilbert, Ross C. C. Leon, Tuomo Tanttu, Philip Mai, Dylan Liang, Jonathan Y. Huang, Yue Su, Wee Han Lim, Fay E. Hudson, Christopher C. Escott, Andrea Morello, Chih Hwan Yang, Andrew S. Dzurak, Andre Saraiva, and Arne Laucht. "Jellybean Quantum Dots in Silicon for Qubit Coupling and On-Chip Quantum Chemistry". *Advanced Materials* 35.19 (2023), p. 2208557.

[204] Ada Warren, Edwin Barnes, and Sophia E. Economou. "Long-distance entangling gates between quantum dot spins mediated by a superconducting resonator". *Phys. Rev. B* 100 (2019), p. 161303.

[205] T. F. Watson, S. G. J. Philips, E. Kawakami, D. R. Ward, P. Scarlino, M. Veldhorst, D. E. Savage, M. G. Lagally, Mark Friesen, S. N. Coppersmith, M. A. Eriksson, and L. M. K. Vandersypen. "A programmable two-qubit quantum processor in silicon". *Nature* 555 (2018), p. 633.

[206] Thomas F. Watson, Bent Weber, Yu-Ling Hsueh, Lloyd C. L. Hollenberg, Rajib Rahman, and Michelle Y. Simmons. "Atomically engineered electron spin lifetimes of 30 s in silicon". *Science Advances* 3.3 (2017), e1602811.

[207] P Weitz, R Haug, K von Klitzing, and F Schäffler. "Tilted magnetic field studies of spin- and valley-splittings in $Si/Si_{1-x}Ge_x$ heterostructures". *Surface Science* 361-362 (1996), pp. 542–546.

[208] Christopher J Wood and Jay M Gambetta. "Quantification and characterization of leakage errors". *Physical Review A* 97.3 (2018), p. 032306.

[209] Benjamin D. Woods, M. A. Eriksson, Robert Joynt, and Mark Friesen. "Spin-orbit enhancement in Si/SiGe heterostructures with oscillating Ge concentration". *Phys. Rev. B* 107 (2023), p. 035418.

[210] Benjamin D. Woods, Hudaiba Soomro, E. S. Joseph, Collin C. D. Frink, Robert Joynt, M. A. Eriksson, and Mark Friesen. "Coupling conduction-band valleys in SiGe heterostructures via shear strain and Ge concentration oscillations". *npj Quantum Information* 10.1 (2024), p. 54.

[211] M Xiao, M. G House, and H. W Jiang. "Measurement of the Spin Relaxation Time of Single Electrons in a Silicon Metal-Oxide-Semiconductor-Based Quantum Dot". *Phys. Rev. Lett.* 104.9 (2010), p. 096801.

[212] Ran Xue, Max Beer, Inga Seidler, Simon Humpohl, Jhih-Sian Tu, Stefan Trellenkamp, Tom Struck, Hendrik Bluhm, and Lars R. Schreiber. "Si/SiGe QuBus for single electron information-processing devices with memory and micron-scale connectivity function". *Nature Communications* 15.1 (2024), p. 2296.

[213] Xiao Xue, Maximilian Russ, Nodar Samkharadze, Brennan Undseth, Amir Sammak, Giordano Scappucci, and Lieven M. K. Vandersypen. "Quantum logic with spin qubits crossing the surface code threshold". *Nature* 601.7893 (2022), pp. 343–347.

[214] Xiao Xue et al. "CMOS-based cryogenic control of silicon quantum circuits". *Nature* 593.7858 (2021), pp. 205–210.

[215] C. H. Yang, K. W. Chan, R. Harper, W. Huang, T. Evans, J. C. C. Hwang, B. Hensen, A. Laucht, T. Tanttu, F. E. Hudson, S. T. Flammia, K. M. Itoh, A. Morello, S. D. Bartlett, and A. S. Dzurak. "Silicon qubit fidelities approaching incoherent noise limits via pulse engineering". *Nature Electronics* 2.4 (2019), pp. 151–158.

[216] C. H. Yang, R. C. C. Leon, J. C. C. Hwang, A. Saraiva, T. Tanttu, W. Huang, J. Camirand Lemyre, K. W. Chan, K. Y. Tan, F. E. Hudson, K. M. Itoh, A. Morello, M. Pioro-Ladrière, A. Laucht, and A. S. Dzurak. "Operation of a silicon quantum processor unit cell above one kelvin". *Nature* 580.7803 (2020), pp. 350–354.

[217] C. H. Yang, W. H. Lim, N. S. Lai, A. Rossi, A. Morello, and A. S. Dzurak. "Orbital and valley state spectra of a few-electron silicon quantum dot". *Phys. Rev. B* 86 (2012), p. 115319.

[218] C. H. Yang, A. Rossi, R. Ruskov, N. S. Lai, F. A. Mohiyaddin, S. Lee, C. Tahan, Gerhard Klimeck, A. Morello, and A. S. Dzurak. "Spin-valley lifetimes in a silicon quantum dot with tunable valley splitting". *Nature Communications* 4 (2013), p. 2069.

[219] Constantine Yannouleas and Uzi Landman. "Molecular formations and spectra due to electron correlations in three-electron hybrid double-well qubits". *Phys. Rev. B* 105 (2022), p. 205302.

[220] Constantine Yannouleas and Uzi Landman. "Valleytronic full configuration-interaction approach: Application to the excitation spectra of Si double-dot qubits". *Phys. Rev. B* 106 (2022), p. 195306.

[221] Constantine Yannouleas and Uzi Landman. "Wigner molecules and hybrid qubits". *Journal of Physics: Condensed Matter* 34.21 (2022), 21LT01.

[222] Jun Yoneda, Wister Huang, Mengke Feng, Chih Hwan Yang, Kok Wai Chan, Tuomo Tanttu, William Gilbert, RCC Leon, FE Hudson, KM Itoh, et al. "Coherent spin qubit transport in silicon". *Nature Communications* 12.1 (2021), p. 4114.

[223] Jun Yoneda, Kenta Takeda, Tomohiro Otsuka, Takashi Nakajima, Matthieu R. Delbecq, Giles Allison, Takumu Honda, Tetsuo Kodera, Shunri Oda, Yusuke Hoshi, Noritaka Usami, Kohei M. Itoh, and Seigo Tarucha. "A quantum-dot spin qubit with coherence limited by charge noise and fidelity higher than 99.9%". *Nature Nanotechnol.* 13 (2018), p. 102.

[224] D. M. Zajac, T. M. Hazard, X. Mi, E. Nielsen, and J. R. Petta. "Scalable Gate Architecture for a One-Dimensional Array of Semiconductor Spin Qubits". *Phys. Rev. Appl.* 6 (2016), p. 054013.

[225] D. M. Zajac, T. M. Hazard, X. Mi, K. Wang, and J. R. Petta. "A reconfigurable gate architecture for Si/SiGe quantum dots". *Appl. Phys. Lett.* 106, 223507 (2015), p. 223507.

[226] D. M. Zajac, A. J. Sigillito, M. Russ, F. Borjans, J. M. Taylor, G. Burkard, and J. R. Petta. "Resonantly driven CNOT gate for electron spins". *Science* 359 (2018), p. 439.

[227] Lijun Zhang, Jun-Wei Luo, Andre Saraiva, Belita Koiller, and Alex Zunger. "Genetic design of enhanced valley splitting towards a spin qubit in silicon". *Nature Comms.* 4 (2013), p. 2396.

[228] Xin Zhang, Hai-Ou Li, Gang Cao, Ming Xiao, Guang-Can Guo, and Guo-Ping Guo. "Semiconductor quantum computation". *National Science Review* 6 (2018), pp. 32–54.

[229] Xinyu Zhao and Xuedong Hu. *Coherent electron transport in silicon quantum dots*. 2018. arXiv: `1803.00749 [cond-mat.mes-hall]`.

[230] Han-Sen Zhong et al. "Quantum computational advantage using photons". *Science* 370.6523 (2020), pp. 1460–1463.

[231] F. A. Zwanenburg, A. S. Dzurak, A. Morello, M. Y. Simmons, L. C. L. Hollenberg, G. Klimeck, S. Rogge, S. N. Coppersmith, and M. A. Eriksson. "Silicon Quantum Electronics". *Rev. Mod. Phys.* 85 (2013), p. 961.

[232] A. M. J. Zwerver, S. V. Amitonov, S. L. de Snoo, M. T. Mądzik, M Rimbach-Russ, A Sammak, G Scappucci, and L. M. K. Vandersypen. "Shuttling an electron spin through a silicon quantum dot array". *PRX Quantum* 4.3 (2023), p. 030303.

[233] A. M. J. Zwerver et al. "Qubits made by advanced semiconductor manufacturing". *Nature Electronics* 5.3 (2022), pp. 184–190.